Macromolecular Carriers for pH-Responsive Immunodrug Delivery

Dissertation zur Erlangung des Grades

„Doctor rerum naturalis“ (Dr. rer. nat.)

im Promotionsfach Chemie

des Fachbereichs 09

Chemie, Pharmazie, Geographie und Geowissenschaften

der Johannes Gutenberg-Universität

in Mainz

Alina Gabriela Heck

geboren in Mainz

Mainz, Mai 2024

JOHANNES GUTENBERG UNIVERSITÄT MAINZ

JG|U

MAX-PLANCK-INSTITUT FÜR POLYMERFORSCHUNG

This thesis was carried out in the period from June 2019 to May 2024 [redacted] at the Max Planck Institute for Polymer Research, Mainz, and the Julius-Maximilians-University, Würzburg.

Reviewer 1: [redacted]

Reviewer 2: [redacted]

Date of Oral Examination: 29.05.2024

FB09 Fachbereich
Chemie, Pharmazie, Geographie
und Geowissenschaften

Versicherung

für das Gesuch um Zulassung zur Promotion im Fachbereich 09 an der
Johannes Gutenberg-Universität Mainz

Hiermit versichere ich, Alina Gabriela Heck, gemäß § 10 Abs. 3d
der Promotionsordnung vom 24.07.2007:

☐ Ich habe die jetzt als Dissertation vorgelegte Arbeit selbst angefertigt und alle benutzten Hilfsmittel (Literatur, Apparaturen, Material) in der Arbeit angegeben.

☐ Ich hatte die jetzt als Dissertation vorgelegte Arbeit als Prüfungsarbeit für folgende Prüfungen eingereicht.

_____

(Bezeichnung der Prüfung)

_____

(Bezeichnung und Ort der Prüfungsstelle)

☐ Ich hatte weder die jetzt als Dissertation vorgelegte Arbeit noch Teile davon bei einer anderen Fakultät bzw. einem anderen Fachbereich als Dissertation eingereicht.

_____

Datum, Unterschrift

CONTENTS

ABSTRACT

The implementation of nanotechnologies in the advancement of new medicines has presented substantive potential to improve the therapeutic outcomes for numerous patients and has now become integrated into several clinical routines. In this context, the covalent attachment of potent immune modulators to nanosized carrier systems can enhance the drugs' bioavailability and minimize toxic side effects, however, also affects their biological properties and activities. To maximize the beneficial effect of drug-loaded nanocarriers, smart materials with pH-sensitive functional groups are well-suited to overcome different biological barriers and delivery limitations but assure the release of intact drugs at diseased sites and intracellularly inside endolysosomes. Hence, this thesis covers the development of novel dimethylmaleic anhydride-based macromolecular carrier platforms as promising systems in nanomedicine that facilitate a fast and reversible conjugation of immune stimuli or targeting units and, thus, promoting advanced tools for cancer immunotherapy.

Within this aspect, polymetharcylamides with pendant 2-propionic-3-methylmaleic anhydride side groups were synthesized by controlled radical polymerization. By investigation of the pH-sensitive release profile with different primary and secondary amines, the amidation process was fine-tuned and served as an effective approach for the conjugation of fluorescent dyes or immunomodulating TLR 7/8 agonists. Initial biological evaluations demonstrated an efficient cellular uptake and promoted immune stimulating effect compared to control groups. Based on the designed macromolecular carrier system, a cholesteryl functionality and useful stealth properties were introduced for directed immunomodulation *in vivo*. Thereby, the extended drug delivery system demonstrated a spatiotemporal control over the stimulation of antigen presenting cells in the draining lymph nodes.

Furthermore, amphiphilic pH-responsive block copolymers were synthesized by Reversible Addition-Fragmentation Chain Transfer (RAFT) polymerization and evaluated towards their application as adjustable micellar compartments insight cells. To this end, the pH-dependent self-assembly behavior was carefully investigated and tuned through chemical modifications of the 2-propionic-3-methylmaleic anhydride side groups. By appropriate choice of different fluorescent dyes, the controlled self-assembly was traced in several biological compartments and clearly exhibited the formulation of spherical structures which may be used as an adaptable system for potential nanomedical applications.

Regarding the beneficial properties emanating from smart materials, amphiphilic block copolymers bearing reactive ester side groups were finally expanded towards the formulation of DBCO core-functionalized nanogels suitable as a bioorthogonally addressable platform for advanced cancer therapies. The well-defined nanogels could subsequently be modified inside their cores either irreversibly with azide-functional targeting units or reversibly with a 2-propionic-3-methylmaleic anhydride linker system, enabling a controlled and pH-responsive delivery of potent TLR 7/8 agonists.

In summary, this thesis delves into the investigation of functional polymer systems and their advancement as stimuli-triggered macromolecular carrier platforms for promising applications in nanomedicine.

ZUSAMMENFASSUNG

Der Einsatz von Nanotechnologien für die Entwicklung neuer Arzneimittel bietet ein erhebliches Potenzial zur Verbesserung der therapeutischen Ergebnisse für zahlreiche Patienten und ist inzwischen bei zahlreichen Anwendungen in der klinischen Routine mitintegriert worden. In diesem Zusammenhang kann die kovalente Anbindung potenter Immunmodulatoren an nanodimensionale Trägersysteme die Bioverfügbarkeit der Wirkstoffe verbessern und toxische Nebenwirkungen minimieren, gleichzeitig allerdings auch deren biologische Eigenschaften und Aktivität beeinträchtigen. Um den positiven Effekt der mit Wirkstoff beladenen Nanoträger zu maximieren, werden geschickte Materialien mit pH-sensitiven funktionellen Gruppen benötigt, die in der Lage sind, verschiedene biologische Barrieren und Transporteinschränkungen zu überwinden, wobei dabei aber auch die Freisetzung des intakten Wirkstoffes gewährleistet werden sollte. Daher befasst sich diese Arbeit mit der Entwicklung neuer makromolekularer Trägerplattformen auf der Basis von Dimethylmaleinsäureanhydriden als vielversprechende Strategie in der Nanomedizin, um eine schnelle und reversible Konjugation von Immunstimulatoren oder Targeting-Einheiten und damit eine verbesserte Anwendbarkeit in der Krebsimmuntherapie zu ermöglichen.

In diesem Zusammenhang wurden Polymetharcylamide mit 2-Propionsäure-3-Methylmaleinsäureanhydrid-Seitengruppen durch kontrollierte radikalische Polymerisation synthetisiert. Nach der Untersuchung des pH-sensitiven Freisetzungsprofils verschiedener primärer und sekundärer Amine wurde der Amidierungsprozess exakt abgestimmt und diente zugleich als effektiver Ansatz für die Konjugation von Fluoreszenzfarbstoffen oder immunmodulierenden TLR 7/8-Agonisten. Erste biologische Untersuchungen zeigten die effiziente zelluläre Aufnahme und die verstärkte immunstimulierende Wirkung im Vergleich zu Kontrollgruppen. Basierend auf diesem makromolekularen Trägersystem wurde eine Cholesterinfunktionalität und nützliche „Stealth“-Eigenschaften für eine gezielte Immunmodulation *in vivo* eingeführt. Das erweiterte Wirkstoffträgersystem ermöglichte eine räumliche und zeitliche Kontrolle über die effiziente Stimulierung von Antigen-präsentierenden Zellen in den drainierenden Lymphknoten.

Darüber hinaus wurden amphiphile, pH-responsive Blockcopolymere durch die Reversible Addition-Fragmentation Chain Transfer (RAFT)-Polymerisation synthetisiert und im Hinblick auf ihre Anwendung als regulierbare, mizellare Kompartimente in der Zelle untersucht. Zu diesem Zweck wurde das pH-abhängige Selbstassemblierungsverhalten sorgfältig untersucht und durch chemische Modifikationen der 2-Propionsäure-3-Methylmaleinsäureanhydrid-

Seitengruppen abgestimmt. Durch die geeignete Wahl verschiedener Fluoreszenzfarbstoffe konnte die kontrollierte Selbstassemblierung in mehreren biologischen Kompartimenten verfolgt werden und zeigte deutlich die Bildung sphärischer Strukturen, die als anpassungsfähiges System für potenzielle nanomedizinische Anwendungen genutzt werden können.

Im Hinblick auf die vorteilhaften Eigenschaften, die von geschickten Materialien ausgehen, wurden letztlich amphiphile Blockcopolymere mit Reaktivester-Seitengruppen zur Formulierung von DBCO-Kern-funktionalisierten Nanogelen erweitert, um sie als bioorthogonal adressierbare Plattform für angepasste Krebstherapien zu verwenden. Diese gut definierten Nanogele konnten unmittelbar in ihrem Kern entweder irreversibel mit Azid-funktionellen Targeting-Einheiten oder reversibel mit einem 2-Propionsäure-3-Methylmaleinsäureanhydrid Linker-System funktionalisiert werden, wodurch eine kontrollierte und pH-abhängige Abgabe von potenten TLR 7/8-Agonisten ermöglicht wurde.

Zusammenfassend erarbeitete diese Arbeit neuartige funktionelle Polymersysteme und deren Weiterentwicklung als reizinduzierte, makromolekulare Trägerplattformen für eine vielversprechende Anwendungen in der Nanomedizin.

INTRODUCTION AND BASIC CONCEPT

Nanomedicine

The application of nanotechnology in the development of new medicines has defined the important field of nanomedicine. Especially in the past few years, there has been a remarkable growth in the utilization of nanomedicine formulations for diagnostic, prevention, and the treatment of diseases.[1,2] The COVID-19 pandemic has demonstrated the flexibility and high efficacy of nanomaterials and raised the awareness for high quality targeted therapeutic treatments.[3,4] In general, nanomedicine can be considered as the application of nanostructured materials with dimensions of 1-100(0) nm intentionally designed with unique medical properties to overcome deficiencies of small molecular drugs.[5,6] First and foremost, nanoparticles have the potential to increase the solubility and stability of hydrophobic small drugs. At the same time, they improve the biodistribution, pharmacokinetic profile and facilitate a localized delivery across different biological barriers.[7,8] In the last decades more than 207 companies purchased several nanomaterials, while more than 50 of them are already on the market and another 563 are in clinical trials.[9,10] All of them investigating a wide range of nanostructures, including lipid based nanocarriers, as well as polymer or inorganic nanoparticles or small drug conjugates (Figure 1).[11,12]

With cancer remaining on of the leading causes of death worldwide, nanosized-drug delivery systems have emerged as novel therapeutic modalities for cancer treatment. Insufficient binding to the target site is a common issue observed in most small anti-cancer drugs, primarily due to their low molecular weight, high hydrophobicity, and short circulation time. Additionally, fast distribution to the whole body with accumulation in healthy tissues causing unwanted side effects and critically limits the efficient application of these potent drugs while increasing the risk of toxicity.[13–15] PEGylated liposomes loaded with the cancer therapeutic doxorubicin (Doxil®) have been the initial category of approved nanomedicine products for cancer treatment, but also other nano-formulations like paclitaxel with albumin (Abraxane®) or mPEG-based amphiphilic macromolecules (Genexol™) demonstrated significant potential and successfully passed clinical trials.[16–20] Compared to the free therapeutic entities, each carrier system provides a unique combination of properties and applies the precise design of nano-sized carriers for a successful therapeutic treatment. This becomes particularly evident for the delivery of nucleic acids (mRNA), where a nanoparticular carrier is required for protection and facilitating the cellular internalization, as realized by the applied lipid-based nanocarriers for the COVID-19 vaccines.[21]

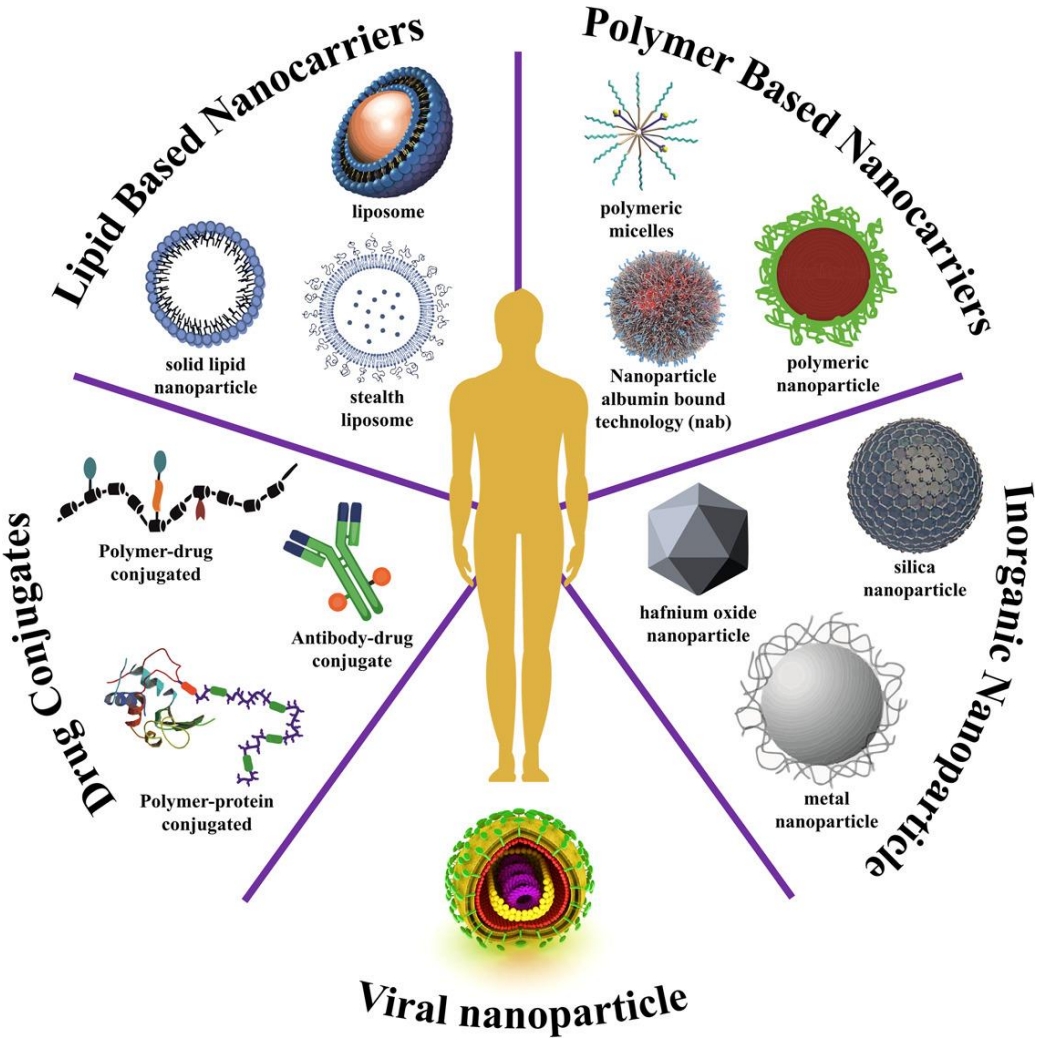

Figure 1. Schematic overview of different nanomaterials applied in the field of nanomedicine (reprinted with permission from reference[11]).

The choice of the appropriate nano-sized architecture relies not only on the requirements of the intended therapeutic application but also on the physicochemical characteristics of the cargo to guarantee an optimized therapeutic outcome.[22] For instance, polymeric micelles with a hydrophobic core represent ideal properties for the transport of hydrophobic drugs. Solely the attachment or encapsulation into such spherical vesicles facilitates a higher acceptance and efficient drug delivery into cells. In contrast to that, hydrophilic drugs are often entrapped into hydrophilic cores of nanohydrogels or polymersomes.[11,12,23] Among the variety of specific nano-sized particles most of them exhibit a typical core-shell structure, leading to an improved biodistribution and reduced clearance.[12,24] The physicochemical nature of the core enables the efficient conjugation or encapsulation of the cargo, whereas the shielding corona guarantees a stabilized delivery by preventing interactions of drug and carrier with the surrounding medium. Towards successfully protecting the implemented drug molecules, the corona should be

hydrophilic, non-charged, with hydrogen-bond acceptors and no hydrogen-bond donors. In this case, the depicted architecture can resist interactions with proteins or the immune system.[25–27] Poly(ethylene glycol) (PEG), poly(2-oxazoline)s (pOX), polysarcosine (pSar) and poly(N-(2-hydroxypropyl)methacrylamide (pHPMA) have been identified to provide such "stealth"-like properties for the nanoparticle shell and, thus, facilitate a more stabilized transport of the cargo with prolonged blood circulation, while increasing safety and efficacy.[28-31]

Nanotechnology finally made the medical potential of a variety of highly potent drugs accessible to patients. These drugs would otherwise not be applicable by conventional therapies based on their non-specific toxicity and unfavorable distribution in the body. As already indicated, the task of nanocarriers includes an improvement of the stability and solubility of drugs with high hydrophobicity, resulting in a significant increase in their bioavailability.[6,32] Moreover, further characteristics that are relevant for the delivery process can be finetuned by the precise design of the size, shape and surface of nanoparticles, providing drug-loaded nanomaterials with a large surface area and sizes above 10 nm. By surpassing the renal threshold, this can repress a rapid clearance of the drug molecules from the body and further improve their pharmacokinetic profile.[8,10,33] With an increased set of opportunities, nanocarrier delivery alters the therapeutic drugs' metabolism, prolongs their circulation time and facilitates overcoming physiological barriers, like blood vessels or cellular membranes.[1,34,35]

The ability of long circulating nano-sized drug delivery systems to selectively reach specific organs or tissues often relies on the increased permeability and followed by prolonged residence. Certain solid tumors, for instance, provide neovascularized tissues that are particularly permeable to macromolecules and coupled with an impaired lymphatic drainage. Such a nanoparticle accumulation is also known as the enhanced permeability and retention (EPR) effect (Figure 2).[35] Matsumura and Madea first introduced this concept in 1986.[36] In general, abnormal endothelium of blood vessels in inflamed tissues and tumors demonstrate a higher permeability comparted to normal tissues, enabling the increased accumulation of drug-loaded nanoparticles with a sized of 10-200 nm.[19,37,38] Additionally, most solid tumors generate a substantial amount of vascular permeability factors to ensure the efficient supply with nutrients and oxygen, contributing to the abnormal architecture and permeability of tumor blood vessels.[39,40] Notably, such a passive accumulation by the EPR effect varies through different tumor types and patients and, thus, limits the overall efficacy of nanoparticle-delivered therapeutics. Furthermore, other tissues may exhibit similar characteristics (e.g. after an infection), misleading to the preferential accumulation in these

inflamed regions. These factors highlight the need for precisely targeted and personalized drug delivery by the development of patient-tailored nanocarriers and individualized precision therapies.[41–43]

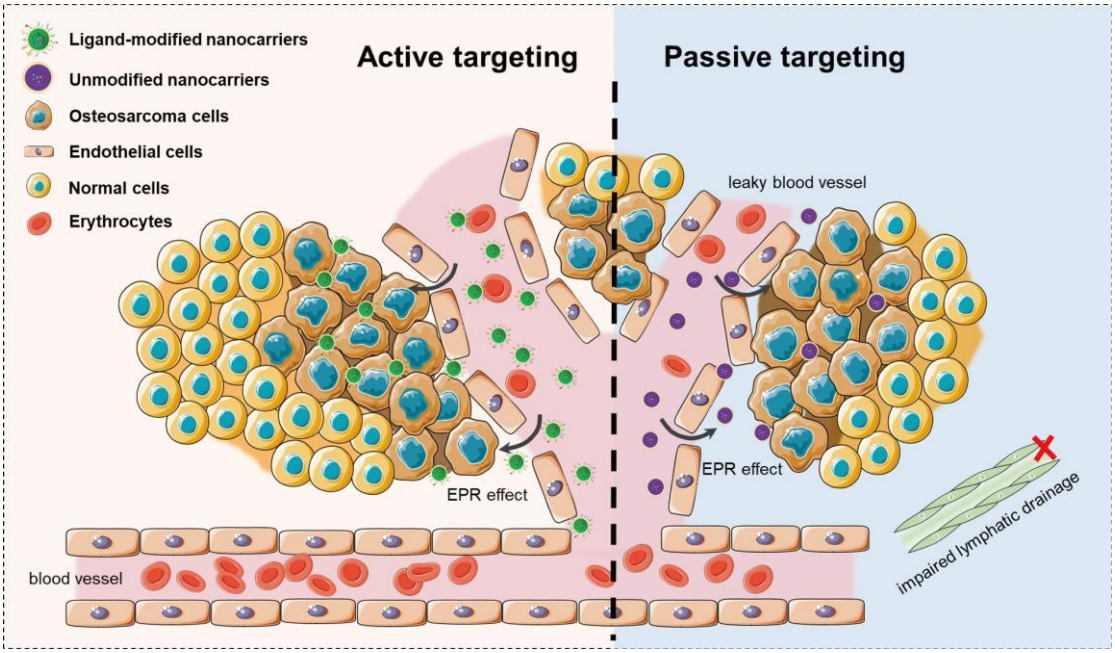

Figure 2. Schematic illustration of the active or passive targeting of nanomaterials in anti-cancer therapy. Passive targeting is characterized by the EPR-mediated tumor targeting while active targeting can be achieved by the interaction of ligand-modified carriers with receptors on the tumor surface (adapted from the reference[44]).

A promising alternative to the passive targeting by EPR effect represents the surface decoration of nanomaterials with targeting ligands. This active strategy is specified to bind corresponding receptors selectively expressed by tumor cells without effecting normal tissues (Figure 2).[44,45] Various molecules can be used for controlled targeting, including full antibodies, their fragments or other modern variants as well as peptides, carbohydrates or nucleic acid based aptamers that provide a selectively high affinity to the overexpressed receptors on the tumor cell surface.[43,46] Nevertheless, in analogy to passive targeting such active targeting strategies strictly depend on long circulation times for remaining long enough in the body in order to allow the targeting molecules meeting their receptors and facilitating a cellular internalization of the nanocarriers for triggering the therapeutic effect.[47,48] In addition to delivering drugs specifically to tumor cells, active targeting can further be applied to various diseases as well as immune cells. Especially, the targeted immunotherapy has emerged as highly promising approach in cancer treatment. Tailoring the surface of nanoparticles for the controlled delivery of therapeutic drugs to macrophages, dendritic cells or T cells boosts the activation and resulting attack of cancer cells by natural mechanisms.[49,50]

Although the introduction of nano-sized materials for medical applications has improved the safety and mobility of small molecular drugs, their nanotoxicity, biodegradation and elimination in the body gained increasing attention, too. Stabilization and shielding strategies influence the physicochemical properties of applied nanomaterials but also their toxicity profile. Several strategies have been explored to alter the mechanical or electrical surface characteristics to enhance the circulation time and tumor accumulation. Especially the increased surface to volume ratio effects the biodistribution and interaction with several organs and tissues.[51–54] For the efficient targeting of solid tumors, for instance, nanomedicines are primarily administrated parenterally. This results in the rapid exposure to various biological barriers and blood components, including plasma proteins, immune cells and red blood cells.[55,56] Thereby, most nanomaterials are naturally sequestered by cells of the mononuclear phagocyte system (MPS). The MPS is a network of bone marrow progenitor cells, monocytes and tissue macrophages mainly present in organs such as the liver, spleen, and bone marrow, destined for the clearance of foreign material from the bloodstream, as illustrated in Figure 3.[57,58] While nanoparticles with a size below 5 nm in diameter may rapidly be cleared by the kidneys, nanomaterials lager than 150 nm can immediately be removed by the MPS in the liver and the spleen, or may even accumulate in the lung capillaries (>200 nm).[32,53,59]

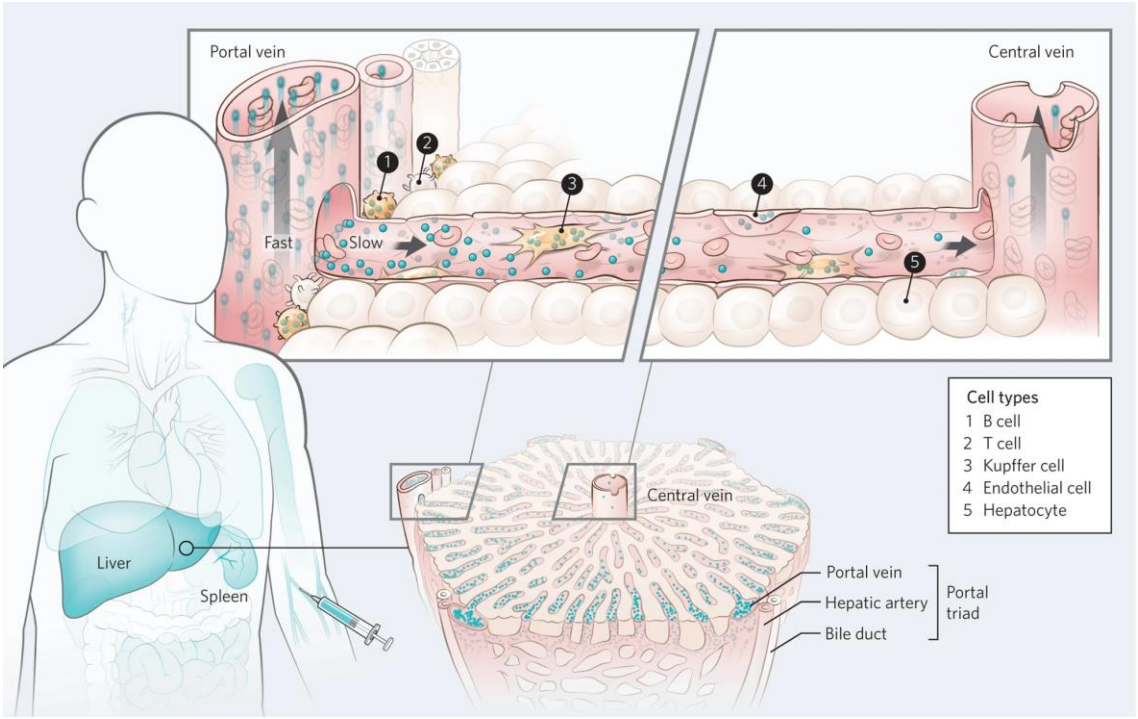

Figure 3. Interactions of carrier systems with the mononuclear phagocyte system (MPS) after intravenous injection. Most nanomaterials interact with monocytes and tissue macrophages localizes in spleen and liver, leading to the fast clearance of the systems from the bloodstream. Furthermore, nanoparticles can accumulate in the lung or bone marrow. The blue color demonstrates the degree of transported nanomaterial into the MPS organs. The Figure is reprinted with permission from the reference[58].

Generally, nanomedicines that enter the body should ideally possess a high-water solubility and biocompatibility that promotes the extended drug circulation but does not bring along further bioactivity.[60] As already mentioned above, strategies to promote these features include a surface decoration with macromolecular structures that have "stealth"-like properties. Such polymers follow the Whitesides' rules and are resistant to protein adsorption.[27,61] Such features are mainly provided by poly(ethylene glycol) (PEG) which reduces recognition and clearance by the MPS, while enhancing the stability and shielding efficacy for many nanoparticles.[28,62] Nevertheless, only little is known about the long-term circulation effects of nanomaterials and their toxicological risks. Even slight variations in the particle design can cause entirely different behaviors for the increased penetration and accumulation in organs, tissues, and cells, inducing toxicological effects. This impedes the precise identification of nanotoxicity in biological systems and increases the development of not only biocompatible but also disintegrating nanostructures.[63,64] For example, biodegradable polymer micelles have appeared as suitable structure for nanomedicine. Biodegradation facilitates the decomposition of nanocarriers by enzymic or metabolic processes into small, non-toxic fragments with sizes below 5 nm that can easily be eliminated from the body by renal clearance.[60,65,66] Furthermore, stimuli-responsive nanoparticles gained an increasing attention as multi-functional carrier systems. The integration of stimuli responsive motifs guarantees the delivery of a cargo in a spatially and temporally more controlled manner and allows the degradation or disassembly into smaller fragments by endogenous stimuli.[67–69]

Nanomedicine for Cancer Immunotherapy

In the landscape of cancer management, immunotherapy has emerged as new paradigm in the treatment of diseases and particularly revolutionized tumor therapy in recent years tremendously. With the ability to harness the body's immune system for recognizing and eliminating cancer cells, cancer immunotherapy can potentially lead to a long-lasting antitumor response and reduced chances for metastasis.[70,71] Already in 2013 the Journal *Science* declared Cancer Immunotherapy as the "breakthrough of the year" and five years later T. Honjo and J. P. Allision were awarded with the Nobel Prize in Physiology or Medicine for their achievements in the field of immune checkpoint inhibitions, which highlights the significance for the development of immune-related cancer treatments.[72–74]

In general, the immune system is a complex network of cells and molecules that can be categorized into two essentially systems: the innate (or natural) immune system and the

adaptive immune system. The innate immune system serves as an initial barrier which is primarily able to recognize non-self and dangerous signals e.g. during microbial invasion or tissue injury. Rapidly, a variety of immune cells such as macrophages, dendritic cells (DC), natural killer cells, neutrophiles, or monocytes are encountering bacteria, viruses, or fungi.[75–77] In this "first-line defense" macrophages, dendritic cells and natural killer are defined as antigen presenting cells (APC) that identify the microbial pathogens by universal pathogen associated molecular patterns (PAMPs) *via* specific pattern recognition receptors (PRRs) and subsequently mediate an inflammatory response. The second set of defense comprises the adaptive immune response and the expression of antigen-specific T and B cells. These cells play a canonical role in the production of antibodies, cytotoxic effector cells and the secretion of cytokines to direct the function of innate immune cells. Additionally, memory T and B cells are generated, ensuring a long-lasting defense.[75,78,79]

A fundamental requirement for an effective immune response against cancer is the maturation of APC, especially dendritic cells, and the uptake of tumor-specific antigens, followed by their presentation to different immune cells using histocompatibility class I and II (MHC-I/MHC-II) complexes. In the draining lymph nodes, activated DC collaboratively orchestrate the innate and adaptive immunity resulting in the priming and activation of CD4+ and CD8+ T cells against cancer specific antigens. Finally, activated effector T cells penetrate to the tumor side and initiate tumor cell apoptosis by specific binding to the cancer cells and additional release of cytotoxic chemokines. That allows for a further secretion of tumor-associated antigens (TAAs) back to the APCs and intrinsically fostering of the whole process (Figure 4).[70,80–82]

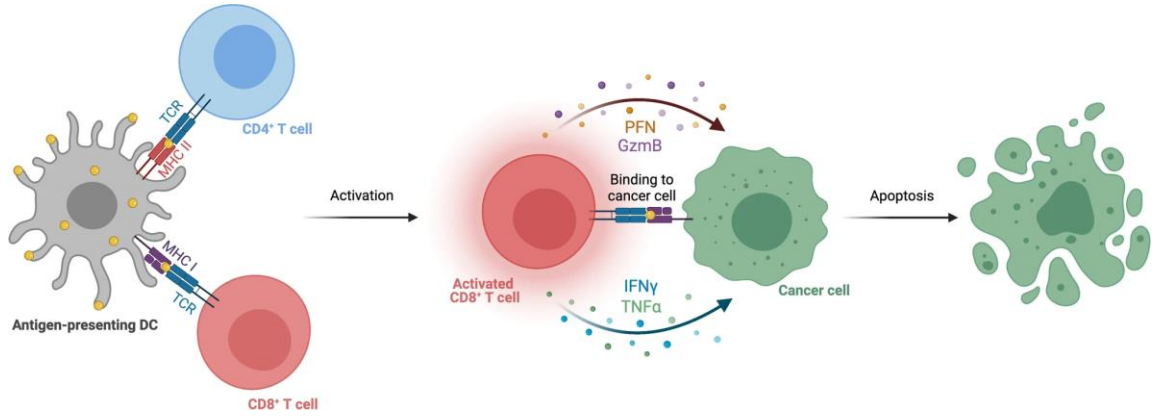

Figure 4. Demonstration of the interaction between antigen presenting dendritic cells (DC) and $CD4^+/CD8^+$ cells by MHCI and II molecules. Activated cytotoxic $CD8^+$ cells migrate into tumors, recognize expressed antigens on the cell surface and induce the elimination of the cancer cell by perforin (PFN), granzyme B (GzmB) pathway as well as interferon gramma (INFγ) and necrosis factor α (TNF α), (reprinted with permission from reference[81]).

However, the efficacy of immunological cancer treatment strategies is limited, since only a minority of patients exhibit acceptable responses, while most tumor patients generate mechanisms to evade the host immune recognition. Several tumors lack the presentation by MHC class I and II molecules or secrete mediators which inhibit the sufficient differentiation of DCs all resulting in a suppressed T cell activity.[83,84] Moreover, checkpoint receptors like the anti-cytotoxic T-lymphocyte associated antigent-4 (CTLA-4) and the programmed death 1 (PD-1) receptor on the surface of T cells have a significant impact on their functionality during MHC recognition. As such, programmed death ligands PD-L1 or PD-L2 can be overexpressed on tumor cells, forcing the conversion of the effector T cell into an ineffective state.[84,85] Furthermore, different immune suppressive molecules, signal factors and cells in the tumor microenvironment (TME) can additionally introduce immunotherapeutic resistance. For instance, the constant release of relevant immunosuppressive chemokines and cytokines into the TME triggers the differentiation of macrophages into tumor-associated macrophages (TAMs) of M2-type. These TAMs secrete IL-10 instead of IL-12 and thereby inhibit the CD8+ T cells response, while promoting tumor growth. Additional, the depletion of metabolites such as glucose, lactate, tryptophane and glutamine in the TME further suppress the activity of anticancer T cells, macrophages or DC.[86,87]

However, steady advances in immunotherapy and the application of immunomodulators enhance the safety and regeneration of the immune system. Thereby, different immunotherapeutic strategies have been employed to promote the antitumor immune response and survival times. The main achievements focus on the direct targeting of cancer cells to foster immunogenic apoptosis, the targeting of immune cells such as macrophages, dendritic cells or T cells in the tumor microenvironment as well as the peripheral immune system in lymph nodes or spleen.[49,88] Beyond the application of oncolytic viruses for cancer cell death, monoclonal antibodies demonstrated highest potential in cancer immunotherapy. Furthermore, adoptive cell therapy (ACT), based on the replication and re-injection of autologous tumor-directed T cells and the blockage of inhibitory checkpoint molecules significantly impact the personalized treatment of cancer patients. Although cancer immunotherapy has elicited significant progress throughout the last years, only few patients can so far benefit from its potential due to unpredictable efficacy as well as off-target toxicity.[71,89]

Thereby, nano-guided cancer immunotherapy can provide several advantages in improving various tumor immuno-treatments, while reducing undesired side effects. A variety of nanoparticles can serve as a platform to deliver immunomodulators such cytokines or

modulatory drugs as well as antigens or adjuvants that enable a controlled immune response e.g. during vaccination.[13,71,88] As already indicated, a promising approach to modulate the immune system can be the stimulation of pattern-recognition receptors (PRRs) through pathogen-associated molecular patterns (PAMPs) derived from microorganisms or danger-associated molecular patterns (DAMPs) from damaged tissue. PRRs are localized in various subcellular compartments, including cellular and endosomal membranes, the cytosol and even secreted in the bloodstream and interstitial fluid.[90,91]

Among PRRs, Toll-like receptors play a major role in immune responses linking the innate and adaptive immunity. They recognize a variety of infectious pathogens and cancer fragments extracellularly as well as intracellularly. TLRs are typ I transmembrane receptors especially characterized by their ligand specificity. Some TLRs, such as TLR1 and TLR2, TLR4 or TLR5 and TLR6 are present on the cell membrane, while TLR3, TLR7/8 and TLR9 are located within endosomal compartments. They are primarily expressed by immune cells like DCs, B cells or macrophages as well as non-immune cells, such as epithelial cells.[92–94] TLRs are stimulated by ligands with various origins and characteristics, as triacyl-lipopeptides and oligosaccharides (TLR1 and TLR2), lipopolysaccharides (LPS, TLR4) or nucleic acids such as double-stranded RNA (dsRNA, TLR3), single-stranded RNA (ssRNA, TLR7/8) as well as unmethylated cytosine-phosphate-guanine (CpG) DNA (TLR9).[95,96] Once the TLR receptors recognize the respective ligands followed by a receptor dimerization, the recruitment of cytosolic adapter molecules is initiated, including the myeloid differentiation primary response protein 88 (MyD88) and the TIR domain-containing adapter protein (TIRAP). This whole signal cascade subsequently initiates the activation of interleukin-1 receptor-associated kinases (IRAKs) and the transcription factor NF-κB, leading to the expression of inflammatory genes and the production of inflammatory cytokines. Additional, activation of TLR3 and TLR4 stimulates the IRF pathway and the generation of Typ I interferons (Figure 5).[95,97,98]

Furthermore, small synthetic molecules like imidazoquinolines stimulate the TLR 7/8 and consequently demonstrate great potential in preclinical and clinical studies. For instance, the imidazoquinoline imiquimod has already been approved by the FDA for treatment of basal cell carcinoma, but only by surface application. Imidazoquinolines suffer from rather poor pharmacokinetic profiles and rapid biodistribution which results in inflammatory off-target reactions and unwanted systemic toxicities.[69,94,99] For their successful application, nanoparticles facilitate an efficient delivery e.g. by a more focused transport into relevant immunological regions, like lymph nodes and spleen.[94,100] Particularly, nanoparticles with sizes

from 20 to 50 nm exhibit the same size as viruses and fragments of bacteria, leading to a natural recognition by the immune system and enhanced accumulation in the lymph nodes.[101,102]

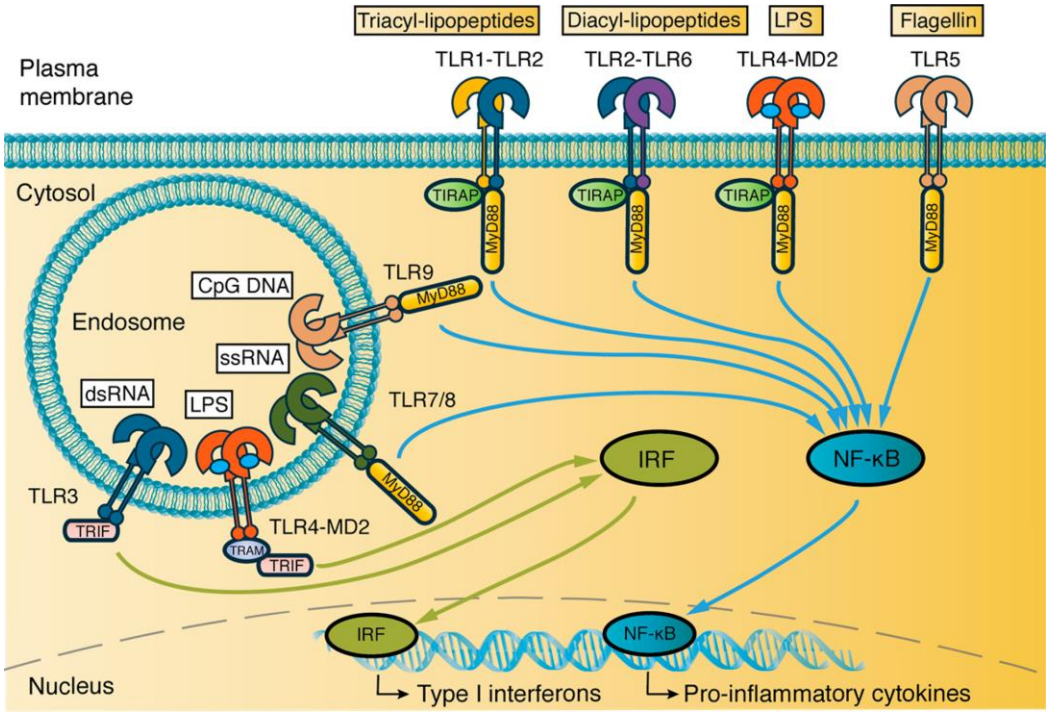

Figure 5. Toll-like receptors, their associated molecular patterns (PAMPs and DAMPs) and their corresponding signaling pathways. Activation of TLRs on the plasma membrane or in endosomes triggers the MyD88 and TRFI dependent pathway and the translocation of NF-κB and IRF into the nucleus. This leads to the transcription of inflammatory cytokines and typ I interferons and the regulation of the adaptive and innate immune response (reprinted with permission from reference[95]).

Therefore, nanocarriers are highly promising systems to support the controlled initiation of immune responses and thereby further suppress autoimmunities.[103] Especially, stimuli-responsive structures confirmed the beneficial interplay between endogenous or exogenous stimuli for achieving controlled accumulation and drug release at the desired site of action. The versatile design of stimuli-responsive architectures promotes the specific delivery of small drug molecules and provides the basis for advanced next generation immunodrug delivery systems.[68,104]

Stimuli-Responsive Nanocarriers

Polymeric nanocarriers become increasingly prominent in nanomedicine as they are applied to transport a variety of active compounds including small molecules drugs, peptides, or genes. In addition to improve the properties of conjugated or encapsulated drugs, such as solubility,

bioavailability, and prolonged circulation times, these nanocarriers can be engineered to selectively deliver and release their cargo at the target site. This promoted the development of a novel category of polymers with the ability of dynamically altering their physical and/or chemical properties in accordance with their environment.[105,106] By carefully tailoring their composition, these smart/stimuli-responsive polymeric systems can be programmed to react to a specific stimulus, enabling the spatiotemporal control over their function, including the sensing of their environment, releasing their cargo, and amplifying therapeutic effects.[13]

There are three main classifications for stimuli: chemical, physical, and biological factors. In general, chemical stimuli trigger intermolecular interactions, exemplified by variations in pH, solvent, ionic strength, hypoxia, and oxidation-reduction reactions. Enzymatic reactions are commonly associated with biological stimuli, while mechanical stress, temperature, light, or magnetic and electrical changes are categorized as physical triggers (Figure 6). The latter can also be defined as exogenous stimuli. In contrast, chemical and biological stimuli are summarized as endogenous and can usually be related to the targeted diseased tissue.[13,68,104]

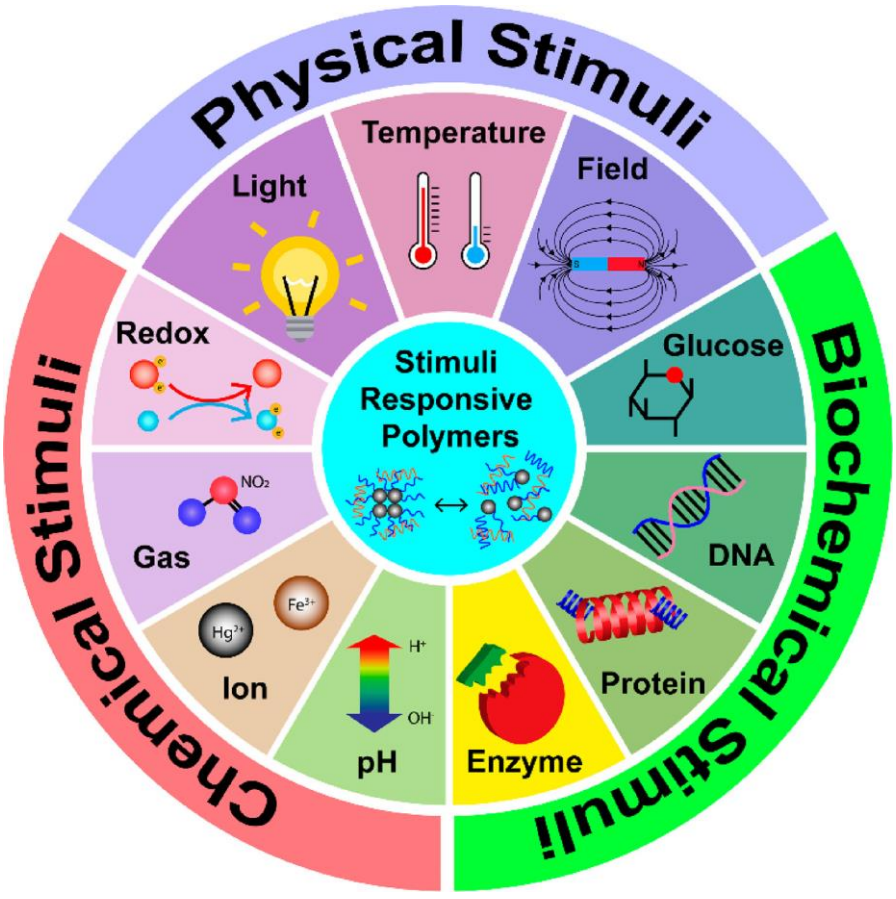

Figure 6. Demonstration of the three main categories of stimuli: physical, chemical, and biological utilized for the synthesis of smart polymers (adapted with permission from reference[107]).

Enzymes play an essential role in a variety of biological and metabolic processes. Due to their high specificity and remarkable catalytic characteristics under mild conditions enzymes attract great potential as biological triggers for a controlled drug targeting.[108] Particularly, the tumor microenvironment can be equipped with a variety of overexpressed receptors, an elevated redox potential, and an increased presence of enzymes, like specific proteases and lipases.[109,110] Therefore, dysregulated enzymes have been investigated as potential biomarkers for diagnostics and prognostics in various cancer types. Furthermore, the incorporation of specific motifs to polymeric nanocarriers enables their selective recognition and degradation by enzymes of the extra- and intracellular tumor microenvironment.[108,111] An even broader range of drug targeting can be achieved by implementing polymers with dual- or multi-responsive motifs, like e.g. pH- and enzyme-responsive poly(esteracetal)s.[67,112]

Another commonly applied internal stimulus is the disparity in redox potential between the intracellular and extracellular environment or the tumor and healthy tissue. In comparison to normal tissues the tumor microenvironment is characterized by a more reductive environment, induced by the presence of the tripeptide glutathione (GSH) bearing reducing thiol (SH) groups from cysteine. Normal cells typically possess intracellular GSH concentrations within the range of 1-10 mM, whereas extracellular GSH levels are considerably lower with 2-20 µM. In addition, tumor cells display GSH concentrations that can reach more than four times higher GSH concentrations than healthy tissues.[111,113] Thereby, GSH is rapidly degraded by different enzymes in human plasma, resulting in varying GSH concentrations in extra- or intracellular compartments.[114] Interestingly, the special reductive tumor microenvironment acts as a unique internal signal for redox-responsive nanocarriers and the controlled release of loaded cargos into tumor cells. For the design of redox-responsive nanoparticles, disulfide-based polymeric systems have been well studied. While disulfide-crosslinked polymeric micelles can improve the stability without premature release of the cargo during long circulation times, they guarantee a rapid degradation and release in GSH-rich tumors. This ensures a safe transport of therapeutic drugs and reduces the risk for toxic side effects.[115–118]

Among the available physical stimuli, temperature may play a relevant role for cancer therapy as it can be addressed by the synthesis of various thermo-responsive polymers. Based on their structural design properties, certain polymers provide a critical solution temperature, leading to a phase transition. In general, these polymers undergo several intra- and intermolecular changes within a small temperature range, causing the contraction or expansion of different polymer chains. Typically, phase transition can be separated into two physicochemical states: the lower critical solution temperature (LCST) where polymers turn insoluble above a specific

temperature or the upper critical solution temperature (UCST), at which polymers remain monophasic and turn insoluble or bi-phasic below this temperature. Different thermo-responsive polymers are characterized such as poly(N-isopropylacrylamide) with a LCST of 32 °C or poly(methoxy tri(ethylene glycol) methacrylate) p(mTEGMA).[67,119,120] These, thermo-responsive polymer systems have great potential for biomedical applications and have improved the creation of *in situ* gel-forming systems at body temperature, leading to significant advancements in tissue engineering and drug delivery.[121,122] In addition, most cells reveal a high temperature sensitivity, as temperatures above 43 °C induce a significant decrease in enzymatic function and protein deactivation, which ultimately results in apoptosis. Specifically, cancer cells are characterized by a heightened sensitivity to heat in contrast to normal cells, combined with a slightly elevated temperature of the tumor microenvironment (1-2 °C above healthy tissue). Thus, the mild hypothermia can be applied as a combined cancer treatment in nanomedicine. Several thermos-responsive polymers have been investigated as smart drug delivery systems for the targeted release of encapsulated drug in the tumor microenvironment and can be effectively used as an adjunct treatment to thermo- or radiotherapy.[123–125]

pH-Sensitive Nanocarriers

Regarding the design of stimuli-responsive nanocarriers for controlled drug delivery, pH as a stimulus is one of the most promising endogenous triggers since different compartments in the human body demonstrate a varying pH. Interestingly, the diversity of pH-sensitive structures facilitates the synthesis of different pH-responsive drug delivery systems matching with the anticipated pH deviation. In particular, the human body is equipped with several pH gradients across various biological systems ranging from very acidic to physiological pH values as illustrated in Figure 7. [105,126,127]

The drastic shift in pH levels within the gastrointestinal system ranging from highly acidic (pH 1 in the stomach) to physiological pH (7.35 in the small intestine) has been a significant factor in the development of orally-active pH-sensitive prodrugs and controlled release systems. The pH stimulus becomes even more essential and influential at the cellular and sub-cellular level. Especially, abnormal tissues like inflamed, infected or malignant tissue commonly exhibit lower pH values.[105,126,128] Notably, even the tumor microenvironment is characterized as slightly acidic (pH 6.5-6.9) compared to normal tissue (pH 7.4). The increased acidity in tumor tissues is attributed to the excessive generation of lactic acid as a product of rapid proliferation and resulting accelerated aerobic glycolysis in tumor cells, often referred to as Warburg effect. In

addition to an increase in proton concentrations, the impaired lymphatic drainage and elevated pressure of tumors may contribute to an insufficient proton clearance and further establishment of an acidic microenvironment. This can be applied to pH-sensitive cancer treatments.[104,127,129,130] Furthermore, intracellular compartments such as endosomes (5-6) and lysosomes (4-5) also reveal an intrinsic acidic pH gradient. The relevance for this pH gradient is highlighted by the fact that many nanocarriers are generally internalized through endocytosis and subsequently located or trapped within endosomes or lysosomes. These acidic environments may trigger the controlled drug release from pH-responsive carrier systems after arrival at the anticipated site of action.[105,131,132]

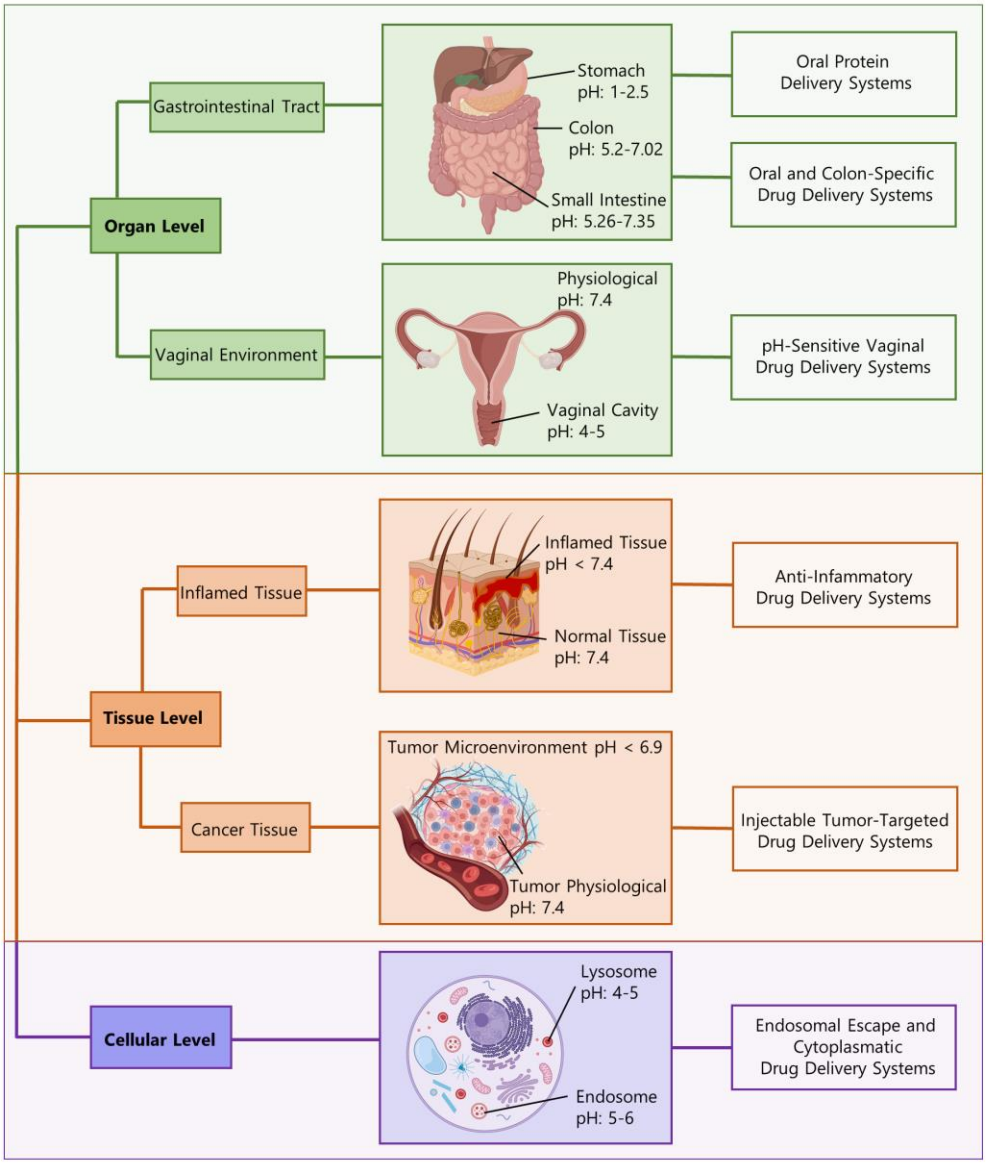

Figure 7. Graphical presentation of the pH variation within the human body and the prospective application of pH-responsive drug delivery systems.[126]

In general, pH-responsive polymers can be characterized by ionizable acidic or basic functional groups that alter their structure and properties under different pH conditions. Ideally, the designed systems are stable and inert under physiological pH values while responding rapidly by fluctuating pH values.[104] Typically, weak acidic conditions promote a protonation of functional groups along the polymer chain, while increasing pH-values afford the release of protons. These characteristics affect the polymers' hydrophilicity and solubility under aqueous conditions and can therefore be applied in physical dissociation and destabilization processes (e.g. swelling or collapse) of polymeric drug vehicles.[104,133,134] This concept is also often referred to as the proton sponge effect and is usually applied in nucleic acid delivery.[135,136] Most frequently reported pH-responsive acidic polymers are poly(acrylic acid) (PAAc) or poly(methacrylic acid) (PMAAc) as well as poly(2-acrylamido-2-methylpropane sulfonic acid) (PAMPS), which conjugate protons at slightly acidic environments and release protons at neutral to basic conditions. Notable basic polymers are amine-containing systems like poly[(2-dimethylamino)ethylmethacrylate] (PDMA) or poly[(2-*N*-morpholino)ethylmethacrylate] (PMEMA).[133]

Alternatively, a pH sensitivity can also be introduced which leads to the cleavage of a chemical covalent bond by hydrolysis upon respective pH conditions. Such bonds can easily be introduced by post-polymerization modifications of functional polymers or nanoparticles with acid labile linkers or crosslinkers. Thereby, the cleavable linkers prevent a premature drug leakage during blood circulation while ensuring a controlled drug release and high accumulation at the targeted acidic site. Such features are widely used in polymers, nanoparticles and antibody-drug conjugates.[137–139] In addition to acid-sensitive drug linkers, acid-degradable crosslinkers offer an alternative approach to optimize the release of active drugs. Several reversible crosslinkers demonstrate an increased stability of micellar nanocarriers under physiological pH values as well as efficient drug release through swelling or disassembly upon extra- and intracellular acidification.[69,137,140] The most commonly applied acid-cleavable systems are acetals and ketals, imines, hydrazones, oximes, orthoesters or 2,3-dialkylmaleamidic amides, as presented in Figure 8.[127]

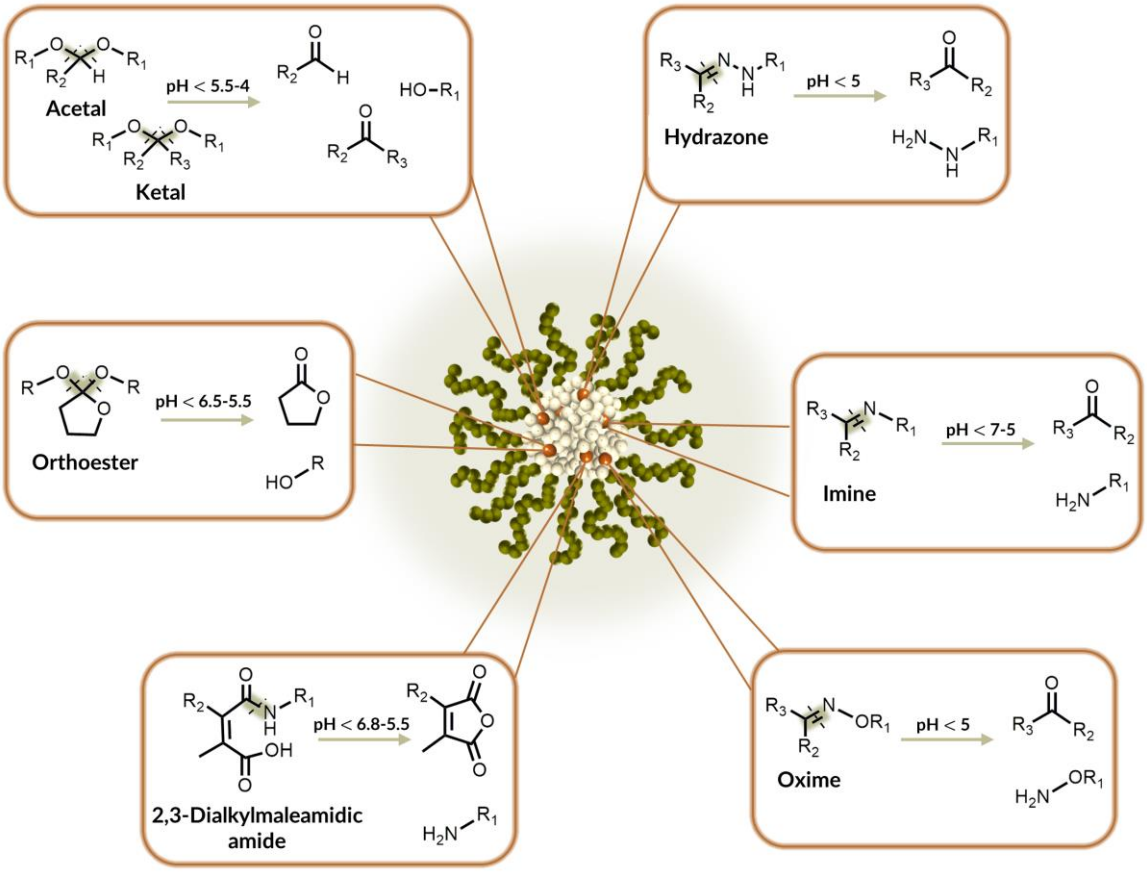

Figure 8. Acid-catalyzed hydrolysis of classical pH-sensitive linker systems applied for controlled drug delivery.[105,127]

Among the variety of pH-sensitive chemical structures, acetal and ketal linkers have been extensively investigated and applied for controlled drug delivery. Since 1960 there has been continuous interest in the hydrolysis mechanism of acetals and ketals. First synthesis approaches for the generation of linear and crosslinked polyacetals and poly(orthoesters) have been reported by Heller et al.[132,141,142] In general, acidic conditions promote the fast hydrolysis of acetals and ketals following first-order kinetics. Protonation of the oxygen induces the generation of a reactive resonance stabilized carboxonium ion intermediate. Thus, the carbocation reactivity is affected by steric and induction effects of the conjugated substituents. Subsequently, the addition of water initiates the rapid cleavage of the carbon bond, leading to the formation of corresponding charge neutral and nontoxic aldehydes/ketones and two alcohols.[127,138,143,144] Nowadays, ketals and acetal are used in several research fields, for instance implemented in degradable polymers or nanoparticles for controlled drug release and nucleic acid delivery as well as masking structure for polymers.[132,138] For example, ketal-crosslinked nanogels possess a remarkable stability at physiological pH, but acidification

to pH 5.5 forces a subsequent disassembly of the micellar carrier system followed by an anticipated drug release.[69,100,145]

Hydrazone structures in pharmaceutical materials gained increasing attention as pH-sensitive linkers and are now commonly used for the reversible conjugation of ketone-bearing anticancer drugs (e.g. doxorubicin). Hydrazones can easily be synthesized by a condensation reaction of aldehydes or ketones with hydrazine, while the conversion with hydroxylamines reveals the formation of more pH-stable oximes, and the reaction with primary amines affords more pH-sensitive imines. All these structures are characterized by their acid-responsive C=N bond, whereas hydrazones represent a significant modality and stability towards hydrolytic cleavage at physiological pH.[129,146]

Based on the mesomeric effect and delocalization effect of the π electrons, hydrazone structures exhibit a decreased electrophilicity and thus, an increased stability. Therefore, hydrazones are commonly known to be kinetically inert under neural conditions. Nevertheless, by exposure to acidic conditions they can undergo hydrolysis, exchange or metathesis, similar to imines.[147] Hydrazones and related oxime or imine functionalities have been extensively investigated for controlled polymer drug conjugation, surface patterning and tissue engineering. Several pH-sensitive hydrazone-linked doxorubicin-polymer conjugates demonstrated high potential as anticancer drug delivery system.[132,148,149] For instance, Van Driessche et al. exhibited the fast formulation of hydrazone-linked doxorubicin nanogels by synthesis and self-assembly of reactive ester block copolymers into acid-responsive hydrazone-functionalized nanogels.[150]

Another pH-responsive chemical structure often involved in various biological and chemical processes are imines. The imine structure, also referred to as “Schiff base”, was initially discovered by Hugo Schiff in 1864. Typically, they are synthesized by condensation reaction of aldehydes or ketones with primary amines under thermodynamical control and the removal of water. Based on their C=N bond, imines exhibit a high hydrolysis sensitivity that is further enhanced by acidic conditions. Imines are then very easily cleaved off at slightly lower pH values like the tumor microenvironment (~pH 6.8).[129,151–153] However, high instability under physiological pH prevents the application of imine-conjugated drug delivery systems. Consequently, recent developments focus on $\pi - \pi$ stabilized imines such as benzoic imines for a controlled delivery and release of anticancer drugs at the target site.[129,147,154]

The reaction of aldehydes/ketones with hydroxylamine results in the rapid an efficient formation of pH-sensitive oximes. In general, oximes as well as hydrazones possess a higher

hydrolytic stability than imines. Additionally, the pH sensitivity can be further fine-tuned by variation of the conjugated substituents, leading to an increased intrinsic stability. Hence, pH-sensitive oximes can be utilized as powerful tool for controlled release of biologically active compounds.[155–157] Zhu Xinyuan and his coworkers demonstrated an interesting example by the synthesis of self-assembling triblock copolymers, including an oxime-tethered polycarprolactone block for the efficient conjugation of the anticancer drug doxorubicin. The resulting pH-sensitive nanoparticles revealed a fast release of the conjugated drug especially in acidic tumor tissues compared to normal tissues.[158,159] Nevertheless, the bioconjugation of oximes has certain limitations due to their increased thermodynamic stability, causing a prolonged drug release in acidic environments[129], while faster release rates would actually be favored.

Among the various acid-sensitive functionalities, orthoesters demonstrate enough pH sensitivity to respond to slightly acidic environments such as the tumor or inflamed tissue. Despite their similar chemical structure to acetals and ketals, orthoesters can rapidly hydrolyze under mild acidic conditions.[160,161] In general, orthoesters are structurally characterized by three alkoxy groups attached to one carbon atom, which can be synthesized by the conversion of nitriles with alcohols and the presence of acid catalysts. Additionally, the acidic hydrolysis can be further modified by variation of the structure patterns and substituents, such as the introduction of methyl groups or integration into a six-membered ring.[162,163] Depending on the cleavage mechanism (exo- or endocyclic), hydrolysis reveals two different products.[164] The specific properties enable the flexible application of orthoesters as pH-responsive linker, polymer or as protecting group for esters.[163,165]

Dimethylmaleic Anhydride-Based Structures

The remarkable features of all the described pH-sensitive structures highlight the advantages of pH-responsive polymer systems and their multiple applications, such as drug or gene delivery, sensing and surface modifications.[130,133] Nevertheless, most pH-sensitive motifs exhibit an insufficient or slow degradation rate under relevant acidic environments within the human body, like the tumor tissue or intracellularly in endosomes. Furthermore, several conjugated small molecular drugs require a sophisticated modification to ensure a pH-reversible conjugation. These strategies often simply prevent the efficient release of the molecular drugs in their native form and thus, affect the drugs' specific activity.[129,166,167]

In contrast to that, dimethylmaleic anhydride-based systems provide several beneficial properties and, most importantly, guarantee a traceless release of the conjugated molecules in their native form under mild acidic conditions.[168] First investigations of maleic anhydrides described the fast and specific conjugation of amino groups of proteins or peptides.[169,170] Thereby, maleic anhydrides appeared to be an efficient protecting group especially for the proteins' lysine residues. Extensive modifications with maleic anhydride-based systems induced a charge conversion of the positively charged amino groups into negatively charged compounds, whereas the constant reversibility of the modification guaranteed a release of the unmodified protein under acidic conditions.[171,172]

Nowadays, cyclic, pH-responsive structural elements, such as dimethylmaleic anhydride, demonstrate versatile biological and chemical applications. In general, cyclic anhydrides provide a high intrinsic reactivity as electrophilic acid derivative towards nucleophiles, including amines or alcohols, under mild reaction conditions. The maleic anhydride group can easily react with amines forming the corresponding ring-opened amide. The reaction is especially favored at basic pH conditions, leading to the deprotonation of the carboxylate group. Additionally, the classical conjugation can be prepared without any coupling agents, which ensures a fast reaction without secondary byproducts. Particularly, the conjugation of amines is attractive because these reactions can be performed in aqueous media and favor amines than alcohols.[172,173] The amine conjugation is depicted in Figure 9:

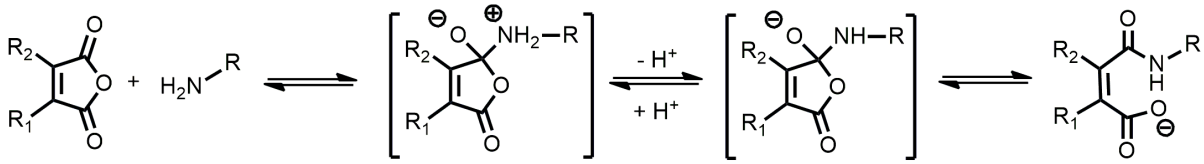

Figure 9. Sequential pH-reversible amidation of dimethylmaleic anhydride-based systems with primary amines.[172]

Interestingly, the nucleophilic addition of amines to asymmetric substituted maleic anhydrides leads to the formation of two regioisomers. Employing mixtures of the regioisomers exhibit a thermodynamic and kinetic product. Thereby, α-substituted maleic acid amides seemed to be the more stable thermodynamic product, while β-substituted maleic acid amides are reported as the kinetically favored product (Figure 10). Further variation of the reaction conditions, such as high temperatures and long reaction times induce the intramolecular transformation of the β-substituted maleic acid amide into stable α-substituted products.[174] This underlines also the dynamics of the conjugate[175] and explains why this bond is often classified among other dynamic covalent bonds[176] applied in macromolecular chemistry.[177]

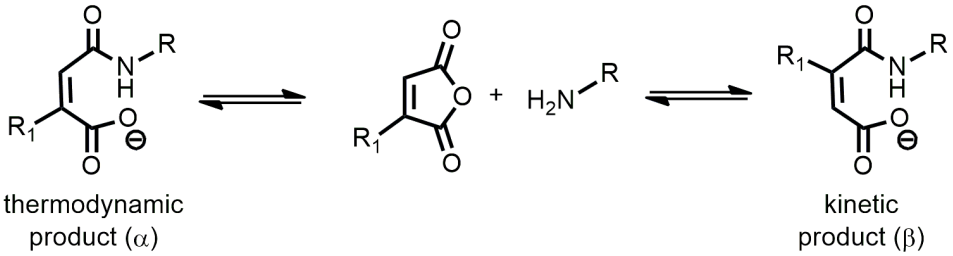

Figure 10. Different regioisomers as result of the amine conjugation to asymmetric substituted maleic anhydrides. Revealing a thermodynamic product (left) and a kinetic product (right).[174]

The generated amide bond can easily release the amine again under slightly acidic conditions, while it remains stable under neutral and alkaline pH levels. Usually, substituted maleic anhydrides reveal a pH sensitivity similar to tumor or inflammatory tissues (pH < 6.8-5.5), making them a promising tool to produce pH-sensitive carrier systems for selective drug delivery.[105,173,178] The pH-dependent nature of maleic acid amide derivates can be attributed to the *cis*-double bond of the system and the neighbored carboxylate group, which can readily attack the amide carbonyl group, forming a tetrahedral intermediate (Figure 11). The intramolecular hydrolysis can be increased under mild acidic conditions by protonation of the amide. Thus, the amide hydrolysis is very much affected by the basicity of the released amine and the acidity of the environment.[179–182]

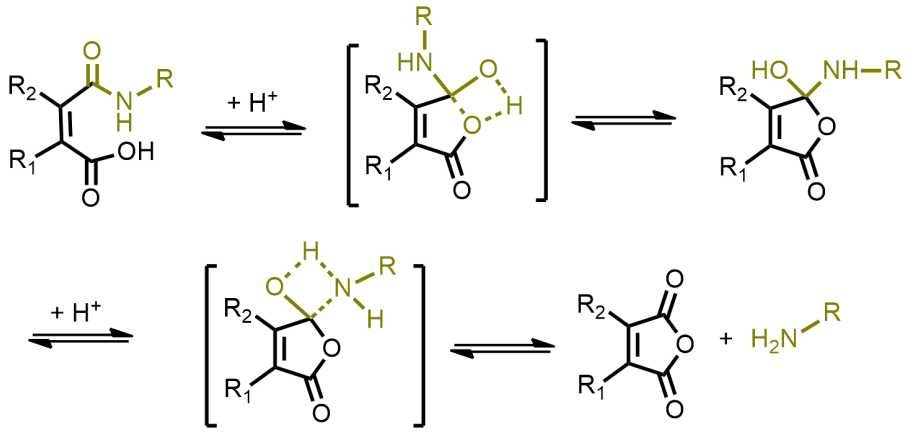

Figure 11. Schematic illustration of the acidic release mechanism of amine-conjugated disubstituted maleic anhydride-based structures.[179,180]

The pH sensitivity of maleic acid amide derivates can be further controlled by modification of the chemical structure focusing on the substituents attached to the *cis*-double bond. Based on the Thorpe-Ingold effect disubstituted maleic acid amide derivates exhibit an accelerated cyclization reaction compared to mono-substituted maleic acid amides, such as citraconic acid

amide or maleic acid amide with two hydrogen substituents. The steric repulsion effect of the substituents reduces the distance between maleic acid amide derivates and the carboxylate group, forcing the intramolecular ring closure. In addition, adjacent substituents to the *cis*-double bond serve as a barrier and reduce the sensitivity to undesired side reactions.[174,180,181,183]

Despite to the fast and traceless intramolecular hydrolysis, the reaction competes with the formation of pH-irreversible imide structures, especially in organic solvents. Only few groups report on the arising side product and the potential equilibrium between the pH-reversible and irreversible system at neutral pH conditions (Figure 12).[175,184,185] Nevertheless, different reaction conditions may impact the formation of imide systems, such as solvent, temperature or basic catalysts. Thereby, basic catalysts like TEA may promote the amine conjugation to the anhydride and further prevent the formation of the imide by-product by deprotonation of the *in situ* generated carboxylate.[174]

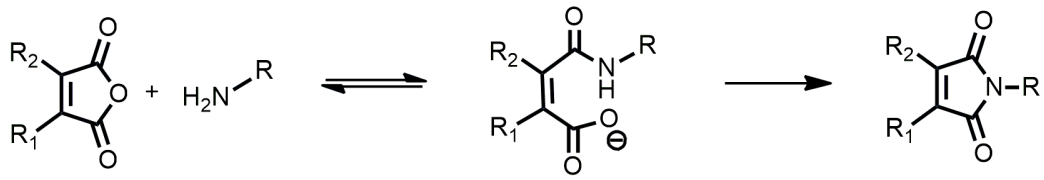

Figure 12. Illustration of possible disubstituted maleic acid amide derivate hydrolysis products: (left) the pH-sensitive release of conjugated primary amines or (right) the formation of pH-irreversible maleimides.[174,184]

As already mentioned, under basic conditions maleic acid amide derivates exhibit negative charges due to the deprotonated β-carboxylic groups after amine conjugation, while they release positively charged amines after degradation in acidic media. This negative-to-positive charge conversion has been extensively exploited for the development of smart drug delivery systems.[180,181,185] Considering the negative charge of cell membranes, positively charged polymeric structures and nanoparticles reveal an increased cellular internalization and localization than negatively charged systems.[186,187] Nevertheless, negatively charged systems suffer from a fast clearance from the bloodstream. Therefore, charge-reversible carrier systems can be exploited for new therapeutic approaches. Disubstituted maleic acid anhydride derivates as pH-sensitive and charge convertible structures can be applied for negative surface decoration and reduced cell internalization, while promoted cell uptake can be found in tumor cells, since they are surrounded by an acidic tumor microenvironment where the carrier system undergoes charge conversion.[188–190]

Furthermore, substituted maleic anhydride derivates have expanded the field of protein conjugation. Protein-based therapeutics are assuming an increasingly important role in the treatment of various diseases, including cancer or autoimmune disorders. Nonetheless, their clinical application is significantly limited by low bioavailability, fast degradation, and renal clearance, as well as high immunogenicity. Protein PEGylation is considered as the most efficient concept for protection but may limit the proteins' activity because of irreversible conjugation. Hence, substituted maleic anhydride derivates are highly suitable for the pH-reversible conjugation of proteins to a nanocarrier. As an example, poly(ethylene glycol)-poly(lysine) micellar systems can complex the transiently negatively charged proteins and further release them in their native form upon cell internalization.[168,176,191–193] Besides to pH-reversible protein conjugation, substituted maleic anhydride derivates can be applied as a versatile pH-sensitive linker for a variety of anticancer drugs and carrier systems.[194–197] Different applications of substituted maleic anhydride derivates are depicted in Figure 13.

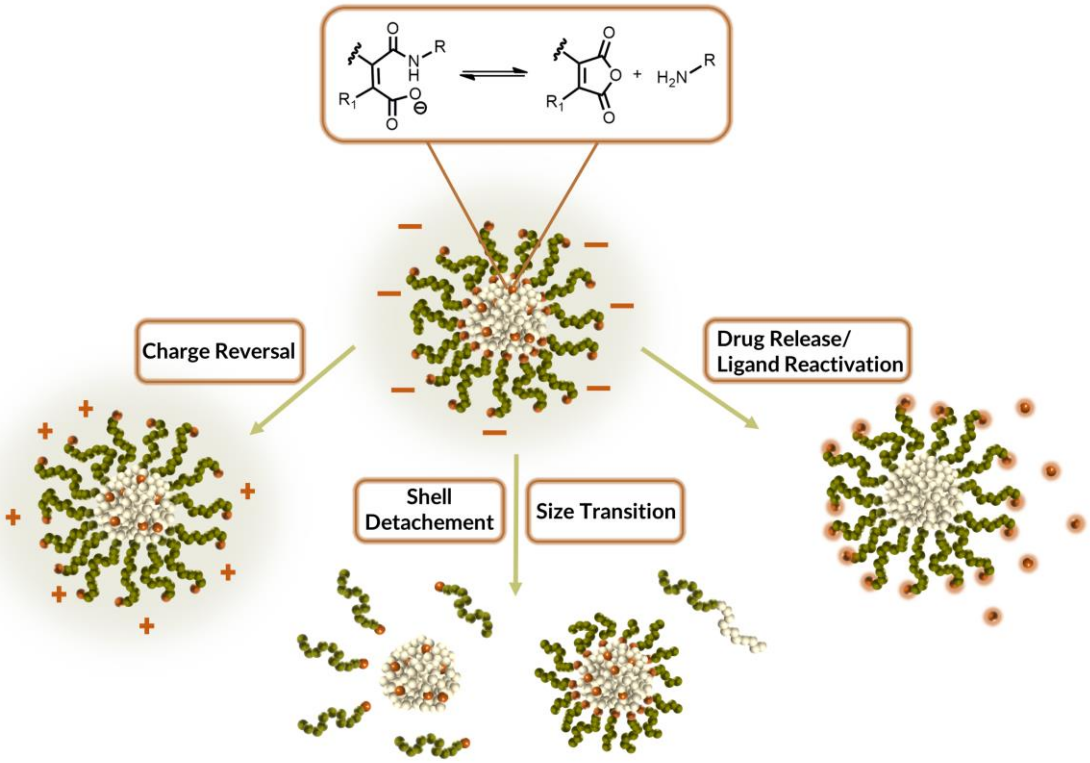

Figure 13. Possible substituted maleic anhydride derivate applications for an efficient, pH-sensitive drug delivery.[180]

The incorporation of cell-penetrating peptides onto the nanoparticles surface facilitates their intracellular delivery. However, such conjugated targeting units can induce an undesired cellular uptake into any cell. To prevent this and facilitate cell uptake only in acidic tumor cells,

Li D. et al. reported a smart modification of TAT (transactivation or transcription)-decorated nanoparticles with pH-sensitive dimethylmaleic anhydrides. Upon accumulation in the tumor microenvironment the pH-sensitive dimethylmaleic amides dissociate and expose the TAT-groups for intracellular nanoparticle delivery.[180,198]

Alternatively, another versatile application of substituted maleic anhydride systems is a shell detachment or controlled size variation of micellar carrier systems. PEGylation provides efficient stealth-properties but inhibits the cellular uptake leading to an ineffective delivery, often referred to as “PEG dilemma”.[28,199] Hence, a controlled cleavage of the PEG-shell at the side of activation may offer several advantages. PEG-substituted maleic anhydride derivates reveal suitable characteristics as acid-sensitive shell polymer structures and demonstrated the efficient cleavage at acid environments, such as the tumor micromilieu for the improved cellular uptake and cancer treatment.[200–203] Furthermore, dimethylmaleic anhydride-based structures could extended the design of size-switchable micellar systems for efficient biodistribution and promoted tumor penetration.[180,204,205] Consequently, dimethylmaleic anhydride-based structures provide versatile applications and could extend the development and evolution of stimuli-responsive polymer systems for the fabrication of smart drug delivery systems in nanomedicine.

References

(1) Soares, S.; Sousa, J.; Pais, A.; Vitorino, C. Nanomedicine: Principles, Properties, and Regulatory Issues. *Front. Chem.* **2018**, *6* (AUG), 1–15.

(2) Rizzo, L. Y.; Theek, B.; Storm, G.; Kiessling, F.; Lammers, T. Recent Progress in Nanomedicine: Therapeutic, Diagnostic and Theranostic Applications. *Curr. Opin. Biotechnol.* **2013**, *24* (6), 1159–1166.

(3) Vahedifard, F.; Chakravarthy, K. Nanomedicine for COVID-19: The Role of Nanotechnology in the Treatment and Diagnosis of COVID-19. *Emergent Mater.* **2021**, *4* (1), 75–99.

(4) Germain, M.; Caputo, F.; Metcalfe, S.; Tosi, G.; Spring, K.; Aslund, A. K. O.; Pottier, A.; Schiffelers, R.; Geccaldi, A.; Schmid, R. Delivering the Power of Nanomedicine to Patients Today. *J. Control. Release* **2020**, *326* (January), 164–171.

(5) Etheridge, M. L.; Campbell, S. A.; Erdman, A. G.; Haynes, C. L.; Wolf, S. M.; McCullough Jeffrey. THE BIG PICTURE ON SMALL MEDICINE: THE STATE OF NANOMEDICINE PRODUCTS APPROVED FOR USE OR IN CLINICAL TRIALS. *Nanomedicine* **2013**, *9* (1), 1–14.

(6) Talelli, M.; Barz, M.; Rijcken, C. J. F.; Kiessling, F.; Hennink, W. E.; Lammers, T. Core-Crosslinked Polymeric Micelles: Principles, Preparation, Biomedical Applications and Clinical Translation. *Nano Today* **2015**, *10* (1), 93–117.

(7) Kumari, A.; Yadav, S. K.; Yadav, S. C. Biodegradable Polymeric Nanoparticles Based Drug Delivery Systems. *Colloids Surfaces B Biointerfaces* **2010**, *75* (1), 1–18.

(8) Wicki, A.; Witzigmann, D.; Balasubramanian, V.; Huwyler, J. Nanomedicine in Cancer Therapy: Challenges, Opportunities, and Clinical Applications. *J. Control. Release* **2015**, *200*, 138–157.

(9) Wagner, V.; Dullaart, A.; Bock, A. K.; Zweck, A. The Emerging Nanomedicine Landscape. *Nat. Biotechnol.* **2006**, *24* (10), 1211–1217.

(10) Thapa, R. K.; Kim, J. O. Nanomedicine-Based Commercial Formulations: Current Developments and Future Prospects. *J. Pharm. Investig.* **2023**, *53* (1), 19–33.

(11) Aghebati-Maleki, A.; Dolati, S.; Ahmadi, M.; Baghbanzhadeh, A.; Asadi, M.; Fotouhi, A.; Yousefi, M.; Aghebati-Maleki, L. Nanoparticles and Cancer Therapy: Perspectives for Application of Nanoparticles in the Treatment of Cancers. *J. Cell. Physiol.* **2020**, *235* (3), 1962–1972.

(12) Mandal, A.; Bisht, R.; Rupenthal, I. D.; Mitra, A. K. Polymeric Micelles for Ocular Drug Delivery: From Structural Frameworks to Recent Preclinical Studies. *J. Control. Release* **2017**, *248*, 96–116.

(13) Cabral, H.; Miyata, K.; Osada, K.; Kataoka, K. Block Copolymer Micelles in Nanomedicine Applications. *Chem. Rev.* **2018**, *118* (14), 6844–6892.

(14) Russell, L. M.; Liu, C. H.; Grodzinski, P. Nanomaterials Innovation as an Enabler for Effective Cancer Interventions. *Biomaterials* **2020**, *242* (October 2019), 119926.

(15) Davis, M. E.; Chen, Z.; Shin, D. M. Nanoparticle Therapeutics: An Emerging Treatment Modality for Cancer. *Nat. Rev. Drug Discov.* **2008**, *7* (9), 771–782.

(16) Andriyanov, A. V.; Koren, E.; Barenholz, Y.; Goldberg, S. N. Therapeutic Efficacy of Combining PEGylated Liposomal Doxorubicin and Radiofrequency (RF) Ablation: Comparison between Slow-Drug-Releasing, Non-Thermosensitive and Fast-Drug-Releasing, Thermosensitive Nano-Liposomes. *PLoS One* **2014**, *9* (5), e92555.

(17) Barenholz, Y. Doxil® - The First FDA-Approved Nano-Drug: Lessons Learned. *J. Control. Release* **2012**, *160* (2), 117–134.

(18) Shi, J.; Kantoff, P. W.; Wooster, R.; Farokhzad, O. C. Cancer Nanomedicine: Progress, Challenges

and Opportunities. *Nat. Rev. Cancer* **2017**, *17* (1), 20–37.

(19) Varela-Moreira, A.; Shi, Y.; Fens, M. H. A. M.; Lammers, T.; Hennink, W. E.; Schiffelers, R. M. Clinical Application of Polymeric Micelles for the Treatment of Cancer. *Mater. Chem. Front.* **2017**, *1* (8), 1485–1501.

(20) Miele, E.; Spinelli, G. P.; Miele, E.; Tomao, F.; Tomao, S. Albumin-Bound Formulation of Paclitaxel (Abraxane® ABI-007) in the Treatment of Breast Cancer. *Int. J. Nanomedicine* **2009**, *4* (1), 99–105.

(21) Watson, O. J.; Barnsley, G.; Toor, J.; Hogan, A. B.; Winskill, P.; Ghani, A. C. Global Impact of the First Year of COVID-19 Vaccination: A Mathematical Modelling Study. *Lancet Infect. Dis.* **2022**, *22* (9), 1293–1302.

(22) Cho, K.; Wang, X.; Nie, S.; Chen, Z.; Shin, D. M. Therapeutic Nanoparticles for Drug Delivery in Cancer. *Clin. Cancer Res.* **2008**, *14* (5), 1310–1316.

(23) Blanco, E.; Kessinger, C. W.; Sumer, B. D.; Gao, J. Multifunctional Micellar Nanomedicine for Cancer Therapy. *Exp. Biol. Med.* **2009**, *234* (2), 123–131.

(24) Chatterjee, K.; Sarkar, S.; Jagajjanani Rao, K.; Paria, S. Core/Shell Nanoparticles in Biomedical Applications. *Adv. Colloid Interface Sci.* **2014**, *209*, 8–39.

(25) Alexis, F.; Pridgen, E.; Molnar, L. K.; Farokhzad, O. C. Factors Affecting the Clearance and Biodistribution of Polymeric Nanoparticles. *Mol. Pharm.* **2008**, *5* (4), 505–515.

(26) Fam, S. Y.; Chee, C. F.; Yong, C. Y.; Ho, K. L.; Mariatulqabtiah, A. R.; Tan, W. S. Stealth Coating of Nanoparticles in Drug-Delivery Systems. *Nanomaterials* **2020**, *10* (4), 1–18.

(27) Ostuni, E.; Chapman, R. G.; Holmlin, R. E.; Takayama, S.; Whitesides, G. M. A Survey of Structure-Property Relationships of Surfaces That Resist the Adsorption of Protein. *Langmuir* **2001**, *17* (18), 5605–5620.

(28) Otsuka, H.; Nagasaki, Y.; Kataoka, K. PEGylated Nanoparticles for Biological and Pharmaceutical Applications. *Adv. Drug Deliv. Rev.* **2003**, *55* (3), 403–419.

(29) Bludau, H.; Czapar, A. E.; Pitek, A. S.; Shukla, S.; Jordan, R.; Steinmetz, N. F. POxylation as an Alternative Stealth Coating for Biomedical Applications. *Eur. Polym. J.* **2017**, *88*, 679–688.

(30) Barz, M.; Luxenhofer, R.; Zentel, R.; Vicent, M. J. Overcoming the PEG-Addiction: Well-Defined Alternatives to PEG, from Structure-Property Relationships to Better Defined Therapeutics. *Polym. Chem.* **2011**, *2* (9), 1900–1918.

(31) Nuhn, L.; Barz, M.; Zentel, R. New Perspectives of HPMA-Based Copolymers Derived by Post-Polymerization Modification. *Macromol. Biosci.* **2014**, *14* (5), 607–618.

(32) Bertrand, N.; Leroux, J. C. The Journey of a Drug-Carrier in the Body: An Anatomo-Physiological Perspective. *J. Control. Release* **2012**, *161* (2), 152–163.

(33) Hoshyar, N.; Samantha, G.; Hongbin, H.; Gang, B. The Effect of Nanoparticle Size on in Vivo Pharmacokinetics and Cellular Interaction Nanoparticle-Based. *Nanomedicine* **2016**, *11* (6), 673–692.

(34) Ahmad, Z.; Shah, A.; Siddiq, M.; Kraatz, H. B. Polymeric Micelles as Drug Delivery Vehicles. *RSC Adv.* **2014**, *4* (33), 17028–17038.

(35) Cabral, H.; Kataoka, K. Progress of Drug-Loaded Polymeric Micelles into Clinical Studies. *J. Control. Release* **2014**, *190*, 465–476.

(36) Maeda, H.; Nakamura, H.; Fang, J. The EPR Effect for Macromolecular Drug Delivery to Solid Tumors: Improvement of Tumor Uptake, Lowering of Systemic Toxicity, and Distinct Tumor Imaging in Vivo. *Adv. Drug Deliv. Rev.* **2013**, *65* (1), 71–79.

(37) Noble, G. T.; Stefanick, J. F.; Ashley, J. D.; Kiziltepe, T.; Bilgicer, B. Ligand-Targeted Liposome Design: Challenges and Fundamental Considerations. *Trends Biotechnol.* **2014**, *32* (1), 32–45.

(38) Hobbs, S. K.; Monsky, W. L.; Yuan, F.; Roberts, W. G.; Griffith, L.; Torchilin, V. P.; Jain, R. K. Regulation of Transport Pathways in Tumor Vessels: Role of Tumor Type and Microenvironment. *Proc. Natl. Acad. Sci. U. S. A.* **1998**, *95* (8), 4607–4612.

(39) Greish, K. Enhanced Permeability and Retention of Macromolecular Drugs in Solid Tumors: A Royal Gate for Targeted Anticancer Nanomedicines. *J. Drug Target.* **2007**, *15* (7–8), 457–464.

(40) Fang, J.; Nakamura, H.; Maeda, H. The EPR Effect: Unique Features of Tumor Blood Vessels for Drug Delivery, Factors Involved, and Limitations and Augmentation of the Effect. *Adv. Drug Deliv. Rev.* **2011**, *63* (3), 136–151.

(41) Danhier, F. To Exploit the Tumor Microenvironment: Since the EPR Effect Fails in the Clinic, What Is the Future of Nanomedicine? *J. Control. Release* **2016**, *244*, 108–121.

(42) Azzopardi, E. A.; Ferguson, E. L.; Thomas, D. W. The Enhanced Permeability Retention Effect: A New Paradigm for Drug Targeting in Infection. *J. Antimicrob. Chemother.* **2013**, *68* (2), 257–274.

(43) Lammers, T.; Kiessling, F.; Hennink, W. E.; Storm, G. Drug Targeting to Tumors: Principles, Pitfalls and (Pre-) Clinical Progress. *J. Control. Release* **2012**, *161* (2), 175–187.

(44) Shi, P.; Cheng, Z.; Zhao, K.; Chen, Y.; Zhang, A.; Gan, W.; Zhang, Y. Active Targeting Schemes for Nano-Drug Delivery Systems in Osteosarcoma Therapeutics. *J. Nanobiotechnology* **2023**, *21* (1), 1–27.

(45) Danhier, F.; Feron, O.; Préat, V. To Exploit the Tumor Microenvironment: Passive and Active Tumor Targeting of Nanocarriers for Anti-Cancer Drug Delivery. *J. Control. Release* **2010**, *148* (2), 135–146.

(46) Gullotti, E.; Yeo, Y. Extracellularly Activated Nanocarriers: A New Paradigm of Tumor Targeted Drug Delivery. *Mol. Pharm.* **2009**, *6* (4), 1041–1051.

(47) Byrne, J. D.; Betancourt, T.; Brannon-Peppas, L. Active Targeting Schemes for Nanoparticle Systems in Cancer Therapeutics. *Adv. Drug Deliv. Rev.* **2008**, *60* (15), 1615–1626.

(48) Kou, L.; Bhutia, Y. D.; Yao, Q.; He, Z.; Sun, J.; Ganapathy, V. Transporter-Guided Delivery of Nanoparticles to Improve Drug Permeation across Cellular Barriers and Drug Exposure to Selective Cell Types. *Front. Pharmacol.* **2018**, *9* (JAN), 1–16.

(49) Shi, Y.; Lammers, T. Combining Nanomedicine and Immunotherapy. *Acc. Chem. Res.* **2019**, *52* (6), 1543–1554.

(50) Riley, R. S.; June, C. H.; Langer, R.; Mitchell, M. J. Delivery Technologies for Cancer Immunotherapy. *Nat. Rev. Drug Discov.* **2019**, *18* (3), 175–196.

(51) Yang, W.; Wang, L.; Mettenbrink, E. M.; Deangelis, P. L.; Wilhelm, S. Nanoparticle Toxicology. *Annu. Rev. Pharmacol. Toxicol.* **2021**, *61*, 269–289.

(52) Gupta, D.; Yadav, P.; Garg, D.; Gupta, T. K. Pathways of Nanotoxicity: Modes of Detection, Impact, and Challenges. *Front. Mater. Sci.* **2021**, *15* (4), 512–542.

(53) Blanco, E.; Shen, H.; Ferrari, M. Principles of Nanoparticle Design for Overcoming Biological Barriers to Drug Delivery. *Nat. Biotechnol.* **2015**, *33* (9), 941–951.

(54) Baetke, S. C.; Lammers, T.; Kiessling, F. Applications of Nanoparticles for Diagnosis and Therapy of Cancer. *Br. J. Radiol.* **2015**, *88* (1054), 20150207.

(55) Docter, D.; Distler, U.; Storck, W.; Kuharev, J.; Wünsch, D.; Hahlbrock, A.; Knauer, S. K.; Tenzer, S.; Stauber, R. H. Quantitative Profiling of the Protein Coronas That Form around Nanoparticles.

Nat. Protoc. **2014**, *9* (9), 2030–2044.

(56) Owen, S. C.; Chan, D. P. Y.; Shoichet, M. S. Polymeric Micelle Stability. *Nano Today* **2012**, *7* (1), 53–65.

(57) Zhao, Y.; Sultan, D.; Liu, Y. Biodistribution, Excretion, and Toxicity of Nanoparticles. *Theranostic Bionanomaterials* **2019**, 27–53.

(58) Tsoi, K. M.; Macparland, S. A.; Ma, X. Z.; Spetzler, V. N.; Echeverri, J.; Ouyang, B.; Fadel, S. M.; Sykes, E. A.; Goldaracena, N.; Kaths, J. M.; Conneely, J. B.; Alman, B. A.; Selzner, M.; Ostrowski, M. A.; Adeyi, O. A.; Zilman, A.; McGilvray, I. D.; Chan, W. C. W. Mechanism of Hard-Nanomaterial Clearance by the Liver. *Nat. Mater.* **2016**, *15* (11), 1212–1221.

(59) Thomas, O. S.; Weber, W. Overcoming Physiological Barriers to Nanoparticle Delivery—Are We There Yet? *Front. Bioeng. Biotechnol.* **2019**, *7*, 415.

(60) Deng, C.; Jiang, Y.; Cheng, R.; Meng, F.; Zhong, Z. Biodegradable Polymeric Micelles for Targeted and Controlled Anticancer Drug Delivery: Promises, Progress and Prospects. *Nano Today* **2012**, *7* (5), 467–480.

(61) Le, T. C.; Penna, M.; Winkler, D. A.; Yarovsky, I. Quantitative Design Rules for Protein-Resistant Surface Coatings Using Machine Learning. *Sci. Rep.* **2019**, *9* (1), 1–12.

(62) Suk, J. S.; Xu, Q.; Kim, N.; Hanes, J.; Ensign, L. M. PEGylation as a Strategy for Improving Nanoparticle-Based Drug and Gene Delivery. *Adv. Drug Deliv. Rev.* **2016**, *99*, 28–51.

(63) Jesus, S.; Schmutz, M.; Som, C.; Borchard, G.; Wick, P.; Borges, O. Hazard Assessment of Polymeric Nanobiomaterials for Drug Delivery: What Can We Learn From Literature So Far. *Front. Bioeng. Biotechnol.* **2019**, *7*, 261.

(64) Elsaesser, A.; Howard, C. V. Toxicology of Nanoparticles. *Adv. Drug Deliv. Rev.* **2012**, *64* (2), 129–137.

(65) Vroman, I.; Tighzert, L. Biodegradable Polymers. *Materials (Basel).* **2009**, *2* (2), 307–344.

(66) Czysch, C.; Medina-Montano, C.; Zhong, Z.; Fuchs, A.; Stickdorn, J.; Winterwerber, P.; Schmitt, S.; Deswarte, K.; Raabe, M.; Scherger, M.; Combes, F.; De Vrieze, J.; Kasmi, S.; Sandners, N. N.; Lienenklaus, S.; Koynov, K.; Räder, H. J.; Lambrecht, B. N.; David, S. A.; Bros, M.; Schild, H.; Grabbe, S.; De Geest, B. G.; Nuhn, L. Transient Lymph Node Immune Activation by Hydrolysable Polycarbonate Nanogels. *Adv. Funct. Mater.* **2022**, *32* (35), 2203490.

(67) Schattling, P.; Jochum, F. D.; Theato, P. Multi-Stimuli Responsive Polymers-the All-in-One Talents. *Polym. Chem.* **2014**, *5* (1), 25–36.

(68) Blum, A. P.; Kammeyer, J. K.; Rush, A. M.; Callmann, C. E.; Hahn, M. E.; Gianneschi, N. C. Stimuli-Responsive Nanomaterials for Biomedical Applications. *J. Am. Chem. Soc.* **2015**, *137* (6), 2140–2154.

(69) Nuhn, L.; Vanparijs, N.; De Beuckelaer, A.; Lybaert, L.; Verstraete, G.; Deswarte, K.; Lienenklaus, S.; Shukla, N. M.; Salyer, A. C. D.; Lambrecht, B. N.; Grooten, J.; David, S. A.; De Koker, S.; De Geest, B. G. PH-Degradable Imidazoquinoline-Ligated Nanogels for Lymph Node-Focused Immune Activation. *Proc. Natl. Acad. Sci. U. S. A.* **2016**, *113* (29), 8098–8103.

(70) Song, W.; Musetti, S. N.; Huang, L. Nanomaterials for Cancer Immunotherapy. *Biomaterials* **2017**, *148*, 16–30.

(71) Shields, C. W.; Wang, L. L. W.; Evans, M. A.; Mitragotri, S. Materials for Immunotherapy. *Adv. Mater.* **2020**, *32* (13), 1–56.

(72) Abbott, M.; Ustoyev, Y. Cancer and the Immune System: The History and Background of Immunotherapy. *Semin. Oncol. Nurs.* **2019**, *35* (5), 150923.

(73) Leach, D. R.; Krummel, M. F.; Allison, J. P. Enhancement of Antitumor Immunity by CTLA-4 Blockade. *Science (80-.).* **1996**, *271* (5256), 1734–1736.

(74) Ishida, Y.; Agata, Y.; Shibahara, K.; Honjo, T. Induced Expression of PD-1, a Novel Member of the Immunoglobulin Gene Superfamily, upon Programmed Cell Death. *EMBO J.* **1992**, *11* (11), 3887–3895.

(75) Irvine, D. J.; Hanson, M. C.; Rakhra, K.; Tokatlian, T. Synthetic Nanoparticles for Vaccines and Immunotherapy. *Chem. Rev.* **2015**, *115* (19), 11109–11146.

(76) Delvers, P. J.; Roitt, I. M. First of Two Parts THREE LEVELS OF DEFENSE. *N. Engl. J. Med.* **2000**, *343* (1), 37–49.

(77) Hato, T.; Dagher, P. C. How the Innate Immune System Senses Trouble and Causes Trouble. *Clin. J. Am. Soc. Nephrol.* **2015**, *10* (8), 1459–1469.

(78) Iwasaki, A.; Medzhitov, R.; Haven, N. Control of Adaptive Immunity by the Innate Immune System. *Nat. Immunol.* **2015**, *16* (4), 343–353.

(79) Eiz-Vesper, B.; Schmetzer, H. M. Antigen-Presenting Cells: Potential of Proven Und New Players in Immune Therapies. *Transfus. Med. Hemotherapy* **2020**, *47* (6), 429–431.

(80) Chen, D. S.; Mellman, I. Oncology Meets Immunology: The Cancer-Immunity Cycle. *Immunity* **2013**, *39* (1), 1–10.

(81) Bulte, J. W. M.; Shakeri-Zadeh, A. In Vivo MRI Tracking of Tumor Vaccination and Antigen Presentation by Dendritic Cells. *Mol. Imaging Biol.* **2022**, *24* (2), 198–207.

(82) Liu, K. Dendritic Cells. *Encycl. Cell Biol.* **2016**, *3*, 741–749.

(83) Kerkar, S. P.; Restifo, N. P. Cellular Constituents of Immune Escape within the Tumor Microenvironment. *Cancer Res.* **2012**, *72* (13), 3125–3130.

(84) Sambi, M.; Bagheri, L.; Szewczuk, M. R. Current Challenges in Cancer Immunotherapy: Multimodal Approaches to Improve Efficacy and Patient Response Rates. *J. Oncol.* **2019**, *2019*, 4508794.

(85) Kalbasi, A.; Ribas, A. Tumour-Intrinsic Resistance to Immune Checkpoint Blockade. *Nat. Rev. Immunol.* **2020**, *20* (1), 25–39.

(86) Bronte, V.; Mocellin, S. Suppressive Influences in the Immune Response to Cancer. *J. Immunother.* **2009**, *32* (1), 1–11.

(87) Kim, S. K.; Cho, S. W. The Evasion Mechanisms of Cancer Immunity and Drug Intervention in the Tumor Microenvironment. *Front. Pharmacol.* **2022**, *13*, 868695.

(88) Cabral, H.; Kinoh, H.; Kataoka, K. Tumor-Targeted Nanomedicine for Immunotherapy. *Acc. Chem. Res.* **2020**, *53* (12), 2765–2776.

(89) Milling, L.; Zhang, Y.; Irvine, D. J. Delivering Safer Immunotherapies for Cancer. *Adv. Drug Deliv. Rev.* **2017**, *114*, 79–101.

(90) Amarante-Mendes, G. P.; Adjemian, S.; Branco, L. M.; Zanetti, L. C.; Weinlich, R.; Bortoluci, K. R. Pattern Recognition Receptors and the Host Cell Death Molecular Machinery. *Front. Immunol.* **2018**, *9*, 2379.

(91) O'Neill, L. A. J.; Golenbock, D.; Bowie, A. G. The History of Toll-like Receptors-Redefining Innate Immunity. *Nat. Rev. Immunol.* **2013**, *13* (6), 453–460.

(92) Sameer, A. S.; Nissar, S. Toll-Like Receptors (TLRs): Structure, Functions, Signaling, and Role of Their Polymorphisms in Colorectal Cancer Susceptibility. *Biomed Res. Int.* **2021**, *2021*, 1157023.

(93) Zakeri, A.; Russo, M. Dual Role of Toll-like Receptors in Human and Experimental Asthma

Models. *Front. Immunol.* **2018**, *9*, 1027.

(94) Van Herck, S.; De Geest, B. G. Nanomedicine-Mediated Alteration of the Pharmacokinetic Profile of Small Molecule Cancer Immunotherapeutics. *Acta Pharmacol. Sin.* **2020**, *41* (7), 881–894.

(95) Ignacio, B. J.; Albin, T. J.; Esser-Kahn, A. P.; Verdoes, M. Toll-like Receptor Agonist Conjugation: A Chemical Perspective. *Bioconjug. Chem.* **2018**, *29* (3), 587–603.

(96) Mancini, R. J.; Stutts, L.; Ryu, K. A.; Tom, J. K.; Esser-Kahn, A. P. Directing the Immune System with Chemical Compounds. *ACS Chem. Biol.* **2014**, *9* (5), 1075–1085.

(97) Kawai, T.; Akira, S. TLR Signaling. *Cell Death Differ.* **2006**, *13* (5), 816–825.

(98) Dias, M. L.; O'Connor, K. M.; Dempsey, E. M.; O'Halloran, K. D.; McDonald, F. B. Targeting the Toll-like Receptor Pathway as a Therapeutic Strategy for Neonatal Infection. *Am. J. Physiol. - Regul. Integr. Comp. Physiol.* **2021**, *321* (6), R879–R902.

(99) Bhagchandani, S.; Johnson, J. A.; Irvine, D. J. Evolution of Toll-like Receptor 7/8 Agonist Therapeutics and Their Delivery Approaches: From Antiviral Formulations to Vaccine Adjuvants. *Adv. Drug Deliv. Rev.* **2021**, *175*, 113803.

(100) Stickdorn, J.; Nuhn, L. Reactive-Ester Derived Polymer Nanogels for Cancer Immunotherapy. *Eur. Polym. J.* **2020**, *124* (September 2019), 109481.

(101) Howard, G. P.; Verma, G.; Ke, X.; Thayer, W. M.; Hamerly, T.; Baxter, V. K.; Lee, J. E.; Dinglasan, R. R.; Mao, H. Q. Critical Size Limit of Biodegradable Nanoparticles for Enhanced Lymph Node Trafficking and Paracortex Penetration. *Nano Res.* **2019**, *12* (4), 837–844.

(102) Grabbe, S.; Landfester, K.; Schuppan, D.; Barz, M.; Zentel, R. Nanoparticles and the Immune System: Challenges and Opportunities. *Nanomedicine* **2016**, *11* (20), 2621–2624.

(103) Moon, J. J.; Huang, B.; Irvine, D. J. Engineering Nano- and Microparticles to Tune Immunity. *Adv. Mater.* **2012**, *24* (28), 3724–3746.

(104) Wagner, A. M.; Spencer, D. S.; Peppas, N. A. Advanced Architectures in the Design of Responsive Polymers for Cancer Nanomedicine. *J. Appl. Polym. Sci.* **2018**, *135* (24), 46154.

(105) Fleige, E.; Quadir, M. A.; Haag, R. Stimuli-Responsive Polymeric Nanocarriers for the Controlled Transport of Active Compounds: Concepts and Applications. *Adv. Drug Deliv. Rev.* **2012**, *64* (9), 866–884.

(106) Wei, M.; Gao, Y.; Li, X.; Serpe, M. J. Stimuli-Responsive Polymers and Their Applications. *Polym. Chem.* **2017**, *8* (1), 127–143.

(107) Sun, X.; Agate, S.; Salem, K. S.; Lucia, L.; Pal, L. Hydrogel-Based Sensor Networks: Compositions, Properties, and Applications - A Review. *ACS Appl. Bio Mater.* **2021**, *4* (1), 140–162.

(108) Hu, J.; Zhang, G.; Liu, S. Enzyme-Responsive Polymeric Assemblies, Nanoparticles and Hydrogels. *Chem. Soc. Rev.* **2012**, *41* (18), 5933–5949.

(109) Park, J. B.; Lee, C. S.; Jang, J. H.; Ghim, J.; Kim, Y. J.; You, S.; Hwang, D.; Suh, P. G.; Ryu, S. H. Phospholipase Signalling Networks in Cancer. *Nat. Rev. Cancer* **2012**, *12* (11), 782–792.

(110) Fernandes, C.; Suares, D.; Yergeri, M. C. Tumor Microenvironment Targeted Nanotherapy. *Front. Pharmacol.* **2018**, *9*, 1230.

(111) Zhou, Q.; Zhang, L.; Yang, T. H.; Wu, H. Stimuli-Responsive Polymeric Micelles for Drug Delivery and Cancer Therapy. *Int. J. Nanomedicine* **2018**, *13*, 2921–2942.

(112) Bixenmann, L.; Stickdorn, J.; Nuhn, L. Amphiphilic Poly(Esteracetal)s as Dual PH-and Enzyme-Responsive Micellar Immunodrug Delivery Systems. *Polym. Chem.* **2020**, *11* (13), 2441–2456.

(113) Abed, H. F.; Abuwatfa, W. H.; Husseini, G. A. Redox-Responsive Drug Delivery Systems: A Chemical Perspective. *Nanomaterials* **2022**, *12* (18), 1–26.

(114) Moriarty-Craige, S. E.; Jones, D. P. Extracellular Thiols and Thiol/Disulfide Redox in Metabolism. *Annu. Rev. Nutr.* **2004**, *24*, 481–509.

(115) Scherger, M.; Pilger, Y. A.; Komforth, P.; Räder, H. J.; Nuhn, L. Reversible Polymer-Protein Functionalization by Stepwise Introduction of Amine-Reactive, Reductive-Responsive Self-Immolative End Groups onto RAFT-Derived Polymers. *ACS Biomater. Sci. Eng.* **2024**, *10* (1), 129–138.

(116) Guo, X.; Cheng, Y.; Zhao, X.; Luo, Y.; Chen, J.; Yuan, W. E. Advances in Redox-Responsive Drug Delivery Systems of Tumor Microenvironment. *J. Nanobiotechnology* **2018**, *16* (1), 1–10.

(117) Lai, T. C.; Cho, H.; Kwon, G. S. Reversibly Core Cross-Linked Polymeric Micelles with PH- and Reduction-Sensitivities: Effects of Cross-Linking Degree on Particle Stability, Drug Release Kinetics, and Anti-Tumor Efficacy. *Polym. Chem.* **2014**, *5* (5), 1650–1661.

(118) Klinker, K.; Schäfer, O.; Huesmann, D.; Bauer, T.; Capelôa, L.; Braun, L.; Stergiou, N.; Schinnerer, M.; Dirisala, A.; Miyata, K.; Osada, K.; Cabral, H.; Kataoka, K.; Barz, M. Secondary-Structure-Driven Self-Assembly of Reactive Polypept(o)Ides: Controlling Size, Shape, and Function of Core Cross-Linked Nanostructures. *Angew. Chemie - Int. Ed.* **2017**, *56* (32), 9608–9613.

(119) Ganesh, V. A.; Baji, A.; Ramakrishna, S. Smart Functional Polymers - A New Route towards Creating a Sustainable Environment. *RSC Adv.* **2014**, *4* (95), 53352–53364.

(120) Jiang, C.; Xu, G.; Gao, J. Stimuli-Responsive Macromolecular Self-Assembly. *Sustain.* **2022**, *14* (18), 11738.

(121) Sarwan, T.; Kumar, P.; Choonara, Y. E.; Pillay, V. Hybrid Thermo-Responsive Polymer Systems and Their Biomedical Applications. *Front. Mater.* **2020**, *7*, 73.

(122) Doberenz, F.; Zeng, K.; Willems, C.; Zhang, K.; Groth, T. Thermoresponsive Polymers and Their Biomedical Application in Tissue Engineering-A Review. *J. Mater. Chem. B* **2020**, *8* (4), 607–628.

(123) Seynhaeve, A. L. B.; Amin, M.; Haemmerich, D.; van Rhoon, G. C.; ten Hagen, T. L. M. Hyperthermia and Smart Drug Delivery Systems for Solid Tumor Therapy. *Adv. Drug Deliv. Rev.* **2020**, *163–164*, 125–144.

(124) Abulateefeh, S. R.; Spain, S. G.; Aylott, J. W.; Chan, W. C.; Garnett, M. C.; Alexander, C. Thermoresponsive Polymer Colloids for Drug Delivery and Cancer Therapy. *Macromol. Biosci.* **2011**, *11* (12), 1722–1734.

(125) Akimoto, J.; Nakayama, M.; Okano, T. Temperature-Responsive Polymeric Micelles for Optimizing Drug Targeting to Solid Tumors. *J. Control. Release* **2014**, *193*, 2–8.

(126) Bazban-Shotorbani, S.; Hasani-Sadrabadi, M. M.; Karkhaneh, A.; Serpooshan, V.; Jacob, K. I.; Moshaverinia, A.; Mahmoudi, M. Revisiting Structure-Property Relationship of PH-Responsive Polymers for Drug Delivery Applications. *J. Control. Release* **2017**, *253*, 46–63.

(127) Jazani, A. M.; Oh, J. K. Development and Disassembly of Single and Multiple Acid-Cleavable Block Copolymer Nanoassemblies for Drug Delivery. *Polym. Chem.* **2020**, *11* (17), 2934–2954.

(128) Gao, W.; Chan, J. M.; Farokhzad, O. C. Reviews PH-Responsive Nanoparticles for Drug Delivery. *Mol. Pharm.* **2010**, *7* (6), 1913–1920.

(129) Kanamala, M.; Wilson, W. R.; Yang, M.; Palmer, B. D.; Wu, Z. Mechanisms and Biomaterials in PH-Responsive Tumour Targeted Drug Delivery: A Review. *Biomaterials* **2016**, *85*, 152–167.

(130) Felber, A. E.; Dufresne, M. H.; Leroux, J. C. PH-Sensitive Vesicles, Polymeric Micelles, and Nanospheres Prepared with Polycarboxylates. *Adv. Drug Deliv. Rev.* **2012**, *64* (11), 979–992.

(131) Schmaljohann, D. Thermo- and PH-Responsive Polymers in Drug Delivery. *Adv. Drug Deliv. Rev.* **2006**, *58* (15), 1655–1670.

(132) Tong, R.; Tang, L.; Ma, L.; Tu, C.; Baumgartner, R.; Cheng, J. Smart Chemistry in Polymeric Nanomedicine. *Chem. Soc. Rev.* **2014**, *43* (20), 6982–7012.

(133) Kocak, G.; Tuncer, C.; Bütün, V. PH-Responsive Polymers. *Polym. Chem.* **2017**, *8* (1), 144–176.

(134) Mu, Y.; Gong, L.; Peng, T.; Yao, J.; Lin, Z. Advances in PH-Responsive Drug Delivery Systems. *OpenNano* **2021**, *5* (2021), 100031.

(135) Midoux, P.; Pichon, C.; Yaouanc, J. J.; Jaffrès, P. A. Chemical Vectors for Gene Delivery: A Current Review on Polymers, Peptides and Lipids Containing Histidine or Imidazole as Nucleic Acids Carriers. *Br. J. Pharmacol.* **2009**, *157* (2), 166–178.

(136) Behr, J.-P. The Proton Sponge:A Trick to Enter Cells the Viruses Did Not Exploit. *Chimia (Aarau).* **1997**, *51* (1), 34–36.

(137) Deirram, N.; Zhang, C.; Kermaniyan, S. S.; Johnston, A. P. R.; Such, G. K. PH-Responsive Polymer Nanoparticles for Drug Delivery. *Macromol. Rapid Commun.* **2019**, *40* (10), 1–23.

(138) Liu, B.; Thayumanavan, S. Substituent Effects on the PH Sensitivity of Acetals and Ketals and Their Correlation with Encapsulation Stability in Polymeric Nanogels. *J. Am. Chem. Soc.* **2017**, *139* (6), 2306–2317.

(139) Pang, X.; Jiang, Y.; Xiao, Q.; Leung, A. W.; Hua, H.; Xu, C. PH-Responsive Polymer-Drug Conjugates: Design and Progress. *J. Control. Release* **2016**, *222*, 116–129.

(140) Shao, Y.; Huang, W.; Shi, C.; Atkinson, S. T.; Luo, J. Reversibly Crosslinked Nanocarriers for On-Demand Drug Delivery in Cancer Treatment. *Ther. Deliv.* **2012**, *3* (12), 1409–1427.

(141) Heller, J.; Penhale, D. W. H.; Helwing, R. F. Preparation of Poly(Ortho Esters) by the Reaction of Diketene Acetals and Polyols. *J. Polym. Sci. Polym. Lett. Ed.* **1980**, *18* (9), 619–624.

(142) Fife, T. H. General Acid Catalysis of Acetal, Ketal, and Ortho Ester Hydrolysis. *Acc. Chem. Res.* **1972**, *5* (8), 264–272.

(143) Cordes, E. H.; Bull, H. G. Mechanism and Catalysis for Hydrolysis of Acetals, Ketals, and Ortho Esters. *Chem. Rev.* **1974**, *74* (5), 581–603.

(144) Ramasamy, T.; Ruttala, H. B.; Gupta, B.; Poudel, B. K.; Choi, H. G.; Yong, C. S.; Kim, J. O. Smart Chemistry-Based Nanosized Drug Delivery Systems for Systemic Applications: A Comprehensive Review. *J. Control. Release* **2017**, *258* (April), 226–253.

(145) Stickdorn, J.; Stein, L.; Arnold-Schild, D.; Hahlbrock, J.; Medina-Montano, C.; Bartneck, J.; Ziß, T.; Montermann, E.; Kappel, C.; Hobernik, D.; Haist, M.; Yurugi, H.; Raabe, M.; Best, A.; Rajalingam, K.; Radsak, M. P.; David, S. A.; Koynov, K.; Bros, M.; Grabbe, S.; Schild, H.; Nuhn, L. Systemically Administered TLR7/8 Agonist and Antigen-Conjugated Nanogels Govern Immune Responses against Tumors. *ACS Nano* **2022**, *16* (3), 4426–4443.

(146) Sonawane, S. J.; Kalhapure, R. S.; Govender, T. Hydrazone Linkages in PH Responsive Drug Delivery Systems. *Eur. J. Pharm. Sci.* **2017**, *99*, 45–65.

(147) Belowich, M. E.; Stoddart, J. F. Dynamic Imine Chemistry. *Chem. Soc. Rev.* **2012**, *41* (6), 2003–2024.

(148) Bae, Y.; Nishiyama, N.; Kataoka, K. In Vivo Antitumor Activity of the Folate-Conjugated PH-Sensitive Polymeric Micelle Selectively Releasing Adriamycin in the Intracellular Acidic Compartments. *Bioconjug. Chem.* **2007**, *18* (4), 1131–1139.

(149) Wahbeh, J.; Milkowski, S. The Use of Hydrazones for Biomedical Applications. *SLAS Technol.* **2019**, *24* (2), 161–168.

(150) Van Driessche, A.; Kocere, A.; Everaert, H.; Nuhn, L.; Van Herck, S.; Griffiths, G.; Fenaroli, F.; De Geest, B. G. PH-Sensitive Hydrazone-Linked Doxorubicin Nanogels via Polymeric-Activated

Ester Scaffolds: Synthesis, Assembly, and in Vitro and in Vivo Evaluation in Tumor-Bearing Zebrafish. *Chem. Mater.* **2018**, *30* (23), 8587–8596.

(151) Patil, R. D.; Adimurthy, S. Catalytic Methods for Imine Synthesis. *Asian J. Org. Chem.* **2013**, *2* (9), 726–744.

(152) Ciaccia, M.; Di Stefano, S. Mechanisms of Imine Exchange Reactions in Organic Solvents. *Org. Biomol. Chem.* **2015**, *13* (3), 646–654.

(153) Zhang, Z.; He, C.; Chen, X. Hydrogels Based on PH-Responsive Reversible Carbon-Nitrogen Double-Bond Linkages for Biomedical Applications. *Mater. Chem. Front.* **2018**, *2* (10), 1765–1778.

(154) Hu, X.; Jazani, A. M.; Oh, J. K. Recent Advances in Development of Imine-Based Acid-Degradable Polymeric Nanoassemblies for Intracellular Drug Delivery. *Polymer (Guildf).* **2021**, *230* (May), 124024.

(155) Kölmel, D. K.; Kool, E. T. Oximes and Hydrazones in Bioconjugation: Mechanism and Catalysis. *Chem. Rev.* **2017**, *117* (15), 10358–10376.

(156) Kalia, J.; Raines, R. T. Hydrolytic Stability of Hydrazones and Oximes. *Angew. Chemie - Int. Ed.* **2008**, *47* (39), 7523–7526.

(157) Collins, J.; Xiao, Z.; Müllner, M.; Connal, L. A. The Emergence of Oxime Click Chemistry and Its Utility in Polymer Science. *Polym. Chem.* **2016**, *7* (23), 3812–3826.

(158) Zhuo, S.; Zhang, F.; Yu, J.; Zhang, X.; Yang, G.; Liu, X. PH-Sensitive Biomaterials for Drug Delivery. *Molecules* **2020**, *25* (23), 1–20.

(159) Jin, Y.; Song, L.; Su, Y.; Zhu, L.; Pang, Y.; Qiu, F.; Tong, G.; Yan, D.; Zhu, B.; Zhu, X. Oxime Linkage: A Robust Tool for the Design of PH-Sensitive Polymeric Drug Carriers. *Biomacromolecules* **2011**, *12* (10), 3460–3468.

(160) Wang, J.; Wang, X.; Yan, G.; Fu, S.; Tang, R. PH-Sensitive Nanogels with Ortho Ester Linkages Prepared via Thiol-Ene Click Chemistry for Efficient Intracellular Drug Release. *J. Colloid Interface Sci.* **2017**, *508*, 282–290.

(161) Cheng, J.; Ji, R.; Gao, S. J.; Du, F. S.; Li, Z. C. Facile Synthesis of Acid-Labile Polymers with Pendent Ortho Esters. *Biomacromolecules* **2012**, *13* (1), 173–179.

(162) Masson, C.; Garinot, M.; Mignet, N.; Wetzer, B.; Mailhe, P.; Scherman, D.; Bessodes, M. PH-Sensitive PEG Lipids Containing Orthoester Linkers: New Potential Tools for Nonviral Gene Delivery. *J. Control. Release* **2004**, *99* (3), 423–434.

(163) Binauld, S.; Stenzel, M. H. Acid-Degradable Polymers for Drug Delivery: A Decade of Innovation. *Chem. Commun.* **2013**, *49* (21), 2082–2102.

(164) Tang, R.; Ji, W.; Wang, C. Amphiphilic Block Copolymers Bearing Ortho Ester Side-Chains: PH-Dependent Hydrolysis and Self-Assembly in Water. *Macromol. Biosci.* **2010**, *10* (2), 192–201.

(165) Bruyère, H.; Westwell, A. D.; Jones, A. T. Tuning the PH Sensitivities of Orthoester Based Compounds for Drug Delivery Applications by Simple Chemical Modification. *Bioorganic Med. Chem. Lett.* **2010**, *20* (7), 2200–2203.

(166) Wang, B.; Van Herck, S.; Chen, Y.; Bai, X.; Zhong, Z.; Deswarte, K.; Lambrecht, B. N.; Sanders, N. N.; Lienenklaus, S.; Scheeren, H. W.; David, S. A.; Kiessling, F.; Lammers, T.; De Geest, B. G.; Shi, Y. Potent and Prolonged Innate Immune Activation by Enzyme-Responsive Imidazoquinoline TLR7/8 Agonist Prodrug Vesicles. *J. Am. Chem. Soc.* **2020**, *142* (28), 12133–12139.

(167) Paramonov, S. E.; Bachelder, E. M.; Beaudette, T. T.; Standley, S. M.; Lee, C. C.; Dashe, J.; Fréchet, J. M. J. Fully Acid-Degradable Biocompatible Polyacetal Microparticles for Drug Delivery.

Bioconjug. Chem. **2008**, *19* (4), 911–919.

(168) Maier, K.; Wagner, E. Acid-Labile Traceless Click Linker for Protein Transduction. *J. Am. Chem. Soc.* **2012**, *134* (24), 10169–10173.

(169) Butler, P. J.; Harris, J. I.; Hartley, B. S.; Lebeman, R. The Use of Maleic Anhydride for the Reversible Blocking of Amino Groups in Polypeptide Chains. *Biochem. J.* **1969**, *112* (5), 679–689.

(170) Aldersley, M. F.; Kirby, A. J.; Lancaster, P. W.; McDonald, R. S.; Smith, C. R. Intramolecular Catalysis of Amide Hydrolysis by the Carboxy-Group. Rate Determining Proton Transfer from External General Acids in the Hydrolysis of Substituted Maleamic Acids. *J. Chem. Soc. Perkin Trans. 2* **1974**, No. 12, 1487–1495.

(171) Nieto, M. A.; Palacián, E. Effects of Temperature and PH on the Regeneration of the Amino Groups of Ovalbumin after Modification with Citraconic and Dimethylmaleic Anhydrides. *Biochim. Biophys. Acta (BBA)/Protein Struct. Mol.* **1983**, *749* (2), 204–210.

(172) Palacián, E.; González, P. J.; Piñeiro, M.; Hernández, F. Dicarboxylic Acid Anhydrides as Dissociating Agents of Protein-Containing Structures. *Mol. Cell. Biochem.* **1990**, *97* (2), 101–111.

(173) Spanedda, M. V.; Bourel-Bonnet, L. Cyclic Anhydrides as Powerful Tools for Bioconjugation and Smart Delivery. *Bioconjug. Chem.* **2021**, *32* (3), 482–496.

(174) Su, S.; Du, F. S.; Li, Z. C. Synthesis and PH-Dependent Hydrolysis Profiles of Mono- and Dialkyl Substituted Maleamic Acids. *Org. Biomol. Chem.* **2017**, *15* (39), 8384–8392.

(175) Matysiak, B. M.; Monreal Santiago, G.; Otto, S. Teaching an Old Compound New Tricks: Reversible Transamidation in Maleamic Acids. *Chem. - A Eur. J.* **2022**, *28* (40), e20220143.

(176) Su, S.; Wang, Y. Y.; Du, F. S.; Lu, H.; Li, Z. C. Dynamic Covalent Bond-Assisted Programmed and Traceless Protein Release: High Loading Nanogel for Systemic and Cytosolic Delivery. *Adv. Funct. Mater.* **2018**, *28* (48), 1805287.

(177) Zheng, N.; Xu, Y.; Zhao, Q.; Xie, T. Dynamic Covalent Polymer Networks: A Molecular Platform for Designing Functions beyond Chemical Recycling and Self-Healing. *Chem. Rev.* **2021**, *121* (3), 1716–1745.

(178) Zhang, X.; Zhang, K.; Haag, R. Multi-Stage, Charge Conversional, Stimuli-Responsive Nanogels for Therapeutic Protein Delivery. *Biomater. Sci.* **2015**, *3* (11), 1487–1496.

(179) Park, H.; Suh, J.; Lee, S. Ab Initio Studies of the Intramolecular Amide Hydrolysis in N-Methylmaleamic Acids. *J. Mol. Struct. THEOCHEM* **1999**, *490* (1–3), 47–54.

(180) Du, J. Z.; Li, H. J.; Wang, J. Tumor-Acidity-Cleavable Maleic Acid Amide (TACMAA): A Powerful Tool for Designing Smart Nanoparticles to Overcome Delivery Barriers in Cancer Nanomedicine. *Acc. Chem. Res.* **2018**, *51* (11), 2848–2856.

(181) Kang, S.; Kim, Y.; Song, Y.; Choi, J. U.; Park, E.; Choi, W.; Park, J.; Lee, Y. Comparison of PH-Sensitive Degradability of Maleic Acid Amide Derivatives. *Bioorganic Med. Chem. Lett.* **2014**, *24* (10), 2364–2367.

(182) Cai, J.; Wu, Z. Solvent and Substituent Effects on The Intramolecular Amide Hydrolysis of N-Methylmaleamic Acid. *J. Theor. Comput. Chem.* **2009**, *8* (6), 1217–1226.

(183) Baumann, M. E.; Bosshard, H. *Dimethyl-Maleic Anhydride, A New Synthesis and Versatile Uses of an Old Compound*, Second Edi.; International Union of Pure and Applied Chemistry, 1979; Vol. 264, pp 85-93.

(184) Zhang, A.; Yao, L.; An, M. Reversing the Undesirable PH-Profile of Doxorubicin: Via Activation of a Di-Substituted Maleamic Acid Prodrug at Tumor Acidity. *Chem. Commun.* **2017**, *53* (95), 12826–12829.

(185) Dal Corso, A.; Pignataro, L.; Belvisi, L.; Gennari, C. Innovative Linker Strategies for Tumor-Targeted Drug Conjugates. *Chem. - A Eur. J.* **2019**, *25* (65), 14740–14757.

(186) Arvizo, R. R.; Miranda, O. R.; Thompson, M. A.; Pabelick, C. M.; Bhattacharya, R.; David Robertson, J.; Rotello, V. M.; Prakash, Y. S.; Mukherjee, P. Effect of Nanoparticle Surface Charge at the Plasma Membrane and Beyond. *Nano Lett.* **2010**, *10* (7), 2543–2548.

(187) Mailänder, V.; Landfester, K. Interaction of Nanoparticles with Cells. *Biomacromolecules* **2009**, *10* (9), 2379–2400.

(188) Ma, B. A.; Sun, C. Y. Tumor PH-Triggered "Charge Conversion" Nanocarriers with on-Demand Drug Release for Precise Cancer Therapy. *J. Mater. Chem. B* **2020**, *8* (40), 9351–9361.

(189) Du, J. Z.; Mao, C. Q.; Yuan, Y. Y.; Yang, X. Z.; Wang, J. Tumor Extracellular Acidity-Activated Nanoparticles as Drug Delivery Systems for Enhanced Cancer Therapy. *Biotechnol. Adv.* **2014**, *32* (4), 789–803.

(190) Han, S. S.; Li, Z. Y.; Zhu, J. Y.; Han, K.; Zeng, Z. Y.; Hong, W.; Li, W. X.; Jia, H. Z.; Liu, Y.; Zhuo, R. X.; Zhang, X. Z. Dual-PH Sensitive Charge-Reversal Polypeptide Micelles for Tumor-Triggered Targeting Uptake and Nuclear Drug Delivery. *Small* **2015**, *11* (21), 2543–2554.

(191) Lyu, M.; Yazdi, M.; Lin, Y.; Höhn, M.; Lächelt, U.; Wagner, E. Receptor-Targeted Dual PH-Triggered Intracellular Protein Transfer. *ACS Biomater. Sci. Eng.* **2024**, *10* (1), 99–114.

(192) Tao, A.; Huang, G. Lo; Igarashi, K.; Hong, T.; Liao, S.; Stellacci, F.; Matsumoto, Y.; Yamasoba, T.; Kataoka, K.; Cabral, H. Polymeric Micelles Loading Proteins through Concurrent Ion Complexation and PH-Cleavable Covalent Bonding for In Vivo Delivery. *Macromol. Biosci.* **2020**, *20* (1), 1–11.

(193) Lee, Y.; Fukushima, S.; Bae, Y.; Hiki, S.; Ishii, T.; Kataoka, K. A Protein Nanocarrier from Charge-Conversion Polymer in Response to Endosomal PH. *J. Am. Chem. Soc.* **2007**, *129* (17), 5362–5363.

(194) Lang, S.; Tan, Z.; Wu, X.; Huang, X. Synthesis of Carboxy-Dimethylmaleic Amide Linked Polymer Conjugate Based Ultra-PH-Sensitive Nanoparticles for Enhanced Antitumor Immunotherapy. *ACS Macro Lett.* **2020**, *9* (11), 1693–1699.

(195) He, N.; Chen, Z.; Yuan, J.; Zhao, L.; Chen, M.; Wang, T.; Li, X. Tumor PH-Responsive Release of Drug-Conjugated Micelles from Fiber Fragments for Intratumoral Chemotherapy. *ACS Appl. Mater. Interfaces* **2017**, *9* (38), 32534–32544.

(196) Wang, Q.; Wang, C.; Li, S.; Xiong, Y.; Wang, H.; Li, Z.; Wan, J.; Yang, X.; Li, Z. Influence of Linkers within Stimuli-Responsive Prodrugs on Cancer Therapy: A Case of Five Doxorubicin Dimer-Based Nanoparticles. *Chem. Mater.* **2022**, *34* (5), 2085–2097.

(197) Chen, J.; Ding, J.; Zhang, Y.; Xiao, C.; Zhuang, X.; Chen, X. Polyion Complex Micelles with Gradient PH-Sensitivity for Adjustable Intracellular Drug Delivery. *Polym. Chem.* **2015**, *6* (3), 397–405.

(198) Li, D.; Ma, Y.; Du, J.; Tao, W.; Du, X.; Yang, X.; Wang, J. Tumor Acidity/NIR Controlled Interaction of Transformable Nanoparticle with Biological Systems for Cancer Therapy. *Nano Lett.* **2017**, *17* (5), 2871–2878.

(199) Fang, Y.; Xue, J.; Gao, S.; Lu, A.; Yang, D.; Jiang, H.; He, Y.; Shi, K. Cleavable PEGylation: A Strategy for Overcoming the "PEG Dilemma" in Efficient Drug Delivery. *Drug Deliv.* **2017**, *24* (0), 22–32.

(200) Sui, H.; Gao, Z.; Guo, J.; Wang, Y.; Yuan, J.; Hao, J.; Dong, S.; Cui, J. Dual PH-Responsive Polymer Nanogels with a Core-Shell Structure for Improved Cell Association. *Langmuir* **2019**, *35* (51), 16869–16875.

(201) Ding, Y.; Du, C.; Qian, J.; Zhou, L.; Su, Y.; Zhang, R.; Dong, C. M. Tumor PH and Intracellular

Reduction Responsive Polypeptide Nanomedicine with a Sheddable PEG Corona and a Disulfide-Cross-Linked Core. *Polym. Chem.* **2018**, *9* (25), 3488–3498.

(202) Sun, C. Y.; Liu, Y.; Du, J. Z.; Cao, Z. T.; Xu, C. F.; Wang, J. Facile Generation of Tumor-PH-Labile Linkage-Bridged Block Copolymers for Chemotherapeutic Delivery. *Angew. Chemie - Int. Ed.* **2016**, *55* (3), 1010–1014.

(203) Gao, Z.; Zhang, Z.; Guo, J.; Hao, J.; Zhang, P.; Cui, J. Polypeptide Nanoparticles with PH-Sheddable PEGylation for Improved Drug Delivery. *Langmuir* **2020**, *36* (45), 13656–13662.

(204) Tang, S.; Meng, Q.; Sun, H.; Su, J.; Yin, Q.; Zhang, Z.; Yu, H.; Chen, L.; Gu, W.; Li, Y. Dual PH-Sensitive Micelles with Charge-Switch for Controlling Cellular Uptake and Drug Release to Treat Metastatic Breast Cancer. *Biomaterials* **2017**, *114*, 44–53.

(205) Suma, T.; Cui, J.; Müllner, M.; Ju, Y.; Guo, J.; Hu, M.; Caruso, F. Generalizable Strategy for Engineering Protein Particles with PH-Triggered Disassembly and Recoverable Protein Functionality. *ACS Macro Lett.* **2015**, *4* (2), 160–164.

MOTIVATION AND OBJECTIVES

The progress of nano-sized drug delivery systems in the field of nanomedicine has accelerated significantly and presently holds crucial functions in several therapeutic methods.[1] At the latest, the Covid-19 pandemic clearly illustrated the great potential of nano-based therapeutics and contributed to the growing importance of nanomedicines in global healthcare.[2,3] The application of nanocarriers provides unique features to improve the pharmacokinetic and pharmacodynamic profile of small molecular drugs, while reducing detrimental side reactions and the risk of systemic toxicities. Moreover, nanocarriers can focus the biodistribution of conjugated drugs and facilitate a targeted delivery across biological barriers, thereby reducing undesired off-target effects.[4,5] In this respect, the design of novel macromolecular delivery systems needs to be specifically adapted to the therapeutic applications and characteristics of the cargo.[6]

In recent years, immunotherapy has introduced a promising perspective to treat severe diseases and achieved great clinical successes, especially cancer therapy. Thereby, cancer immunotherapy centers the suppression or activation of the immune system to eliminate tumorous cells, while protecting healthy cells. The stimulation of multiple coordinated signaling pathways elicits long-lasting and tissue-specific responses.[7,8] Especially the combination of nanomedicine and cancer immunotherapy offers new pathways towards individualized and improved cancer treatment. Nano-scaled carrier systems with sizes of 1-100(0) nm enable the selective delivery of anticancer drugs, genes, or immune modulatory small molecules to the main targets in cancer nano-immunotherapy. Notable immunomodulatory approaches encompass the evoked apoptosis of cancer cells, the modulation of the tumor immune microenvironment and targeting the peripheral immune system to promote precise anticancer immune responses.[9–11] Despite certain advancements in patients, nano-immunotherapy encounters a complex set of obstacles attenuating efficacious therapeutic responses.[12]

In this regard, the development of new carrier systems with controlled delivery properties should be investigated that are able to overcome different biological barriers and enhance the therapeutic effect at the target site. Stimuli-responsive systems gained an increasing attention in the field of advanced materials and yielded novel carrier systems capable of dynamically adjusting their physical and chemical properties dependent on their environment.[13,14] The versatile design of smart drug delivery systems with tailor-made functionalities should exhibit beneficial responses to exogenous or endogenous stimuli in order to precisely release the conjugated or encapsulated drugs at the desired site of action.[13,15,16]

Among the variety of stimuli that can be applied, (patho-)physiological pH gradients are one of the most interesting endogenous triggers for controlled drug delivery. Considering the pH variations within the human body, the mild tumor microenvironment (pH ~ 6.5-6.9) as well as endosomal intracellular compartments (pH ~ 5-6) may stimulate a highly controlled and localized drug release of conjugated small molecules, making them a promising target in nano-immunotherapy.[17–19] In general, the design of new pH-sensitive macromolecular carrier systems can be achieved by the synthesis of functional polymers that change their polarity at varying pH values. Alternatively, they can benefit from the incorporation of pH-degradable groups, for instance by post-polymerization modifications.[20,21] Interestingly, dimethylmaleic anhydride-based motifs offer a high pH sensitivity (pH ~ 5.5-6.8) and fast release of conjugated small molecules under mild conditions without the formation of undesired by-products. Due to their intrinsic reactivity, these structures can directly conjugate nucleophilic amines affording a reversible charge reversion for the positively charged amines into negatively charged carboxylates.[16,22,23] Moreover, the pH-sensitive release profile of maleic acid amide derivates can be fine-tuned through the variation of adjacent substituents to the *cis*-double bond, making them a powerful structure for the design of new pH-responsive carrier systems in cancer immunotherapy.[24–26]

This thesis delves into the development and investigation of novel functional polymers and their capabilities as stimuli-responsive macromolecular carrier platforms for the precise delivery of immune stimulatory small molecules. In this respect, 2-propionic-3-methylmaleic anhydride-based polymers are synthesized and characterized as pH-sensitive carrier systems and micellar compartments in nanomedicine.

The first chapter of this thesis includes the synthesis of a new pH-sensitive methacrylamide-based polymer with pendant 2-propionic-3-methylmaleic anhydride groups and its initial application in immunodrug delivery. Thus far, the primary application of dimethylmaleic anhydride-based structures has mainly focused on the generation of functional linker systems[23] and the subsequent incorporation into macromolecular structures.[25,27,28] However, direct polymerization of dimethylmaleic anhydride monomers has yet not been achieved and presents an attractive strategy for the facile generation of advanced carrier systems. Followingly, a polymerizable propionic methyl maleic anhydride methacrylamide monomer is introduced and examined for its exclusive methacrylamide conversion under RAFT conditions.[29] By considering the pH-sensitive postmodification of the stable 2-propionic-3-methylmaleic anhydride side groups, various chemical or biological structures can be incorporated to the polymer systems. In this respect, the pH-reversible conjugation of primary or secondary

amine-bearing entities is evaluated and fine-tuned to generate fully hydrophilic stimuli-responsive polymers. Additionally, a novel immune stimulatory drug can be formulated and conjugated to the macromolecular carrier system to exploit the beneficial contribution of the installed pH sensitivity of the polymers in immunotherapy. The initial impact of the pH-sensitive carrier system is carefully investigated by *in vitro* studies on reporter cells as well as primary immune cells.

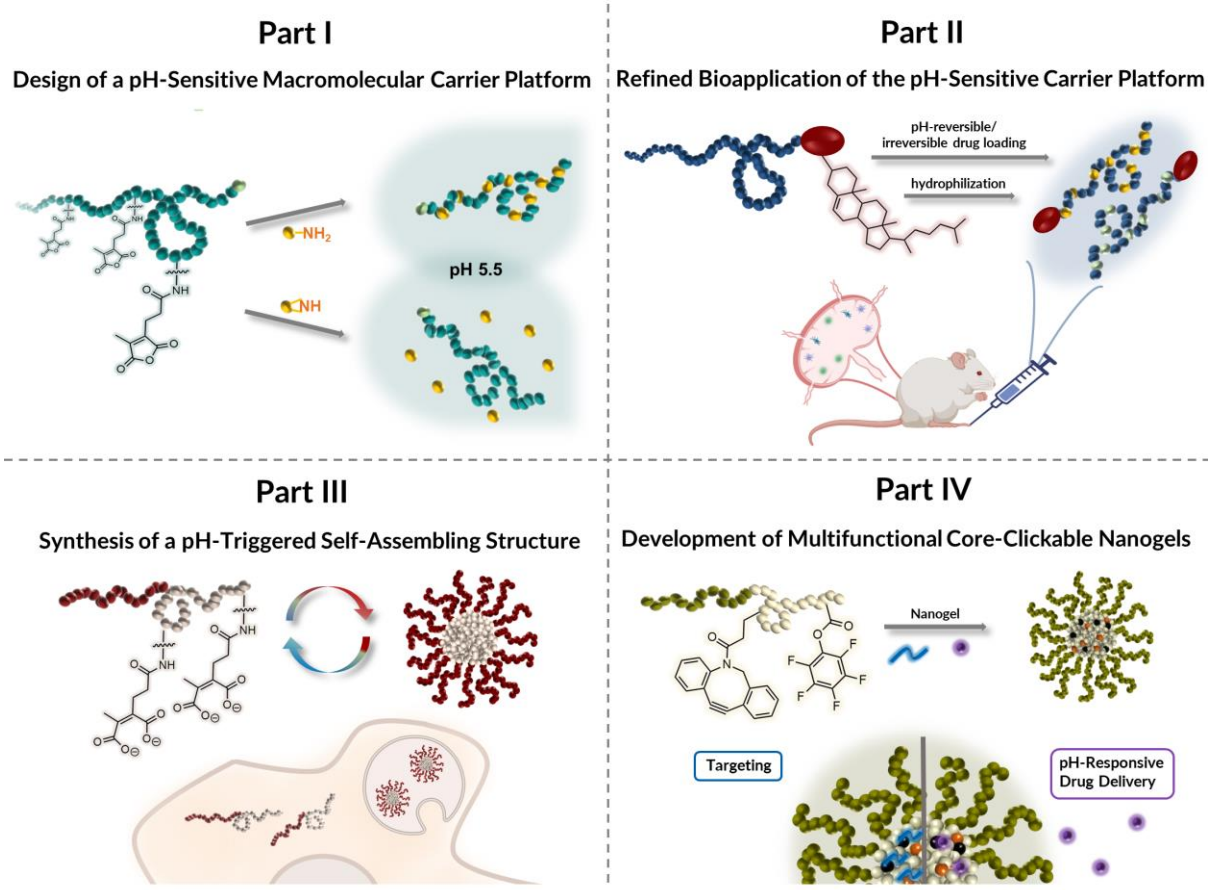

Figure 1. Graphical abstract demonstrating the objectives of this thesis ranging from the development of dimethylmaleic anhydride-based pH-sensitive macromolecular carrier platforms for cancer immunotherapy to the formulations of pH-triggered micellar compartments insight cells and the investigation of pH-responsive DBCO-modified nanogels as smart drug delivery systems. This Figure is partially created with BioRender.com.

The second part covers the enhancement of the novel pH-sensitive methacrylamide-based polymer system to a controlled *in vivo* stimulation of antigen-presenting cells (APCs) in the draining lymph nodes. Majority of the successful anti-cancer immune responses depend on an increased activation of APCs and cytotoxic T-cells *via* an effective delivery of immune stimulatory drugs to the lymphatic system.[7,30] On this account, cholesteryl-modified structures should be developed as lymphatic targeting system *via* albumin-hitchhiking processes. Various approaches have already demonstrated an improved immunotherapeutic treatment by

applying this endogenous trafficking pathway of albumin through the lymphatic system.[31–33] In this respect, a new cholesterol chain transfer agents (chol-CTA) is designed and applied during controlled radical polymerization of the propionic methyl maleic anhydride methacrylamide monomer. The implementation of the cholesteryl-unit to the pH-sensitive macromolecular carrier platform should increase the cellular uptake[34,35] and lymphatic targeting of the polymer. To explore the potential of the carrier system to effectively stimulate an immune response *in vitro* and *in vivo*, post-polymerization modification needs to be applied for reversible or irreversible conjugation of immune stimulatory drugs and dyes for monitoring. Additionally, the cholesteryl-linked polymer should be compared to the similar carrier system without cholesterol in order to evaluate the beneficial impact of the advanced polymer structure on macrophage reporter cells and primary dendritic cells *in vitro* as well as in draining lymph nodes of reporter mice *in vivo*.

In the third chapter, 2-propionic-3-methylmaleic anhydride-functionalized block copolymers are synthesized and employed as a pH-triggered self-assembling structure to form reversible micellar compartments insight cells. As intracellular pH variations can induce the alteration of polymers surface activity, chain conformation, solubility, charge and configuration[21,36], properties of the 2-propionic-3-methylmaleic anhydride-functionalized block copolymer can be controllably exploited in biological media. Thus, it is crucial to conduct a thorough analysis of these structures. After RAFT polymerization of the propionic methyl maleic anhydride methacrylamide monomers onto mPEG-based macro-CTAs, the resulting block copolymers provide a reversible pH-dependent self-assembly behavior both before and after amine modification in aqueous media. Furthermore, the self-assembly properties can be investigated inside cells, too. For that purpose, covalent fluorescent dye labelling can be selected to follow the polymers insight living cells and further investigate their self-assembly *via* Förster/Fluorescence Resonance Energy Transfer (FRET) strategies. Real-time analyses of molecular modifications and interactions can be traced with various quantitative FRET tools on cellular levels.[37–39] Based on the pH sensitivity profile of the 2-propionic-3-methylmaleic anhydride-functionalized block copolymer, FRET analyses can identify reversible micellar structures as potential new intracellular compartments and their localization inside acidic endolysosomes can be verified by correlative light electron microscopies (CLEM).

Chapter four covers the development of a new DBCO core-functionalized nanogel a as smart clickable carrier system for the implementation of targeting units or pH-reversible immunodrug conjugation. Most immunostimulatory adjuvants leak from their carrier and afford a rapid systemic biodistribution that exceeds the desired immunological effects. The covalent

attachment of targeting structures to nanocarriers as well as the reversible incorporation of small molecular immunostimulatory adjuvants can facilitate their controlled delivery and minimize their risk of toxicity.[40,41] The advancement of promsing nanogel-based carrier systems with core-clickable functional structures can benefit from the fast biorthogonal conjugation of azide-bearing structures and prevent a prolongated stimulation of the immune system.[41–44] In this regard, amphiphilic block copolymers based on methoxy tri(ethylene glycol) methacrylate (mTEGMA) and reactive ester pentafluorophenyl methacrylate (PFPMA) can be deployed as a macromolecular platform, sensitive for the versatile conjugation of amine-bearing structures. To this aim, DBCO-PEG_4-amine units can further be conjugated onto the block copolymer followed by conversion into fully hydrophilic and core-crosslinked nanogels. The impact of incorporated DBCO-units to the size, stability and further attachment of azide-functionalized structures is evaluated and compared to nanogels without DBCO. Trimannosylation, renowned for its high specificity, offers a promising approach for selectively targeting immune cells that highly express mannose-binding receptors, including macrophages or dendritic cells.[45,46] Thus, azide-trimannose conjugation to the DBCO nanogels is realized and the ability for controlled targeting is characterized *in vitro*. While targeting should remain irreversibly, the carrier system should be evaluated for a pH-reversible attachment of small molecular drugs by an azide-containing 2-propionic-3-methylmaleic anhydride linker. Subsequently, cell uptake and receptor stimulation can be analyzed *in vitro*.

In the last chapter the pH-sensitive profile of the bifunctional 2-propionic-3-methylmaleic anhydride linkers is further investigated towards their utilization in nanomedicine. While dimethylmaleic anhydride-based structures provide advantageous properties to molecular drugs, biomolecules or nanocarriers, the application to primary amines affords several limitations.[24,47–49] Based on the observations of the linker system described in chapter four, the pH-reversible conjugation of several primary and secondary amines should be explored. For this purpose, amidations of the azide-functional 2-propionic-3-methylmaleic anhydride linkers are conducted under different reaction conditions and detailed analysis will evaluate their pH reversibility and suitability in nanomedicine.

Overall, this thesis has the objective to design new 2-propionic-3-methylmaleic anhydride-based macromolecular carrier platforms for the pH-sensitive delivery of small molecular drugs or targeting units towards advancing the development of future nanocarrier-based treatments in cancer immunotherapy.

References

(1) Russell, L. M.; Liu, C. H.; Grodzinski, P. Nanomaterials Innovation as an Enabler for Effective Cancer Interventions. *Biomaterials* **2020**, *242* (October 2019), 119926.

(2) Germain, M.; Caputo, F.; Metcalfe, S.; Tosi, G.; Spring, K.; Aslund, A. K. O.; Pottier, A.; Schiffelers, R.; Geccaldi, A.; Schmid, R. Delivering the Power of Nanomedicine to Patients Today. *J. Control. Release* **2020**, *326* (January), 164–171.

(3) Vahedifard, F.; Chakravarthy, K. Nanomedicine for COVID-19: The Role of Nanotechnology in the Treatment and Diagnosis of COVID-19. *Emergent Mater.* **2021**, *4* (1), 75–99.

(4) Wicki, A.; Witzigmann, D.; Balasubramanian, V.; Huwyler, J. Nanomedicine in Cancer Therapy: Challenges, Opportunities, and Clinical Applications. *J. Control. Release* **2015**, *200*, 138–157.

(5) Alonso, M. J. Nanomedicines for Overcoming Biological Barriers. *Biomed. Pharmacother.* **2004**, *58* (3), 168–172.

(6) Cho, K.; Wang, X.; Nie, S.; Chen, Z.; Shin, D. M. Therapeutic Nanoparticles for Drug Delivery in Cancer. *Clin. Cancer Res.* **2008**, *14* (5), 1310–1316.

(7) Song, W.; Musetti, S. N.; Huang, L. Nanomaterials for Cancer Immunotherapy. *Biomaterials* **2017**, *148*, 16–30.

(8) Shields, C. W.; Wang, L. L. W.; Evans, M. A.; Mitragotri, S. Materials for Immunotherapy. *Adv. Mater.* **2020**, *32* (13), 1–56.

(9) Cabral, H.; Kataoka, K. Progress of Drug-Loaded Polymeric Micelles into Clinical Studies. *J. Control. Release* **2014**, *190*, 465–476.

(10) Talelli, M.; Barz, M.; Rijcken, C. J. F.; Kiessling, F.; Hennink, W. E.; Lammers, T. Core-Crosslinked Polymeric Micelles: Principles, Preparation, Biomedical Applications and Clinical Translation. *Nano Today* **2015**, *10* (1), 93–117.

(11) Shi, Y.; Lammers, T. Combining Nanomedicine and Immunotherapy. *Acc. Chem. Res.* **2019**, *52* (6), 1543–1554.

(12) Blanco, E.; Shen, H.; Ferrari, M. Principles of Nanoparticle Design for Overcoming Biological Barriers to Drug Delivery. *Nat. Biotechnol.* **2015**, *33* (9), 941–951.

(13) Wagner, A. M.; Spencer, D. S.; Peppas, N. A. Advanced Architectures in the Design of Responsive Polymers for Cancer Nanomedicine. *J. Appl. Polym. Sci.* **2018**, *135* (24).

(14) Wei, M.; Gao, Y.; Li, X.; Serpe, M. J. Stimuli-Responsive Polymers and Their Applications. *Polym. Chem.* **2017**, *8* (1), 127–143.

(15) Schattling, P.; Jochum, F. D.; Theato, P. Multi-Stimuli Responsive Polymers-the All-in-One Talents. *Polym. Chem.* **2014**, *5* (1), 25–36.

(16) Fleige, E.; Quadir, M. A.; Haag, R. Stimuli-Responsive Polymeric Nanocarriers for the Controlled Transport of Active Compounds: Concepts and Applications. *Adv. Drug Deliv. Rev.* **2012**, *64* (9), 866–884.

(17) Tong, R.; Tang, L.; Ma, L.; Tu, C.; Baumgartner, R.; Cheng, J. Smart Chemistry in Polymeric Nanomedicine. *Chem. Soc. Rev.* **2014**, *43* (20), 6982–7012.

(18) Bazban-Shotorbani, S.; Hasani-Sadrabadi, M. M.; Karkhaneh, A.; Serpooshan, V.; Jacob, K. I.; Moshaverinia, A.; Mahmoudi, M. Revisiting Structure-Property Relationship of PH-Responsive Polymers for Drug Delivery Applications. *J. Control. Release* **2017**, *253*, 46–63.

(19) Felber, A. E.; Dufresne, M. H.; Leroux, J. C. PH-Sensitive Vesicles, Polymeric Micelles, and

Nanospheres Prepared with Polycarboxylates. *Adv. Drug Deliv. Rev.* **2012**, *64* (11), 979–992.

(20) Deirram, N.; Zhang, C.; Kermaniyan, S. S.; Johnston, A. P. R.; Such, G. K. PH-Responsive Polymer Nanoparticles for Drug Delivery. *Macromol. Rapid Commun.* **2019**, *40* (10), 1–23.

(21) Kocak, G.; Tuncer, C.; Bütün, V. PH-Responsive Polymers. *Polym. Chem.* **2017**, *8* (1), 144–176.

(22) Spanedda, M. V.; Bourel-Bonnet, L. Cyclic Anhydrides as Powerful Tools for Bioconjugation and Smart Delivery. *Bioconjug. Chem.* **2021**, *32* (3), 482–496.

(23) Maier, K.; Wagner, E. Acid-Labile Traceless Click Linker for Protein Transduction. *J. Am. Chem. Soc.* **2012**, *134* (24), 10169–10173.

(24) Su, S.; Du, F. S.; Li, Z. C. Synthesis and PH-Dependent Hydrolysis Profiles of Mono- and Dialkyl Substituted Maleamic Acids. *Org. Biomol. Chem.* **2017**, *15* (39), 8384–8392.

(25) Du, J. Z.; Li, H. J.; Wang, J. Tumor-Acidity-Cleavable Maleic Acid Amide (TACMAA): A Powerful Tool for Designing Smart Nanoparticles to Overcome Delivery Barriers in Cancer Nanomedicine. *Acc. Chem. Res.* **2018**, *51* (11), 2848–2856.

(26) Du, J. Z.; Mao, C. Q.; Yuan, Y. Y.; Yang, X. Z.; Wang, J. Tumor Extracellular Acidity-Activated Nanoparticles as Drug Delivery Systems for Enhanced Cancer Therapy. *Biotechnol. Adv.* **2014**, *32* (4), 789–803.

(27) Tao, A.; Huang, G. Lo; Igarashi, K.; Hong, T.; Liao, S.; Stellacci, F.; Matsumoto, Y.; Yamasoba, T.; Kataoka, K.; Cabral, H. Polymeric Micelles Loading Proteins through Concurrent Ion Complexation and PH-Cleavable Covalent Bonding for In Vivo Delivery. *Macromol. Biosci.* **2020**, *20* (1), 1–11.

(28) Lyu, M.; Yazdi, M.; Lin, Y.; Höhn, M.; Lächelt, U.; Wagner, E. Receptor-Targeted Dual PH-Triggered Intracellular Protein Transfer. *ACS Biomater. Sci. Eng.* **2022**.

(29) Lechner, M. D.; Nordmeier, E. H.; Gehrke, K. *Makromolekulare Chemie*; 2010.

(30) Lynn, G. M.; Laga, R.; Jewell, C. M. Induction of Anti-Cancer T Cell Immunity by in Situ Vaccination Using Systemically Administered Nanomedicines. *Cancer Lett.* **2019**, *459* (January), 192–203.

(31) Hoogenboezem, E. N.; Duvall, C. L. Harnessing Albumin as a Carrier for Cancer Therapies. *Adv. Drug Deliv. Rev.* **2018**, *130*, 73–89.

(32) Abdallah, M.; Müllertz, O. O.; Styles, I. K.; Mörsdorf, A.; Quinn, J. F.; Whittaker, M. R.; Trevaskis, N. L. Lymphatic Targeting by Albumin-Hitchhiking: Applications and Optimisation. *J. Control. Release* **2020**, *327* (May), 117–128.

(33) De Vrieze, J.; Louage, B.; Deswarte, K.; Zhong, Z.; De Coen, R.; Van Herck, S.; Nuhn, L.; Kaas Frich, C.; Zelikin, A. N.; Lienenklaus, S.; Sanders, N. N.; Lambrecht, B. N.; David, S. A.; De Geest, B. G. Potent Lymphatic Translocation and Spatial Control Over Innate Immune Activation by Polymer–Lipid Amphiphile Conjugates of Small-Molecule TLR7/8 Agonists. *Angew. Chemie - Int. Ed.* **2019**, *58* (43), 15390–15395.

(34) Irby, D.; Du, C.; Li, F. Lipid-Drug Conjugate for Enhancing Drug Delivery. *Mol. Pharm.* **2017**, *14* (5), 1325–1338.

(35) Raffy, S.; Teissié, J. Control of Lipid Membrane Stability by Cholesterol Content. *Biophys. J.* **1999**, *76* (4), 2072–2080.

(36) Schmaljohann, D. Thermo- and PH-Responsive Polymers in Drug Delivery. *Adv. Drug Deliv. Rev.* **2006**, *58* (15), 1655–1670.

(37) Roy, R.; Hohng, S.; Ha, T. A Practical Guide to Single-Molecule FRET. *Nat. Methods* **2008**, *5* (6), 507–516.

(38) Nuhn, L.; Van Herck, S.; Best, A.; Deswarte, K.; Kokkinopoulou, M.; Lieberwirth, I.; Koynov, K.; Lambrecht, B. N.; De Geest, B. G. FRET Monitoring of Intracellular Ketal Hydrolysis in Synthetic Nanoparticles. *Angew. Chemie - Int. Ed.* **2018**, *57* (33), 10760–10764.

(39) Shrestha, D.; Jenei, A.; Nagy, P.; Vereb, G.; Szöllősi, J. Understanding FRET as a Research Tool for Cellular Studies. *Int. J. Mol. Sci.* **2015**, *16* (4), 6718–6756.

(40) Pearce, A. K.; O'Reilly, R. K. Insights into Active Targeting of Nanoparticles in Drug Delivery: Advances in Clinical Studies and Design Considerations for Cancer Nanomedicine. *Bioconjug. Chem.* **2019**, *30* (9), 2300–2311.

(41) Nuhn, L.; Vanparijs, N.; De Beuckelaer, A.; Lybaert, L.; Verstraete, G.; Deswarte, K.; Lienenklaus, S.; Shukla, N. M.; Salyer, A. C. D.; Lambrecht, B. N.; Grooten, J.; David, S. A.; De Koker, S.; De Geest, B. G. PH-Degradable Imidazoquinoline-Ligated Nanogels for Lymph Node-Focused Immune Activation. *Proc. Natl. Acad. Sci. U. S. A.* **2016**, *113* (29), 8098–8103.

(42) Stickdorn, J.; Nuhn, L. Reactive-Ester Derived Polymer Nanogels for Cancer Immunotherapy. *Eur. Polym. J.* **2020**, *124* (September 2019), 109481.

(43) D. Hein, Christopher. Liu, Xin-Ming. Wang, D. Click Chemistry, a Powerful Tool for Pharmaceutical Sciences. *Natl. Inst. Heal. J.* **2008**, *25* (10), 1–7.

(44) Stickdorn, J.; Stein, L.; Arnold-Schild, D.; Hahlbrock, J.; Medina-Montano, C.; Bartneck, J.; Ziß, T.; Montermann, E.; Kappel, C.; Hobernik, D.; Haist, M.; Yurugi, H.; Raabe, M.; Best, A.; Rajalingam, K.; Radsak, M. P.; David, S. A.; Koynov, K.; Bros, M.; Grabbe, S.; Schild, H.; Nuhn, L. Systemically Administered TLR7/8 Agonist and Antigen-Conjugated Nanogels Govern Immune Responses against Tumors. *ACS Nano* **2022**, *16* (3), 4426–4443.

(45) Duan, Z.; Luo, Y. Targeting Macrophages in Cancer Immunotherapy. *Signal Transduct. Target. Ther.* **2021**, *6* (1), 1–21.

(46) Kawakami, S.; Hashida, M. Glycosylation-Mediated Targeting of Carriers. *J. Control. Release* **2014**, *190*, 542–555.

(47) Zhang, X.; Zhang, K.; Haag, R. Multi-Stage, Charge Conversional, Stimuli-Responsive Nanogels for Therapeutic Protein Delivery. *Biomater. Sci.* **2015**, *3* (11), 1487–1496.

(48) Zhang, A.; Yao, L.; An, M. Reversing the Undesirable PH-Profile of Doxorubicin: Via Activation of a Di-Substituted Maleamic Acid Prodrug at Tumor Acidity. *Chem. Commun.* **2017**, *53* (95), 12826–12829.

(49) Matysiak, B. M.; Monreal Santiago, G.; Otto, S. Teaching an Old Compound New Tricks: Reversible Transamidation in Maleamic Acids. *Chem. - A Eur. J.* **2022**, *28* (40).

CHAPTER I: POLYMERIZABLE 2-PROPIONIC-3-METHYL-MALEIC ANHYDRIDES AS A MACROMOLECULAR CARRIER PLATFORM FOR PH-RESPONSIVE IMMUNODRUG DELIVERY

The following chapter was published in the Journal of the American Chemical Society (JACS). As first author I was responsible for the synthesis of the monomer and optimization of the Reversible Addition-Fragmentation Chain Transfer (RAFT) polymerization of the polymers. I functionalized the polymers with several primary or secondary amines and investigated their pH sensitivity under acidic conditions. The project was supported by my bachelor student Jonas Woller. He reproduced the previously obtain results, optimized the reaction conditions, and fine-tuned the reactivity of the pH-responsive polymers. Additionally, the evaluation of the pH-sensitive release profile of the modified polymers was conducted with the assistance of Katharina Eigen. First *in vitro* studies on RAW-Dual macrophages for cellular uptake and cell viability analyses were conducted by me and Judith Stickdorn. The small molecular agonist IMDQ was provided by Maximilian Scherger. The further modification and analysis of the immunostimulatory drug was performed by me. Finally, I evaluated the immunostimulatory properties of the drugs and polymer conjugates *in vitro*. Additional investigations regarding the maturation of primary immune cells were accomplished by Laura J. Rosenberger. I wrote the first draft of the manuscript with included feedback from the co-authors.

Published in J. Am. Chem. Soci. **2023**, *145*, 50, 27424-27436. DOI: 10.1021/jacs.3c08511

POLYMERIZABLE 2-PROPIONIC-3-METHYLMALEIC ANHYDRIDES AS A MACROMOLECULAR CARRIER PLATFORM FOR PH-RESPONSIVE IMMUNODRUG DELIVERY

Alina G. Heck[1], Judith Stickdorn[1], Laura R. Rosenberger[2], Maximilian Scherger[1], Jonas Woller[1], Katharina Eigen[3], Matthias Bros[2], Stephan Grabbe[2] and Lutz Nuhn[,1,3]*

Dedicated to Professor Rudolf Zentel on the occasion of his 70th birthday.

1: Max Planck Institute for Polymer Research, 55128 Mainz, Germany

2: Department of Dermatology, University Medical Center (UMC) of the Johannes Gutenberg-University Mainz, 55131 Mainz, Germany

3: Institute of Functional Materials and Biofabrication, Department of Chemistry and Pharmacy, Julius-Maximilians-Universität Würzburg, 97070 Würzburg, Germany

*: corresponding author: Prof. Dr. Lutz Nuhn (E-mail: lutz.nuhn@uni-wuerzburg.de)

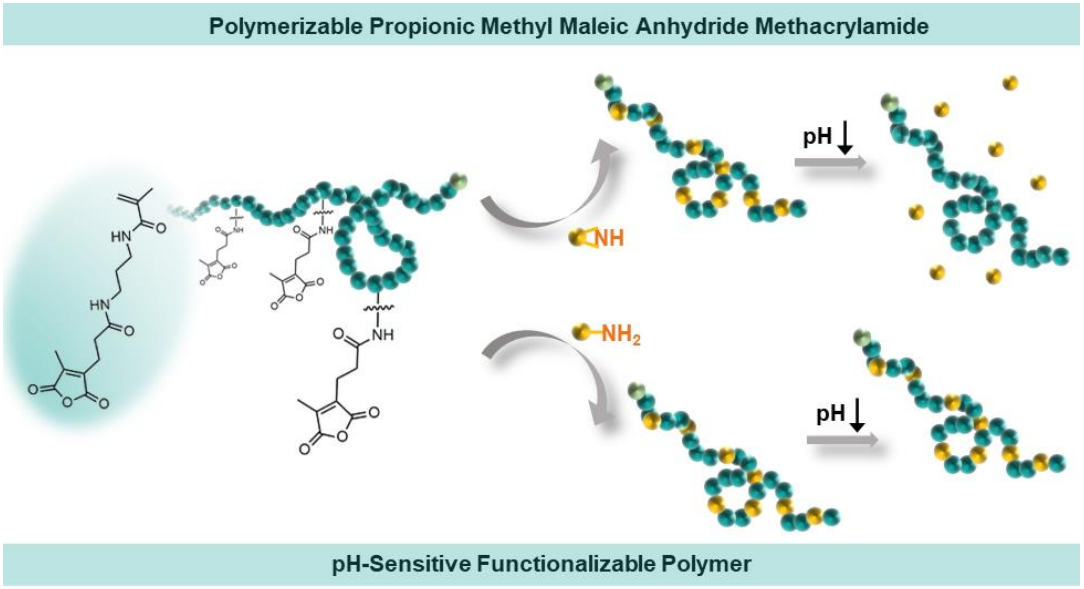

Keywords: pH-responsive, maleic anhydride, RAFT-polymerization, polymer-drug conjugate, immunodrug delivery.

Abstract

The design of functional polymers coupled with a stimuli-triggered drug release mechanisms is a promising achievement to overcome various biological barriers. pH trigger methods yield significant potential for controlled targeting and release of therapeutics due to their simplicity and relevance, especially upon cell internalization. Here, we introduce reactive polymers that conjugate primary or secondary amines and release potential drugs under acidic conditions. For that purpose, we introduced methacrylamide-based monomers with pendant 2-propionic-3-methylmaleic anhydride groups. Such groups allow the conjugation of primary and secondary amines but are resistant to radical polymerization conditions. We, therefore, polymerized 2-propionic-3-methylmaleic anhydride amide-based methacrylates *via* reversible addition-fragmentation chain transfer (RAFT) polymerization. Their amine-reactive anhydrides could sequentially be derivatized by primary or secondary amines into hydrophilic polymers. Acidic pH-triggered drug release from the polymeric systems was fine-tuned by comparing different amines. Thereby, the conjugation of primary amines led to the formation of irreversible imide bonds in dimethyl sulfoxide, while secondary amines could quantitatively be released upon acidification. *In vitro*, this installed pH-responsiveness can contribute to an effective release of conjugated immune stimulatory drugs under endosomal pH conditions. Interestingly, the amine-modified polymers generally showed no toxicity and a high cellular uptake. Furthermore, secondary amine-modified immune stimulatory drugs conjugated to the polymers yielded better receptor activity and immune cell maturation than their primary amine derivatives due to their pH-sensitive drug release mechanism. Consequently, 2-propionic-3-methylmaleic anhydride-based polymers can be considered as a versatile platform for pH-triggered delivery of various (immuno)drugs, thus enabling new strategies in macromolecule-assisted immunotherapy.

Introduction

Antitumor immunotherapy has become a promising approach for cancer treatment. Multiple strategies such as immune checkpoint blockage, in situ cancer vaccines, and chimeric antigen receptor (CAR) T-cell-based therapies have improved the therapeutic outcome for patients.[1,2] Thereby, dendric cells (DCs) are of particular interest in immune engineering. They are the most potent antigen-presenting cells (APCs) able to activate T cells, exerting an antitumoral effect.[3] One method of activating DCs is a stimulation of their pattern recognition receptors (PRRs) *via* small molecular agonists.[4,5] A promising category are agonists of the Toll-like receptors (TLRs) expressed by different APCs, like DCs, macrophages, and B cells.[6] These receptors are either localized on the cell surface (TLR 3/4) or inside endosomes (TLR3/7/8/9) and can be triggered by dsRNA, like poly(I:C) (TLR3), lipopolysaccharides (LPS, TLR4), imidazoquinolines (TLR7/8), or CpG-oligonucleotides (TLR9), leading to the maturation of APCs and the release of cytokines. This causes the promotion of both humoral and cellular immune responses.[7–9]

However, highly potent immune stimulatory small molecules like the TLR7/8 agonist 1-(4-(aminomethyl)benzyl)-butyl-1*H*-imidazo[4,5-*c*]quinoline-4-amine (IMDQ) are often immediately distributed systemically and are therefore, susceptible to off-target toxicity and nonspecific systemic inflammation.[10,11] Conjugation of TLR agonists to different nanosized carriers enables a focused delivery to cancer cells, the tumor immune microenvironment, and the peripheral immune system while minimizing off-target side effects.[12,13] This objective has been addressed using a variety of carrier systems such as polysaccharides,[14] lipids,[15] synthetic polymers,[16] micelles,[17] and nanogels.[18,19] One method for the conjugation of TLR agonists like IMDQ is the reaction with self-assembling reactive ester block copolymers.[20] By Reversible Addition-Fragmentation Chain Transfer (RAFT) polymerization of methoxy tri(ethylene glycol) methacrylate (mTEGMA) and reactive ester pentafluorophenyl methacrylate (PFPMA) we have previously formulated well-defined amphiphilic block copolymers, which enable a covalent attachment of IMDQ and further transformation into fully hydrophilic carriers.[21–23] Although the application of pentafluorophenyl ester guarantees fast and selective conjugation of primary amines, it results in an irreversible conjugation of IMDQ to the carrier system, which can result in an alteration of the biological properties and, thus, can reduce the drugs' biological activity.[14,24]

To enhance the chemical translatability and the effect of TLR agonists, a subcellular delivery by advanced stimuli-responsive materials into receptor-associated organelles would be favorable.[25,26] There are a variety of possibilities for an effective stimuli-induced drug release

such as redox, enzymatic, or pH.[27–29] However, pH-sensitive systems have gained the most significant potential for drug delivery control. Several endogenously relevant stimuli at different locations exhibit an acidic pH, such as the tumor microenvironment (pH = 6.5-6.9), inflammatory tissues (pH = 5-6), and finally, on a subcellular level, endolysosomes (pH = 4.5-5.5).[29–31] The latter compartments become particularly relevant for IMDQ as their corresponding receptor TLR 7/8 is localized in these organelles as well. Notable examples of acid-responsive architectures are ketals[23] or acetals,[32] hydrazones,[33] oximes,[34] or imines.[35,36] Unfortunately, not all of these chemical motifs are fast enough to fully degrade under physiologically relevant conditions (e.g., endolysosomal pH values) and, in addition, require severe chemical modification for reversible drug conjugation. These modifications then reduce the drugs' specific activity after release.[37]

In contrast to that, dimethylmaleic anhydride-based systems are more promising, due to their high pH sensitivity (pH = 5.5-6.8) and fast release of conjugated amines.[38,39] Especially, the *cis*-orientated double bond structure enables a rapid attack of the amide carbonyl group by the β-carboxylate under mild acidic conditions. The release of the amine derivatives can be controlled by substituents of the double bond, reducing the distance between maleic acid amide derivatives and β-carboxylate.[40,41] Besides, maleic acid amide derivatives are negatively charged, due to the introduced carboxylate groups while releasing positively charged amines under acidic conditions.[38] Thus, an anhydride modification represents a reversible charge conversion of amine-bearing molecules.[42,43] Interestingly, IMDQ is equipped with one single benzyl amine that would be susceptible for conjugation to dimethylmaleic anhydrides and release under endolysosomal pH conditions.

So far, it has been shown that dimethylmaleic anhydride motifs were mostly used as linkers for amine-containing molecules or proteins.[44,45] However, most reported structures require a complex synthesis to ligate single linkers to a macromolecular carrier for accessing pH-sensitive delivery systems.[46] In this study, however, we present an elegant way to design methacrylamide-based polymers with appended pH-sensitive 2-propionic-3-methylmaleic anhydride groups for controlled delivery and efficient release of the TLR agonist IMDQ. 2-Propionic-3-methylmaleic anhydride amide-based methacrylamides are synthesized in a multistep reaction and polymerized under controlled radical polymerization (CRP) conditions affording an amine-reactive macromolecular carrier platform (Figure 1). The anhydride groups can be functionalized with primary or secondary amines to yield fully hydrophilic polymers. Investigating the releasing process upon acidification exhibits the formation of irreversible imide structures when primary amines are conjugated, while secondary amines can be released

under acidic conditions. Due to its pH-responsive profile, a new TLR 7/8 agonist IMDQ-Me is synthesized bearing a secondary amine for reversible conjugation to the polymer platform. *In vitro* studies on reporter cell lines as well as primary immune cells confirm IMDQ-Me's exclusive immune stimulatory potential under endosomal pH conditions without any toxicities. Based on its chemical design, the herein described carrier system allows facile conjugation for a variety of small molecules with fast release under acidic conditions and, therefore, might be a promising carrier for an effective immunodrug delivery.

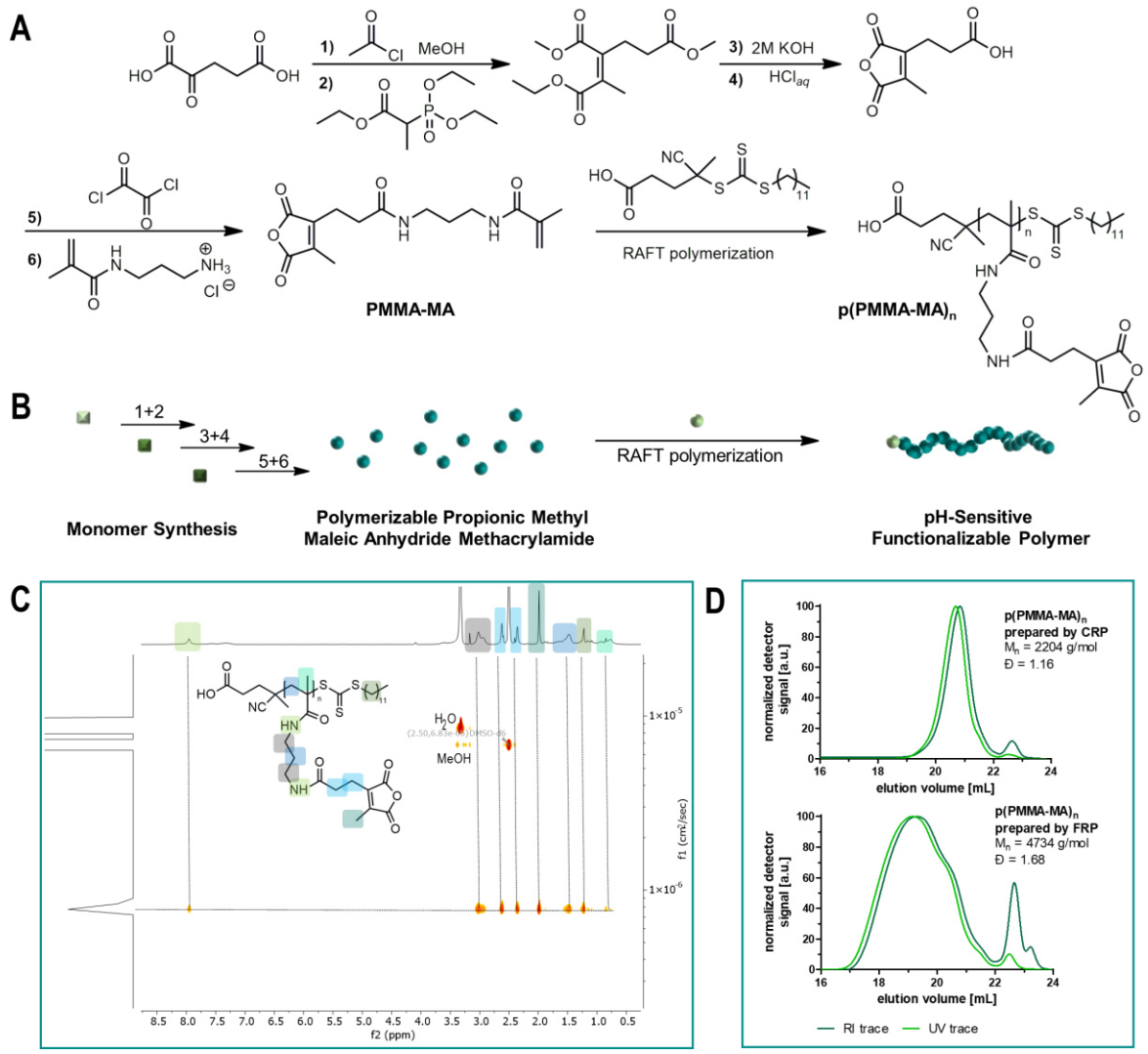

Figure 1. Synthesis and characterization of methacrylamide-based polymers with pendant pH-sensitive 2-propionic-3-methylmaleic anhydride groups. (**A**) Synthesis route of the 2-propionic-3-methylmaleic anhydride methacrylamide monomer (PMMA-MA) and the corresponding pH-sensitive polymer p(PMMA-MA)$_n$ obtained by RAFT polymerization using a small molecular trithiocarbonate chain transfer agent (TTC-CTA). (**B**) Schematic illustration of the synthesis concept. (**C**) ^{1}H DOSY NMR spectroscopy of the polymer generated *via* RAFT polymerization. All proton signals appear at a macromolecular diffusion coefficient. (**D**) SEC in [HFIP (hexafluoroisopropyl alcohol), calibrated with PMMA standards] of the polymer prepared by CRP compared to the polymer obtained by FRP.

Results and Discussion

Polymeric maleic anhydride structures have mostly been applied as linkers[46] or conjugated to polylysine[44] as pH-sensitive carriers. To the best of our knowledge, polymerizable monomers with pendant 2-propionic-3-methylmaleic anhydride groups have not been reported. Based on the reactivity ratios of methacrylamides versus maleic anhydrides, an exclusive radical polymerization of methacrylamides can be expected.[47] For that purpose, we first employed a methacrylamide-based monomer with pendant 2-propionic-3-methylmaleic anhydride groups and investigated its reactivity towards CRP conditions.

Monomer and Polymer Synthesis

N-(3-(3-(4-Methyl-2,5-dioxo-2,5-dihydrofuran-3-yl)propanamido)-propyl)methacrylamide (PMMA-MA) could be synthesized in a multistep reaction starting with the methyl esterification of 2-oxoglutaric acid. Thereby, we observed the generation of dimethyl 2,2-dimethoxypentanedioate as the byproduct, which could be treated with trifluoroacetic acid (TFA) to isolate pure dimethyl 2-oxoglutarate (Figures 1A; S1, S2). Next, in a Horner-Wadsworth-Emmons reaction, dimethyl-2-oxoglutarate and triethyl-2-phosphonopropionate yielded (Z)-4-ethyl 1,3-dimethyl pent-3-ene-1,3,4-tricarboxylate bearing a *cis*-double bond, which could be converted into substituted maleic anhydride structures (Figures 1A; S3, S4). For that purpose, the ester groups were cleaved by a strong base, followed by subsequent cyclization under acidic conditions. As residuals of ring-opened pent-3-ene-1,3,4-tricarboxylic acids could potentially interfere during further reactions, the anhydride product was recrystallized from tetrahydrofuran (THF) and n-hexane (1:3) to yield pure 2-propionic-3-methylmaleic anhydride as colorless crystals (Figures 1A, S5-S7). In the last step, we decided to fuse this pH-sensitive moiety to a polymerizable methacrylamide. Therefore, 2-propionic-3-methymaleic anhydride was converted into a highly reactive acid chloride and then reacted with the commercially available N-(3-aminopropyl)methacrylamide hydrochloride catalyzed by triethylamine (Figures 1A and S8). The synthesis afforded a stable 2-propionic-3-methylmaleic anhydride methacrylamide monomer characterized by NMR analysis and electrospray ionization mass spectrometry (ESI-MS, Figures S9-S14). The use of conventional (meth)acrylate-based monomers should be avoided, as they are more sensitive to exothermic conditions and may suffer from autopolymerization.[48] Moreover, during base-catalyzed amidation of the anhydride, the methacrylate may also get aminolyzed, affording an irreversible ligation of the respective amine.[49]

To this end, the synthesized propionic methyl maleic anhydride methacrylamide (PMMA-MA) was polymerized under different conditions by RAFT polymerization. The polymerization technique had to be optimized, and a variety of solvents, reaction times, and different initiators were investigated to achieve sufficient polymerization of the new monomer (Table 1). Successful polymerization in methanol (MeOH) at 70 °C with azobis(isobutyronitrile) (AIBN) as the initiator and trithiocarbonate as the chain transfer agent (TTC-CTA) revealed the formation of well-defined polymers *p*(PMMA-MA)$_n$, providing narrowly dispersed polymers with *Đ* below 1.2 (Figure 1A, D). According to the controlled reaction conditions, a polymerization seemed to occur exclusively at the methacrylate function, while the anhydride remained intact. This is in accordance with literature-reported copolymerization parameters of methacrylamide/dimethylmaleic anhydride and the high reactivity ratio for methacrylamides.[47] Intact maleic anhydride was further supported by ^{1}H NMR analysis yielding a sharp methyl anhydride signal at δ (ppm) = 1.99 ppm, with the disappearance of the methacrylamide vinyl protons [δ (ppm) = 5.62, 5.31] and the formation of a broad poly(methacrylamide) backbone [δ (ppm) = 1.75–0.60] (Figures S9 and S16). Additionally, ^{1}H diffusion-ordered NMR spectroscopy (^{1}H DOSY NMR) showed only one single diffusing species at high-molecular-weight diffusion units (Figure 1C).

Table 1. Characterization of RAFT-Derived Polymers Synthesized under Different Reaction Conditions.

solvent	initiator[a]	time [h][b]	temperature [°C][c]	conversion [%][d]	DP $_{(NMR)}$[e]	$M_{n\,(NMR)}$ [g/mol][f]	$Đ_{(SEC)}$[g]
DMF	AMDVN	24	30	42	21	6878	1.48 polydisperse
DMF	AIBN	24	70	52	26	8450	1.86 polydisperse
DMSO	AIBN	24	70	15	8	2870	-
dioxane: H_2O	AIBN	24/48	70	37/30	19/15	6261/5029	1.36/2.31 polydisperse
DMAc	AIBN	72	70	43	22	7187	1.38 polydisperse
DMAc: MeOH	AIBN	72	70	45	23	7495	1.47 polydisperse
MeOH	AIBN	24/48/72	70	43/63/72	22/32/36	7180/10270/ 11504	1.20/1.19/1.16 monodisperse

[a]Initiators used for CRP: 2,2'-azo-di(4-methoxy-2,4-dimethylvaleronitrile) (AMDVN) or azobis(isobutyronitrile) (AIBN). [b]Reaction times in hours. [c]Reaction temperatures in °C. [d]Monomer conversion determined by ^{1}H NMR. [e]Degree of polymerization (DP) quantified by ^{1}H NMR. [f]Number-average molar mass (M_n) derived from ^{1}H NMR. [g]Dispersity (Đ) defined by SEC.

Even free radical polymerization (FRP), conducted at 70 °C and applying more AIBN as the initiator, still afforded similar ^{1}H NMR spectra (Figure S17) and confirmed once more the exclusive reactivity of the methacrylamide vinyl protons. Under these conditions no polymer chain cross-linking was observed, as all polymers could be analyzed in hexafluoroisopropanol

(HFIP) serving as the solvent for size exclusion chromatography (SEC). A broadly distributed polymer with a *Đ* around 1.68 was recorded (Figure 1D), which is typical for FRP. Thus, it can be assumed that only the methacrylamide group ensures polymerization, and under controlled RAFT polymerization conditions, well-defined polymers can be accessed. Furthermore, ^{1}H NMR monomer conversion studies confirmed first-order kinetics of the RAFT polymerization process (Figures S18 and S19).

Amidation with Primary or Secondary Amines

After successfully establishing a procedure to synthesize suitable polymers with pendant pH-sensitive 2-propionic-3-methymaleic anhydride groups, the amine reactivity and pH reversibility of the polymer were verified in dimethyl sulfoxide (DMSO). Different primary and secondary amines, such as ethylmethylamine or butylamine serving as short aliphatic structures, hydrophilic compounds, like morpholine, or aromatic structures, using benzyl- or dibenzylamine, were added to a polymer solution in DMSO and triethylamine (TEA, Figure S20). These amines were selected due to their solubility, commercial availability, and fast spectroscopic quantification. After overnight treatment, the modified polymers were precipitated in diethyl ether and characterized by ^{1}H NMR and DOSY NMR measurements. All amine-treated polymers demonstrated a successful and quantitative modification, as indicated in Figures S21 and S22. Interestingly, reactions with secondary amines exhibited significant proton signal shifts, proving the formation of a ring-opened maleic acid amide derivate. All modifications revealed a decreasing chemical shift of the methyl and ethylene unit adjacent to the vinyl group of the anhydride structure caused by the amidation (Figures S23, S24 and S26 top, neutral). The strongly electron-withdrawing character of the anhydride group decreases, leading to an increased proton shielding. Additionally, we observed a split signal of the α-positioned methyl unit. This is generated by two corresponding regioisomers that are formed during amidation of the maleic anhydride structure.

Successful conjugation of primary and secondary amines was further confirmed by DOSY measurements and, most notably, provided a platform to analyze the release profile under acidic conditions (Figures 2 and S25, S27, and S29). We realized a significant difference by direct comparison between primary and secondary amines under neutral and acidic conditions. Those samples that were modified with primary amines in DMSO (e.g., benzylamine) showed no pH sensitivity upon treatment with TFA (Figure 2B1, B2). A closer look by ^{1}H NMR spectroscopy indicated the formation of an irreversible imide structure (Figures 2B and S23). In stark contrast to benzylamine-modified polymers, dibenzylamine as a secondary amine

provided one single diffusing species with high-molecular-weight diffusion units under neutral conditions (Figure 2C1) but liberated low-molecular-weight diffusing species by treatment with TFA (Figure 2C2). This confirmed the expected pH-sensitive release of dibenzylamine (Figure 2C) and was additionally supported by ^{1}H NMR analysis (Figure S23).

Moreover, dibenzylamine-modified polymers provided a peak shift from broad polymer signals to sharp signals for the liberated amine species, as well as a reformation of one single α-positioned anhydride methyl signal at δ (ppm) = 1.99. The spectra of the benzylamine-conjugated polymers, however, did not provide any difference between neutral or acidic conditions at all (Figure S23, neutral and acidic color highlights). Consequently, primary amines are not suitable for pH-reversible conjugation and release from this polymer platform with pendant pH-sensitive 2-propionic-3-methylmaleic anhydrides. Beyond benzylamine, other primary amines were also irreversibly conjugated as imides to the polymer, while secondary amines could be released quantitatively (Figures S24-S29—relevant proton signal shifts under neutral and acidic conditions are highlighted). One exceptional case are secondary aromatic amines such as N-methylaniline, which exhibited no conversion with the anhydride (Figure S28 top and Figure S29A).

Following the design concept of amidation with secondary amines, we were interested in the chemical release mechanism managed by the *cis*-vinylic β-carboxylate. For that purpose, dibenzylamine-modified polymers were redissolved in DMSO and treated with benzyl bromide and *N*,*N*-diisopropylethylamine (DIPEA) (Figures 2A and S30). After precipitation in diethyl ether, dually modified polymers were obtained with their maleic anhydride functions converted into dibenzyl amides as well as benzyl esters (an increase in molecular weight was found by SEC—compare Figure S32). They were again further analyzed by ^{1}H NMR and DOSY NMR spectroscopy under both, neutral and acidic conditions. Both conditions revealed successful dual conversion but a loss of pH reversibility. No differences occurred upon acidification (Figures 2D1, D2, and S31) underlining the necessity of free *cis*-vinylic β-carboxylates. The acid-triggered release of conjugated secondary amines was ensured *via* nucleophilic cyclization at the adjacent amides.

Altogether, these results highlight the versatile application of 2-propionic-3-methylmaleic anhydrides as functionalizable polymer side groups, although pH sensitivity must be considered critically. Only secondary amine-modified polymers guarantee quantitative release upon acidification.

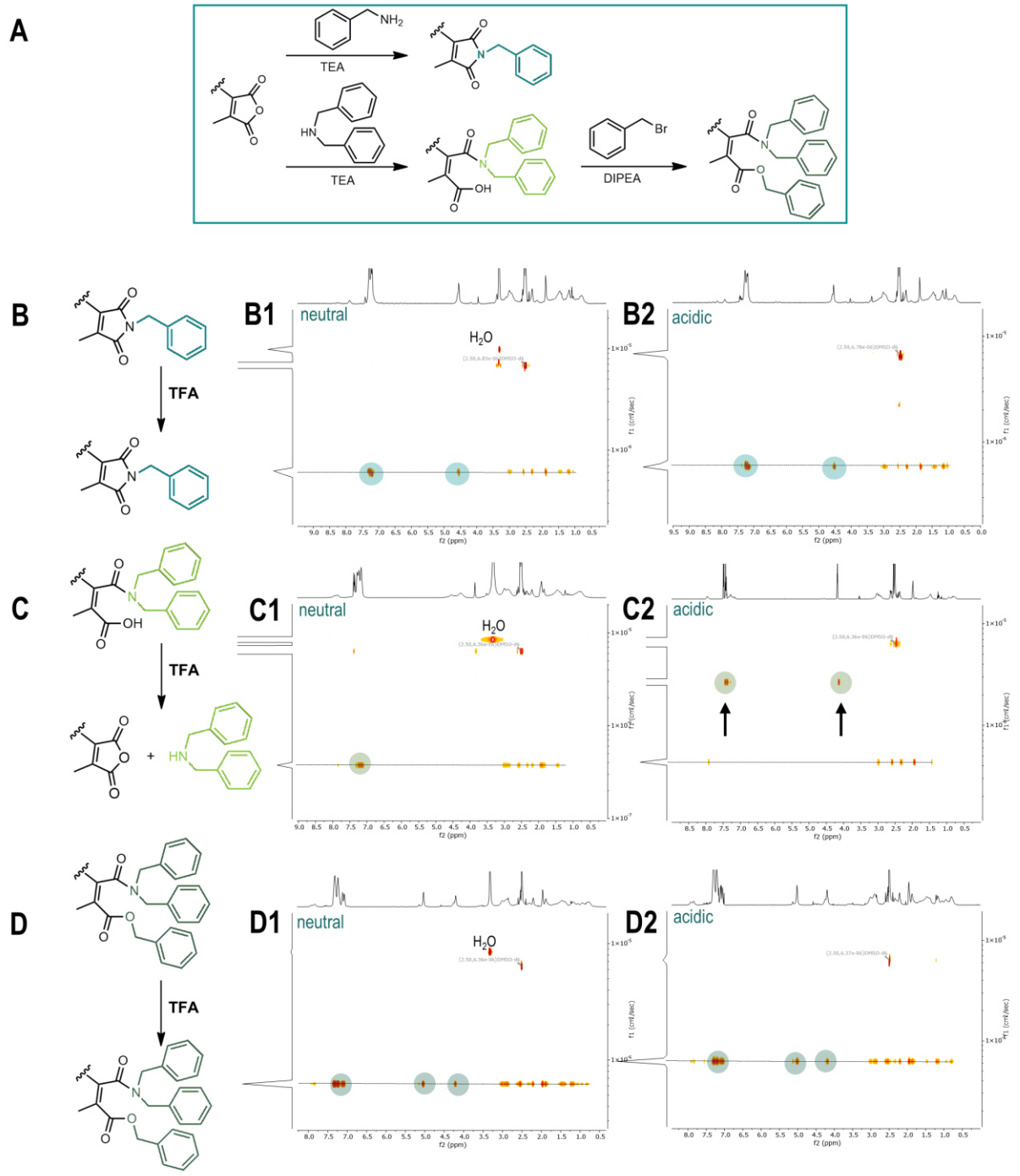

Figure 2. pH-sensitive profile of amine-modified maleic anhydride side groups of *p*(PMMA-MA)$_n$. (**A**) Reaction scheme for the amidation of *p*(PMMA-MA)$_n$ with benzylamine or dibenzylamine and a further conversion of resulting carboxylate units with benzyl bromide. (**B**) Chemical structure of benzylamine, (**C**) dibenzylamine and (**D**) dually conjugated maleic anhydride groups before and after treatment with TFA. (**B1**) ^{1}H DOSY NMR experiments under neutral conditions showing the covalent conjugation of benzylamine, (**C1**) dibenzylamine and (**D1**) additional modification with benzyl bromide to *p*(PMMA-MA)$_n$. (**B2**) ^{1}H DOSY NMR under acidic conditions reveals the resistance of conjugated benzylamine, (**C2**) the reversible release of dibenzylamine and (**D2**) the loss of the pH-sensitivity by dually modified maleic anhydride groups.

In Vitro Performance of Dye-Labeled Hydrophilic Polymers

Based on the amidation results, we investigated the polymers' *in vitro* behavior. To ensure the high solubility of the anhydride-containing polymers in phosphate-buffered saline (PBS), the systems were reacted with hydrophilic amines. Morpholine was selected as the pH-reversible structure, while short methoxypoly(ethylene glycol)$_{11}$-amine (mPEG$_{11}$-amine) served as irreversible, soluble analogues. According to previous modifications, the well-defined polymer *p*(PMMA-MA)$_{38}$ was dissolved in DMSO with TEA. Prior to hydrophilization, we labeled the polymers with a fluorescent dye bearing a primary amine (tetramethylrhodamine cadaverine, TMR) as the irreversibly conjugated tracer for monitoring the cellular uptake (Figure 3A). The prepared polymers increased in molecular weight from the unmodified polymer, determined by SEC characterization in HFIP (Figure S39A), and together with ^{1}H NMR analysis, quantitative hydrophilic modification of the polymers was confirmed (Figures S37 and S38). Ultimately, both polymers became fully water-soluble and showed similar absorbance maxima intensities around 550 nm, as determined by UV-vis spectroscopy in PBS (Figure S39B).

These properties motivated us to apply the polymers as carrier systems in further biological studies. Initial *in vitro* experiments focusing on the toxicity profile of the modified polymers on a macrophage cell line (RAW-Dual) exhibited no major influence on the cell viability, as verified by MTT assay. Even high concentrations up to 1 mg/mL did not impair the viability of the macrophages (Figure 3B). RAW-Dual macrophages were used as a model cell line for phagocytosing cells that ingest polymeric structures after administration. Therefore, cellular uptake of the hydrophilic, dye-labeled polymers could be studied using flow cytometry and fluorescence confocal microscopy. Cells were incubated with different polymer concentrations (10, 30, and 100 µg/mL) for 24 h at 37 °C prior to analysis. Resulting histograms (Figure 3C) and mean fluorescence intensities (Figure 3D, %TMR positive cells in Figure S64) revealed a linear dose-dependent internalization of the polymers into the cells, probably by endocytosis. Interestingly, morpholine-hydrophilized polymers confirmed a significantly enhanced uptake compared with mPEG$_{11}$-amine-conjugated systems (Figure 3E). Poly(ethylene glycol) (PEG) is well-known for its efficient stealth properties enabling different polymeric structures or nanoparticles to increase their residence time in the blood circulation. It decreases protein adsorption and reduces recognition by macrophages affording less cellular uptake.[50,51] Our data regarding the mPEG$_{11}$-amine-conjugated systems align with these findings. However, for applying the 2-propionic-3-methylmaleic anhydrides as functionalizable polymers for TLR 7/8 delivery with sufficient *in vitro* uptake, we opted for morpholine-hydrophilized structures in the following studies.

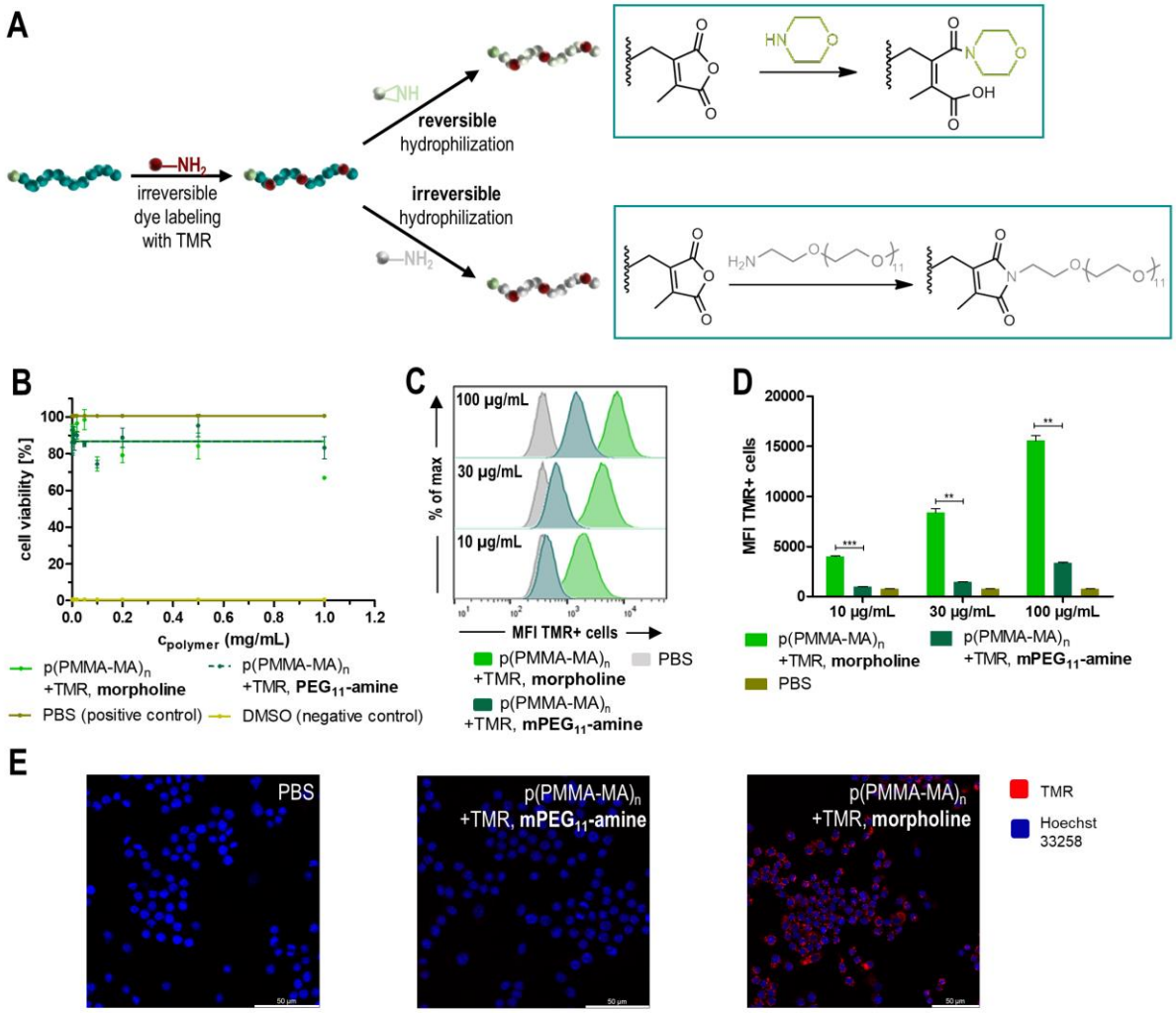

Figure 3. Evaluation of tetramethylrhodamine cadaverine (TMR)-labeled and morpholine or $mPEG_{11}$-amine-hydrophilized polymer *in vitro*. (**A**) Schematic overview for the gradual conversion of *p*(PMMA-MA)$_n$ 2-propionic-3-methylmaleic anhydride groups with TMR and morpholine or $mPEG_{11}$-amine as the hydrophilizing agent. (**B**) Cell viability assay (MTT) of RAW-Dual macrophages incubated with the modified polymers, PBS (positive control, 100% viability) and DMSO (negative control, 0% viability) (n = 4). (**C**) Flow cytometry of the morpholine- or $mPEG_{11}$-amine-hydrophilized polymers at 10, 30, and 100 µg/mL characterized by histogram and (**D**) mean fluorescence intensity (MFI, n = 3, statistical t-test: $^*p \leq 0.05$, $^{**}p \leq 0.01$, $^{***}p \leq 0.001$, ns = nonsignificant). (**E**) Fluorescence confocal microscope images of RAW-Dual macrophages incubated with 100 µg/mL PBS (control), $mPEG_{11}$-amine- or morpholine-modified polymer (red: TMR-labeled polymer, blue: nuclei stained with Hoechst 33258).

pH-Sensitive Properties of Dye-Labeled Polymers

To further elucidate the water-soluble polymers' behavior upon exposure to extracellular and endolysosomal pH variations, we first analyzed the release kinetics of a dually dye-labeled polymer at both pH 5.5 and pH 4.0. For that purpose, the polymer *p*(PMMA-MA)$_{38}$ was irreversibly dye-labeled with TMR and additionally reversibly modified with 4-nitro-7-piperazino-2,1,3-benzoxadiazole (NBD-PZ). NBD-PZ can be readily synthesized in a one-step reaction (Figures S33 and S34), provides a secondary amine for reversible conjugation, and can

be monitored at an absorbance maximum around 480 nm (Figure S35A)/a fluorescence emission maximum around 540 nm (Figure S35B). After dye conjugation, the polymer was treated with $mPEG_{11}$-amine or morpholine, to ensure high solubility in water, and characterized by ^{1}H NMR, SEC, and UV-vis measurement (Figures S40-42). A polymer solution, hydrophilized with $mPEG_{11}$-amine was prepared at 2 mg/mL in PBS at pH 7.4 and dialyzed against PBS at pH 5.5 or against ultrapure water of pH 4.0 (both adjusted with hydrochloric acid) for 48 h (Figures 4A and S43). The acidic hydrolysis of the reversibly conjugated small-molecule NBD-PZ was tracked by frequent UV-vis measurement of the polymer solution inside the dialysis bag. These studies may serve as a model for the release of a reversibly attached drug molecule (Figures 4B1 and S44A). In relation to the irreversibly conjugated TMR, the absorbance of NBD-PZ showed a decay over time and confirmed again the exclusive pH-responsiveness for secondary amine-conjugated species in water (Figures 4B1 and S44A). Interestingly, after baseline correction, we could interpret the release kinetics at pH 5.5 and 4.0 by a fast NBD-PZ release at the beginning with a half-lifetime of around 1.7 h followed by a slower release rate exhibiting a half-lifetime of around 12 h (Figures 4B2, B3, and S44B, C).

Moreover, the performance of the dually dye-labeled polymers, hydrophilized with morpholine was analyzed *in vitro* by flow cytometry and fluorescence confocal microscopy. RAW-Dual macrophages were incubated with different samples at same UV-vis absorbance intensities (Figures S39B and S42B) for 24 h at 37 °C. TMR fluorescence detection provided information about the polymers' cell uptake, indicating almost identical internalization for mono-labeled (TMR) and dual-labeled (TMR and NBD-PZ) polymers (Figures 4C1 and S65). The additional conjugation of a pH-sensitive dye had no effect on the polymer. On the contrary, the conjugation of NBD-PZ to the carrier allows an improved uptake of this small molecule compared to its application as a free dye. By detection of the NBD-PZ fluorescence, a significantly higher amount was recorded for polymers that were mono-labeled with NBD-PZ vs soluble NBD-PZ (Figures 4C2 and S65). Such an enhanced NBD-PZ uptake could similarly be achieved for dual-labeled polymers carrying both the irreversibly conjugated dye (TMR) and the reversibly conjugated dye (NBD-PZ). The additional conjugation of TMR seems not to affect the delivery properties of $p(PMMA\text{-}MA)_n$ carrying reversibly attached small molecules like NBD-PZ into cells (Figures 4C2 and S66).

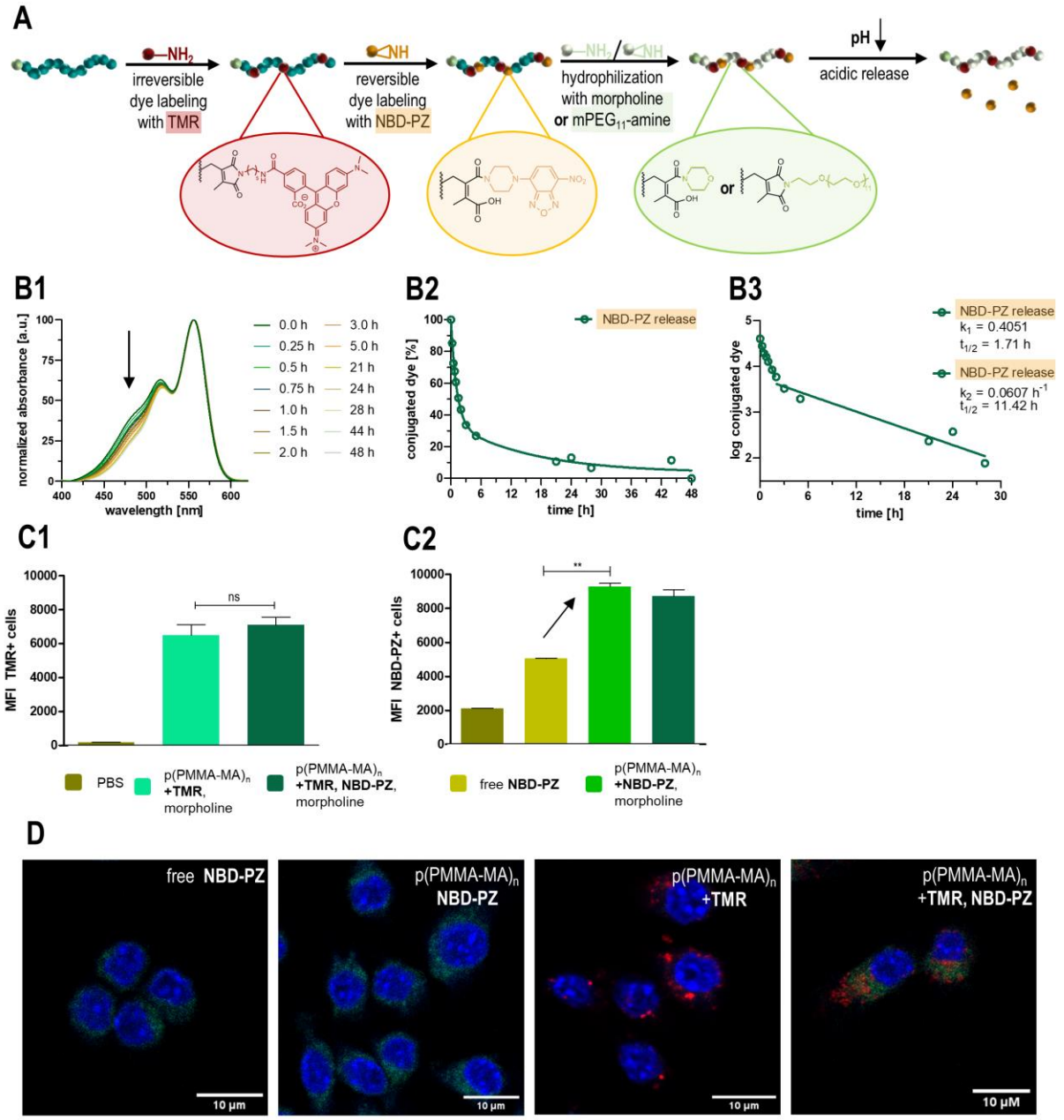

Figure 4. pH-dependent release profile of reversible and irreversible dye-labeled hydrophilic p(PMMA-MA)$_n$ polymer carriers. (**A**) Synthetic design concept of TMR- and/or 4-nitro-7-piperazino-2,1,3-benzoxadiazole (NBD-PZ)-labeled polymers hydrophilized with morpholine or mPEG$_{11}$-amine. (**B**) UV-vis spectra of TMR- and NBD-PZ-labeled, PEGylated polymer dialyzed against PBS at pH 5.5. (**B1**) UV-vis spectra recorded at pH 5.5. (**B2+B3**) Corresponding amount of conjugated NBD-PZ over time and the respective half-lifetime determined by UV-vis absorbance. (**C1+C2**) Flow cytometry data of RAW-Dual macrophages incubated with TMR- and/or NBD-PZ-labeled polymer, or free NBD-PZ analyzed by mean fluorescence intensity (MFI, n = 3, statistical t-test: $^*p \leq 0.05$, $^{**}p \leq 0.01$, $^{***}p \leq 0.001$, ns = nonsignificant). (**D**) Fluorescence confocal microscope images of RAW-Dual macrophages treated with 10 µg/mL free NBD-PZ, NBD-PZ-labeled polymers, TMR-labeled polymers, or TMR- and NBD-PZ-labeled polymers hydrophilized with morpholine (green: NBD-PZ fluorescence, red: TMR-labeled polymer, blue: nuclei stained with Hoechst 33258).

To finally elucidate the intracellular acid-induced release of the NBP-PZ small molecule from the dye-labeled polymers, further fluorescence confocal microscopy studies were conducted. Again, the fluorescence images substantiate an increased cellular uptake of the NBD-PZ polymer compared to that of the free dye (Figures 4D and S67). Most interestingly, NBD-PZ-conjugated systems revealed very diffuse signals, indicating a release of the small molecule into the cells. Especially, the corecording of both dyes in case of the dual-modified polymer strongly confirmed the hypothesis of a release of the secondary amine-containing dye NBD-PZ, while the TMR fluorescence is rather located inside vesicular compartments, as it remains conjugated to the polymer system (Figure 4D right and Figure S67).

Altogether, these findings nicely demonstrate the high potential of the pH-sensitive 2-propionic-3-methymaleic anhydride-based polymer system to foster the uptake of small molecules with secondary amines into cells and even promote their intracellular release upon acidification.

Immune Stimulatory Effect of IMDQ or IMDQ-Me Drug-Loaded Hydrophilic Polymers

To investigate the delivery of immune stimulatory drugs by the pH-reversible polymer system, we designed a new TLR 7/8 agonist, IMDQ-Me bearing a secondary amine for reversible conjugation to the polymer platform. IMDQ itself is a highly potent small molecule, able to activate the Toll-like receptor TLR7/8 in endosomal compartments inside cells. In previous studies, we could show that covalent attachment of IMDQ bearing a primary amine improved the biodistribution and turned off systemic side effects.[21,23,52,53]

For this study, IMDQ was reacted with ethyl chloroformate and $LiAlH_4$, providing a secondary amine for reversible conjugation to our polymer system (IMDQ-Me, Figures S45-S51). It could be compared head-to-head with the primary amine IMDQ, affording an irreversible polymer conjugate. Covalent attachment of both drugs by their benzylic primary or secondary amines followed by subsequent polymer hydrophilization *via* aminolysis with morpholine revealed the formation of two drug-loaded, water-soluble polymers (Figure 5A). They either carried the IMDQ irreversibly or could release IMDQ-Me upon acidification (Figures S52-S60). Quantification of IMDQ or IMDQ-Me was conducted by ^{1}H NMR and DOSY measurement as well as UV-vis spectroscopy and confirmed the successful conjugation of both drugs to the polymers (Figures 5B and S53-S60). Release upon acidification was exclusively found for IMDQ-Me by DOSY, while IMDQ remained irreversibly bound to the polymer (Figures S56 and

S60). The amount of covalently attached IMDQ or IMDQ-Me was determined as 4.6 wt % for IMDQ and 5.7 wt % for IMDQ-Me (Figure 5B and Figure S61 and S62).

Next, we aimed at investigating the cellular delivery potency of the two polymer-drug conjugates. Therefore, RAW-Dual macrophages were treated with either different concentrations of the drug-loaded polymers or the corresponding free drugs. RAW-Dual cells provide a reporter function for TLR stimulation. They express different pattern recognition receptors, including the endosomal TLR 7/8 receptor. Moreover, they are genetically modified to secrete embryonic alkaline phosphatase upon receptor stimulation and activation of the NF-κB pathway, which can be quantified spectrophotometrically by the Quanti Blue Assay. Consequently, they could be applied for studying the endosomal delivery of the two TLR 7/8 agonists.

In analogy to the unmodified soluble IMDQ, the new IMDQ-Me exhibited a slightly reduced but still very high TLR stimulation at submicromolar concentrations (Figure 5C brown and dark green curve). In contrast to that, the conjugation of IMDQ to the polymer carrier led to a strongly reduced TLR activation. The irreversible IMDQ-polymer conjugate shifted the activity into the micromolar concentration range (Figure 5C yellow curve). However, better preservation of TLR activity was achieved only with the reversible IMDQ-Me-loaded polymer. It provided a 10-fold higher activity than the irreversible IMDQ conjugate (Figure 5C, light green curve), probably associated with its pH-sensitive endosomal release. Nevertheless, the IMDQ-Me-loaded polymer revealed in this assay a further reduced TLR activity compared to the soluble drug, which may corroborate a prolongated internalization. In this regard, longer incubation times probably enforce an increased endosomal internalization and pH-triggered release, whereas systemic immune activation may be prevented. Simultaneously, the RAW-Dual macrophage viability was characterized by an MTT assay. Neither the soluble small molecules nor the polymer carriers exhibited any impact on the cellular viability (Figure S68).

These promising studies finally motivated us to further investigate the improved TLR activity for the IMDQ-Me-loaded polymers and trigger primary immune cell maturation. For that purpose, murine bone marrow cells were isolated from femurs and tibiae of C57BL/6 mice and differentiated for 1 week in the presence of GM-CSF-supplemented media yielding inflammatory bone-marrow-derived dendritic cells (BMDCs).[54,55] These could subsequently be treated overnight with IMDQ- and IMDQ-Me-loaded polymers as well as empty polymers (Figure 5D). *Via* flow cytometric analysis (Figure S69), the immunostimulatory phenotype of

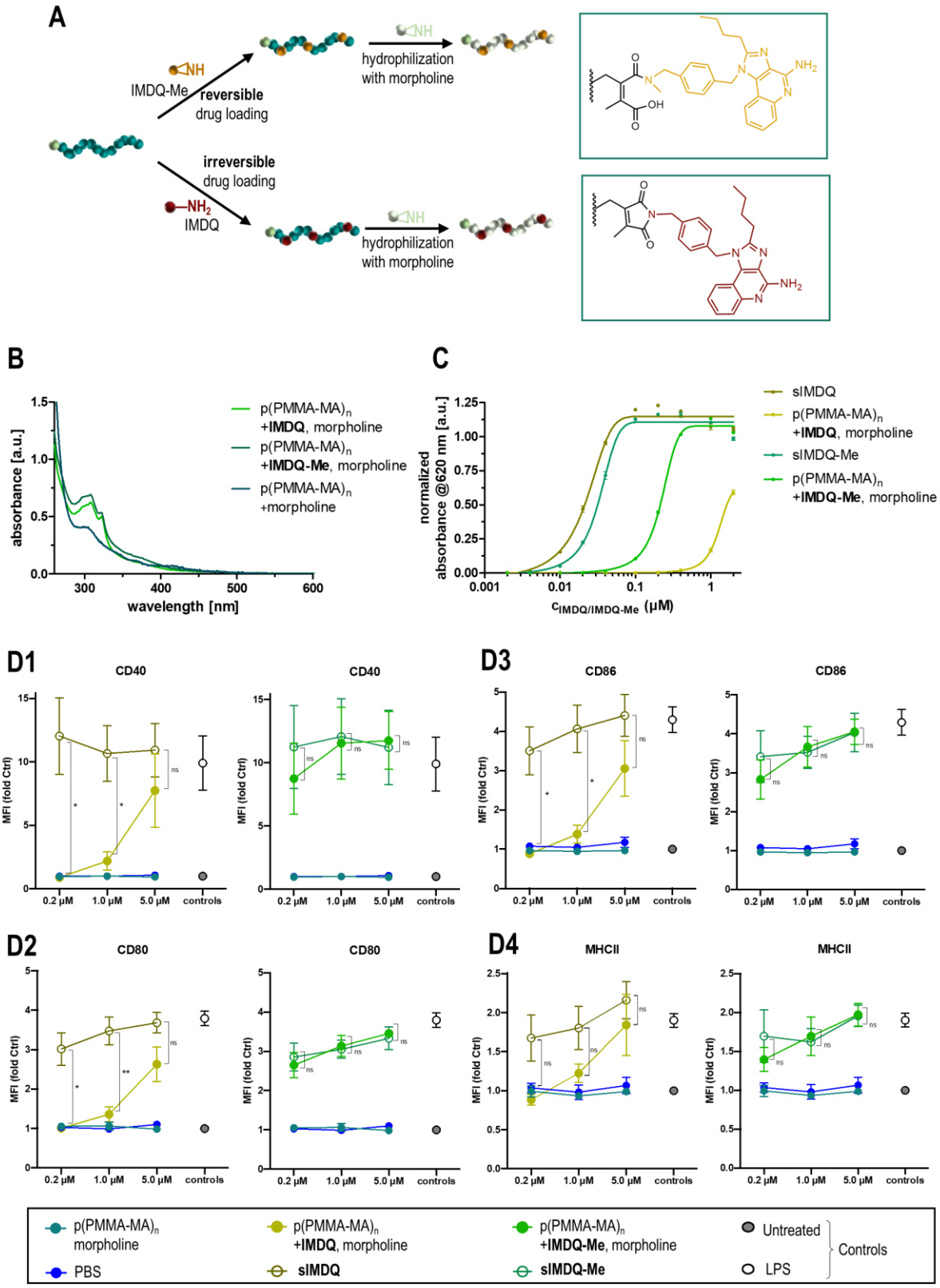

Figure 5. 2-Propionic-3-methyl maleic anhydride methacrylamide polymer with irreversibly or reversibly conjugated TLR7/8 agonist IMDQ or IMDQ-Me. (**A**) Synthesis scheme of irreversible or reversible drug-loaded polymers and their corresponding chemical composition. (**B**) UV-vis spectra of IMDQ- or IMDQ-Me-loaded polymers as well as the corresponding water-soluble control polymer. (**C**) TLR receptor stimulation of RAW-Dual macrophages determined by RAW blue assay (*n* = 4). **(D)** Maturation of bone marrow-derived dendritic cells after incubation with

agonists and TLR 7/8 agonist carrying polymers (IMDQ left, IMDQ-Me right). To delineate the cellular activation state, the expression of the costimulatory markers CD40 **(D1)**, CD80 **(D2),** and CD86 **(D3)** as well as of the antigen-presenting molecule MHC-II **(D4)** was quantified *via* flow cytometry by mean fluorescence intensity (MFI) fold of the untreated control sample (n = 4, statistical t-test: $^{*}p \leq 0.05$, $^{**}p \leq 0.01$, $^{***}p \leq 0.001$, ns = nonsignificant).

these BMDCs could be assessed by quantification of the surface-expressed costimulatory molecules CD40 (Figure 5D1), CD80 (Figure 5D2) and CD86 (Figure 5D3) as well as the antigen-presenting receptor MHCII (Figure 5D4). These constitute relevant markers of dendritic cell maturation (untreated cells and incubation with TLR 4 agonist LPS served as controls—Figure 5D). Interestingly, polymers without IMDQ or IMDQ-Me could not increase the expression of any of these markers, thereby remaining at similar levels as PBS or untreated cells and, thus, underlining the carriers' immunological inertness. On the contrary, soluble IMDQ or IMDQ-Me immediately increased the expression of either activation markers to similar levels as LPS. According to their previously confirmed high TLR 7/8 activity, both agonists conferred BMDC maturation when applied at 0.2, 1, and 5 µM in the case of soluble IMDQ or IMDQ-Me. Surprisingly, this was also the case for IMDQ-Me-loaded polymers, as at each concentration, all maturation markers were already at similar levels as observed for soluble IMDQ-Me (green curves in Figure 5D1-4 right). This again confirms the reversible intracellular release of secondary amines from the macromolecular carrier, which may also occur inside the primary immune cells and promote their maturation by IMDQ-Me. In contrast to that, the conjugation of IMDQ to the polymer carrier, resulting in irreversible IMDQ-polymer conjugates, yielded much weaker primary immune cell maturation. While significantly reduced maturation expression levels for CD40, CD80, CD86 and MHCII were found for 0.2 µM and 1 µM IMDQ equivalent concentrations (yellow curves in Figure 5D1-4 left—although the expression levels of MHCII were less significant), only the highest dose of 5 µM IMDQ equivalents was able to induce some BDMC maturation, with expression levels for CD40, CD80, CD86 and MHCII almost matching those of soluble IMDQ (yellow curves in Figure 5D1-4, left).

Overall, these results confirm that 2-propionic-3-methylmaleic anhydride amide-based polymethacrylamides are a valuable platform to control the delivery and release of secondary amine-containing small molecules under acidic endosomal conditions. They represent an elegant and promising tool for the controlled cellular delivery of immune stimulatory drugs.

Conclusions

Substituted maleic anhydrides are well-known for their acid-triggered release of conjugated amines. In this study, we demonstrated the successful synthesis of a novel polymerizable 2-propionic-3-methylmaleic anhydride as a methacrylamide monomer. It could be applied during CRPs and afforded well-defined polymer carriers for pH-reversible post-polymerization modifications. To the best of our knowledge, the incorporation of functional 2-propionic-3-methylmaleic anhydride groups into polymerizable methacrylamides has not been reported before. The modification of polymer anhydrides with primary amines resulted in the conversion of maleic anhydrides into imide bonds. These imide bonds are resistant to pH changes, affording a loss of the polymers' release behavior in acidic environments. Only secondary amines maintained the responsiveness of the polymeric 2-propionic-3-methylmaleic anhydrides and ensured a quantitative release. A conversion of the polymers into water-soluble derivatives yielded nontoxic carriers with high dose-dependent uptake into macrophages. During these experiments, the cellular delivery and intracellular release of secondary amine conjugates were confirmed by fluorescence microscopy and flow cytometry. These studies finally led to the conjugation of imidazoquinoline-based TLR 7/8 agonists to control their receptor activity. Compared to the primary amine-bearing IMDQ, a novel TLR 7/8 agonist IMDQ-Me retained its immune stimulation activity after conjugation to the carrier in both reporter cell lines as well as primary immune cells. Due to its secondary amine, it can be released intracellularly and, thus, promote TLR 7/8 receptor stimulation.

Altogether, these experiments underline the high potential of 2-propionic-3-methylmaleic anhydride-based polymers as a suitable platform for pH-triggered delivery of various (immuno)-drugs, thus paving the way for new opportunities in macromolecule-assisted immunotherapy.

Author Contributions

The manuscript was written through contributions of all authors. All authors have given approval to the final version of the manuscript.

Funding

The authors kindly acknowledge financial support by the DFG through the Emmy Noether program (L. N.) and the SFB 1066 Projects B03 (L.N.), B04 (S.G., L.N.) and B015 (M.B.).

Notes

The authors declare no competing financial interest.

Acknowledgements

A.G.H. and L.N. want to thank Manfred Wagner and Stefan Spang for NMR measurements as well as Tanja Weil for providing access to excellent laboratory facilities.

References

(1) Lybaert, L.; Vermaelen, K.; De Geest, B. G.; Nuhn, L. Immunoengineering through Cancer Vaccines – A Personalized and Multi-Step Vaccine Approach towards Precise Cancer Immunity. *J. Control. Release* **2018**, *289*, 125–145.

(2) Milling, L.; Zhang, Y.; Irvine, D. J. Delivering Safer Immunotherapies for Cancer. *Adv. Drug Deliv. Rev.* **2017**, *114*, 79–101.

(3) Teijeira, A.; Cueto, F. J.; Garasa, S.; Pe, J. L.; Sancho, D.; Melero, I. Antigen Cross-Presentation and T-Cell Cross-Priming in Cancer Immunology and Immunotherapy. *Ann. Oncol.* **2017**, *28* (September), 44–55.

(4) Palucka, K.; Banchereau, J. Cancer Immunotherapy via Dendtritic Cells. *Nat. Rev. Cancer* **2013**, *12* (4), 1–19.

(5) Yap, T. A.; Parkes, E. E.; Peng, W.; Moyers, J. T.; Curran, M. A.; Tawbi, H. A. Development of Immunotherapy Combination Strategies in Cancer. *Cancer Discov.* **2021**, *11* (6), 1368–1397.

(6) Salem, M. L. Triggering of Toll-like Receptor Signaling Pathways in T Cells Contributes to the Anti-Tumor Efficacy of T Cell Responses. *Immunol. Lett.* **2011**, *137* (1–2), 9–14.

(7) Van Herck, S.; De Geest, B. G. Nanomedicine-Mediated Alteration of the Pharmacokinetic Profile of Small Molecule Cancer Immunotherapeutics. *Acta Pharmacol. Sin.* **2020**, *41* (7), 881–894.

(8) Mancini, R. J.; Stutts, L.; Ryu, K. A.; Tom, J. K.; Esser-Kahn, A. P. Directing the Immune System with Chemical Compounds. *ACS Chem. Biol.* **2014**, *9* (5), 1075–1085.

(9) Iwasaki, A.; Medzhitov, R.; Haven, N. Control of Adaptive Immunity by the Innate Immune System. *Nat. Immunol.* **2015**, *16* (4), 343–353.

(10) Shields, C. W.; Wang, L. L. W.; Evans, M. A.; Mitragotri, S. Materials for Immunotherapy. *Adv. Mater.* **2020**, *32* (13), 1–56.

(11) Beesu, M.; Salyer, A. C. D.; Brush, M. J. H.; Trautman, K. L.; Hill, J. K.; David, S. A. Identification of High-Potency Human TLR8 and Dual TLR7/TLR8 Agonists in Pyrimidine-2,4-Diamines. *J. Med. Chem.* **2017**, *60* (5), 2084–2098.

(12) Cabral, H.; Kinoh, H.; Kataoka, K. Tumor-Targeted Nanomedicine for Immunotherapy. *Acc. Chem. Res.* **2020**, *53* (12), 2765–2776.

(13) Shi, Y.; Lammers, T. Combining Nanomedicine and Immunotherapy. *Acc. Chem. Res.* **2019**, *52* (6), 1543–1554.

(14) Wang, B.; Van Herck, S.; Chen, Y.; Bai, X.; Zhong, Z.; Deswarte, K.; Lambrecht, B. N.; Sanders, N. N.; Lienenklaus, S.; Scheeren, H. W.; David, S. A.; Kiessling, F.; Lammers, T.; De Geest, B. G.; Shi, Y. Potent and Prolonged Innate Immune Activation by Enzyme-Responsive Imidazoquinoline TLR7/8 Agonist Prodrug Vesicles. *J. Am. Chem. Soc.* **2020**, *142* (28), 12133–12139.

(15) De Vrieze, J.; Louage, B.; Deswarte, K.; Zhong, Z.; De Coen, R.; Van Herck, S.; Nuhn, L.; Kaas Frich, C.; Zelikin, A. N.; Lienenklaus, S.; Sanders, N. N.; Lambrecht, B. N.; David, S. A.; De Geest, B. G. Potent Lymphatic Translocation and Spatial Control Over Innate Immune Activation by Polymer–Lipid Amphiphile Conjugates of Small-Molecule TLR7/8 Agonists. *Angew. Chemie - Int. Ed.* **2019**, *58* (43), 15390–15395.

(16) Lynn, G. M.; Chytil, P.; Francica, J. R.; Lagová, A.; Kueberuwa, G.; Ishizuka, A. S.; Zaidi, N.; Ramirez-Valdez, R. A.; Blobel, N. J.; Baharom, F.; Leal, J.; Wang, A. Q.; Gerner, M. Y.; Etrych, T.; Ulbrich, K.; Seymour, L. W.; Seder, R. A.; Laga, R. Impact of Polymer-TLR-7/8 Agonist (Adjuvant) Morphology on the Potency and Mechanism of CD8 T Cell Induction. *Biomacromolecules* **2019**, *20* (2), 854–870.

(17) Van Herck, S.; Deswarte, K.; Nuhn, L.; Zhong, Z.; Portela Catani, J. P.; Li, Y.; Sanders, N. N.; Lienenklaus, S.; De Koker, S.; Lambrecht, B. N.; David, S. A.; De Geest, B. G. Lymph-Node-Targeted Immune Activation by Engineered Block Copolymer Amphiphiles-TLR7/8 Agonist Conjugates. *J. Am. Chem. Soc.* **2018**, *140* (43), 14300–14307.

(18) Nuhn, L.; De Koker, S.; Van Lint, S.; Zhong, Z.; Catani, J. P.; Combes, F.; Deswarte, K.; Li, Y.; Lambrecht, B. N.; Lienenklaus, S.; Sanders, N. N.; David, S. A.; Tavernier, J.; De Geest, B. G. Nanoparticle-Conjugate TLR7/8 Agonist Localized Immunotherapy Provokes Safe Antitumoral Responses. *Adv. Mater.* **2018**, *30* (45), 1–9.

(19) Nuhn, L.; Bolli, E.; Massa, S.; Vandenberghe, I.; Movahedi, K.; Devreese, B.; Van Ginderachter, J. A.; De Geest, B. G. Targeting Protumoral Tumor-Associated Macrophages with Nanobody-Functionalized Nanogels through Strain Promoted Azide Alkyne Cycloaddition Ligation. *Bioconjug. Chem.* **2018**, *29* (7), 2394–2405.

(20) Nuhn, L.; Van Hoecke, L.; Deswarte, K.; Schepens, B.; Li, Y.; Lambrecht, B. N.; De Koker, S.; David, S. A.; Saelens, X.; De Geest, B. G. Potent Anti-Viral Vaccine Adjuvant Based on PH-Degradable Nanogels with Covalently Linked Small Molecule Imidazoquinoline TLR7/8 Agonist. *Biomaterials* **2018**, *178*, 643–651.

(21) Stickdorn, J.; Stein, L.; Arnold-Schild, D.; Hahlbrock, J.; Medina-Montano, C.; Bartneck, J.; Ziß, T.; Montermann, E.; Kappel, C.; Hobernik, D.; Haist, M.; Yurugi, H.; Raabe, M.; Best, A.; Rajalingam, K.; Radsak, M. P.; David, S. A.; Koynov, K.; Bros, M.; Grabbe, S.; Schild, H.; Nuhn, L. Systemically Administered TLR7/8 Agonist and Antigen-Conjugated Nanogels Govern Immune Responses against Tumors. *ACS Nano* **2022**, *16* (3), 4426–4443.

(22) Stickdorn, J.; Nuhn, L. Reactive-Ester Derived Polymer Nanogels for Cancer Immunotherapy. *Eur. Polym. J.* **2020**, *124* (September 2019), 109481.

(23) Nuhn, L.; Vanparijs, N.; De Beuckelaer, A.; Lybaert, L.; Verstraete, G.; Deswarte, K.; Lienenklaus, S.; Shukla, N. M.; Salyer, A. C. D.; Lambrecht, B. N.; Grooten, J.; David, S. A.; De Koker, S.; De Geest, B. G. PH-Degradable Imidazoquinoline-Ligated Nanogels for Lymph Node-Focused Immune Activation. *Proc. Natl. Acad. Sci. U. S. A.* **2016**, *113* (29), 8098–8103.

(24) Fu, J.; Yu, C.; Li, L.; Yao, S. Q. Intracellular Delivery of Functional Proteins and Native Drugs by Cell-Penetrating Poly(Disulfide)S. *J. Am. Chem. Soc.* **2015**, *137* (37), 12153–12160.

(25) Wei, M.; Gao, Y.; Li, X.; Serpe, M. J. Stimuli-Responsive Polymers and Their Applications. *Polym. Chem.* **2017**, *8* (1), 127–143.

(26) Schattling, P.; Jochum, F. D.; Theato, P. Multi-Stimuli Responsive Polymers-the All-in-One Talents. *Polym. Chem.* **2014**, *5* (1), 25–36.

(27) Iyer, R.; Nguyen, T.; Padanilam, D.; Xu, C.; Saha, D.; Nguyen, K. T.; Hong, Y. Glutathione-Responsive Biodegradable Polyurethane Nanoparticles for Lung Cancer Treatment. *J. Control. Release* **2020**, *321* (November 2019), 363–371.

(28) Bixenmann, L.; Stickdorn, J.; Nuhn, L. Amphiphilic Poly(Esteracetal)s as Dual PH-and Enzyme-Responsive Micellar Immunodrug Delivery Systems. *Polym. Chem.* **2020**, *11* (13), 2441–2456.

(29) Kanamala, M.; Wilson, W. R.; Yang, M.; Palmer, B. D.; Wu, Z. Mechanisms and Biomaterials in PH-Responsive Tumour Targeted Drug Delivery: A Review. *Biomaterials* **2016**, *85*, 152–167.

(30) Liu, B.; Thayumanavan, S. Substituent Effects on the PH Sensitivity of Acetals and Ketals and Their Correlation with Encapsulation Stability in Polymeric Nanogels. *J. Am. Chem. Soc.* **2017**, *139* (6), 2306–2317.

(31) Cao, H.; Dong, Y.; Bre, L.; Tapeinos, C.; Wang, W.; Pandit, A. An Acetal-Based Polymeric Crosslinker with Controlled PH-Sensitivity. *RSC Adv.* **2016**, *6* (12), 9604–9611.

(32) Murthy, N.; Thng, Y. X.; Schuck, S.; Xu, M. C.; Fréchet, J. M. J. A Novel Strategy for Encapsulation and Release of Proteins: Hydrogels and Microgels with Acid-Labile Acetal Cross-Linkers. *J. Am. Chem. Soc.* **2002**, *124* (42), 12398–12399.

(33) Van Driessche, A.; Kocere, A.; Everaert, H.; Nuhn, L.; Van Herck, S.; Griffiths, G.; Fenaroli, F.; De Geest, B. G. PH-Sensitive Hydrazone-Linked Doxorubicin Nanogels via Polymeric-Activated Ester Scaffolds: Synthesis, Assembly, and in Vitro and in Vivo Evaluation in Tumor-Bearing Zebrafish. *Chem. Mater.* **2018**, *30* (23), 8587–8596.

(34) Liu, Z.; Zhang, N. PH-Sensitive Polymeric Micelles for Programmable Drug and Gene Delivery. *Curr. Pharm. Des.* **2012**, *18* (23), 3442–3451.

(35) Wang, C.; Wang, G.; Wang, Z.; Zhang, X. A PH-Responsive Superamphiphile Based on Dynamic Covalent Bonds. *Chem. - A Eur. J.* **2011**, *17* (12), 3322–3325.

(36) Jazani, A. M.; Oh, J. K. Development and Disassembly of Single and Multiple Acid-Cleavable Block Copolymer Nanoassemblies for Drug Delivery. *Polym. Chem.* **2020**, *11* (17), 2934–2954.

(37) Kamada, H.; Tsutsumi, Y.; Sato-Kamada, K.; Yamamoto, Y.; Yoshioka, Y.; Okamoto, T.; Nakagawa, S.; Nagata, S.; Mayumi, T. Synthesis of a Poly(Vinylpyrrolidone-Co-Dimethyl Maleic Anhydride) Co-Polymer and Its Application for Renal Drug Targeting. *Nat. Biotechnol.* **2003**, *21* (4), 399–404.

(38) Du, J. Z.; Li, H. J.; Wang, J. Tumor-Acidity-Cleavable Maleic Acid Amide (TACMAA): A Powerful Tool for Designing Smart Nanoparticles to Overcome Delivery Barriers in Cancer Nanomedicine. *Acc. Chem. Res.* **2018**, *51* (11), 2848–2856.

(39) Zhang, X.; Zhang, K.; Haag, R. Multi-Stage, Charge Conversional, Stimuli-Responsive Nanogels for Therapeutic Protein Delivery. *Biomater. Sci.* **2015**, *3* (11), 1487–1496.

(40) Kang, S.; Kim, Y.; Song, Y.; Choi, J. U.; Park, E.; Choi, W.; Park, J.; Lee, Y. Comparison of PH-Sensitive Degradability of Maleic Acid Amide Derivatives. *Bioorganic Med. Chem. Lett.* **2014**, *24* (10), 2364–2367.

(41) Su, S.; Du, F. S.; Li, Z. C. Synthesis and PH-Dependent Hydrolysis Profiles of Mono- and Dialkyl Substituted Maleamic Acids. *Org. Biomol. Chem.* **2017**, *15* (39), 8384–8392.

(42) Spanedda, M. V.; Bourel-Bonnet, L. Cyclic Anhydrides as Powerful Tools for Bioconjugation and Smart Delivery. *Bioconjug. Chem.* **2021**, *32* (3), 482–496.

(43) Butler, P. J.; Harris, J. I.; Hartley, B. S.; Lebeman, R. The Use of Maleic Anhydride for the Reversible Blocking of Amino Groups in Polypeptide Chains. *Biochem. J.* **1969**, *112* (5), 679–689.

(44) Tao, A.; Huang, G. Lo; Igarashi, K.; Hong, T.; Liao, S.; Stellacci, F.; Matsumoto, Y.; Yamasoba, T.; Kataoka, K.; Cabral, H. Polymeric Micelles Loading Proteins through Concurrent Ion Complexation and PH-Cleavable Covalent Bonding for In Vivo Delivery. *Macromol. Biosci.* **2020**, *20* (1), 1–11.

(45) Maier, K.; Wagner, E. Acid-Labile Traceless Click Linker for Protein Transduction. *J. Am. Chem. Soc.* **2012**, *134* (24), 10169–10173.

(46) Lyu, M.; Yazdi, M.; Lin, Y.; Höhn, M.; Lächelt, U.; Wagner, E. Receptor-Targeted Dual PH-Triggered Intracellular Protein Transfer. *ACS Biomater. Sci. Eng.* **2022**.

(47) Lechner, M. D.; Nordmeier, E. H.; Gehrke, K. *Makromolekulare Chemie*; **2010**.

(48) Mätzig, J.; Drache, M.; Beuermann, S. Self-Initiated Butyl Acrylate Polymerizations in Bulk and in Solution Monitored by in-Line Techniques. *Polymers (Basel).* **2021**, *13* (12).

(49) Van Guyse, J. F. R.; Bernhard, Y.; Podevyn, A.; Hoogenboom, R. Non-activated Esters as Reactive Handles in Direct Post-polymerization Modification. *Angew. Chemie Int. Ed.* **2023**, *62* (40), e202303841.

(50) Fang, Y.; Xue, J.; Gao, S.; Lu, A.; Yang, D.; Jiang, H.; He, Y.; Shi, K. Cleavable PEGylation: A Strategy for Overcoming the "PEG Dilemma" in Efficient Drug Delivery. *Drug Deliv.* **2017**, *24* (0), 22–32.

(51) Pozzi, D.; Colapicchioni, V.; Caracciolo, G.; Piovesana, S.; Capriotti, A. L.; Palchetti, S.; De Grossi, S.; Riccioli, A.; Amenitsch, H.; Laganà, A. Effect of Polyethyleneglycol (PEG) Chain Length on the Bio-Nano- Interactions between PEGylated Lipid Nanoparticles and Biological Fluids: From Nanostructure to Uptake in Cancer Cells. *Nanoscale* **2014**, *6* (5), 2782–2792.

(52) Bhagchandani, S.; Johnson, J. A.; Irvine, D. J. Evolution of Toll-like Receptor 7/8 Agonist Therapeutics and Their Delivery Approaches: From Antiviral Formulations to Vaccine Adjuvants. *Adv. Drug Deliv. Rev.* **2021**, *175*, 113803.

(53) Huppertsberg, A.; Kaps, L.; Zhong, Z.; Schmitt, S.; Stickdorn, J.; Deswarte, K.; Combes, F.; Czysch, C.; De Vrieze, J.; Kasmi, S.; Choteschovsky, N.; Klefenz, A.; Medina-Montano, C.; Winterwerber, P.; Chen, C.; Bros, M.; Lienenklaus, S.; Sanders, N. N.; Koynov, K.; Schuppan, D.; Lambrecht, B. N.; David, S. A.; De Geest, B. G.; Nuhn, L. Squaric Ester-Based, PH-Degradable Nanogels: Modular Nanocarriers for Safe, Systemic Administration of Toll-like Receptor 7/8 Agonistic Immune Modulators. *J. Am. Chem. Soc.* **2021**, *143* (26), 9872–9883.

(54) Czysch, C.; Medina-Montano, C.; Zhong, Z.; Fuchs, A.; Stickdorn, J.; Winterwerber, P.; Schmitt, S.; Deswarte, K.; Raabe, M.; Scherger, M.; Combes, F.; De Vrieze, J.; Kasmi, S.; Sandners, N. N.; Lienenklaus, S.; Koynov, K.; Räder, H. J.; Lambrecht, B. N.; David, S. A.; Bros, M.; Schild, H.; Grabbe, S.; De Geest, B. G.; Nuhn, L. Transient Lymph Node Immune Activation by Hydrolysable Polycarbonate Nanogels. *Adv. Funct. Mater.* **2022**, *32* (35), 2203490.

(55) Czysch, C.; Medina-Montano, C.; Dal, N. J. K.; Dinh, T.; Fröder, Y.; Winterwerber, P.; Maxeiner, K.; Räder, H. J.; Schuppan, D.; Schild, H.; Bros, M.; Biersack, B.; Feranoli, F.; Grabbe, S.; Nuhn, L. End Group Dye-Labeled Polycarbonate Block Copolymers for Micellar (Immuno-)Drug Delivery. *Macromol. Rapid Commun.* **2022**, *43* (12), 202200095.

POLYMERIZABLE 2-PROPIONIC-3-METHYLMALEIC ANHYDRIDES AS A MACROMOLECULAR CARRIER PLATFORM FOR PH-RESPONSIVE IMMUNODRUG DELIVERY

-Supporting Information-

Alina G. Heck[1], Judith Stickdorn[1], Laura R. Rosenberger[2], Maximilian Scherger[1], Jonas Woller[1], Katharina Eigen[3], Matthias Bros[2], Stephan Grabbe[2] and Lutz Nuhn[,1,3]*

Dedicated to Professor Rudolf Zentel on the occasion of his 70th birthday.

1: Max Planck Institute for Polymer Research, 55128 Mainz, Germany

2: Department of Dermatology, University Medical Center (UMC) of the Johannes Gutenberg-University Mainz, 55131 Mainz, Germany

3: Institute of Functional Materials and Biofabrication, Department of Chemistry and Pharmacy, Julius-Maximilians-Universität Würzburg, 97070 Würzburg, Germany

*: corresponding author: Prof. Dr. Lutz Nuhn (E-mail: lutz.nuhn@uni-wuerzburg.de)

Materials and Methods

Unless otherwise described, all reagents and solvents were purchased from commercial sources, such as TCI Chemicals (Tokyo, Japan), Sigma Aldrich (Taufkirchen, Germany) or Rapp Polymers (Tübingen, Germany) and used without further purification. N-(3-aminopropyl)methacrylamide hydrochloride (APMA) was purchased from abcr GmbH (Karlsruhe, Germany), tetramethylrhodamine cadaverine from Biotium (Fermont, CA, USA) and oxalyl chloride was obtained from Thermo Fisher Scientific (Waltham, MA, USA).

TLR7/8 agonist 1-(4-(aminomethyl)benzyl)-2-butyl-1-H-imidazo[4,5-c]quinoline-4-amine (IMDQ) was kindly provided from Maximilian Scherger (Max Planck Institute for Polymer Research, Germany).[1] Prior to use, azobis(isobutyronitrile) (AIBN) was recrystallized from ethanol twice.

Hexafluoroisopropyl alcohol (HFIP) was purchased from Fluorochem Ltd. (Hadfield, UK) and deuterated solvents were bought from Sigma Aldrich. Ultrapure (up) water was prepared using a MILLI-Q® Reference A+ System. Dialysis was performed using Spectra/Por7™ membranes with a molecular weight cut-off of 1,000 g/mol. For silica gel chromatography silica with particle size of 0.063-0.2 mm from Macherey-Nagel GmbH & Co. KG (Dueren, Germany) was used.

Dulbecco's phosphate-buffered saline (PBS), cell culture medium and supplements were obtained from Thermo Fisher Scientific. The RAW-Dual™ (IRF-Lucia/KI-[MIP-2]SEAP) murine macrophage reporter cell line as well as QUANTI-Blue™ solution were purchased from InvivoGen (San Diego, CA, USA). RAW-Dual™ cells were cultured in DMEM-GlutaMAX™ medium, containing 10% fetal bovine serum, 1% penicillin/streptomycine, 0.02% normocine, and 0.01% zeocin at 37 °C with 5% CO_2 saturation.

Instrumentation

Nuclear Magnetic Resonance (NMR) Spectroscopy

^{1}H, ^{13}C and 2D NMR spectra were recorded on a Bruker Avance III 300 MHz, Bruker Avance III 400 MHz, Bruker Avance III 500 MHz or Bruker Avance III 700 MHz spectrometer. Samples were prepared in deuterated solvents and the corresponding spectra analyzed using MestReNova 14.2.0 by Mestrelab Research. The chemical shifts are specified in parts per million (ppm) relative to tetramethylsilane (TMS). Diffusion ordered spectroscopy (DOSY) were

recorded on a Bruker Avance III 500 MHz or Bruker Avance III 700 MHz spectrometer at room temperature. All spectra were referenced to the respective solvent signals.

Size Exclusion Chromatography (SEC)

SEC characterization was performed on a SECcurity^{2}instrument from PPS, Mainz, equipped with SECcurtity^{2}isocratic pump, a degasser, an autosampler, a column thermostat, an UV and RI detector. HFIP containing 3 g/L potassium trifluoroacetate was used as an eluent at a flow rate of 0.8 mL/min and a column temperature of 40 °C. The columns were packed with modified silica gel (PFG columns, particle size 7 µM, porosity: 100 Å and 1000 Å), obtained from PSS Polymer Standards Service GmbH, Mainz, Germany. Calibration was carried out with poly(methyl methacrylate) (PMMA) standards, purchased from PSS, Mainz. Polymer samples were prepared at 1 mg/mL and filtered through GHP syringe filters (0.2 µm pore size, Acrodisc) before injection.

Ultraviolet-Visible Spectroscopy (UV-vis) and Fluorescence Spectroscopy

UV-vis spectra were recorded on a Thermo Scientific™ NanoDrop™ 2000c spectrophotometer with a Hellma Quartz Cuvette.

Fluorescence spectroscopy as well as RAW-blue and MTT assay absorbance read-out were performed using a Spark 20M Multimode Microplate Reader from Tecan Trading AG (Mannedorf, Switzerland).

Electrospray-Ionization Mass Spectrometry (ESI-MSI)

ESI mass spectra were conducted using an Agilent 6545 QTOF-MS (Santa Clara, CA, USA). Samples were prepared at 0.1 mg/mL in methanol.

Fluorescence Confocal Microscopy

Fluorescence confocal laser scanning microscopy images were recorded on a Leica SP5 confocal microscope with a 63x oil immersion objective. Images were processed using Leica Application Suite X 3.7.4.23463 by Leica Microsystems.

Fluorescence-Activated Cell Scanning (FACS)

Flow cytometric analyses were performed on a BD Accuri C6 from BD Biosciences or on an Attune NxT from Thermo Fischer. The obtained data were analyzed with FloJo™_v10.8.1_CL by BD Biosciences or Attune NxT Flow cytometer software by Thermo Fisher.

Syntheses

Monomer

Synthesis of Dimethyl 2-Oxoglutarate

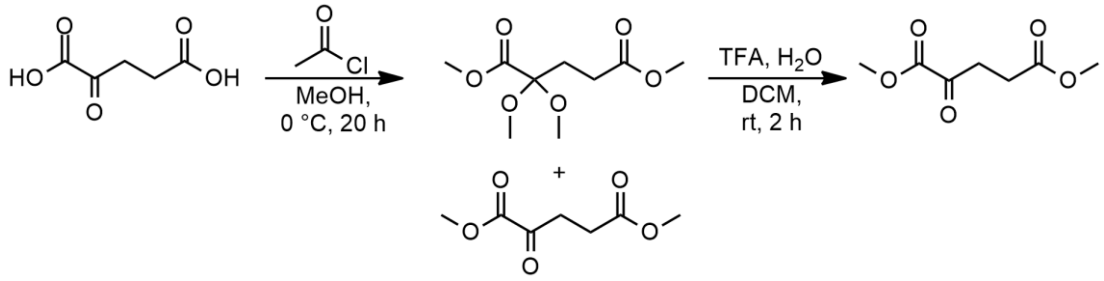

Figure S1: Synthesis of dimethyl 2-oxoglutarate in two steps.

The synthesis of dimethyl 2-oxoglutarate was adapted from the literature with minor modification.[2] Acetyl chloride (27.3 mL, 383 mmol, 2.24 eq) was placed in a three-neck round bottom flask equipped with a Dimroth condenser and dropping funnel. The gas outlet led into an aqueous sodium hydroxide solution to neutralize resulting HCl. Then, 2-oxoglutaric acid (25 g, 171 mmol, 1 eq) was dissolved in methanol (214 mL) and slowly added *via* dropping funnel over 4 h, under cooling. The reaction solution was stirred for another 16 h at 0 °C and after complete conversion concentrated under vacuum, redissolved in ethyl acetate (100 mL) and extracted five times with a solution of bicarbonate and sodium chloride (2:3, 50 mL). The organic phase was dried over Na_2SO_4 and evaporated. The resulting crude product was further purified according to the literature and dissolved in 80 mL DCM and H_2O (7.83 mL, 434 mmol, 6 eq).[3] Trifluoroacetic acid (TFA, 39.08 mL, 507 mmol, 7 eq) was added dropwise under nitrogen atmosphere and the reaction mixture was stirred for 2 h at RT. After complete reaction the solvent mixture was removed under vacuum. The residue was redissolved in DCM, washed with a $NaHCO_3$ solution, dried over Na_2SO_4 and evaporated. The product was obtained as a colorless oil (10.83 g, 86%).

^{1}H NMR (300 MHz, $CDCl_3$): δ (ppm) = 3.88 (s, 3H, **a**), 3.69 (s, 3H, **b**), 3.16 (t, J = 6.5 Hz, 2H, **c**), 2.68 (t, J = 6.5 Hz, 2H, **d**).

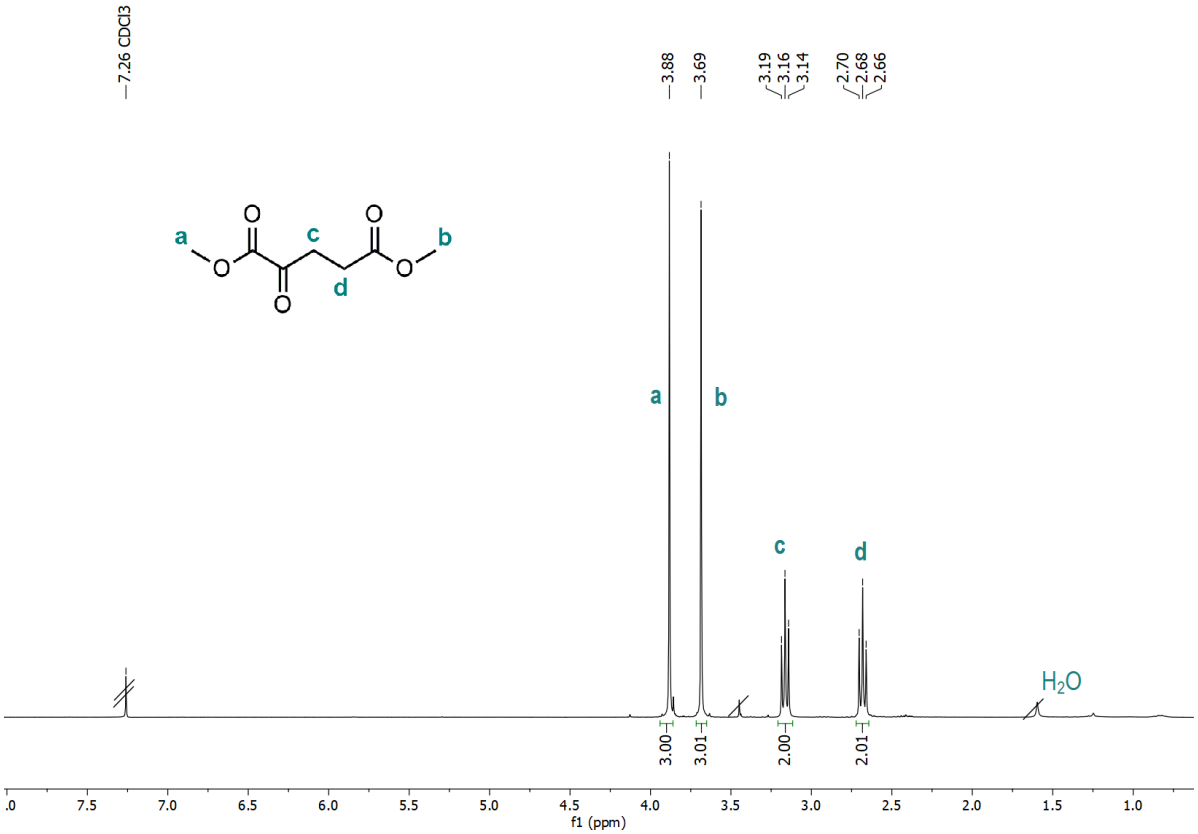

Figure S2: ^{1}H NMR spectrum (300 MHz) of dimethyl 2-oxoglutarate in $CDCl_3$.

Synthesis of (Z)-4-Ethyl 1,3-Dimethyl-Pent-3-Ene-1,3,4-Tricarboxylate

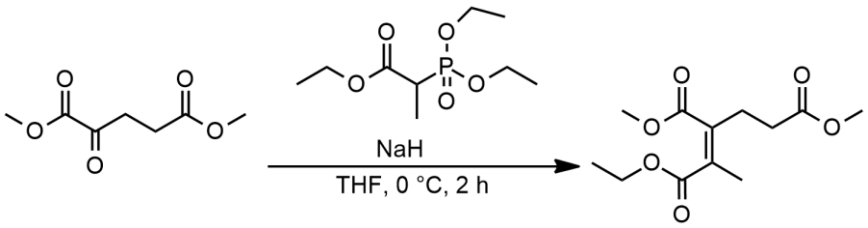

Figure S3: Synthesis of (Z)-4-ethyl 1,3-dimethyl-pent-3-ene-1,3,4-tricarboxylate.

The procedure was adapted from the literature and modified.[4] In an oven-dried two neck round bottom flask, sodium hydride (1.38 g, 57.43 mmol, 1.25 eq) was suspended in dry THF (125 mL) and cooled to 0 °C. Triethyl-2-phosphonopropionate (14.79 mL, 68.91 mmol, 1.5 eq) was slowly added to the suspension *via* dropping funnel. After completion of H_2 gas formation, dimethyl-2-oxoglutarate (6.6 mL 45.94 mmol, 1 eq) was dropped to the solution under ice cooling. The reaction mixture was allowed to stir for another 2 h, before a saturated ammonium chloride solution (140 mL) was added, followed by extraction with diethyl ether (4x40 mL). The combined organic layers were dried over Na_2SO_4, filtrated, and concentrated under reduced

pressure. The crude product was further purified by silica gel chromatography using a mixture of diethyl ether and n-hexane (2:1). The product was obtained as colorless oil (8.85 g, 74%).

^{1}H NMR (300 MHz, $CDCl_3$): δ (ppm) = 4.22 (q, J = 7.2 Hz, 2H, **a**), 3.75 (s, 3H, **b**), 3.68 (s, 3H, **c**), 2.66 (t, J = 7.5 Hz, 2H, **d**) 2.47 (t, J = 7.5 Hz, 2H, **e**), 1.99 (s, 3H, **f**), 1.29 (t, J = 7.1, 3H, **g**).

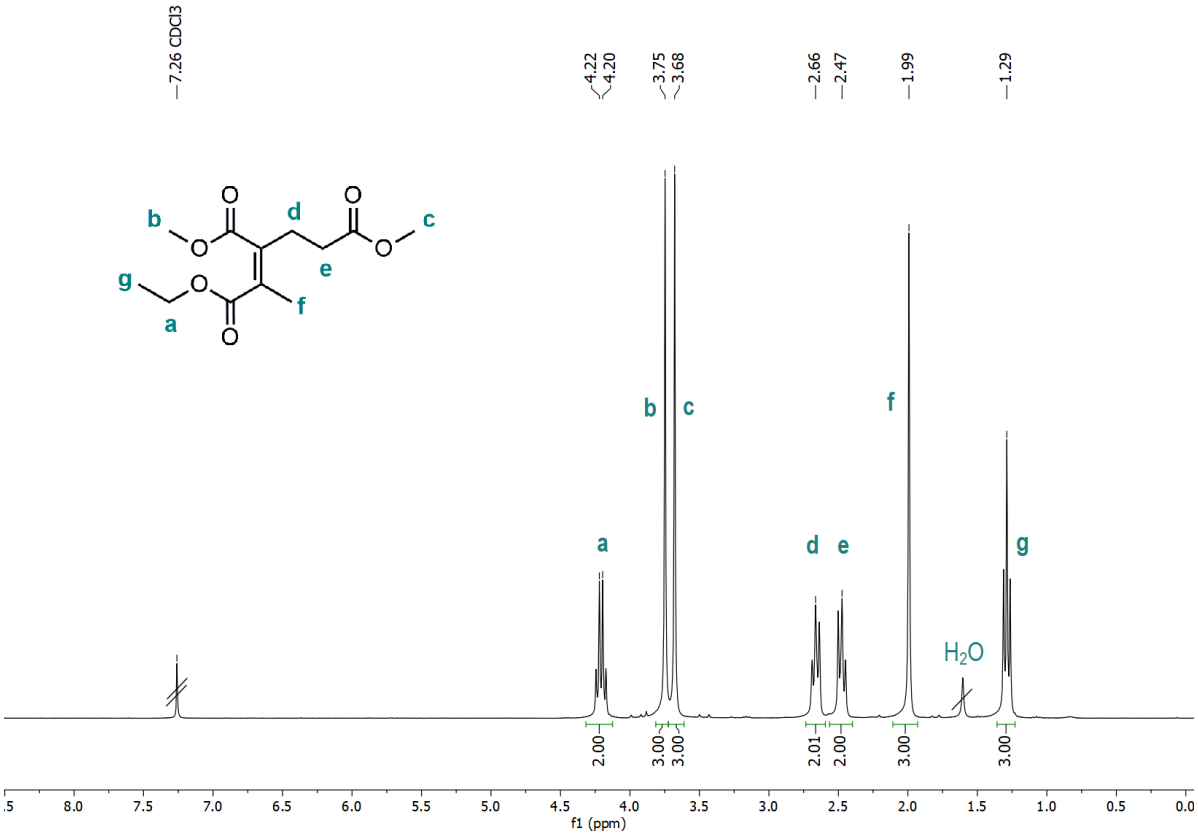

Figure S4: ^{1}H NMR spectrum (300 MHz) of (Z)-4-ethyl 1,3-dimethyl pent-3-ene-1,3,4-tricarboxylate in $CDCl_3$.

Synthesis of 2-Propionic-3-Methylmaleic Anhydride

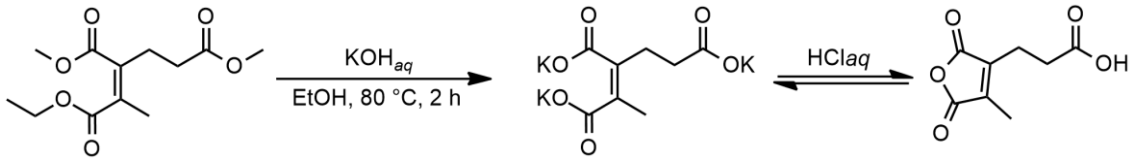

Figure S5: Synthesis of 2-propionic-3-methylmaleic anhydride.

2-Propionic-3-methylmaleic anhydride was synthesized according to the literature with minor modification.[4] In a two neck round bottom flask (Z)-4-ethyl 1,3-dimethyl pent-3-ene-1,3,4-tricarboxylate (8.85 g, 34.3 mmol, 1 eq) was dissolved in ethanol (108 mL) under nitrogen atmosphere. A potassium hydroxide solution (60 mL, 2 mol/L) was added *via* dropping funnel

and heated to reflux for 2 h. During the addition of the potassium hydroxide solution the reaction mixture turned yellow. The solution was allowed to cool to room temperature and acidified with a HCl_{aq} solution to pH 2. The reaction mixture was washed with ethyl acetate (3x40 mL), dried over Na_2SO_4, filtrated, and concentrated *in vacuo*. The crude product was recrystallized twice from THF and n-hexane (1:3) to give 2-propionic-3-methylmaleic anhydride as colorless crystals (4.05 g, 64%).

^{1}H NMR (700 MHz, $CDCl_3$): δ (ppm) = 2.76 (s, 4H, **a+b**), 2.11 (s, 3H, **c**).

^{13}C NMR (176 MHz, $CDCl_3$): δ (ppm) = 177.41 (**a**), 165.71 (**b**), 165.48 (**c**), 142.40 (**d**), 141.74 (**e**), 30.70 (**f**), 19.52 (**g**), 9.66 (**h**).

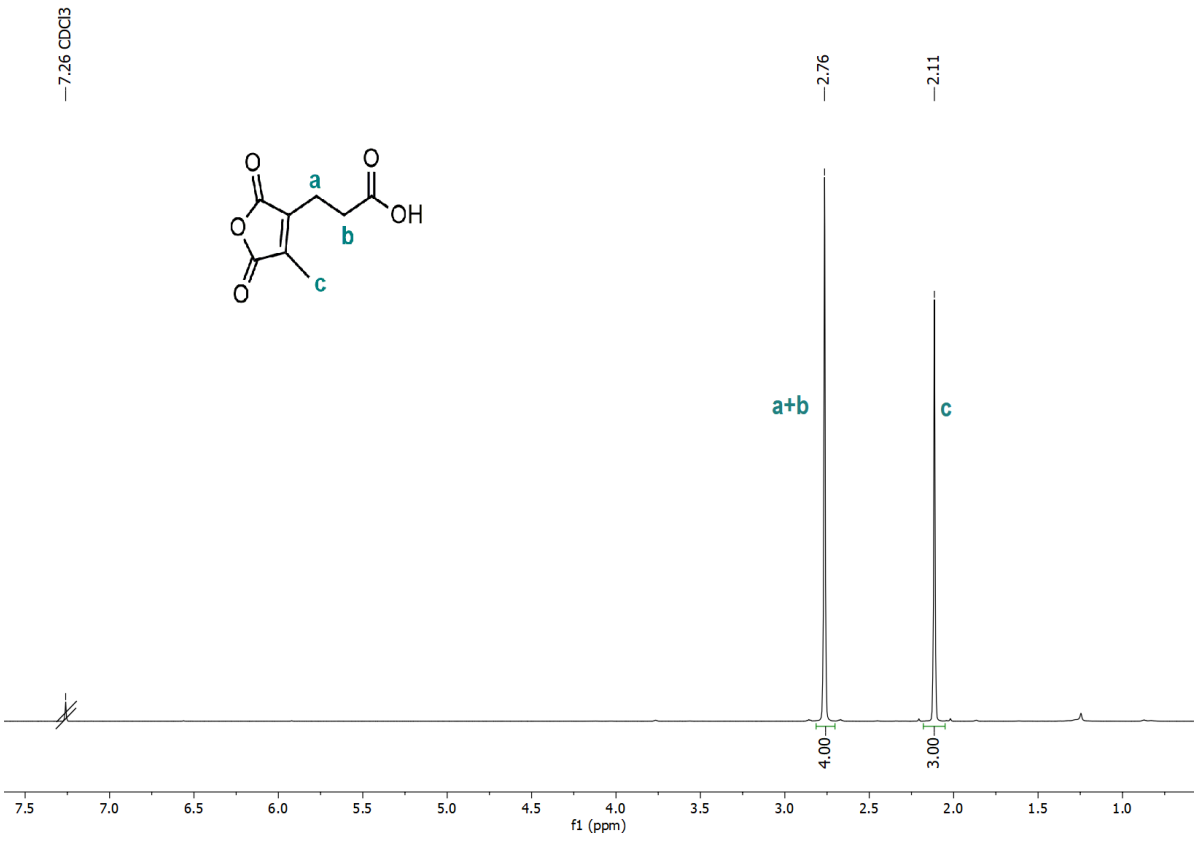

Figure S6: ^{1}H NMR spectrum (700 MHz) of 2-propionic-3-methylmaleic anhydride in $CDCl_3$.

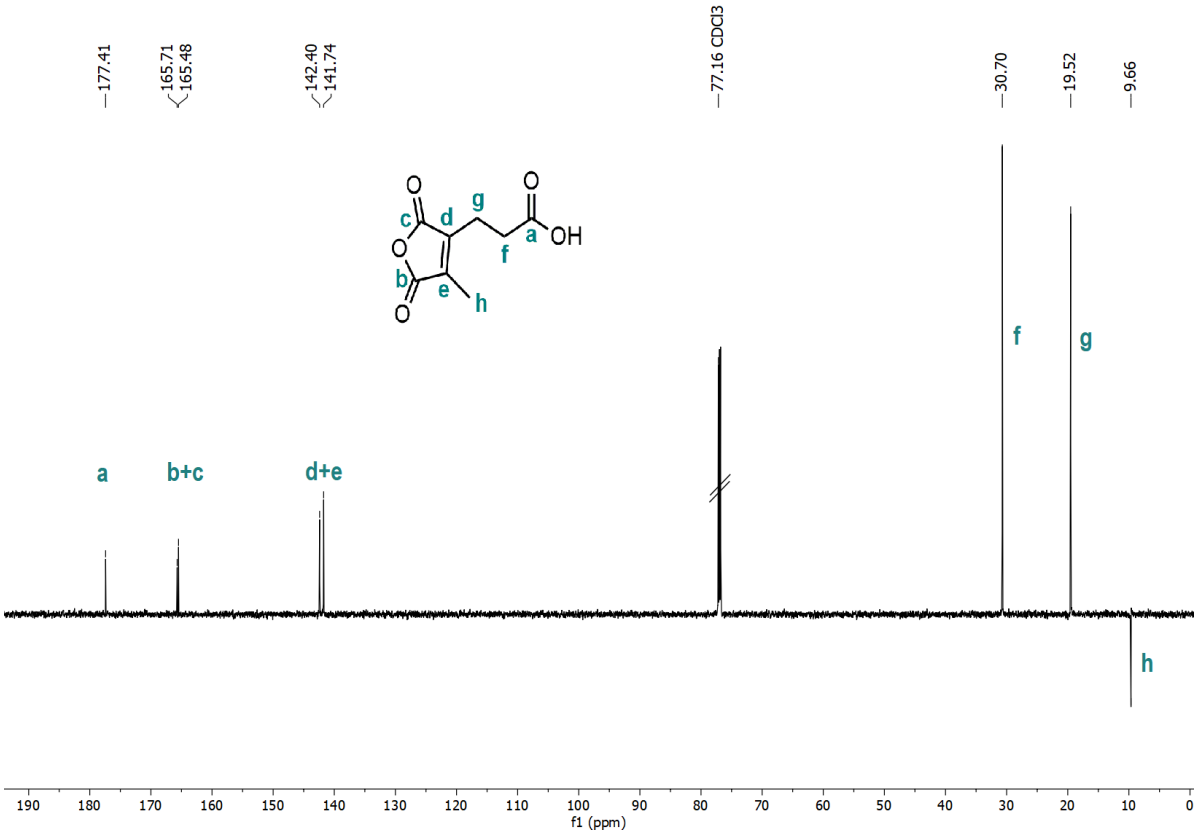

Figure S7: ^{13}C NMR spectrum (176 MHz) of 2-propionic-3-methylmaleic anhydride in $CDCl_3$.

Synthesis of N-(3-(3-(4-Methyl-2,5-Dioxo-2,5-Dihydrofuran-3-yl)propanamido)-Propyl)methacrylamide

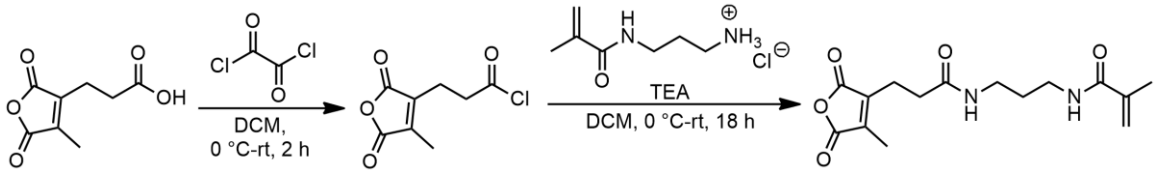

Figure S8: Synthesis of N-(3-(3-(4-methyl-2,5-dioxo-2,5-dihydrofuran-3-yl)propanamido)-propyl)-methacrylamide in two steps.

The synthesis of the monomer was adapted from literature and modified.[4,5] In an oven-dried round bottom flask, 2-propionic-3-methylmaleic anhydride (1.5 g, 8 mmol, 1 eq) was dissolved under nitrogen atmosphere in anhydrous DCM (40 mL). The solution was cooled for 20 min using an ice bath, before 5 drops of DMF and oxalyl chloride (2.3 mL, 27 mmol, 3.3 eq) were added dropwise. After 30 min reaction at 0 °C the mixture was allowed to stir for 1.5 h at room temperature. The solution was concentrated *in vacuo* and then redissolved in anhydrous DCM under nitrogen atmosphere. To this solution N-(3-aminopropyl)methacrylamide hydrochloride

(APMA) (1.0 g, 5.6 mmol, 0.7 eq) dissolved in a mixture of DMF (1.5 mL) and TEA (1.54 mL, 11.12 mmol, 1.5 eq) was slowly added under ice cooling and reacted for further 30 min, before stirred overnight at room temperature. The reaction mixture was washed with a saturated ammonium chloride solution (4x50 mL), dried over Na_2SO_4 and evaporated. To first remove MEHQ inhibitor from the crude product it was dissolved in ethyl acetate (40 mL) and passed through an activated basic alumina column. The solvent was removed by evaporation and the residue further purified by silica gel chromatography using ethyl acetate as eluent. The pure monomer was isolated as slightly yellow, viscose oil (856 mg, 35%).

^{1}H NMR (700 MHz, DMSO-d_6): δ (ppm) = 7.91 (s, 1H, **a**), 7.87 (s, 1H, **b**), 5.62 (s, 1H, **c**), 5.31 (s, 1H, **d**), 3.08 (q, J = 6.8 Hz, 2H, **e**), 3.02 (q, J = 6.8 Hz, 2H, **f**), 2.62 (t, J = 7.4 Hz, 2H, **g**), 2.35 (t, J = 7.4 Hz, 2H, **h**), 1.98 (s, 3H, **i**), 1.84 (s, 3H, **j**), 1.53 (quin, J = 8.4 Hz, 2H, **k**).

^{13}C NMR (176 MHz, DMSO-d_6): δ (ppm) = 170.61 (**a**), 167.64 (**b**), 166.61 (**c**), 166.15 (**d**), 143.12 (**e**), 141.22 (**f**), 140.27 (**g**), 119.04 (**h**). 36.90 (**i+j**), 32.87 (**k**), 29.58 (**l**), 20.51 (**m**), 19.08 (**n**), 9.68 (**o**).

ESI-MS [m/z] = 309.10 $[M+H]^+$ (calc. 309.15), 331.15 $[M+Na]^+$ (calc. 331.13), 347.10 $[M+K]^+$ (calc. 347.10).

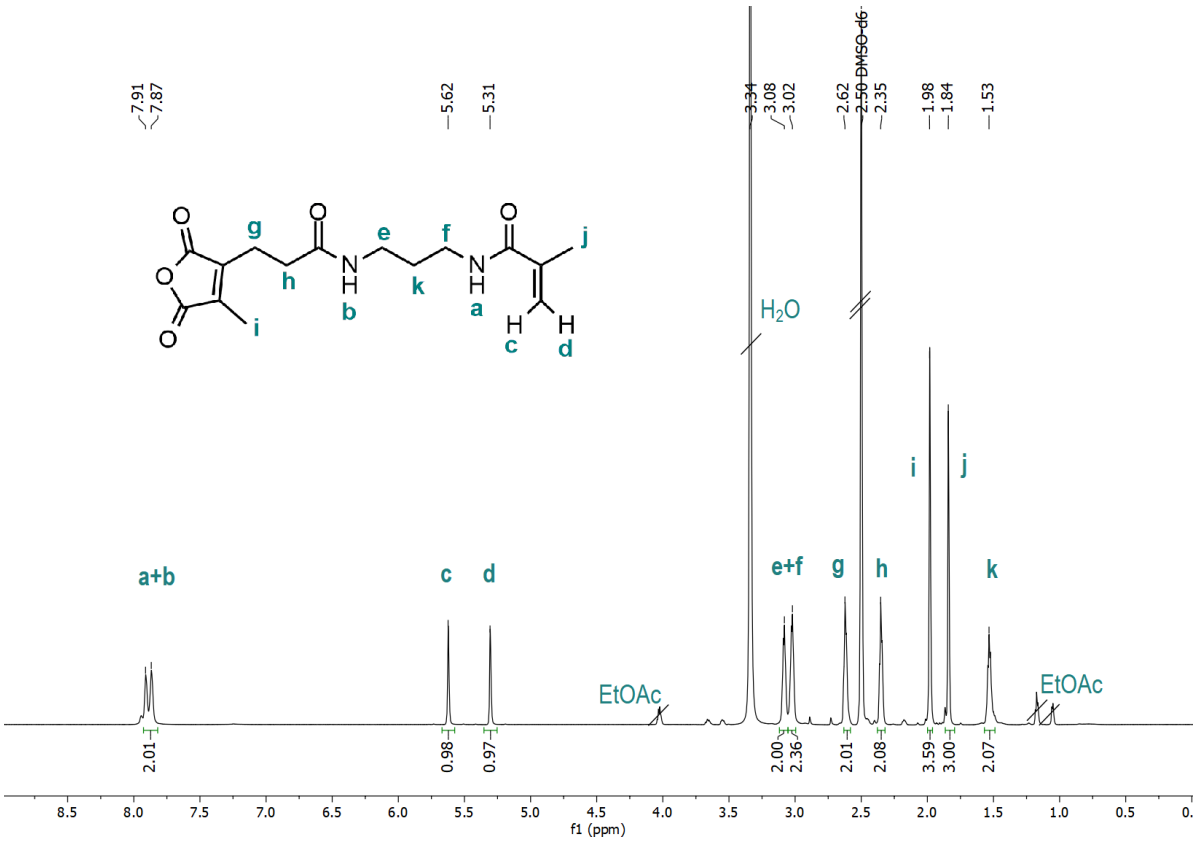

Figure S9: ^{1}H NMR spectrum (700 MHz) of N-(3-(3-(4-methyl-2,5-dioxo-2,5-dihydrofuran-3-yl)propanamido)-propyl)methacrylamide in DMSO-d_6.

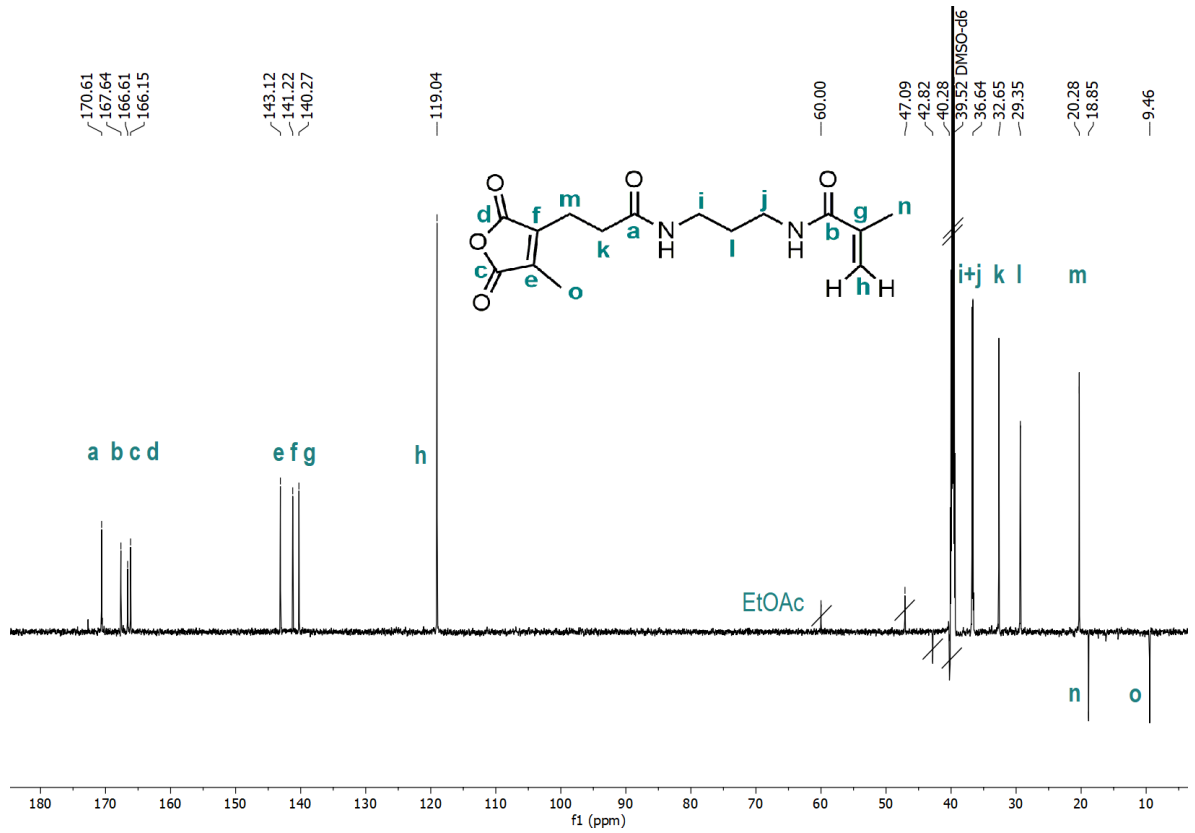

Figure S10: ^{13}C NMR spectrum (176 MHz) of N-(3-(3-(4-methyl-2,5-dioxo-2,5-dihydrofuran-3-yl)propanamido)-propyl)methacrylamide in DMSO-d_6.

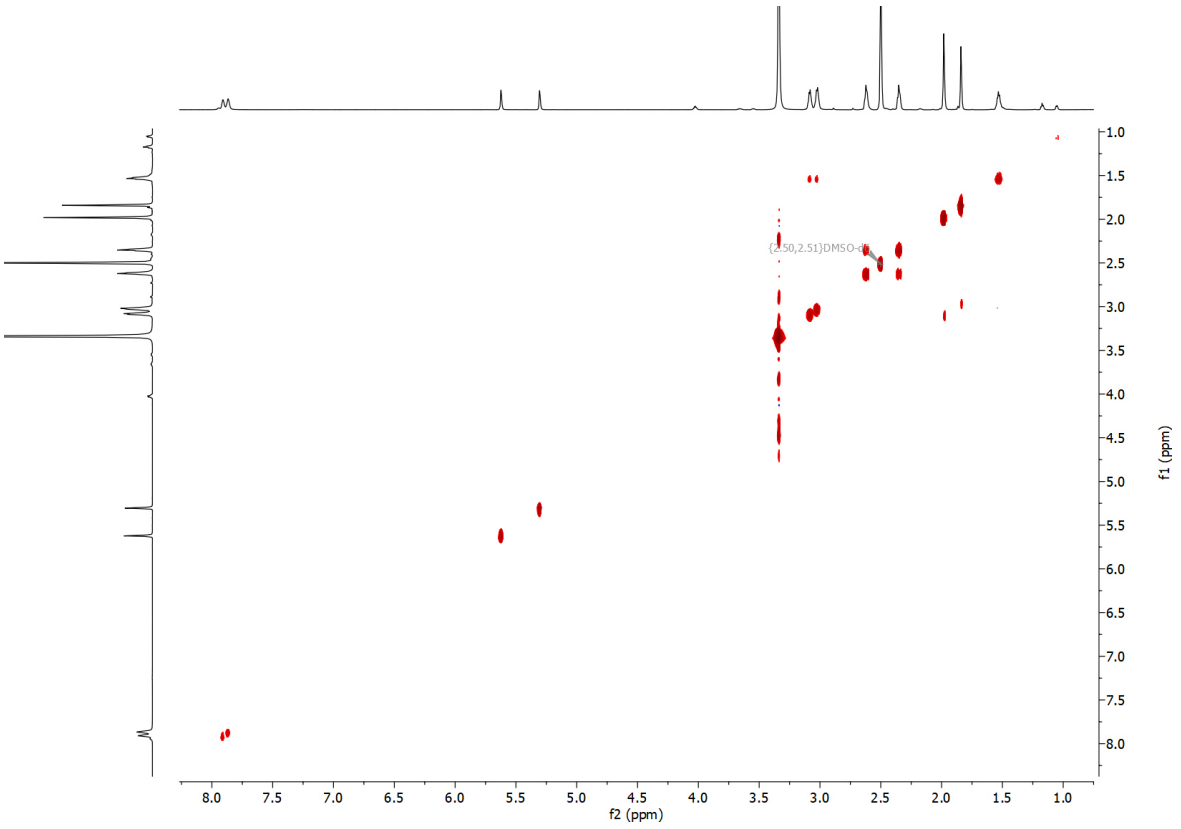

Figure S11: 2D COSY NMR spectrum of N-(3-(3-(4-methyl-2,5-dioxo-2,5-dihydrofuran-3-yl)propanamido)-propyl)methacrylamide in DMSO-d_6.

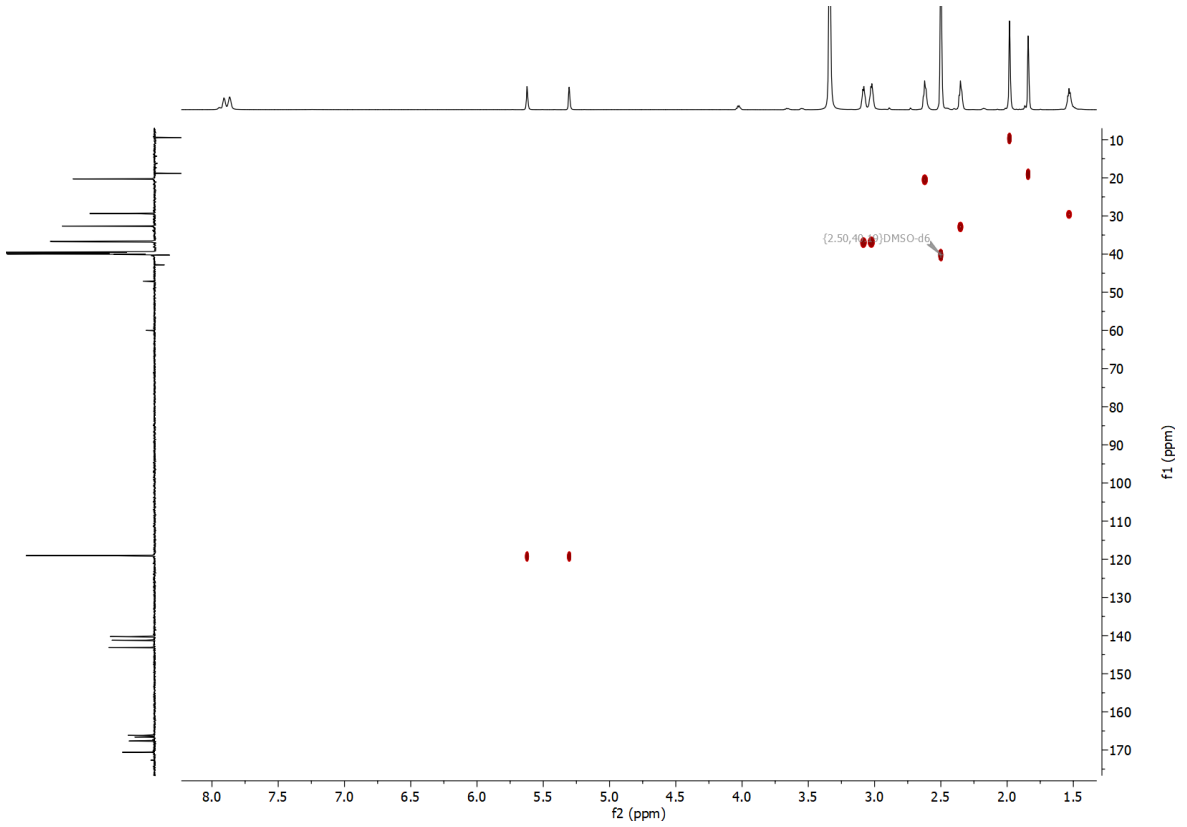

Figure S12: 2D HSQC NMR spectrum of N-(3-(3-(4-methyl-2,5-dioxo-2,5-dihydrofuran-3-yl)propanamido)-propyl)methacrylamide in DMSO-d_6.

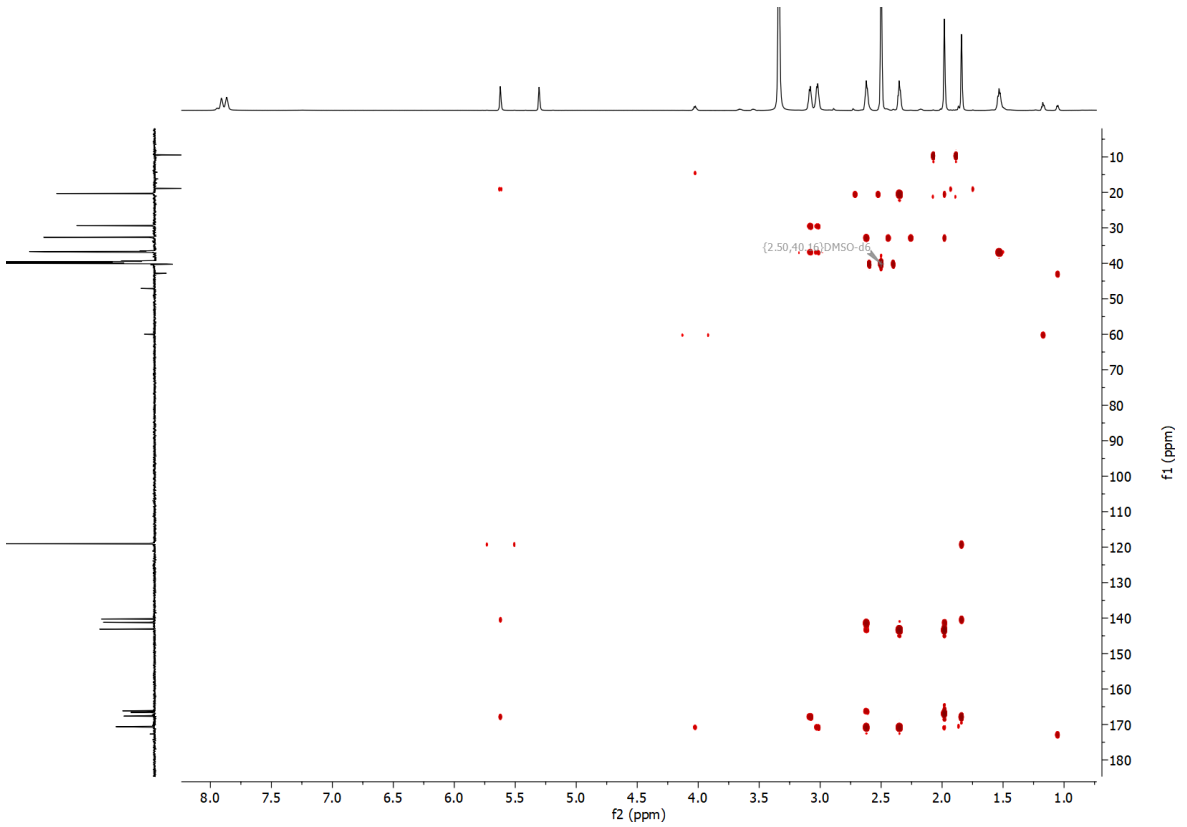

Figure S13: 2D HMBC NMR spectrum of N-(3-(3-(4-methyl-2,5-dioxo-2,5-dihydrofuran-3-yl)propanamido)-propyl)methacrylamide in DMSO-d_6.

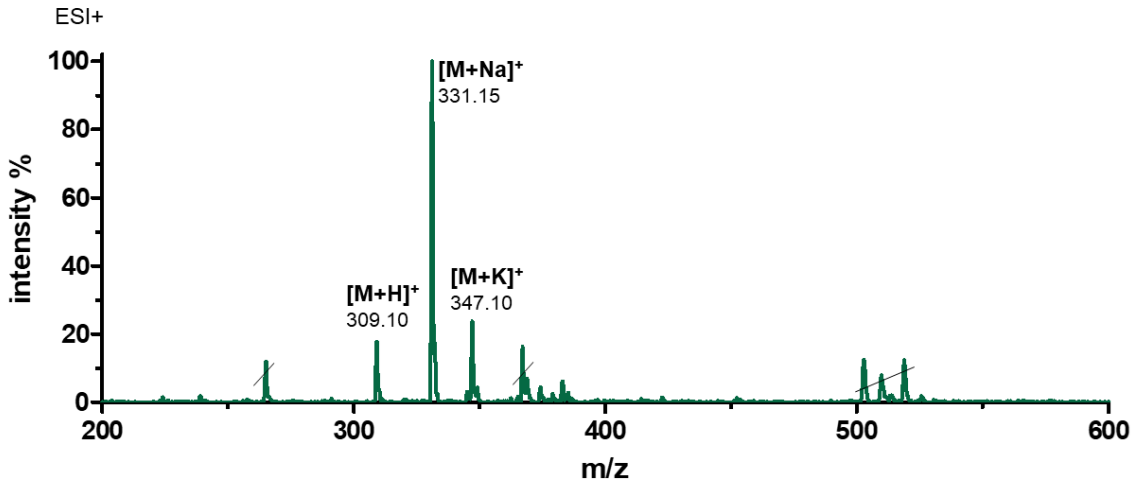

Figure S14: ESI-MS spectrum of N-(3-(3-(4-methyl-2,5-dioxo-2,5-dihydrofuran-3-yl)propanamido)-propyl)methacrylamide in MeOH (positive ion mode).

Polymerization Procedure

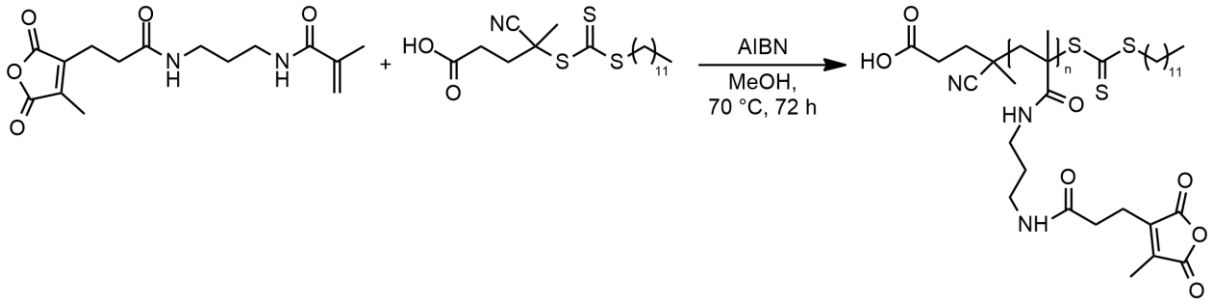

Figure S15: Synthesis of the polymer with TTC-CTA and AIBN in MeOH for 72 h.

The polymer was synthesized by RAFT-polymerization according to the literature and modified.[6] AIBN (0.48 mg, 2.9 µmol, 0.3 eq) and 4-cyano-4-(((dodecylthio)carbonothioyl)thio)pentanoic acid (TTC-CTA) (3.92 mg, 9.7 µmol, 1 eq) were weighed into an oven-dried Schlenk flask. PMMA-MA (150 mg, 486 µmol, 50 eq) was dissolved in 0.6 mL anhydrous methanol and transferred to the Schlenk flask. The solution was degassed by four freeze-pump-thaw cycles, followed by heating at 70 °C in its evacuated state. After a reaction time of 72 h, ^{1}H NMR analysis indicated a conversion of 72%. The polymer was precipitated in an excess of cold diethyl ether (-20 °C), centrifuged (4000 rpm, 20 min, 4 °C) and decanted. The residue was redissolved in ~ 0.5 mL methanol and precipitated dropwise into cold diethyl ether. The process was repeated three times and the product dried *in vacuo* for 16 h. The polymer was isolated as a colorless solid (83 mg, 74%).

^{1}H NMR (700 MHz, DMSO-d_6): δ (ppm) = 7.95 (s, 1H, **a**), 7.54-7.32 (m, 1H, **b**), 3.02-2.95 (m, 4H, **c+d**), 2.62 (m, 2H, **e**), 2.36 (m, 2H, **f**), 1.99 (s, 3H, **g**), 1.68-1.41 (m, 4H, **h+i**), 1.22 (s, 2H, **j**) 1.14-0.56 (m, 3H, **k**).

SEC (HFIP): M_n = 2204 g/mol, M_w = 2557 g/mol, Đ = 1.16

Free radical polymerization was performed analogously to controlled polymerization conditions without TTC-CTA. AIBN (0.85 mg, 5.2 µmol, 1 eq) was weighed in a Schlenk flask and PMMA-MA (80 mg, 260 µmol, 50 eq.), dissolved in 0.5 mL methanol, was transferred to the flask. After the reaction time, conversion was determined by ^{1}H NMR analysis (69% conversion) and the polymer was precipitated in cold diethyl ether. The polymer was isolated as slightly yellow solid (29.3 mg, 53%).

SEC (HFIP): M_n = 4734 g/mol, M_w = 5312 g/mol, Đ = 1.68.

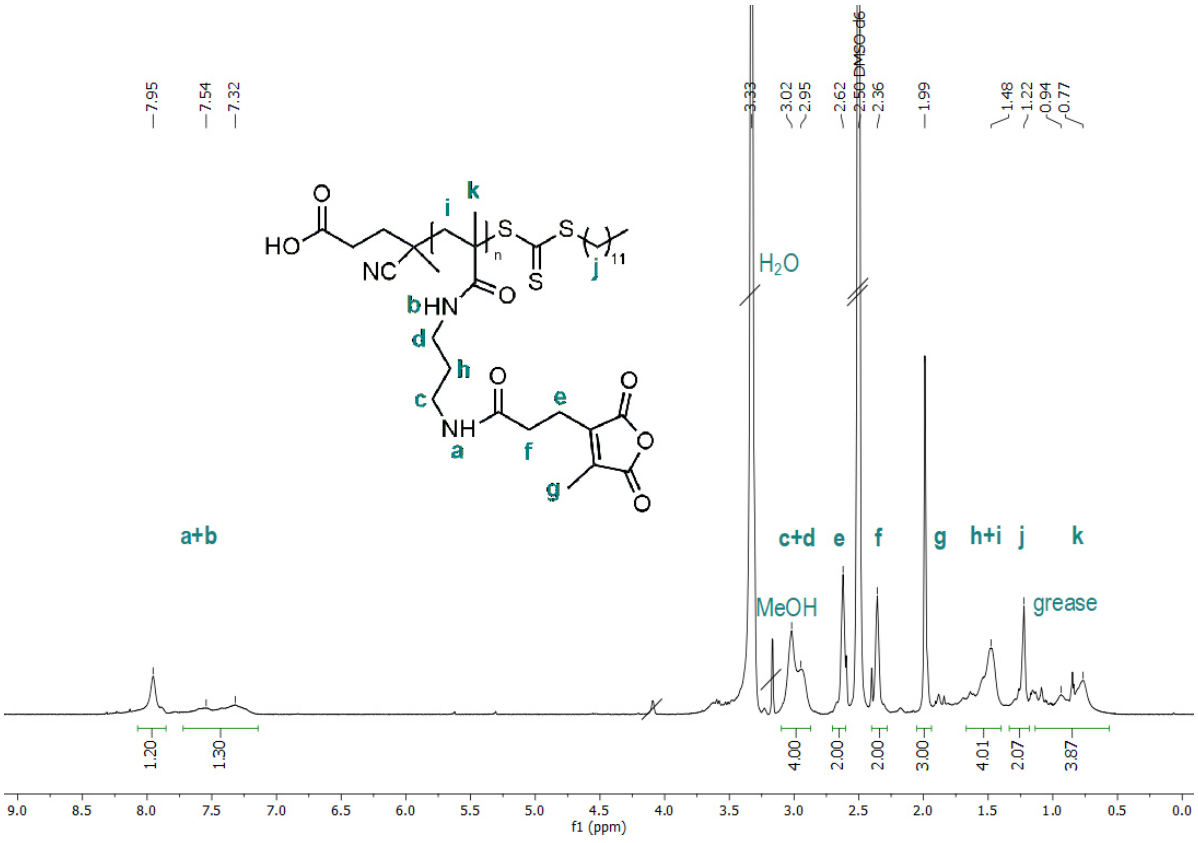

Figure S16: ^{1}H NMR spectrum (700 MHz) of the polymer synthesized under RAFT conditions in DMSO-d_6.

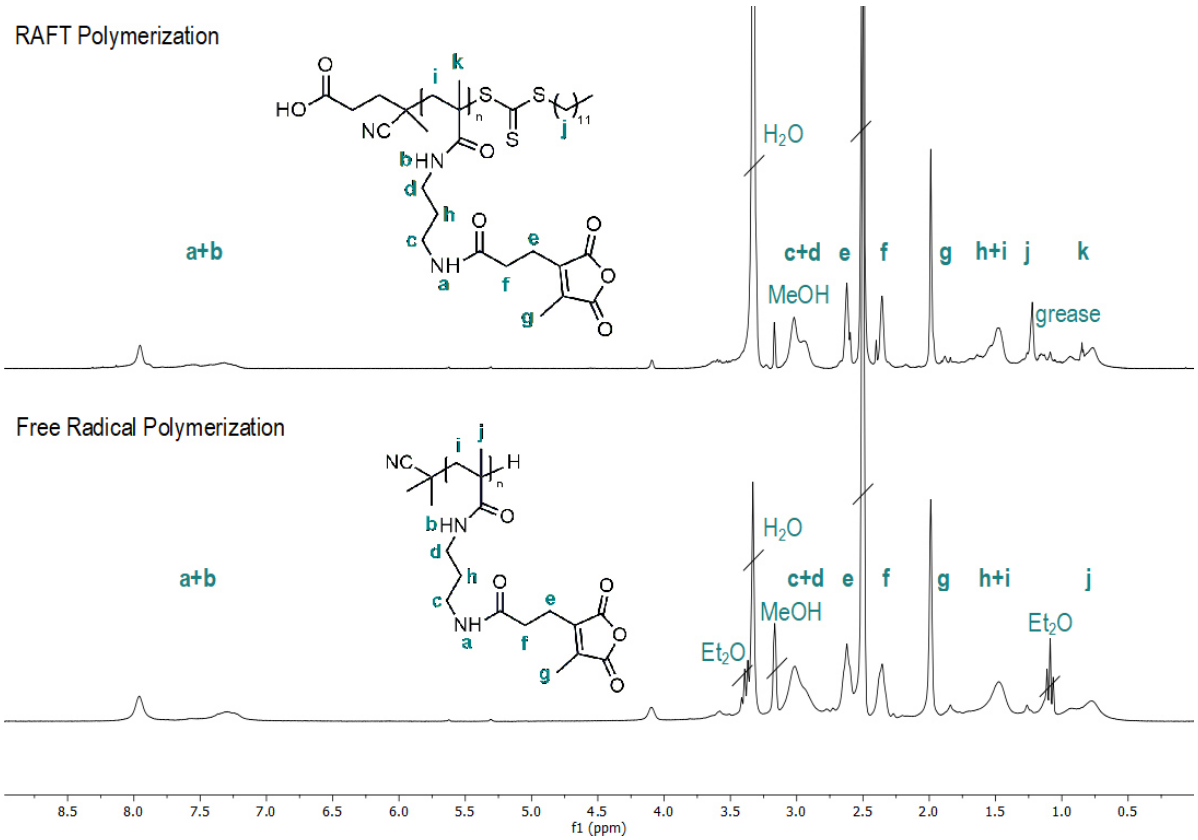

Figure S17: ^{1}H NMR spectrum (700 MHz) of the polymer synthesized under RAFT conditions compared to the polymer prepared by free radical polymerization in DMSO-d_6.

Kinetic Study RAFT-Polymerization

The kinetics of RAFT polymerization was investigated by monomer conversion determined by ^{1}H NMR measurements. After 0, 2, 4, 10, 24 and 30 h samples were taken from the reaction mixture, while the reaction remained in its evacuated state. Prior to ^{1}H NMR analysis, samples were diluted with DMSO-d_6 and exposed to air. The monomer conversion was determined by the ratio between the integrals of the polymer (CH2-NH-C- at 7.8 and -NH-CH2-CH2-CH2-NH, -C-CH2-C- at 1.5 ppm) to integrals of the monomer (CH2=C- at 5.6 and 5.3 ppm) as well as the integrals of the polymer (-NHCO-CH2-, =C-CH3, -NH-CH2-CH2-CH2-NH, -C-CH3, -C-CH2-C at 2.4-0.5 ppm) to integrals of the monomer (CH2=C- at 5.6 and 5.3 ppm).

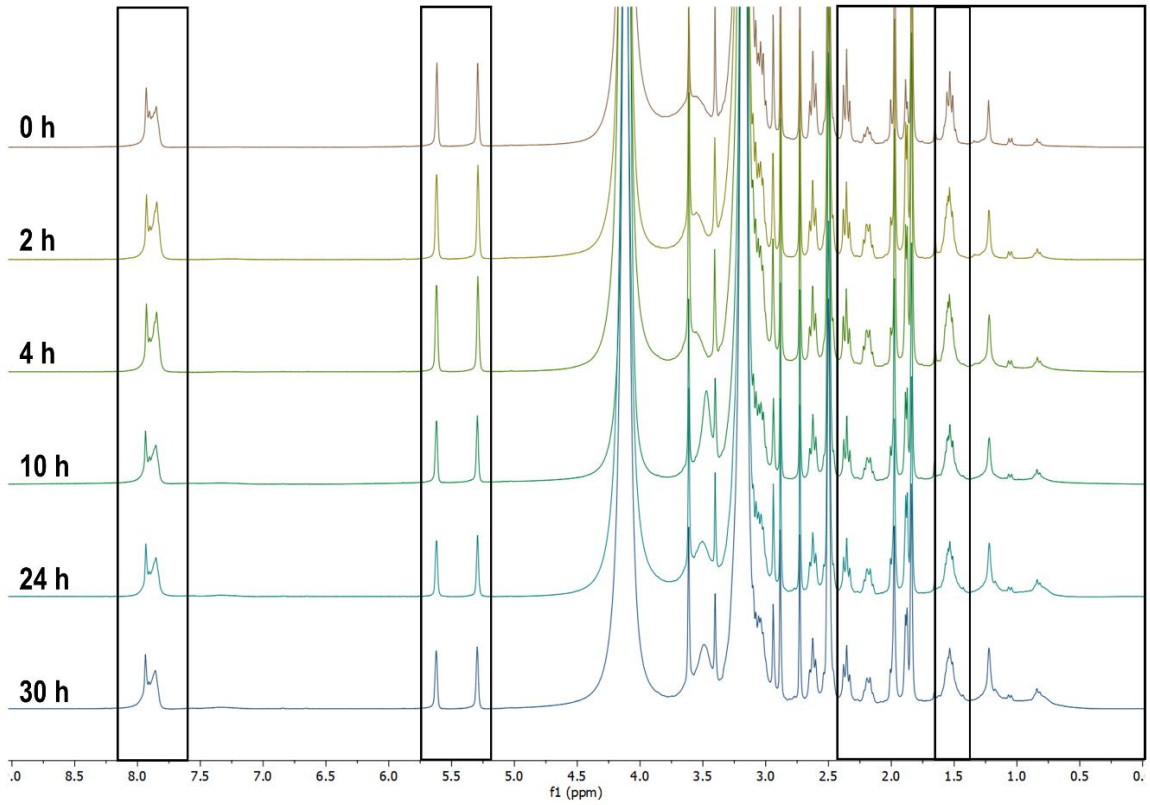

Figure S18: ^{1}H NMR spectrum (300 MHz) of the RAFT polymerization reaction mixture at different time points in DMSO-d_6.

A

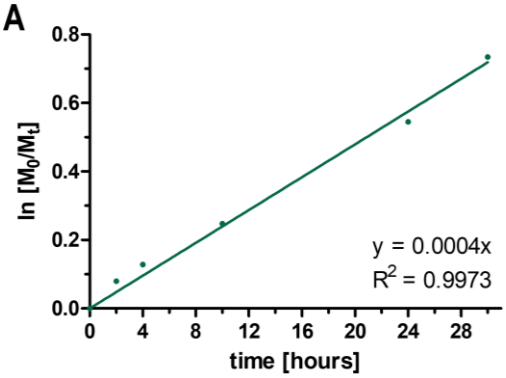

B

t [h]	conv. [%]	c [M]	$\ln(M_0/M_t)$
0	0	0.65	0
2	8	0.598	0.080
4	12	0.572	0.128
10	22	0.507	0.248
24	42	0.377	0.537
30	52	0.312	0.740

Figure S19: Monomer conversion $\ln(M_0/M_t)$ over time (A) and conversion (conv), concentration (c) and $\ln(M_0/M_t)$ over time (B).

Polymer Modification by Amidation with Primary or Secondary Amines

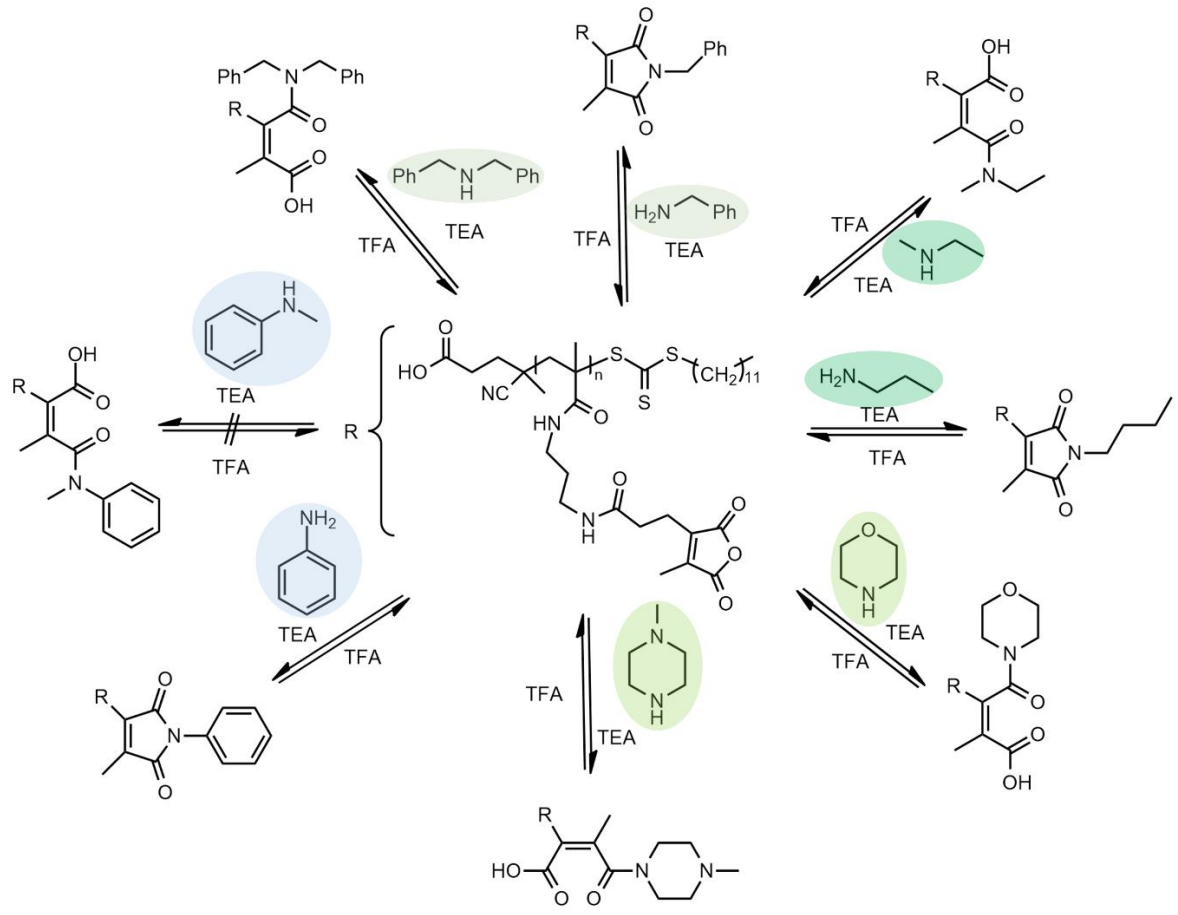

Figure S20: Schematic reaction of anhydride containing polymer p(PMMA-MA)$_{36}$ with different primary or secondary amines.

The ability for amine modification with primary or secondary amines was characterized by ^{1}H NMR and DOSY analysis. Therefore, 15 mg polymer (1.30 µmol/46.8 µmol related to the number of anhydride groups, 1 eq) was dissolved in DMSO under nitrogen atmosphere and triethylamine (TEA) (32.44 µL, 234 µmol, 5 eq) was added to the solution. Corresponding amines, like dibenzylamine (27.08 µL, 140 µmol, 3 eq) were dropped to the reaction mixture and stirred at 50 °C for 16 h. The product was three times precipitated in diethyl ether and dried *in vacuo* for 16 h. The modified polymer was isolated as slightly yellow solid (23 mg, 95%).

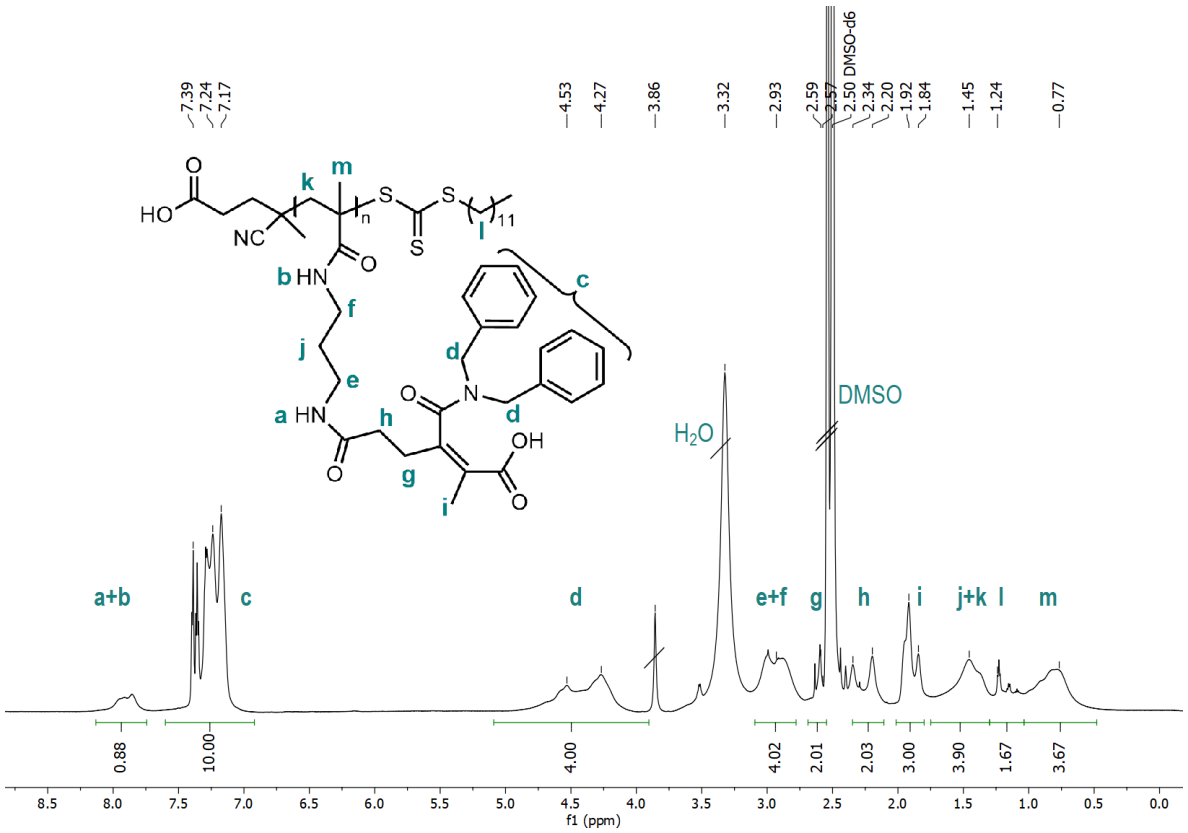

Figure S21: ^{1}H NMR spectrum (700 MHz) of the polymer after modification with dibenzylamine synthesized in DMSO-d_6.

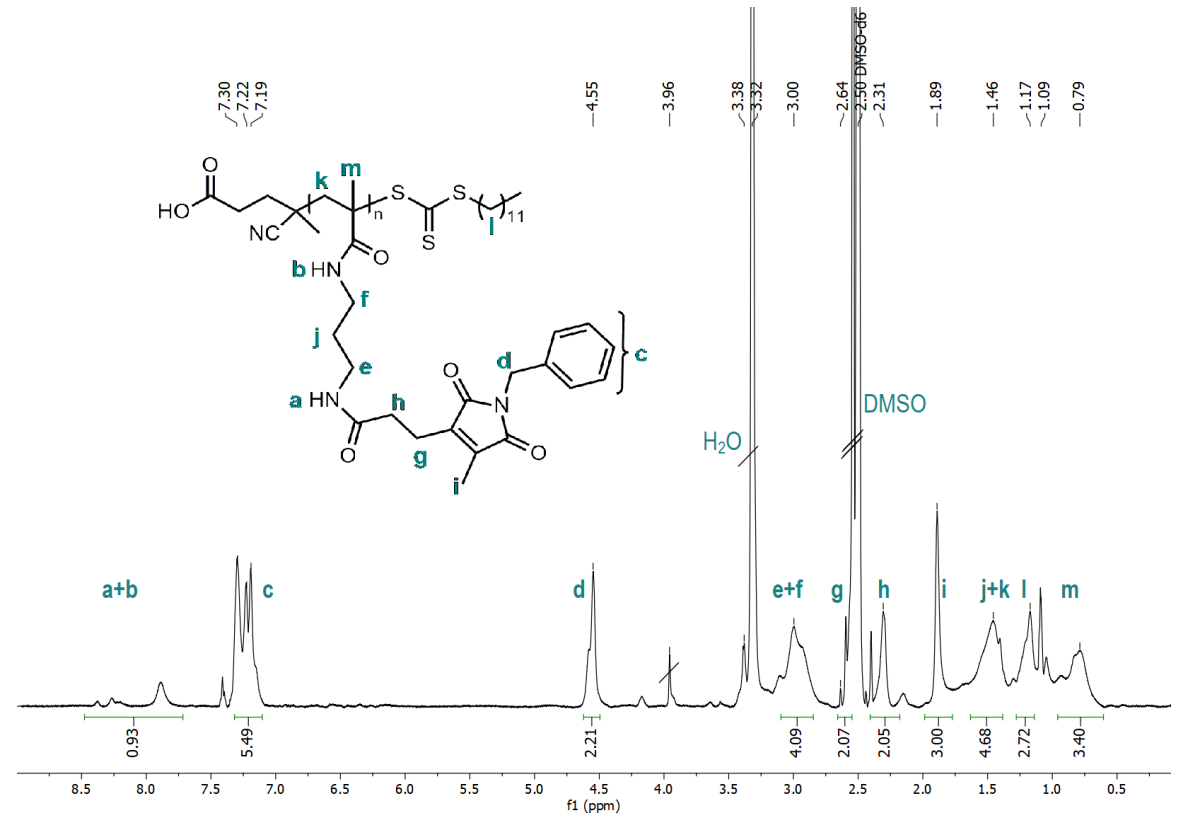

Figure S22: ^{1}H NMR spectrum (700 MHz) of the polymer after modification with benzylamine synthesized in DMSO-d_6.

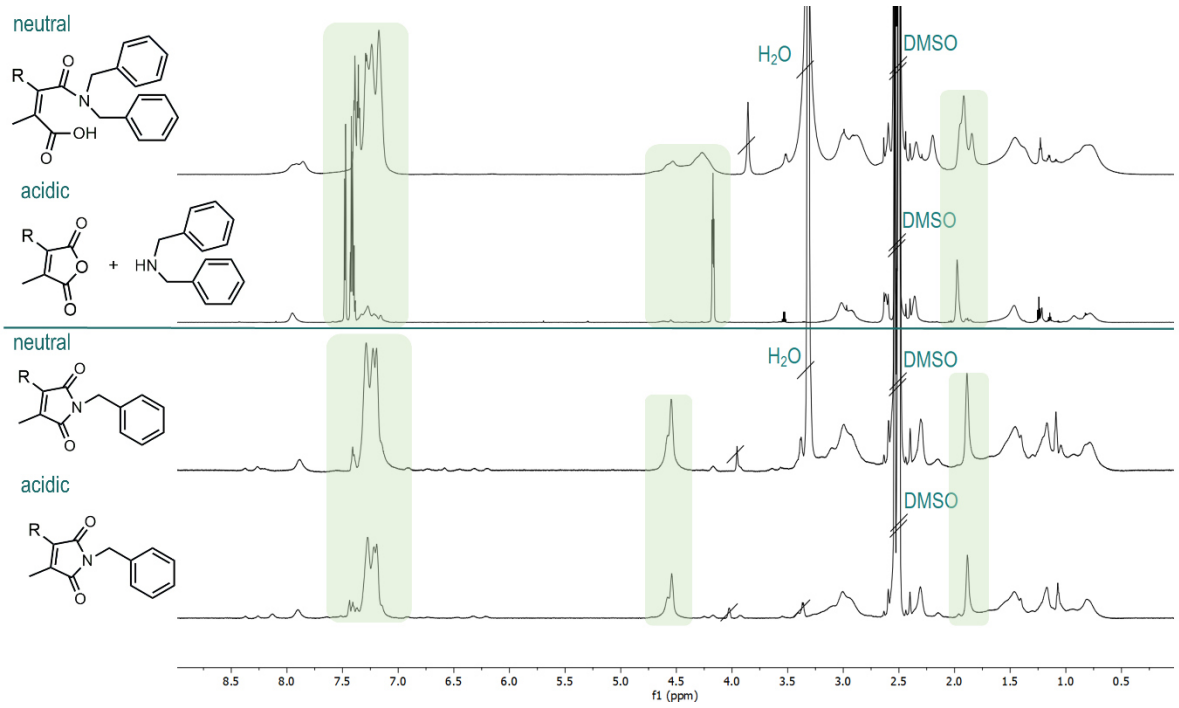

Figure S23: ^{1}H NMR spectra (700 MHz) of the polymer after modification with dibenzylamine or benzylamine under neutral and acidic conditions in DMSO-d_6.

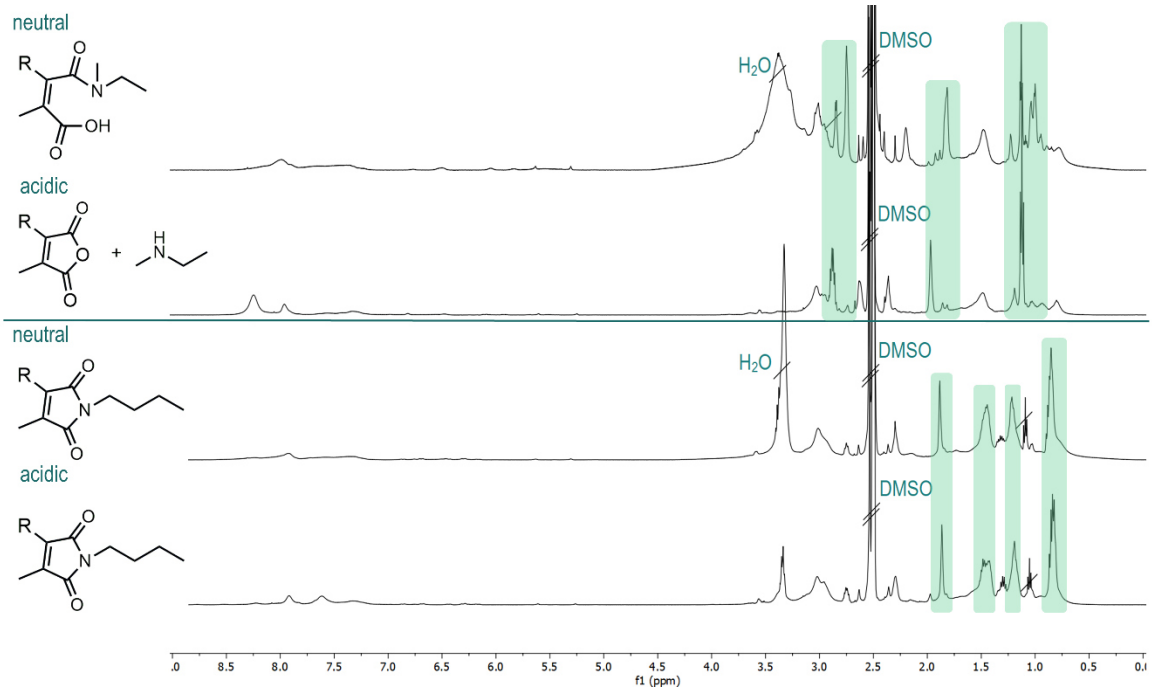

Figure S24: ^{1}H NMR spectra (500 MHz) of the polymer after modification with ethylmethylamine or butylamine under neutral and acidic conditions in DMSO-d_6.

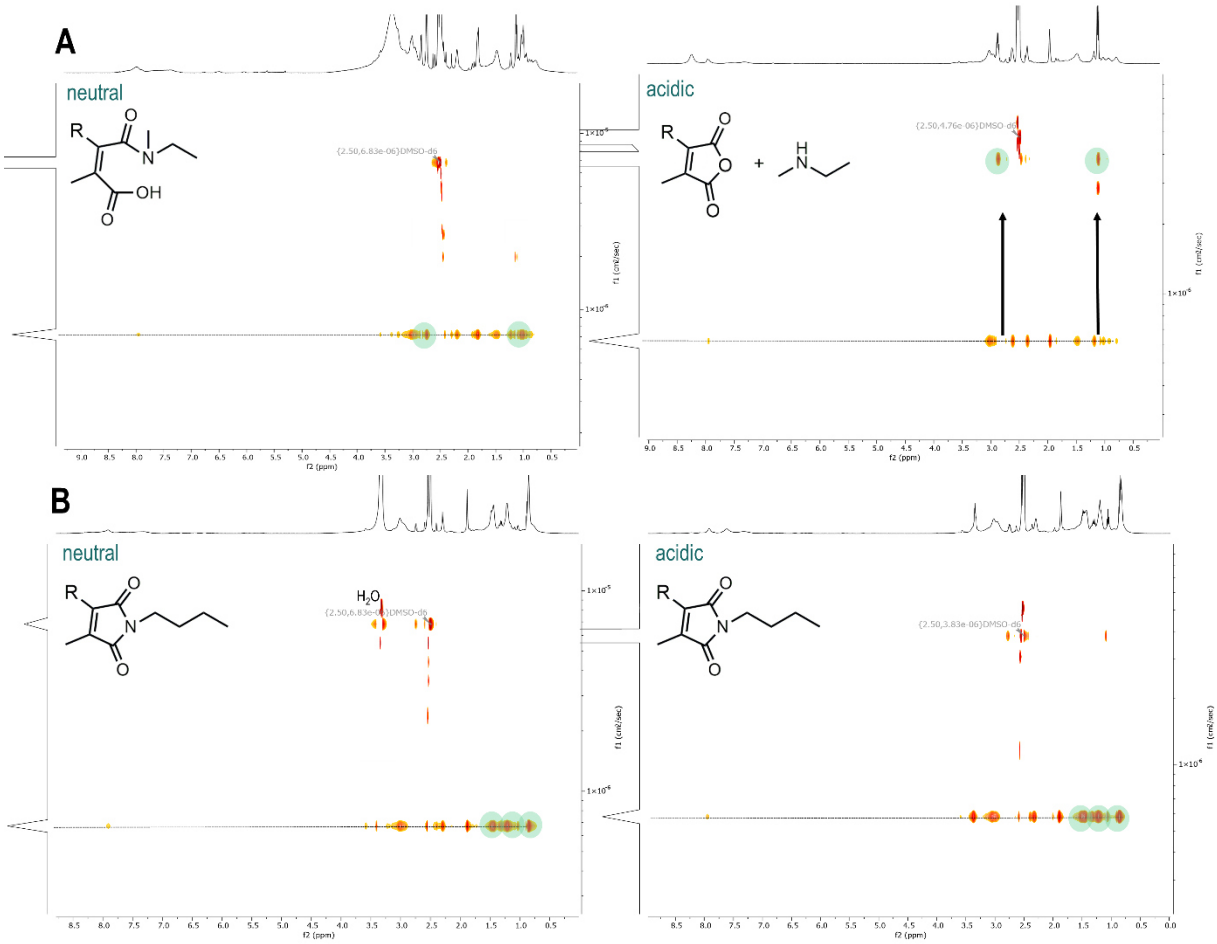

Figure S25: DOSY spectra (500 MHz) of the polymer after modification with ethylmethylamine (A) or butylamine (B) under neutral and acidic conditions in DMSO-d_6.

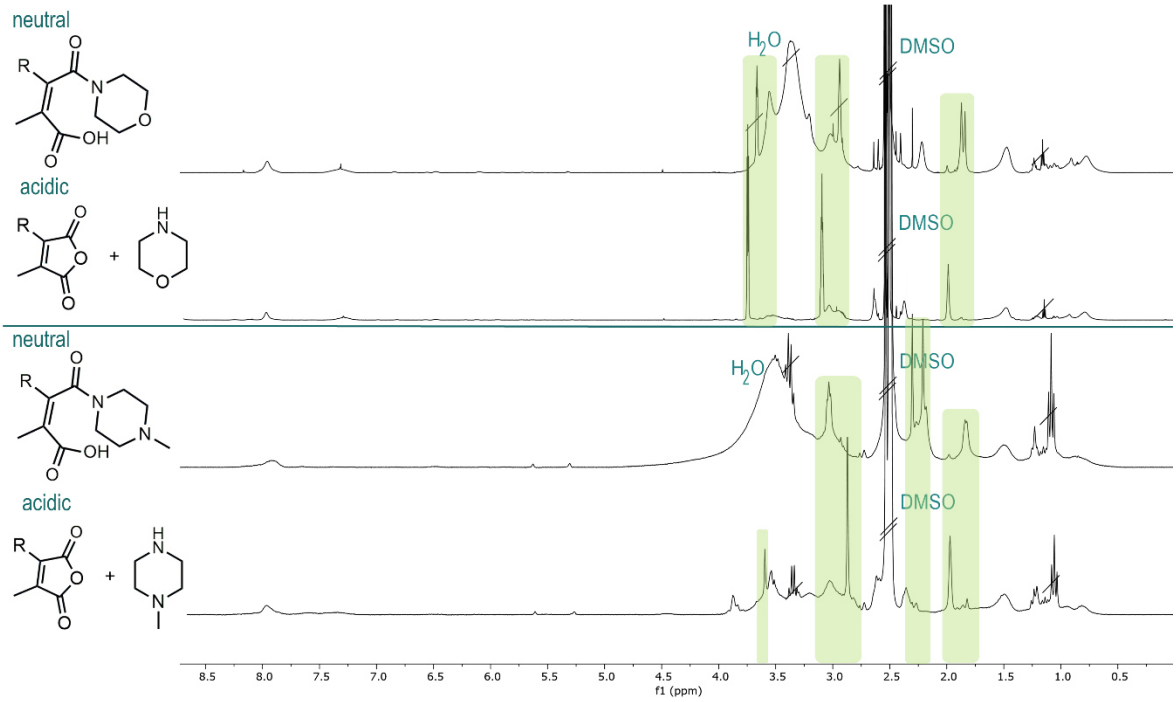

Figure S26: ^{1}H NMR spectra (700 MHz) of the polymer after modification with morpholine or N-methylpiperazine under neutral and acidic conditions in DMSO-d_6.

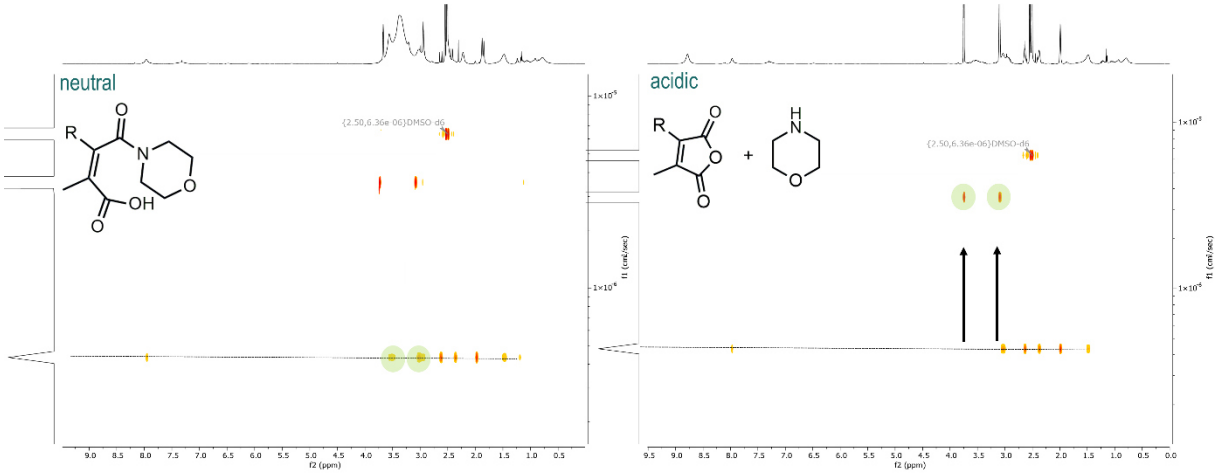

Figure S27: DOSY spectra (700 MHz) of the polymer after modification with morpholine under neutral and acidic conditions in DMSO-d_6.

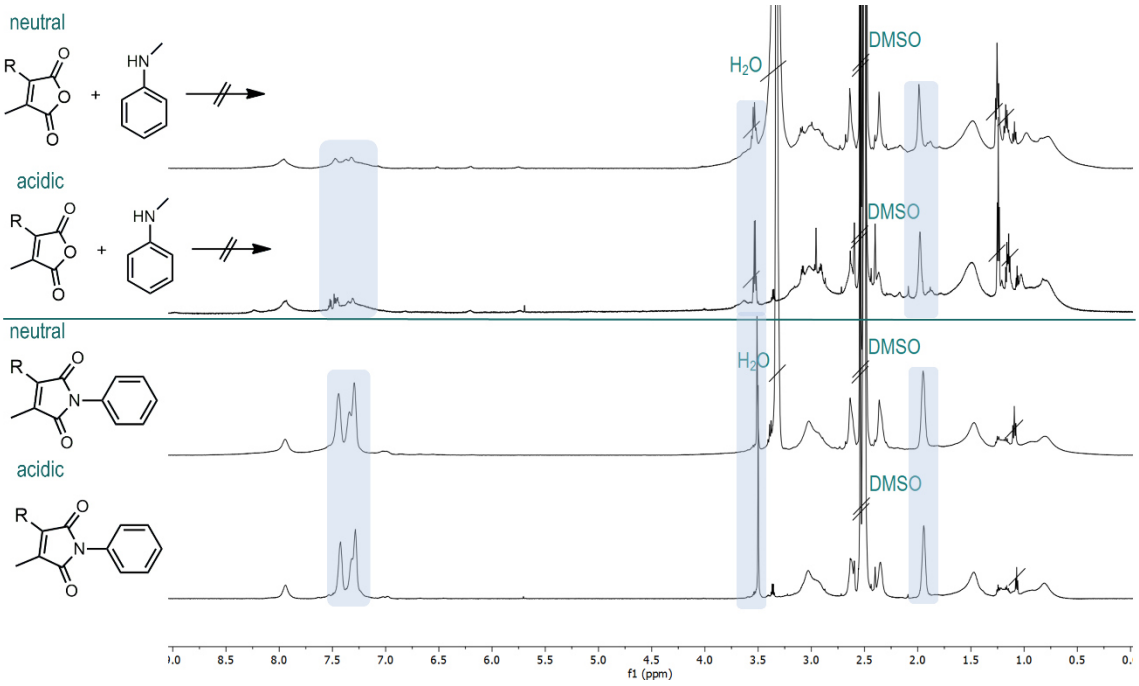

Figure S28: ^{1}H NMR spectra (500 MHz) of the polymer after modification with N-methylaniline or aniline under neutral and acidic conditions in DMSO-d_6.

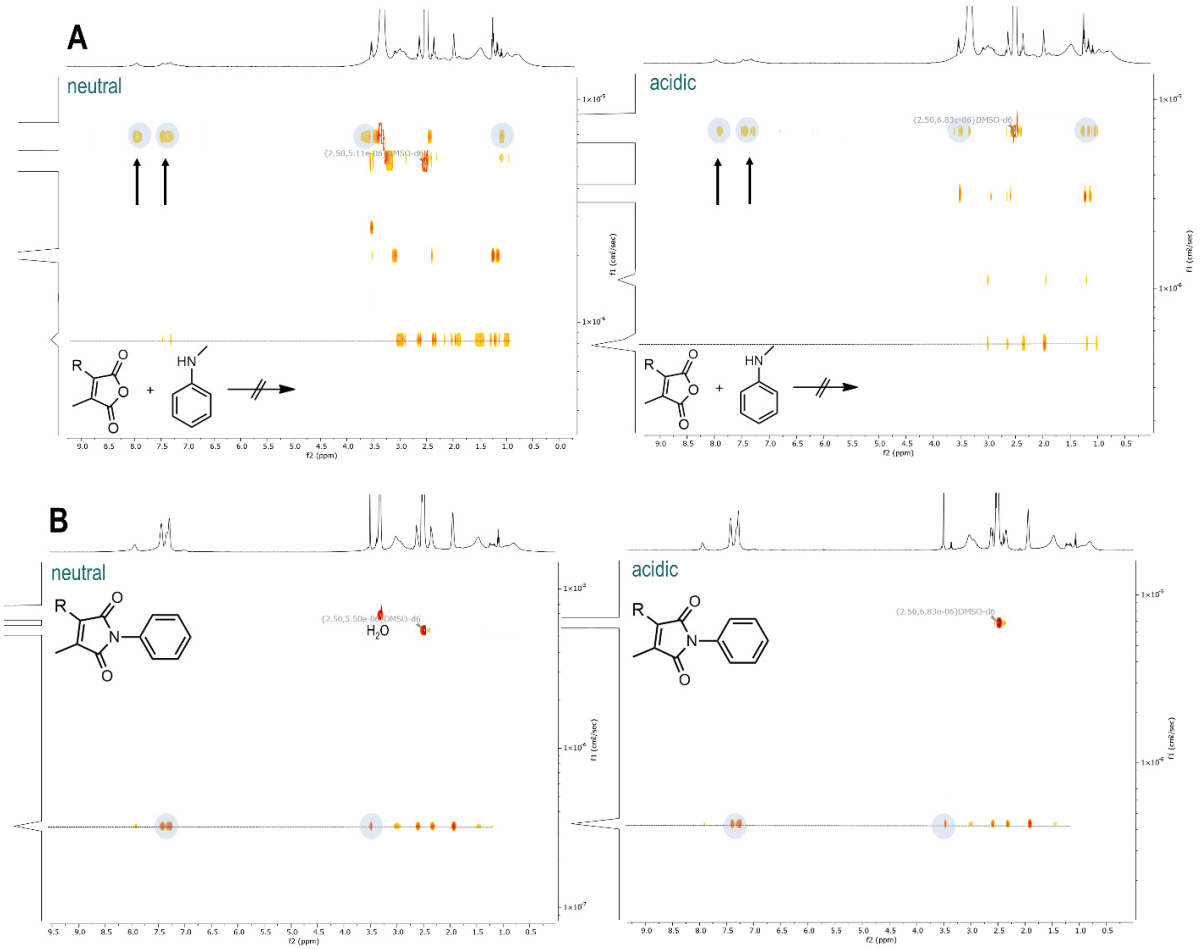

Figure S29: DOSY spectra (500 MHz) of the polymer after modification with N-methylaniline (A) or aniline (B) under neutral and acidic conditions in DMSO-d_6.

Polymer Modification by Dual Anhydride Conjugation

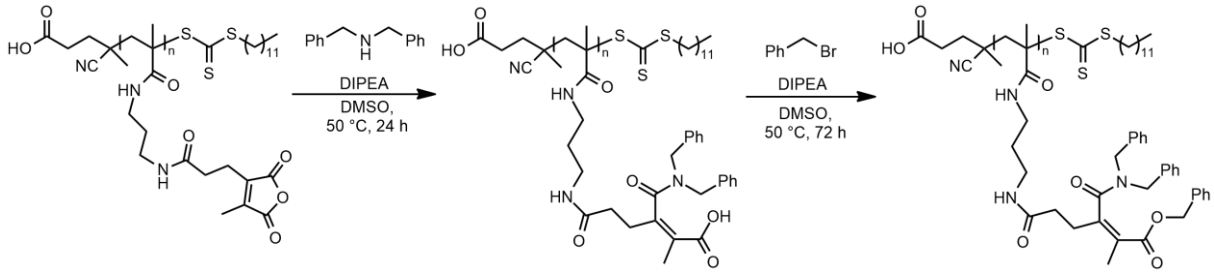

Figure S30: Reaction scheme of anhydride containing polymer p(PMMA-MA)$_{36}$ with dibenzylamine and further modification with benzyl bromide.

In an oven-dried Schlenk tube the polymer p(PMMA-MA)$_{36}$ (10 mg, 0.869 µmol/31.29 µmol reactive anhydride groups, 1 eq) was dissolved in 0.5 mL dry DMSO under nitrogen atmosphere. N,N-diisopropylethylamine (DIPEA) (15.97 µL, 93.88 µmol, 3 eq) and dibenzylamine (12.03 µL, 62.58 µmol, 2 eq) were dropped to the solution and the reaction mixture was allowed to stir for 16 h at 50 °C. The modified polymer was precipitated three

times in cold diethyl ether (-20°C) and isolated by subsequent centrifugation. After drying under high vacuum, the polymer (10 mg, 0.537 µmol/19.35 µmol reactive anhydride groups, 1 eq) was redissolved in 0.5 mL dry DMSO. Benzyl bromide (9.19 µL, 77.39 µmol, 4 eq) and DIPEA (32.91 µL, 193.5 µmol, 10 eq) were added to the solution and stirred for 72 h at 50 °C. The resulting polymer was isolated by threefold precipitation into ice cold diethyl ether, centrifugation and drying *in vacuo* overnight (17 mg, 87%).

SEC (HFIP) (+dibenzylamine, step 1): M_n = 2453 g/mol, M_w = 3229 g/mol, Đ = 1.33

SEC (HFIP) (+dibenzylamine, benzyl bromide, step 2): M_n = 6118 g/mol, M_w = 8207 g/mol, Đ = 1.34

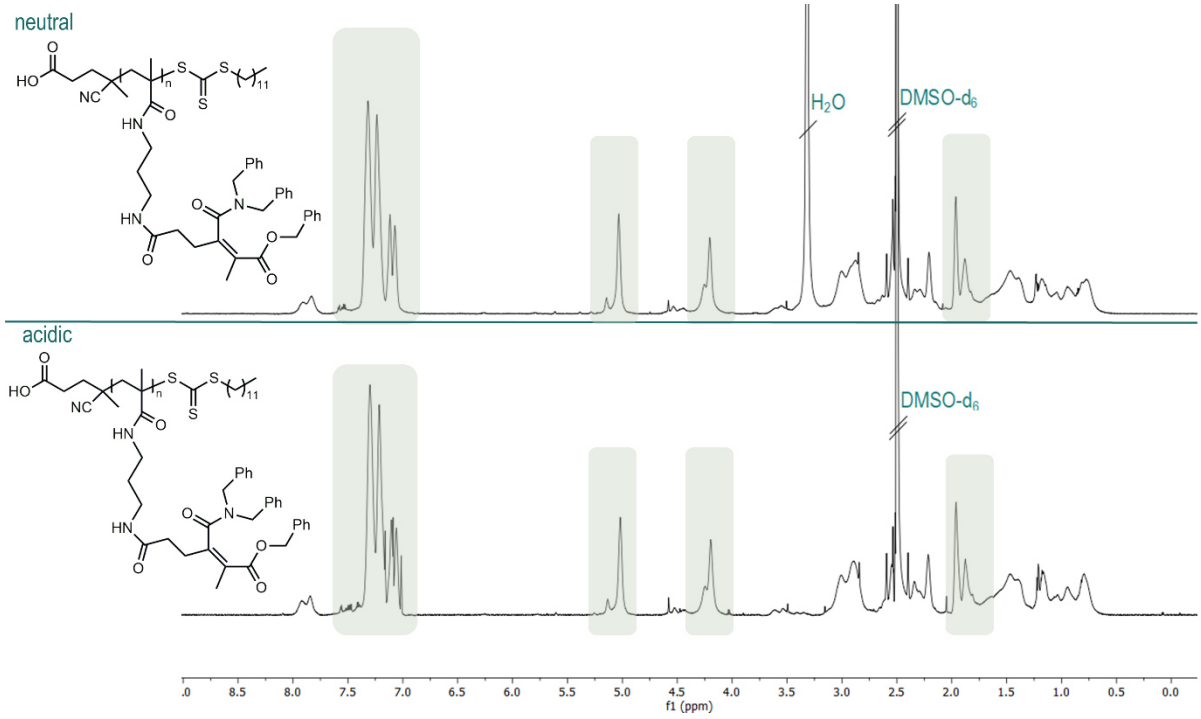

Figure S31: ^{1}H NMR spectra (700 MHz) of the polymer after modification with benzylamine and benzyl bromide to the same anhydride under neutral and acidic conditions in DMSO-d_6.

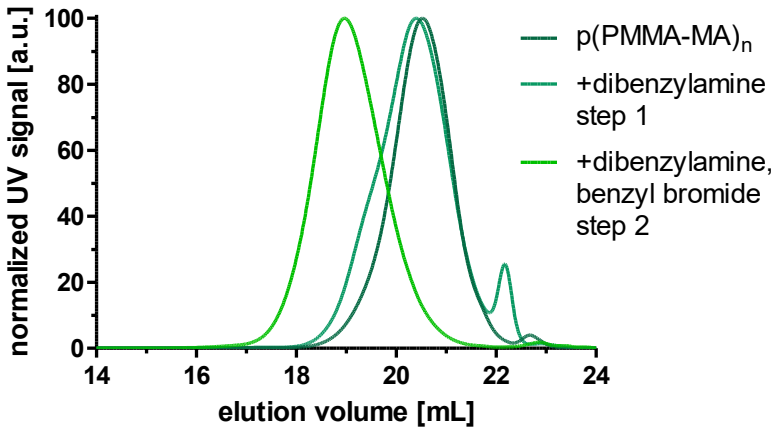

Figure S32: SEC elugrams of the polymer p(PMMA-MA)$_{38}$ before and after anhydride modification with benzylamine and benzyl bromide.

Formulation of pH-Reversible and Irreversible Dye-Labeled Hydrophilic Polymers by Amidation

Synthesis of 4-Nitro-7-Piperazino-2,1,3-Benzoxadiazole (NBD-PZ)

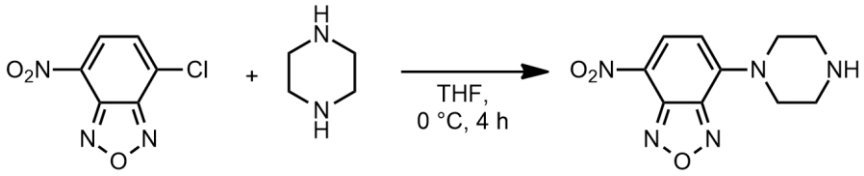

Figure S33: Synthesis of 4-Nitro-7-piperazino-2,1,3-benzoxadiazole (NBD-PZ/NBD).

The synthesis of 4-nitro-7-piperazino-2,1,3-benzoxadiazole (NBD-PZ/NBD) was adapted from literature and modified.[7] In a two neck round bottom flask piperazine (1.34 g, 15.5 mmol, 3.1 eq) was dissolved under nitrogen atmosphere in dry THF (50 mL). After cooling for 30 min using an ice bath, NBD-chloride (1.0 g, 5.01 mmol, 1 eq) dissolved in dry THF (40 mL) was slowly added *via* dropping funnel to the reaction mixture. During the addition of NBD-chloride the solution changed immediately from slightly yellow to orange and then became red. The reaction solution was stirred for one hour and after complete conversion, concentrated under vacuum, redissolved in a mixture of methanol and acetone (1:1) and added to an excess of chloroform (250 mL). The resulting organic solution was extracted with water, dried over Na_2SO_4 and evaporated. The pure NDB-PZ was isolated as a red powder (1.28 g, 100%).

^{1}H NMR (500 MHz, DMSO-d$_6$): δ (ppm) = 8.44 (d, J = 9.2 Hz, 1H, **a**), 6.63 (d, J = 9.3 Hz, 1H, **b**), 4.07 (m, 4H, **c**), 2.92 (m, 4H, **d**).

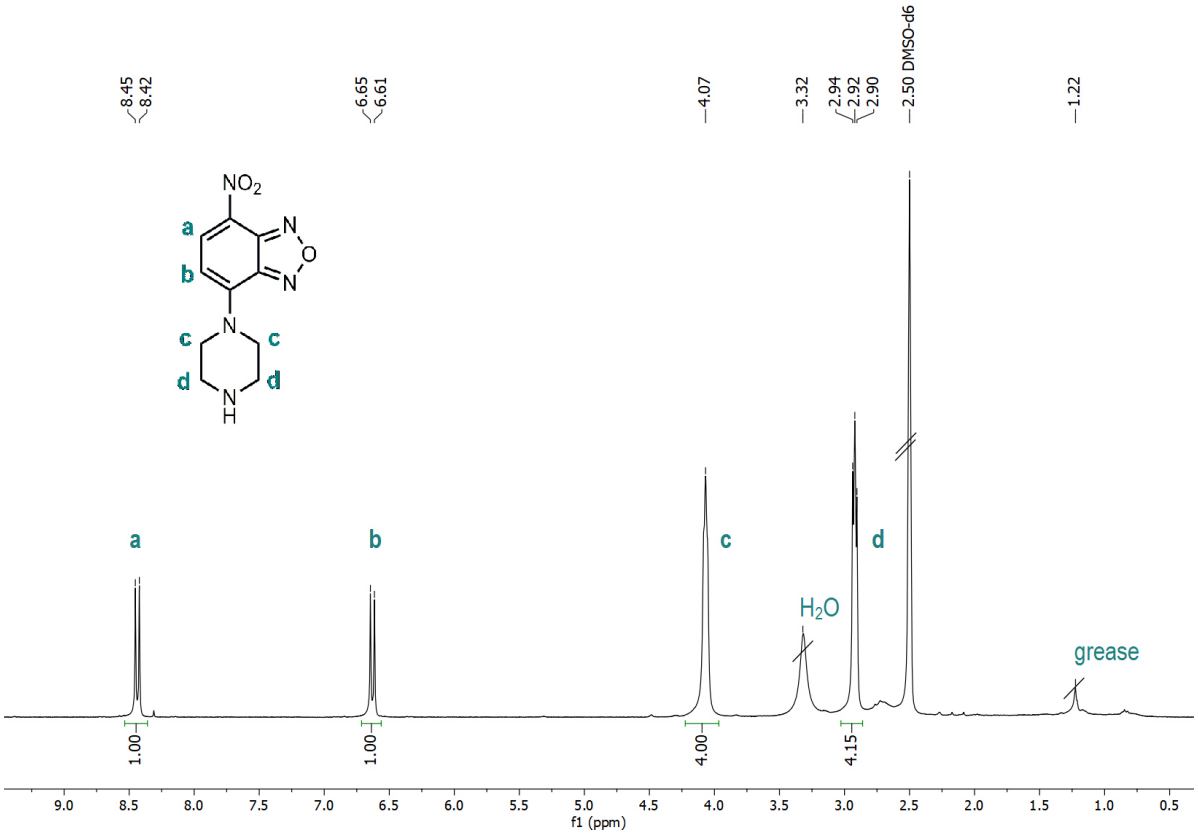

Figure S34: ^{1}H NMR spectrum (500 MHz) of 4-Nitro-7-piperazino-2,1,3-benzoxadiazole (NBD-PZ/NBD) in DMSO-d_6.

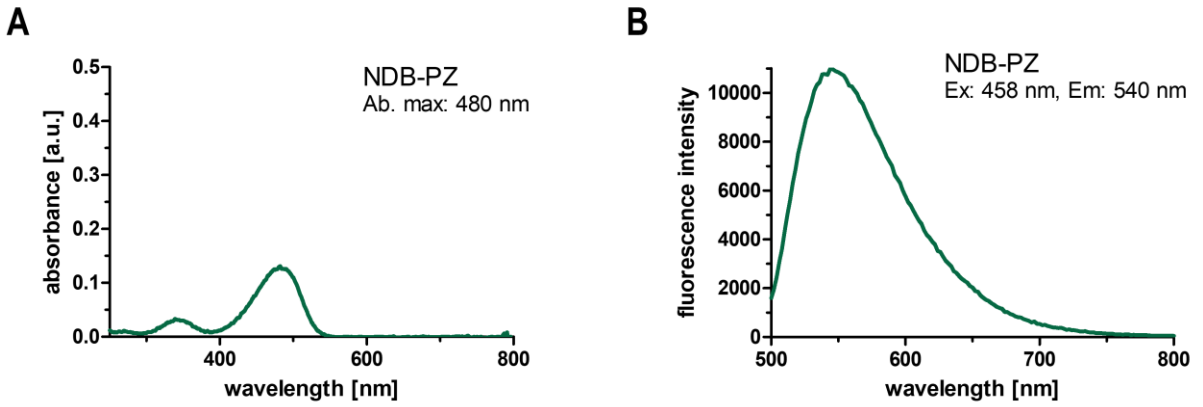

Figure S35: UV-vis spectrum of 4-Nitro-7-piperazino-2,1,3-benzoxadiazole (A) and the corresponding fluorescence spectrum in PBS (B).

Polymer Dye Labeling and Hydrophilization by Covalent Attachment of Primary and Secondary Amines to Polymer Anhydride Groups

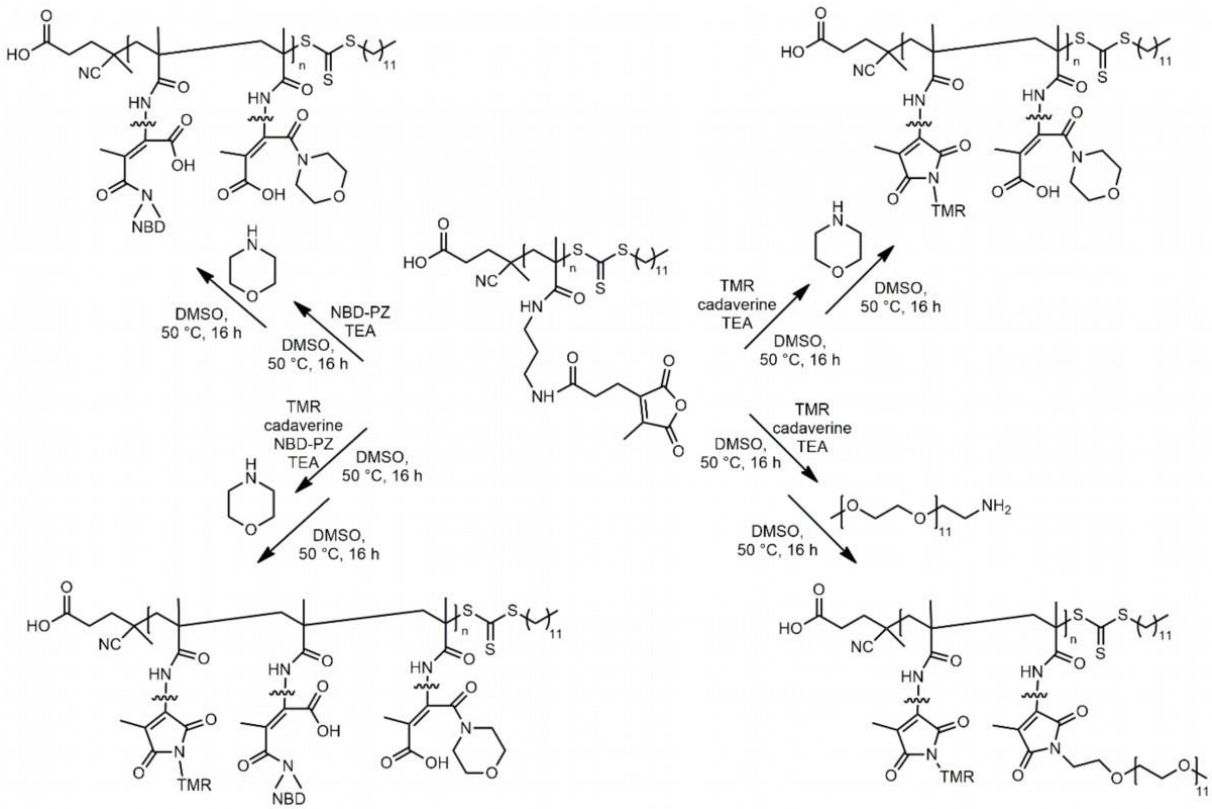

Figure S36: Schematic reaction of the polymer p(PMMA-MA)$_{38}$ with TMR and NBD-PZ/NBD followed by hydrophilization with morpholine or mPEG$_{11}$-amine.

In a Schlenk tube equipped with a stir bar the polymer p(PMMA-MA)$_{38}$ (80 mg, 6.6 µmol/250.8 µmol reactive anhydride groups, 1 eq) was dissolved in 4 mL dry DMSO under nitrogen atmosphere and TEA (174 µL, 1.25 mmol, 5 eq) was added to the solution. 20 mg of the polymer (1.65 µmol/62.71 µmol reactive anhydride units, 1 eq) was transferred into a new Schlenk tube and NBD-PZ (77.26 µL, 0.63 µmol, 0.01 eq) was added from a 2 mg/mL stock solution in DMSO (77.25 µL, 0.63 µmol, 0.01 eq). Then, tetramethylrhodamine cadaverine stock solution (TMR) (5 mg/mL in DMSO, 195 µL, 1.89 µmol, 0.01 eq) was added to the remaining polymer and the mixture was stirred at 50 °C for one day. The obtained dye-labeled polymers were used to generate different pH-reversible and non-reversible hydrophilic systems. Therefore, 20 mg polymer each (1.65 µmol/62.71 µmol reactive anhydride units, 1 eq) was transferred into three Schlenk tubes and reacted with hydrophilic amines, whereby the added equivalents were related to the anhydride units. Morpholine (16.22 µL, 188.1 µmol, 3 eq) or mPEG$_{11}$-amine (M_n 0.75 kDa) (1.41 mL, 100 mg/mL in DMSO, 188.1 µmol, 3 eq) were dropped to the reaction mixtures as reversible or non-reversible hydrophilic amine. The reaction mixtures were stirred at 50 °C for 16 h. For the formulation of a dual dye-labeled

system TMR conjugated polymer was reacted with NBD-PZ (77.26 µL, 0.63 µmol, 0.01 eq) prior to hydrophilization with morpholine. Finally, the solutions were three times precipitated in an excess of diethyl ether, centrifuged (4000 rpm, 20 min, 4 °C) and decanted. After drying *in vacuo* overnight the polymers were isolated as pink or orange powder (25 mg, 98%).

SEC (HFIP) (p(PMMA-MA)$_{38}$): M_n = 3932 g/mol, M_w = 4689 g/mol, Đ = 1.19

SEC (HFIP) (+TMR, morpholine): M_n = 6674 g/mol, M_w = 13614 g/mol, Đ = 1.59

SEC (HFIP) (+TMR, mPEG$_{11}$-amine): M_n = 28073 g/mol, M_w = 37958 g/mol, Đ = 1.35

SEC (HFIP) (+NBD-PZ, morpholine): M_n = 1927 g/mol, M_w = 3045 g/mol, Đ = 1.58

SEC (HFIP) (+NBD-PZ, TMR, morpholine): M_n = 7192 g/mol, M_w = 10768 g/mol, Đ = 1.49

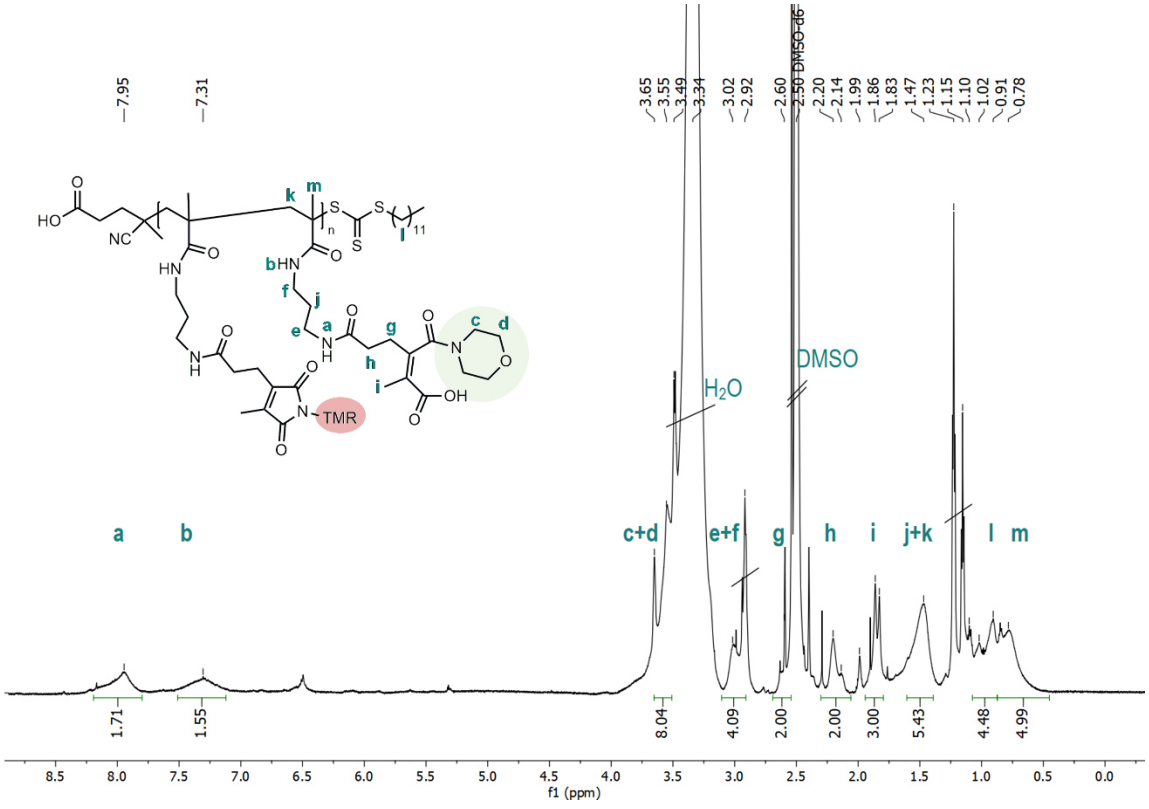

Figure S37: ^{1}H NMR spectrum (700 MHz) of the polymer after modification with TMR and morpholine in DMSO-d$_6$

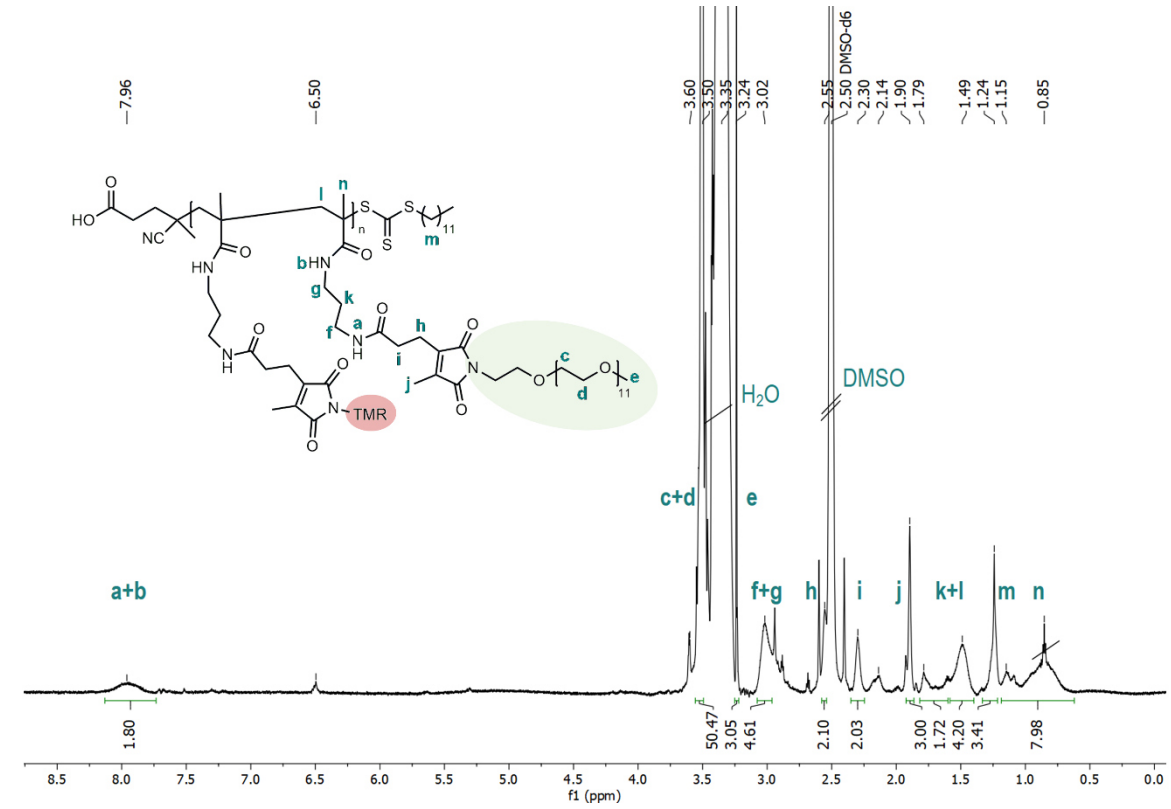

Figure S38: ^{1}H NMR spectrum (700 MHz) of the polymer after modification with TMR and mPEG$_{11}$-amine in DMSO-d$_6$.

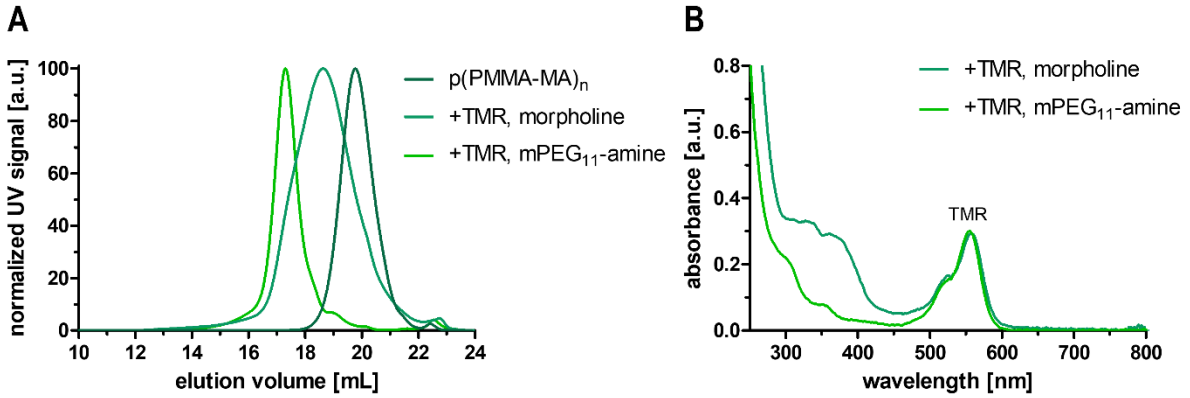

Figure S39: SEC elugrams of the polymer before and after dye labeling and hydrophilization (A) and the corresponding UV-vis spectra in PBS (B).

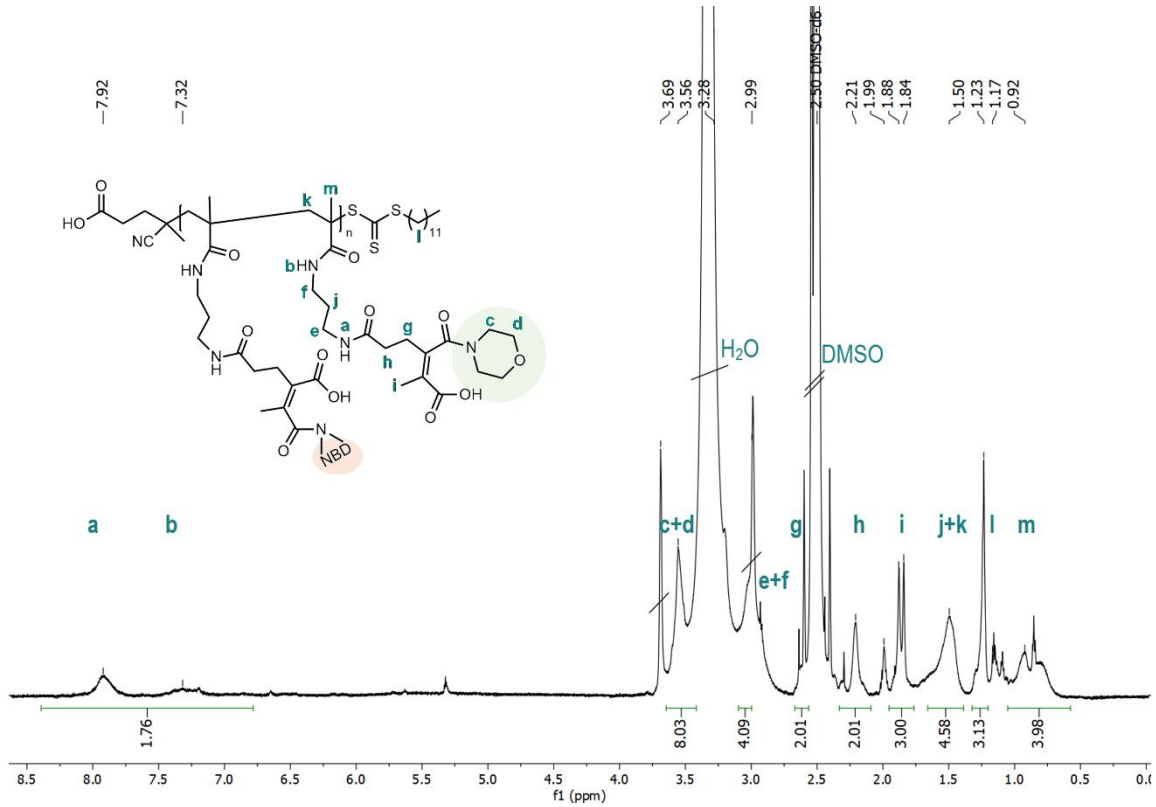

Figure S40: ^{1}H NMR spectrum (700 MHz) of the polymer after modification with NBD-PZ and morpholine or TMR, NBD-PZ and morpholine in DMSO-d_6

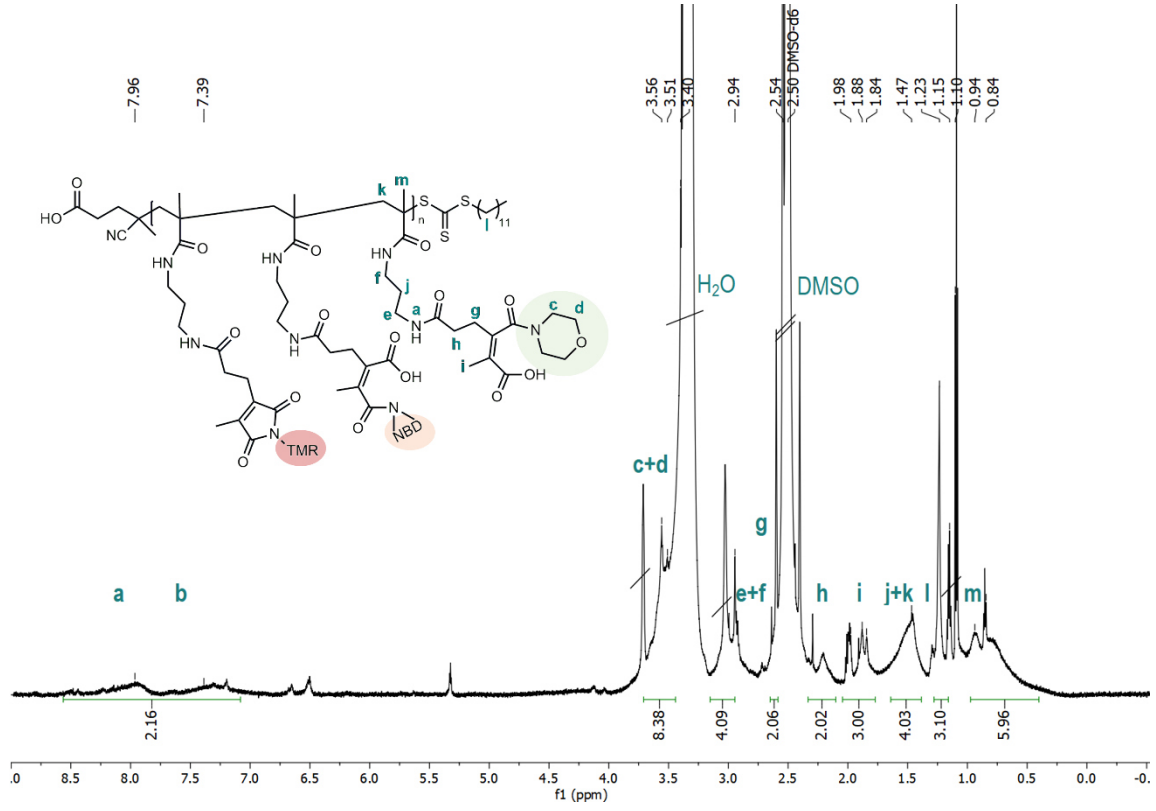

Figure S41: ^{1}H NMR spectrum (700 MHz) of the polymer after modification with TMR, NBD-PZ and morpholine in DMSO-d_6.

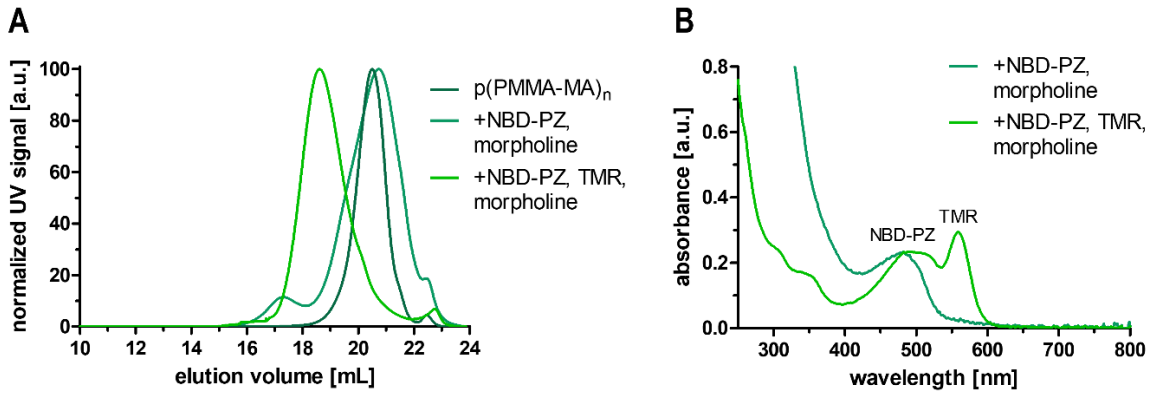

Figure S42: SEC elugrams of the polymer before and after dye labeling and hydrophilization (A) and the corresponding UV-vis spectra in PBS (B).

Acidic Hydrolysis Study of pH-Reversible Dye-Labeled Hydrophilic Polymers

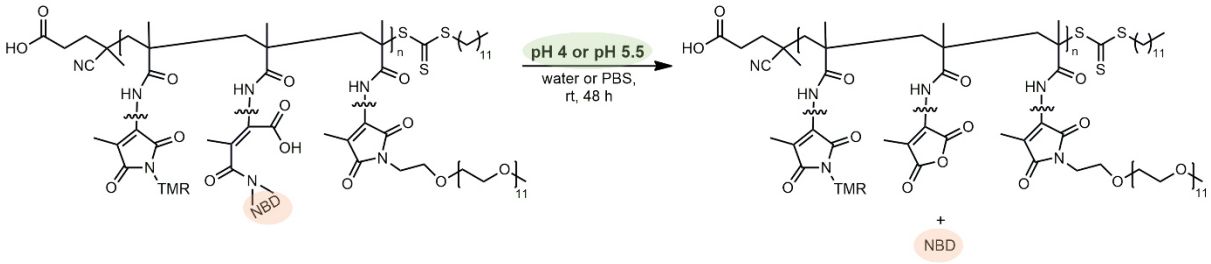

Figure S43: Schematic amine release reaction of pH-reversible NBD-PZ/NBD- and TMR-labeled hydrophilic polymer at pH 4 or pH 5.5 over time.

The release kinetics of a reversible dye-labeled polymer under acidic conditions was analyzed by UV-vis absorbance measurement. 2 mg of a TMR and NBD-PZ dye-labeled hydrophilic polymer was dissolved in 1 mL PBS (pH 7.4) and transferred to a dialyse tube with MWCO 1 kDa cut-off. The polymer was dialyzed against ultrapure water pH 4 or PBS at pH 5.5 (adjusted with hydrochloric acid) for 48 h. UV-vis spectra of the polymer were recorded at different time points. TMR absorbance served as internal standard while NBD-PZ was gradually released from the polymer.

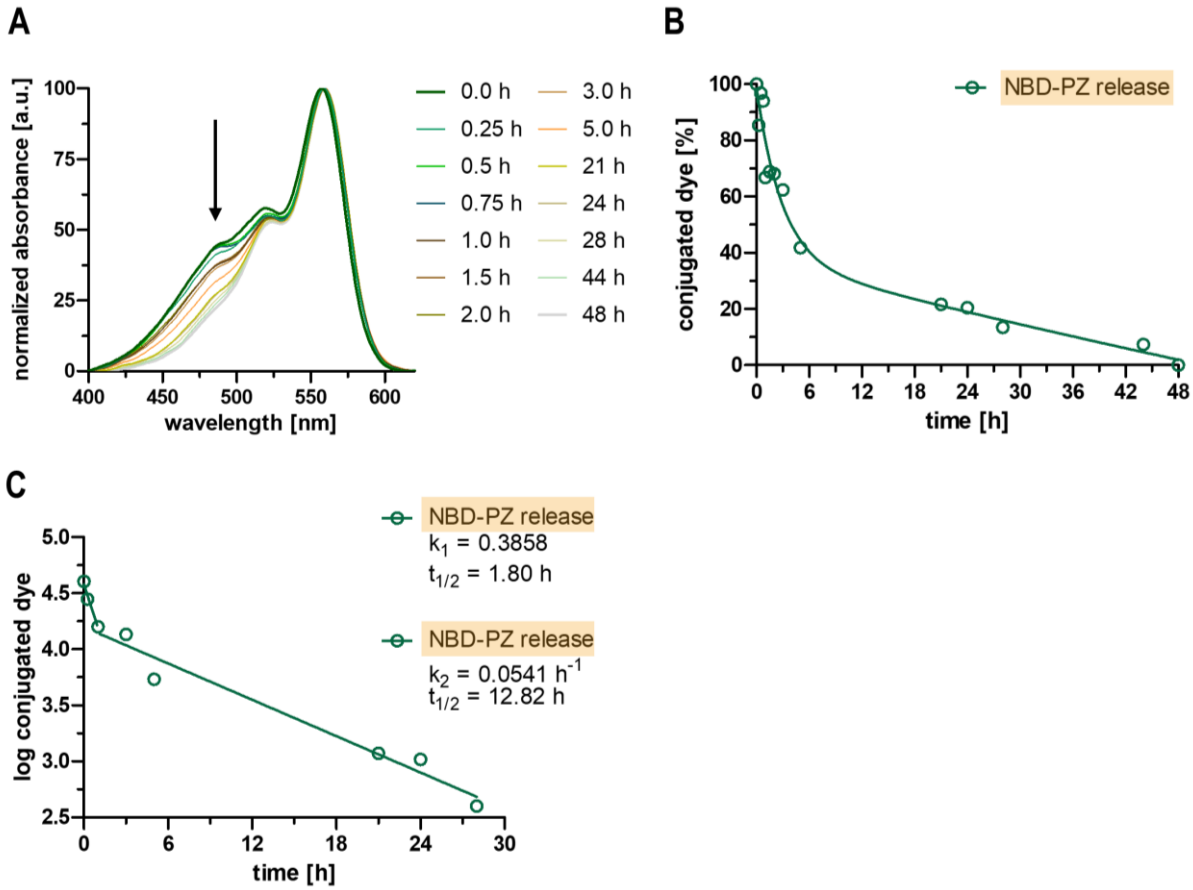

Figure S44: UV-vis spectra of NBD-PZ/NBD- and TMR-labeled hydrophilic polymer at pH 4 over time (A), the corresponding amount of conjugated NBD-PZ/NBD over time (B) and the half-life time determined by UV-vis absorbance measurements (C).

Preparation of pH-Reversible and Irreversible Drug-Loaded Hydrophilic Polymers

Methylation of the Toll-like Receptor 7/8 Agonist Imidazoquinoline IMDQ

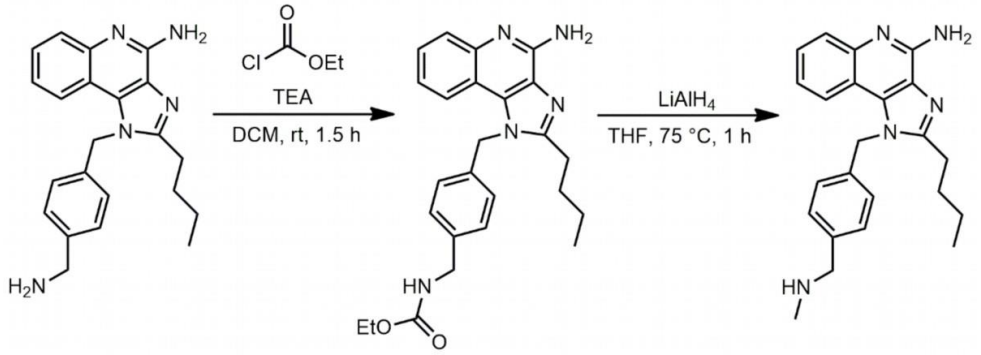

Figure S45: Synthesis of 2-butyl-1-(4-((methylamino)methyl)benzyl)-1H-imidazo[4,5-c]quinolin-4-amine (IMDQ-Me).

IMDQ-Me was synthesized according to the literature with minor modification.[8] In a 10 mL Schlenk tube equipped with a stir bar 50 mg IMDQ (0.14 mmol, 1 eq) was dissolved in 3 mL dry DCM under nitrogen atmosphere. Ethyl chloroformate (17.14 µL, 0.18 mmol, 1.3 eq) and TEA (24.95 µL, 0.18 mmol, 1.3 eq) were dropped to the solution and the reaction mixture was allowed to stir for 1.5 h at room temperature. After complete conversion water was added to the reaction mixture (6 mL) and extracted with chloroform (10 mL). The resulting organic layer was dried over $MgSO_4$, filtrated, and evaporated. In an oven-dried two neck round-bottom flask the crude product was redissolved in 10 mL dry THF. $LiAlH_4$ (26.6 mg, 0.7 mmol, 5 eq) was added in small portions and then refluxed for 1 h. The solution was cooled to room temperature before water (10 mL) was poured to the reaction mixture. The product was extracted with chloroform (10 mL), dried over $MgSO_4$, filtrated, and concentrated under reduced pressure. Further purification was performed by silica gel chromatography using chloroform and methanol (10-20%) as eluent. The desired product was obtained as a yellow powder (28 mg, 54%).

^{1}H NMR (700 MHz, DMSO-d_6): δ (ppm) = 7.78 (d, J = 8.8 Hz,1H, **a**), 7.57 (d, J = 8.8 Hz, 1H, **b**), 7.37 (m, 3H, **c+d**), 7.01 (m, 3H, **e+f**), 6.53 (s, 2H, **g**), 5.85 (s, 2H, **h**), 3.73 (s, 2H, **i**), 2.90 (m, 2H, **j**), 2.30 (s, 3H, **k**), 1.70 (m, 2H, **l**), 1.38 (m, 2H, **m**), 1.23 (s, 1H, **n**), 0.86 (t, 3H, **o**).

^{13}C NMR (176 MHz, DMSO-d_6): δ (ppm) = 153.68 (**a**), 151.82 (**b**), 144.91 (**c**), 135.89 (**d**), 132.95 (**e**), 129.24 (**f**), 126.57-125.60 (**g-k**), 120.95 (**l**). 120.19 (**m**), 114.68 (**n**), 53.47 (**o**), 47.96 (**p**), 34.50 (**q**), 29.71 (**r**), 26.34 (**s**), 21.95 (**t**), 13.83 (**u**).

ESI-MS [m/z] = 374.24 $[M+H]^+$ (calc. 374.49).

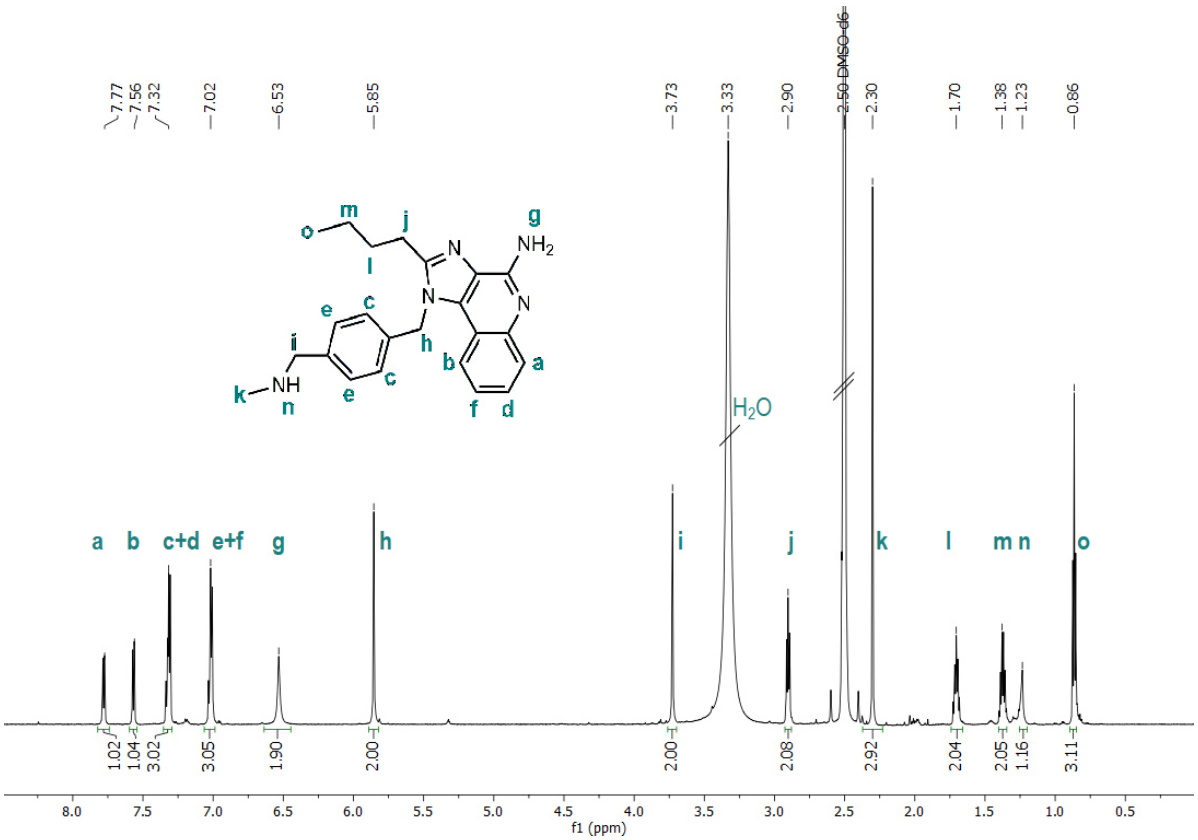

Figure S46: ^{1}H NMR spectrum (700 MHz) of 2-butyl-1-(4-((methylamino)methyl)benzyl)-1H-imidazo[4,5-c]quinolin-4-amine (IMDQ-Me) in DMSO-d_6.

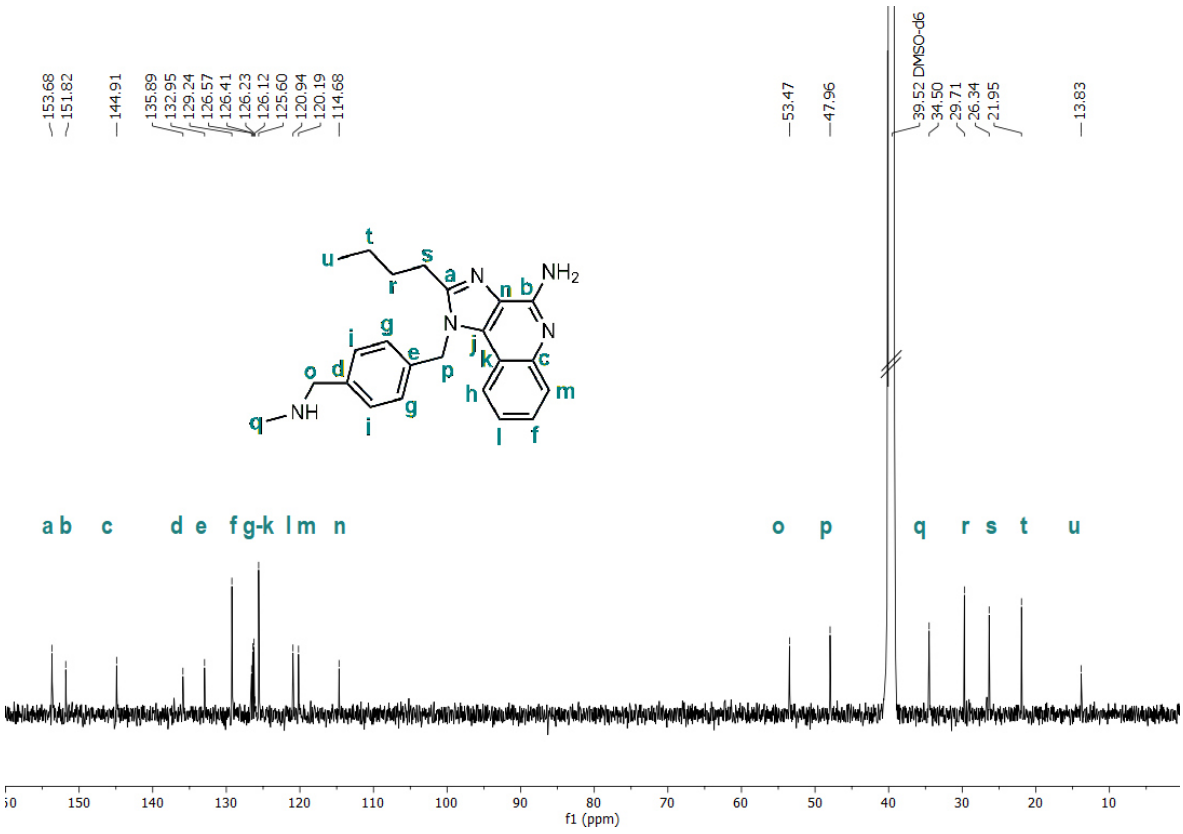

Figure S47: ^{13}C NMR spectrum (176 MHz) of 2-butyl-1-(4-((methylamino)methyl)benzyl)-1H-imidazo[4,5-c]quinolin-4-amine (IMDQ-Me) in DMSO-d_6.

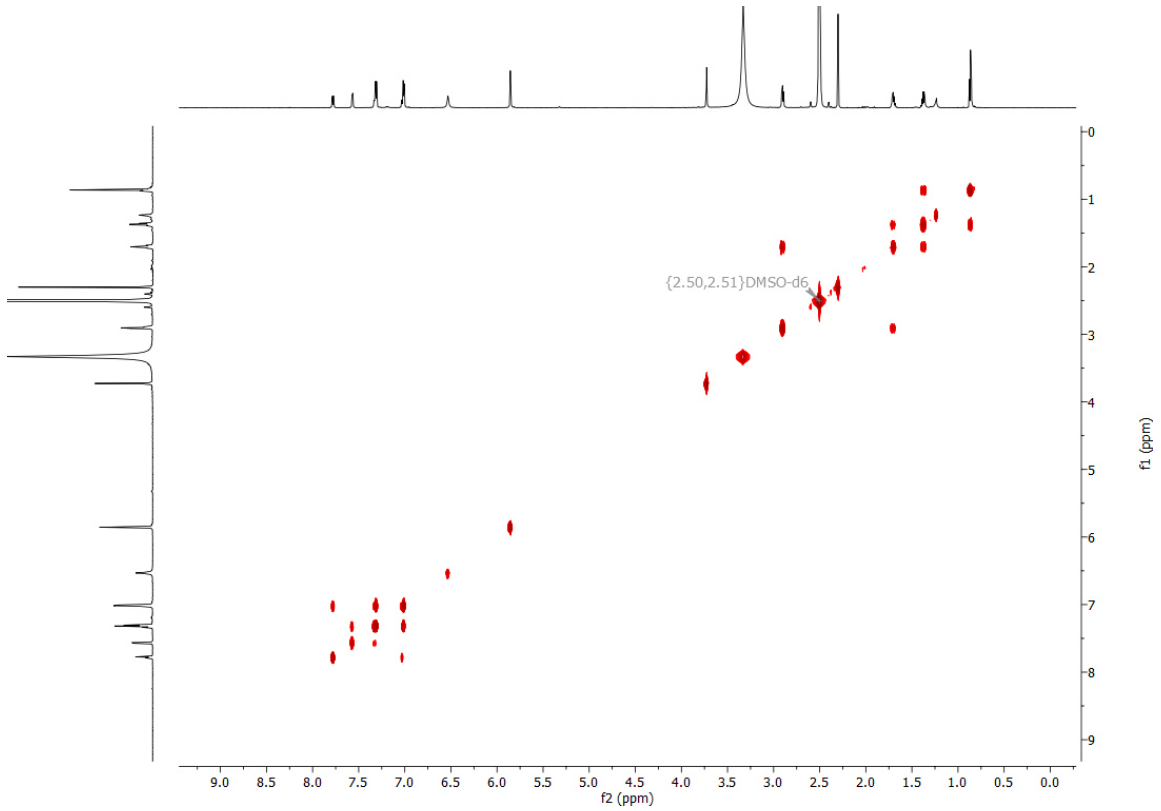

Figure S48: 2D COSY NMR spectrum of 2-butyl-1-(4-((methylamino)methyl)benzyl)-1H-imidazo[4,5-c]quinolin-4-amine (IMDQ-Me) in DMSO-d_6.

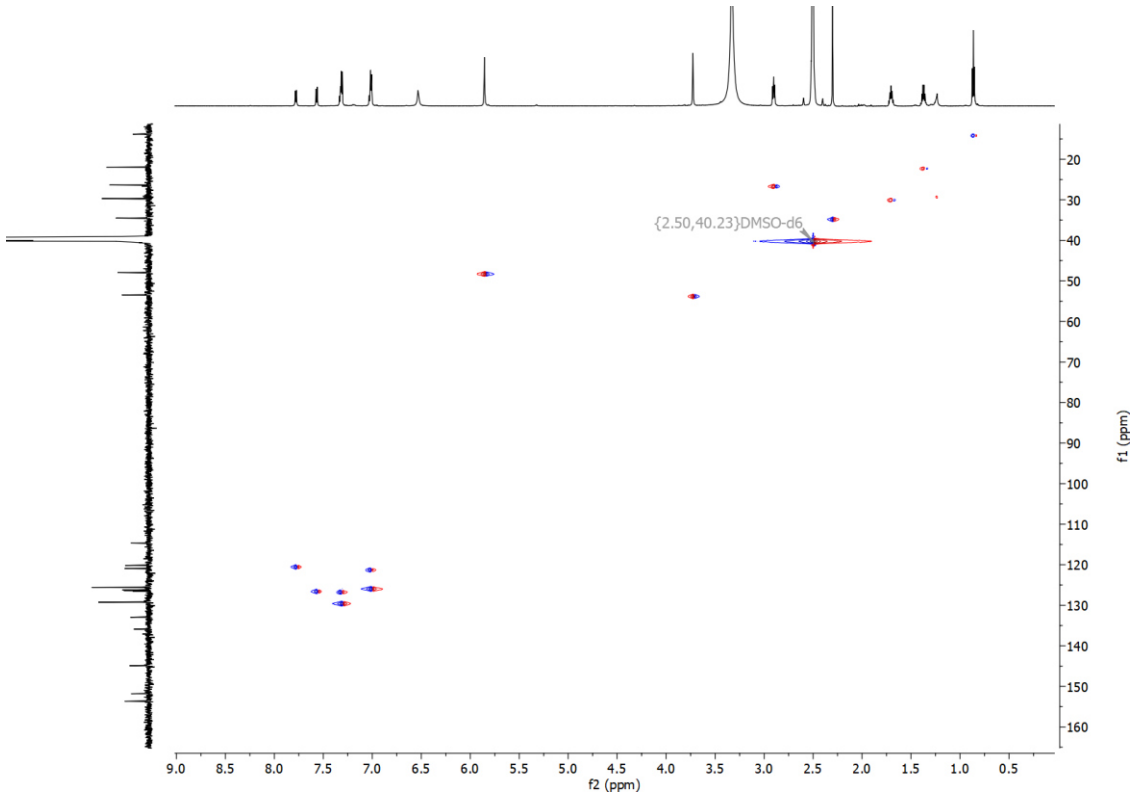

Figure S49: 2D HSQC NMR spectrum of 2-butyl-1-(4-((methylamino)methyl)benzyl)-1H-imidazo[4,5-c]quinolin-4-amine (IMDQ-Me) in DMSO-d_6.

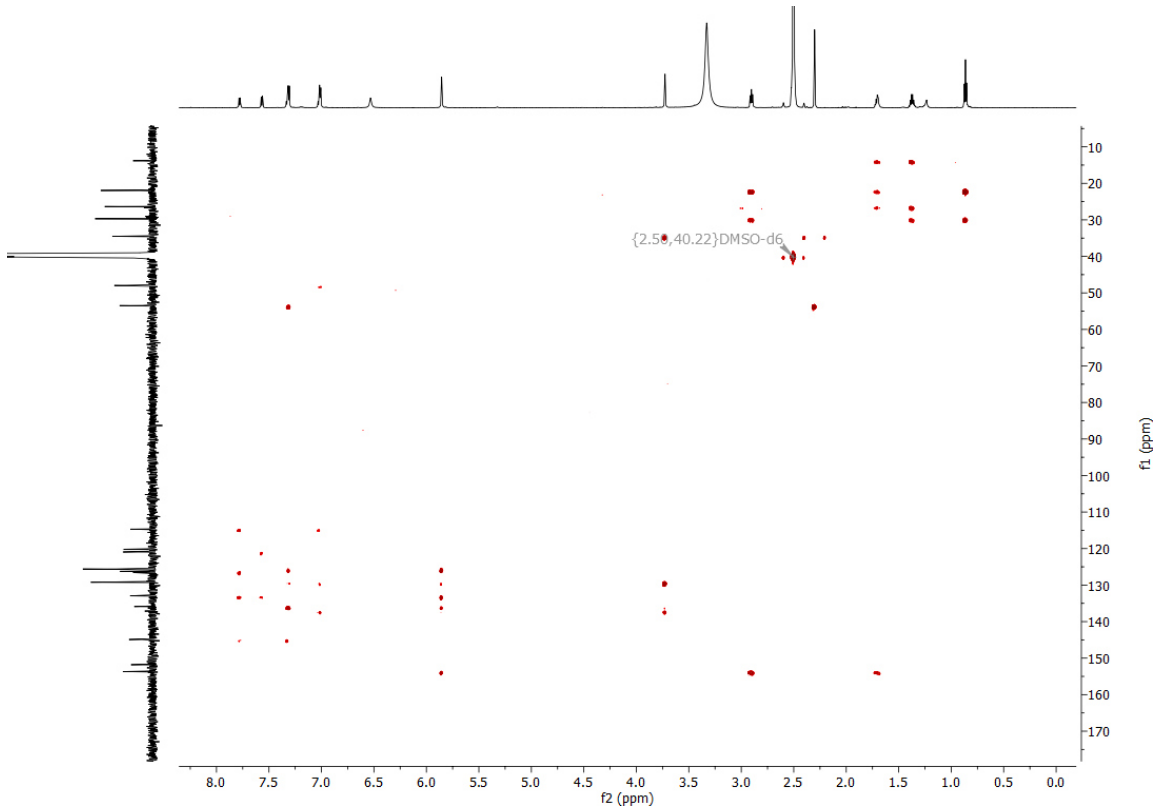

Figure S50: 2D HMBC NMR spectrum of 2-butyl-1-(4-((methylamino)methyl)benzyl)-1H-imidazo[4,5-c]quinolin-4-amine (IMDQ-Me) in DMSO-d_6.

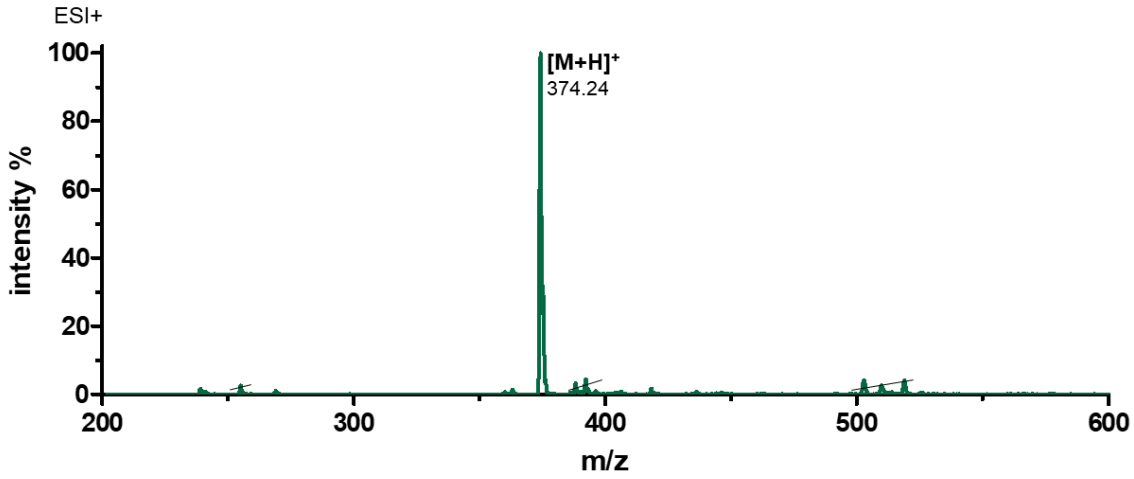

Figure S51: ESI-MS spectrum of 2-butyl-1-(4-((methylamino)methyl)benzyl)-1H-imidazo[4,5-c]quinolin-4-amine (IMDQ-Me) in MeOH (positive ion mode).

Polymer Drug Conjugation and Hydrophilization by Covalent Attachment of IMDQ or IMDQ-Me to Polymer Anhydride Groups

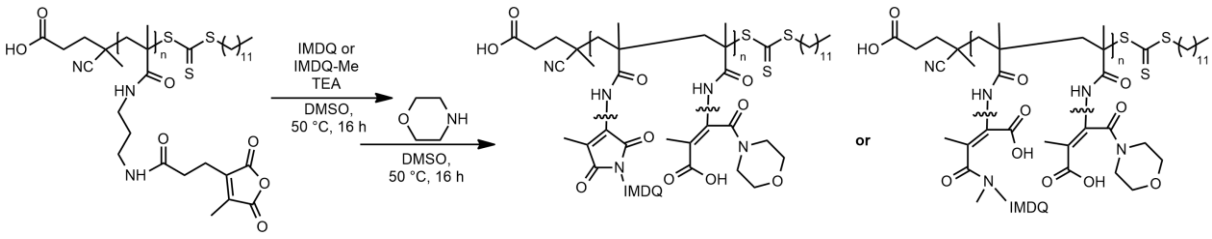

Figure S52: Schematic reaction of the polymer p(PMMA-MA)$_{36}$ with IMDQ or IMDQ-Me followed by hydrophilization with morpholine.

Analogous to the previously described amine modifications, the polymer p(PMMA-MA)$_{36}$ (15 mg each, 1.30 µmol/46.94 µmol reactive anhydride groups, 1 eq) was dissolved in two Schlenk tubes under nitrogen atmosphere in dry DMSO (0.5 mL). TEA (19.52 µL, 140.8 µmol, 3 eq) was dropped to the solutions, followed by the addition of IMDQ (84.0 µL, 2.35 µmol, 0.05 eq) or IMDQ-Me (87.7 µL, 2.35 µmol, 0.05 eq) from a 10 mg/mL stock solution in DMSO. The reaction mixtures were stirred at 50 °C for 16 h. For hydrophilization of the polymers an excess of morpholine (6.07 µL,70.41 µmol, 1.5 eq) was added to the solutions and the mixtures were stirred for further 16 h at 50 °C. Subsequently, the drug-loaded polymers were isolated by threefold precipitation into diethyl ether and centrifuged (4000 rpm, 15 min, 10 °C). After drying in high vacuum for 16 h the modified polymers were isolated as slightly yellow powder (19 mg, 97%).

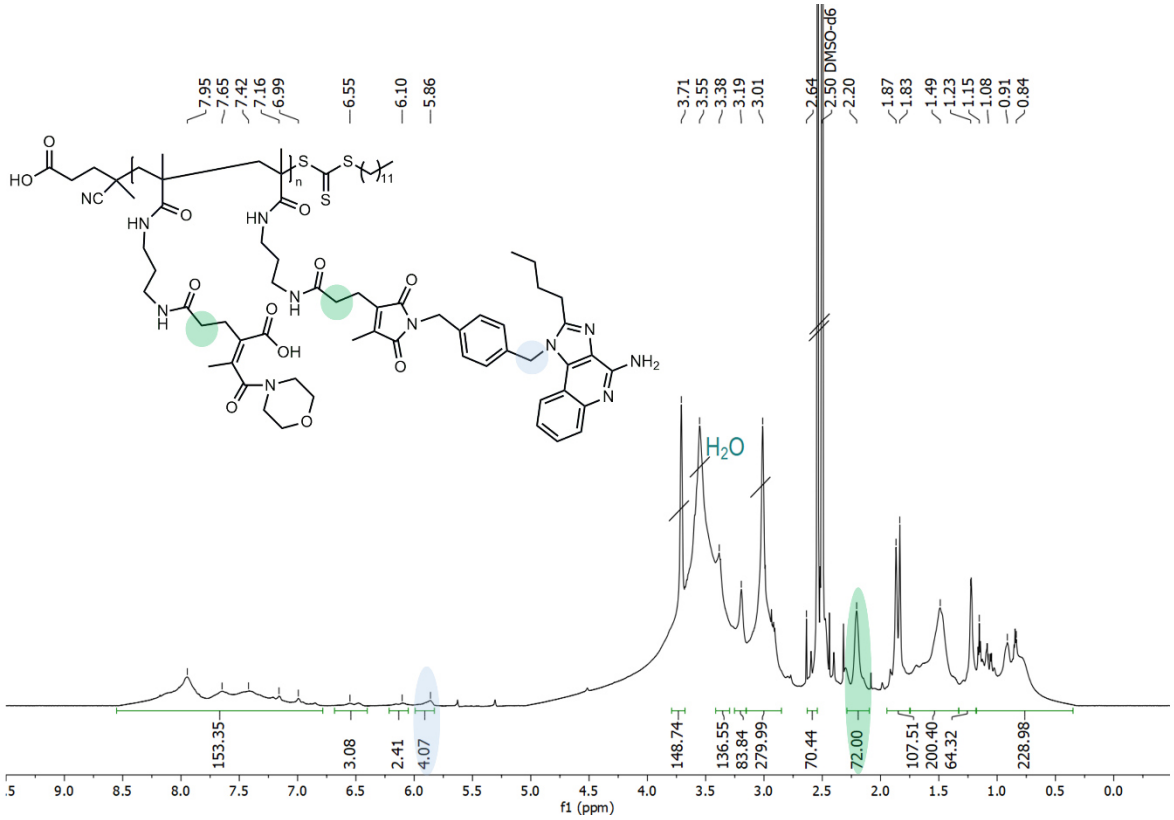

Figure S53: ^{1}H NMR spectrum (700 MHz) of the polymer p(PMMA-MA)$_{36}$ after drug loading with IMDQ and hydrophilization with morpholine in DMSO-d$_6$.

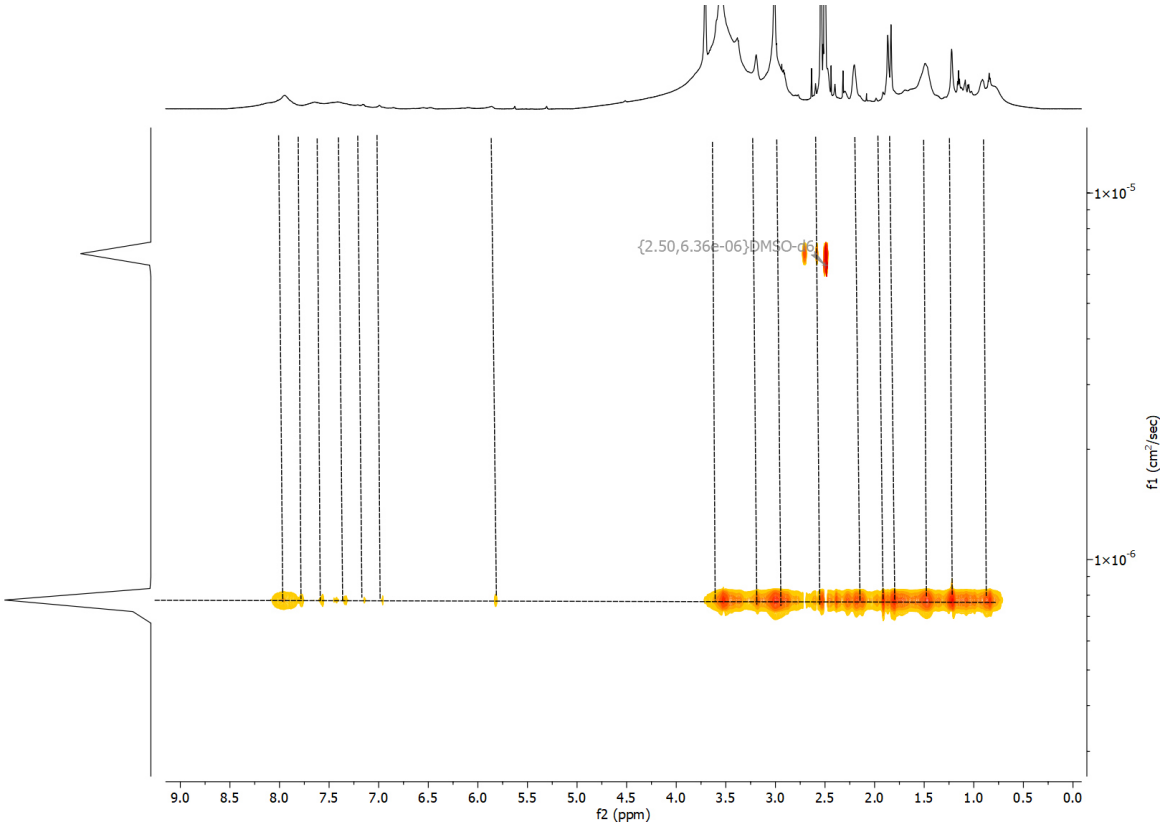

Figure S54 ^{1}H DOSY NMR spectrum (700 MHz) of the polymer p(PMMA-MA)$_{36}$ after drug loading with IMDQ and hydrophilization with morpholine in DMSO-d$_6$.

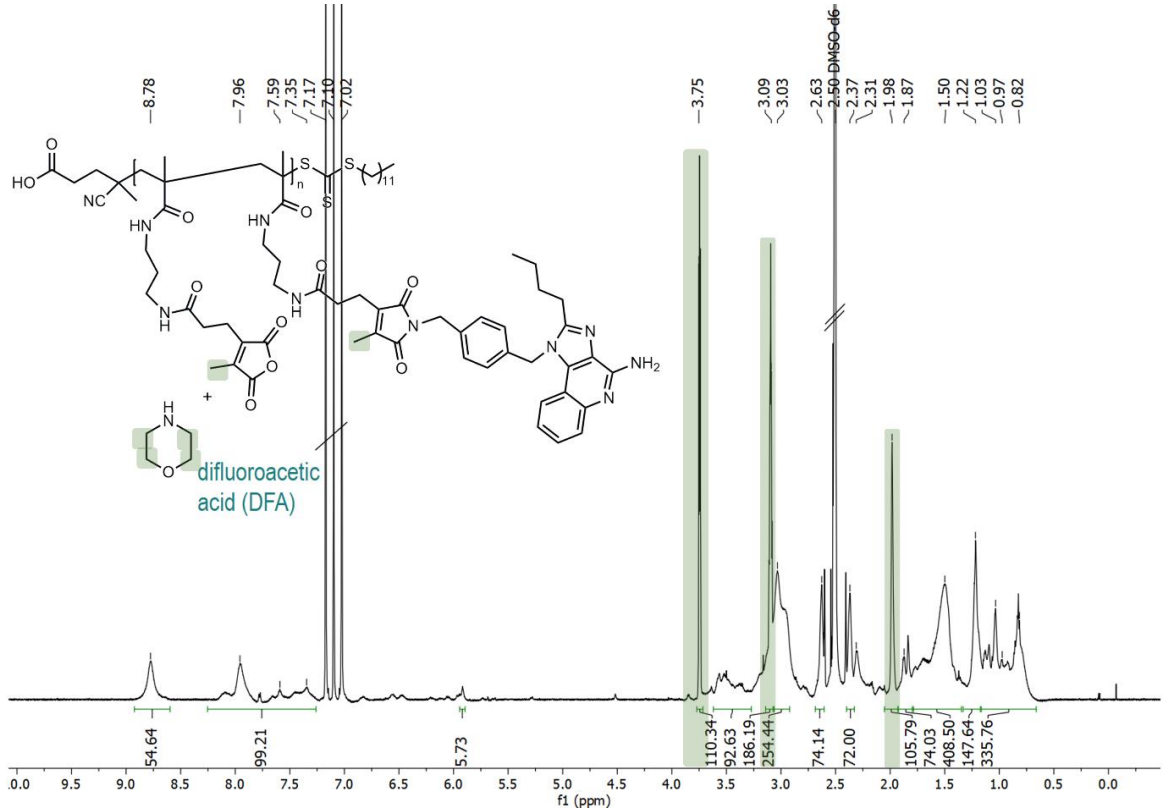

Figure S55: ^{1}H NMR spectrum (700 MHz) of the polymer p(PMMA-MA)$_{36}$ after drug loading with IMDQ and hydrophilization with morpholine at acidic conditions in DMSO-d$_6$.

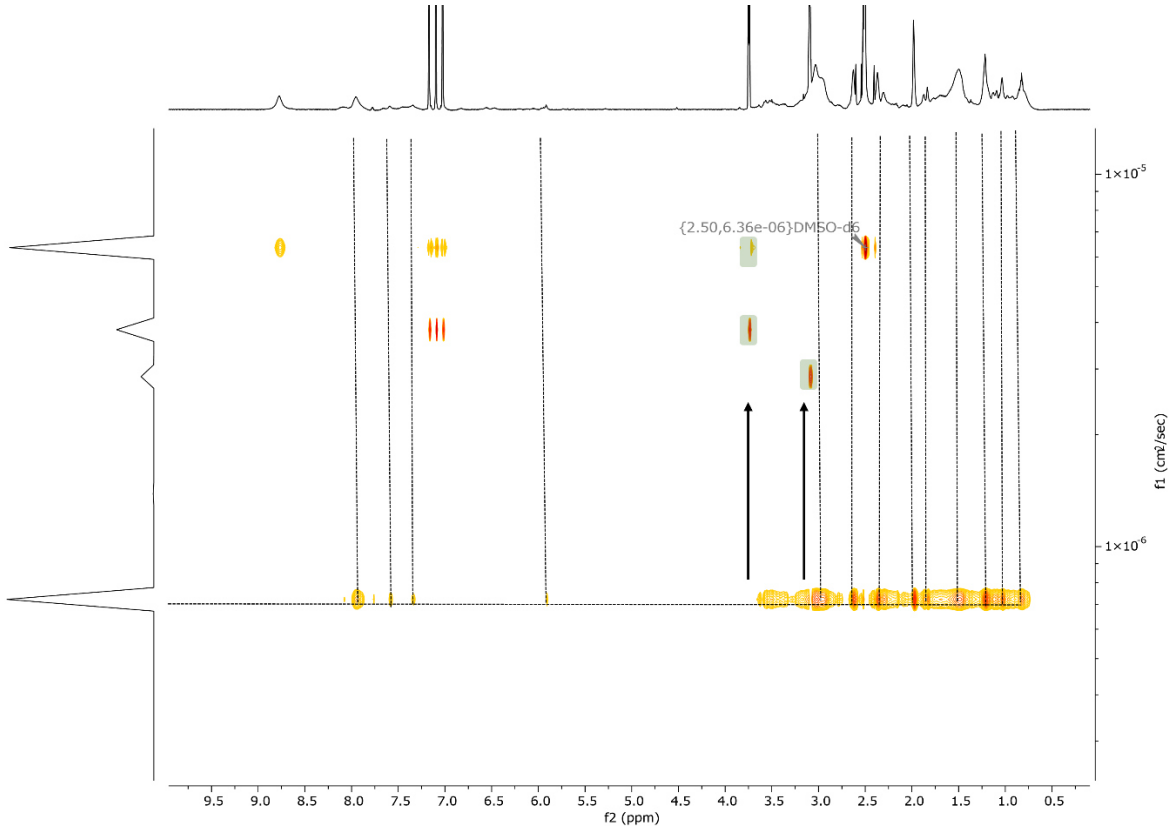

Figure S56: ^{1}H DOSY NMR spectrum (700 MHz) of the polymer p(PMMA-MA)$_{36}$ after drug loading with IMDQ and hydrophilization with morpholine at acidic conditions in DMSO-d$_6$.

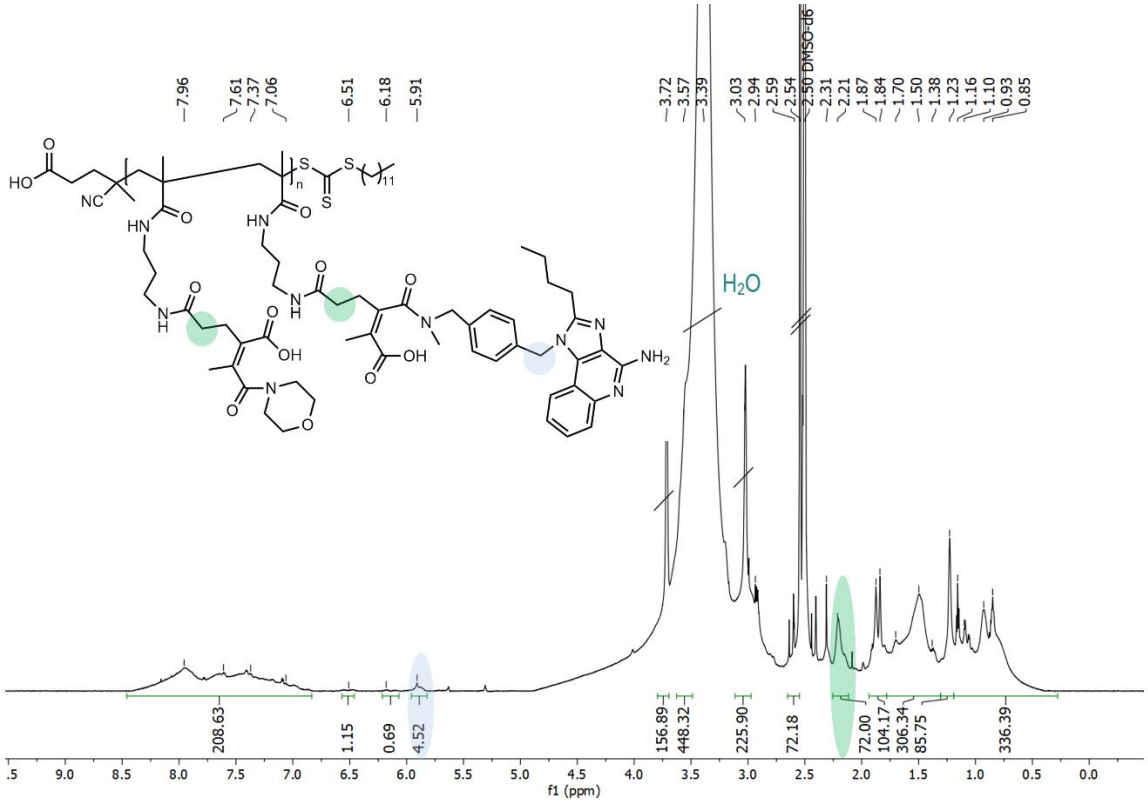

Figure S57: ^{1}H NMR spectrum (700 MHz) of the polymer p(PMMA-MA)$_{36}$ after drug loading with IMDQ-Me and hydrophilization with morpholine in DMSO-d$_6$.

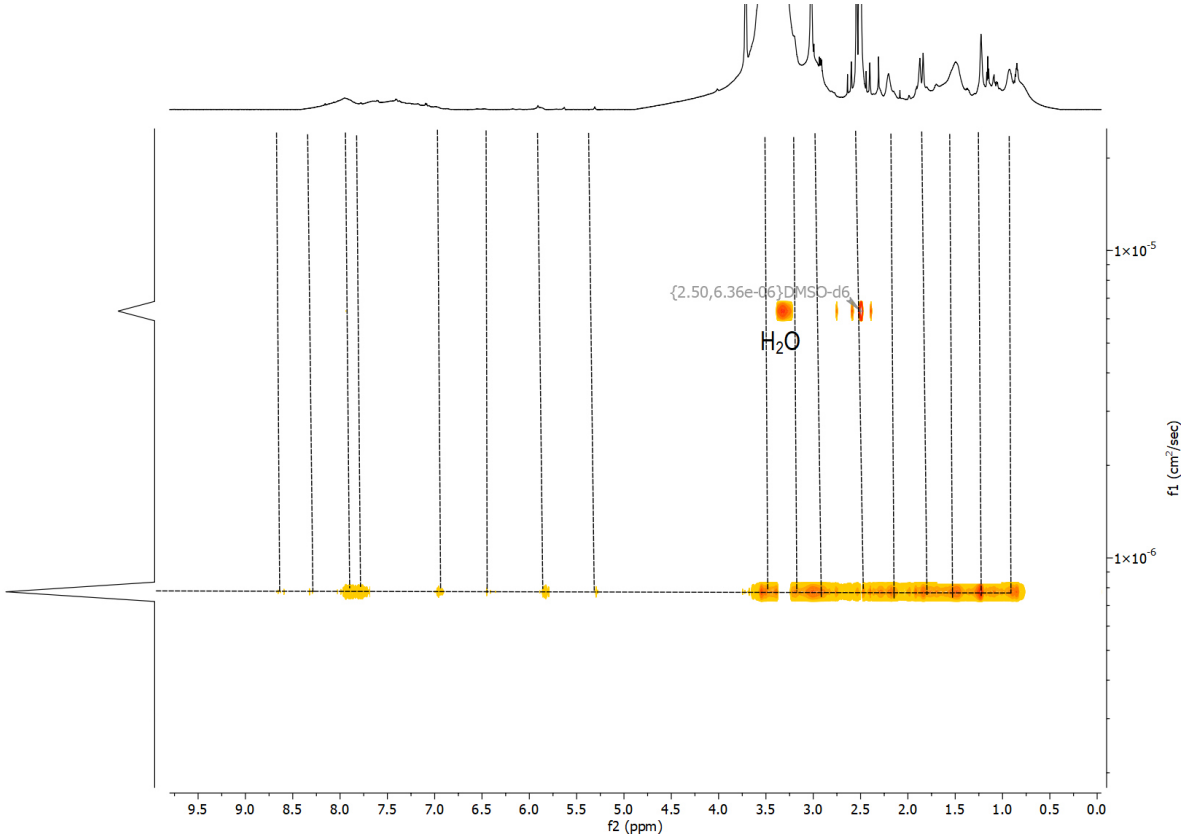

Figure S58: ^{1}H DOSY NMR spectrum (700 MHz) of the polymer p(PMMA-MA)$_{36}$ after drug loading with IMDQ-Me and hydrophilization with morpholine in DMSO-d$_6$.

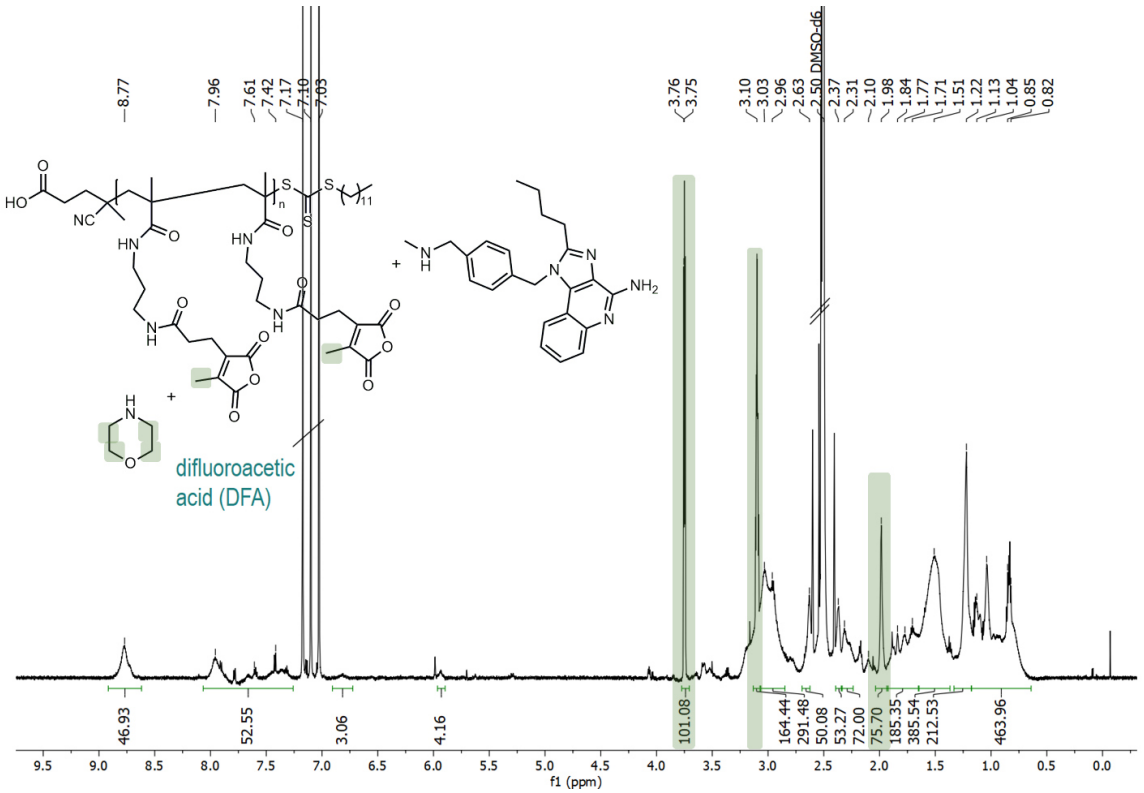

Figure S59: ^{1}H NMR spectrum (700 MHz) of the polymer p(PMMA-MA)$_{36}$ after drug loading with IMDQ-Me and hydrophilization with morpholine at acidic conditions in DMSO-d$_6$.

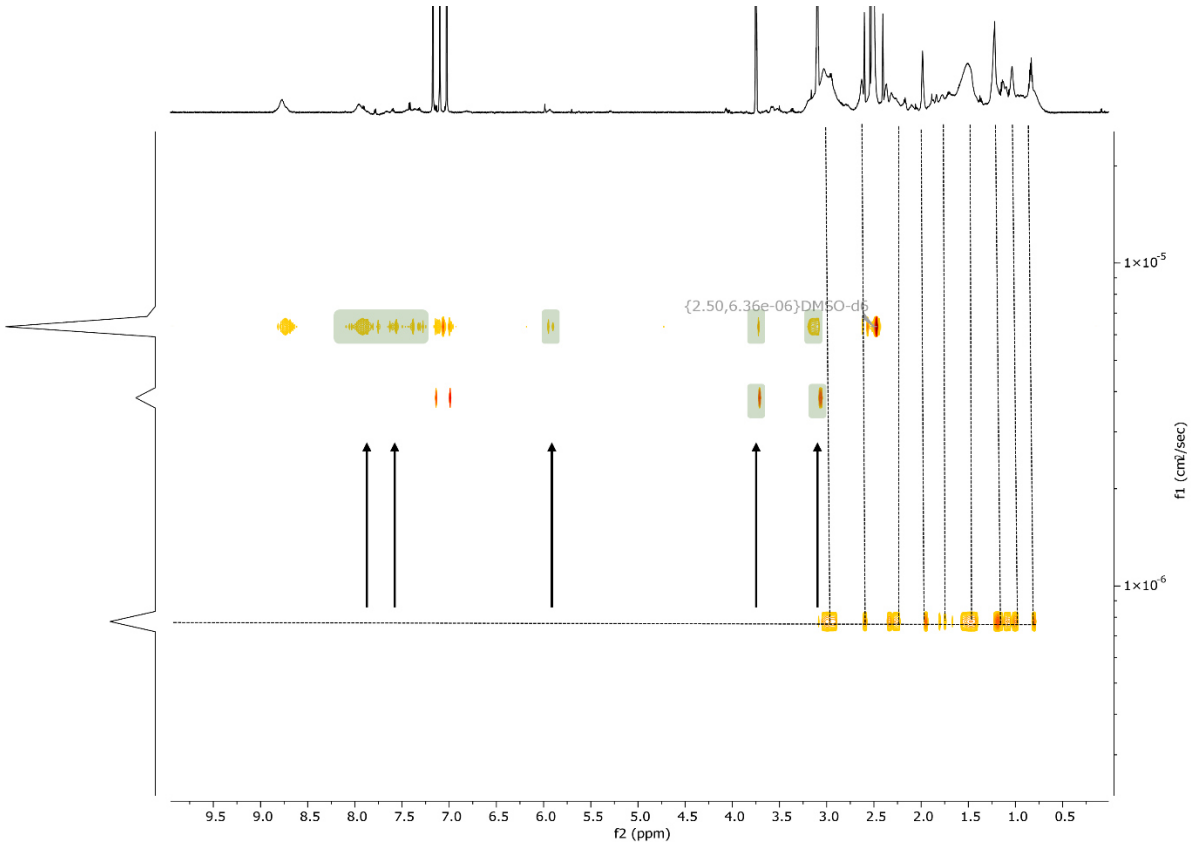

Figure S60: ^{1}H DOSY NMR spectrum (700 MHz) of the polymer p(PMMA-MA)$_{36}$ after drug loading with IMDQ-Me and hydrophilization with morpholine at acidic conditions in DMSO-d$_6$.

Calculation of IMDQ or IMDQ-Me Drug Loading by ^{1}H NMR and UV-vis Analyses

To determine the drug load of the synthesized polymers ^{1}H NMR and UV-vis analyses were utilized. For ^{1}H NMR analysis the polymers were dissolved in deuterated DMSO and 2 H of -C-CH2-CH2-CO-NH- were used as a reference.

Calculation of IMDQ-drug load:

Polymer DP = 36

2 H of -C-CH2-CH2-CO-NH → **72 H**

IMDQ proton signal: 4.07 H → 2 H of Bn-CH2-N → 2.04 IMDQ / polymer

2.04 · 359 g/mol : 15105 g/mol → **4.9 wt%**

Calculation of IMDQ-Me-drug load:

Polymer DP = 36

2 H of -C-CH2-CH2-CO-NH → **72 H**

IMDQ-Me proton signal: 4.52 H → 2 H of Bn-CH2-N → 2.26 IMDQ-Me / polymer

2.26 · 373 g/mol : 15361 g/mol → **5.5 wt%**

To investigate the drug load by UV-vis analysis free drug stock solutions (10 mg/mL) were diluted in PBS. The resulting aqueous solutions were used for determining calibration curves ranging from 0.1 to 0.0016 mg/mL. According to the literature, the drug load of the formulated polymers could be calculated.[9] Both drugs and the drug-loaded polymers show distinct absorbance maxima in PBS at 322 nm.

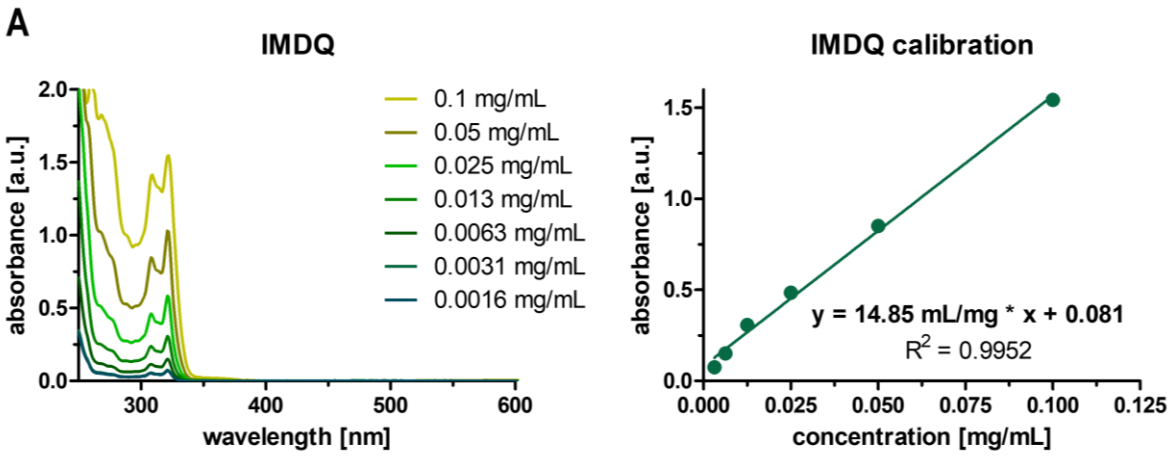

Figure S61: UV-vis spectra of IMDQ at different concentrations in PBS (left) and the corresponding calibration curve (right).

Calculation for IMDQ drug load:

$$X = \frac{(\Delta A - b)}{m - (A_{empty} / c)}$$

$X = 0.010 / 0.25$ mg/mL

$X =$ **4.2 wt%**

$\mathbf{\Delta A} = A_{max}$ (IMDQ polymer) $- A_{max}$ (morph. polymer)
$= 0.499 - 0.276 = 0.223$

b $= 0.081$

m $= 14.85$ mL/mg

$\mathbf{A_{empty}} = 0.276$

c $= 0.25$ mg/mL

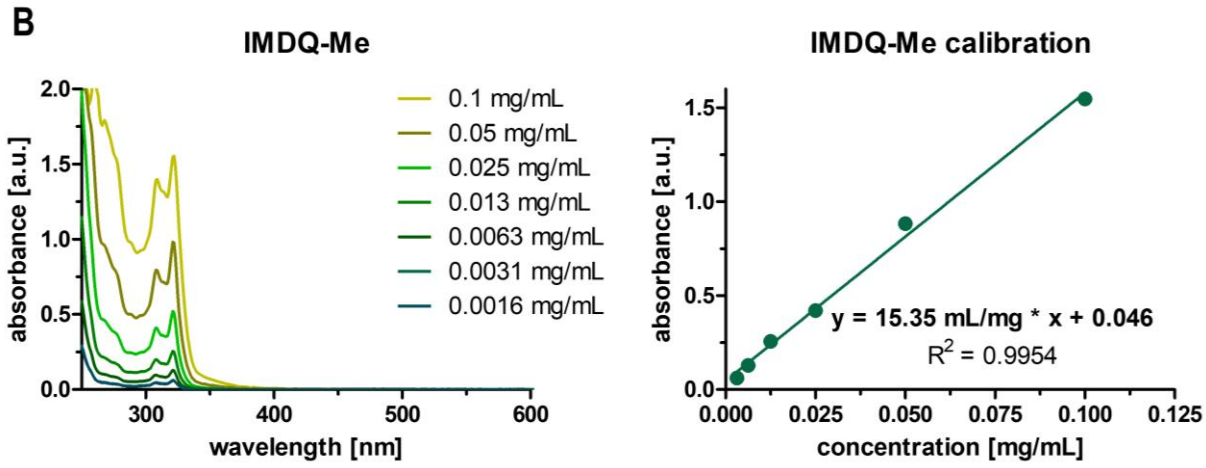

Figure S62: UV-vis spectra of IMDQ-Me at different concentrations in PBS (left) and the corresponding calibration curve (right).

Calculation for IMDQ-Me drug load:

$$X = \frac{(\Delta A - b)}{m - (A_{empty} / c)}$$

$X = 0.015 / 0.25$ mg/mL

$X =$ **5.9 wt%**

$\mathbf{\Delta A} = A_{max}$ (IMDQ-Me polymer) $- A_{max}$ (morph. polymer)
$= 0.536 - 0.276 = 0.260$

b $= 0.046$

m $= 15.35$ mL/mg

$\mathbf{A_{empty}} = 0.276$

c $= 0.25$ mg/mL

The relative drug load of the polymers was calculated by the average of ^{1}H NMR and UV-vis analysis.

IMDQ-polymer drug load = **4.6 wt%**

IMDQ-Me-polymer drug load = **5.7 wt%**

In vitro Experiments

Cell Uptake Analysis in RAW-Dual Macrophages by Flow Cytometry (FACS)

RAW-Dual macrophages were seeded into 24-well plates (250000 cells/well suspended in 900 µL of culture medium) and incubated overnight to allow cells settling and adhering to the bottom of the wells. Then, cells were incubated with 100 µL of tetramethylrhodamine (TMR)- or NBD-PZ-labeled hydrophilic polymers in PBS (resulting in a total concentration of 10, 30, or 100 µg/mL). All samples were performed in triplicates (n = 3) and after 24 h of incubation time the medium was removed, and cells were washed with 1 mL PBS. 500 µL cell dissociation buffer was added, and cells were incubated for 15 min at 37 °C. Cells were detached by pipetting and cell suspensions were transferred into Eppendorf tubes on ice. After centrifugation at 300 g for 10 minutes at 5 °C the supernatant was aspired, and the cell pellets were resuspended in 200 µL of PBS. Cell suspensions were stored on ice to maintain cell integrity prior to flow cytometric analysis by a BD Accuri C6 (BD Biosciences). All data were processed by FlowJo Software.

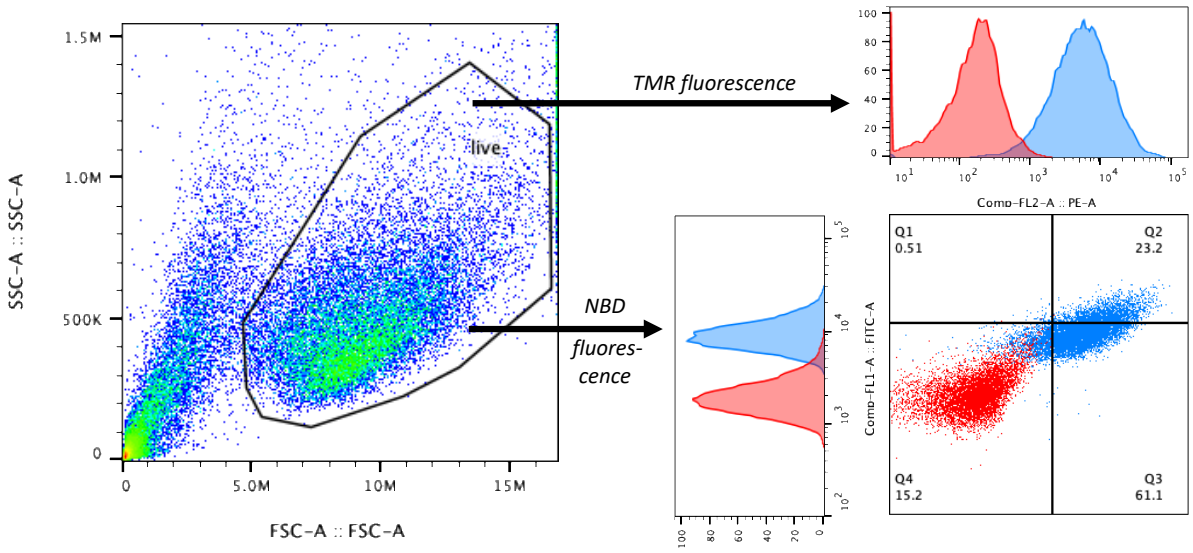

Figure S63: Gating procedure for flow cytometry analysis of RAW-Dual macrophages.

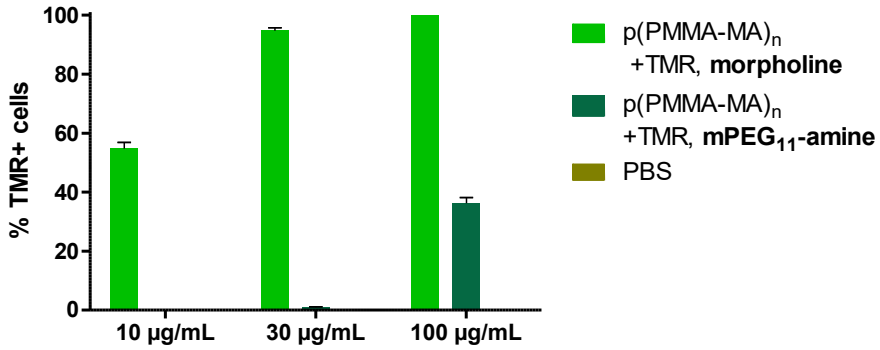

Figure S64: Flow cytometric analysis of RAW-Dual macrophages incubated with PBS (control), TMR-labeled polymers hydrophilized with $mPEG_{11}$-amine or morpholine at 10, 30, and 100 µg/mL for 24 h revealing the percentage of TMR positive cells (% TMR+ cells).

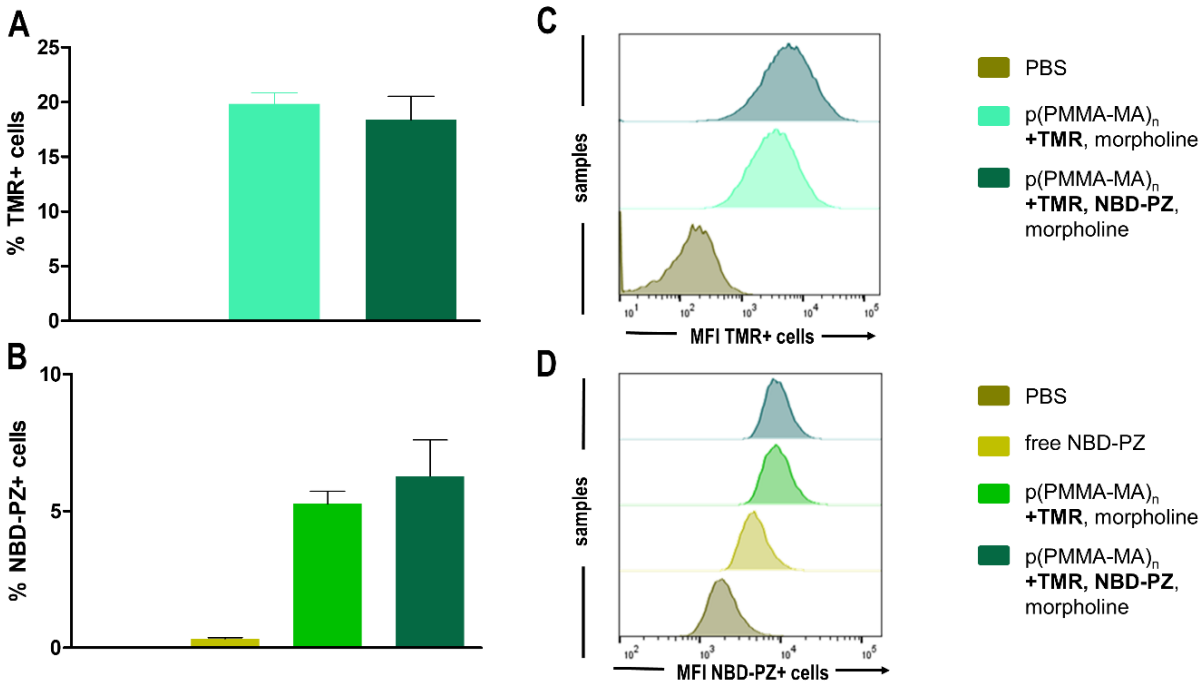

Figure S65: Flow cytometric analysis of RAW-Dual macrophages incubated with PBS (control), TMR-labeled or NBD-PZ-labeled polymers hydrophilized with morpholine at 10 µg/mL for 24 h exposing the percentage of TMR or NDB-PZ positive cells (% TMR+ cells or % NBD-PZ+ cells) (A and B) and the corresponding histograms (C and D).

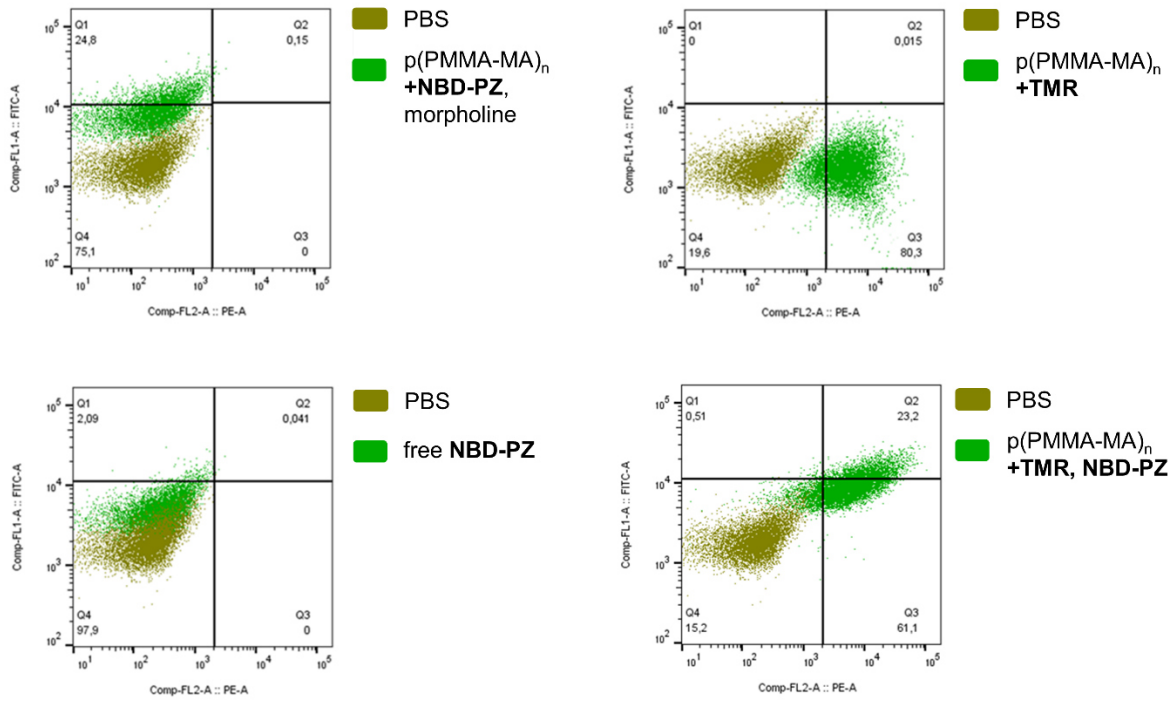

Figure S66: Flow cytometric analysis of RAW-Dual macrophages incubated with PBS (control), TMR-labeled or NBD-PZ-labeled polymers hydrophilized with morpholine at 10 µg/mL for 24 h showing the specific cell population depending on the polymer cell uptake.

Fluorescence Confocal Laser Scanning Microscopy Imaging

For fluorescence microscopy imaging RAW-Dual macrophages were seeded in an Ibidi µ-slide 8-well chamber (50000 cells/well in 180 µL culture medium) and incubated overnight. After treatment with 20 µL TMR- or NBD-PZ-labeled polymer solutions in PBS (total concentration of 10 or 30 µg/mL) for 24 h, cells were three times washed with PBS and fixed with 200 µL 4% paraformaldehyde solution for 15 min at 37 °C. Cells were then washed three times with PBS and cell nuclei were stained with 125 µL 4′,6-diamidino-2-phenylindole (DAPI) (80 µg/mL in PBS) for 20 min at room temperature. Afterwards, cells were washed with PBS three times and samples were stored under aqueous mounting medium. Samples were analyzed on a Leica SP5 confocal microscope (Wetzlar, Germany) with a 63x oil immersion objective. All images were finally processes using Leica Application Suite X 3.7.4.23463 by Leica Microsystems.

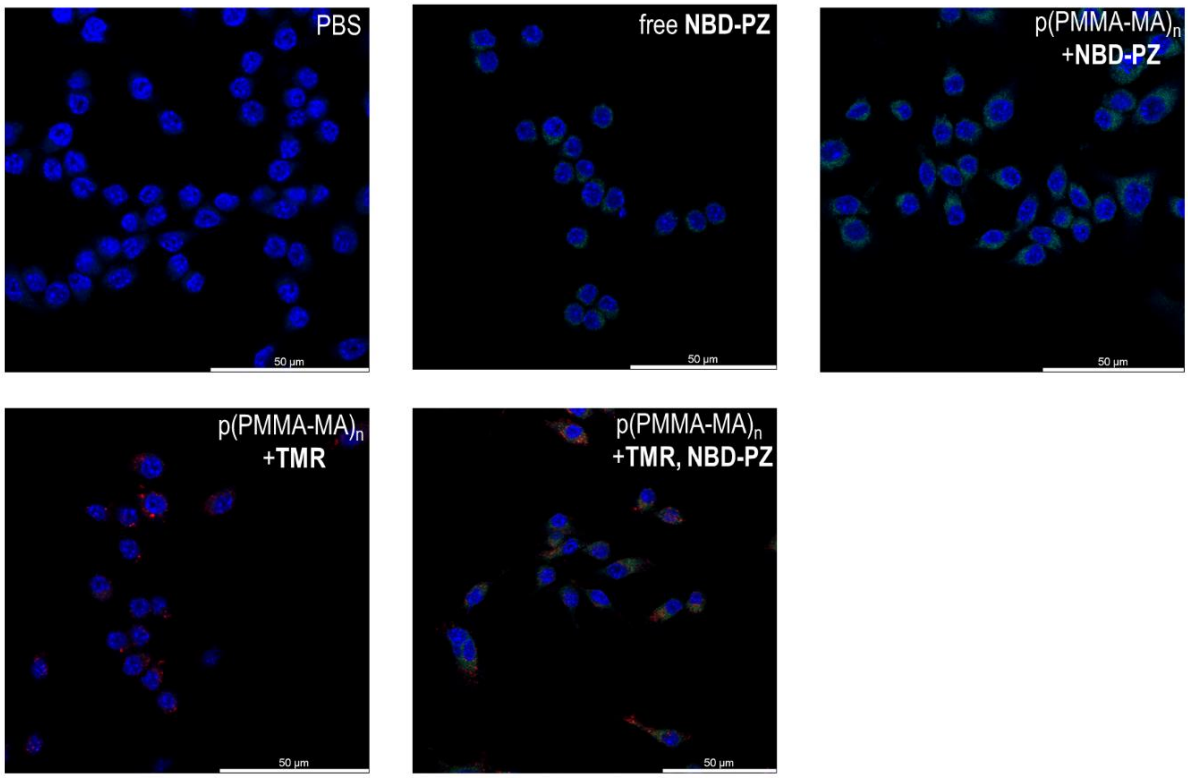

Figure S67: Confocal microscopy images of RAW-Dual macrophages incubated with PBS (control), TMR-labeled or NBD-PZ-labeled polymers hydrophilized with morpholine at 10 µg/mL for 24 h (blue: nuclei stained with Hoechst 33258, red: TMR-labeled polymer, green: NBD-PZ free dye or NBD-PZ-labeled polymer).

Determination of Cellular Metabolic Activity of RAW-Dual Macrophages by MTT Assay

RAW-Dual macrophage viability was quantified by determining their cellular metabolic activity using a colorimetric MTT assay. Cells were seeded in a 96-well plate at a concentration of 90000 cells/well in 180 µL and left to adhere overnight. Each well containing RAW-Dual macrophages was treated with 20 µL IMDQ- or IMDQ-Me-loaded polymer, free drugs, morpholine or $mPEG_{11}$-amine hydrophilized polymer at given concentration (n = 4). After 24 h incubation at 37 °C 30 µL of a 2 mg/mL 3-(4,5-dimethylthiazol-2-yl)-2,5-diphenyltetrazolium bromide solution in PBS was added, and cells were incubated at 37 °C for 1.5 h. The formed formazan crystals were dissolved by addition of 100 µL of 10% m/v SDS/0.01 M HCl solution followed by incubation overnight at 37 °C. Cellular metabolic activity was finally obtained in relation to positive (PBS blank, 100% activity) and negative (10% DMSO, 0% activity) control samples based on the absorbance measurements at 570 nm.

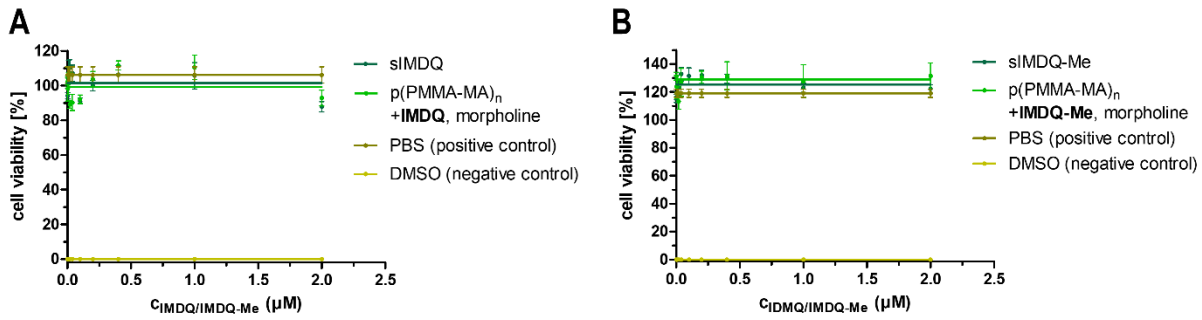

Figure S68: Cell viability of RAW-Dual macrophages treated with sIMDQ or IMDQ-loaded polymer hydrophilized with morpholine (A), sIMDQ-Me or IMDQ-Me-loaded polymer hydrophilized with morpholine (B), PBS and DMSO analyzed by MTT assay (n = 4).

RAW-Dual Macrophage TLR Reporter Assay (QUANTI-Blue Assay)

To evaluate the immune modulating properties of pH-reversible and non-reversible IMDQ-conjugated polymers, the TLR reporter assay was conducted as recommended by InvivoGen. For that purpose, IMDQ-induced stimulation of the TLR receptor and subsequent NF-κB/AP-1 activation was monitored by the secretion of embryonic alkaline phosphatase (SEAP). RAW-Dual cells were seeded analogously to previously described MTT assay and incubated with 20 µL of the respective solution at the given IMDQ/IMDQ-Me concentrations. On the next day, 50 µL of the supernatant was transferred into a new 96-well plate and the SEAP levels were determined by QUANTI-Blue Assay. QUANTI-Blue (150 µL) was added to each sample and incubated for 2 h at 37 °C, followed by read-out for their optical density at 620 nm using a plate reader. All experiments were performed at n = 4.

Maturation of GM-CSF stimulated bone marrow derived dendritic cells (BMDCs)

Bone marrow cells were isolated from femurs and tibiae of C57BL/6 mice and resuspended in IMDM-based culture medium (5% FBS, 2 mM L-glutamine, 100 IU/ml penicillin, 100 µg/ml streptomycin and 50 µM β-mercaptoethanol; all from Sigma-Aldrich, Deisenhofen, Germany) supplemented with 10 ng/ml recombinant murine GM-CSF (R&D Systems, Wiesbaden, Germany). To this end, bone marrow cells were seeded in 12 well suspension cell culture cluster plates at $2x10^5$/mL. On day 3 and 6, cell culture media had to be replenished. On days 7-8, the bone marrow cells differentiated into inflammatory bone marrow derived dendritic cells (BMDCs). They were subsequently incubated over night with the respective polymer solutions at the given concentrations (0.2 µM, 1.0 µM and 5.0 µM equivalents of soluble of polymer bound IMDQ or IMDQ-Me).

On the next day, all cells were harvested and subjected to flow cytometric analysis. After incubation with Fcγ receptor (CD16/CD32) blocking antibody (rat-anti-mouse, clone 2G4) to prevent non-specific binding of other antibodies (15 min, 4 °C), all cells were stained with lineage and activation marker detecting antibodies for 20 min at 4 °C. All antibodies were purchased from BioLegend (San Diego, CA, USA) or Thermo Fisher (Waltham, MA, USA) and served to differentiate the cells and their maturation status (compare Table S1 and Figure S69). Samples left untreated or stained with single antibodies served as controls. Fixable Viable Dye (FVD-eFluor® 780, Thermo, CA, USA) was used to discriminate live/dead cells. Fixed samples were analyzed on a Attune NxT flow cytometer (Thermo Fisher) and the obtained data processed using the Attune NxT Flow cytometer software (Thermo Fisher).

Table S1: Antibodies used to differentiate and characterize the activation state of the BMDCs.

Cell line	Antibody	Clone	Dye
BMDCs (GM-CSF)	CD11c	N418	PE-Cy7-A
	CD80	16-10A1	PE
	CD86	GL1	eF450
	MHC-II	M5/114.152	FITC
	CD40	1C10	APC

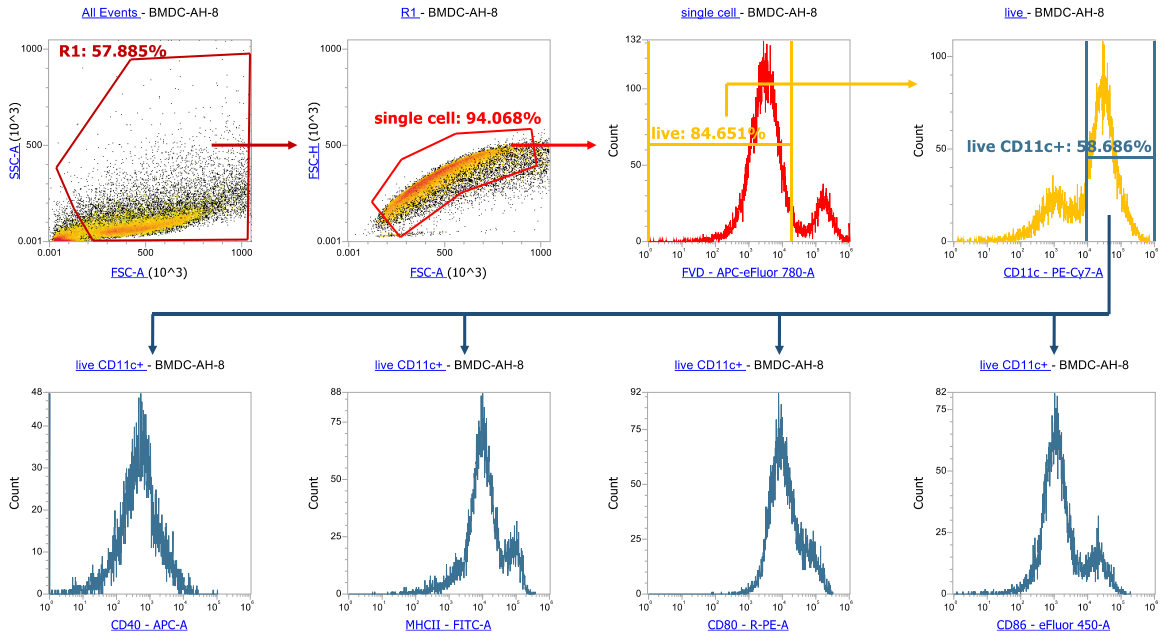

Figure S69: Gating procedure for flow cytometry analysis of bone marrow derived dendritic cells towards analysis of their maturation markers. Cells were first identified as single cells and discriminated by Fixable Viable Dye (FVD-eFluor 780) between live and dead. Viable cells were then identified as dendritic cells by CD11c antibody. The respective population was then characterized by mean fluorescent intensities of the displayed maturation markers.

Statistical Analyses

All data are shown as mean values ± standard deviation (mean ± SD). Samples sizes (n) were mentioned for each data set. To calculate statistical significance of the mean values, unpaired Student's t-test with Welch's correction was performed using Graph Pad Prism 8 software (*$p \leq 0.05$; **$p \leq 0.01$; ***$p \leq 0.001$).

Additional References

(1) Bolli, E.; Scherger, M.; Arnouk, S. M.; Pombo Antunes, A. R.; Straßburger, D.; Urschbach, M.; Stickdorn, J.; De Vlaminck, K.; Movahedi, K.; Räder, H. J.; Hernot, S.; Besenius, P.; Van Ginderachter, J. A.; Nuhn, L. Targeted Repolarization of Tumor-Associated Macrophages via Imidazoquinoline-Linked Nanobodies. *Adv. Sci.* **2021**, *8* (10), 1–12.

(2) He, N.; Chen, Z.; Yuan, J.; Zhao, L.; Chen, M.; Wang, T.; Li, X. Tumor PH-Responsive Release of Drug-Conjugated Micelles from Fiber Fragments for Intratumoral Chemotherapy. *ACS Appl. Mater. Interfaces* **2017**, *9* (38), 32534–32544.

(3) Helaine, V.; Bolte, J. Chemoenzymatic Synthesis of (4S)- and (4R)-4-Methyl-2-Oxoglutaric Acids, Precursors of Glutamic Acid Analogues. *European J. Org. Chem.* **1999**, No. 12, 3403–3406.

(4) Takemoto, H.; Miyata, K.; Hattori, S.; Ishii, T.; Suma, T.; Uchida, S.; Nishiyama, N.; Kataoka, K. Acidic PH-Responsive SiRNA Conjugate for Reversible Carrier Stability and Accelerated

Endosomal Escape with Reduced IFNα-Associated Immune Response. *Angew. Chemie - Int. Ed.* **2013**, *52* (24), 6218–6221.

(5) Ding, Y.; Du, C.; Qian, J.; Zhou, L.; Su, Y.; Zhang, R.; Dong, C. M. Tumor PH and Intracellular Reduction Responsive Polypeptide Nanomedicine with a Sheddable PEG Corona and a Disulfide-Cross-Linked Core. *Polym. Chem.* **2018**, *9* (25), 3488–3498.

(6) Nuhn, L.; Hirsch, M.; Krieg, B.; Koynov, K.; Fischer, K.; Schmidt, M.; Helm, M.; Zentel, R. Cationic Nanohydrogel Particles as Potential SiRNA Carriers for Cellular Delivery. *ACS Nano* **2012**, *6* (3), 2198–2214.

(7) Nudelman, R.; Ardon, O.; Hadar, Y.; Chen, Y.; Libman, J.; Shanzer, A. Modular Fluorescent-Labeled Siderophore Analogues. *J. Med. Chem.* **1998**, *41* (10), 1671–1678.

(8) Honjo, T.; Sano, S.; Shiro, M.; Nagao, Y. Highly Enantioselective Catalytic Thiolysis of Prochiral Cyclic Dicarboxylic Anhydrides Utilizing a Bifunctional Chiral Sulfonamide. *Angew. Chemie - Int. Ed.* **2005**, *44* (36), 5838–5841.

(9) Nuhn, L.; Vanparijs, N.; De Beuckelaer, A.; Lybaert, L.; Verstraete, G.; Deswarte, K.; Lienenklaus, S.; Shukla, N. M.; Salyer, A. C. D.; Lambrecht, B. N.; Grooten, J.; David, S. A.; De Koker, S.; De Geest, B. G. PH-Degradable Imidazoquinoline-Ligated Nanogels for Lymph Node-Focused Immune Activation. *Proc. Natl. Acad. Sci. U. S. A.* **2016**, *113* (29), 8098–8103.

CHAPTER II: PH-TRIGGERED, LYMPH NODE FOCUSED IMMUNODRUG DELIVERY BY POLYMERIC 2-PROPIONIC-3-METHYLMALEIC ANHYDRIDES WITH CHOLESTEROL END GROUPS

The following chapter was submitted to a peer-reviewed journal. As first author, I was responsible for the synthesis and characterization of the pH-sensitive and cholesteryl-coupled polymers. In this regard, the project was elaborated by my research student Katharina Eigen. She started the synthesis of a cholesteryl-bearing chain transfer agent (chol-CTA), which could be used for the controlled radical polymerization of methacrylamide-based monomers. I supported Katharina Eigen regarding the experimental procedures and analysis of the chol-CTA. In addition, I optimized the synthesis process, and further investigated the pH reversibility of the polymer system. Thereby, Johannes Kockelmann performed IR-measurements for the detailed characterization. Subsequently, I transformed the cholesteryl-polymer into dye-labeled, immune stimulant-loaded and hydrophilic polymers, with efficient stealth properties and acidic drug release. Initial *in vitro* studies on RAW-Dual macrophages were performed by me. Confocal microscopy images were recorded by Judith Stickdorn and Maximilian Scherger synthesized the immune stimulatory drug, whereas further modifications were conducted by me. Additional *in vitro* and *in vivo* experiments were performed by Carolina Medina-Montano, Zifu Zhong and further coworkers. Finally, I wrote the first draft of the manuscript and included contributions and feedback from the co-authors.

pH-TRIGGERED, LYMPH NODE FOCUSED IMMUNODRUG DELIVERY BY POLYMERIC 2-PROPIONIC-3-METHYL-MALEIC ANHYDRIDES WITH CHOLESTEROL END GROUPS

Alina G. Heck[1,2], Carolina Medina-Montano[3], Zifu Zhong[4], Kim Deswarte[5], Katharina Eigen[1], Judith Stickdorn[2], Johannes Kockelmann[1], Maximilian Scherger[2], Niek N. Sanders[6], Stefan Lienenklaus[7], Bart N. Lambrecht[5], Stephan Grabbe[3], Bruno G. De Geest[4] and Lutz Nuhn[,1]*

1: Chair of Macromolecular Chemistry, Julius-Maximilians-Universität Würzburg, 97070 Würzburg, Germany

2: Max Planck Institute for Polymer Research, 55128 Mainz, Germany

3: Department of Dermatology, University Medical Center (UMC) of the Johannes Gutenberg-University Mainz, 55131 Mainz, Germany

4: Department of Pharmaceutics and Cancer Research Institute Ghent (CRIG), Ghent University, Ghent 9000, Belgium

5: Department of Internal Medicine and Pediatrics, VIB Center for Inflammation Research, Ghent University, 9052 Ghent, Belgium

6: Laboratory of Gene Therapy, Department of Nutrition, Genetics and Ethology, Ghent University, 9820 Merelbeke, Belgium

7: Institute for Laboratory Animal Science and Institute of Immunology, Hannover Medical School, 30625 Hannover, Germany

*: corresponding author: Prof. Dr. Lutz Nuhn (E-mail: lutz.nuhn@uni-wuerzburg.de)

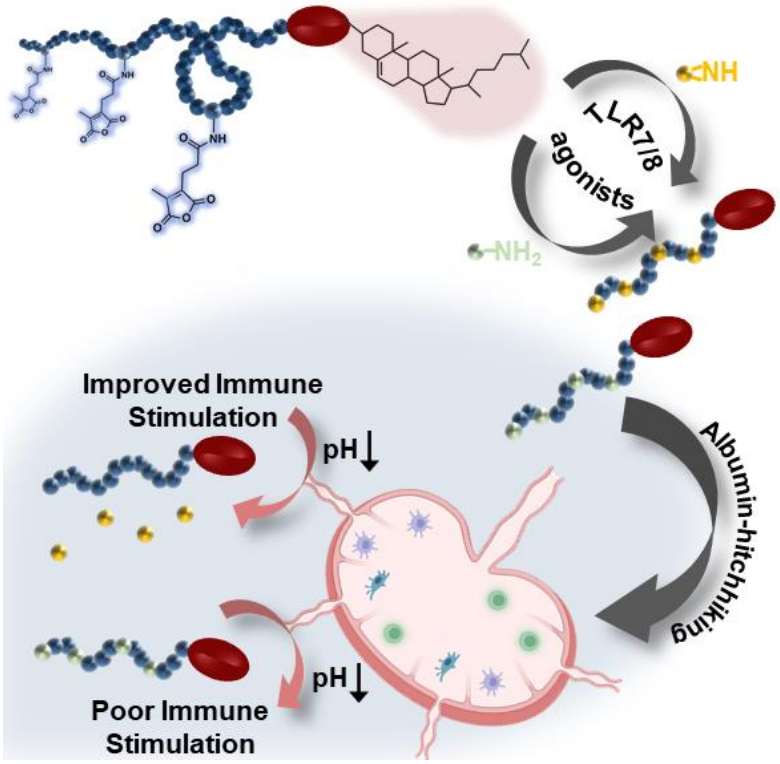

Keywords: 2-propionic-3-methylmaleic anhydride, cholesterol, RAFT-polymerization, pH sensitivity, immunodrug delivery.

Abstract

Gaining spatial-control over innate immune activation is of great relevance during vaccine delivery and anti-cancer therapy, where one aims at activating immune cells at draining lymphoid tissue, while avoiding systemic off-target innate immune activation. Lipid-polymer amphiphiles show high tendency to drain to lymphoid tissue upon local administration. Here we report on pH-sensitive, cholesterol end group functionalized polymers as stimuli-responsive carriers for controlled immunoactivation of draining lymph nodes. Methacrylamide-based monomers bearing pendant 2-propionic-3-methylmaleic anhydride groups were polymerized by Reversible Addition-Fragmentation Chain Transfer (RAFT) polymerization using a cholesterol chain-transfer agent (chol-CTA). The amine-reactive anhydrides were conjugated with various amines, however, while primary amines afforded irreversible imides, secondary amines provided pH-responsive conjugates that were released upon acidification. This could be applied to fluorescent dyes for irreversibly carrier labeling or immunostimulatory Toll-like receptor (TLR) 7/8 agonists as cargos for pH-responsive delivery. Hydrophilization of remaining anhydride repeating units with short PEG-chains yielded cholesterol-polymer amphiphiles that showed efficient cellular uptake and increased drug release at endosomal pH. Moreover, reversibly conjugated TLR 7/8 agonist amphiphiles efficiently drained to lymph nodes and increased the number of effectively maturated antigen-presenting cells after subcutaneous injection *in vivo*. Consequently, cholesterol-linked methacrylamide-based polymers with pH-sensitive 2-propionic-3-methylmaleic anhydride side groups provide ideal features for immunodrug delivery.

Introduction

The immune system is a complex organization of different cells and lymphoid organs with the function to protect the human body from infection as well as possibly preventing tumor growth. Separated into two essential types, the innate immune response on the one hand uses a variety of cells including macrophages, natural killer cells or dendritic cells that immediately recognize pathogens or abnormal features. The adaptive response, on the other hand, is characterized by the precise activation of T- and B-cell subsets localized in lymphoid organs or tissues and their ability to form long-lived memory.[1–5] Thereby, the lymphoid organs are further subdivided into the primary organs – thymus and bone marrow – responsible for the T- and B-cell generation, while cell activation occurs in the spleen, Peyer's patches, mucosa-associated lymphoid tissue, and lymph nodes, summarized as secondary lymphoid organs.[6–8]

Precisely controlling the activation of those immune components facilitates advanced opportunities for the treatment of infectious diseases and, more recently, also cancer. The application of immune modulators, monoclonal antibodies or vaccines providing antigens or adjuvants revealed the effective stimulation of innate and adaptive immune cells.[9,10] In particular, adaptive immune responses require well-orchestrated contributions by the innate immune system, most effectively *via* addressing pathogen-associated molecular patterns (PAMPs). For that purpose, small molecules or viral nucleic acids can be applied to get recognized by various pattern-recognition receptors (PRRs) for triggering necessary inflammatory responses. Toll-like receptors (TLRs) localized on the plasma membrane of macrophages, dendritic cells, or in endosomes constitute an important category of PPRs and can be activated by many diverse agonists.[11,12] Imidazoquinoline derivates, such as 1-(4-(aminomethyl)benzyl)-butyl-1*H*-imidazo[4,5-*c*]quinoline-4-amine (IMDQ), are very potent activators, stimulating the TLR7/8 signaling pathway.[13,14] However, for effective therapy such types of immune modulators need to reach the target site in sufficient concentration, whereas most of them show a poor selectivity and rapidly diffuse after administration, inducing immune-related inflammatory toxicities all over the body.[14–16]

Directing the immune activation to the site of interest by conjugating, encapsulating or entrapping immune modulatory cues to the matrix of carrier systems can significantly increase the therapeutic window.[17,18] For advancing transport into lymph nodes, a variety of materials, including synthetic polymers[19], micelles[20], nanoparticles[21,22], dendrimers[23] or lipids[24] demonstrated to improve the pharmacokinetic and biodistribution of potent small molecule immune modulators.[25] In particular, lipid motives emerged as an auspicious new approach for

albumin-hitchhiking to the lymph node, and cholesterol, mono- and diacyl lipids have been characterized for that purpose intensively.[26,27,28,29–33] Besides, covalent cholesterol conjugation affects the cell membranes' fluidity and, thus, the permeability, which further advanced cell internalization and the activity of intracellularly active immune modulators, too.[34–36]

However, most drugs show reduced or even no activity when conjugated to a carrier, hence, necessitating the introduction of a cleavable linker.[37,38] In this context, acid-labile linkers[39–41] such as ketals[42], acetals[43] and hydrazones[44] are of greatest interest, as macromolecular drug conjugates typically enter the cells through endocytosis and are transported into endosomal vesicles with gradually decreasing pH values. In this context, 2,3-dialkymaleic anhydrides have less been explored but offer several advantages.[45,46] They enable a fast release of amine-containing proteins or drugs under mild acidic conditions (pH = 5.5-6.8).[45,47] Furthermore, the hydrolysis rate can be adjusted by varying the substitutes of the *cis*-double bond and, thus, the internal angle between the amide and the carboxylic acid group.[48,49] Most importantly, as traceless linker 2,3-dialkymaleic anhydride structures release their conjugated molecules in their native form and, consequently, do not affect the drugs' acitivity.[50,51]

For that purpose, we here report on the use of cholesterol-polymer scaffolds with pendant amine-reactive 2-propionic-3-methylmaleic anhydrides[52] for the design of acid-labile amphiphile immuno-drug conjugates that efficiently target lymph nodes (Figure 1).[25,53] RAFT polymerization using a cholesterol-functionalized CTA enabled the controlled polymerization of methacrylamides with 2-propionic-3-methylmaleic anhydride side groups. Post-polymerization conjugation of IMDQ analogues and amine-functionalized short hydrophilic PEG-chains yielded water-soluble IMDQ-conjugated cholesterol-polymer amphiphiles. We demonstrated that an IMDQ bearing a primary amine remained irreversibly conjugated to the polymer backbone, whereas an IMDQ bearing a secondary amine could be liberated from the carrier at endosomal pH and, thus, re-installed its bioactivity *in vitro*. Moreover, *in vivo* the amphiphile conjugates efficiently drained to lymph nodes upon local injection and increased the number of effectively maturated antigen-presenting cells. Altogether, these characteristics demonstrate the advances of cholesterol-linked methacrylamide-based polymers with pendant 2-propionic-3-methylmaleic anhydride units as versatile platform for effectively localized and pH-stimulative immunodrug delivery.

Results and Discussion

Synthesis and Characterization of Methacrylamide-Based Polymers with Pendant 2-Propionic-3-Methmaleic Anhydride Groups

We previously identified the propionic-methylmaleic anhydride methacrylamide monomer PMMA-MA (Figure S22-S24) as suitable monomer for Reversible Addition-Fragmentation Chain Transfer (RAFT) polymerization yielding well defined polymers suitable for the design of pH-labile drug conjugates.[52] A trithiocarbonate as chain transfer agent (TTC-CTA) with azobisisobutyronitrile (AIBN) as initiator provided well-defined narrowly distributed homopolymers p(PMMA-MA)$_n$ (Figure 1 and Figure S28) with a number-average molecular weight (M_n) of 2314 g/mol (determined by size-exclusion chromatography (SEC) in hexafluoroisopropanol (HFIP) with poly(methyl methacrylate) (PMMA) calibration) and a polydispersity index (Đ) of 1.20 (Figure 1C). Noteworthy, under these conditions the PMMA-MA monomer solely polymerizes by the methacrylamide function, while its maleic anhydride group is not affected.[54]

To extend this polymer concept to lipid-polymer amphiphiles, a cholesterol-functionalized chain transfer agent was synthesized in order to combine the albumin-hitchhiking properties[25,29,35] with the polymeric 2-propionic-3-methylmaleic anhydride. For that purpose, the hydrophilic 3-hydroxy headgroup of cholesterol was gradually converted into a primary amine (Figure S1-S11) and subsequently treated with a pentafluorophenyl ester-activated trithiocarbonate chain transfer agent[42] (Figure S12-S14) affording the desired cholesteryl-CTA (Figure S15-S21). Of note, we opted for an amide-conjugated cholesteryl-CTA rather than an ester-linked structure, due the hydrolytic resistance of the amide bond during later applications.

Subsequent RAFT polymerization of PMMA-MA by the obtained cholesteryl-CTA and initiated by AIBN in methanol (Figure 1A+B and Figure S25) yielded well-defined chol-p(PMMA-MA)$_n$ polymers, e.g. with a number-average molecular weight (M_n) of 2489 g/mol and a narrow Đ of 1.23 (Figure 1D) (determined by SEC in HFIP with PMMA calibration). ^{1}H diffusion ordered NMR spectroscopy (^{1}H DOSY NMR) revealed one diffusing species at high diffusing units, giving proof of a single macromolecular entity with cholesteryl end groups (Figure S26-S27). The homopolymers p(PMMA-MA)$_n$ obtained from the parent CTA served as control lacking the cholesteryl end group (Fig. 1C and Figure S28-S30).

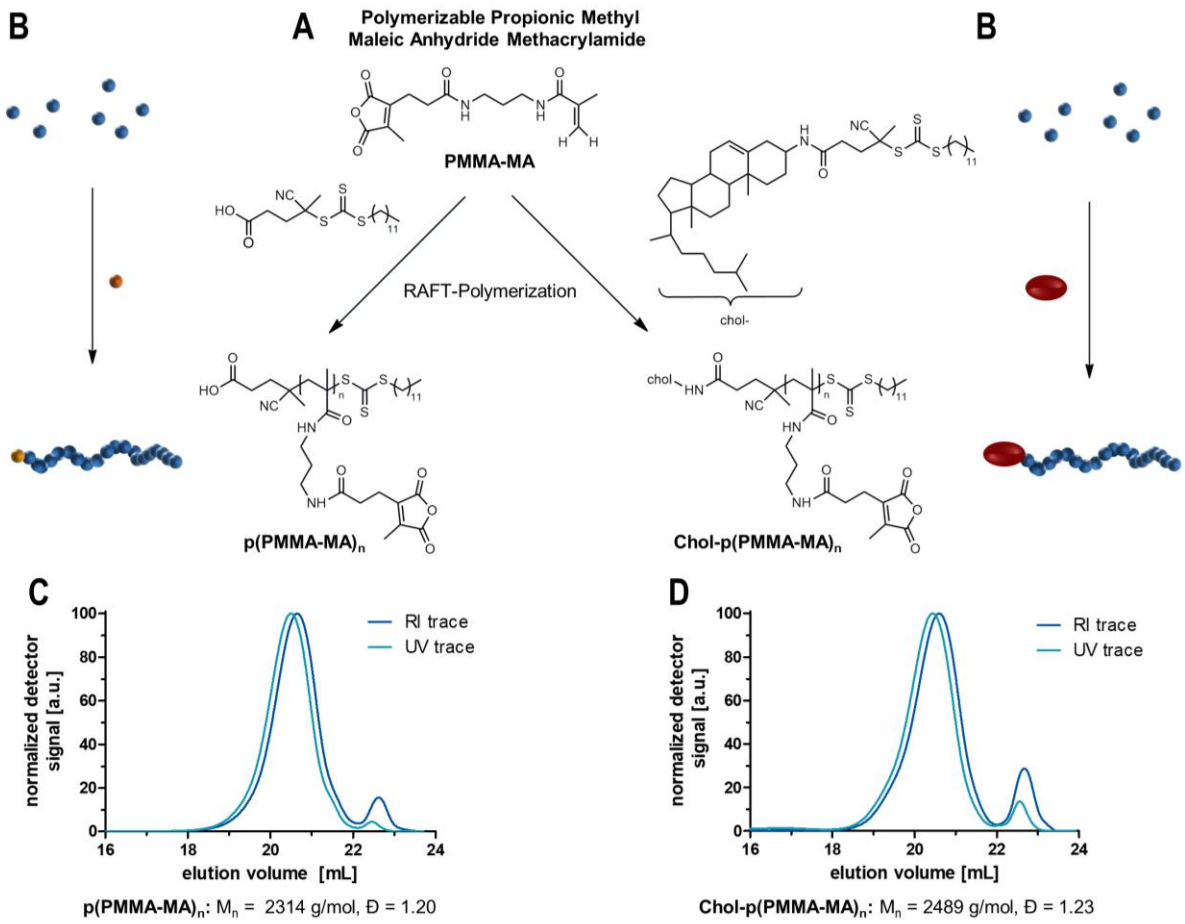

Figure 1. 2-Propionic-3-methyl maleic anhydride methacrylamides (PMMA-MA) as RAFT polymerizable monomers for the formulation of pH-sensitive polymers. (**A**) Reaction scheme for polymerizations of PMMA-MA with a small molecular trithiocarbonate chain transfer agent (TTC-CTA) or a cholesterol chain transfer agent (chol-TTC) and the resulting polymers. (**B**) Schematic reaction overview. (**C**) SEC traces of the polymers obtained by the reaction with the TTC-CTA (analyzed in HFIP (hexafluoroisopropanol) and calibrated with PMMA standards). (**D**) SEC analysis of the polymer obtained by the reaction with the chol-CTA.

pH-Reversible or Irreversible Chol-Polymer Modification by Amidation with Primary and Secondary Amines

We then verified the accessibility of the anhydride groups for pH-reversible conjugation of different amines (Figure 2A). For this purpose, chol-p(PMMA-MA)$_{30}$ was dissolved in DMSO, mixed with triethylamine (TEA) and incubated with benzylamine or dibenzylamine (Figure 2B and Figure S31). Similar to our previous studies on p(PMMA-MA)$_{38}$, also chol-p(PMMA-MA)$_{30}$ could successfully be conjugated with secondary amines under pH-responsive release conditions.[52] ^{1}H NMR spectroscopy confirmed the covalent attachment of dibenzylamine, as evidenced by the broadening of specific dibenzylamine signals. Due to the formation of two ring-opened 2-propionic-3-methylmaleic anhydride regioisomers, the related α-positioned

methyl signal splits into two signals (Figure S32, top, neutral). By contrast, the modification with benzylamine resulted in the formation of one single sharp peak (Figure S33, top, neutral), representing the pH-resistant imide structure.

We then treated the amine-modified chol-p(PMMA-MA)$_{30}$ polymers with trifluoroacetic acid (TFA) and measured the release of dibenzylamine and benzylamine, respectively, by ^{1}H diffusion ordered NMR spectroscopy (^{1}H DOSY NMR) (Figure 2C1 and Figure 2D1). For the dibenzylamine-modified polymers, the aromatic signals of dibenzylamine disappeared at the diffusing polymer species and faster aromatic diffusion species were immediately recorded (Figure 2C2). By contrast, for the benzylamine modified polymer no signal shift was observed upon acidification (Figure 2D2). This behavior could further be confirmed by ^{1}H NMR measurements (Figure S32, bottom, acidic and Figure S33, bottom, acidic) emphasizing the complete acid-triggered cleavage of the secondary amines from the polymer affording the release of dibenzylamine and the regeneration of the disubstituted maleic anhydrides. The primary amines, however, like the conjugated benzylamine, provoked a deprivation of the pH sensitivity by irreversible emergence of the corresponding imide system.

Overall, the obtained results demonstrated the successful synthesis of a cholesterol-linked methacrylamide-based polymer with pH-sensitive 2-propionic-3-methylmaleic anhydride groups for conjugation of amines. However, only the use of secondary amines ensured a quantitative acidic-triggered release from the macromolecular carrier, whereas primary amines formed irreversible imide bonds.

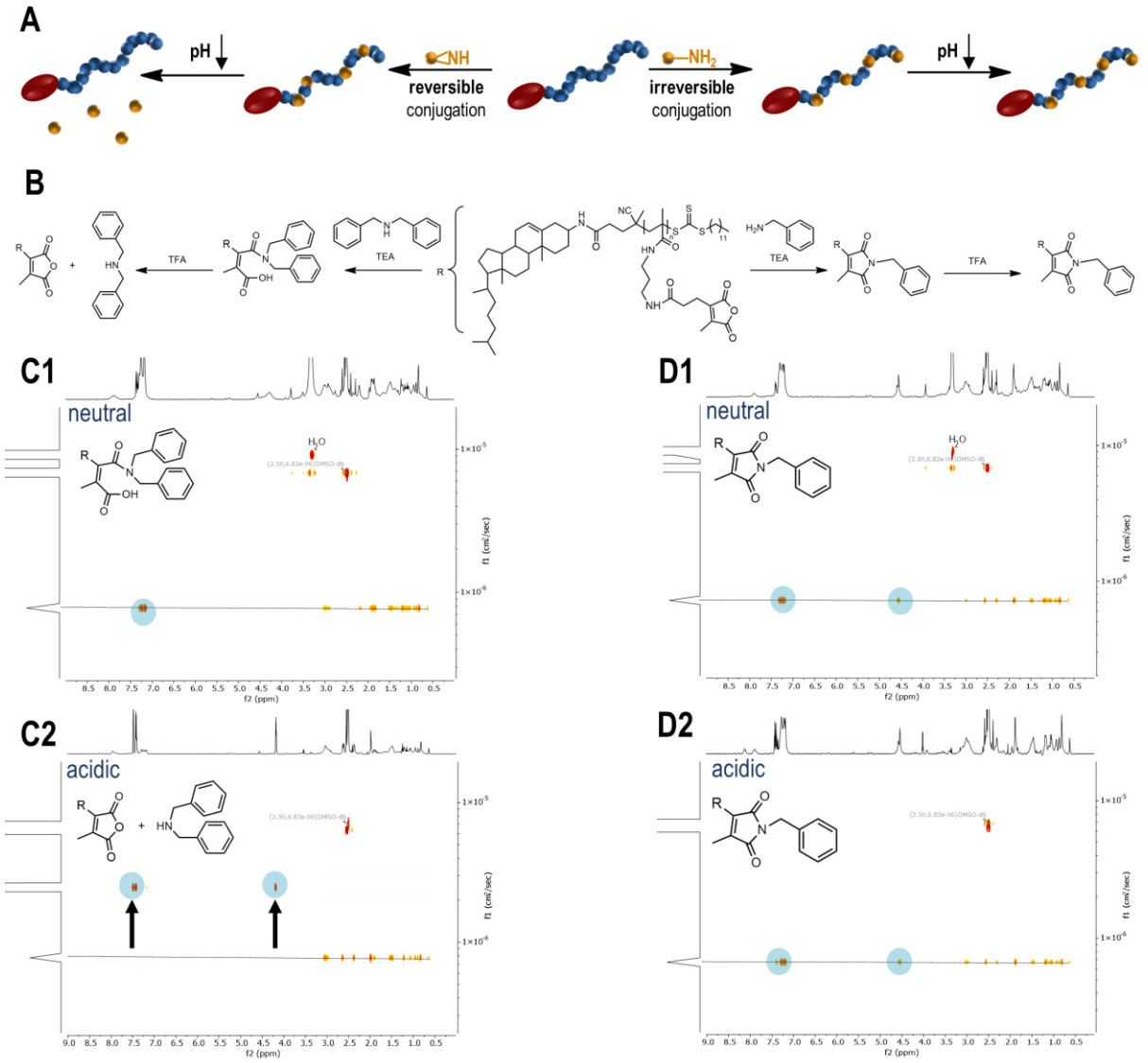

Figure 2. pH sensitivity of chol-p(PMMA-MA)$_{30}$ conjugated with different amines. (**A**) Scheme for the conversion of chol-polymeric 2-porpionic-3-methylmaleic anhydride groups with primary or secondary amines and their corresponding pH-response. (**B**) Amidation of 2-porpionic-3-methylmaleic anhydride side groups with benzyl- or dibenzylamine affording a pH-reversible or irreversible polymer system. (**C1**) ^{1}H DOSY NMR spectrum of the chol-polymer treated with dibenzylamine providing an identical diffusion species under neutral conditions and (**C2**) the related ^{1}H DOSY NMR spectrum upon acidification showing the successful release of the aromatic compound. (**D1**) ^{1}H DOSY NMR spectrum of the chol-polymer treated with benzylamine under neutral and (**D2**) acidic conditions affording only one diffusion species and no release of the primary amine upon acidification.

In vitro Properties of Dye-Labeled and PEG-Modified Methacrylamide-Based Polymers with Pendant 2-Propionic-3-Methylmaleic Anhydride Groups

Encouraged by the selective reversible amidation results, we aimed to convert chol-p(PMMA-MA)$_{30}$ polymers into lipid-polymer amphiphiles using short amine-functionalized polyethylene glycols (PEG) to increase the carriers' water-solubility, biocompatibility, as well as low intrinsic affinity to serum proteins and cell membranes.[55,56,57]

For that purposes, chol-p(PMMA-MA)$_{30}$ and p(PMMA-MA)$_{38}$ were dissolved in DMSO supplemented with TEA and subsequently treated with the fluorescent dye tetramethylrhodamine cadaverine (TMR) followed by mPEG$_{11}$-amine (M_n = 0.75 kDa) (Figure 3A and Figure S34) (note that primary amines were applied yielding two pH-resistant and completely hydrophilic polymers). Successful polymer modifications were confirmed by ^{1}H NMR spectroscopy (Figure S35 A and B) as well as size exclusion chromatography (SEC). In both cases, narrow polymer distributions with increased number-average molecular weights (M_n) of 26,910 g/mol for chol-p(PMMA-MA)$_{30}$ and 28,073 g/mol for p(PMMA-MA)$_{38}$ were found compared to the unmodified polymers (Figure S36 A and B). In addition, due to intensive purifications by precipitation, a covalent conjugation of the fluorescent dye TMR was evidenced by the remaining appearance of a TMR absorbance maxima at the respective wavelength 550 nm, detected by UV-Vis spectroscopy measurements for both purified polymers (Figure 3E).

Due to the hydrophilic properties of PEG, the covalently functionalized polymers could easily be redissolved in PBS. To ensure no aggregation during further experiments, the polymer solutions were analyzed by dynamic light scattering (DLS) measurements. Both chol-p(PMMA-MA)$_{30}$ and p(PMMA-MA)$_{38}$, conjugated with TMR and mPEG$_{11}$-amine, exhibited exclusively soluble polymer chains with volume sizes of 4.51 nm (chol-p(PMMA-MA)$_{30}$) and 5.21 nm (p(PMMA-MA)$_{38}$) (Figure 3B). Notably, the cholesterol moiety itself is insufficient to trigger micellar self-assembling of the polymers in water. Subsequently, the cellular internalization of TMR-labeled, hydrophilic polymers was analyzed by flow cytometry and fluorescence confocal microscopy. For that purpose, RAW-Dual macrophages were incubated with different concentrations of fluorescent dye-labeled polymers for 24 h at 37 °C. Flow cytometry showed a concentration-dependent uptake of both polymers (Figure 3C and 3D, as well as Figure S48). Interestingly, PEGylated polymers with cholesterol end group exhibited a much higher internalization compared to the analogous polymer without cholesterol (Figure 3C and 3D, as well as Figure S48). These results were also confirmed by confocal fluorescence

microscopy. Only the cholesterol end group-containing polymers exhibited sufficient intracellular fluorescence (Figure 3F and Figure S49) and, thus, evidenced the favorable intracellular delivery features mediated by the cholesteryl end group.

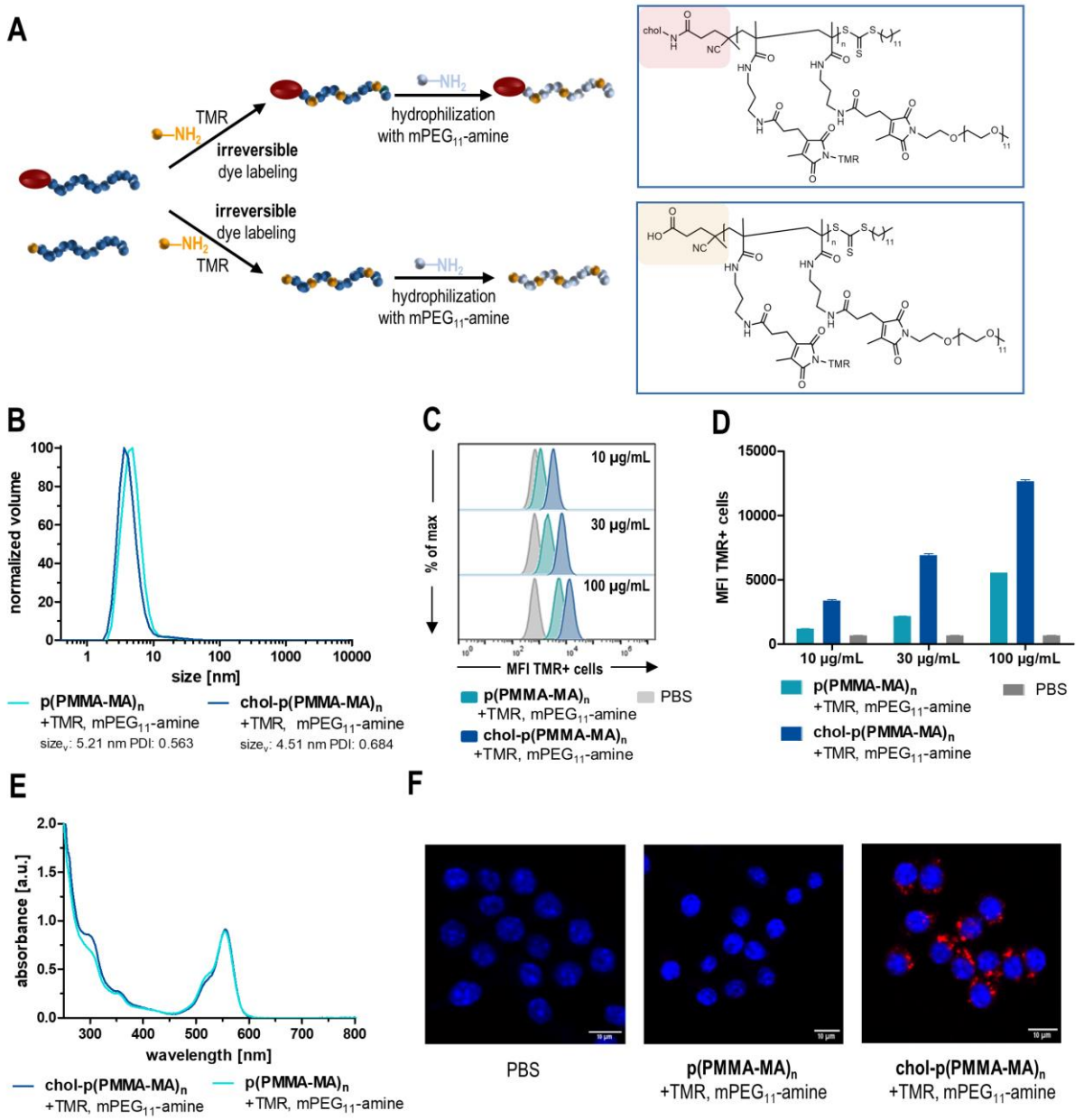

Figure 3. *In vitro* evaluation of PEGylated 2-propionic-3-methylmaleic anhydride-containing polymers with and without cholesterol end groups. (**A**) Synthetic scheme and resulting chemical structure of tetramethylrhodamine cadaverine (TMR)-labeled and PEGylated p(PMMA-MA)$_{38}$ (yellow) and chol-p(PMMA-MA)$_{30}$ (red). (**B**) DLS polymer size distribution showing fully water-soluble polymers in PBS with a volume mean of 5.21 nm for modified p(PMMA-MA)$_{38}$ (light blue) and 4.51 nm for chol-p(PMMA-MA)$_{30}$ (dark blue). (**C**) Flow cytometric histograms of TMR-labeled, PEGylated p(PMMA-MA)$_{38}$ and chol-p(PMMA-MA)$_{30}$ and their concentration dependent uptake in RAW-Dual macrophages. (**D**) Concentration dependent mean fluorescence intensity (MFI) of RAW-Dual macrophages incubated with the respective polymers (n=3). (**E**) UV-Vis absorbance spectra of the TMR-labeled polymers revealing similar labeling efficiencies. (**F**) Fluorescent confocal microscopy images of the modified p(PMMA-MA)$_{38}$ and chol-p(PMMA-MA)$_{30}$ as well as PBS, confirming an efficient cholesteryl-induced cellular uptake (red: TMR-labeled polymer, blue: nuclei stained with Hoechst 33258).

In vitro Effect of IMDQ or IMDQ-Me Loaded and PEG-Modified Cholesterol-Linked Methacrylamide-Based Polymers with Pendant 2-Propionic-3-Methylmaleic Anhydride Groups

Next, we wanted to combine these two delivery properties to small immune stimulatory imidazoquinoline-based TLR 7/8 agonists. For that purpose, an imidazoquinoline analogue bearing an aliphatic primary amine, IMDQ, was further modified as previously reported[52] into a secondary amine derivative (2-butyl-1-(4-((methylamino)methyl)benzyl)-1*H*-imidazo[4,5-c]quinolin-4-amine, IMDQ-Me) (Figure S37-S39). Both IMDQ or IMDQ-Me were conjugated to the chol-polymers and further treated with TMR and $mPEG_{11}$-amine (Figure 4A and Figure S40), affording water-soluble lipid-polymer amphiphiles that either carried the immunostimulatory cue irreversibly (IMDQ) or reversibly (IMDQ-Me). Successful dye-labeling and IMDQ- or IMDQ-Me-loading were verified by UV-Vis spectroscopy (Figure 4B) as well as ^{1}H NMR spectroscopy analyses (Figure S41 and S43). Both drug-conjugated chol-polymers revealed an almost similar drug load of 4.4 wt% (IMDQ) and 4.7 wt% (IMDQ-Me) (compare Supporting Information and Figure S46+S47). Hydrophilization of the chol-polymers was confirmed by ^{1}H DOSY NMR spectroscopy measurements (Figure S42+S44), where all IMDQ-related aromatic protons provided similar diffusion coefficients as the polymer backbone and the PEG side chains. No unbound IMDQ species were detectable. In addition, SEC analysis showed a significant elution volume shift compared to the unmodified polymer (Figure S45A), and *via* DLS measurements in PBS single non-aggregating polymer chain species were recorded, too (Figure S45B).

We then tested the ability of the IMDQ(-Me) conjugates to trigger an innate immune stimulation. For that purpose, we applied a RAW-Dual macrophage reporter cell line in which a NF-κB activation by TLR7/8 triggering is coupled to the expression of the alkaline embryonic phosphatase (SEAP). The immune stimulation can readily be quantified by colorimetric Quanti Blue Assay (Figure 4D), and cell viability subsequently determined by MTT assay (Figure 4C). Upon RAW-Dual macrophage incubation with our samples, both the native IMDQ and IMDQ-Me as unbound drugs demonstrated effective TLR 7/8 stimulation at sub-micromolar concentrations, albeit methylation of IMDQ resulted in a slight reduction in activity (Figure 4D). While unmodified polymer (chol-p(PMMA-MA)$_n$) did not affect TLR activation, only a very low stimulation could be detected for the irreversibly conjugated IMDQ-chol-polymer (chol-p(PMMA-MA)$_n$, +IMDQ, TMR, $mPEG_{11}$-amine) (Figure 4D). By contrast, the pH-reversible IMDQ-Me conjugate (chol-p(PMMA-MA)$_n$, +IMDQ-Me, TMR, $mPEG_{11}$-amine)

exhibited a significantly increased activity and the observed stimulation was only marginally lower when compared to the native IMDQ-Me (Figure 4D). This underlines the potential of an intracellular release of the TLR agonist exclusively for the secondary amine derivative, restoring its full receptor activity upon cellular delivery. Besides, no relevant reduction in cellular viability could be observed for all samples at the given concentrations, either (Figure 4C).

Based on these highly promising results, we further investigated the pH-sensitive immune stimulatory potency of the PEGylated chol-polymer conjugated with IMDQ or IMDQ-Me on primary dendritic cells (DC) derived from murine bone marrow (BMDC). DCs are considered as one of the most effective cellular sensors of antigen-presenting cells (APCs) and represent an essential link between adaptive and innate immune response.[58] After bone marrow differentiation in GM-CSF-supplemented media, the affording BMDCs were incubated with soluble IMDQ or IMDQ-Me and the corresponding drug-loaded chol-polymers, as well as empty chol-polymer and PBS. *Via* flow cytometric analysis, the subsequent immunostimulatory phenotype of the incubated BMDCs could be determined after 24 h by quantification of the surface-expressed co-stimulatory molecules CD80 and CD86. Interestingly, IMDQ that was irreversibly conjugated to the chol-p(PMMA-MA)$_n$ polymer barely triggered any maturation, neither for CD80 nor CD86. Only the chol-polymers with the reversibly conjugated IMDQ-Me were able to induce BMDC maturation in analogy to the native sIMDQ and sIMDQ-Me, while the carrier polymer chol-p(PMMA-MA)$_n$ alone was immunologically silent. Additionally, the supernatants of the cell cultures were collected and quantified for the cells' secretion of the proinflammatory cytokines TNFα, IL-1β and IL-6, as further markers for BMDCs' immunostimulatory phenotype maturation. Again, the polymers with the irreversibly conjugated IMDQ were hardly able to induce the secretion of all three cytokines. To a same extent as the native sIMDQ and sIMDQ-Me, only the polymers with reversibly conjugated IMDQ-Me were able to trigger sufficient secretion of TNFα, IL-1β and IL-6. These data support once more the ability of the chol-p(PMMA-MA)$_n$ platform to exclusively release the secondary amine TLR agonists intracellularly, and thereby restore their full receptor activity.

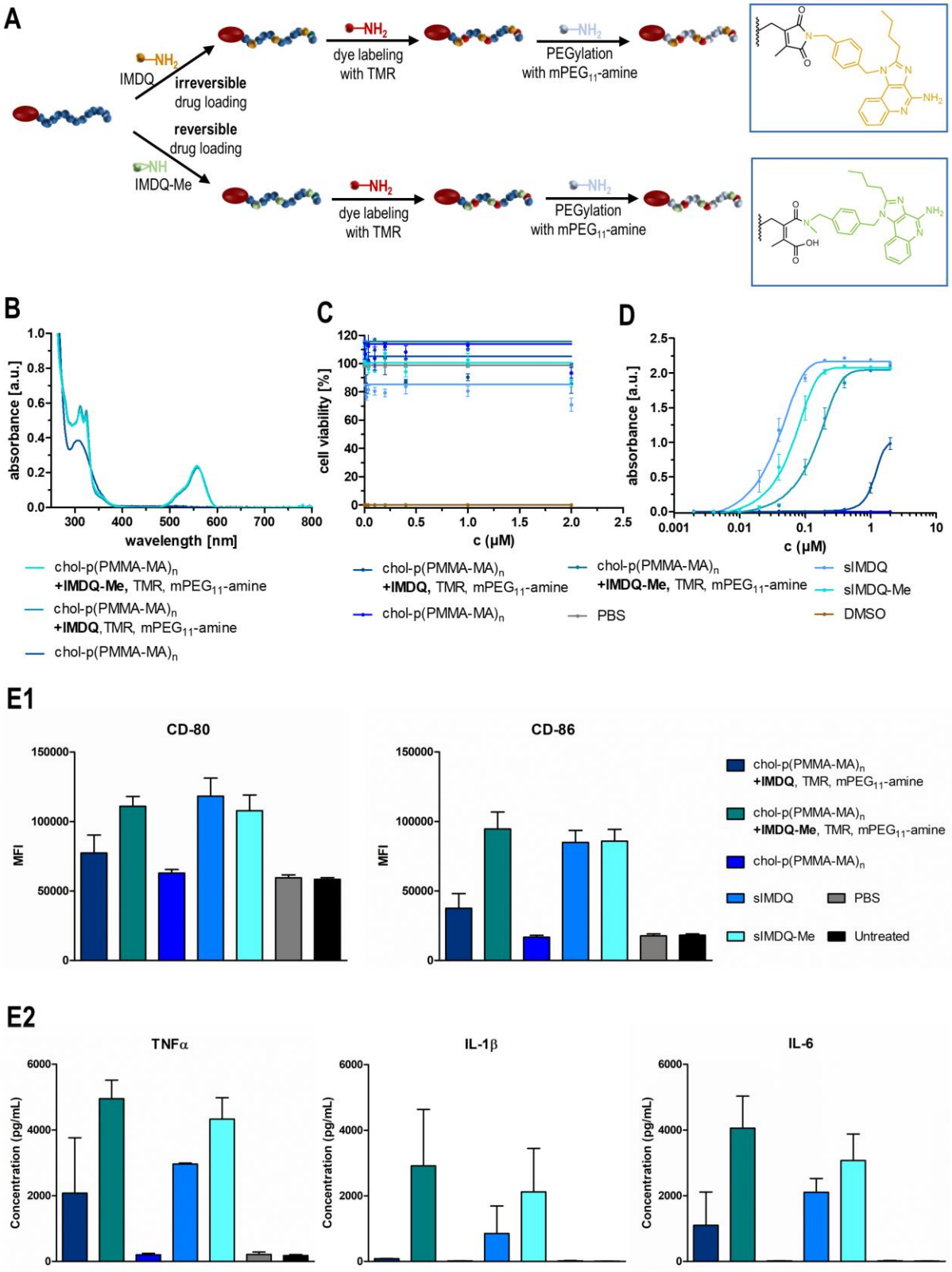

Figure 4. *In vitro* characterization of drug-loaded cholesterol-linked polymers with 2-propionic-3-methylmaleic anhydride side groups. (**A**) Synthetic strategy for the formulation of a reversibly (IMDQ-Me) or irreversibly (IMDQ)-loaded and TMR-labeled chol-p(PMMA-MA)$_{32}$ hydrophilized with PEG$_{11}$-amine. (**B**) UV-Vis spectra of the corresponding drug-loaded and dye-labeled polymer systems as well as the unmodified chol-polymer. (**C**) Cell

viability assay (MTT) of RAW-Dual macrophages incubated with the soluble drugs (IMDQ and IMDQ-Me) and respective drug-loaded chol-polymers, the unmodified chol-polymer as well as PBS (positive control) and DMSO (negative control) (n=4). (**D**) TLR receptor activation of RAW-Dual macrophages incubated with the drug-conjugated chol-polymers, free drugs or empty chol-polymer quantified by RAW blue assay (n=4). (**E**) Maturation of bone marrow-derived dendritic cells after incubation with soluble drugs (IMDQ and IMDQ-Me) and respective drug-loaded chol-polymers, the unmodified chol-polymer as well as PBS. (**E1**) To delineate the cellular activation state, the expression of the costimulatory markers CD80 and CD86 was quantified *via* flow cytometry by mean fluorescence intensity (MFI) (n = 3). (**E2**) Additionally, the secretion of the proinflammatory cytokines TNFα, IL 1β and IL-6 into the cell culture media was quantified by cytometric bead assay (n = 3).

In vivo Performance of IMDQ- or IMDQ-Me-Loaded and PEG-Modified Cholesterol-Linked Methacrylamide-Based Polymers with Pendant 2-Propionic-3-Methylmaleic Anhydride Groups

Based on the remarkable *in vitro* results, we finally investigated whether chol-polymer conjugated IMDQ and IMDQ-Me could induce a controlled immune activation *in vivo* upon local administration in draining lymph nodes (Figure 5A).[21,59–61] To monitor the biodistribution of innate immune activation, we injected the respective test samples subcutaneously in the footpad of IFN-$\beta^{+/\Delta\beta\text{-luc}}$ reporter mice, a transgenic mouse model that provides luciferase co-expression upon expression of the type I interferon IFN-β.[16,62] Bioluminescence imaging 4 and 24 h post injection revealed a spatially resolved innate immune activation (Figure 5B and Figure S51). For the injected native TLR 7/8 agonists IMDQ and IMDQ-Me a widespread systemic innate activation was observed immediately, indicative of a rapid diffusion of the injected TLR 7/8 agonists from the site of injection into the circulation. Similar effects had been reported in earlier studies that were accompanied by severe acute toxic inflammatory responses.[14,21,42,59,60] Irreversible IMDQ-chol-p(PMMA-MA)$_n$ conjugates had negligible activity, confirming our *in vitro* observation. Reversible IMDQ-Me-chol-p(PMMA-MA)$_n$ conjugates, by contrast, did show activation in the draining popliteal lymph node at 4 h post-injection and resulted in a strongly reduced systemic response (Figure 5B and Figure S51) (as well as a subtle higher background activity, which increases after 24 h – Figure 5B1). Corresponding luminescence quantification of full body activity and targeted lymph node activity confirm the improved immunostimulation for the reversibly conjugated IMDQ-Me agonist (Figure 5B2) and, consequently, evidence the *in vivo* release of the molecule from its chol-p(PMMA-MA)$_n$ carrier, too.

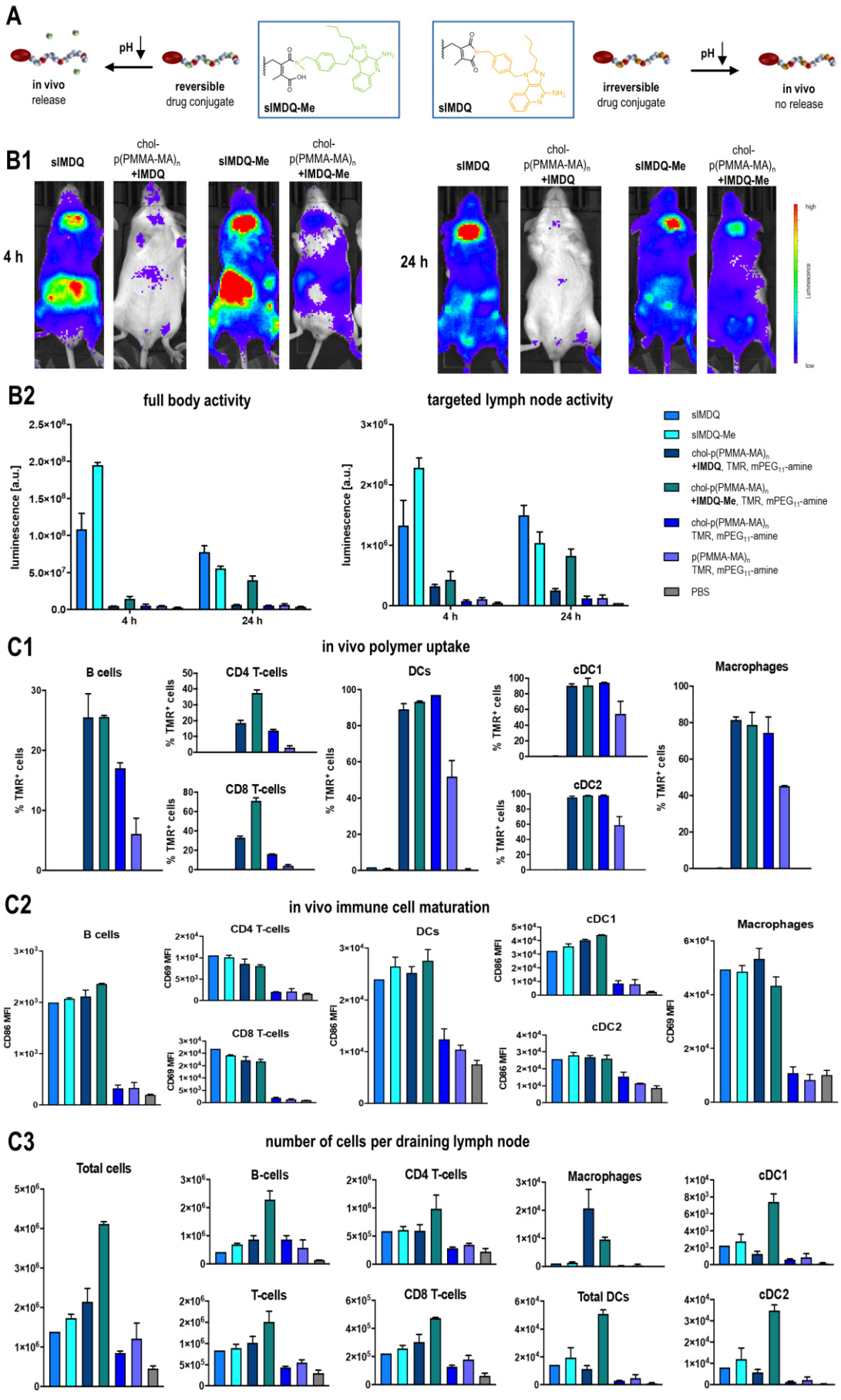
A
in vivo release
pH
reversible drug conjugate
sIMDQ-Me
sIMDQ
irreversible drug conjugate
pH
in vivo no release
B1
sIMDQ
chol-p(PMMA-MA)n +IMDQ
sIMDQ-Me
chol-p(PMMA-MA)n +IMDQ-Me
4 h
24 h
high
Luminescence
low
B2
full body activity
targeted lymph node activity
luminescence [a.u.]
4 h
24 h
sIMDQ
sIMDQ-Me
chol-p(PMMA-MA)n +IMDQ, TMR, mPEG11-amine
chol-p(PMMA-MA)n +IMDQ-Me, TMR, mPEG11-amine
chol-p(PMMA-MA)n TMR, mPEG11-amine
p(PMMA-MA)n TMR, mPEG11-amine
PBS
C1
in vivo polymer uptake
B cells
CD4 T-cells
CD8 T-cells
DCs
cDC1
cDC2
Macrophages
% TMR+ cells
C2
in vivo immune cell maturation
B cells
CD4 T-cells
CD8 T-cells
DCs
cDC1
cDC2
Macrophages
CD86 MFI
CD69 MFI
C3
number of cells per draining lymph node
Total cells
B-cells
T-cells
CD4 T-cells
CD8 T-cells
Macrophages
Total DCs
cDC1
cDC2

Figure 5. *In vivo* performance of chol-polymer with pendant 2-propionic-3-methylmaleic anhydride groups covalently attached with the TLR 7/8 agonist IMDQ or methylated IMDQ-Me. (**A**) Scheme for the exclusive acid-triggered drug release for IMDQ-Me compared to IMDQ, mediated by the dye- and drug-loaded chol-p(PMMA-MA)$_{32}$ polymer, further PEGylated with mPEG$_{11}$-amine. (**B**) Immune stimulatory properties of those samples after footpad injection into BALB/c INF-β (IFN- $\beta^{+/\Delta\beta\text{-luc}}$) luciferase reporter. (**B1**) Representative luminescence images of the respective samples after 4 h and 24 h and (**B2**) corresponding luminescence quantification of full body activity and targeted lymph node activity, which is only fully restored for the mice treated with IMDQ-Me-loaded chol-p(PMMA-MA)$_{32}$ (n = 3 or 4). (**C**) Flow cytometric analyses of the draining popliteal lymph nodes 24 h after footpad injection (n = 2 or 3): (**C1**) The uptake of the (chol)-p(PMMA-MA)$_{32}$ polymer was followed by TMR fluorescence and confirmed effective cholesteryl end group mediated delivery; (**C2**) the maturation of the respective immune cell subpopulations was evaluated by mean fluorescence intensity of the respective maturation markers CD86 or CD69 and confirmed the immunostimulatory activity of the TLR 7/8 agonists; (**C3**) the number of cells in the lymph node was determined in relation to count beads and revealed effective immunodrug delivery properties for chol-p(PMMA-MA)$_n$ carrying the pH-releasable TLR 7/8 agonist IMDQ-Me.

Flow cytometry analysis (Figure 5C – for detailed gating procedures compare Supporting Information Figure S52) of the TMRs signal in dissected popliteal lymph nodes, 24 h post-injection, revealed that all chol-p(PMMA-MA)$_n$ conjugates exhibited greatly enhanced lymphatic drainage compared to p(PMMA-MA)$_n$ conjugates that lacked the cholesteryl motif (Figure 5C1). For all immune cell subpopulations, the amount of TMR$^+$ cells was at least twice as high for the cholesterol-functionalized p(PMMA-MA)$_n$ carriers than without cholesterol. While for DCs (cDC1s and cDC2s) as well as macrophages almost all recorded cells were TMR$^+$ when the mice were treated with cholesterol-functionalized p(PMMA-MA)$_n$, for B cells it was only more effective, if the carrier was also equipped with IMDQ or IMDQ-Me. Remarkably, for T-cells only the IMDQ-Me-carrying chol-p(PMMA-MA)$_n$ triggered highest cell uptake (Figure 5C1).

Next, the expression of typical co-stimulatory surface markers like CD69 or CD86 on those immune cells was examined by flow cytometry, too (Figure 5C2). Given the strong immune stimulatory response that the native TLR 7/8 agonists sIMDQ and sIMDQ-Me triggered all over the body, the expression of CD69 or CD86 could be found here in all immune subpopulations, too. Despite the IMDQ- and IMDQ-Me-carrying chol-p(PMMA-MA)$_n$ polymers not exhibiting systemic activity in the INF-β reporter mice (Figure 5B), they still provided an efficient lymph node focused expression of CD69 on T lymphocytes (CD4 and CD8) and macrophages, as well as CD86 on B lymphocytes, cDC1s and cDC2s, all to a similar extent as the soluble derivatives (Figure 5C2). Interestingly, for cDC1s – renown for their ability to cross-present cellular antigens to CD8+ T cells and elicit antitumor immunity – the CD86 expression levels were highest after treatment with the reversibly conjugated polymeric IMDQ-Me.

With that in mind, we finally analyzed the absolute cellularity of those immune populations in the draining lymph nodes, which is finally required to initiate effective immune responses (for

that purpose, the number of cells was counted during flow cytometry analysis in relation to a defined amount of added beads). Remarkably, the chol-p(PMMA-MA)$_n$ polymers with reversibly conjugated IMDQ-Me featured the highest influx of all immune cells compared to all samples (Figure 5C3). A strong increase of B cells, T cells (CD4+ and CD8+) and dendritic cells (cDC1s and cDC2s) was found exclusively upon treatment with chol-p(PMMA-MA)$_n$ carrying the pH-releasable TLR 7/8 agonist IMDQ-Me. The lymph node targeting and pH-responsive IMDQ-Me releasing polymers were most efficient in recruiting those relevant immune cell populations which are required for effective vaccination or cancer immunotherapy.

Altogether, our results support the successful *in vivo* release of the secondary amines from polymeric 2-propionic-3-methylmaleic anhydrides, thereby, restoring the drugs' bioactivity, which can potentially be applied for further immunotherapeutic delivery scenarios.

Conclusions

In this study, we herein reported the successful introduction of a cholesteryl-functionalized pH-sensitive polymeric delivery system derived from 2-propionic-3-methylmaleic anhydride amide-based methacrylamides. The resulting polymers can serve as a controlled pH-responsive polymer carrier platform for delivering small immune stimulatory cues into draining lymph nodes after subcutaneous injection and, thereby, restoring their full bioactivity *in vivo*.

Via RAFT polymerization by a cholesteryl-amide functionalized chain transfer agent, well-defined propionic-methylmaleic anhydride methacrylamide polymers were obtained that could sequentially be post-modified with primary or secondary amines, albeit only the secondary amines revealed the desired pH-responsive release upon acidification. Further conversion of the remaining anhydrides with short PEG-amine yielded fully water-soluble lipid-polymer amphiphiles. Exemplified for imidazoquinoline TLR7/8 agonists, only the secondary amine drug derivative could reversibly be released from the carrier in its native form, thereby, preserving its biological activity in contrast to its primary amine derivative. The cholesteryl-motif exhibited efficient lymphatic translocation *in vivo* upon local subcutaneous administration. Whereas native IMDQs induced systemic innate immune activation, the administration of IMDQ-Me-chol-p(PMMA-MA)$_n$ provoked a potent, but localized activation in draining lymph nodes. Notably, irreversible IMDQ-chol-p(PMMA-MA)$_n$ neither induced innate immune activation *in vitro*, nor sufficiently *in vivo*, thereby, underscoring the key

contribution of the reversible bond formed between the IMDQ-Me, bearing a secondary amine, and the polymer. Overall, our findings demonstrate the potential of the cholesterol-linked pH-sensitive carrier system for lymph node-targeted immune activation and suggest future applications in vaccination or cancer immunotherapy.

Author Contributions

The manuscript was written through contributions of all authors. All authors have given approval to the final version of the manuscript.

Notes

The authors declare no competing financial interest.

Acknowledgements

This work was gratefully supported by the DFG through the Emmy Noether program and the CRC/SFB 1006 Projects B03 and B04 (both to L.N.). Stephan Türk, Manfred Wagner, Stefan Spang and Detlev-Walter Scholdei are acknowledged for technical assistance during the analytical measurements, and Tanja Weil for providing access to excellent laboratory facilities.

References

(1) Delvers, P. J.; Roitt, I. M. First of Two Parts THREE LEVELS OF DEFENSE. *N. Engl. J. Med.* **2000**, *343* (1), 37–49.

(2) Andersen, M. H.; Schrama, D.; Thor Straten, P.; Becker, J. C. Cytotoxic T Cells. *J. Invest. Dermatol.* **2006**, *126* (1), 32–41.

(3) Moon, J. J.; Huang, B.; Irvine, D. J. Engineering Nano- and Microparticles to Tune Immunity. *Adv. Mater.* **2012**, *24* (28), 3724–3746.

(4) Irvine, D. J.; Hanson, M. C.; Rakhra, K.; Tokatlian, T. Synthetic Nanoparticles for Vaccines and Immunotherapy. *Chem. Rev.* **2015**, *115* (19), 11109–11146.

(5) Sallusto, F.; Lanzavecchia, A.; Araki, K.; Ahmed, R. From Vaccines to Memory and Back. *Immunity* **2010**, *33* (4), 451–463.

(6) Randall, T. D.; Carragher, D. M.; Rangel-Moreno, J. Development of Secondary Lymphoid Organs. *Annu. Rev. Immunol.* **2008**, *26*, 627–650.

(7) Ruddle, N. H.; Akirav, E. M. Secondary Lymphoid Organs: Responding to Genetic and Environmental Cues in Ontogeny and the Immune Response. *J. Immunol.* **2009**, *183* (4), 2205–2212.

(8) Kim, S.; Shah, S. B.; Graney, P. L.; Singh, A.; Shah, S. B.; Graney, P. L. Multiscale Engineering of Immune Cells and Lymphoid Organs. *Nat Rev Mater* **2019**, *4* (6), 355–378.

(9) Lynn, G. M.; Laga, R.; Jewell, C. M. Induction of Anti-Cancer T Cell Immunity by in Situ Vaccination Using Systemically Administered Nanomedicines. *Cancer Lett.* **2019**, *459* (January), 192–203.

(10) Shields, C. W.; Wang, L. L. W.; Evans, M. A.; Mitragotri, S. Materials for Immunotherapy. *Adv. Mater.* **2020**, *32* (13), 1–56.

(11) Mancini, R. J.; Stutts, L.; Ryu, K. A.; Tom, J. K.; Esser-Kahn, A. P. Directing the Immune System with Chemical Compounds. *ACS Chem. Biol.* **2014**, *9* (5), 1075–1085.

(12) Iwasaki, A.; Medzhitov, R.; Haven, N. Control of Adaptive Immunity by the Innate Immune System. *Nat. Immunol.* **2015**, *16* (4), 343–353.

(13) Van Herck, S.; De Geest, B. G. Nanomedicine-Mediated Alteration of the Pharmacokinetic Profile of Small Molecule Cancer Immunotherapeutics. *Acta Pharmacol. Sin.* **2020**, *41* (7), 881–894.

(14) Nuhn, L.; Vanparijs, N.; De Beuckelaer, A.; Lybaert, L.; Verstraete, G.; Deswarte, K.; Lienenklaus, S.; Shukla, N. M.; Salyer, A. C. D.; Lambrecht, B. N.; Grooten, J.; David, S. A.; De Koker, S.; De Geest, B. G. PH-Degradable Imidazoquinoline-Ligated Nanogels for Lymph Node-Focused Immune Activation. *Proc. Natl. Acad. Sci. U. S. A.* **2016**, *113* (29), 8098–8103.

(15) Cabral, H.; Miyata, K.; Osada, K.; Kataoka, K. Block Copolymer Micelles in Nanomedicine Applications. *Chem. Rev.* **2018**, *118* (14), 6844–6892.

(16) Bhagchandani, S.; Johnson, J. A.; Irvine, D. J. Evolution of Toll-like Receptor 7/8 Agonist Therapeutics and Their Delivery Approaches: From Antiviral Formulations to Vaccine Adjuvants. *Adv. Drug Deliv. Rev.* **2021**, *175*, 113803.

(17) Shi, J.; Kantoff, P. W.; Wooster, R.; Farokhzad, O. C. Cancer Nanomedicine: Progress, Challenges and Opportunities. *Nat. Rev. Cancer* **2017**, *17* (1), 20–37.

(18) Sur, S.; Rathore, A.; Dave, V.; Reddy, K. R.; Chouhan, R. S.; Sadhu, V. Recent Developments in Functionalized Polymer Nanoparticles for Efficient Drug Delivery System. *Nano-Structures and Nano-Objects* **2019**, *20*, 100397.

(19) Lynn, G. M.; Chytil, P.; Francica, J. R.; Lagová, A.; Kueberuwa, G.; Ishizuka, A. S.; Zaidi, N.; Ramirez-Valdez, R. A.; Blobel, N. J.; Baharom, F.; Leal, J.; Wang, A. Q.; Gerner, M. Y.; Etrych, T.; Ulbrich, K.; Seymour, L. W.; Seder, R. A.; Laga, R. Impact of Polymer-TLR-7/8 Agonist (Adjuvant) Morphology on the Potency and Mechanism of CD8 T Cell Induction. *Biomacromolecules* **2019**, *20* (2), 854–870.

(20) Van Herck, S.; Deswarte, K.; Nuhn, L.; Zhong, Z.; Portela Catani, J. P.; Li, Y.; Sanders, N. N.; Lienenklaus, S.; De Koker, S.; Lambrecht, B. N.; David, S. A.; De Geest, B. G. Lymph-Node-Targeted Immune Activation by Engineered Block Copolymer Amphiphiles-TLR7/8 Agonist Conjugates. *J. Am. Chem. Soc.* **2018**, *140* (43), 14300–14307.

(21) Nuhn, L.; De Koker, S.; Van Lint, S.; Zhong, Z.; Catani, J. P.; Combes, F.; Deswarte, K.; Li, Y.; Lambrecht, B. N.; Lienenklaus, S.; Sanders, N. N.; David, S. A.; Tavernier, J.; De Geest, B. G. Nanoparticle-Conjugate TLR7/8 Agonist Localized Immunotherapy Provokes Safe Antitumoral Responses. *Adv. Mater.* **2018**, *30* (45), 1–9.

(22) Stickdorn, J.; Nuhn, L. Reactive-Ester Derived Polymer Nanogels for Cancer Immunotherapy. *Eur. Polym. J.* **2020**, *124* (September 2019), 109481.

(23) Kaminskas, L. M.; Kota, J.; McLeod, V. M.; Kelly, B. D.; Karellas, P.; Porter, C. J. PEGylation of Polylysine Dendrimers Improves Absorption and Lymphatic Targeting Following SC Administration in Rats. *J. Control. Release* **2009**, *140* (2), 108–116.

(24) De Vrieze, J.; Louage, B.; Deswarte, K.; Zhong, Z.; De Coen, R.; Van Herck, S.; Nuhn, L.; Kaas Frich, C.; Zelikin, A. N.; Lienenklaus, S.; Sanders, N. N.; Lambrecht, B. N.; David, S. A.; De Geest, B. G. Potent Lymphatic Translocation and Spatial Control Over Innate Immune Activation by Polymer–Lipid Amphiphile Conjugates of Small-Molecule TLR7/8 Agonists. *Angew. Chemie - Int. Ed.* **2019**, *58* (43), 15390–15395.

(25) De Vrieze, J.; Baptista, A. P.; Nuhn, L.; Van Herck, S.; Deswarte, K.; Yu, H.; Lambrecht, B. N.; De Geest, B. G. Lipid Nature and Alkyl Length Influence Lymph Node Accumulation of Lipid-Polyethylene Glycol Amphiphiles. *Adv. Ther.* **2021**, *4* (8), 1–9.

(26) Schudel, A.; Francis, D. M.; Thomas, S. N. Material Design for Lymph Node Drug Delivery. *Nat. Rev. Mater.* **2019**, *4* (6), 415–428.

(27) Liu, H.; Moynihan, K. D.; Zheng, Y.; Szeto, G. L.; Li, A. V.; Huang, B.; Van Egeren, D. S.; Park, C.; Irvine, D. J. Structure-Based Programming of Lymph-Node Targeting in Molecular Vaccines. *Nature* **2014**, *507* (7493), 519–522.

(28) Wan, D.; Que, H.; Chen, L.; Lan, T.; Hong, W.; He, C.; Yang, J.; Wei, Y.; Wei, X. Lymph-Node-Targeted Cholesterolized TLR7 Agonist Liposomes Provoke a Safe and Durable Antitumor Response. *Nano Lett.* **2021**, *21* (19), 7960–7969.

(29) Famta, P.; Shah, S.; Jain, N.; Srinivasarao, D. A.; Murthy, A.; Ahmed, T.; Vambhurkar, G.; Shahrukh, S.; Singh, S. B.; Srivastava, S. Albumin-Hitchhiking: Fostering the Pharmacokinetics and Anticancer Therapeutics. *J. Control. Release* **2023**, *353* (September 2022), 166–185.

(30) Spada, A.; Emami, J.; Tuszynski, J. A.; Lavasanifar, A. The Uniqueness of Albumin as a Carrier in Nanodrug Delivery. *Mol. Pharm.* **2021**, *18* (5), 1862–1894.

(31) Hoogenboezem, E. N.; Duvall, C. L. Harnessing Albumin as a Carrier for Cancer Therapies. *Adv. Drug Deliv. Rev.* **2018**, *130*, 73–89.

(32) Lacroix, A.; Fakih, H. H.; Sleiman, H. F. Detailed Cellular Assessment of Albumin-Bound Oligonucleotides: Increased Stability and Lower Non-Specific Cell Uptake. *J. Control. Release* **2020**, *324* (April), 34–46.

(33) Abdallah, M.; Müllertz, O. O.; Styles, I. K.; Mörsdorf, A.; Quinn, J. F.; Whittaker, M. R.; Trevaskis, N. L. Lymphatic Targeting by Albumin-Hitchhiking: Applications and Optimisation. *J. Control. Release* **2020**, *327* (May), 117–128.

(34) Raffy, S.; Teissié, J. Control of Lipid Membrane Stability by Cholesterol Content. *Biophys. J.* **1999**, *76* (4), 2072–2080.

(35) Albuquerque, H. M. T.; Santos, C. M. M.; Silva, A. M. S. Cholesterol-Based Compounds: Recent Advances in Synthesis and Applications. *Molecules* **2019**, *24* (1).

(36) Irby, D.; Du, C.; Li, F. Lipid-Drug Conjugate for Enhancing Drug Delivery. *Mol. Pharm.* **2017**, *14* (5), 1325–1338.

(37) Duncan, R.; Gaspar, R. Nanomedicine (s) under the Microscope. *Mol. Pharm.* **2011**, *8* (6), 2101–2141.

(38) Kanamala, M.; Wilson, W. R.; Yang, M.; Palmer, B. D.; Wu, Z. Mechanisms and Biomaterials in PH-Responsive Tumour Targeted Drug Delivery: A Review. *Biomaterials* **2016**, *85*, 152–167.

(39) Tong, R.; Tang, L.; Ma, L.; Tu, C.; Baumgartner, R.; Cheng, J. Smart Chemistry in Polymeric Nanomedicine. *Chem. Soc. Rev.* **2014**, *43* (20), 6982–7012.

(40) Schattling, P.; Jochum, F. D.; Theato, P. Multi-Stimuli Responsive Polymers-the All-in-One Talents. *Polym. Chem.* **2014**, *5* (1), 25–36.

(41) Liu, B.; Thayumanavan, S. Substituent Effects on the PH Sensitivity of Acetals and Ketals and Their Correlation with Encapsulation Stability in Polymeric Nanogels. *J. Am. Chem. Soc.* **2017**, *139* (6), 2306–2317.

(42) Huppertsberg, A.; Kaps, L.; Zhong, Z.; Schmitt, S.; Stickdorn, J.; Deswarte, K.; Combes, F.; Czysch, C.; De Vrieze, J.; Kasmi, S.; Choteschovsky, N.; Klefenz, A.; Medina-Montano, C.; Winterwerber, P.; Chen, C.; Bros, M.; Lienenklaus, S.; Sanders, N. N.; Koynov, K.; Schuppan, D.; Lambrecht, B. N.; David, S. A.; De Geest, B. G.; Nuhn, L. Squaric Ester-Based, PH-Degradable Nanogels: Modular Nanocarriers for Safe, Systemic Administration of Toll-like Receptor 7/8 Agonistic Immune Modulators. *J. Am. Chem. Soc.* **2021**, *143* (26), 9872–9883.

(43) Bixenmann, L.; Stickdorn, J.; Nuhn, L. Amphiphilic Poly(Esteracetal)s as Dual PH-and Enzyme-Responsive Micellar Immunodrug Delivery Systems. *Polym. Chem.* **2020**, *11* (13), 2441–2456.

(44) Van Driessche, A.; Kocere, A.; Everaert, H.; Nuhn, L.; Van Herck, S.; Griffiths, G.; Fenaroli, F.; De Geest, B. G. PH-Sensitive Hydrazone-Linked Doxorubicin Nanogels via Polymeric-Activated Ester Scaffolds: Synthesis, Assembly, and in Vitro and in Vivo Evaluation in Tumor-Bearing Zebrafish. *Chem. Mater.* **2018**, *30* (23), 8587–8596.

(45) Fleige, E.; Quadir, M. A.; Haag, R. Stimuli-Responsive Polymeric Nanocarriers for the Controlled Transport of Active Compounds: Concepts and Applications. *Adv. Drug Deliv. Rev.* **2012**, *64* (9), 866–884.

(46) Jazani, A. M.; Oh, J. K. Development and Disassembly of Single and Multiple Acid-Cleavable Block Copolymer Nanoassemblies for Drug Delivery. *Polym. Chem.* **2020**, *11* (17), 2934–2954.

(47) Du, J. Z.; Li, H. J.; Wang, J. Tumor-Acidity-Cleavable Maleic Acid Amide (TACMAA): A Powerful Tool for Designing Smart Nanoparticles to Overcome Delivery Barriers in Cancer Nanomedicine. *Acc. Chem. Res.* **2018**, *51* (11), 2848–2856.

(48) Su, S.; Du, F. S.; Li, Z. C. Synthesis and PH-Dependent Hydrolysis Profiles of Mono- and Dialkyl Substituted Maleamic Acids. *Org. Biomol. Chem.* **2017**, *15* (39), 8384–8392.

(49) Kang, S.; Kim, Y.; Song, Y.; Choi, J. U.; Park, E.; Choi, W.; Park, J.; Lee, Y. Comparison of PH-Sensitive Degradability of Maleic Acid Amide Derivatives. *Bioorganic Med. Chem. Lett.* **2014**, *24* (10), 2364–2367.

(50) Lyu, M.; Yazdi, M.; Lin, Y.; Höhn, M.; Lächelt, U.; Wagner, E. Receptor-Targeted Dual PH-Triggered Intracellular Protein Transfer. *ACS Biomater. Sci. Eng.* **2022**.

(51) Wang, Q.; Wang, C.; Li, S.; Xiong, Y.; Wang, H.; Li, Z.; Wan, J.; Yang, X.; Li, Z. Influence of Linkers within Stimuli-Responsive Prodrugs on Cancer Therapy: A Case of Five Doxorubicin Dimer-Based Nanoparticles. *Chem. Mater.* **2022**, *34* (5), 2085–2097.

(52) Heck, A. G.; Stickdorn, J.; Rosenberger, L. J.; Scherger, M.; Woller, J.; Eigen, K.; Bros, M.; Grabbe, S.; Nuhn, L. Polymerizable 2-Propionic-3-Methylmaleic Anhydrides as a Macromolecular Carrier Platform for PH-Responsive Immunodrug Delivery. *J. Am. Chem. Soc.* **2023**, *145* (50), 27424–27436.

(53) Jangra, S.; De Vrieze, J.; Choi, A.; Rathnasinghe, R.; Laghlali, G.; Uvyn, A.; Van Herck, S.; Nuhn, L.; Deswarte, K.; Zhong, Z.; Sanders, N. N.; Lienenklaus, S.; David, S. A.; Strohmeier, S.; Amanat, F.; Krammer, F.; Hammad, H.; Lambrecht, B. N.; Coughlan, L.; García-Sastre, A.; De Geest, B. G.; Schotsaert, M. Sterilizing Immunity against SARS-CoV-2 Infection in Mice by a Single-Shot and Lipid Amphiphile Imidazoquinoline TLR7/8 Agonist-Adjuvanted Recombinant Spike Protein Vaccine**. *Angew. Chemie - Int. Ed.* **2021**, *60* (17), 9467–9473.

(54) Lechner, M. D.; Nordmeier, E. H.; Gehrke, K. *Makromolekulare Chemie*; 2010.

(55) Rabanel, J. M.; Hildgen, P.; Banquy, X. Assessment of PEG on Polymeric Particles Surface, a Key Step in Drug Carrier Translation. *J. Control. Release* **2014**, *185* (1), 71–87.

(56) Fang, Y.; Xue, J.; Gao, S.; Lu, A.; Yang, D.; Jiang, H.; He, Y.; Shi, K. Cleavable PEGylation: A Strategy for Overcoming the "PEG Dilemma" in Efficient Drug Delivery. *Drug Deliv.* **2017**, *24* (0), 22–32.

(57) Shyh-Dar, L.; Leaf, H. Stealth Nanoparticles: High Density but Sheddable PEG Is a Key for Tumor Targeting. *J. Control. Release* **2011**, *145* (3), 178–181.

(58) Palucka, K.; Banchereau, J. Cancer Immunotherapy via Dendtritic Cells. *Nat. Rev. Cancer* **2013**, *12* (4), 1–19.

(59) Czysch, C.; Medina-Montano, C.; Zhong, Z.; Fuchs, A.; Stickdorn, J.; Winterwerber, P.; Schmitt, S.; Deswarte, K.; Raabe, M.; Scherger, M.; Combes, F.; De Vrieze, J.; Kasmi, S.; Sandners, N. N.; Lienenklaus, S.; Koynov, K.; Räder, H. J.; Lambrecht, B. N.; David, S. A.; Bros, M.; Schild, H.; Grabbe, S.; De Geest, B. G.; Nuhn, L. Transient Lymph Node Immune Activation by Hydrolysable Polycarbonate Nanogels. *Adv. Funct. Mater.* **2022**, *32* (35), 2203490.

(60) Stickdorn, J.; Stein, L.; Arnold-Schild, D.; Hahlbrock, J.; Medina-Montano, C.; Bartneck, J.; Ziß, T.; Montermann, E.; Kappel, C.; Hobernik, D.; Haist, M.; Yurugi, H.; Raabe, M.; Best, A.; Rajalingam, K.; Radsak, M. P.; David, S. A.; Koynov, K.; Bros, M.; Grabbe, S.; Schild, H.; Nuhn, L. Systemically Administered TLR7/8 Agonist and Antigen-Conjugated Nanogels Govern Immune Responses against Tumors. *ACS Nano* **2022**, *16* (3), 4426–4443.

(61) Stickdorn, J.; Czysch, C.; Medina-Montano, C.; Stein, L.; Xu, L.; Scherger, M.; Schild, H.; Grabbe, S.; Nuhn, L. Peptide-Decorated Degradable Polycarbonate Nanogels for Eliciting Antigen-Specific Immune Responses. *Int. J. Mol. Sci.* **2023**, *24* (20).

(62) Lienenklaus, S.; Cornitescu, M.; Ziętara, N.; Łyszkiewicz, M.; Gekara, N.; Jabłońska, J.; Edenhofer, F.; Rajewsky, K.; Bruder, D.; Hafner, M.; Staeheli, P.; Weiss, S. Novel Reporter Mouse Reveals

Constitutive and Inflammatory Expression of IFN-β In Vivo. *J. Immunol.* **2009**, *183* (5), 3229–3236.

pH-TRIGGERED, LYMPH NODE FOCUSED IMMUNODRUG DELIVERY BY POLYMERIC 2-PROPIONIC-3-METHYLMALEIC ANHYDRIDES WITH CHOLESTEROL END GROUPS

-Supporting Information-

Alina G. Heck[1,2], Carolina Medina-Montano[3], Zifu Zhong[4], Kim Deswarte[5], Katharina Eigen[1], Judith Stickdorn[2], Johannes Kockelmann[1], Maximilian Scherger[2], Niek N. Sanders[6], Stefan Lienenklaus[7], Bart N. Lambrecht[5], Stephan Grabbe[3], Bruno G. De Geest[4] and Lutz Nuhn[,1]*

1: Chair of Macromolecular Chemistry, Julius-Maximilians-Universität Würzburg, 97070 Würzburg, Germany

2: Max Planck Institute for Polymer Research, 55128 Mainz, Germany

3: Department of Dermatology, University Medical Center (UMC) of the Johannes Gutenberg-University Mainz, 55131 Mainz, Germany

4: Department of Pharmaceutics and Cancer Research Institute Ghent (CRIG), Ghent University, Ghent 9000, Belgium

5: Department of Internal Medicine and Pediatrics, VIB Center for Inflammation Research, Ghent University, 9052 Ghent, Belgium

6: Laboratory of Gene Therapy, Department of Nutrition, Genetics and Ethology, Ghent University, 9820 Merelbeke, Belgium

7: Institute for Laboratory Animal Science and Institute of Immunology, Hannover Medical School, 30625 Hannover, Germany

*: corresponding author: Prof. Dr. Lutz Nuhn (E-mail: lutz.nuhn@uni-wuerzburg.de)

Materials and Methods

All reagents and solvents were purchased from TCI Chemicals (Tokyo, Japan), Sigma Aldrich (Taufkirchen, Germany) or Rapp Polymers (Tübingen, Germany) and used as received, unless otherwise described. Oxalyl chloride was obtained from Thermo Fisher Scientific (Waltham, MA, USA). Benzylamine, dibenzylamine, triethylamine, dimethyl sulfoxide (DMSO), *N*,*N*-dimethylformamide (DMF), chloroform ($CHCl_3$), dichloromethane (DCM) and all deuterated solvents were bought from Sigma Aldrich. N-(3-aminopropyl)methacrylamide hydrochloride (APMA) was purchased from abcr GmbH (Karlsruhe, Germany) and tetramethylrhodamine cadaverine from Biotium (Fermont, CA, USA).

Immunodrug 1-(4-(aminomethyl)benzyl)-2-butyl-1*H*-imidazo[4,5-c]quinoline-4-amine (IMDQ) was synthesized by Maximilian Scherger (Max Planck Institute for Polymer Research, Germany).[1–3] Azobisisobutyronitrile (AIBN) was recrystallized from ethanol twice.

Hexafluoroisopropanol (HFIP) was obtained from Fluorochem Ltd. (Hadfield, UK). Millipore (mp) water was prepared using a MILLI-Q® Reference A+ System. For silica gel chromatography silica with particle size of 0.063-0.2 mm from Macherey-Nagel GmbH & Co. KG (Dueren, Germany) was used.

Dulbecco's phosphate-buffered saline (PBS), cell culture medium and supplements were bought from Thermo Fisher Scientific. The RAW-Dual™ (IRF-Lucia/KI-[MIP-2]SEAP) murine macrophage reporter cell line and the QUANTI-Blue™ solution were obtained from InvivoGen (San Diego, CA, USA). RAW-Dual™ cells were cultured in Dulbecco's modified Eagle's medium DMEM, containing 10% fetal bovine serum, 1% penicillin/streptomycine, 0.02% normocine, and 0.01% zeocin at 37 °C with 5% CO_2 saturation.

Instrumentation

Nuclear Magnetic Resonance (NMR) Spectroscopy

^{1}H, ^{13}C, ^{19}F and 2D NMR spectra were recorded on a Bruker Avance III 300 MHz, Bruker Avance III 400 MHz, Bruker Avance III 500 MHz or Bruker Avance III 700 MHz spectrometer at room temperature. Diffusion ordered spectroscopy (DOSY) were measured on a Bruker Avance III 500 MHz or Bruker Avance III 700 MHz spectrometer. Calibration of the spectra was achieved using the solvent signal. NMR spectra were analyzed using MestReNova 14.2.0 by Mestrelab Research.

Size Exclusion Chromatography (SEC)

Analytical SEC was performed in HFIP as an eluant, containing 3 g/L potassium trifluoroacetate at a flow rate of 0.8 mL/min at 40 °C. Measurements were carried out on a SECcurity2instrument from PPS, Mainz equipped with SECcurtity2isocratic pump, a degasser, an autosampler, a column thermostat, an UV and RI detector. The column material was composed with modified silica gel (PFG columns, particle size 7 µM, porosity: 100 Å and 1000 Å), obtained from PSS Polymer Standards Service GmbH, Mainz, Germany. The molecular weights were determined by using a calibration with poly(methyl methacrylate) (PMMA) standard, purchased from PSS, Mainz. Polymer samples were prepared at 1mg/mL and filtered through GHP syringe filters (0.2 µm pore size, Acrodisc) prior to injection.

Dynamic Light Scattering (DLS)

Single-angle dynamic light scattering measurements were performed on a Malvern Z Nano instrument equipped with a He-Ne-Laser (λ = 632.8 nm) using the ZetaSizer Software 7.12. All samples were measured in triplicates at 25 °C and a detection angle of 173°. The resulting data were processes by cumulant fitting for D_z and PDI, or by CONTIN fitting for intensity-, volume- and number-weighted particle size distribution. Samples were prepared at 0.1 mg/mL and dust was removed by filtration through GHP syringe filters (0.2 µm pore size, Acrodisc).

Ultraviolet-Visible Spectroscopy (UV-Vis) and Fluorescence Spectroscopy

UV-Vis spectra were recorded using a Thermo Scientific™ NanoDrop™ 2000c spectrophotometer with a Hellma Quartz Cuvette.

Fluorescence spectroscopy as well as RAW-blue and MTT assay absorbance read-out were performed using a Spark 20M Multimode Microplate Reader from Tecan Trading AG (Mannedorf, Switzerland).

Mass Spectrometry (ESI-MS and MALDI-ToF)

ESI mass spectra were measured on an Agilent 6545 QTOF-MS (Santa Clara, CA, USA). Samples were dissolved in methanol with a concentration of 0.1 mg/mL. Mass spectrometry data were analyzed using Advion Data Express software.

Matrix Assisted Laser Desorption Ionization-Time of Flight (MALDI-ToF) measurement were acquired on a rapifleX™ MALDI-ToF/ToF mass spectrometer from Bruker Daltonik GmbH (Bremen, Germany). The instrument was fitted with a 10 kHz scanning smartbeam Nd:YAG laser at 355 nm wavelength and a 10 bit 5 GHz digitizer. Mass spectra were recorded in a positive ion mode using DCTB (trans-2-[3-(4-tbutylphenyl)-2-methyl-2-propenylidene]-

malononitrile) acid as a matrix. Samples were prepared at 0.1 mg/mL and the resulting data were processed by mMass software.

Fluorescent Confocal Microscopy

Fluorescent confocal laser scanning microscopy images were recorded on a Leica STELLARIS 8 Leica DMi8 confocal microscope with a HC PL APO CS2 40x/1.25 GLYC oil immersion objective. Images were processed using Leica Application Suite X 3.7.4.23463 by Leica Microsystems.

Fluorescence-Activated Cell Scanning (FACS)

Flow cytometric analyses were conducted on a BD Accuri C6 from BD Biosciences. All obtained data were processed using FloJo™_v10.8.1_CL by BD Biosciences.

Syntheses

Cholesterol-CTA

Synthesis of Cholesteryl tosylate

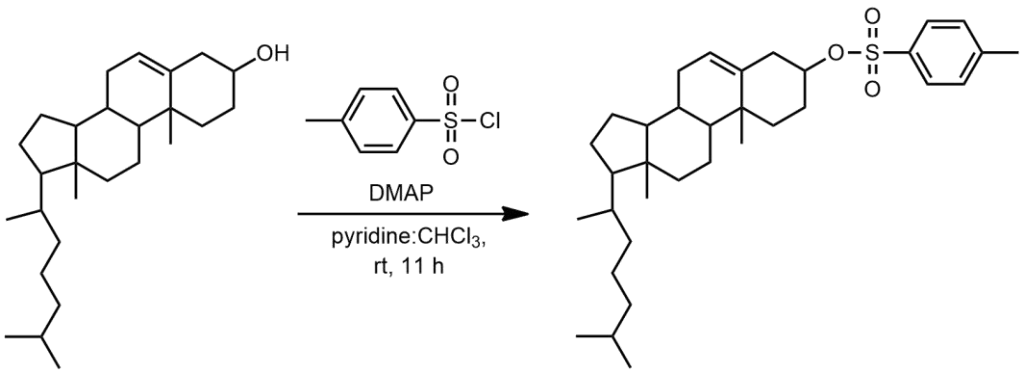

Figure S1: Synthesis of cholesteryl tosylate.

The synthesis was adapted from the literature and modified.[4] Cholesterol (5.0 g, 12.93 mmol, 1 eq) and 4-dimethylaminopyridine (DMAP) (0.158 g, 1.29 mmol, 0.1 eq) were dissolved in a mixture of dry $CHCl_3$ and pyridine (1:1) and cooled to 0 °C. Tosyl chloride (3.08 g, 16.16 mmol, 1.25 eq) dissolved in $CHCl_3$ (10 mL) was added dropwise *via* dropping funnel. After 1 h, the reaction mixture was allowed to warm to room temperature and stirred overnight, follow by extraction with brine (2x 50 mL), 1M HCl solution (2x 50 mL) and H_2O (2x 50 mL). The

combined organic layers were dried over Na_2SO_4, filtrated, and concentrated *in vacuo*. The product was obtained as slightly yellow crystals (7.0 g, 100%).

^{1}H NMR (300 MHz, $CDCl_3$): δ (ppm) = 7.97 (d, J = 8.4 Hz, 2H, **A**), 7.33 (d, J = 8.3 Hz, 2H, **B**), 5.30 (dd, J = 5.3 Hz, 1H, **a**), 4.32 (tt, J = 11.0 Hz, 1H, **b**), 2.44 (s, 3H, **C**), 2.32-2.22 (m, 1H, **c**) 2.09-1.96 (m, 1H, **c'**), 1.86-1.74 (m, 3H, **d+e**), 1.72-1.29 (m, 12H, **f-l**), 1.28-0.97 (m, 10 H, **m-p**), 0.96 (s, 3H, **q**) 0.91 (d, 3H, **r**), 0.90-0.80 (m, 7H, **s-u**), 0.65 (s, 3H, **v**).

ESI-MS [m/z] = th.: 541.84 $[M+H]^+$, res.: 369.20 $[C_{27}H_{45}]^+$ (calc. 369.35), 448.20 $[C_{27}H_{45}\text{-}OSO_2]^+$ (calc. 448.31).

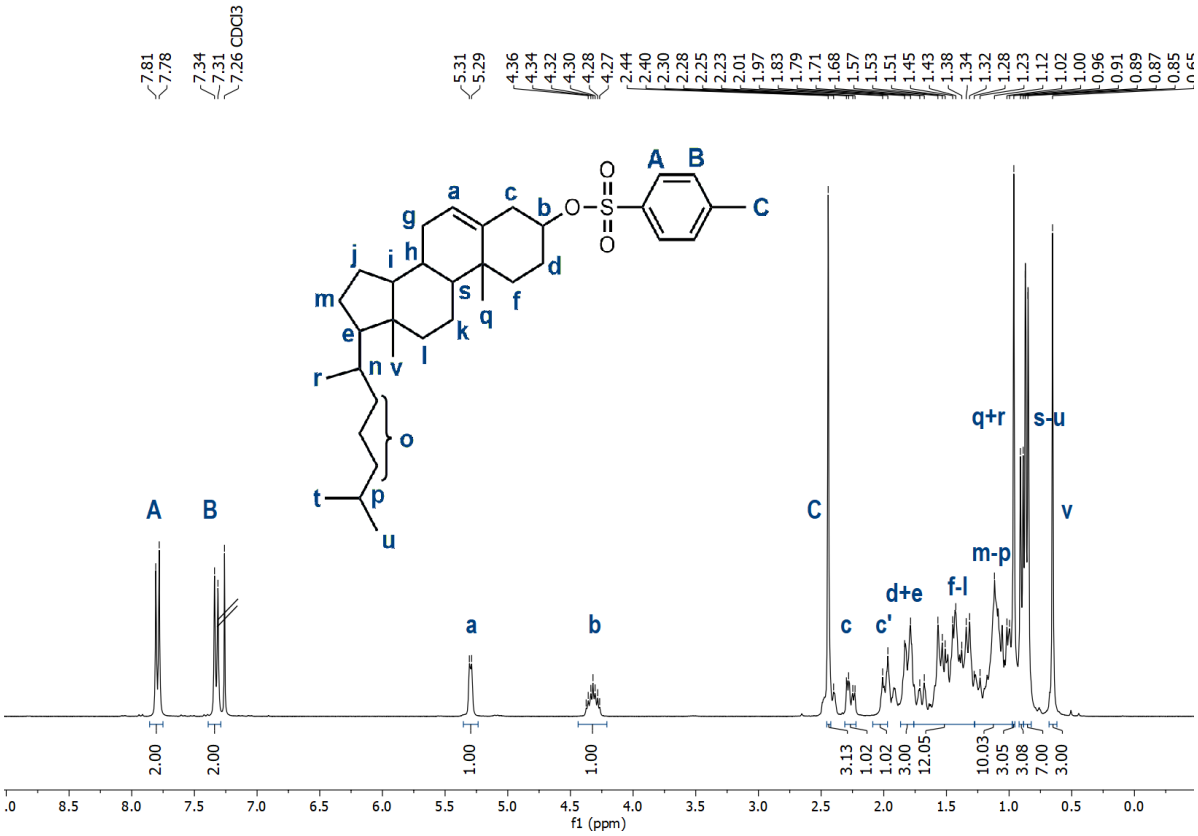

Figure S2: ^{1}H NMR spectrum (300 MHz) of cholesteryl tosylate in $CDCl_3$.

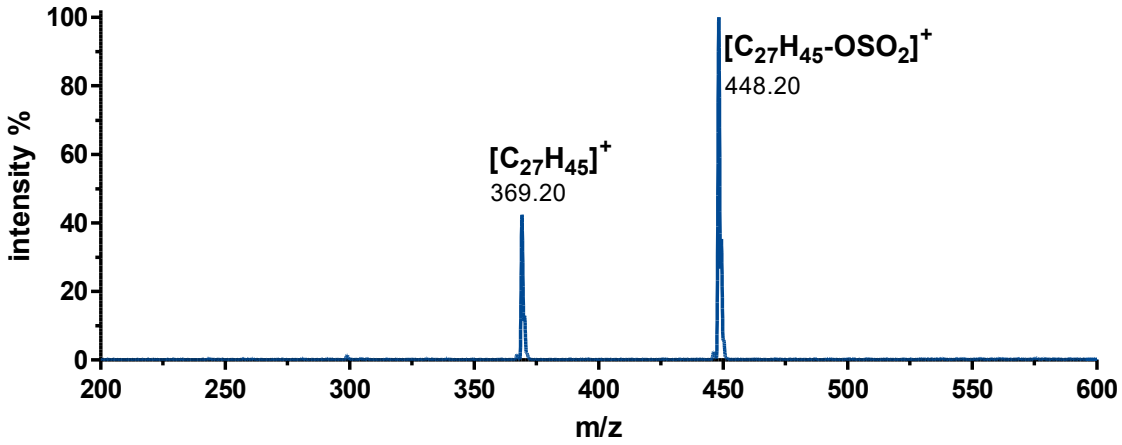

Figure S3: ESI-MS spectrum of cholesteryl tosylate in MeOH (positive ion mode).

Synthesis of Cholesteryl azide

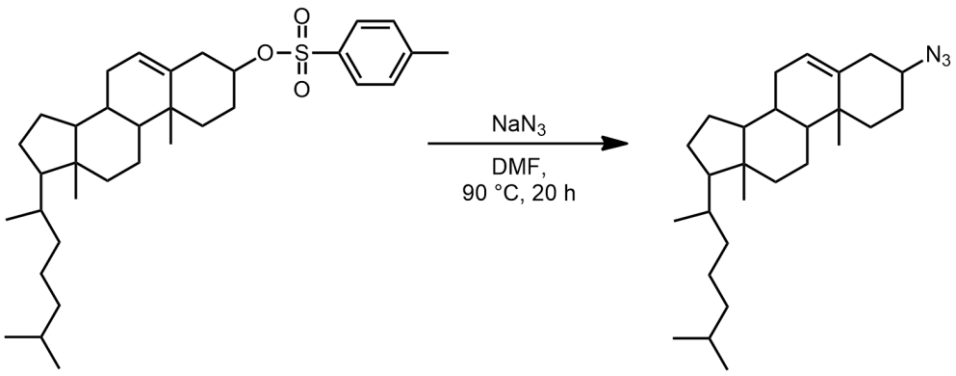

Figure S4: Synthesis of cholesteryl azide.

Cholesteryl azide was synthesized according to the literature with minor modification.[5,6] In an oven-dried two neck round bottom flask, cholesteryl tosylate (3.5 g, 6.47 mmol, 1 eq) was dissolved in dry DMF (50 mL) under nitrogen atmosphere. NaN_3 (0.841 mg, 12.94 mmol, 2 eq) was slowly added to the solution under nitrogen flow and stirred at 90 °C for 18 h. Thereafter, the reaction mixture was cooled to room temperature and quenched with water (100 mL). The organic phase was extracted with water (3x 30 mL) and the combined aqueous layer were washed with ethyl acetate (3x 30 mL). The organic solvent was dried over Na_2SO_4, filtrated, and evaporated under reduced pressure. The crude reaction product was purified by silica gel chromatography using cyclohexane and ethyl acetate (10:1) as eluent. Cholesteryl azide was isolated as colorless crystals (2.21 g, 89%).

^{1}H NMR (700 MHz, $CDCl_3$): δ (ppm) = 5.39 (s, 1H, **a**), 3.88 (s, 1H, **b**), 2.05-192 (m, 2H, **c**), 1.92-1.77 (m, 3H, **d+e**) 1.57-1.29 (m, 12H, **f-l**), 1.21-1.07 (m, 10H, **m-p**), 1.01 (s, 3H, **q**), 0.87 (d, *J* = 3.1 MHz, 3H, **r**), 0.87-0.85 (m, 7H, **s-u**), 0.68 (s, 3H, **v**).

^{13}C NMR (176 MHz, $CDCl_3$): δ (ppm) = 138.42 (**1**), 123.50 (**2**), 58.62 (**3**), 57.02 (**4**), 56.44 (**5**), 50.22 (**6**), 42.63 (**7**), 40.06 (**8**), 39.85 (**9**), 38.49 (**10**), 36.52 (**11**), 35.65 (**12**), 36.40 (**13**), 33.95 (**14**), 32.16 (**15**), 32.12 (**16**), 28.56 (**17**), 28.35 (**18**), 26.43 (**19**), 24.60 (**20**), 24.17 (**21**), 23.11 (**22**), 22.85 (**23**), 21.05 (**24**), 19.29 (**25**), 19.01 (**26**), 12.22 (**27**).

IR (ATR) ũ [cm^{-1}] = 840-790 (s, υ, CHR_3), 1390-1370 (m, δ, -CH_3), 1479-1430 (m, δ, -CH_2), 2160-2250 (m, υ, -N_3), 2960-2850 (s, υ, C-H).

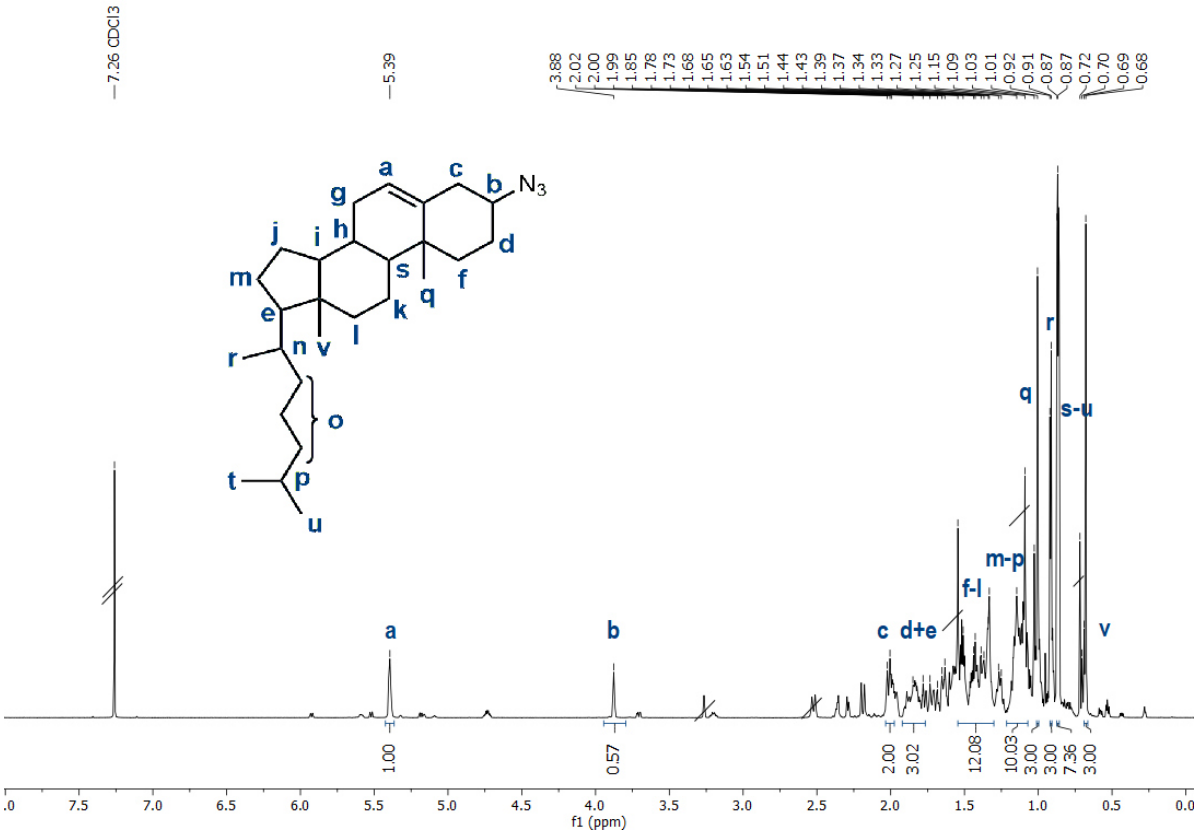

Figure S5: ^{1}H NMR spectrum (700 MHz) of cholesteryl azide in $CDCl_3$.

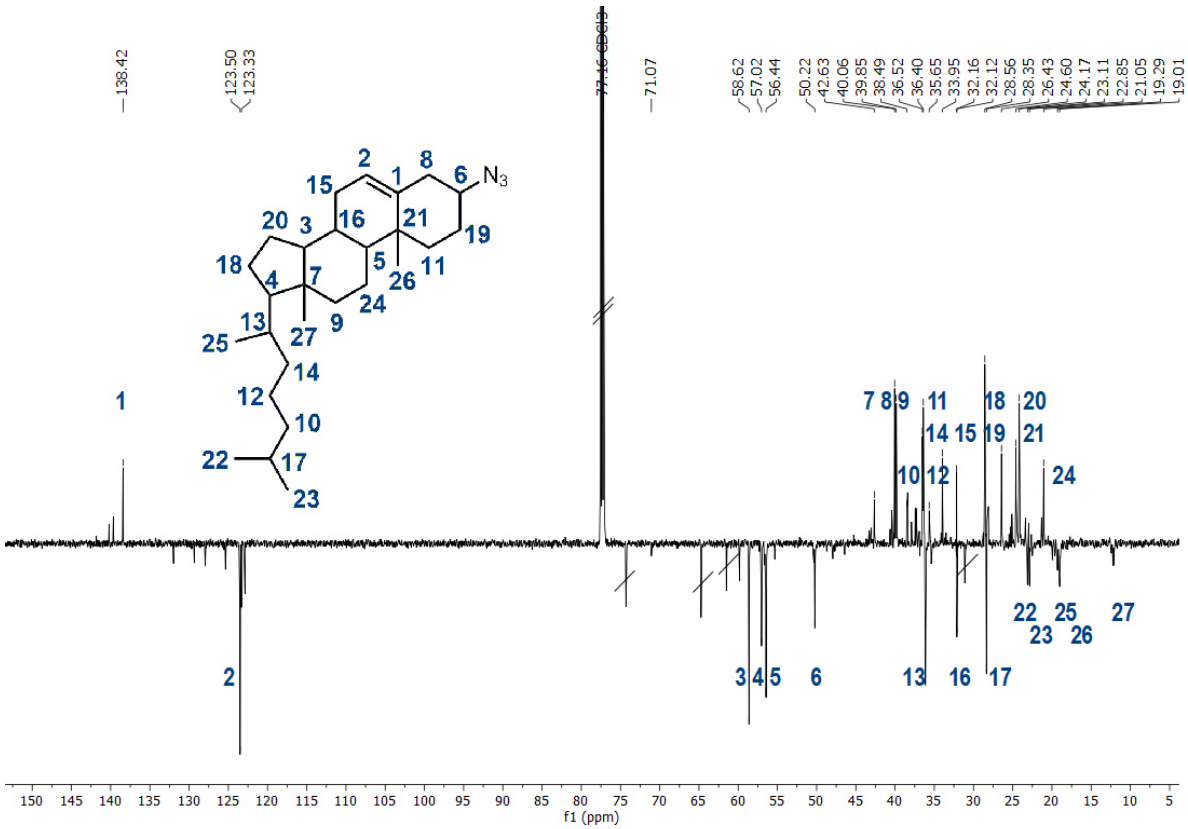

Figure S6: ^{13}C NMR spectrum (176 MHz) of cholesteryl azide in $CDCl_3$.

Synthesis of Cholesteryl amine

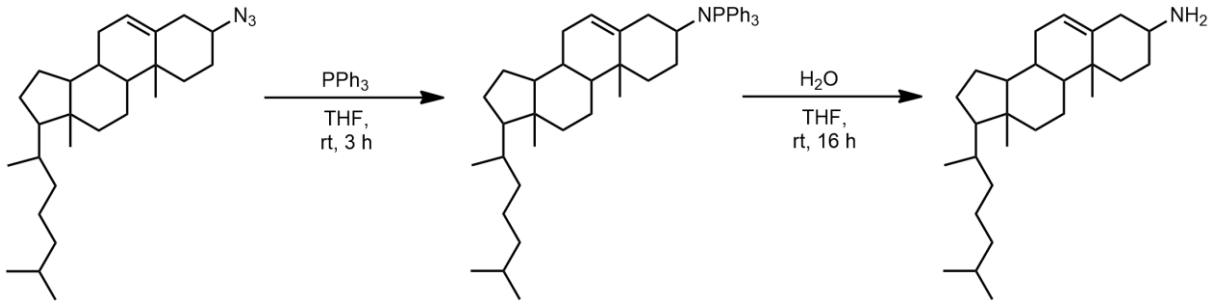

Figure S7: Synthesis of cholesteryl amine by Staudinger Reaction.

The synthesis of cholesteryl amine was conducted according to the literature and modified.[7] In a three neck round bottom flask, cholesteryl azide (2.0 g, 4.86 mmol, 1 eq) was dissolved in anhydrous THF (30 mL) under nitrogen atmosphere. To this solution triphenylphosphine (PPh_3) (6.37 g, 24.29 mmol, 5 eq) dissolved in dry THF (20 mL) was slowly added *via* dropping funnel. The reaction mixture was stirred at room temperature for 3 h. Afterwards, water (10 mL) was added, and the suspension was stirred for further 16 h. The reaction mixture was diluted with toluene (3x 200 mL) to remove THF and water by azeotropic evaporation *in vacuo*. The crude

product was purified by column chromatography (DCM/MeOH 95:5 + 1% TEA) yielding cholesteryl amine as colorless powder (1.50 g, 80%).

^{1}H NMR (700 MHz, $CDCl_3$): δ (ppm) = 5.38 (s, 1H, **a**), 3.20 (d, J = 5.8 MHz, **b**), 2.61-2.51 (m, 1H, **c**), 2.13-2.07 (m, 1H, **c'**), 1.89-1.78 (m, 3H, **d+e**) 1.54-1.32 (m, 12H, **f-l**), 1.18-1.06 (m, 10H, **m-p**), 1.00 (s, 3H, **q**), 0.92 (d, J = 3.7 MHz, 3H, **r**), 0.86-0.85 (m, 7H, **s-u**), 0.67 (s, 3H, **v**).

^{13}C NMR (176 MHz, $CDCl_3$): δ (ppm) = 138.85 (**1**), 123.69 (**2**), 56.91 (**3**), 56.31 (**4**), 50.54 (**5**), 47.19 (**6**), 42.97 (**7**), 42.46 (**8**), 39.94 (**9**), 39.67 (**10**), 37.56 (**11**), 36.35 (**12**), 35.96 (**13**), 33.20 (**14**), 32.14 (**15**), 32.01 (**16**), 28.22 (**17**), 29.38 (**18**), 28.16 (**19**), 24.44 (**20**), 24.01 (**21**), 23.01 (**22**), 22.75 (**23**), 20.94 (**24**), 19.04 (**25**), 18.84 (**26**), 11.97 (**27**).

ESI-MS [m/z] = th.: 386.67 $[M+H]^+$, res.: 386.35 $[M+H]^+$, 369.09 $[C_{27}H_{45}]^+$ (calc. 369.35), 771.30 $[2M+H]^+$ (calc. 771.34).

IR (ATR) ũ [cm^{-1}] = 840-790 (s, υ, CHR_3), 1390-1370 (m, δ, -CH_3), 1479-1430 (m, δ, -CH_2), 1650-1560 (m, δ, -NH_2), 2960-2850 (s, υ, C-H), 3550-3050 (m, υ, N-H).

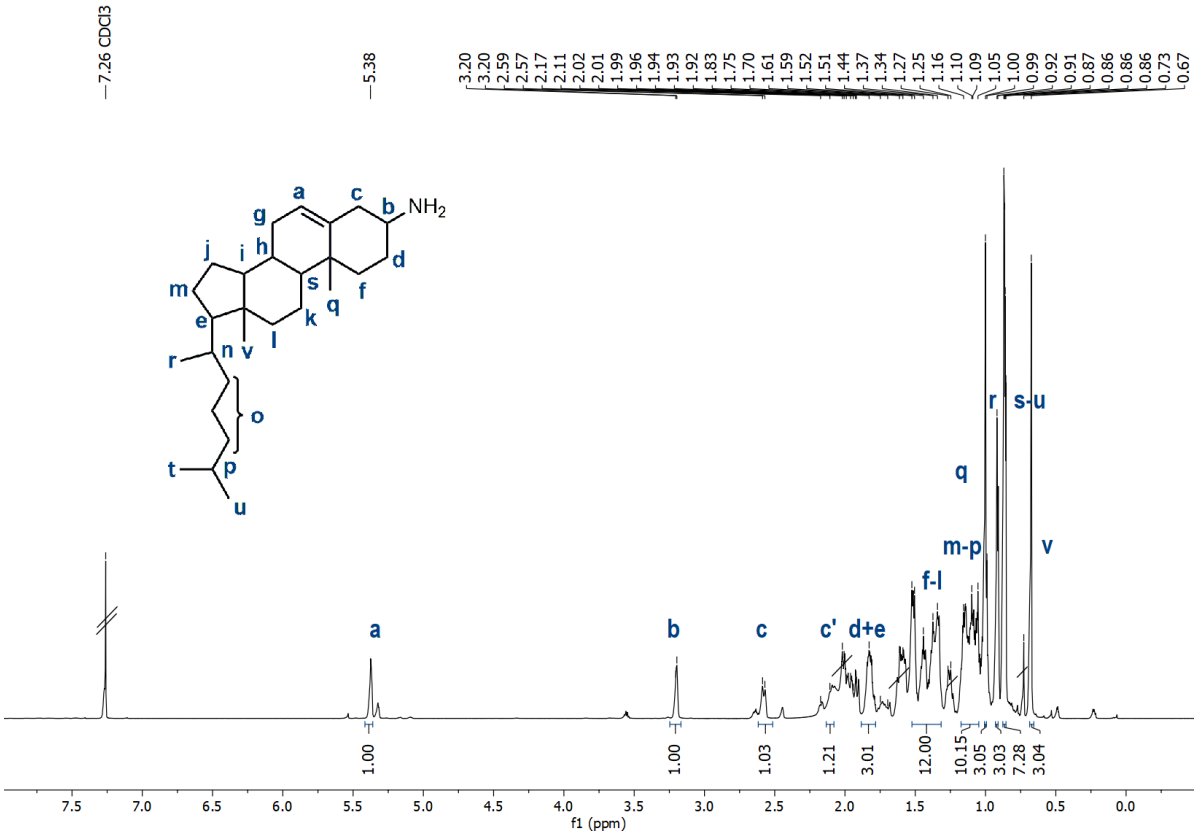

Figure S8: ^{1}H NMR spectrum (700 MHz) of cholesteryl amine in $CDCl_3$.

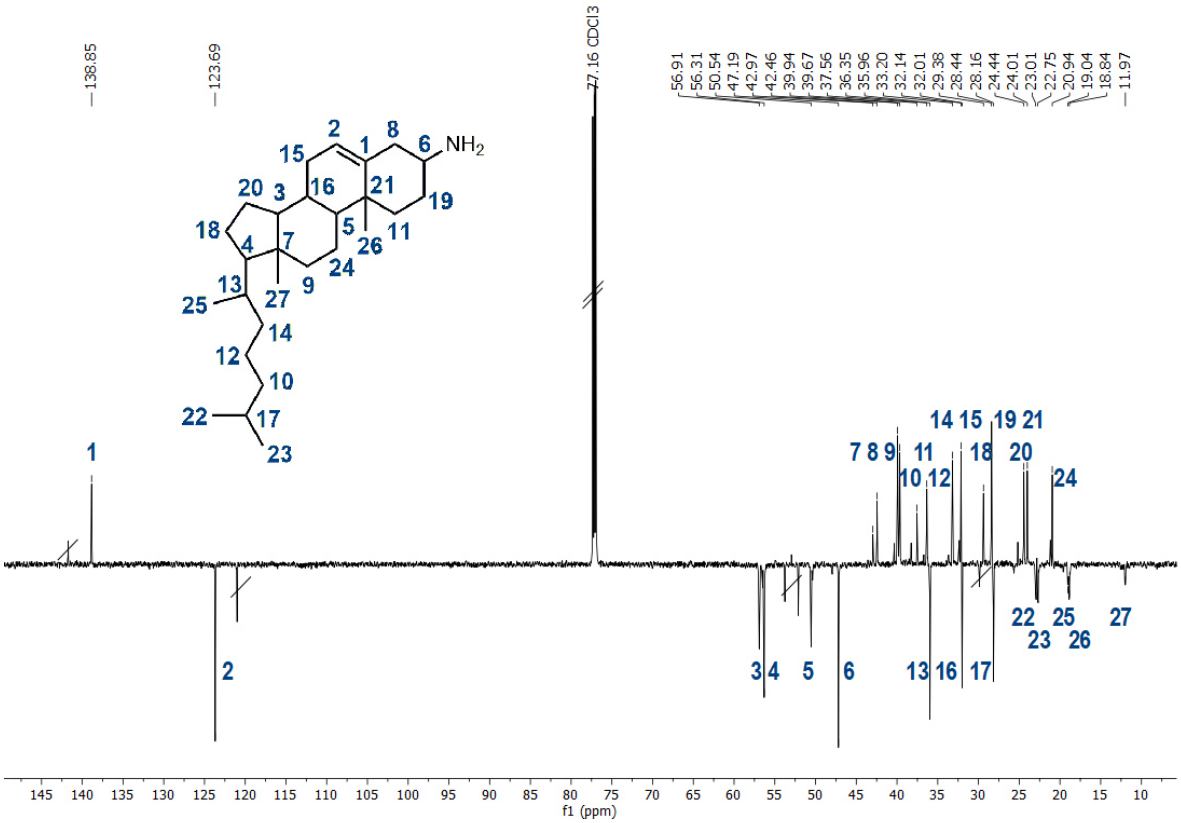

Figure S9: ^{13}C NMR spectrum (176 MHz) of cholesteryl amine in $CDCl_3$.

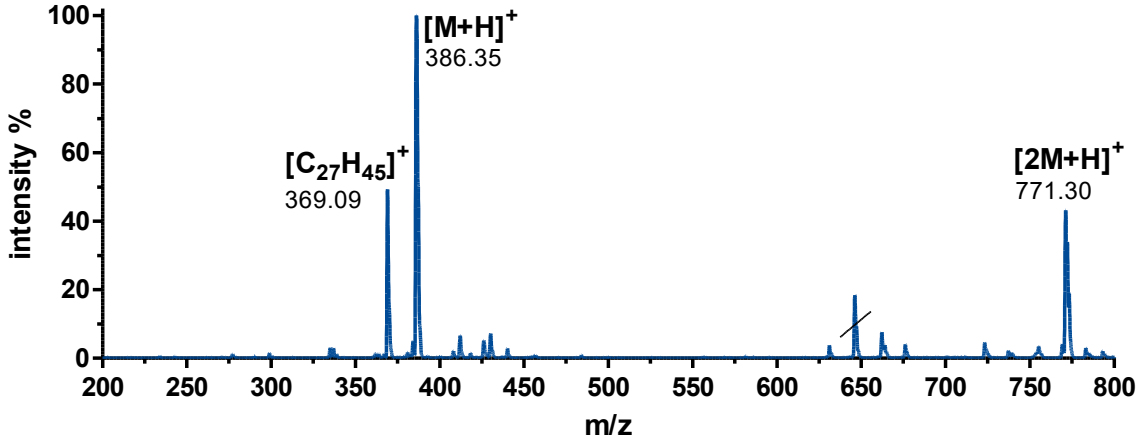

Figure S10: ESI-MS spectrum of cholesteryl amine in MeOH (positive ion mode).

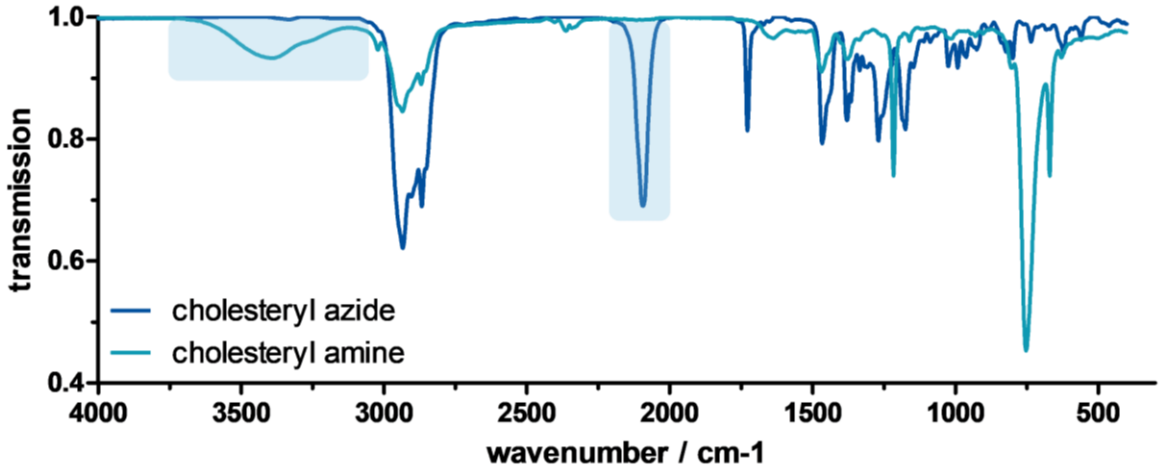

Figure S11: IR spectrum of cholesteryl azide (dark blue) and cholesteryl amine (light blue).

Synthesis of Pentafluorophenyl-trithiocarbonate Chain Transfer Agent

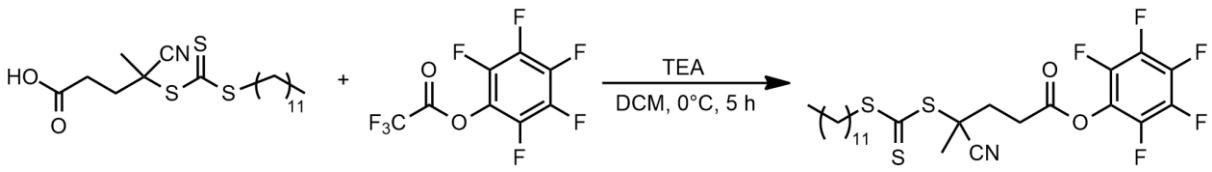

Figure S12: Synthesis of pentafluorophenyl-trithiocarbonate chain transfer agent (PFP-TTC-CTA).

Pentafluorophenyl-trithiocarbonate chain transfer agent (PFP-TTC-CTA) was synthesized by an adapted literature protocol.[8] 0.7 g 4-cyano-4-[(dodecylsulfanylthiocarbonyl)sulfanyl]-pentanoic acid (TTC-CTA) (1.75 mmol, 1 eq) was weighed into a dry round bottom flask and dissolved in anhydrous DCM (20 mL) under nitrogen atmosphere. Triethylamine (TEA) (0.605 mL, 4.67 mmol, 2.5 eq) was added and the solution was cooled to 0 °C using an ice bath. Protected from light pentafluorophenyl trifluoroacetate (0.802 mL, 4.67 mmol, 2.5 eq) was dropped to the reaction mixture *via* a syringe and stirred for 5 h at 0 °C. After complete conversion, the solution was diluted with DCM (15 mL) and the organic phase was extracted with water (3x 25 mL), dried over Na_2SO_4, filtrated, and evaporated *in vacuo*. The reaction product was purified *via* column chromatography (PE/EA 15:1). The product was isolated as yellow oil (0.75 g, 77 %).

^{1}H NMR (700 MHz, $CDCl_3$): δ (ppm) = 3.34 (t, J = 7.4 Hz, 2H, **a**), 3.05-2.98 (m, 2H, **b**), 2.68 (dt, J = 15.5 Hz, J = 8.0 Hz 1H, **c**), 2.53 (dt, J = 14.2 Hz, J = 7.6 Hz 1H, **c'**), 1.93 (s, 3H, **d**), 1.70 (quin, J = 7.1 Hz, 2H, **e**), 1.44-1.36 (m, 2H, **f**), 1.26 (s, 16H, **g**), 0.88 (t, J = 7.0 Hz, 3H, **h**).

^{19}F NMR (659 MHz, $CDCl_3$): δ (ppm) = -152.51 (d, J = 18 Hz, 2F, **a**), -157.29 (t, J = 21.6 Hz, 1F, **b**), -161.89 (d, J = 19.9 Hz, 2F, **c**).

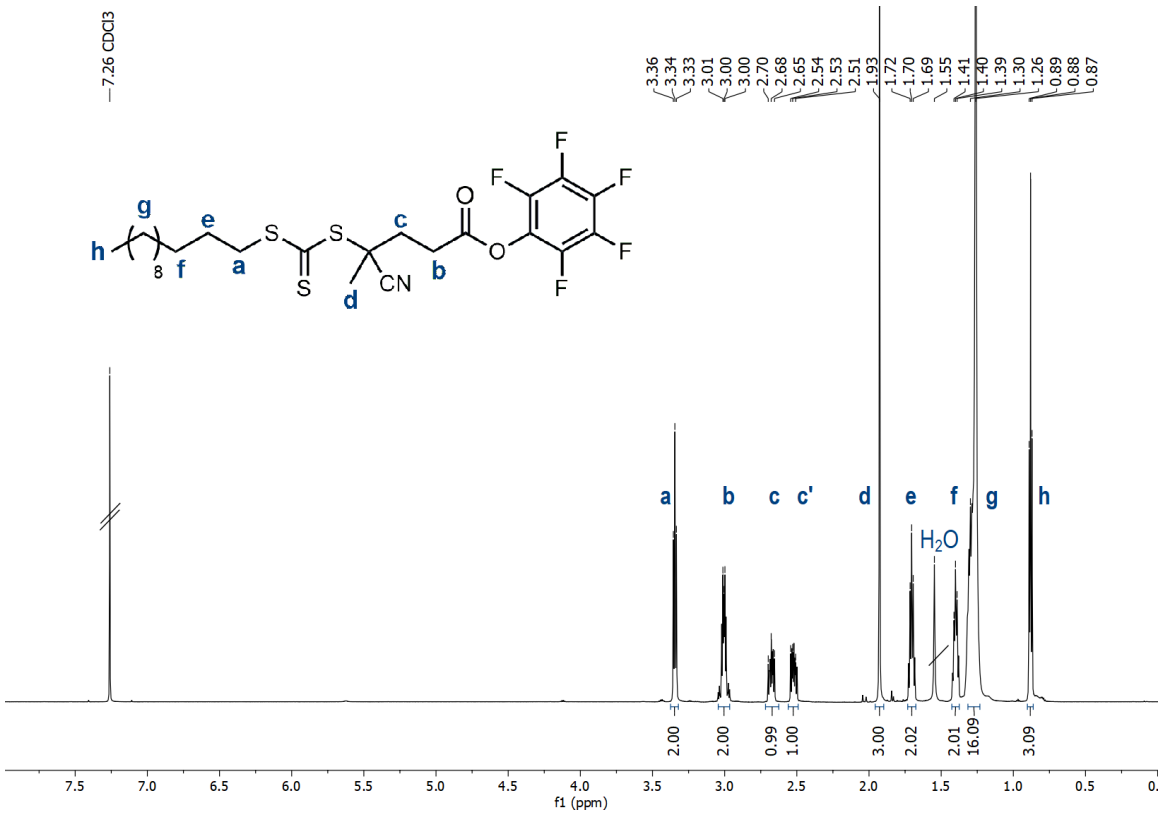

Figure S13: ^{1}H NMR spectrum (700 MHz) of pentafluorophenyl-trithiocarbonate chain transfer agent (PFP-TTC-CTA) in $CDCl_3$.

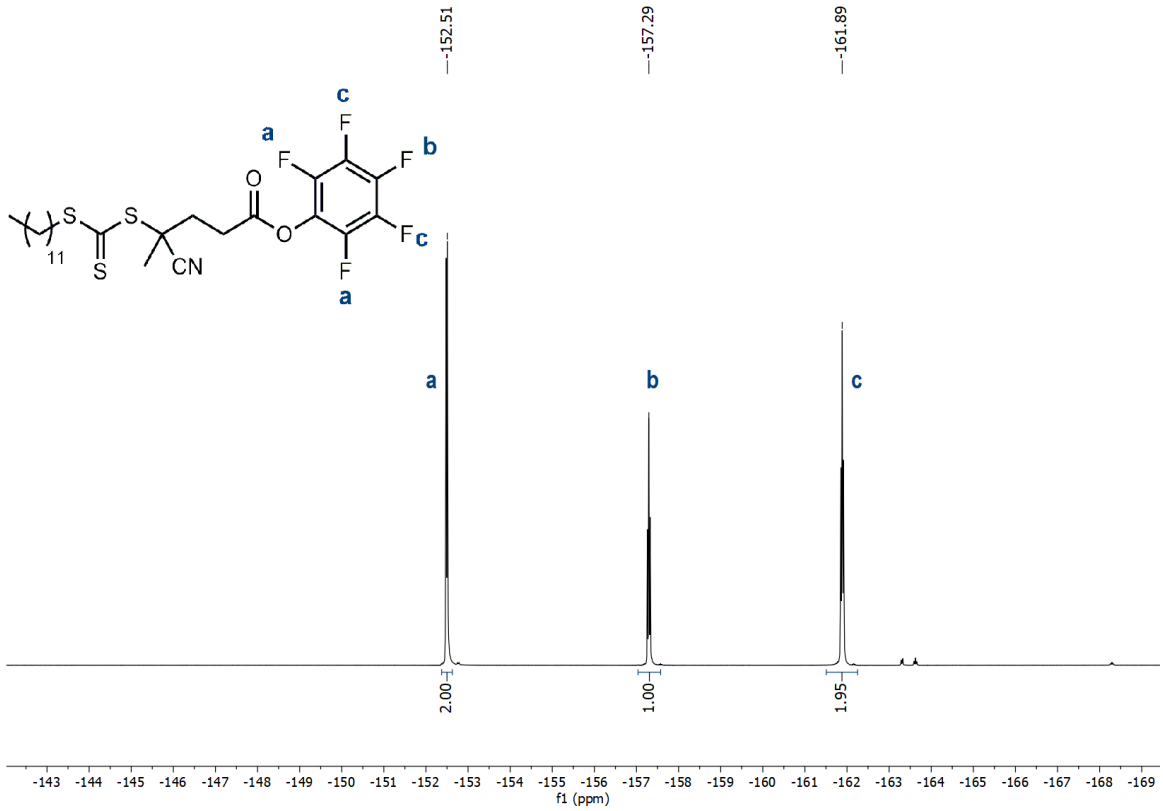

Figure S14: ^{19}F NMR spectrum (659 MHz) of pentafluorophenyl-trithiocarbonate chain transfer agent (PFP-TTC-CTA) in $CDCl_3$.

Synthesis of Cholesterol-trithiocarbonate Chain Transfer Agent (Chol-TTC-CTA)

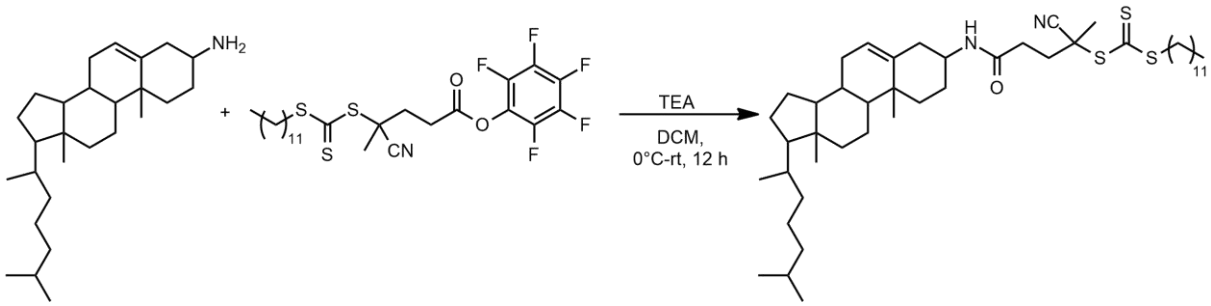

Figure S15: Synthesis of cholesterol-trithiocarbonate chain transfer agent (Chol-TTC-CTA).

The synthesis of cholesterol-trithiocarbonate chain transfer agent (Chol-TTC-CTA) was adapted from the literature and modified.[9] PFP-TTC-CTA (716 mg, 1.29 mmol, 2 eq) was weighed into a pre-dried two neck round bottom flask and dissolved in dry DCM (15 mL) under nitrogen atmosphere. The solution was cooled for 30 min using an ice bath and protected from light cholesteryl amine (250 mg, 0.648 mmol, 1 eq) dissolved in DCM (15 mL) and TEA (0.269 mL, 1.94, 3 eq) were dropwise added *via* dropping funnel. The reaction mixture was warmed to room temperature and stirred overnight. Then, the volatiles were evaporated under reduced pressure and the crude product was purified by silica gel chromatography using a gradient mixture of n-hexane and ethyl acetate (90:10, 80:20, 70:30 + 1% TEA). The cholesterol-TTC-CTA was obtained as yellow crystals (293 mg, 59 %).

^{1}H NMR (700 MHz, $CDCl_3$): δ (ppm) = 5.59 (d, *J* = 7.8 MHz, 1H, A), 5.41 (s, 1H, a), 4.13 (s, 1H, b), 3.33 (t, *J* = 7.5 MHz, 2H, B), 2.64-2.57 (m, 1H, c), 2.56-2.48 (m, 1H, C), 2.49-2.43 (m, 2H, D), 2.40-2.32 (m, 1H, C'), 2.07-2.00 (m, 1H, c'), 2.01 (s, 3H, E)1.87-1.72 (m, 3H, d+e), 1.74-1.64 (m, 2H, F), 1.58-1.31 (m, 12H, f-l), 1.30-1.27 (m, 2H, G), 1.26 (s, 16H, H), 1.22-1.06 (m, 10H, m-p), 1.02 (s, 3H, q), 0.92 (d, *J* = 6.6 MHz, 3H, r), 0.90-0.84 (m, 10H, I, s-u), 0.68 (s, 3H, v).

^{13}C NMR (176 MHz, $CDCl_3$): δ (ppm) = 217.47 (1), 169.32 (2), 138.78 (3), 124.14 (4), 119.46 (5), 56.85 (6), 56.34 (7), 50.52 (8), 46.96 (9), 46.01 (10), 42.46 (11), 39.85 (12), 39.65 (13), 37.52 (14), 37.21 (15), 36.33 (16), 35.96 (17), 34.75 (18), 34.28 (19), 32.26 (20), 32.05 (21), 31.95 (22), 29.76-29.09 (23-32), 28.95 (33), 28.38 (34), 28.15 (35), 26.14 (36), 25.23 (37), 24.41 (38), 24.03 (39), 23.00 (40), 22.66 (41), 20.91 (42), 19.01 (43), 18.96 (44), 14.30 (46), 12.02 (46).

MALDI-ToF [m/z] = 771.62 $[M]^+$ (calc. 771.32), 493.46 $[C_{33}H_{53}N_2O]^+$ (calc. 493.42).

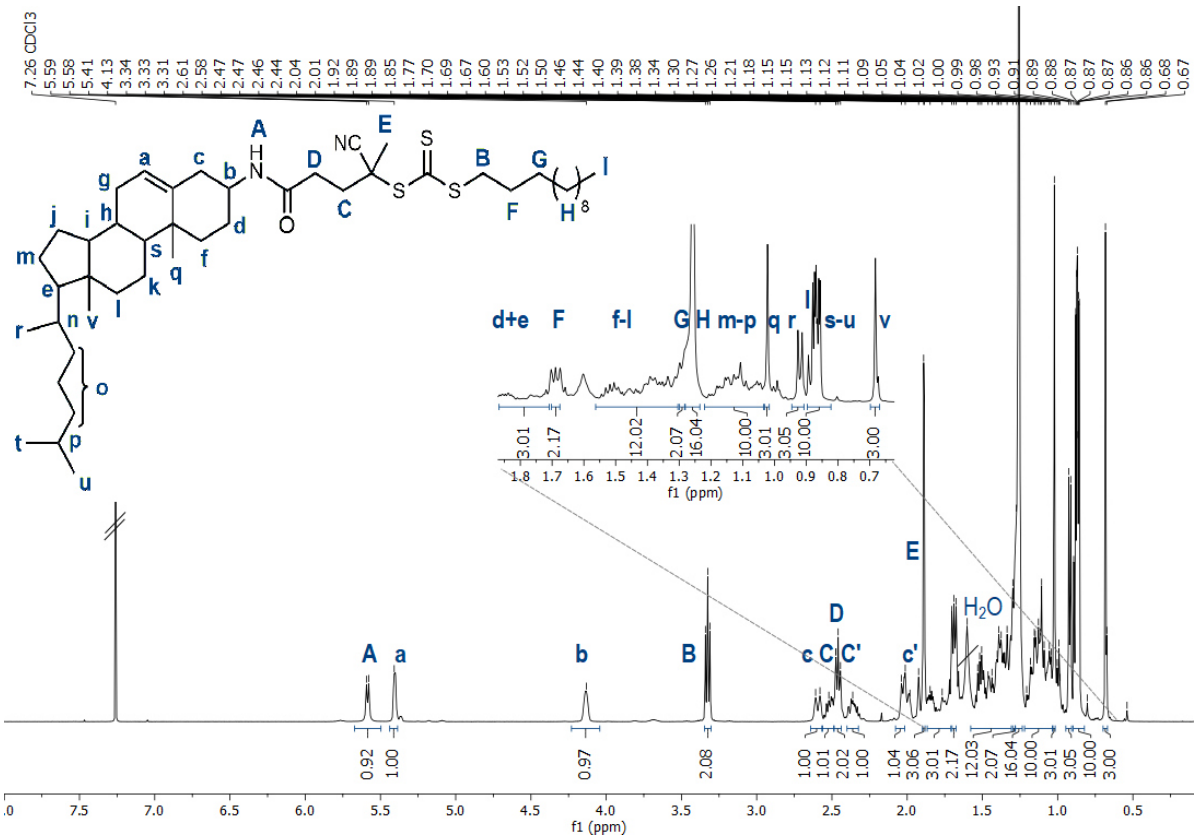

Figure S16: ^{1}H NMR spectrum (700 MHz) of Cholesterol-TTC-CTA in $CDCl_3$.

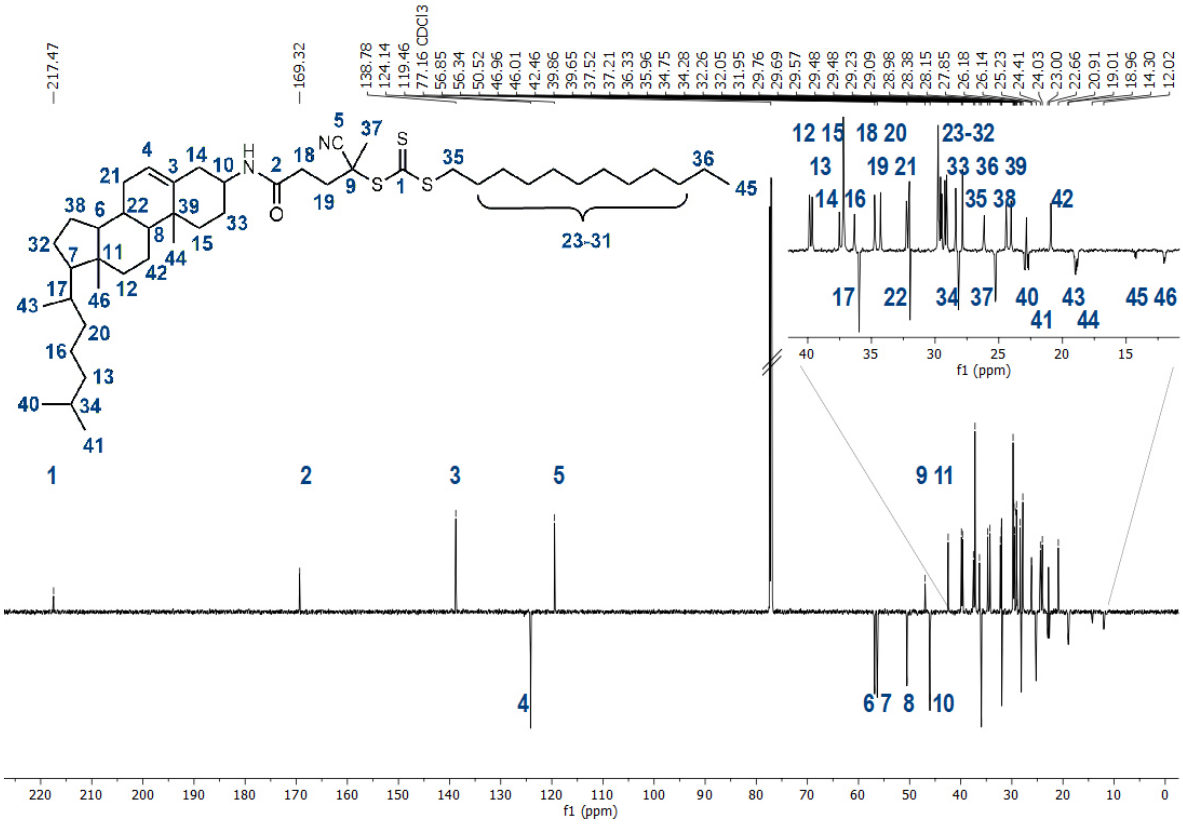

Figure S17: ^{13}C NMR spectrum (176 MHz) of Cholesterol-TTC-CTA in $CDCl_3$.

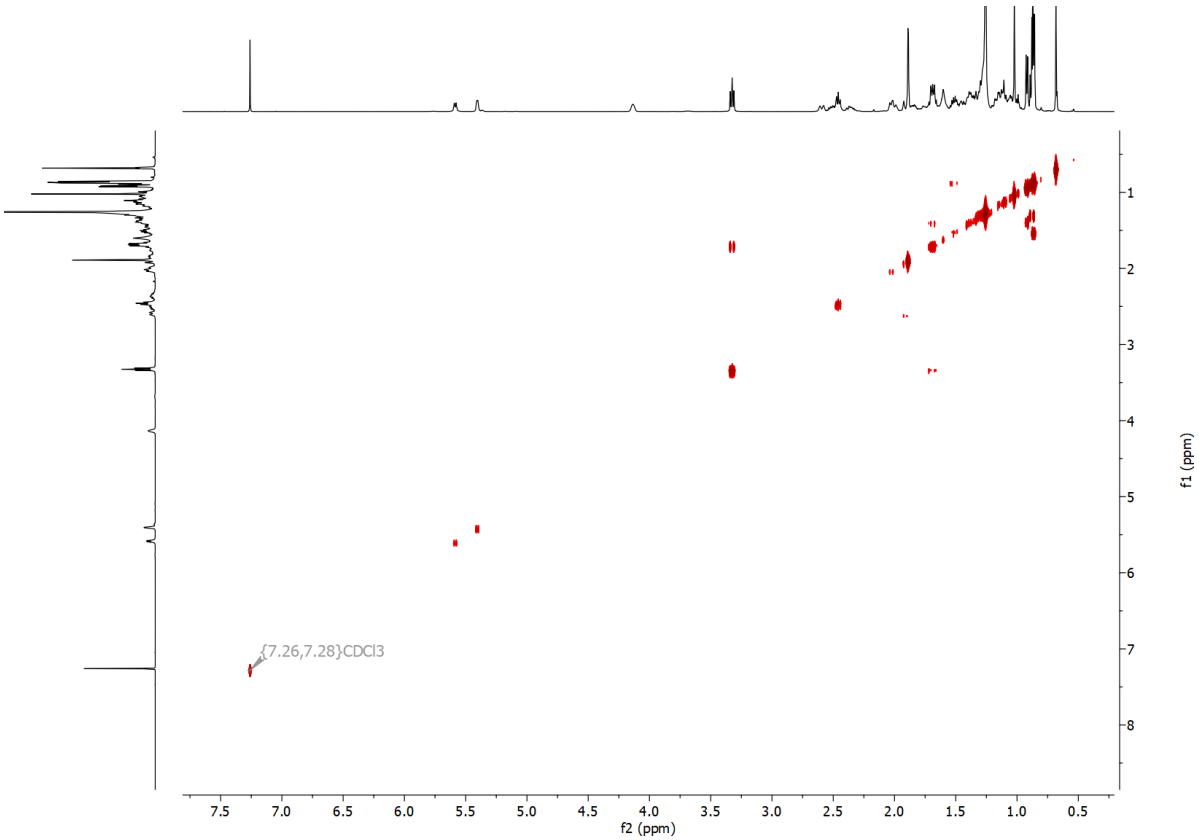

Figure S18: 2D COSY NMR spectrum of Cholesterol-TTC-CTA in $CDCl_3$.

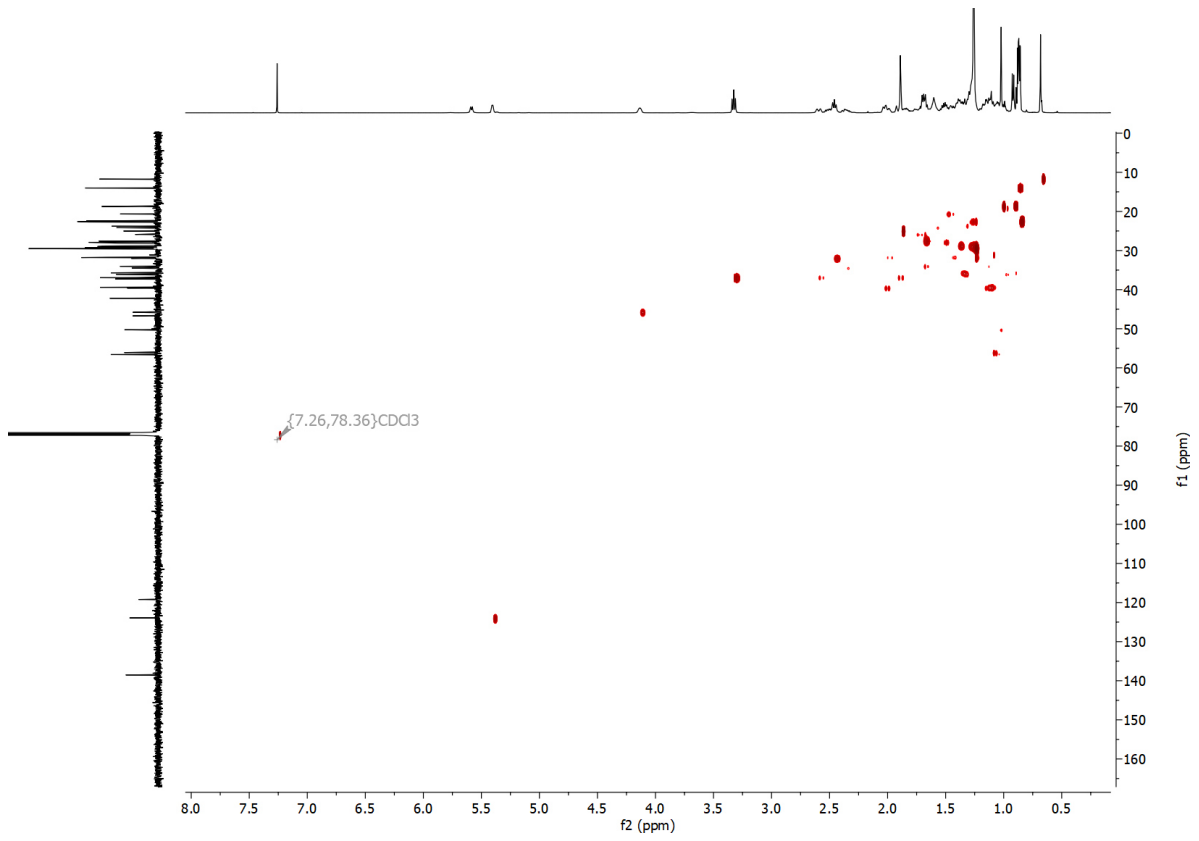

Figure S19: 2D HSQC NMR spectrum of Cholesterol-TTC-CTA in $CDCl_3$.

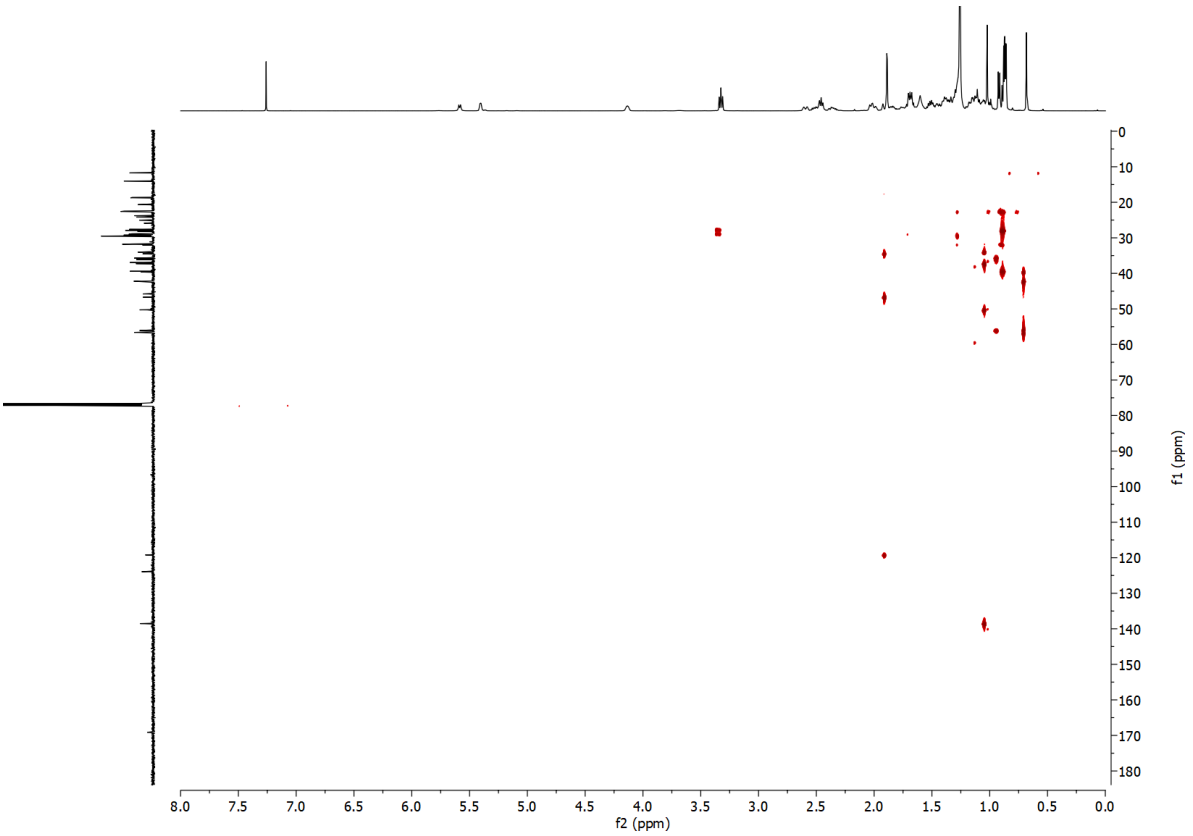

Figure S20: 2D HMBC NMR spectrum of Cholesterol-TTC-CTA in $CDCl_3$.

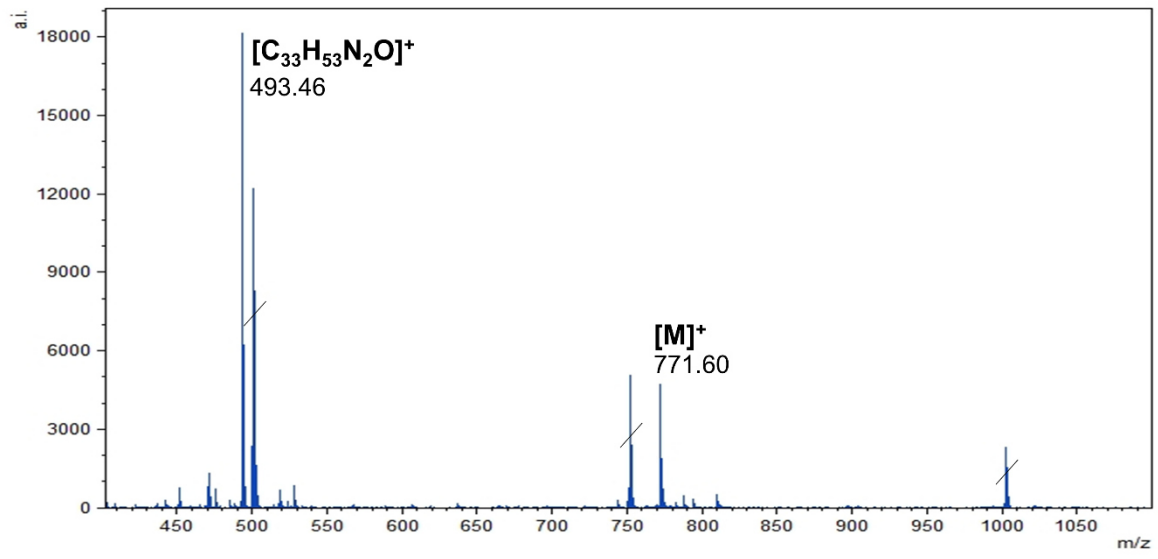

Figure S21: MALDI-ToF spectrum of Cholesterol-TTC-CTA in DCM.

Polymerization Procedure

Monomer Synthesis (PMMA-MA)

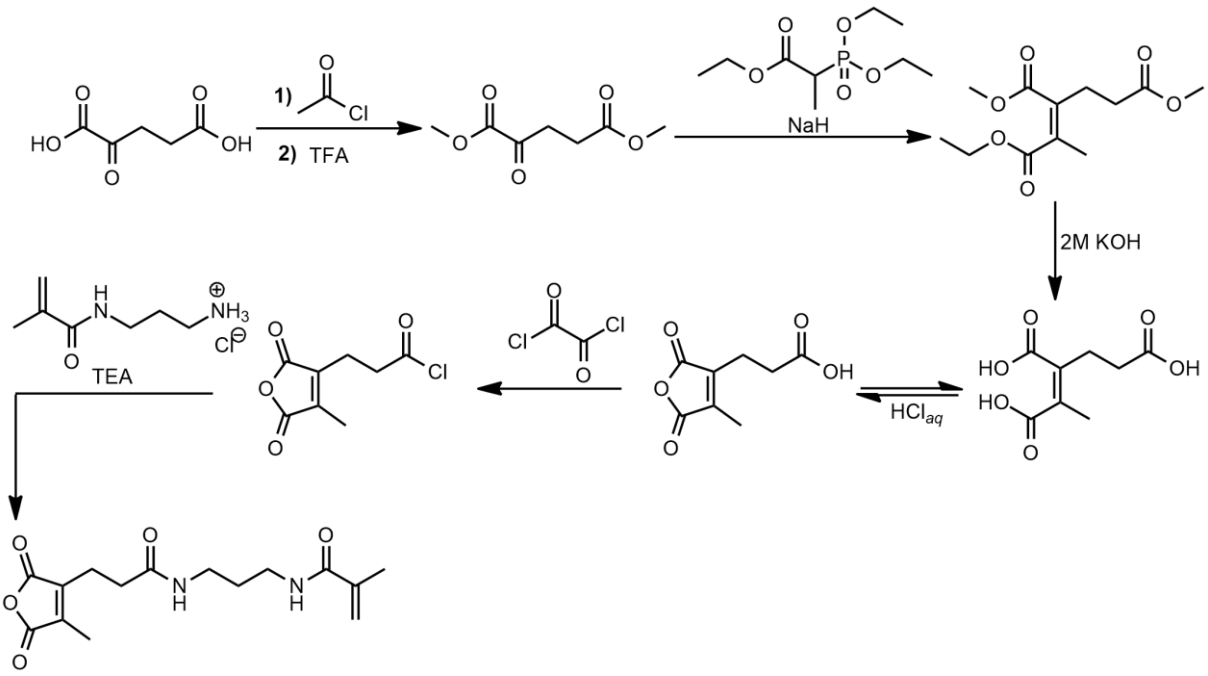

Figure S22: Synthesis scheme of the monomer N-(3-(3-(4-methyl-2,5-dioxo-2,5-dihydrofuran-3-yl)propanamido)-propyl)methacrylamide (PMMA-MA).

The monomer was synthesized as previously reported.[10]

^{1}H NMR (700 MHz, DMSO-d$_6$): δ (ppm) = 7.91 (s, 1H, **a**), 7.87 (s, 1H, **b**), 5.62 (s, 1H, **c**), 5.31 (s, 1H, **d**), 3.08 (q, *J* = 6.8 Hz, 2H, **e**), 3.02 (q, *J* = 6.8 Hz, 2H, **f**), 2.62 (t, *J* = 7.4 Hz, 2H, **g**), 2.35 (t, *J* = 7.4 Hz, 2H, **h**), 1.98 (s, 3H, **i**), 1.84 (s, 3H, **j**), 1.53 (quin, *J* = 8.4 Hz, 2H, **k**).

ESI-MS [m/z] = 309.10 $[M+H]^+$ (calc. 309.15), 331.15 $[M+Na]^+$ (calc. 331.13), 347.10 $[M+K]^+$ (calc. 347.10).

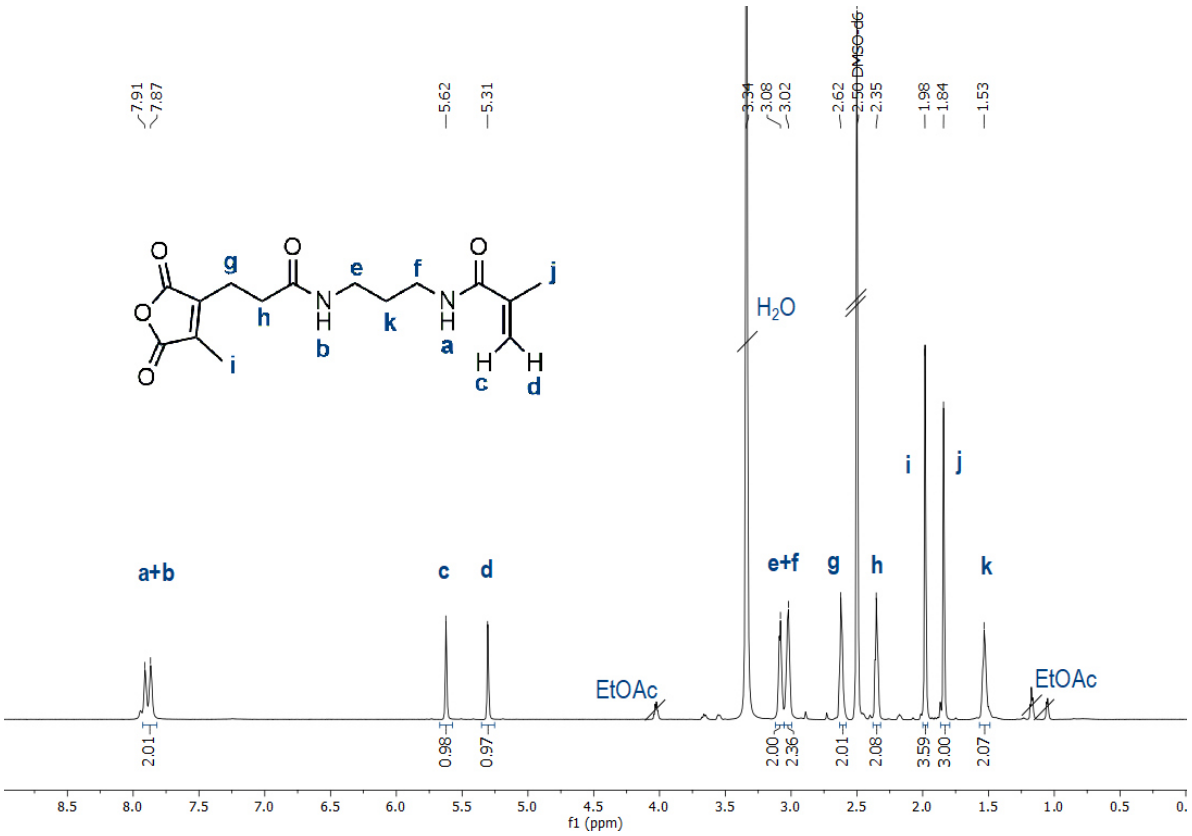

Figure S23: ^{1}H NMR spectrum (700 MHz) of the monomer N-(3-(3-(4-methyl-2,5-dioxo-2,5-dihydrofuran-3-yl)propanamido)-propyl)methacrylamide (PMMA-MA) in DMSO-d_6.

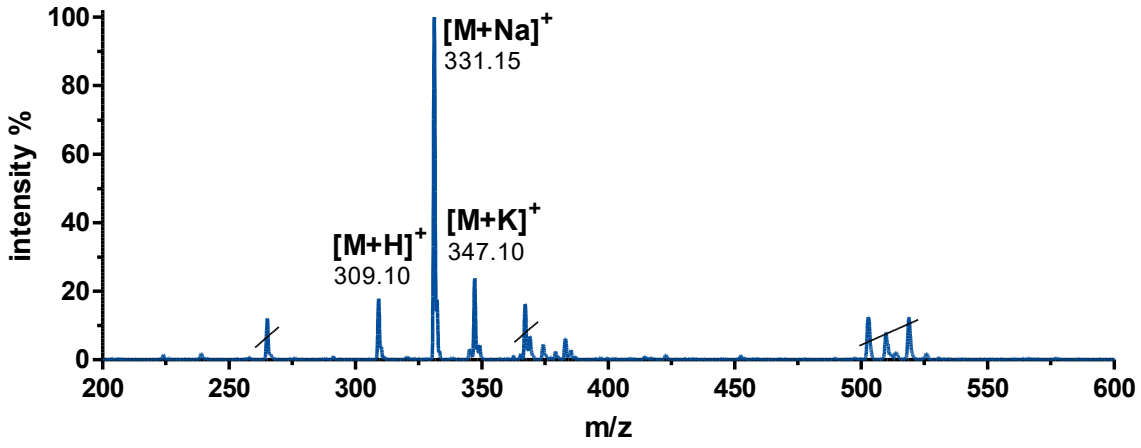

Figure S24: ESI-MS spectrum of N-(3-(3-(4-methyl-2,5-dioxo-2,5-dihydrofuran-3-yl)propanamido)-propyl)methacrylamide (PMMA-MA) in MeOH (positive ion mode).

Chol-Polymer Synthesis

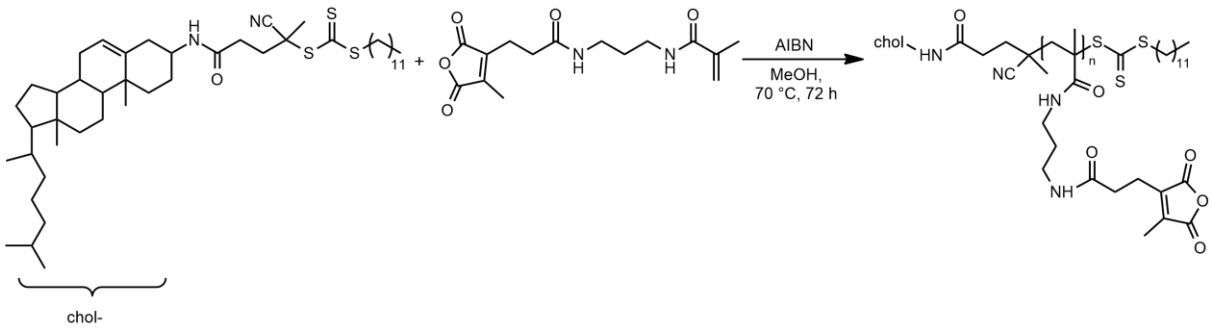

Figure S25: Synthesis of the chol-polymer with Chol-TTC-CTA and AIBN in MeOH for 72 h.

The chol-polymer was synthesized by RAFT polymerization according to the literature with minor modification.[10] Chol-TTC-CTA (7.48 mg, 9.7 µmol, 1 eq) and AIBN (0.48 mg, 2.9 µmol, 0.3 eq) were transferred into a pre-dried Schlenk flask and dissolved in 0.3 mL anhydrous methanol. PMMA-MA (150 mg, 486 µmol, 50 eq), dissolved in 0.3 mL dry methanol, was added to the mixture, followed by four freeze-pump-thaw cycles. The clear, yellow solution was stirred at 70 °C in the absence of light and oxygen. After a reaction time of 72 h, ^{1}H NMR analysis showed a monomer conversion of 60%. Threefold precipitation in cold diethyl ether (-20 °C) and drying *in vacuo* for 16 h yielded 75 mg of a pale-yellow solid (77%).

^{1}H NMR (700 MHz, DMSO-d$_6$): δ (ppm) = 7.95 (s, 1H, a), 7.81-7.14 (m, 1H, b), 5.23 (m, 1H, c), 4.09 (m, 1H, d), 3.75-3.45 (m, 2H, e), 3.08-2.94 (m, 4H, f+g), 2.62 (m, 2H, h), 2.36 (m, 2H, i), 1.99 (s, 3H, j), 1.84 (s, 3H, k), 1.57-1.44 (m, 4H, l+m), 1.33 (s, 16H, n), 1.06 (s, 3H, o), 1.00-0.83 (m, 12H, p-s), 0.82-0.68 (m, 3H, t), 0.65 (s, 3H, u).

SEC (HFIP): M_n = 2489 g/mol, M_w = 3075 g/mol, Đ = 1.23

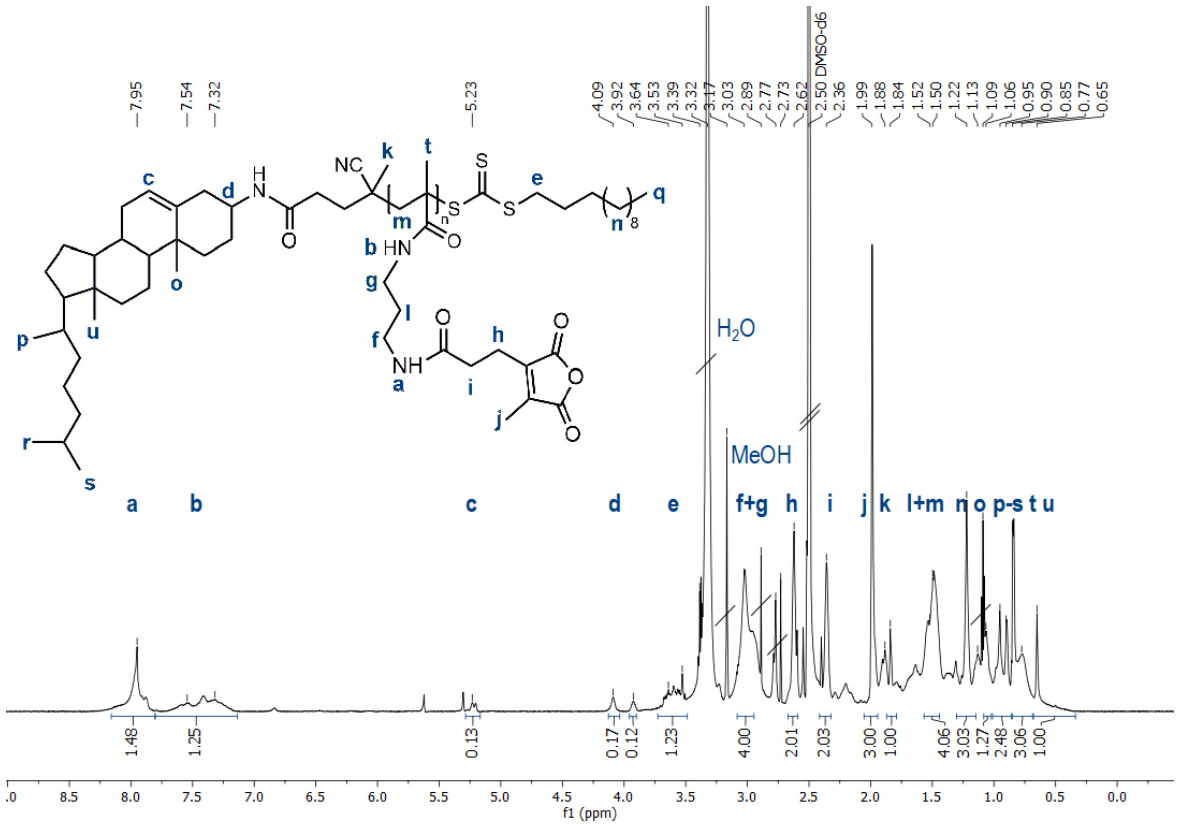

Figure S26: ^{1}H NMR spectrum (700 MHz) of the chol-polymer synthesized by RAFT polymerization in DMSO-d_6.

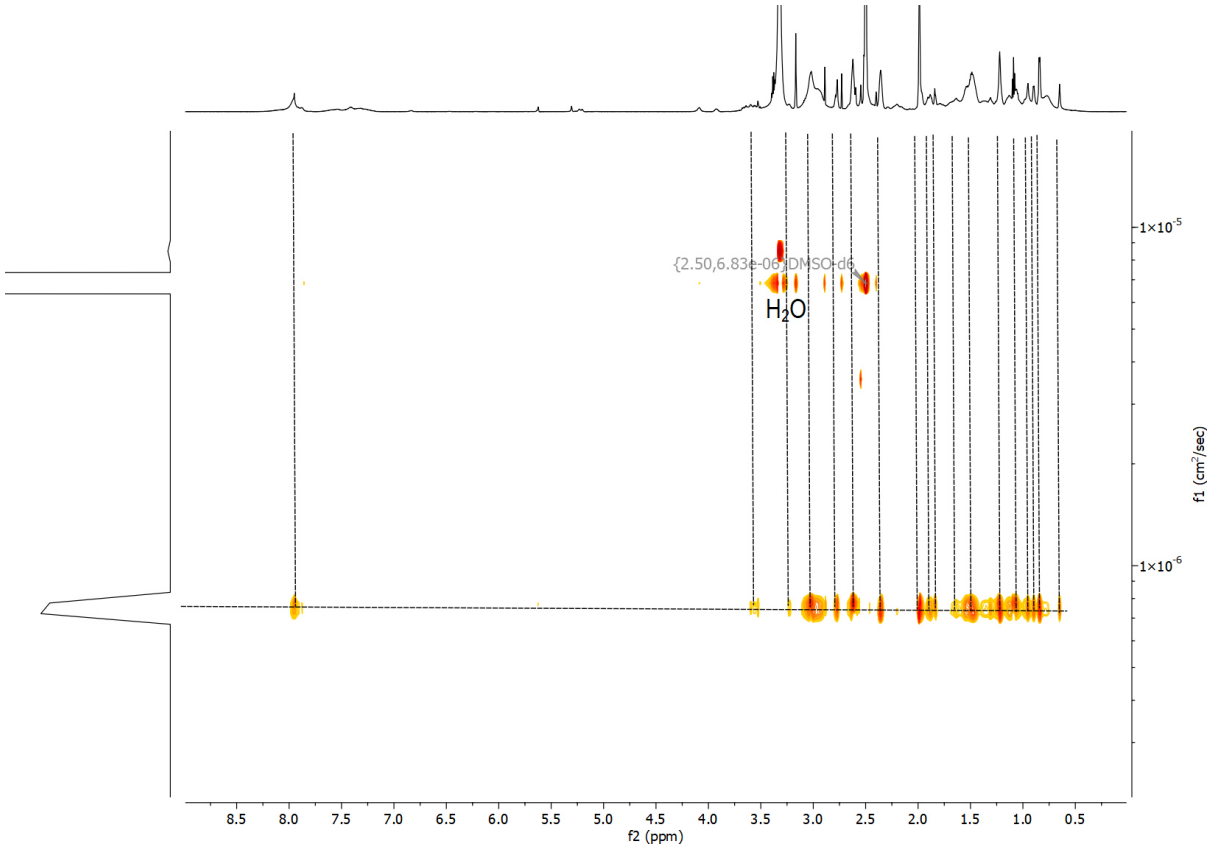

Figure S27: DOSY spectrum (700 MHz) of the chol-polymer synthesized by RAFT polymerization in DMSO-d_6.

Homopolymer Synthesis

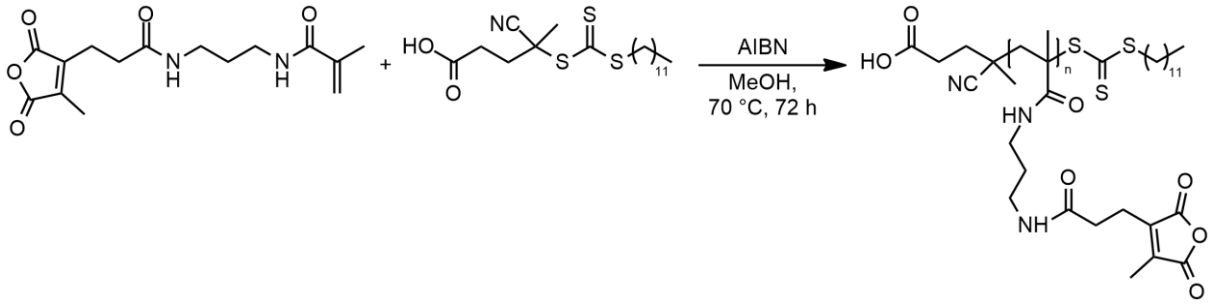

Figure S28: Synthesis of the polymer with TTC-CTA and AIBN in MeOH for 72 h.

The homopolymer was synthesized analogously to the chol-polymer procedure with 4-cyano-4-(((dodecylthio)carbonothioyl)thio)pentanoic acid (TTC-CTA) as chain transfer agent. AIBN (0.48 mg, 2.9 µmol, 0.3 eq) and TTC-CTA (3.92 mg, 9.7 µmol, 1 eq) were weighed in a Schlenk flask and dissolved in 0.3 mL dry methanol. Then, PMMA-MA (150 mg, 486 µmol, 50 eq), dissolved in 0.3 mL methanol, was transferred to the flask and the reaction mixture was degassed by four freeze-pump-thaw cycles. After heating at 70 °C for 72 h the conversion was determined by ^{1}H NMR analysis (69% conversion) and the polymer was precipitated in cold diethyl ether. The polymer was isolated as colorless solid (79 mg, 67%).

^{1}H NMR (700 MHz, DMSO-d_6): δ (ppm) = 7.95 (s, 1H, a), 7.72-7.18 (m, 1H, b), 3.02-2.95 (m, 4H, c+d), 2.62 (m, 2H, e), 2.36 (m, 2H, f), 1.99 (s, 3H, g), 1.69-1.41 (m, 4H, h+i), 1.22 (s, 2H, j) 1.04-0.53 (m, 3H, k).

SEC (HFIP): M_n = 2314 g/mol, M_w = 2866 g/mol, Đ = 1.20

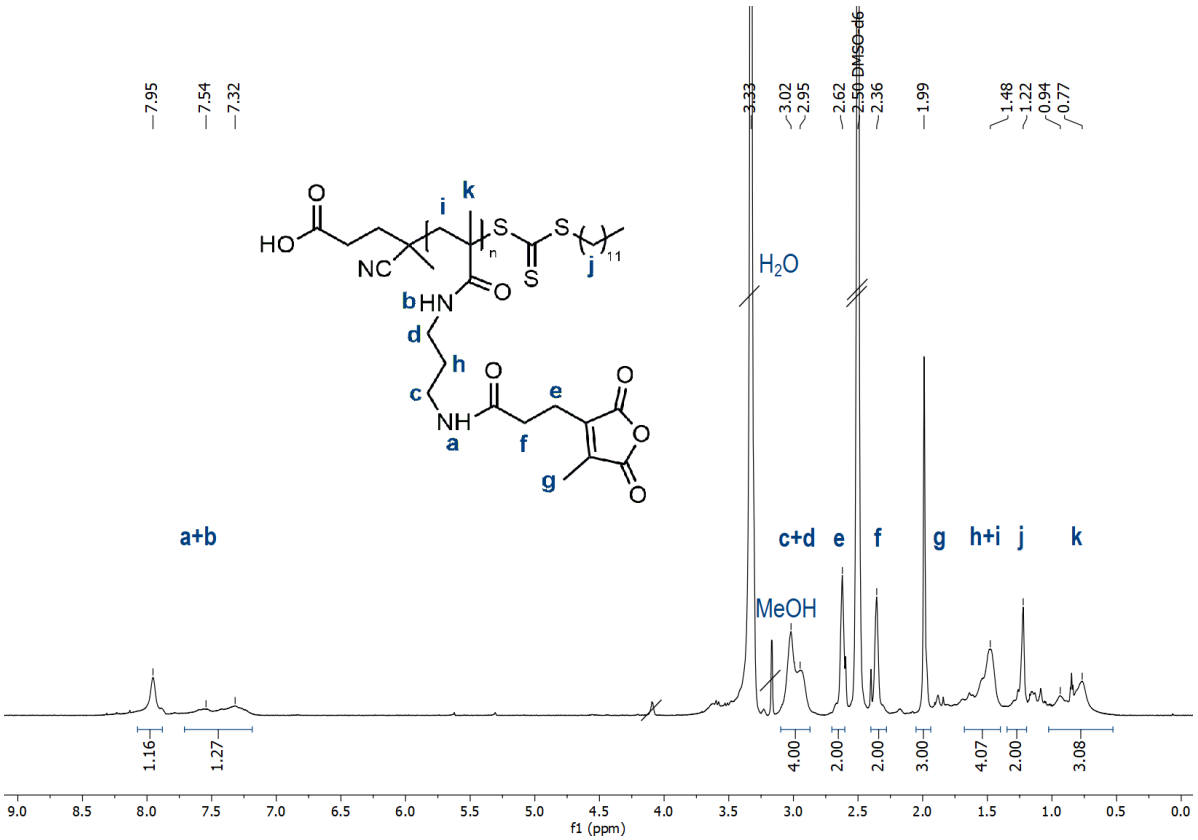

Figure S29: ^{1}H NMR spectrum (700 MHz) of the polymer synthesized under RAFT conditions in DMSO-d_6.

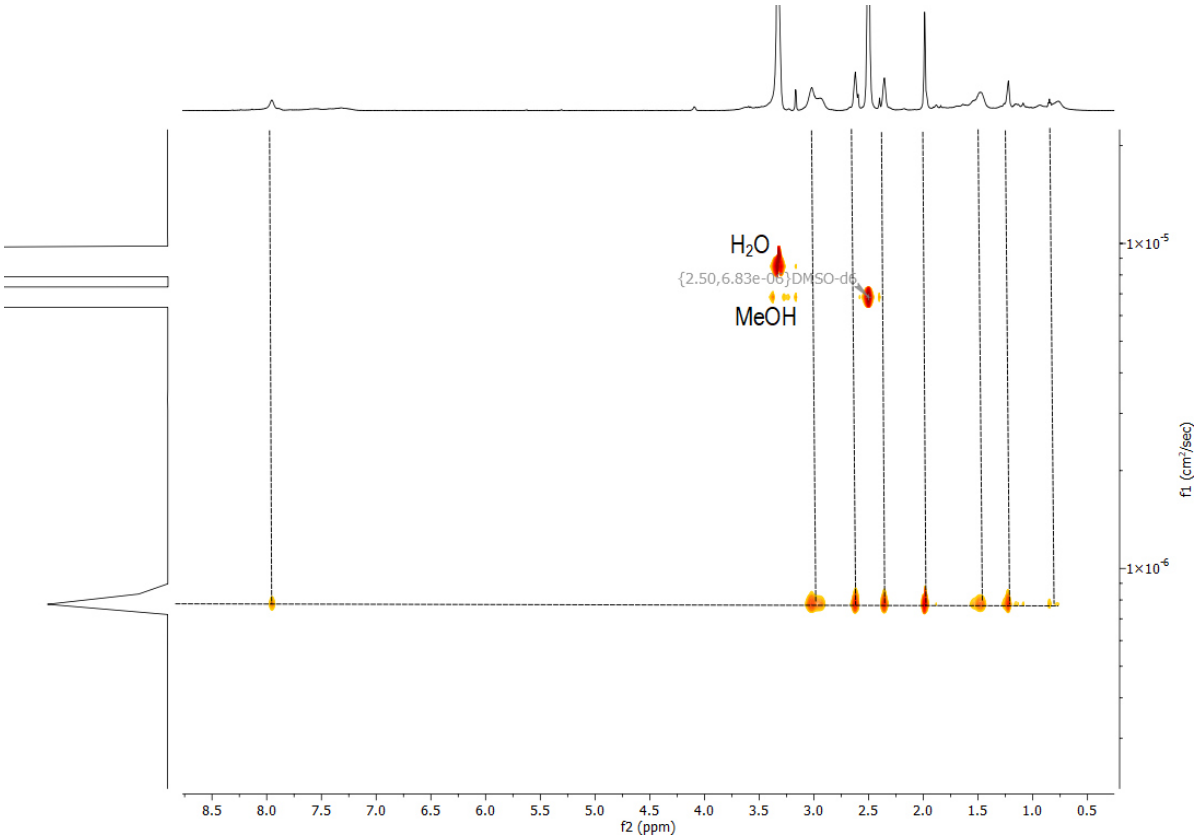

Figure S30: DOSY spectrum (700 MHz) of the polymer synthesized under RAFT conditions in DMSO-d_6.

pH-Reversible or Irreversible Polymer Modification by Amidation with Primary and Secondary Amines

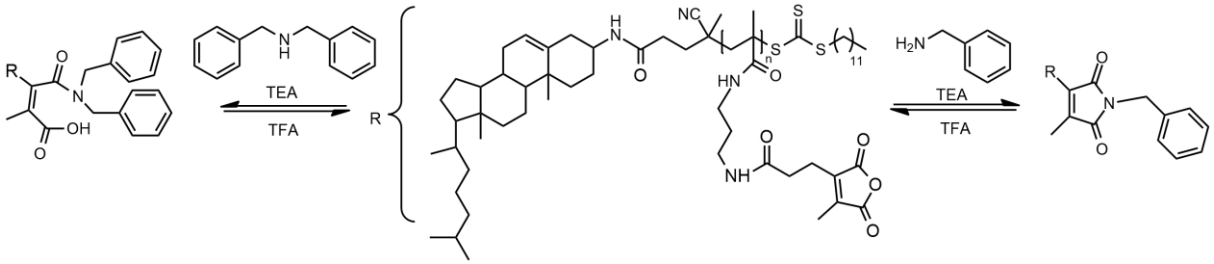

Figure S31: Schematic pH-sensitive reaction of chol-polymer chol-p(PMMA-MA)$_{30}$ with dibenzylamine or benzylamine.

The ability for pH-reversible amine conjugation was analyzed by reacting primary (benzylamine) or secondary (dibenzylamine) amines with the chol-polymer. In a Schlenk tube equipped with a stirring bar 10 mg chol-polymer (1.0 µmol/29.9 µmol reactive anhydride groups, 1 eq) was dissolved in DMSO under nitrogen atmosphere. Triethylamine (TEA) (20.79 µL, 150 µmol, 5 eq) and the corresponding amines, such as dibenzylamine (17.25 µL, 89.7 µmol, 3 eq) or benzylamine (9.81 µL, 89.7 µmol, 3 eq) were dropped to the reaction mixture. After 16 h heating at 50 °C the product was precipitated three times in diethyl ether and dried under reduced pressure overnight. The modified polymers were isolated as pale-yellow solid (14 mg, 88%) and analyzed by ^{1}H NMR and DOSY measurement.

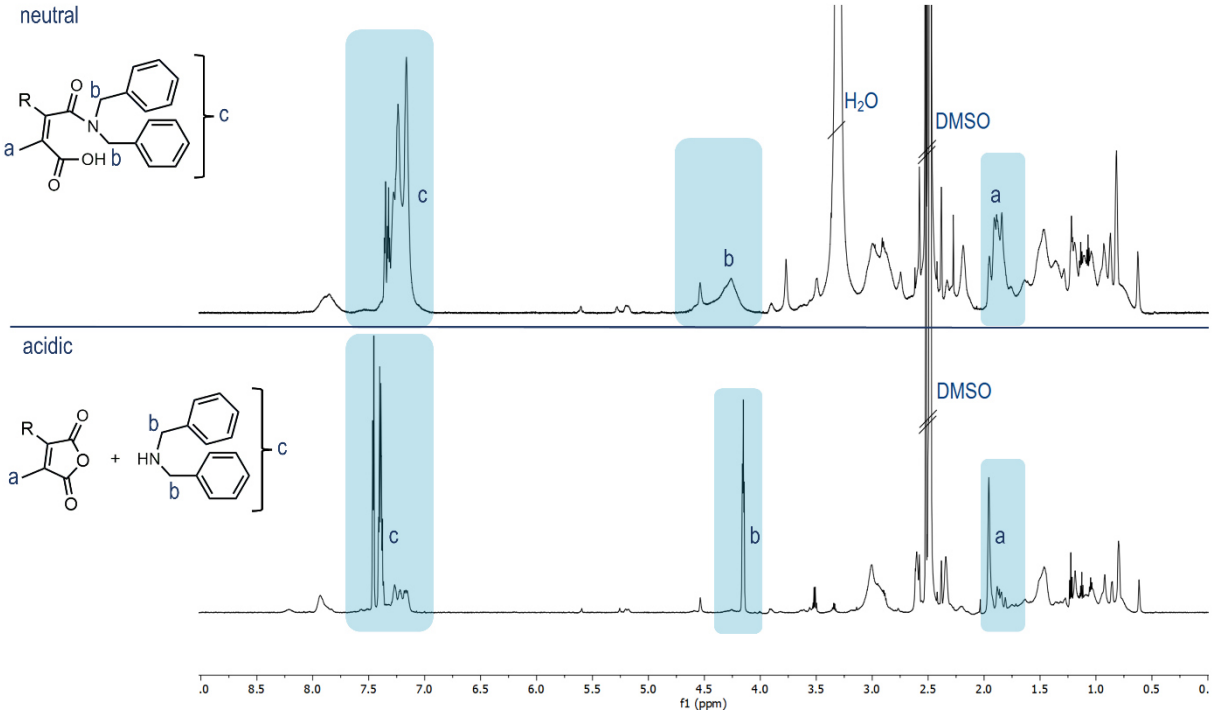

Figure S32: ^{1}H NMR spectra (700 MHz) of the chol-polymer after modification with dibenzylamine under neutral and acidic conditions in DMSO-d_6.

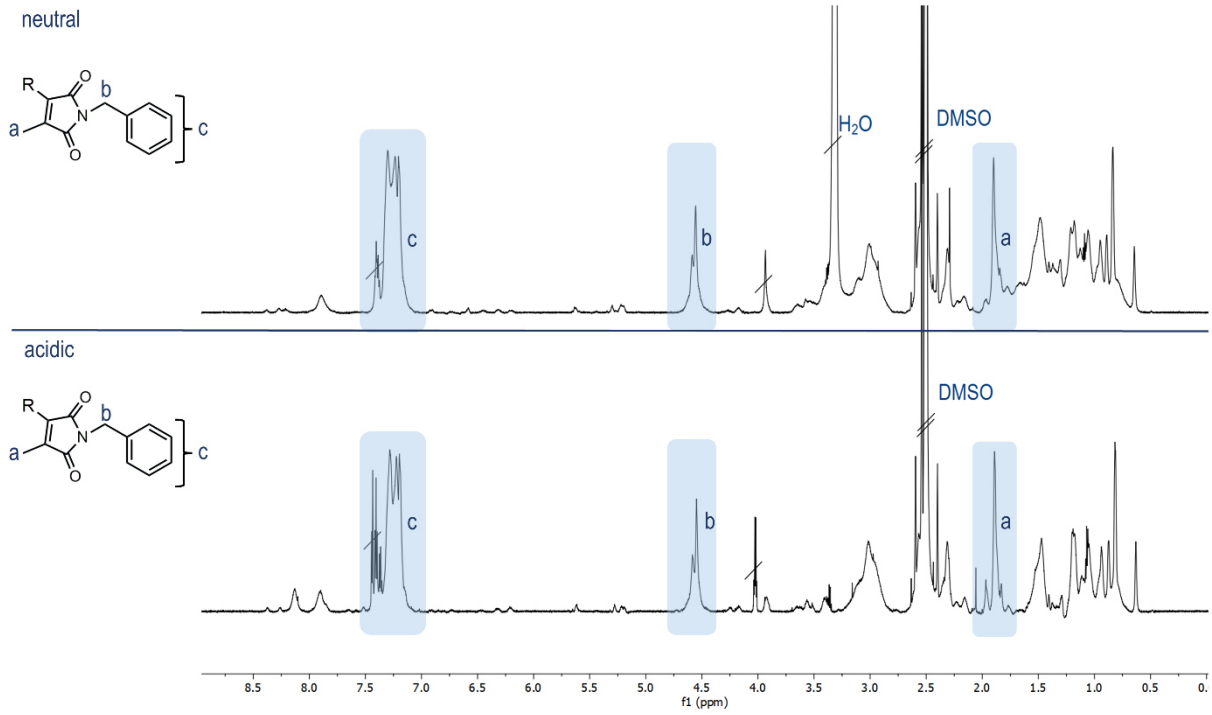

Figure S33: 1H NMR spectra (700 MHz) of the chol-polymer after modification with benzylamine under neutral and acidic conditions in DMSO-d_6.

Formulation of Dye-Labeled and PEG-Conjugated Polymers by Amidation

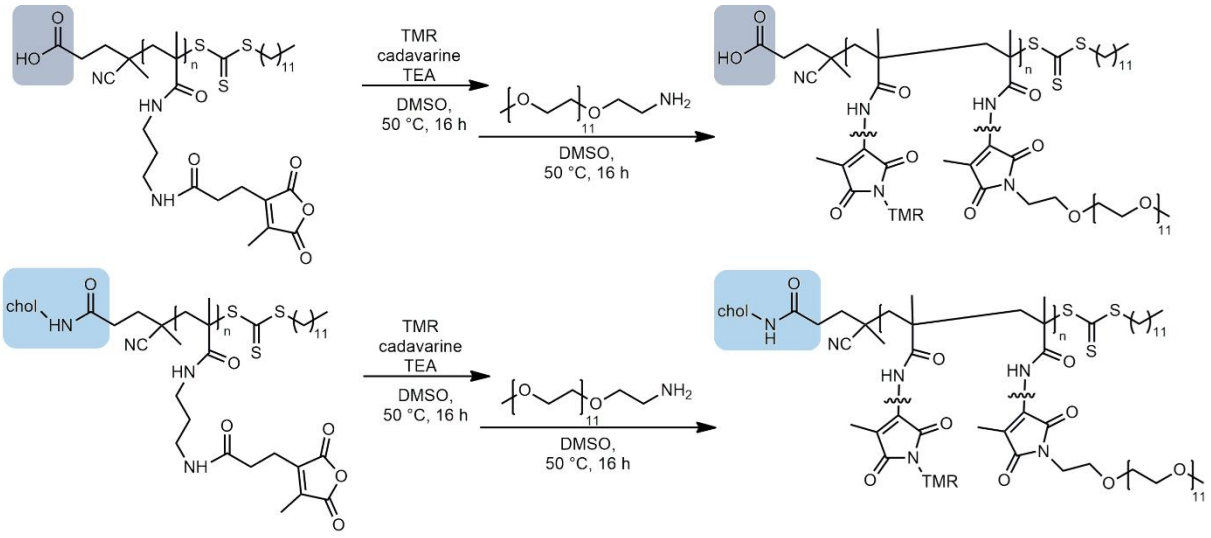

Figure S34: Schematic reaction of the homopolymer p(PMMA-MA)$_{38}$ or the chol-polymer chol-p(PMMA-MA)$_{30}$ with TMR cadaverine and mPEG$_{11}$-amine.

15 mg chol-polymer (1.50 µmol/45.0 µmol reactive anhydride groups, 1 eq) or homopolymer (1.24 µmol/47.0 µmol reactive anhydride groups, 1 eq) were dissolved in 0.5 mL anhydrous DMSO under nitrogen atmosphere. Next, TEA (31.15 µL, 225 µmol, 5 eq) / (32.57 µL, 235 µmol, 5 eq) and tetramethylrhodamine cadaverine (46.31 µL of a 5 mg/mL stock solution in DMSO, 0.45 µmol, 0.01 eq) / (48.84 µL of a 5 mg/mL stock solution in DMSO, 0.47 µmol, 0.01 eq) were added to the solutions. The reaction mixtures were stirred at 50 °C overnight. After dye conjugation, the chol-polymer and the homopolymer were reacted with mPEG$_{11}$-amine (M_n: 0.75 kDa) (1.04 mL of a 100 mg/mL stock solution in DMSO, 138 µmol, 3 eq)/ (1.06 mL, 100 mg/mL in DMSO, 141 µmol, 3 eq) and stirred for further 16 h at 50 °C. Finally, the solutions were three times precipitated in an excess of diethyl ether, centrifuged (4000 rpm, 20 min, 4 °C) and decanted. After drying *in vacuo* for 16 h the polymers were isolated as pink powder (36 mg, 74%).

SEC (HFIP) chol-p(PMMA-MA)$_{30}$: M_n = 2489 g/mol, M_w = 3075 g/mol, Đ = 1.23

SEC (HFIP) chol-p(PMMA-MA)$_{30}$ (+TMR, mPEG$_{11}$-amine): M_n = 26910 g/mol, M_w = 29879 g/mol, Đ = 1.11

SEC (HFIP) p(PMMA-MA)$_{38}$: M_n = 3932 g/mol, M_w = 4689 g/mol, Đ = 1.19

SEC (HFIP) p(PMMA-MA)$_{38}$ (+TMR, mPEG$_{11}$-amine): M_n = 28073 g/mol, M_w = 37958 g/mol, Đ = 1.35

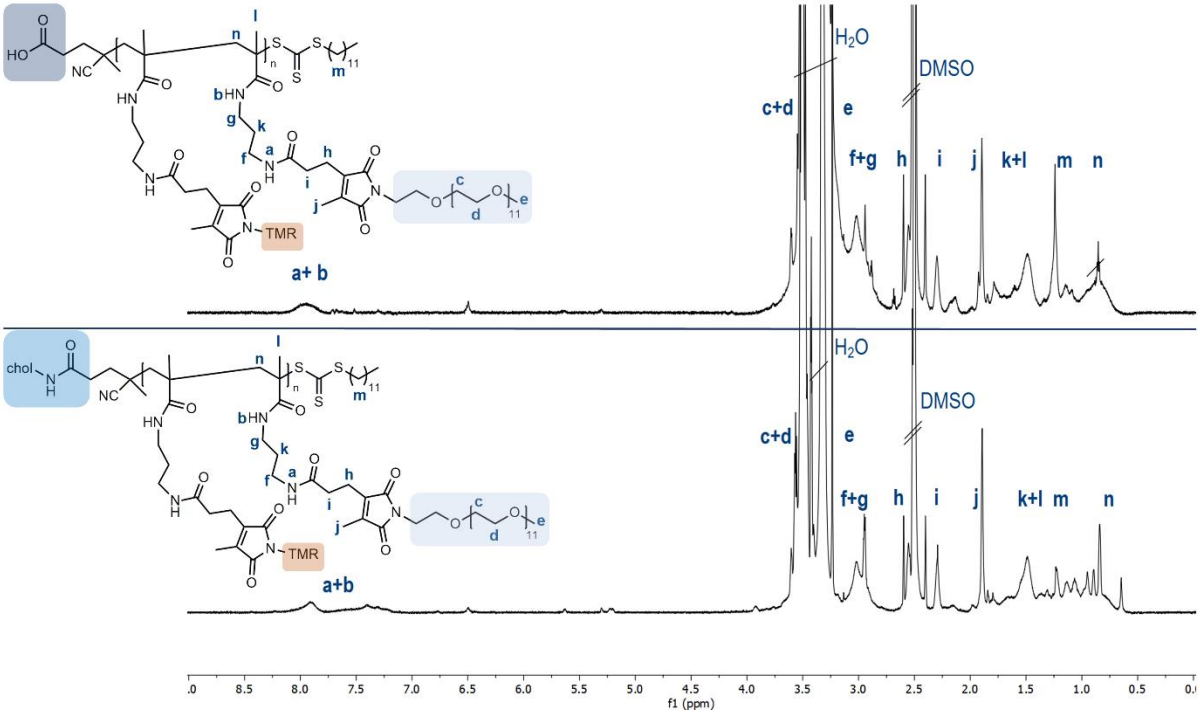

Figure S35: ^{1}H NMR spectra (700 MHz) of the homopolymer p(PMMA-MA)$_{38}$ (top) and the chol-polymer chol-p(PMMA-MA)$_{30}$ (down) after modification with TMR and mPEG$_{11}$-amine in DMSO-d$_6$.

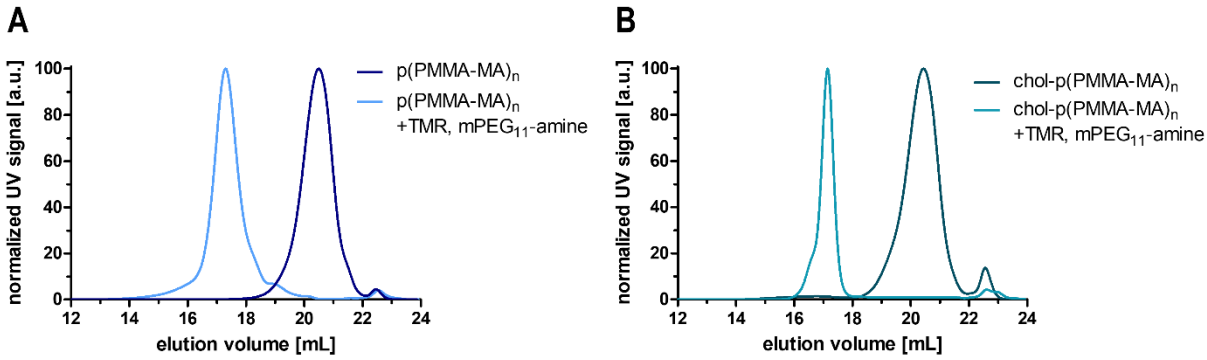

Figure S36: HFIP SEC elugrams of the homopolymer p(PMMA-MA)$_{38}$ before and after dye labeling and PEGylation (A), elugrams of the chol-polymer chol-p(PMMA-MA)$_{30}$ before and after modification (B).

Preparation of pH-Reversible and Irreversible Drug Loaded Chol-Polymers

Methylation of the Immune Stimulatory Drug Imidazoquinoline IMDQ

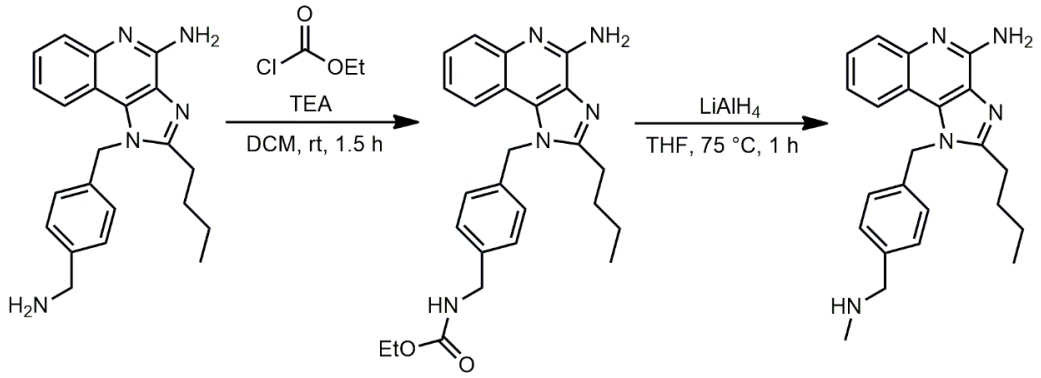

Figure S37: Synthesis of 2-butyl-1-(4-((methylamino)methyl)benzyl)-1H-imidazo[4,5-c]quinolin-4-amine (IMDQ-Me).

The synthesis of IMDQ-Me was performed similarly as previously reported[10].

^{1}H NMR (700 MHz, DMSO-d_6): δ (ppm) = 7.78 (d, *J* = 8.8 Hz,1H, a), 7.57 (d, *J* = 8.8 Hz, 1H, b), 7.37 (m, 3H, c+d), 7.01 (m, 3H, e+f), 6.53 (s, 2H, g), 5.85 (s, 2H, h), 3.73 (s, 2H, i), 2.90 (m, 2H, j), 2.30 (s, 3H, k), 1.70 (m, 2H, l), 1.38 (m, 2H, m), 1.23 (s, 1H, n), 0.86 (t, 3H, o).

ESI-MS [m/z] = 374.24 $[M+H]^+$ (calc. 374.49).

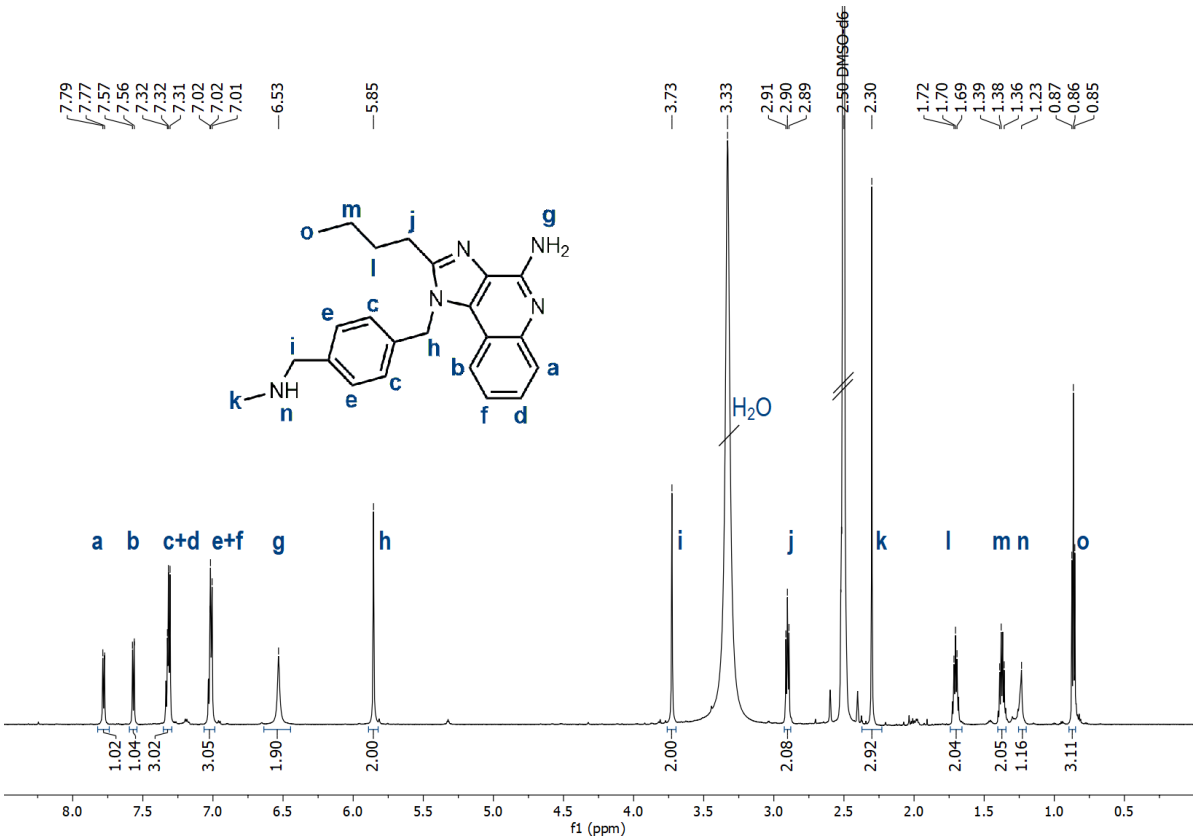

Figure S38: ^{1}H NMR spectrum (700 MHz) of 2-butyl-1-(4-((methylamino)methyl)benzyl)-1H-imidazo[4,5-c]quinolin-4-amine (IMDQ-Me) in DMSO-d_6.

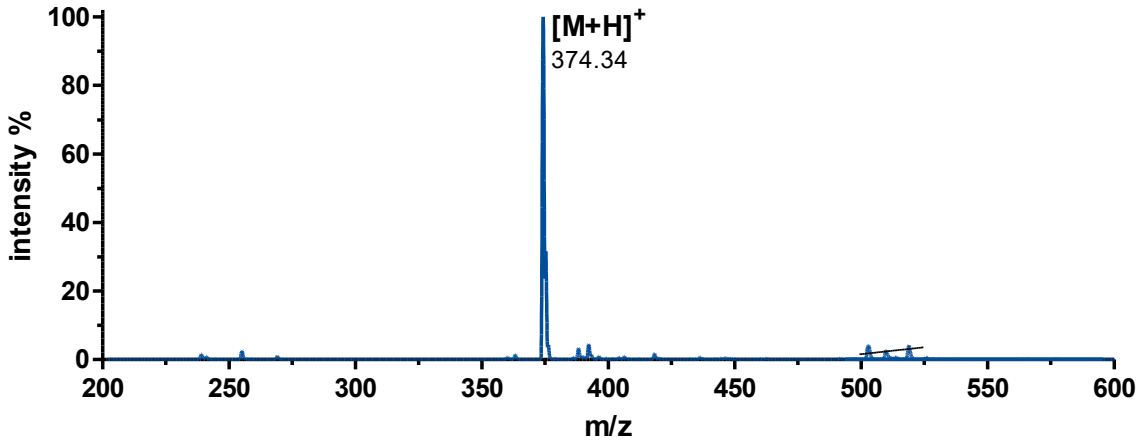

Figure S39: ESI-MS spectrum of 2-butyl-1-(4-((methylamino)methyl)benzyl)-1H-imidazo[4,5-c]quinolin-4-amine (IMDQ-Me) in MeOH (positive ion mode).

Polymer Drug Conjugation and PEGylation by Covalent Attachment of IMDQ or IMDQ-Me to the Chol-Polymer

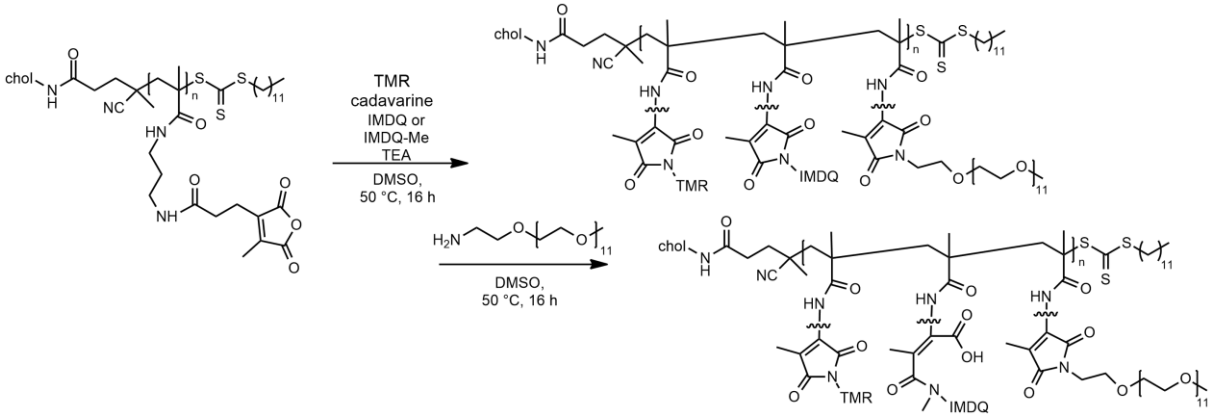

Figure S40: Schematic reaction of the chol-polymer chol-p(PMMA-MA)$_{32}$ with IMDQ or IMDQ-Me followed by PEGylation with mPEG$_{11}$-amine.

In two pre-dried Schlenk tubes the chol-polymer chol-p(PMMA-MA)$_{32}$ (2x15 mg, 1.41 µmol/45.12 µmol reactive anhydride groups, 1 eq) was dissolved in dry DMSO (0.5 mL) under nitrogen atmosphere. IMDQ (81.13 µL of a 10 mg/mL stock solution in DMSO, 2.26 µmol, 0.05 eq) or IMDQ-Me (84.30 µL of a 10 mg/mL stock solution in DMSO, 2.26 µmol, 0.05 eq) and TEA (18.76 µL, 135.4 µmol, 3 eq) were added to the solutions. The reaction mixtures were stirred at 50 °C for 16 h, followed by PEGylation with mPEG$_{11}$-amine (M_n: 0.75 kDa) (0.508 mL of a 100 mg/mL stock solution in DMSO, 67.68 µmol, 1.5 eq). The mixtures were stirred for further 16 h at 50 °C. Next, the drug-loaded polymers were precipitated three times in diethyl ether. Diethyl ether was decanted, and the obtained chol-polymers were dried under high vacuum for 16 h. The modified chol-polymers were isolated as pink powder (38 mg, 83%).

SEC (HFIP) chol-p(PMMA-MA)$_{32}$: M_n = 1993 g/mol, M_w = 2463 g/mol, Đ = 1.23

SEC (HFIP) chol-p(PMMA-MA)$_{32}$ (+IMDQ, TMR, mPEG$_{11}$-amine): M_n = 35609 g/mol, M_w = 40116 g/mol, Đ = 1.13

SEC (HFIP) p(PMMA-MA)$_{32}$ (+IMDQ-Me, TMR, mPEG$_{11}$-amine): M_n = 36572 g/mol, M_w = 40822 g/mol, Đ = 1.12

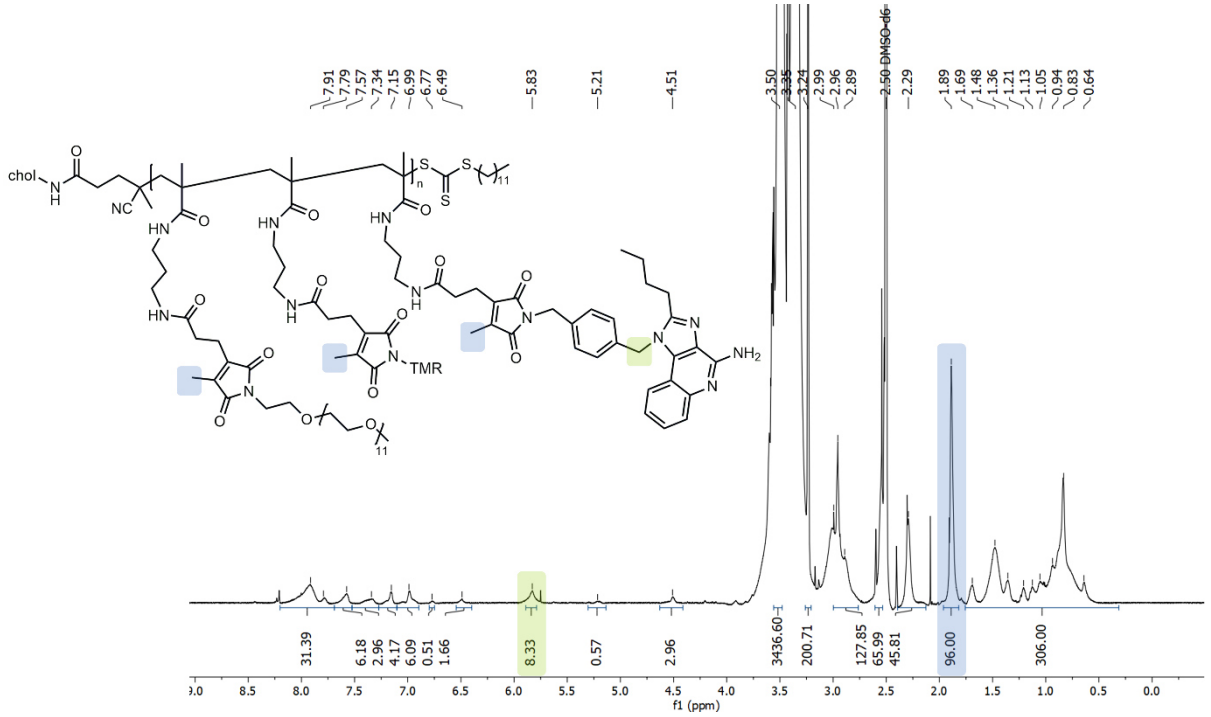

Figure S41: ^{1}H NMR spectrum (700 MHz) of the chol-p(PMMA-MA)$_{32}$ after dye labeling, drug loading with IMDQ and PEGylation with mPEG$_{11}$-amine in DMSO-d$_6$.

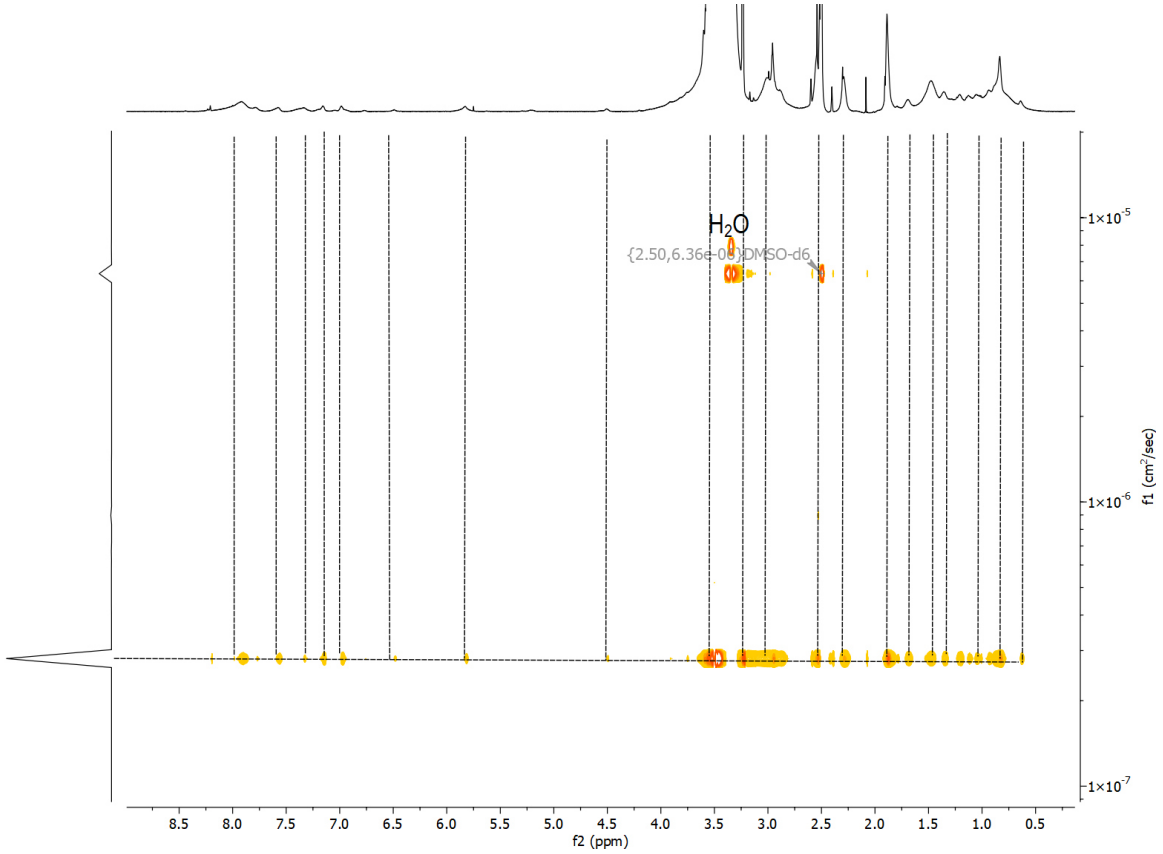

Figure S42: DOSY spectrum (700 MHz) of the chol-polymer p(PMMA-MA)$_{32}$ after dye labeling, drug loading with IMDQ and PEGylation with mPEG$_{11}$-amine in DMSO-d$_6$.

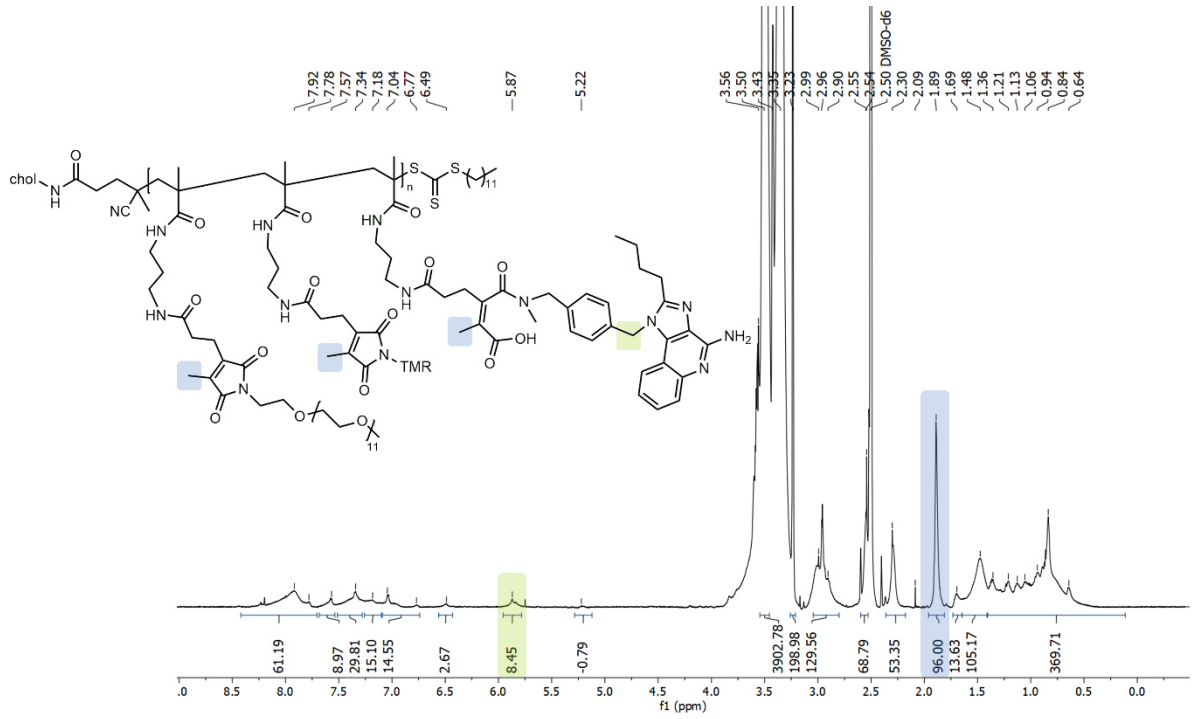

Figure S43: ^{1}H NMR spectrum (700 MHz) of the chol-polymer chol-p(PMMA-MA)$_{32}$ after dye labeling, drug loading with IMDQ-Me and PEGylation with mPEG$_{11}$-amine in DMSO-d$_6$.

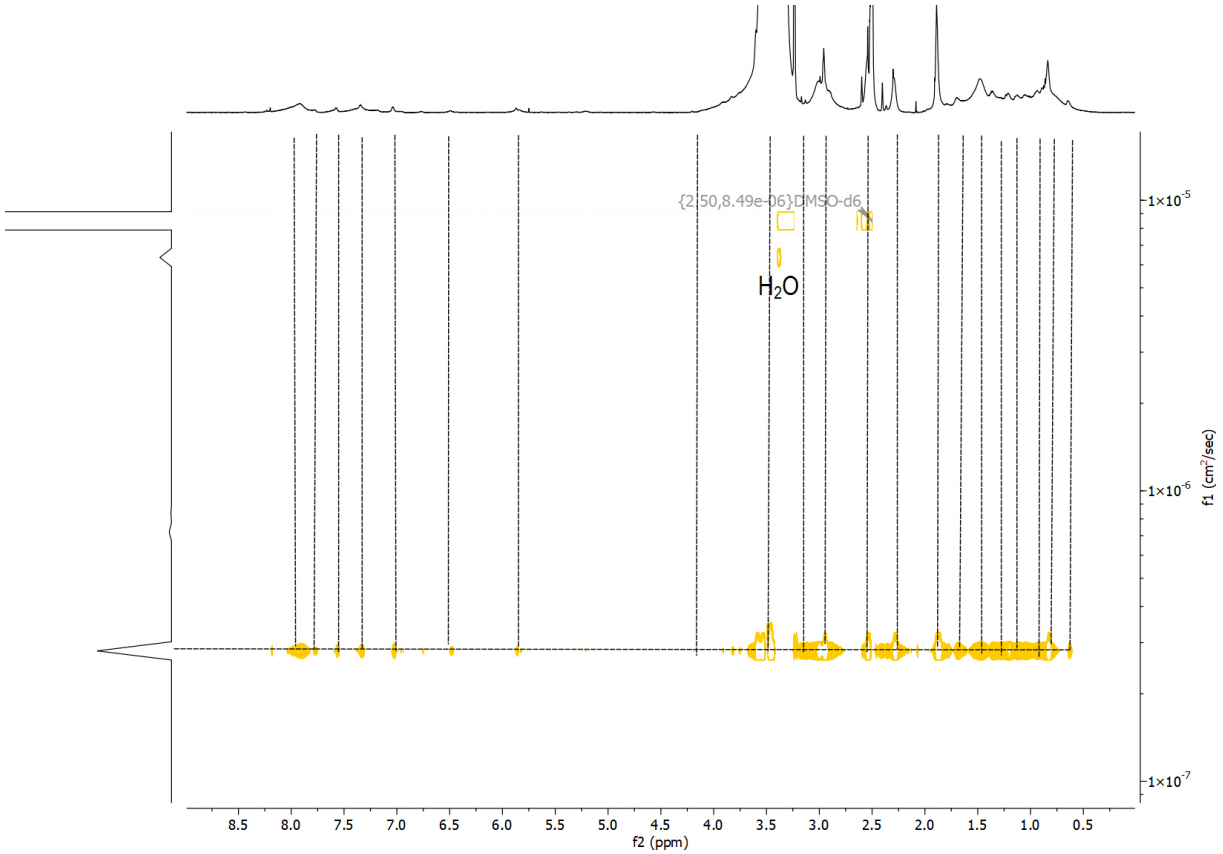

Figure S44: DOSY spectrum (700 MHz) of the chol-polymer chol-p(PMMA-MA)$_{32}$ after dye labeling, drug loading with IMDQ-Me and PEGylation with mPEG$_{11}$-amine in DMSO-d$_6$.

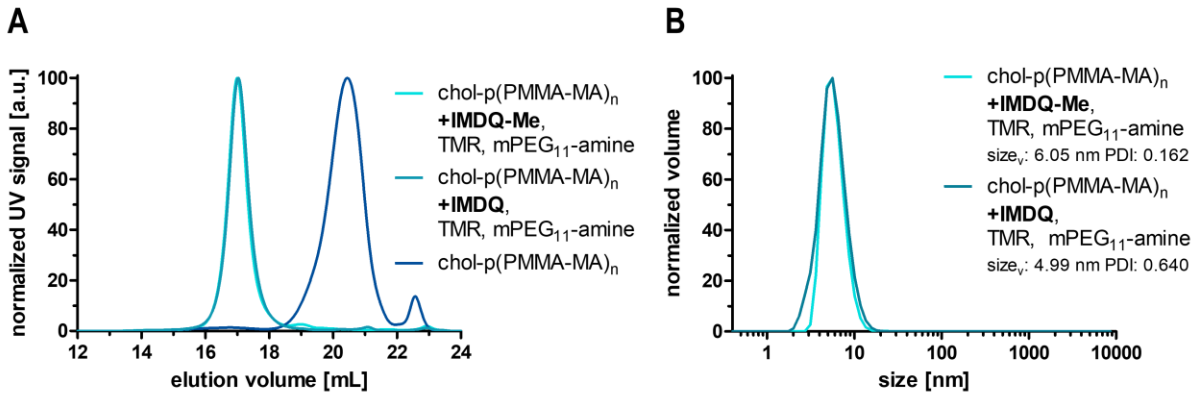

Figure S45: HFIP SEC traces of TMR-labeled, IMDQ- or IMDQ-Me-loaded and PEGylated chol-polymer (A), and the DLS volume-weighted size distribution in PBS of the fully soluble polymers do not forming micelles or aggregates (B).

Calculation of IMDQ or IMDQ-Me Drug Loading by ^{1}H NMR and UV-Vis Analysis

The drug load of the modified chol-polymers was determined by ^{1}H NMR and UV-Vis measurement. For ^{1}H NMR analysis the chol-polymers were dissolved in deuterated DMSO and 3 H of =C-CH3 were used as a reference.

Calculation of the IMDQ-drug load to the chol-polymer:

Polymer DP = 32

3 H of =C-CH3 → **96 H**

IMDQ proton signal: 8.33 H → 2 H of Bn-CH2-N → 4.165 IMDQ/polymer

4.165 · 359 g/mol : 32594 g/mol → **4.6 wt%**

Calculation of the IMDQ-Me-drug load to the chol-polymer:

Polymer DP = 32

3 H of =C-CH3 → **96 H**

IMDQ-Me proton signal: 8.45 H → 2 H of Bn-CH2-N → 4.225 IMDQ-Me/polymer

4.225 · 373 g/mol : 32742 g/mol → **4.8 wt%**

For the determination of the drug load by UV-Vis analysis standard curves were created. Therefore, free drug stock solutions (10 mg/mL) were diluted in PBS and measured at different concentrations (ranging from 0.1 to 0.0031 mg/mL). According to the literature the drug load

of the formulated chol-polymers was calculated.[11] The free drugs IMDQ and IMDQ-Me show a strong absorbance maximum at 322 nm, while the corresponding drug-loaded chol-polymers have absorbance maximum at 324 nm.

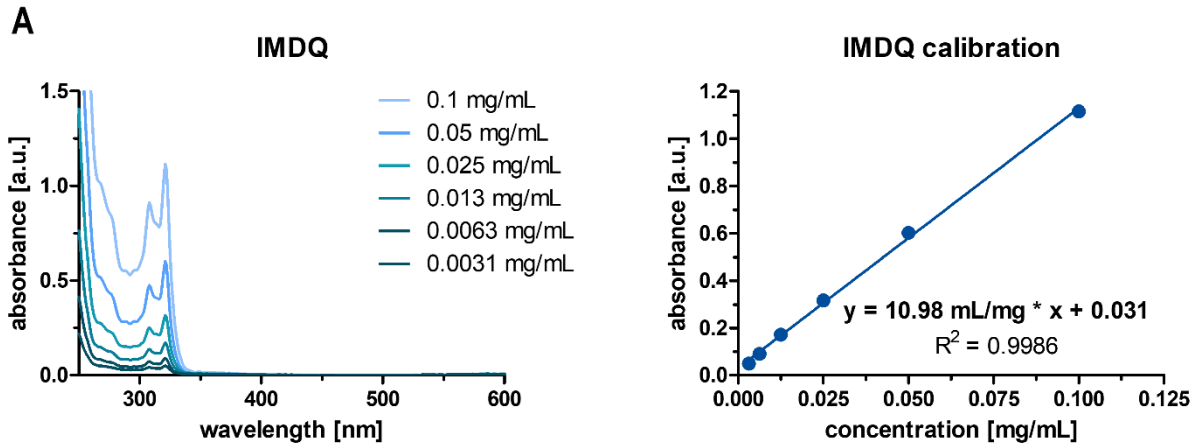

Figure S46: UV-Vis spectra of IMDQ at different concentrations in PBS (left) and the corresponding calibration curve (right).

Calculation of the IMDQ drug load to the chol-polymer:

$$X = \frac{(\Delta A - b)}{m - (A_{empty} / c)}$$

$X = 0.021 / 0.5$ mg/mL

$X =$ **4.2 wt%**

$\mathbf{\Delta A} = A_{max}$ (IMDQ chol-polymer) $- A_{max}$ (chol-polymer)
$= 0.557 - 0.307 = 0.250$

$\mathbf{b} = 0.031$

$\mathbf{m} = 10.98$ mL/mg

$\mathbf{A_{empty}} = 0.307$

$\mathbf{c} = 0.5$ mg/mL

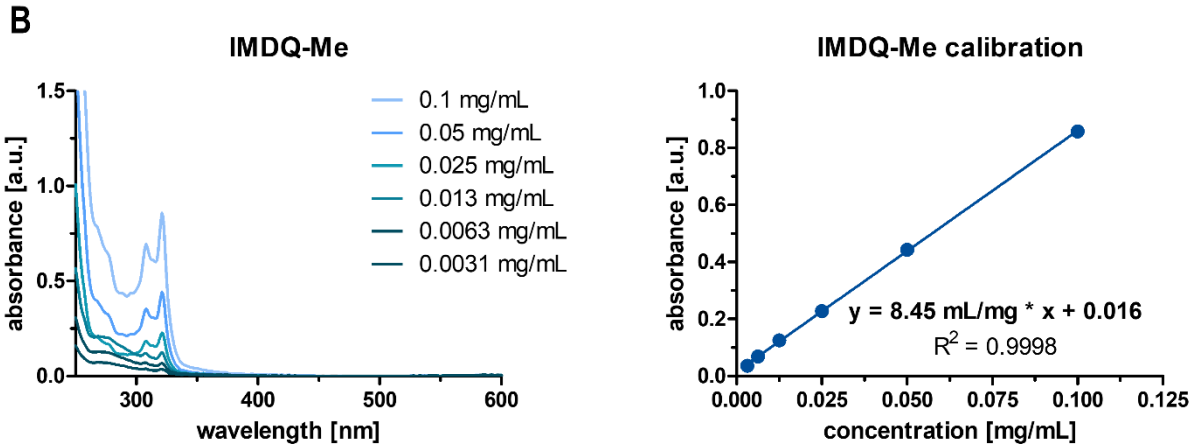

Figure S47: UV-Vis spectra of IMDQ-Me at different concentrations in PBS (left) and the corresponding calibration curve (right). Calculation of the IMDQ-Me drug load to the chol-polymer.

$$X = \frac{(\Delta A - b)}{m - (A_{empty} / c)}$$

$X = 0.023 / 0.5$ mg/mL

$X =$ **4.5 wt%**

$\mathbf{\Delta A} = A_{max}$ (IMDQ-Me chol-polymer) $- A_{max}$ (chol-polymer)
$= 0.507 - 0.307 = 0.200$

$\mathbf{b} = 0.016$

$\mathbf{m} = 8.45$ mL/mg

$\mathbf{A_{empty}} = 0.307$

$\mathbf{c} = 0.5$ mg/mL

The drug load of the chol-polymers was determined by the average of ^{1}H NMR and UV-Vis analysis.

IMDQ chol-polymer drug load = **4.4 wt%**

IMDQ-Me chol-polymer drug load = **4.7 wt%**

In vitro Experiments

Determination of Chol-Polymer/Polymer Cell Uptake by Flow Cytometry (FACS)

For cellular uptake studies in RAW-Dual macrophages, cells were seeded into 24-well plates (250000 cells/well in 900 µL of culture medium) and incubated overnight. After 20 h cells were treated with 100 µL of tetramethylrhodamine-labeled, PEGylated chol-polymer or the corresponding polymer without cholesterol in PBS (yielding a concentration of 10, 30 or 100 µg/mL). The experiment was conducted for 24 h at 37 °C. Then, the medium was removed, cells were washed with 1 mL PBS and incubated with 500 µL cell dissociation buffer for 15 min at 37 °C. Afterwards, the cell suspensions were transferred into Eppendorf tubes on ice and centrifuged at 300 g for 10 minutes at 5 °C. The supernatants were removed, and the cell pellets were resuspended in 200 µL of PBS, to be analyzed on a BD Accuri C6 (BD Biosciences). All data were processed by FlowJo Software and all samples were run in triplicates (n=3).

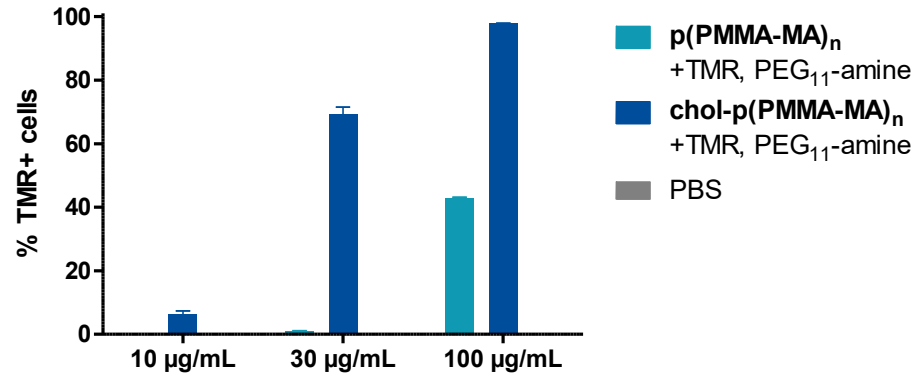

Figure S48: Flow cytometric uptake analysis in RAW-Dual macrophages incubated with PBS (control), TMR-labeled polymer PEGylated with PEG_{11}-amine or TMR-labeled chol-polymer PEGylated with PEG_{11}-amine at 10, 30 and 100 µg/mL for 24 h. Flow cytometry measurements yielding the percentage of TMR positive cells (% TMR+ cells).

Fluorescent Confocal Microscopy Imaging

For fluorescent confocal laser scanning microscopy RAW-Dual macrophages were seeded in an Ibidi µ-slide 8-well chamber (50000 cells/well in 180 µL culture medium) and left to adhere overnight. Next, the cells were incubated with 20 µL TMR-labeled, PEGylated chol-polymer or the corresponding polymer solutions in PBS (total concentration of 100 µg/mL) for 24 h at 37 °C. Then, the medium was removed, and the cells were three times washed with PBS and fixed with 200 µL 4% paraformaldehyde solution for 15 min at 37 °C. Afterwards, the cells were washed again three times with PBS and cell nuclei were stained with 125 µL 4′,6-diamidino-2-phenylindole (DAPI) (80 µg/mL in PBS) for 20 min at room temperature. Finally, after washing with PBS three times the samples were stored under aqueous mounting medium and analyzed on a STELLARIS 8 Leica DMi8 confocal microscope (Wetzlar, Germany) with a HC PL APO CS2 40x/1.25 GLYC oil immersion objective. All images were processes by Leica Application Suite X 3.7.4.23463 of the Leica Microsystem.

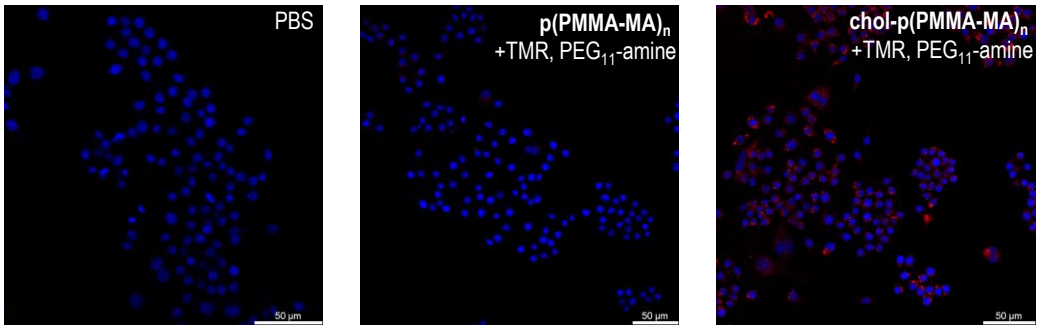

Figure S49: Confocal microscopy images of RAW-Dual macrophages incubated with PBS (control), TMR-labeled, PEGylated **polymer** or TMR-labeled, PEGylated **chol-polymer** at 100 µg/mL for 24 h (blue: nuclei stained with Hoechst 33258, red: TMR-labeled polymer).

Determination of the Cellular Metabolic Activity by MTT Assay on Stimulated RAW-Dual Macrophages

Determination of the cellular metabolic activity can be used as an indicator for cell viability and cytotoxicity. Therefore, RAW-Dual macrophages were seeded in a 96-well plate at a concentration of 90000 cells/well in 180 µL and left to adhere for 20 h. The cells were treated with 20 µL IMDQ- or IMDQ-Me-loaded chol-polymer, free drugs, or chol-polymer solution at given concentration. All experiments were performed in quadruplicates. After 24 h of incubation time at 37 °C 30 µL of a 2 mg/mL 3-(4,5-dimethylthiazol-2-yl)-2,5-diphenyl-tetrazolium bromide solution in PBS was added, and cells were incubated for further 1.5 h at 37 °C. Formed formazan crystals were dissolved by addition of 100 µL of 10% m/v SDS/0.01 M HCl solution and incubated overnight at 37 °C. Quantification of the metabolic activity was done by measuring the absorbance at 570 nm using a plate reader.

RAW-Dual Macrophage TLR Reporter Assay (QUANTI-Blue Assay)

To analyze the immune modulatory properties of IMDQ/IMDQ-Me-conjugated chol-polymers a TLR reporter assay was performed as recommended by the manufacturer (InvivoGen). The IMDQ-induced downstream activation of NF-κB/AP-1 was determined by the secretion of embryonic alkaline phosphatase (SEAP). RAW-Dual cells were seeded similarly as previously reported for the MTT assay and incubated with 20 µL of the respective solutions at the given IMDQ/IMDQ-Me concentration. After 24 h incubation at 37 °C, 50 µL of the supernatant was collected and the SEAP levels were probed by QUANTI-Blue Assay. After incubation for 2 h at 37 °C with 150 µL QUANTI-Blue solution, wells were read-out for their absorbance at 620 nm using a plate reader. All experiments were conducted at n=4.

BMDCs (Bone marrow derived dendritic cells)

Bone marrow (BM) cells were isolated from femurs and tibiae of C57BL/6 mice followed by resuspension in IMDM medium containing 5% FBS, 2 mM L-glutamine, 100 IU/ml penicillin, 100 µg/ml streptomycin and 50 µM β-Mercaptoethanol (all reagents were obtained from Sigma-Aldrich, Deisenhofen, Germany), supplemented with 10 ng/ml recombinant murine GM-CSF (R&D Systems, Wiesbaden, Germany). Next, BM cells were seeded in 12-well suspension cell culture cluster plates ($2x10^5$/ml). After 3 and 6 days the culture media was replenished. On days 7-8, the differentiated cells were treated with IMDQ- or IMDQ-Me-loaded chol-polymer,

soluble IMDQ and IMDQ-Me, or chol-polymer solution. After incubation for 24 h, samples were harvested and analyzed by flow cytometry. All experiments were performed in triplicates.

Flow Cytometry

Prior to flow cytometric analysis all samples were pretreated with a rat anti-mouse CD16/CD32 antibody (15 min, 4 °C) to prevent Fc-mediated binding of subsequently applied antibody (clone 2.4G2; 15 min, room temperature). Afterwards, samples were incubated (20 min, 4 °C) with distinct sets of fluorescence-labeled antibodies as indicated in table S1. Samples were left untreated, incubated with the according cholesterol polymer samples alone or with single antibody serving as controls. Subsequently, FVD was added to all samples to delineate dead cells. Antibodies were purchased from BD Biosciences, Thermo Fisher or BioLegend. FVD was obtained from Thermo Fisher. Afterwards, samples were fixed (4% paraformaldehyde, 2mM EDTA) and analyzed in an Attune NxT flow cytometer (Thermo Fisher). The resulting data were processed by Attune Nxt Software v3.1.1. following the gating strategy (Figure 50).

Table S1: Antibodies used to characterize BMDCs and their maturation/activation.

Cell Type	**Cell Marker**	**Antibody**	**Fluorochrome**	**Clone**
BMDC GM-CSF	DC	CD11c	PE-Cy7, BV421	N418
Others Cell Staining		**Antibody**	**Fluorochrome**	**Clone**
Activation		CD80	PE, PerCP-eFl780	16-10A1
		CD86	FITC	GL1
Fc Block		CD16/32	n.a.	2.4G2
Live/Dead		Fixable Viability Dye	eFl450, eFl780	n.a.

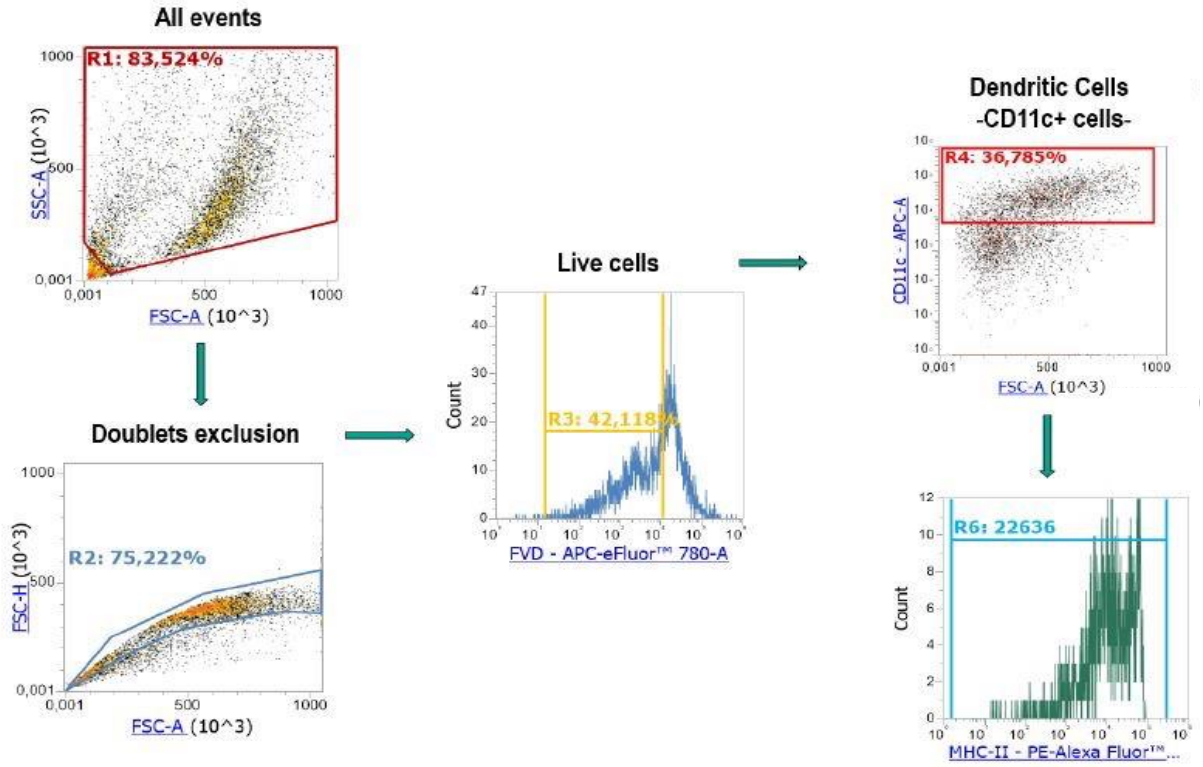

Figure S50: Gating strategy of BMDCs-GM CSF. After exclusion of debris, doublets, and dead cells (fixable viability dye $[FVD]^-$), $CD11c^+$ cells were characterized for the activation markers CD80 and CD86.

Cytometric Bead Assay

Supernatants of cell cultures were retrieved and stored at −20 °C for subsequent analysis. TNFα, IL-1β and IL-6 cytokines were quantified using a Cytometric Bead Assay (CBA; BD Biosciences) as recommended by the manufacturer. For this purpose, the kit used a bead-based multiplex assay with fluorescence–encoded beads that were conjugated with cytokine-specific capture antibodies. Samples were mixed with capture beads, subsequently incubated with detection antibodies and then with PE-conjugated detection antibodies (all at room temperature protected from light under shaking) and subjected to flow cytometric analysis. The obtained results were analyzed using FCAP Array Analysis Software v.1.0.1 (BD Biosciences).

In Vivo Experiments

Bioactivity of IMDQ- or IMDQ-Me-Conjugated Chol-Polymers

To study the immune stimulatory effect of IMDQ- or IMDQ-Me-conjugated chol-polymers, heterozygous BALB/c INF-β (IFN-$\beta^{+/\Delta\beta\text{- luc}}$) reporter mice in the range of 7–9 weeks were housed in individual ventilated cages and given ad libitum access to food and water. 20 µL of the IMDQ- or IMDQ-Me-conjugated chol-polymers as well as soluble IMDQ and IMDQ-Me were injected subcutaneously in the footpad at an equivalent dose of 10 µg IMDQ or IMDQ-Me. Additional, mice treated with PBS or polymer with or without cholesterol served as controls (n = 3 or 4). For subsequent *in vivo* bioactivity imaging, mice were injected subcutaneously with 200 µL D-luciferin (15 mg/ mL, Gold Biotechnology, USA) at 4 and 24 h, and *in vivo* luminescence imaging was recorded 12 min later using the IVIS Lumina II imaging system from PerkinElmer, (Waltham, MA, USA). Photon flux was analyzed by Living Image 4.4 software from Caliper life sciences (Hopkinton, MA, USA).

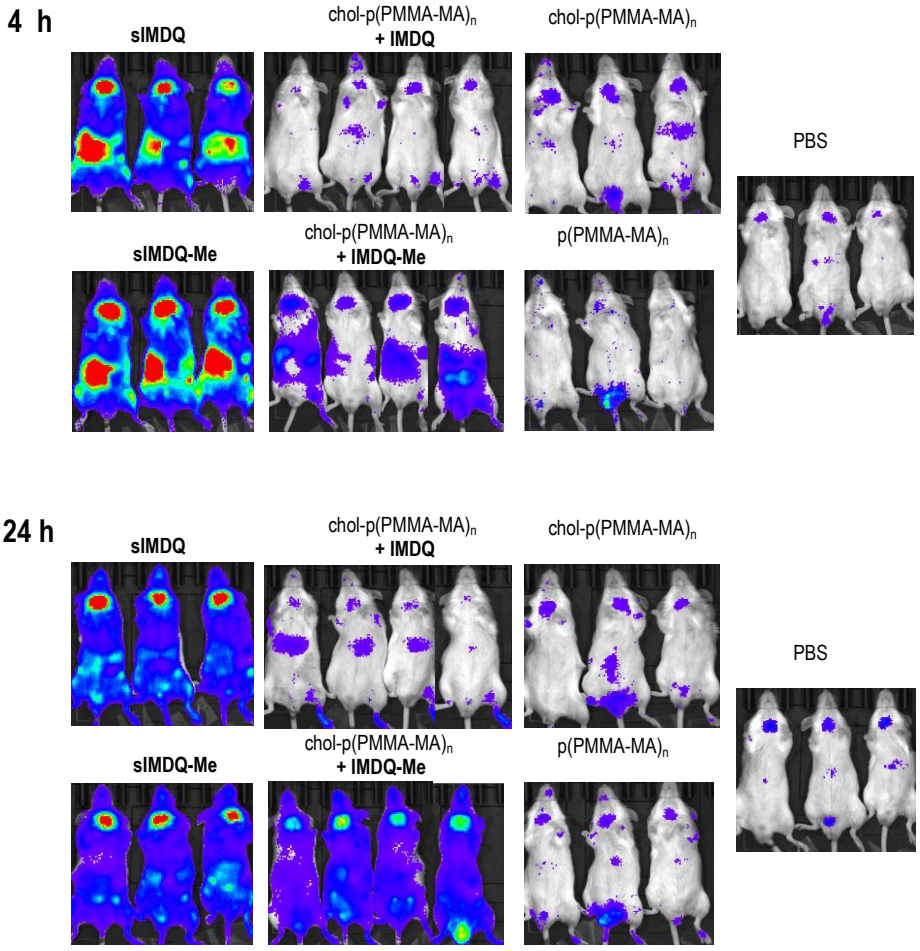

Figure S51: In vivo bioactivity of soluble and chol-p(PMMA-MA)$_n$ conjugated IMDQ and IMDQ-Me as well as chol-p(PMMA-MA)$_n$ and p(PMMA-MA)$_n$ after footpad injection into heterozygous BALB/c IFN-β (IFN-$\beta^{+/\Delta\beta\text{-luc}}$) reporter mice (n = 3 or 4).

Analysis of Lymphocyte Targeting and Activation

Heterozygous BALB/c IFN-β (IFN-β+/Δβ-luc) reporter mice were subcutaneously injected in the footpad with 10 µg IMDQ or IMDQ-Me (soluble or bound to the chol-polymers in 20 µL of PBS, n=3) and sacrificed after 48 h. Popliteal lymph nodes were isolated for flow cytometry. A single cell suspension was prepared form three of the dissected lymph nodes for analysis by flow cytometry. The isolated lymph nodes were collected in ice cold PBS, smashed through 70 µm cell strainers, washed with PBS and stained for 30 min at 4 °C with a live-dead stain and the following primary labeled monoclonal antibodies: CD3, CD4, CD8, CD11c, CD11b, CD19, CD45, CD69, CD86, CD172a, CCR7, XCR7, F4-80, and MHC-II. 123count beads were added to determine cellularity prior to acquiring them by flow cytometry (BD FACS Aria). Analyses were done using the FlowJo software package according to the gating procedure.

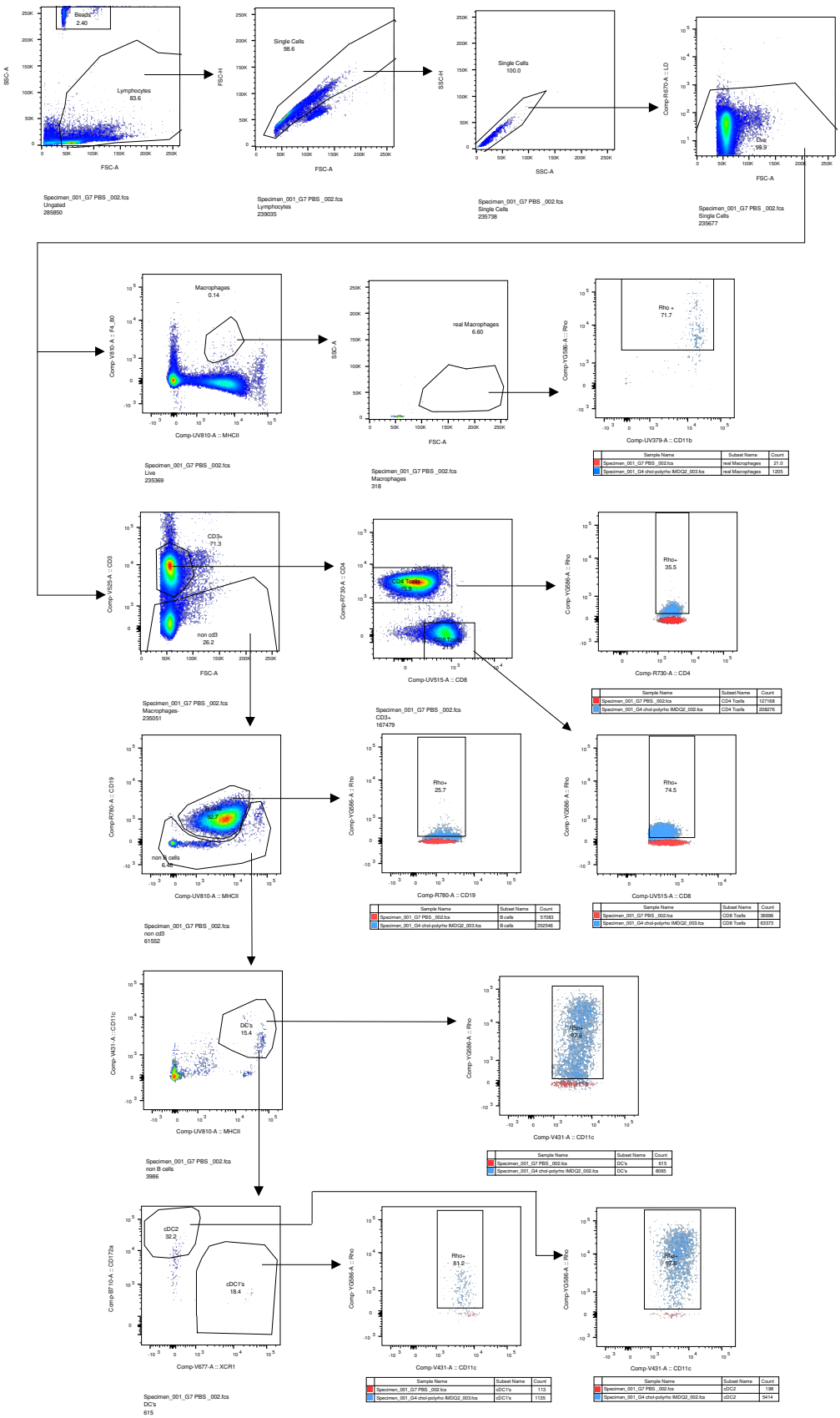

Figure S52: Gating procedure for flow cytometry analysis of popliteal lymph node immune cell targeting (and maturation).

Additional References

(1) Bolli, E.; Scherger, M.; Arnouk, S. M.; Pombo Antunes, A. R.; Straßburger, D.; Urschbach, M.; Stickdorn, J.; De Vlaminck, K.; Movahedi, K.; Räder, H. J.; Hernot, S.; Besenius, P.; Van Ginderachter, J. A.; Nuhn, L. Targeted Repolarization of Tumor-Associated Macrophages via Imidazoquinoline-Linked Nanobodies. *Adv. Sci.* **2021**, *8* (10), 1–12.

(2) Scherger, M.; Pilger, Y. A.; Stickdorn, J.; Komforth, P.; Schmitt, S.; Arnouk, S. M.; Lebegge, E.; Koynov, K.; Räder, H. J.; Van Ginderachter, J. A.; Nuhn, L. Self-Immolative Nanobody-Cysteine Residue Modification for Controlled Immunodrug Delivery. *Adv. Ther.* **2023**, *6* (2300076), 1–8.

(3) Scherger, M.; Pilger, Y. A.; Stickdorn, J.; Komforth, P.; Schmitt, S.; Koynov, K.; Räder, H. J.; Nuhn, L. Efficient Self-Immolative RAFT End Group Modification for Macromolecular Immunodrug Delivery. *Biomacromolecules* **2023**, *24* (5), 2380–2391.

(4) Kim, B. K.; Bae, Y. U.; Doh, K. O.; Hwang, G. B.; Lee, S. H.; Kang, H.; Seu, Y. B. The Synthesis of Cholesterol-Based Cationic Lipids with Trimethylamine Head and the Effect of Spacer Structures on Transfection Efficiency. *Bioorganic Med. Chem. Lett.* **2011**, *21* (12), 3734–3737.

(5) Gonçalves, M.; Estieu-Gionnet, K.; Berthelot, T.; Laïn, G.; Bayle, M.; Canron, X.; Betz, N.; Bikfalvi, A.; Déléris, G. Design, Synthesis, and Evaluation of Original Carriers for Targeting Vascular Endothelial Growth Factor Receptor Interactions. *Pharm. Res.* **2005**, *22* (8), 1411–1421.

(6) Vidya Sagar Reddy, G.; Venkat Rao, G.; Subramanyam, R. V. K.; Iyengar, D. S. A New Novel and Practical One Pot Methodology for Conversion of Alcohols to Amines. *Synth. Commun.* **2000**, *30* (12), 2233–2237.

(7) De Vrieze, J.; Baptista, A. P.; Nuhn, L.; Van Herck, S.; Deswarte, K.; Yu, H.; Lambrecht, B. N.; De Geest, B. G. Lipid Nature and Alkyl Length Influence Lymph Node Accumulation of Lipid-Polyethylene Glycol Amphiphiles. *Adv. Ther.* **2021**, *4* (8), 1–9.

(8) Huppertsberg, A.; Kaps, L.; Zhong, Z.; Schmitt, S.; Stickdorn, J.; Deswarte, K.; Combes, F.; Czysch, C.; De Vrieze, J.; Kasmi, S.; Choteschovsky, N.; Klefenz, A.; Medina-Montano, C.; Winterwerber, P.; Chen, C.; Bros, M.; Lienenklaus, S.; Sanders, N. N.; Koynov, K.; Schuppan, D.; Lambrecht, B. N.; David, S. A.; De Geest, B. G.; Nuhn, L. Squaric Ester-Based, PH-Degradable Nanogels: Modular Nanocarriers for Safe, Systemic Administration of Toll-like Receptor 7/8 Agonistic Immune Modulators. *J. Am. Chem. Soc.* **2021**, *143* (26), 9872–9883.

(9) De Vrieze, J.; Van Herck, S.; Nuhn, L.; De Geest, B. G. Design of PH-Degradable Polymer-Lipid Amphiphiles Using a Ketal-Functionalized RAFT Chain Transfer Agent. *Macromol. Rapid Commun.* **2020**, *41* (18), 1–6.

(10) Heck, A. G.; Stickdorn, J.; Rosenberger, L. J.; Scherger, M.; Woller, J.; Eigen, K.; Bros, M.; Grabbe, S.; Nuhn, L. Polymerizable 2-Propionic-3-Methylmaleic Anhydrides as a Macromolecular Carrier Platform for PH-Responsive Immunodrug Delivery. *J. Am. Chem. Soc.* **2023**, *145* (50), 27424–27436.

(11) Nuhn, L.; Vanparijs, N.; De Beuckelaer, A.; Lybaert, L.; Verstraete, G.; Deswarte, K.; Lienenklaus, S.; Shukla, N. M.; Salyer, A. C. D.; Lambrecht, B. N.; Grooten, J.; David, S. A.; De Koker, S.; De Geest, B. G. PH-Degradable Imidazoquinoline-Ligated Nanogels for Lymph Node-Focused Immune Activation. *Proc. Natl. Acad. Sci. U. S. A.* **2016**, *113* (29), 8098–8103.

CHAPTER III: REVERSIBLE INTRACELLULAR CO-ASSEMBLY OF POLYMERIC 2-PROPIONIC-3-METHYLMALEIC ANHYDRIDES

The following chapter will be submitted to a peer-reviewed journal. As first author of this chapter I synthesized the monomer as well as the corresponding amphiphilic block copolymers and investigated their pH-dependent self-assembly behavior. During his bachelor thesis Jonas Woller synthesized the mPEG-based chain transfer agents, which could be used in following RAFT copolymerization experiments. Transmission Electron Microscopy (TEM) measurements were conducted by David Schwiertz. Furthermore, I prepared, isolated, and characterized all amine-modified polymers. In addition, I analyzed their pH sensitivity and self-assembly properties. Then, I fabricated Cy3- or Cy5-labeled block copolymers and performed the fluorescence spectrometric analyses. Moreover, I investigated their behavior on a cellular level as well as the generation of a FRET signal. Confocal microscopy images were recorded by Judith Stickdorn and David Y. W. Ng. Additionally, David Y. W. Ng detected the fluorescence lifetime images (FLIM). The detection of micellar structures *in vitro* by the combined method of fluorescence staining and electron microscopy, related as correlative light and electron microscopy (CLEM) was carried out by Anke Kaltbeitzel and Christoph Sieber.

REVERSIBLE INTRACELLULAR CO-ASSEMBLY OF POLYMERIC 2-PROPIONIC-3-METHYLMALEIC ANHYDRIDES

Alina G. Heck[1,2], Judith Stickdorn[1], David Schwiertz[3], Jonas Woller[2], Anke Kaltbeitzel[2], Ingo Lieberwirth[2], David Y. W. Ng[2], Katharina Landfester[2], Tanja Weil[2], and Lutz Nuhn[1,2]*

1: Institute of Functional Materials and Biofabrication, Department of Chemistry and Pharmacy, Julius-Maximilians-Universität Würzburg, 97070 Würzburg, Germany

2: Max Planck Institute for Polymer Research, 55128 Mainz, Germany

3: Biotherapeutics Division, Leiden Academic Centre for Drug Research (LACDR), Leiden University, 2333CC Leiden, The Netherlands

*: corresponding author: Prof. Dr. Lutz Nuhn (E-mail: lutz.nuhn@uni-wuerzburg.de)

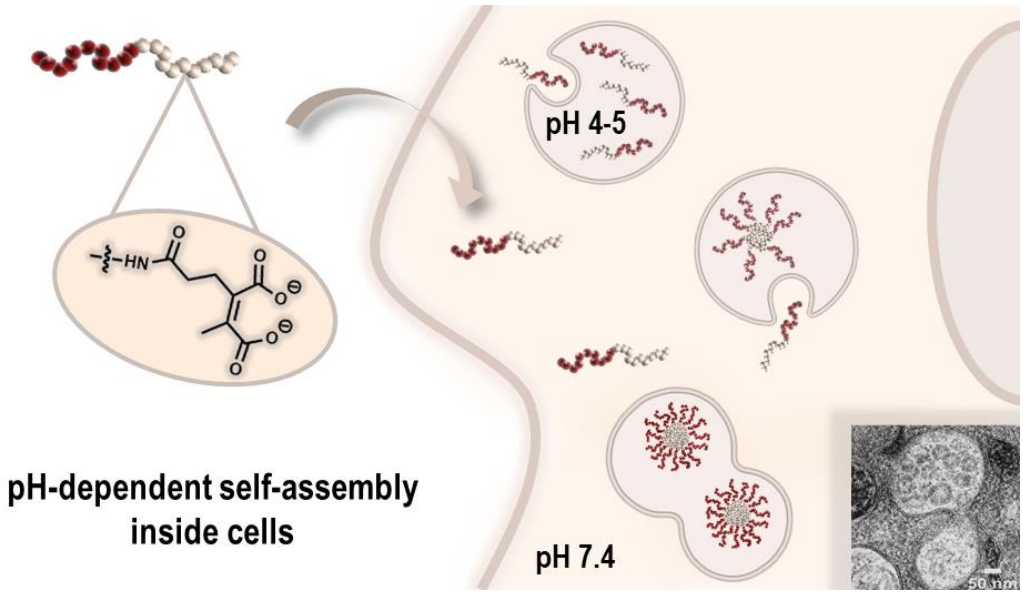

Keywords: RAFT polymerization, block copolymer, maleic anhydride, pH-sensitive, polymer micelle, FRET.

Abstract

The applications of stimuli-responsive polymers are rapidly growing based on the versatile sensitivity to changing environments such as temperature, redox potential, or pH. These changes can be harnessed to deliberately release conjugated small molecules, but they can also induce an intracellular morphological transformation of the delivering vehicle. In particular, the development of pH-responsive materials represents an effective approach to precisely access relevant biological compartments. Here, we demonstrate the synthesis of well-defined polymetharcylamide-based block copolymers with pendant 2-propionic-3-methylmaleic anhydride groups. Following controlled radical polymerization conditions, propionic methylmaleic anhydride methacrylamide (PMMA-MA) monomers can be grafted onto PEG-based chain transfer agents (PEG-TTC-CTA) affording pH-sensitive block copolymers which remain fully soluble under basic conditions but immediately co-assemble into micelles under acidic conditions. Conjugation of primary or secondary amines to the maleic anhydrides further affects the pH sensitivity of the block copolymer. Primary amines convert into pH-irreversible imides and their micelles lose the responsive disassembly behavior. Only secondary amines ensure a permanent pH-responsiveness and allow for reversible self-assembly under acidic conditions. These properties can be investigated on a cellular level by labeling the polymer chains with the two fluorescent dyes Cy3 and Cy5 individually. Upon acid-triggered micellization, they provide Förster Resonance Energy Transfer (FRET) that can be monitored during cell uptake by live cell microscopy and fluorescent lifetime imaging. The collected data suggest that the individual polymer chains find each other upon cell internalization and build up spherical micelles inside endolysosomes which can be confirmed by correlative light and electron microscopy (CLEM), too.

In general, such pH-sensitive polymetharcylamides with pendant 2-propionic-3-methylmaleic anhydride groups display interesting features for a controlled functionalization and simultaneous intracellular morphology transformation. The pH-triggered self-assembly behavior can be utilized to selectively build up well-defined nanostructures in distinct organelles that allow for a controlled compartmentalization inside cells.

Introduction

In the last decades researchers have identified various methods of how to build up functional nanostructured materials derived from well-defined polymers. Controlled radical polymerization techniques offer the opportunity to generate precise macromolecules with defined molecular weights and end group functionalities. The Reversible Addition-Fragmentation Chain Transfer (RAFT) polymerization has emerged as valuable robust polymerization method to access polymers with control over their chain length and narrow dispersity (Đ). Moreover, block copolymers and other complex architectures can be generated with reactive monomers yielding multifunctional nano-structured materials.[1–5]

In particular, RAFT-polymerized bio-responsive and -active polymers revealed great potential in the development of materials for biomedical purposes.[6,7] Various functionalities can be applied to attach or encapsulate small molecular drugs[6,8–10], as well as to integrate stimuli-responsive release features for conjugated cargo molecules[11,12], while controlling polymer degradation reactions.[13,14] One promising approach are stimuli-responsive polymers that respond to their environment and react to biological signals such as light, redox, temperature or pH.[7,15,16] These changes can be utilized to trigger a controlled activation/inactivation of the conjugated cargo as well as initiate a morphology switch of the polymeric carrier systems.[17,18] Among a variety of smart polymers, pH-sensitive polymer structures gained an increasing interest, since relevant biological compartments provide distinct acidic pH gradients, ranging from the organ level (stomach, pH 1-3) to the tissue level, like the tumor microenvironment (pH = 6.0-6.5) or cellular compartments including endosomes and lysosomes (pH 4.5-5.5).[19,20]

Notable examples of pH-responsive acidic or basic polymers are poly((meth)acrylic acid), poly(vinylsulfonic acid) or poly[(2-dimethylamino)ethyl methacrylate]. They all bind or release protons upon pH switch affecting their net charge.[21–23] Alternatively, pH sensitivity can be introduced by pH-sensitive groups that are hydrolyzed and fall apart upon pH drop. This is the case, for instance, for hydrazones[24], acetals[25] and ketals[26], oximes[27] or imines[28], most likely applied as linkers for acid-triggered drug release.[18,27,29]

An important pH-responsive motif that both alters its charge as well as reversibly conjugates amines are dimethylmaleic anhydrides with an exceedingly high pH sensitivity (pH 5.5-6.8). Due to their reactivity towards nucleophiles under mild conditions and in the absence of other coupling agents, cyclic anhydride-based structures strongly suggest their application as stimuli-responsive linkers. By treatment with amine-containing small molecules, corresponding

ring-opened amides are generated that bear a negatively charged carboxylate group, favorable for a charge reversal of related amines as well as subsequent traceless release of the amine upon acidification.[29–32] An intramolecular cyclization thereby converts the amide back into the anhydride. This process depends on the nucleophilicity of the conjugated amine as well as the acidity of the environment. Additional substitutions on the *cis*-double bond control the distance between the maleic acid amide and β-carboxylate group and, thus, further modulate the related pH sensitvity.[33–35] PH-responsive polymeric materials with dimethylmaleic anhydride structures have widely been applied for biomedical purposes in order to induce an acid-triggered ligand activation, size transformation or charge reversion.[36–38] However, detailed investigations on the pH reversibility of the conjugated amines as well as the morphological variations of the resulting polymers have been hardly investigated, in particularly inside cells.

Herein, we report on the development and evaluation of 2-propionic-3-methylmaleic anhydride-functionalized block copolymers as pH-reversible self-assembling systems for the formulation of micellar structures inside acidic cellular compartments. Therefore, 2-propionic-3-methylmaleic anhydride methacrylamides are converted with a polyethylene glycol (PEG)-modified macro-trithiocarbonate chain transfer agent (macro-TTC-CTA) by RAFT polymerization (Figure 1). A pH-dependent self-assembly behavior of the resulting block copolymer is found in aqueous media and reveals the formation of highly defined micelles at pH values below 5.5, while higher pH values cause a rapid disassembly and release of negatively charged polymer chains. Further maleic anhydride functionalization with primary amines affects the pH-reversible micelle disassembly properties due to the formation of stable maleic imides. In contrast, secondary amines retain their reversible self-assembly behavior by an acid-triggered amine release mechanism. The block copolymers can additionally be labeled with primary amine bearing fluorescent dyes (Cy3 and Cy5) affording efficient Förster Resonance Energy Transfer (FRET) upon acid-triggered micellarization.[39,40] This enables us to monitor the co-assembling of the block copolymers inside acidic environments of cells and suggest the formation of new nanostructured compartments *in vitro*. Both live cell microscopy in combination with fluorescent lifetime imaging, as well as correlative light and electron microscopy (CLEM) support our findings. Consequently, the herein described polymer system provides access to a functionalizable and structure-promoting macromolecular platform that might be highly valuable not only for intracellular delivery but also for further building up tailor-made nanostructured materials inside cells.

Results and Discussion

Synthesis of mPEG-based Block Copolymers with Appending pH-Sensitive 2-Propionic-3-Methylmaleic Anhydrides

For the synthesis of well-defined, pH-responsive block copolymers with pendant 2-propionic-3-methylmaleic anhydride groups, we applied a polymerizable propionic methylmaleic anhydride methacrylamide (PMMA-MA) as suitable monomer for Reversible Addition-Fragmentation Chain Transfer (RAFT) polymerization (Figure S1-S4).

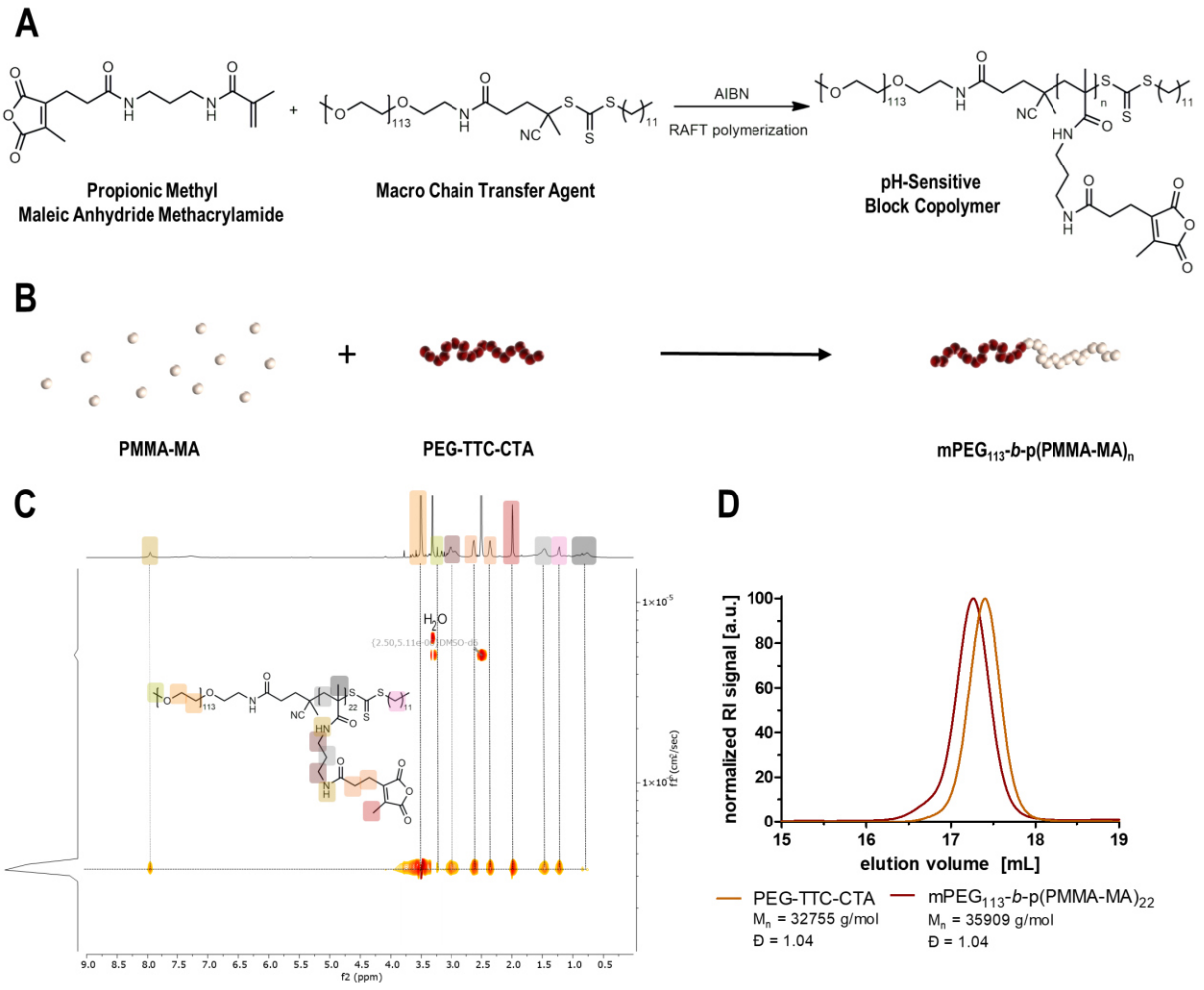

Figure 1. Synthesis and characterization of pH-responsive block copolymers with pendant 2-propionic-3-methylmaleic anhydride groups. (**A**) Synthesis route of mPEG$_{113}$-*b*-p(PMMA-MA)$_n$ by controlled radical polymerization of the propionic methylmaleic anhydride methacrylamide monomer (PMMA-MA) with a mPEG-based macro trithiocarbonate chain transfer agent (PEG-TTC-CTA). (**B**) Schematic overview for the synthesis of the pH-sensitive amphiphilic block copolymer mPEG$_{113}$-*b*-p(PMMA-MA)$_n$. (**C**) ^{1}H DOSY NMR of the block copolymer in DMSO-d$_6$ with colored peak annotations affording one diffusing species with high molecular weight diffusion units. (**D**) Size exclusion chromatography (SEC, in HFIP (hexafluoroisopropanol), calibrated with PMMA standards) of the block copolymer mPEG$_{113}$-*b*-p(PMMA-MA)$_n$ (red) compared to the macro PEG-TTC-CTA (orange).

Previous reports demonstrated the high stability of the maleic anhydride system under controlled radical polymerization conditions in methanol with azobisisobutyronitrile (AIBN) as initiator and trithiocarbonates as chain transfer agent (TTC-CTA).[41] Extending this macromolecular polymer platform for the formulation of amphiphilic block copolymers, we first synthesized a mPEG-based macro trithiocarbonate chain transfer agent (PEG-TTC-CTA). In this context, the PEG block provides excellent hydrophilic properties with high flexibility, suitable as a shell-forming segment for self-assembling, amphiphilic block copolymers. The additional stealth character guarantees high biocompatibility with long circulation in blood, making it an efficient chemical segment for biomedical applications.[26,42] In a two-step reaction 4-cyano-4-[(dodecylsulfanylthiocarbonyl)sulfanyl]-pentanoic acid (TTC-CTA) was treated with pentafluorophenyl trifluoroacetate yielding a reactive ester chain transfer agent (Figure S5-S7) sensitive for aminolysis with methoxypoly(ethylene glycol)amine (mPEG-NH_2 M_n: 5 kDa) (Figure S8). The resulting PEG-TTC-CTA was analyzed by ^{1}H NMR spectroscopy (Figure S9) and size exclusion chromatography (SEC) showing a narrowly distributed, high molecular weight chain transfer agent (number-average molecular weight determined by HFIP SEC and PMMA calibration of M_n = 32755 g/mol) with a narrow dispersity (Đ = 1.04, Figure S10).

Next, amphiphilic block copolymers mPEG$_{113}$-*b*-p(PMMA-MA)$_n$ could be prepared by RAFT polymerization of the pH-sensitive propionic methylmaleic anhydride methacrylamide (PMMA-MA) monomer in methanol (Figure 1A-B and Figure S11). After polymerization for 72 hours, the reaction provided adequate monomer conversions and yielded polymers with a block length of ~ 22 units. The resulting block copolymers were purified by precipitation into cold diethyl ether and dried under reduced pressure. Size exclusion chromatography (SEC) analysis confirmed the successful synthesis of monomodal block copolymers mPEG$_{113}$-*b*-p(PMMA-MA)$_{22}$ of narrow Đ = 1.04. The elugram shifted towards higher molecular weight compared to the PEG-TTC-CTA and yielded a number-average molecular weight (M_n) of 35909 g/mol (determined by HFIP SEC and PMMA calibration, Figure 1D and S13). Further characterization by ^{1}H NMR (Figure S12) and ^{1}H diffusion ordered NMR spectroscopy (^{1}H DOSY NMR, Figure 1C) demonstrated only one single diffusing species with high molecular weight diffusion units and affirmed the grafting of the p(PMMA-MA)-block to the macro-CTA without the generation of homopolymer.

pH-Dependent Self-Assembling Properties of the Block Copolymer mPEG-*b*-p(PMMA-MA)$_n$

Maleic anhydrides are reversibly ionizable structures sensitive for charge reversal and structural transformation at different pH values. Therefore, we were interested whether these properties can be applied for the pH-reversible self-assembly of the mPEG$_{113}$-*b*-p(PMMA-MA)$_{22}$ block copolymers (Figure 2A and Figure S14). Supported by ultrasonication, the block copolymers easily dispersed in water. Their self-assembly was then monitored at different pH values by dynamic light scattering (DLS).

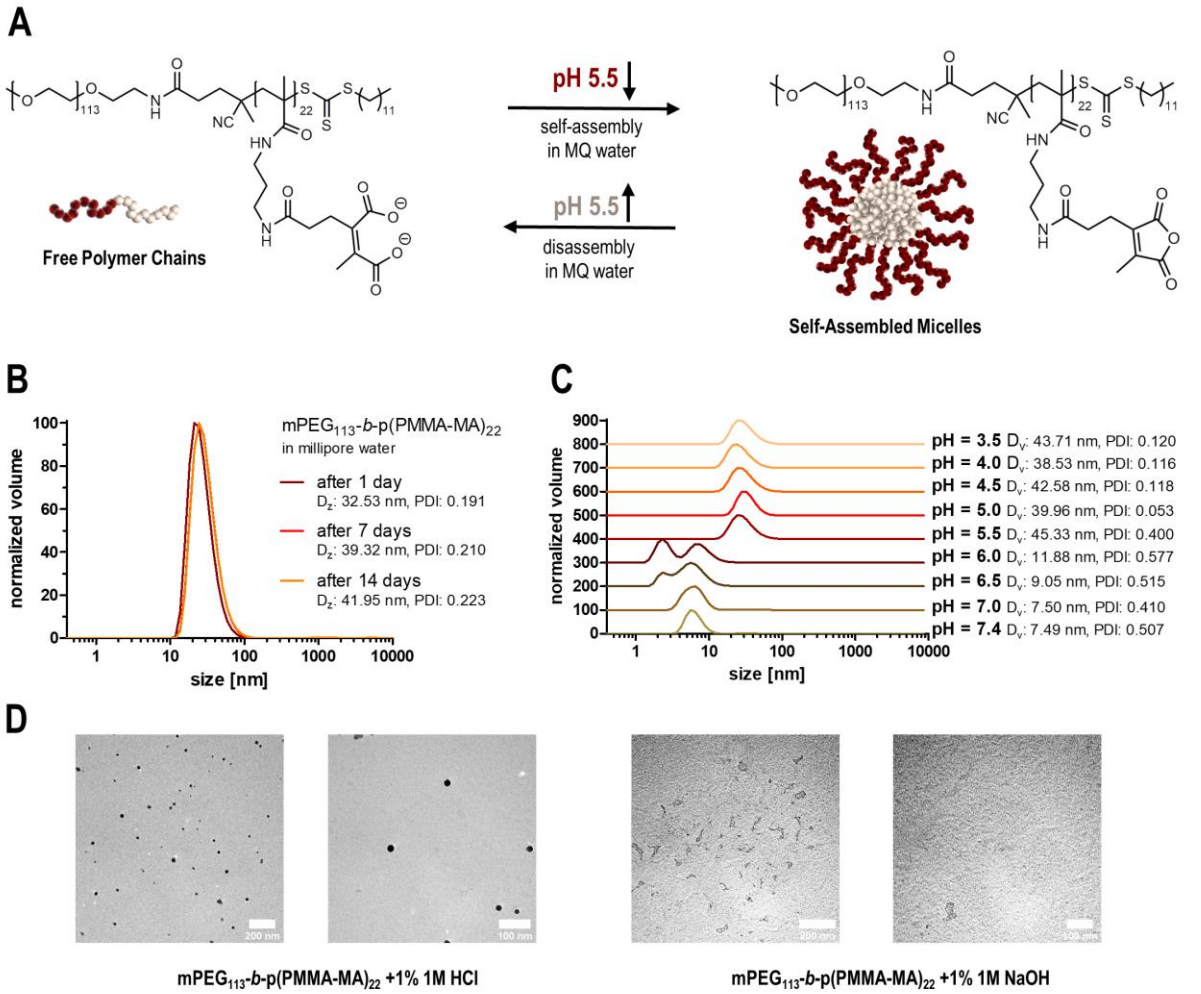

Figure 2. pH-dependent self-assembly behavior of the block copolymer mPEG$_{113}$-*b*-p(PMMA-MA)$_n$. (**A**) Schematic scheme for the pH-reversible self-assembly of mPEG$_{113}$-*b*-p(PMMA-MA)$_n$ at different pH values. (**B**) Micelles recorded by single-angle dynamic light scattering (DLS) in millipore water showing narrow monomodal distributed micelles over 14 days. (**C**) pH-sensitive self-assembly of mPEG$_{113}$-*b*-p(PMMA-MA)$_n$ at different pH values yielded stable micelles at acidic environments up to pH 5.5. (**D**) Transmission Electron Microscopy (TEM) of the block copolymer under acidic conditions formulated spherical micelles (left) or under basic conditions disassembled into soluble and not detectable polymer chains (right).

Only acidic pH values below pH 5.5 afforded monomodal micellar particles with sizes (D_v) around 40 nm and polydispersity values (PDI) below 0.12 (Figure 2C). These conditions trigger the formation of the ring-closed maleic anhydride structure which drives the block copolymers' self-assembly into compact and stable micelles. In contrast to that, maleic anhydride is most likely deprotonated at increasing pH values, leading to a charge repulsion of the maleic dicarboxylate block and a disassembly into single polymer chains (Figure 2A and 2C). Interestingly, pH values above 5.5 already resulted in a decrease in scattering count rates as well as increasing PDI > 0.4 and decreasing volume sizes (Figure 2C and Figure S15). As millipore water contains low ion concentrations and low buffering capacity, carbon dioxide (CO_2) in the air decreases the pH value below 5.5.[43] Even after 2 weeks DLS measurements in millipore water yielded monodisperse micelles with narrow PDI of 0.22 (Figure 2B). Further characterization by transmission electron microscopy (TEM) in dry state displayed the existence of compact, spherical micelles under acidic conditions, while free polymer chains were generated under basic conditions that were not detectable by TEM measurement (Figure 2D) (compare Figure S15 for corresponding DLS measurements).

pH-Sensitive Functionalization by Amidation with Primary or Secondary Amines

Next, we investigated the pH-reversible amidation reaction of the block copolymers' pendant 2-propionic-3-methylmaleic anhydride groups and its resulting impact on the self-assembly properties. In analogy to previously established modification reactions[41], the block copolymer was dissolved in a mixture of DMSO and triethylamine (TEA), followed by the addition of various amines (Figure S16) including dibenzyl- and benzylamine (as shown in Figure 3A and Figurer S24). After incubation for 16 h the modified polymers were precipitated into diethyl ether and characterized (Figure S25). In accordance with our previous reports[41], ^{1}H NMR and ^{1}H DOSY NMR spectroscopy confirmed the successful amidation of the block copolymer with benzylamine, dibenzylamine, butylamine, ethylmethylamine, morpholine and aniline (Figure S17-S23). Thereby, the conjugation of secondary amines displayed remarkable variations compared to primary amines. The formation of two ring-opened 2-propionic-3-methylmaleic anhydride regioisomers resulted in a splitting of the α-position methyl signal (1.89 ppm) into two signals, as shown by the Figures S17, S18 and S20 (top, neutral). However, the successful attachment of primary amines occurred without the presence of two regioisomers. The α-position methyl signal at 1.99 ppm appeared as one single sharp signal by ^{1}H NMR spectroscopy and, thus, implies the formation of a pH-resistant imide structure (Figures S17, S18 and S22 bottom, neutral).

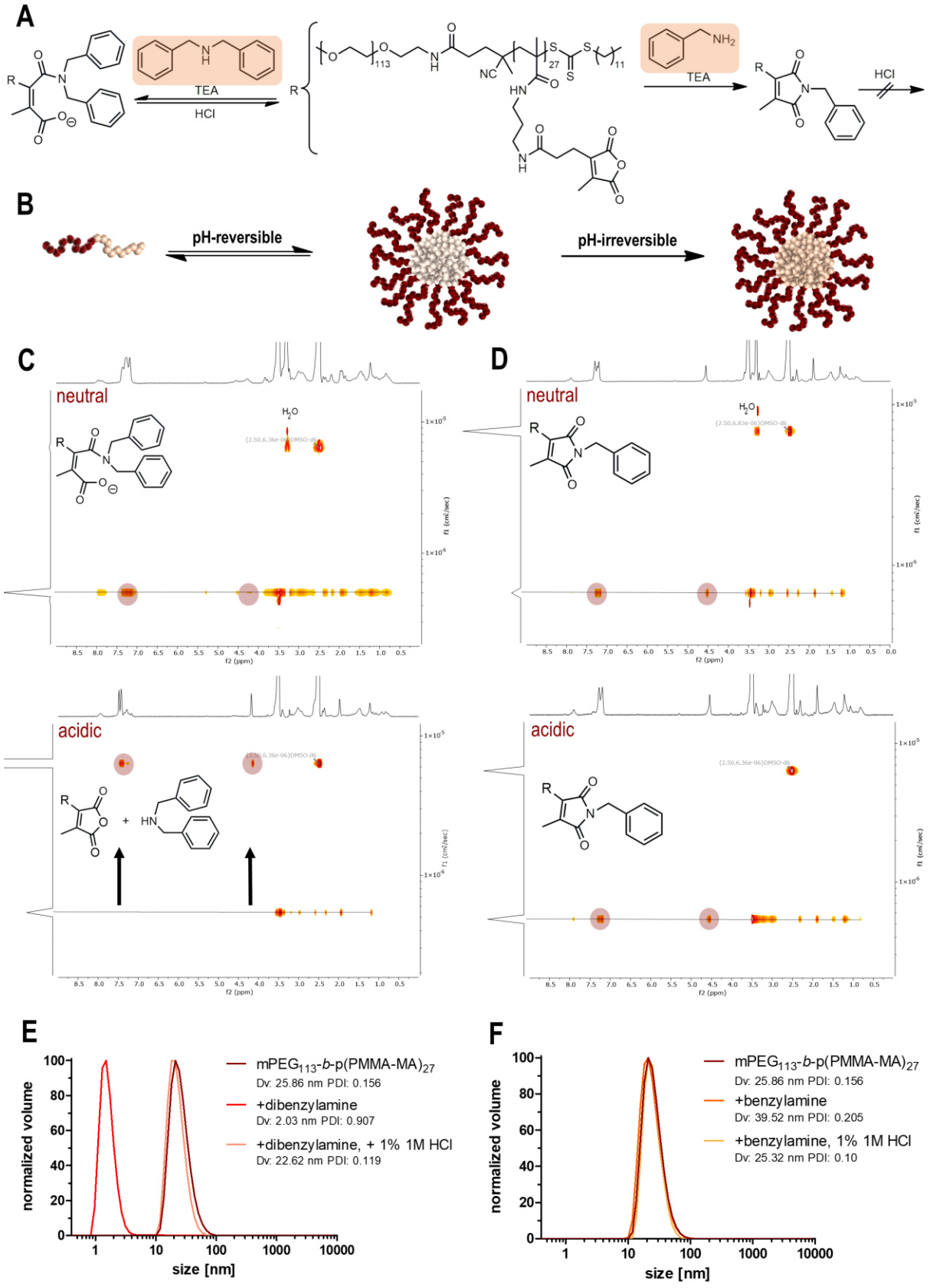

Figure 3. pH-responsiveness and related self-assembly of amine-conjugated maleic anhydride side groups of the block copolymer mPEG$_{113}$-*b*-p(PMMA-MA)$_n$. (**A**) pH-irreversible or reversible conjugation of benzyl- and dibenzylamine to the block copolymer. (**B**) Scheme of amine-modified block copolymers and corresponding

pH-sensitive self-assembly properties. (**C**) ^{1}H DOSY NMR of the pH-reversible dibenzylamine-modified polymer under neutral and acidic conditions. (**D**) ^{1}H DOSY NMR of the pH-irreversible benzylamine-conjugated polymer under neutral and acidic conditions. (**E**) DLS measurement of the secondary amine-modified block copolymer in millipore water, confirming uniform micelles upon acidification and release of dibenzylamine, while (**F**) primary amine-conjugated systems form stable pH-resistant micelles.

In order to assess the pH-dependent release of the amine-modified block copolymers, additional ^{1}H DOSY NMR spectroscopy measurements were conducted. Both the aromatic protons of dibenzylamine or benzylamine appeared at the same diffusion constant as the block copolymers' protons. These measurements confirmed the successful attachment to the appended 2-propionic-3-methylmaleic anhydride groups, too (Figure 3C and 3D, neutral). Yet only the secondary amine modified polymers yielded a quantitative amine release upon acidification. The characteristic signals attributed to dibenzylamine then shifted to low molecular weight diffusing species (Figure 3C, acidic), whereas no signal shift was observed for benzylamine-conjugated block copolymers upon treatment with trifluoroacetic acid (TFA) (Figure 3D, acidic). These findings were in perfect agreement with the corresponding ^{1}H NMR spectra and corroborated the formation of pH-resistant imides after anhydride conversion with primary amines (Figure S17 and S18, acidic). The secondary amines cannot form imides but yield acid-responsive amides. This could be confirmed for all secondary amines (Figure S19-S21), except for secondary aromatic amines (e.g. for *N*-methylaniline no anhydride conversion could be observed – Figure S22, top and Figure S23).

Beyond the pH-responsiveness of the modified block copolymers, we were also interested in their self-assembly behavior (Figure 3B and Figure S24). Therefore, benzylamine- or dibenzylamine-conjugated polymers were dispersed in millipore water followed by DLS characterization (Figure 3E and 3F). Interestingly, benzylamine-modified polymers formed narrowly distributed micelles with sizes (D_v) of 39.59 nm and a PDI of 0.20 (Figure 3F), while dibenzylamine-modified block copolymers remained as individual polymer chains in solution (Figure 3E, D_v = 2.03 nm, PDI = 0.91). Upon acidification with 1% 1M HCl, a self-assembly was observed for them and micellar particles could be detected by DLS (D_v = 22.62 nm, PDI = 0.12). They were of similar sizes as the benzylamine-modified polymers under similar conditions (D_v = 25.32 nm, PDI = 0.10) and correspond to the unmodified anhydride block copolymers forming self-assembled micelles below pH 5.5 (D_v = 25.86 nm, PDI = 0.16 compare Figure 3E and Figure 2C). These findings support again that the micelles lose their pH-responsiveness after modification by primary amines because of their imide formation. Only the secondary

amines allow for a reversible block copolymer modification which can be used for a reversible release of the conjugated secondary amines as well as reversible nanostructure formation.

Interestingly, after secondary amine modification the impact of the *cis*-vinylic β-carboxylate on its self-assembly behavior can be demonstrated, too (Figure S26 and S27). For that purpose, the block copolymers were first treated with dibenzylamine in DMSO supplemented with *N,N*-diisopropylethylamine (DIPEA), followed by subsequent conversion of the ring-opened maleic anhydride with benzyl bromide. The latter reaction results in an additional esterification of the carboxylate into a benzyl ester. The obtained dually modified block copolymers were analyzed by SEC and DLS measurement (Figure S27). The molecular weight distribution obtained by SEC exhibited well-defined block copolymers with an increased molecular weight (M_n = 34414 g/mol by HFIP SEC and PMMA calibration) and narrow Đ of 1.07 (Figure S27A and B). DLS measurement could be used to monitor the polymers' self-assembly behavior under varying pH conditions. Sequential modification with dibenzylamine yielded a pH-reversible, negatively charged polymer which only self-assembled under acidic conditions by the release of conjugated amine (D_v = 40.13 nm, PDI = 0.26, Figure S27C). Basic conditions reversibly afforded single polymer chains due to the deprotonation of the carboxylates derived from the ring-opened maleic anhydrides (D_v = 7.19 nm, PDI = 0.76, Figure S27C). In contrast to that, the dual modification of the maleic anhydride with dibenzylamine followed by benzyl esterification revealed the immediate loss of the pH sensitivity, as stable micelles were recorded by DLS in millipore water (D_v = 46.18 nm, PDI = 0.18, Figure S27D) under both basic as well as acidic conditions (Figure S27D). These results clearly demonstrate the strong impact of the unmodified *cis*-vinylic β-carboxylate not only on the acid-triggered release mechanism, but also on the polymers' acid-triggered self-assembly behavior.

Synthesis of Dye-Labeled Block Copolymers as Fluorescent FRET Couple

Encouraged by the obtained results we were interested in the self-assembly of the block copolymers under physiological conditions *in vitro*. During endosomal internalization, decreasing pH conditions are approached for polymeric carries inside endolysosomal vesicles. Thus, we were interested whether these conditions could also allow for individual block copolymer chains to recognize each other and form micellar self-assemblies inside cells as novel structurally synthetic compartments. To that respect, the application of fluorescence-based techniques have demonstrate their efficacy for sensitive analysis of molecular interaction inside living cells, enabling the investigation of different processes such as phagocytosis or carrier degradation.[40,44] Förster/Fluorescence Resonance Energy Transfer (FRET) is an elegant physical strategy that relies on the distance between two molecules,

allowing for a nonradiative energy transfer from an excited fluorophore (donor) to another fluorophore (acceptor) through long-range intermolecular dipole-dipole coupling, which also decreases the donor's fluorescence lifetime.[45,46] Interestingly, real-time monitoring of FRET dynamics enables the tracking of the polymers and measuring their interactions at a distance of 1-10 nm, which is obtained during co-assembly.[39,47]

For that purpose, separate batches of the block copolymer $mPEG_{113}$-*b*-$p(PMMA\text{-}MA)_{18}$ were first irreversibly dye-labeled with primary amine bearing Cy3 cadaverine or Cy5 cadaverine in a mixture of DMSO and dioxane followed by precipitation into diethyl ether (Figure 4A). Additionally, a small amount of the dye-labeled block copolymers was further pH-reversibly modified with secondary amine-containing morpholine (Figure S28). Two individually fluorescently dye-labeled block copolymers could be obtained and successfully analyzed by SEC, UV-Vis and fluorescence spectroscopy as well as DLS measurement (Figure 4B+C and Figure S29-32). SEC analysis revealed narrowly distributed polymers (Đ = 1.07 for Cy3-labeled polymers, Đ = 1.08 for Cy5-lableled polymers) with slightly increased number-average molecular weight compared to the unmodified block copolymer (M_n = 32794 g/mol for Cy3 and M_n = 33392 g/mol for Cy5, determined by HFIP SEC and PMMA calibration –Figure S29A and B). Further characterization by UV-Vis spectroscopy measurements confirmed the successful conjugation of the fluorescent dyes (Figure 4B and Figure S29C). Cy3-fluorecently labeled block copolymers displayed an absorbance maximum at 545 nm, while Cy5-absorbance appeared at 640 nm. A mixture of the dye-labeled polymers in equimolar amount showed both absorbance maxima with the same intensity (Figure 4B and Figure S29C). The self-assembly of the dye-labeled polymers was measured by DLS in aqueous medium at neutral pH using phosphate-buffered saline (PBS), representing the extracellular medium (Figure 4C and Figure S30). In agreement with our previous analyses, the free polymer chains remained as individual strands under neutral pH conditions (D_v below 10 nm, PDI above 0.50, Figure 4C and Figure S30). Upon acidification with 1% 1M HCl yielding pH levels around pH 5.5, they subsequently self-assembled into monodisperse micelles representing the acidified conditions of endolysosomal compartments during cell uptake (Figure 4C and Figure S30). Remarkably, the self-assembly was directly reversible depending on the pH, as a further treatment with 1% 1M sodium hydroxide (NaOH) caused the deprotonation and disassembly of the propionic methylmaleic anhydride polymethacrylamide block, while subsequent re-assembly by maleic ring-closure and micellization was again obtained by addition of 1% 1M hydrochloric acid (HCl, Figure 4C and Figure S30A and B – note that only Cy3-labeled block copolymers were here

analyzed, as interference of the free Cy5-labeled polymer chains with the laser setup of the DLS device limited their characterization in solution, compare Figure S30C and D).

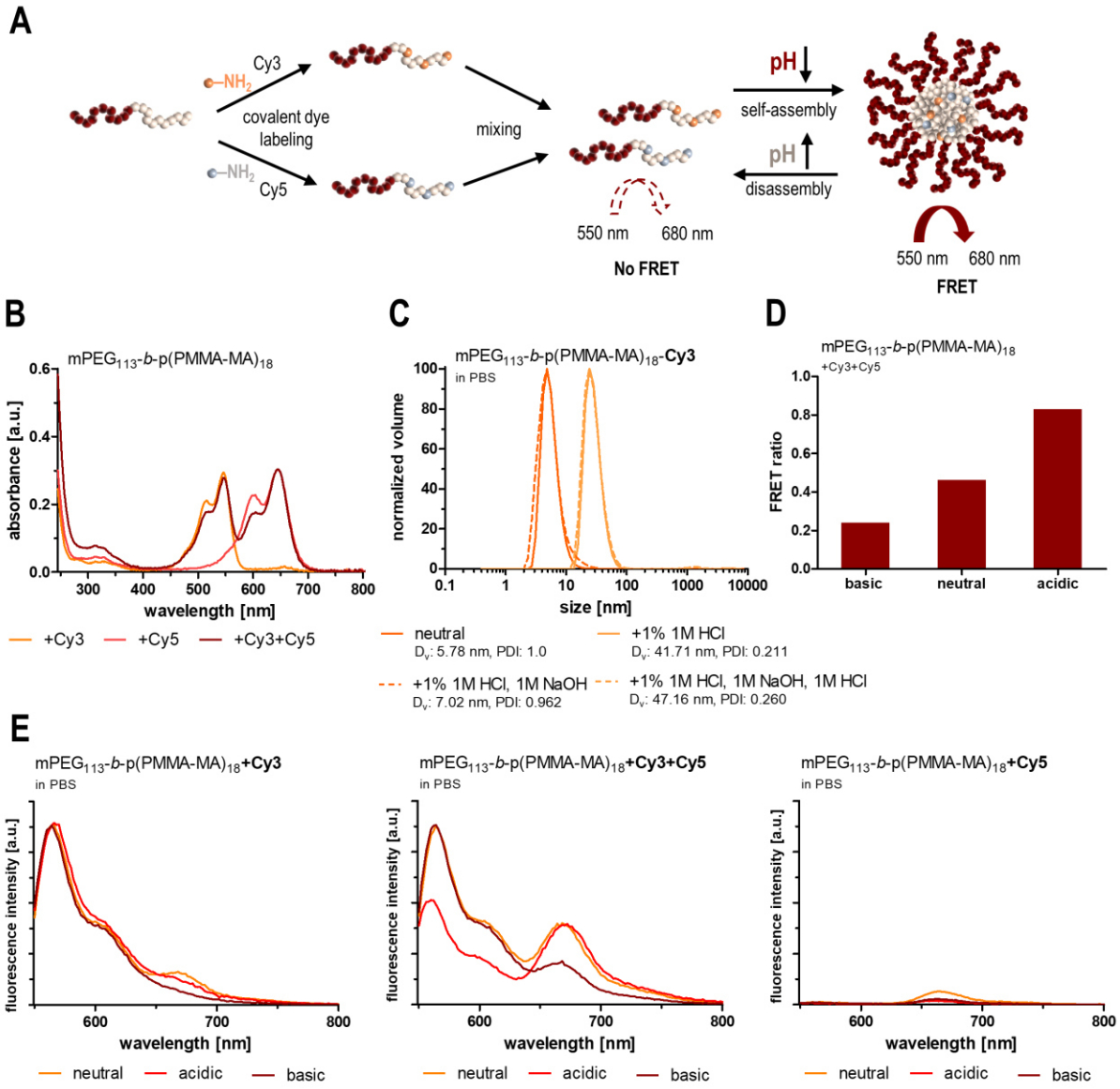

Figure 4. FRET evaluation after acid-triggered self-assembly of fluorescently dye-labeled block copolymers. (**A**) Scheme for the synthesis of Cy3- or Cy5-labeled block copolymers and their acid-triggered formulation as FRET generating micelles. (**B**) UV-Vis spectra of Cy3- or Cy5-labeled block copolymer as well as a mixture of both dye-labeled polymers in PBS. (**C**) Self-assembly behavior of Cy3-conjugated block copolymers under neutral, basic, and acidic conditions quantified by DLS. (**D**) Calculated FRET ratios derived from Cy3 and Cy5 emission spectra under different pH conditions. (**E**) Fluorescence spectra upon excitation at 550 nm under different pH values for Cy3-labeled block copolymers (left), a mixture of Cy3- and Cy5-conjugated polymers (showing a signification FRET emission under acidic conditions) (middle), and Cy5-labeled block copolymers (providing almost no emission) (right).

Next, we evaluated the emission of the Cy5 acceptor dye as a FRET signal upon excitation of the Cy3 donor dye during self-assembly of the dye-labeled block copolymers under varying pH conditions. To this end, first experiments were conducted by fluorescence spectroscopy in

aqueous solutions. Beside the individually dye-labeled polymers, similar concentrations of the Cy3- or Cy5-labeled polymer were mixed and dissolved in PBS (Figure 4B, S29C). All polymer solutions were subsequently excited at 550 nm and corresponding fluorescence spectra were recorded at room temperature. Despite exhibiting different pH conditions, the fluorescence spectra of the Cy3-labeled polymer revealed an intensive emission maximum at 558 nm (Figure 4E left and Figure S31), while the Cy5-labeled polymers provided only a negligible signal at 667 nm, independent from the pH conditions (Figure 4E right and Figure S31). In contrast to that, a mixture of the dye-labeled polymers provided a pH-sensitive change of the emission maxima (Figure 4E middle and Figure S31). While the polymer mixture displayed a high emission maximum from the Cy3-label at neutral and alkaline pH, the acidic pH conditions led to an increased Cy5-emission maximum at 667 nm with reduced Cy3-emission at 558 nm. This clearly confirms FRET between the two dyes which only occurs when both dyes approach each other during the polymer co-assembly into micelles. According to the obtained fluorescence spectra, corresponding FRET ratios (calculated from the emission intensities at 667 nm vs. 558 nm) confirmed increasing FRET with decreasing pH values (Figure 4D and Figure S32).

The obtain results strongly support that the generation of FRET can be used to monitor polymer co-assembly by maleic anhydride formation of block polymers in acidic environments. The individual soluble Cy5- or Cy3-labeld polymer chains co-assemble into narrowly distributed micelles which bring both dyes close to each other in order to promote FRET.

In vitro Co-Assembly of Fluorescently Dye-Labeled Block Copolymers and Reversible Formation of Intracellular Micellar Compartments

We next investigated whether the FRET dye-functionalized block copolymers would allow for an intracellular acid-triggered micellization *in vitro*. For that purpose, RAW macrophages were selected as model for phagocytizing cells, which represent relevant targets for immunodrug delivery purposes.[48,49] They were first investigated for any potential cellular toxicity profiles at increasing polymer doses, but fortunately cell viabilities remained unaffected up to 1 mg/mL determined by MTT assay (Figure S33).

Subsequently, time-dependent cellular uptake and the generation of FRET was monitored as a reporter for intracellular co-assembly of the fluorescently modified block copolymers. For that purpose, cells were incubated with either Cy3- or Cy5-conjugated block copolymers as well as a mixture of both systems for 4 h up to 48 h at 37 °C and then analyzed by flow cytometry (Figure 5A-C and Figure S34A+B). Cy5 could be recorded by a channel which provided excitation at 640 nm and emission between 650 -700 nm, while Cy3 was recorded by a channel

with an excitation at 488 nm and emission between 565-605 nm. The Cy3-Cy5 corresponding FRET signal could be detected independently by a channel with an excitation at 488 nm laser and its FRET emission was recorded beyond 670 nm.

Interestingly, all polymer solutions already demonstrated a strong internalization after 4 hours that gradually increased overtime up to 48 h (Figure 5B and Figure S34A+B). Importantly, only the mixture of both dye-labeled systems, which by itself at neutral pH does not provide any strong FRET emission (compare Fig. 4) yielded an increasing FRET signal over time (Figure 4B+C and Figure S34). To further evaluate the progression of the FRET signal, corresponding FRET ratios were determined by dividing the mean fluorescent intensity of the FRET channel by the Cy3 channel (Figure 5D and Figure S34C). A sufficiently high FRET ratio around 1.5 was found after 4 h, which gradually increased over time and, thus, further confirmed the existence of FRET inside the macrophages assuming a micellar co-assembly of the individual polymer chains inside acidified intracellular compartments (note that also morpholine quenched block copolymers were evaluated, but here the FRET ratio decreased after 48 h, where we assume that the released morpholine might quench the intracellularly acidified pH environments - compare Figure S34C).

The cellular uptake in combination with intracellular co-assembly of the dye-labeled block copolymers by generation of FRET was further confirmed by confocal microscopy (Figure 5E and Figure S35). Based on the previous flow cytometric characterization, macrophages were incubated for 4 h at 37 °C. To enhance the imaging of a FRET emission signal by reduction of any crosstalk, the cells were measure in solution without fixation and nuclei staining (Figure S35). All incubated polymers confirmed a fast cellular uptake after 4 h. By carefully screening the FRET emission signal, the cells treated with the individual dye-labeled polymers showed no FRET but only their respective dye label. For the mixture of Cy3- and Cy5-labeled block copolymers, however, an intracellular colocalization could be recorded for both dyes. This colocalization further evolved as exclusive FRET emission over time (Figure S35).

To visualize the time-related co-assembly monitored by FRET, live cell fluorescence imaging was recorded for 4 h after macrophages exposure to a mixture Cy3- or Cy5-labeled polymers (Figure 5E). Interestingly, the resulting live-cell images confirmed a fast-growing intracellular fluorescence of both Cy3 and Cy5 within the first 2 h, which increased by further incubation for 4 h. Related to the increasing cellular uptake of the dye-labeled polymers, an increasing appearance of the FRET emission signal was recorded, too (Figure 5E). The FRET emission signal evolves at those intracellular areas where the two dyes Cy3 and Cy5 overlap and suggest a co-assembly of the two polymers.

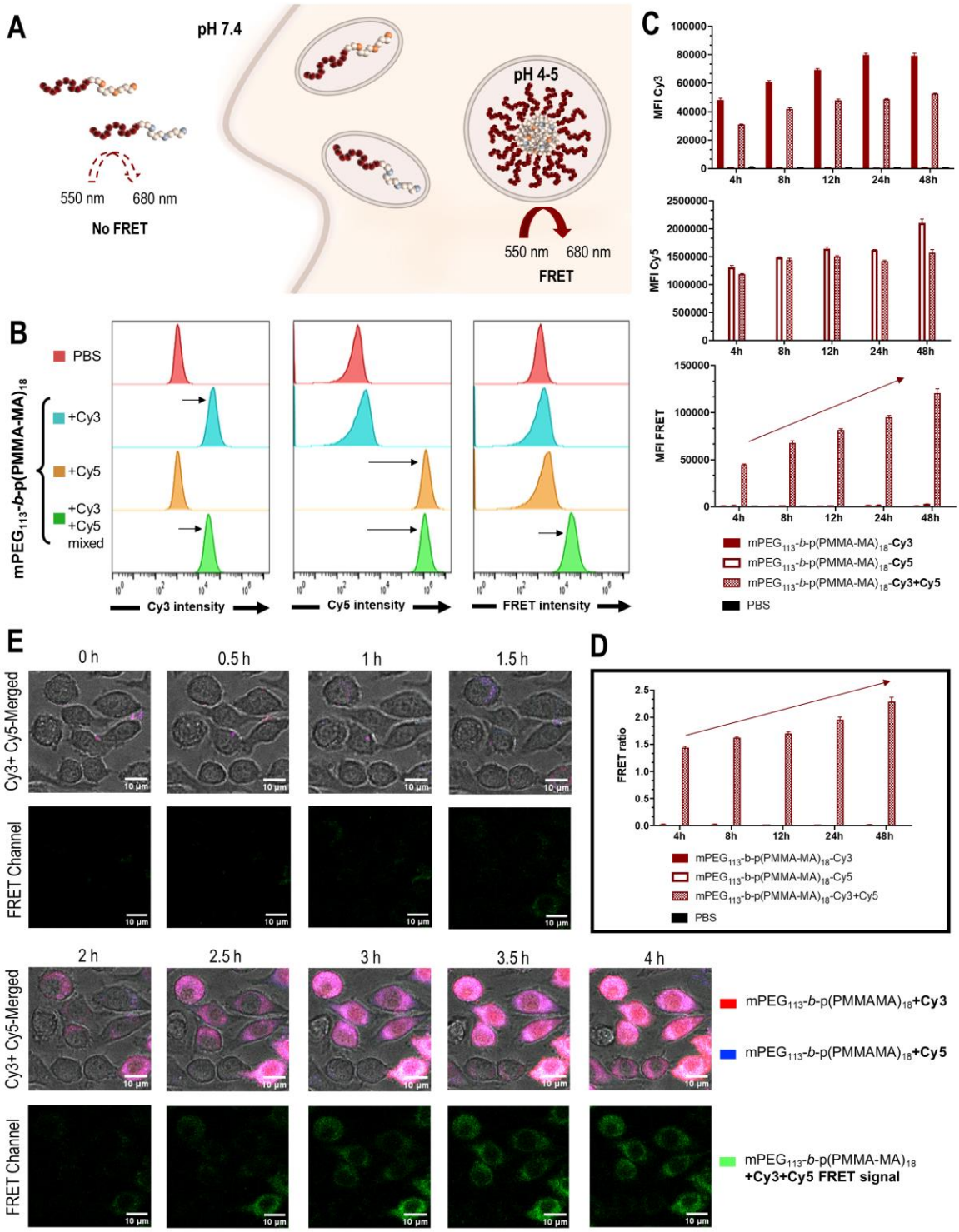

Figure 5. *In vitro* co-assembly of fluorescently dye-labeled block copolymer mPEG$_{113}$-*b*-p(PMMA-MA)$_{18}$ inside RAW macrophages. (**A**) While there is no extracellular FRET emission occurring extracellularly due to the individually solubilized Cy3- and Cy5-labeled block copolymers, upon internalization and accumulation inside acidified endolysosomal compartments a corresponding FRET signal can be detected. (**B**) Flow cytometric histogram for the cells treated with the respective polymer samples after 4 h. (**C**) Time-dependent mean fluorescence intensity (MFI) data for cells treated with the respective dye-labeled polymers and their derived FRET signal. (**D**) Corresponding FRET ratios over time. (**E**) Lifetime confocal microscopy images of RAW macrophages incubated with a mixture of Cy3- and Cy5-conjugated block copolymer at a concentration of 10 µg/mL for 4 h. The fluorescence emission of the two dyes (Cy3 = red, and Cy5 = blue) (top) as well as the resulting FRET emission signal (red) is evolving over time.

Besides the FRET emission, the co-assembly of the two dyes also affects the fluorescence lifetime of the Cy3 donor dye.[40] While the free donor provides a longer fluorescence lifetime, it is reduced during FRET and can as well be monitored over time by live cell fluorescence lifetime imaging microscopy (FLIM) (Figure 6A+B). A robust way to analyze FLIM data can be conducted by the phasor approach (Figure 6A).[50–53] Different lifetime populations can easily be distinguished within the phasor plot and allow a differentiation between states of long lifetimes around 1.2 ns (green circle), representing the free polymers, and short lifetimes around 0.8 ns (red circle), representing the FRET-emitting micelles (Figure 6B, top). For each recorded pixel a contribution for each of these two populations can be derived and visualized over time (Figure 6B, bottom). The collected live cell FLIM data correspond well with the previous FRET emission images (Figure 5E). While long lifetimes were usually present directly after the addition of the polymers (a dim green signal can first be found extracellularly that gradually accumulates inside cells), after 2 h they start to turn into the short lifetimes (a red signal appears inside intracellular vesicles that increases overtime and fills up almost all the intracellular space except for the nuclei). After 4 h, all cells provided short fluorescence lifetimes, indicating again the intracellular co-assembly.

Intrigued by the evolving FRET signal assuming the intracellular co-assembly of the individual polymer strands, we wanted to visualize these co-assemblies and identify polymer micelles *in vitro*. For that purpose, we used the combined method of fluorescence staining and electron microscopy related as correlative light and electron microscopy (CLEM).[54,55] This technique enables the imaging of cellular environments by electron microscopy (EM) and further localization of fluorescently dye-labeled structures. For that purpose, RAW macrophages were incubated with Cy5-labeled polymers for 4 h and subsequently characterized by this method for additional artificial micellar structures (Figure 6C). To ensure a reliable characterization, different cells were investigated and carefully screened for new micellar structures at those spots where a fluorescence was recorded (Figure S36). First, block copolymer-incubated macrophages were detected by EM to define cellular sections, followed by the detection of an overlapping Cy5-fluorescence signal, which confirmed the successful internalization of the dye-labeled polymers. Remarkably, the detailed characterization of the fluorescent cellular regions by a serial of CLEM images revealed indeed the formation of spherical compounds, with sizes around 40-50 nm, localized in endosomal compartments (Figure 5D and Figure S36). These images portend the successful co-assembly of the block copolymers, and according to our previous investigations they presumably occur as block copolymer micelles inside acidic cellular environments.

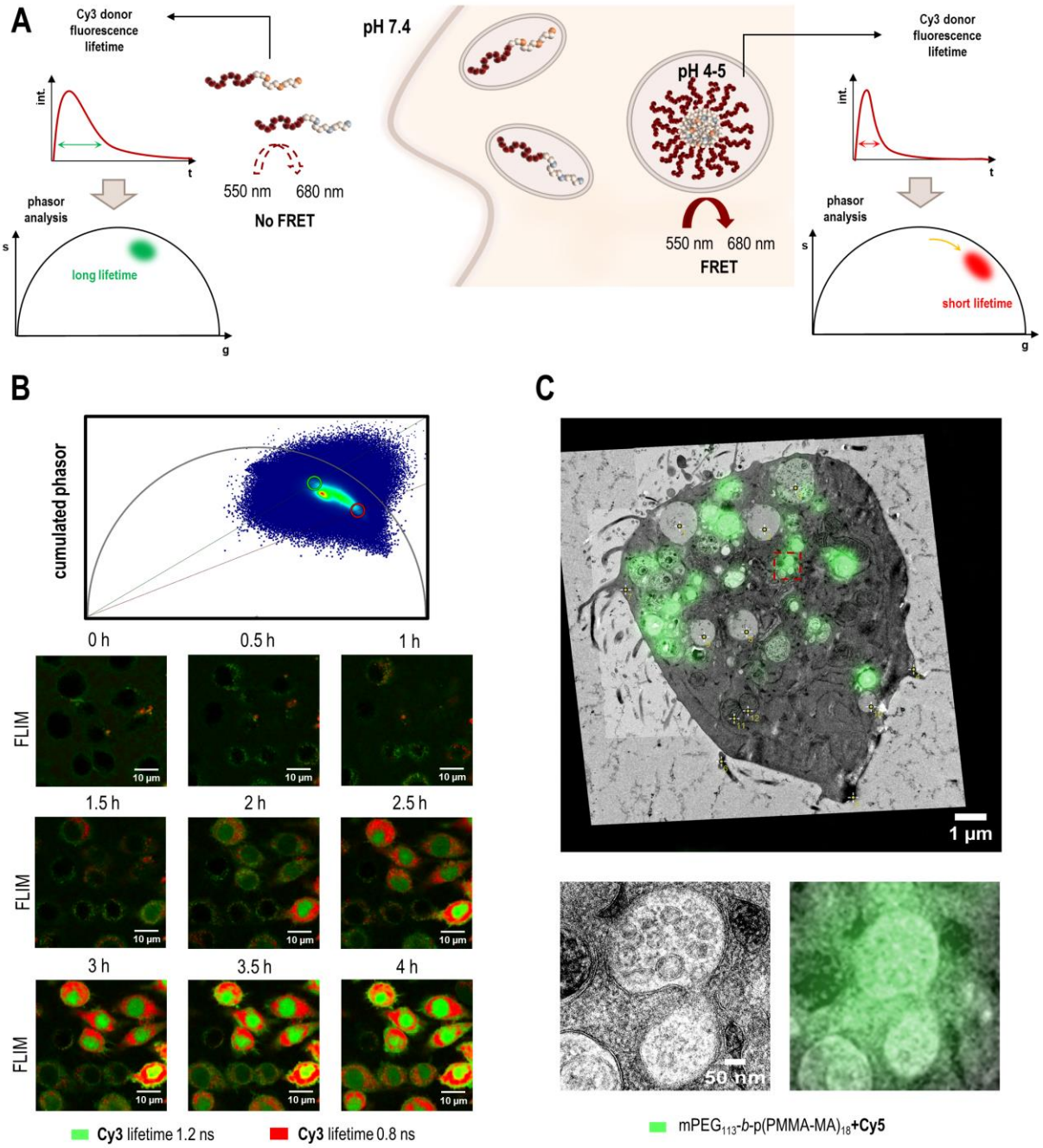

Figure 6. Molecular insight into the *in vitro* co-assembly of the fluorescently dye-labeled block copolymer mPEG$_{113}$-*b*-p(PMMA-MA)$_{18}$ inside RAW macrophages. (**A**) Fluorescence lifetime microscopy (FLIM) imaging allows to distinguish between the absence or presence of FRET for the Cy3- and Cy5-labeled block copolymers. The fluorescence lifetime of the donor dye Cy3 was recorded and then analyzed by the phasor approach to differentiate between the soluble, non-FRET emitting species with longer lifetimes that the co-assembled micellar species providing FRET. (**B**) Phasor plot of the accumulated life cell FLIM data (top) provide two different lifetime species at 1.2 ns (green circle) and 0.8 ns (red circle). The resulting lifetime confocal microscopy images (below) of the RAW macrophages incubated with a mixture of Cy3- and Cy5-conjugated block copolymer at a concentration of 10 µg/mL for 4 h show the evolving co-assembly of the polymers inside the cells. (**C**). Correlative light and electron microscopy (CLEM) of RAW macrophages incubated with 30 µg/mL Cy5-labeled block copolymer solution in PBS for 4 h, showing additional spherical structures at those spots inside endosomes where a Cy5-fluorescence can be associated.

Consequently, our polymeric carrier system, which has previously already demonstrated successful intracellular acid-triggered drug release properties[41,56], can also serve as building block to potentially form reversible nano-structured morphologies inside cells. They may provide additional features to design artificial cellular compartments that might probably accommodate advanced reaction properties or other physicochemical conditions. Fortunately, the pH reversibility assures only transient nano-structuring which immediately disassembles under neutral conditions and, thus, guarantees a safe way for artificial compartmentalization inside cells.

Conclusions

In this study, we could demonstrate the successful synthesis of polymethacrylamide-based block copolymers with pendant 2-propionic-3-methylmaleic anhydride groups which provide pH-sensitive micelles that even self-assemble inside cells. For this purpose, polymerizable propionic methylmaleic anhydride methacrylamide (PMMA-MA) monomers were grafted onto mPEG-based macro trithiocarbonate chain transfer agents (PEG-TTC-CTA) by controlled radical polymerization and afforded well-defined pH-responsive amphiphilic block copolymers. The pH-dependent self-assembling behavior of the substituted maleic anhydride containing block copolymers yielded stable micelles with sizes around 40 nm and narrow PDI below 0.12 at acidic pH values around 5.5 and below. Increasing pH values resulted in a deprotonation of substituted maleic anhydrides into ring-opened systems and forced the disassembly of the micellar self-assemblies. The modification of the polymer anhydrides with primary amines led to the formation of pH-resistant imide structures. In contrast to that, secondary amines assured a quantitative release upon acidification and further pH-reversible self-assembly of the block copolymers. These pH-sensitive properties were additionally investigated by Cy3- and Cy5-labeled polymers that provided a strong FRET signal upon acidification and self-assembly. The latter could also be confirmed during cell internalization monitored by flow cytometry, live cell confocal microscopy and fluorescent lifetime imaging. The collected data suggest that the individual polymer chains co-assemble during cell uptake and build up spherical micelles inside endosomes which could be confirmed by correlative light and electron microscopy.

Overall, these features make polymetharcylamides with pendant 2-propionic-3-methylmaleic anhydride groups a remarkable macromolecular system not only for acid-triggered intracellular release of secondary amines as cargos, but also for the controlled pH-triggered formation of nano-structured compartments by the carrier inside cells. Due to its pH-reversible co-assembly

properties, the polymeric 2-propionic-3-methylmaleic anhydrides allow for transient micellization that immediately disassembles under neutral conditions and, thus, resembles a safe way to install artificial compartmentalization inside cells.

Author Contributions

The manuscript was written through contributions of all authors. All authors have given approval to the final version of the manuscript.

Notes

The authors declare no competing financial interest.

Acknowledgements

This work was gratefully supported by the DFG through the Emmy Noether program, the CRC/SFB 1066 projects B03 and B04 and the CRC/TRR 225 project B05. Moreover, support by the BMBF Clusters4Futer curATime (projects curAIntervent and megATarget) is kindly acknowledged. Stephan Türk, Manfred Wagner, Stefan Spang, Detlev-Walter Scholdei, Joshua Krehan and Christoph Sieber are acknowledged for technical assistance during the analytical measurements.

References

(1) Coessens, V.; Pintauer, T.; Matyjaszewski, K. Functionalized Polymers by Atom Transfer Radical Polymerization. *ACS Symp. Ser.* **2000**, *768* (November 2000), 347–360.

(2) Nothling, M. D.; Fu, Q.; Reyhani, A.; Allison-Logan, S.; Jung, K.; Zhu, J.; Kamigaito, M.; Boyer, C.; Qiao, G. G. Progress and Perspectives Beyond Traditional RAFT Polymerization. *Adv. Sci.* **2020**, *7* (20), 1–12.

(3) Moad, G.; Rizzardo, E.; Thang, S. H. RAFT Polymerization and Some of Its Applications. *Chem. - An Asian J.* **2013**, *8* (8), 1634–1644.

(4) Chiefari, J.; Chong, Y. K.; Ercole, F.; Krstina, J.; Jeffery, J.; Le, T. P. T.; Mayadunne, R. T. A.; Meijs, G. F.; Moad, C. L.; Moad, G.; Rizzardo, E.; Thang, S. H. Living Free-Radical Polymerization by Reversible Addition - Fragmentation Chain Transfer: The RAFT Process. *Macromolecules* **1998**, *31* (16), 5559–5562.

(5) McLeary, J. B.; Calitz, F. M.; McKenzie, J. M.; Tonge, M. P.; Sanderson, R. D.; Klumperman, B. A 1H NMR Investigation of Reversible Addition-Fragmentation Chain Transfer Polymerization Kinetics and Mechanisms. Initialization with Different Initiating and Leaving Groups. *Macromolecules* **2005**, *38* (8), 3151–3161.

(6) Das, A.; Theato, P. Activated Ester Containing Polymers: Opportunities and Challenges for the Design of Functional Macromolecules. *Chem. Rev.* **2016**, *116* (3), 1434–1495.

(7) Ganesh, V. A.; Baji, A.; Ramakrishna, S. Smart Functional Polymers - A New Route towards Creating a Sustainable Environment. *RSC Adv.* **2014**, *4* (95), 53352–53364.

(8) Nuhn, L.; Overhoff, I.; Sperner, M.; Kaltenberg, K.; Zentel, R. RAFT-Polymerized Poly(Hexafluoroisopropyl Methacrylate)s as Precursors for Functional Water-Soluble Polymers. *Polym. Chem.* **2014**, *5* (7), 2484–2495.

(9) Stickdorn, J.; Nuhn, L. Reactive-Ester Derived Polymer Nanogels for Cancer Immunotherapy. *Eur. Polym. J.* **2020**, *124* (September 2019), 109481.

(10) Huppertsberg, A.; Kaps, L.; Zhong, Z.; Schmitt, S.; Stickdorn, J.; Deswarte, K.; Combes, F.; Czysch, C.; De Vrieze, J.; Kasmi, S.; Choteschovsky, N.; Klefenz, A.; Medina-Montano, C.; Winterwerber, P.; Chen, C.; Bros, M.; Lienenklaus, S.; Sanders, N. N.; Koynov, K.; Schuppan, D.; Lambrecht, B. N.; David, S. A.; De Geest, B. G.; Nuhn, L. Squaric Ester-Based, PH-Degradable Nanogels: Modular Nanocarriers for Safe, Systemic Administration of Toll-like Receptor 7/8 Agonistic Immune Modulators. *J. Am. Chem. Soc.* **2021**, *143* (26), 9872–9883.

(11) Scherger, M.; Pilger, Y. A.; Komforth, P.; Räder, H. J.; Nuhn, L. Reversible Polymer-Protein Functionalization by Stepwise Introduction of Amine-Reactive, Reductive-Responsive Self-Immolative End Groups onto RAFT-Derived Polymers. *ACS Biomater. Sci. Eng.* **2024**, *10* (1), 129–138.

(12) Bixenmann, L.; Stickdorn, J.; Nuhn, L. Amphiphilic Poly(Esteracetal)s as Dual PH-and Enzyme-Responsive Micellar Immunodrug Delivery Systems. *Polym. Chem.* **2020**, *11* (13), 2441–2456.

(13) Czysch, C.; Medina-Montano, C.; Zhong, Z.; Fuchs, A.; Stickdorn, J.; Winterwerber, P.; Schmitt, S.; Deswarte, K.; Raabe, M.; Scherger, M.; Combes, F.; De Vrieze, J.; Kasmi, S.; Sandners, N. N.; Lienenklaus, S.; Koynov, K.; Räder, H. J.; Lambrecht, B. N.; David, S. A.; Bros, M.; Schild, H.; Grabbe, S.; De Geest, B. G.; Nuhn, L. Transient Lymph Node Immune Activation by Hydrolysable Polycarbonate Nanogels. *Adv. Funct. Mater.* **2022**, *32* (35), 2203490.

(14) Chen, F.; Qi, R.; Huyer, L. D.; Amsden, B. G. Degradation of Poly(5-Hydroxy-Trimethylene Carbonate) in Aqueous Environments. *Polym. Degrad. Stab.* **2018**, *158*, 83–91.

(15) Moad, G. RAFT Polymerization to Form Stimuli-Responsive Polymers. *Polym. Chem.* **2017**, *8* (1), 177–219.

(16) Schattling, P.; Jochum, F. D.; Theato, P. Multi-Stimuli Responsive Polymers-the All-in-One Talents. *Polym. Chem.* **2014**, *5* (1), 25–36.

(17) Blum, A. P.; Kammeyer, J. K.; Rush, A. M.; Callmann, C. E.; Hahn, M. E.; Gianneschi, N. C. Stimuli-Responsive Nanomaterials for Biomedical Applications. *J. Am. Chem. Soc.* **2015**, *137* (6), 2140–2154.

(18) Tong, R.; Tang, L.; Ma, L.; Tu, C.; Baumgartner, R.; Cheng, J. Smart Chemistry in Polymeric Nanomedicine. *Chem. Soc. Rev.* **2014**, *43* (20), 6982–7012.

(19) Kanamala, M.; Wilson, W. R.; Yang, M.; Palmer, B. D.; Wu, Z. Mechanisms and Biomaterials in PH-Responsive Tumour Targeted Drug Delivery: A Review. *Biomaterials* **2016**, *85*, 152–167.

(20) Gao, W.; Chan, J. M.; Farokhzad, O. C. Reviews PH-Responsive Nanoparticles for Drug Delivery. *Mol. Pharm.* **2010**, *7* (6), 1913–1920.

(21) Schmaljohann, D. Thermo- and PH-Responsive Polymers in Drug Delivery. *Adv. Drug Deliv. Rev.* **2006**, *58* (15), 1655–1670.

(22) Kocak, G.; Tuncer, C.; Bütün, V. PH-Responsive Polymers. *Polym. Chem.* **2017**, *8* (1), 144–176.

(23) Deirram, N.; Zhang, C.; Kermaniyan, S. S.; Johnston, A. P. R.; Such, G. K. PH-Responsive Polymer Nanoparticles for Drug Delivery. *Macromol. Rapid Commun.* **2019**, *40* (10), 1–23.

(24) Van Driessche, A.; Kocere, A.; Everaert, H.; Nuhn, L.; Van Herck, S.; Griffiths, G.; Fenaroli, F.; De Geest, B. G. PH-Sensitive Hydrazone-Linked Doxorubicin Nanogels via Polymeric-Activated Ester Scaffolds: Synthesis, Assembly, and in Vitro and in Vivo Evaluation in Tumor-Bearing Zebrafish. *Chem. Mater.* **2018**, *30* (23), 8587–8596.

(25) Murthy, N.; Thng, Y. X.; Schuck, S.; Xu, M. C.; Fréchet, J. M. J. A Novel Strategy for Encapsulation and Release of Proteins: Hydrogels and Microgels with Acid-Labile Acetal Cross-Linkers. *J. Am. Chem. Soc.* **2002**, *124* (42), 12398–12399.

(26) Nuhn, L.; Vanparijs, N.; De Beuckelaer, A.; Lybaert, L.; Verstraete, G.; Deswarte, K.; Lienenklaus, S.; Shukla, N. M.; Salyer, A. C. D.; Lambrecht, B. N.; Grooten, J.; David, S. A.; De Koker, S.; De Geest, B. G. PH-Degradable Imidazoquinoline-Ligated Nanogels for Lymph Node-Focused Immune Activation. *Proc. Natl. Acad. Sci. U. S. A.* **2016**, *113* (29), 8098–8103.

(27) Liu, Z.; Zhang, N. PH-Sensitive Polymeric Micelles for Programmable Drug and Gene Delivery. *Curr. Pharm. Des.* **2012**, *18* (23), 3442–3451.

(28) Wang, C.; Wang, G.; Wang, Z.; Zhang, X. A PH-Responsive Superamphiphile Based on Dynamic Covalent Bonds. *Chem. - A Eur. J.* **2011**, *17* (12), 3322–3325.

(29) Fleige, E.; Quadir, M. A.; Haag, R. Stimuli-Responsive Polymeric Nanocarriers for the Controlled Transport of Active Compounds: Concepts and Applications. *Adv. Drug Deliv. Rev.* **2012**, *64* (9), 866–884.

(30) Spanedda, M. V.; Bourel-Bonnet, L. Cyclic Anhydrides as Powerful Tools for Bioconjugation and Smart Delivery. *Bioconjug. Chem.* **2021**, *32* (3), 482–496.

(31) Tao, A.; Huang, G. Lo; Igarashi, K.; Hong, T.; Liao, S.; Stellacci, F.; Matsumoto, Y.; Yamasoba, T.; Kataoka, K.; Cabral, H. Polymeric Micelles Loading Proteins through Concurrent Ion Complexation and PH-Cleavable Covalent Bonding for In Vivo Delivery. *Macromol. Biosci.* **2020**, *20* (1), 1–11.

(32) Maier, K.; Wagner, E. Acid-Labile Traceless Click Linker for Protein Transduction. *J. Am. Chem. Soc.* **2012**, *134* (24), 10169–10173.

(33) Park, H.; Suh, J.; Lee, S. Ab Initio Studies of the Intramolecular Amide Hydrolysis in N-Methylmaleamic Acids. *J. Mol. Struct. THEOCHEM* **1999**, *490* (1–3), 47–54.

(34) Kang, S.; Kim, Y.; Song, Y.; Choi, J. U.; Park, E.; Choi, W.; Park, J.; Lee, Y. Comparison of PH-Sensitive Degradability of Maleic Acid Amide Derivatives. *Bioorganic Med. Chem. Lett.* **2014**, *24* (10), 2364–2367.

(35) Song, Y.; Jung, D.; Kang, S.; Lee, Y. Amine-Selective Affinity Resins Based on PH-Sensitive Reversible Formation of Covalent Bonds. *Soft Matter* **2017**, *13* (12), 2295–2298.

(36) Du, J. Z.; Li, H. J.; Wang, J. Tumor-Acidity-Cleavable Maleic Acid Amide (TACMAA): A Powerful Tool for Designing Smart Nanoparticles to Overcome Delivery Barriers in Cancer Nanomedicine. *Acc. Chem. Res.* **2018**, *51* (11), 2848–2856.

(37) Li, Y.; Yang, H. Y.; Thambi, T.; Park, J. H.; Lee, D. S. Charge-Convertible Polymers for Improved Tumor Targeting and Enhanced Therapy. *Biomaterials* **2019**, *217*, 119299.

(38) Zhang, X.; Zhang, K.; Haag, R. Multi-Stage, Charge Conversional, Stimuli-Responsive Nanogels for Therapeutic Protein Delivery. *Biomater. Sci.* **2015**, *3* (11), 1487–1496.

(39) Roy, R.; Hohng, S.; Ha, T. A Practical Guide to Single-Molecule FRET. *Nat. Methods* **2008**, *5* (6), 507–516.

(40) Nuhn, L.; Van Herck, S.; Best, A.; Deswarte, K.; Kokkinopoulou, M.; Lieberwirth, I.; Koynov, K.; Lambrecht, B. N.; De Geest, B. G. FRET Monitoring of Intracellular Ketal Hydrolysis in Synthetic Nanoparticles. *Angew. Chemie - Int. Ed.* **2018**, *57* (33), 10760–10764.

(41) Heck, A. G.; Stickdorn, J.; Rosenberger, L. J.; Scherger, M.; Woller, J.; Eigen, K.; Bros, M.; Grabbe, S.; Nuhn, L. Polymerizable 2-Propionic-3-Methylmaleic Anhydrides as a Macromolecular Carrier Platform for PH-Responsive Immunodrug Delivery. *J. Am. Chem. Soc.* **2023**, *145* (50), 27424–27436.

(42) Otsuka, H.; Nagasaki, Y.; Kataoka, K. PEGylated Nanoparticles for Biological and Pharmaceutical Applications. *Adv. Drug Deliv. Rev.* **2003**, *55* (3), 403–419.

(43) Melnik, L. A.; Krysenko, D. A. Ultrapure Water: Properties, Production, and Use. *J. Water Chem. Technol.* **2019**, *41* (3), 143–150.

(44) Fernández-Arguelles, M. T.; Yakovlev, A.; Sperling, R. A.; Luccardini, C.; Gaillard, S.; Medel, A. S.; Mallet, J. M.; Brochon, J. C.; Feltz, A.; Oheim, M.; Parak, W. J. Synthesis and Characterization of Polymer-Coated Quantum Dots with Integrated Acceptor Dyes as FRET-Based Nanoprobes. *Nano Lett.* **2007**, *7* (9), 2613–2617.

(45) Sekar, R. B.; Periasamy, A. Fluorescence Resonance Energy Transfer (FRET) Microscopy Imaging of Live Cell Protein Localizations. *J. Cell Biol.* **2003**, *160* (5), 629–633.

(46) Förster, T. Zwischenmolekulare Energiewanderung Und Fluoreszenz. *Ann. Phys.* **1948**, *2* (6), 55–75.

(47) Shrestha, D.; Jenei, A.; Nagy, P.; Vereb, G.; Szöllősi, J. Understanding FRET as a Research Tool for Cellular Studies. *Int. J. Mol. Sci.* **2015**, *16* (4), 6718–6756.

(48) Kaps, L.; Huppertsberg, A.; Choteschovsky, N.; Klefenz, A.; Durak, F.; Schrörs, B.; Diken, M.; Eichler, E.; Rosigkeit, S.; Schmitt, S.; Leps, C.; Schulze, A.; Foerster, F.; Bockamp, E.; de Geest, B. G.; Koynov, K.; Räder, H. J.; Tenzer, S.; Marini, F.; Schuppan, D.; Nuhn, L. PH-Degradable, Bisphosphonate-Loaded Nanogels Attenuate Liver Fibrosis by Repolarization of M2-Type Macrophages. *Proc. Natl. Acad. Sci. U. S. A.* **2022**, *119* (12), e2122310119.

(49) Lybaert, L.; Vermaelen, K.; De Geest, B. G.; Nuhn, L. Immunoengineering through Cancer Vaccines – A Personalized and Multi-Step Vaccine Approach towards Precise Cancer Immunity.

J. Control. Release **2018**, *289*, 125–145.

(50) Digman, M. A.; Caiolfa, V. R.; Zamai, M.; Gratton, E. The Phasor Approach to Fluorescence Lifetime Imaging Analysis. *Biophys. J.* **2008**, *94* (2), L14–L16.

(51) Ossato, G. *Phasor Analysis for FLIM (Fluorescence Lifetime Imaging Microscopy)*. Leica Microsystems. https://www.leica-microsystems.com/science-lab/phasor-analysis-for-flim-fluorescence-lifetime-imaging-microscopy/.

(52) Cao, J.; Su, T.; Zhang, L.; Liu, R.; Wang, G.; He, B.; Gu, Z. Polymeric Micelles with Citraconic Amide as PH-Sensitive Bond in Backbone for Anticancer Drug Delivery. *Int. J. Pharm.* **2014**, *471* (1–2), 28–36.

(53) Ren, Y.; Zhou, Z.; Maxeiner, K.; Wu, Y.; Wagner, M.; Landfester, K. Resolving Bioactive Supramolecular Structure Formation in Live Cells by Phasor-Fluorescence Lifetime Imaging. *J. Am. Chem. Soc.* **2024**, 1–15.

(54) Han, S.; Raabe, M.; Hodgson, L.; Mantell, J.; Verkade, P.; Lasser, T.; Landfester, K.; Weil, T.; Lieberwirth, I. High-Contrast Imaging of Nanodiamonds in Cells by Energy Filtered and Correlative Light-Electron Microscopy: Toward a Quantitative Nanoparticle-Cell Analysis. *Nano Lett.* **2019**, *19* (3), 2178–2185.

(55) Han, S.; da Costa Marques, R.; Simon, J.; Kaltbeitzel, A.; Koynov, K.; Landfester, K.; Mailänder, V.; Lieberwirth, I. Endosomal Sorting Results in a Selective Separation of the Protein Corona from Nanoparticles. *Nat. Commun.* **2023**, *14* (1), 295.

(56) Heck, A. G.; Medina-Montano, C.; Zhong, Z.; Deswarte, K.; Eigen, K.; Stickdorn, J.; Kockelmann, J.; Scherger, M.; Sanders, N. N.; Lienenklaus, S.; Lambrecht, B. N.; Grabbe, S.; De Geest, B. G.; Nuhn, L. PH-Triggered, Lymph Node Focused Immunodrug Delivery by Polymeric 2-Propionic-3-Methylmaleic Anhydrides with Cholesterol End Group. **2024-submitted**.

REVERSIBLE INTRACELLULAR CO-ASSEMBLY OF POLYMERIC 2-PROPIONIC-3-METHYLMALEIC ANHYDRIDES

-Supporting Information-

Alina G. Heck[1,2], Judith Stickdorn[1], David Schwiertz[3], Jonas Woller[2], Anke Kaltbeitzel[2], Ingo Lieberwirth[2], David Y. W. Ng[2], Katharina Landfester[2], Tanja Weil[2], and Lutz Nuhn[1,2]*

1: Institute of Functional Materials and Biofabrication, Department of Chemistry and Pharmacy, Julius-Maximilians-Universität Würzburg, 97070 Würzburg, Germany

2: Max Planck Institute for Polymer Research, 55128 Mainz, Germany

3: Biotherapeutics Division, Leiden Academic Centre for Drug Research (LACDR), Leiden University, 2333CC Leiden, The Netherlands

*: corresponding author: Prof. Dr. Lutz Nuhn (E-mail: lutz.nuhn@uni-wuerzburg.de)

Materials and Methods

Unless otherwise described, all reagents and solvents were obtained from TCI Chemicals (Tokyo, Japan), Sigma Aldrich (Taufkirchen, Germany) or Rapp Polymers (Tübingen, Germany) and used without further purification. Dimethyl sulfoxide (DMSO), *N*,*N*-dimethylformamide (DMF), chloroform ($CHCl_3$), dichloromethane (DCM), ethyl acetate (EA), methanol (MeOH), all deuterated solvents as well as benzylamine, dibenzylamine and triethylamine (TEA) were purchased from Sigma Aldrich. Oxalyl chloride and trifluoroacetic acid (TFA) were bought from Thermo Fisher Scientific (Waltham, MA, USA). N-(3-aminopropyl)methacrylamide hydrochloride (APMA) was obtained from abcr GmbH (Karlsruhe, Germany). Cyanine 3 cadaverine (Cy3) and Cyanine 5 cadaverine (Cy5) were purchased from Lumiprobe GmbH (Hannover, Germany). Azobisisobutyronitrile (AIBN) was recrystallized from ethanol twice.

Hexafluoroisopropanol (HFIP) was bought from Fluorochem Ltd. (Hadfield, UK). Millipore (mp) water was prepared using a MILLI-Q® Reference A+ System. Water was used at a resistivity of 18.2 MΩ·cm and total organic caron of <5 ppm. For silica gel chromatography silica with particle size of 0.063-0.2 mm from Macherey-Nagel GmbH & Co. KG (Dueren, Germany) was used. Dialysis was performed with Spectra/Por7™ dialysis membranes with a molecular weight cut-off of 1000 g/mol purchased from Spectrum Labs (Schwerte, Germany).

Dulbecco's phosphate-buffered saline (PBS), cell culture medium and supplements were obtained from Thermo Fisher Scientific. The RAW-Dual™ (IRF-Lucia/KI-[MIP-2]SEAP) murine macrophage reporter cell line and the QUANTI-Blue™ solution were purchased from InvivoGen (San Diego, CA, USA). RAW-Dual™ cells were cultured in Dulbecco's modified Eagle's medium DMEM, containing 10% fetal bovine serum, 1% penicillin/streptomycine, 0.02% normocine, and 0.01% zeocin at 37 °C with 5% CO_2 saturation.

Instrumentation

Nuclear Magnetic Resonance (NMR) Spectroscopy

All ^{1}H, ^{13}C, ^{19}F and 2D NMR spectra were recorded on a Bruker Avance III 300 MHz, Bruker Avance III 400 MHz, Bruker Avance III 500 MHz or Bruker Avance III 700 MHz spectrometer at room temperature. Diffusion ordered spectroscopy (DOSY) were conducted on a Bruker Avance III 500 MHz or Bruker Avance III 700 MHz spectrometer. The samples were dissolved

in deuterated solvents and referenced to residual protons of the solvent signals. NMR spectra were processed and analyzed using MestReNova 14.2.0 by Mestrelab Research.

Size Exclusion Chromatography (SEC)

Analytical SEC was performed using a SECcurity2instrument from PPS, Mainz equipped with a SECcurtity2isocratic pump, a degasser, an autosampler, a column thermostat, an UV and RI detector. HFIP was utilized as an eluant, which contained 3 g/L potassium trifluoroacetate and the flow rate was set at 0.8 mL/min and 40 °C. The column material was packed with modified silica gel (PFG columns, particle size 7 µM, porosity: 100 Å and 1000 Å), obtained from PSS Polymer Standards Service GmbH, Mainz, Germany. Poly(methyl methacrylate) (PMMA) standard was used for calibration, purchased from PSS, Mainz. Polymer samples were dissolved at 1 mg/mL and filtered through GHP syringe filters (0.2 µm pore size, Acrodisc) prior to injection.

Dynamic Light Scattering (DLS)

Single-angle dynamic light scattering measurements were carried out on a Malvern Z Nano instrument equipped with a He-Ne-Laser (λ = 632.8 nm) using the ZetaSizer Software 7.12. All measurements were performed in triplicates at 25 °C and a detection angle of 173°. The resulting data were analyzed by cumulant fitting for z-average mean diameter and PDI, or by CONTIN fitting method for intensity-, volume-, and number-weighted particle size distribution. Samples were prepared at 0.1 mg/mL and dust was removed by filtration through GHP syringe filters (0.2 µm pore size, Acrodisc).

Ultraviolet-Visible Spectroscopy (UV-Vis) and Fluorescence Spectroscopy

UV-Vis spectra were performed on a Thermo Scientific™ NanoDrop™ 2000c spectrophotometer with a Hellma Quartz Cuvette.

Fluorescence spectroscopy and MTT assay absorbance read-out were measured on a Spark 20M Multimode Microplate Reader from Tecan Trading AG (Mannedorf, Switzerland).

Mass Spectrometry (ESI-MS)

ESI mass spectra were recorded using an Agilent 6545 QTOF-MS (Santa Clara, CA, USA). Samples were dissolved in methanol at 0.1 mg/mL. Mass spectrometry data were processed using the Advion Data Express software.

Transmission Electron Microscopy (TEM)

TEM measurements were carried out on a FEI Tecnai G2 Spirit microscope equipped with a Gatan US1000 2k x 2k CCD camera an LaB_6 cathode operated at 120 kV. Images were collected on freshly glow discharged carbon copper grids (CF300-Cu, 300 mesh). For preparation of TEM images 5 µL of the polymer solution (c = 25 mg·L^{-1}, dissolved in Millipore water containing 0.1 wt% hydrochloric acid or ammonia) was added onto the TEM grid and removed with a filter paper after 1 minute. Then, 5 µL uranyl acetate solution (2 wt% in ethanol) was added and removed after 15 seconds incubation time. All sample-deposited grids were air-dried overnight before measurement. Transmission electron microscopy data were processed using the ImageJ 1.52 software (National Institutes of Health, USA).

Fluorescent Confocal Microscopy

Fluorescent confocal laser scanning microscopy images were measured on a STELLARIS 8 Leica DMi8 confocal microscope with a HC PL APO CS2 40x/1.25 GLYC oil immersion objective. Images were processed using Leica Application Suite X 3.7.4.23463 by Leica Microsystems and ImageJ 1.52 software (National Institutes of Health, USA).

Flow Cytometry

Flow cytometric analyses were conducted on a BD Accuri C6 from BD Biosciences. All obtained data were analyzed using FloJo™_v10.8.1_CL by BD Biosciences.

Syntheses

Monomer Synthesis (PMMA-MA)

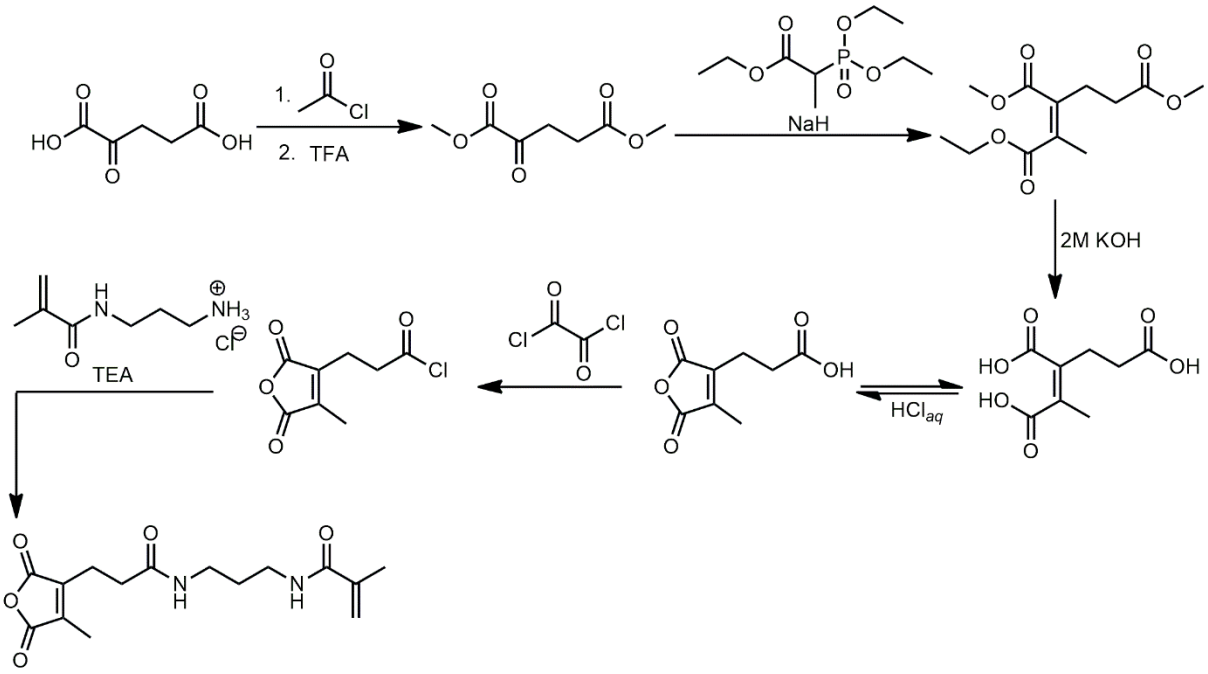

Figure S1: Synthesis route of the monomer N-(3-(3-(4-methyl-2,5-dioxo-2,5-dihydrofuran-3-yl)propanamido)-propyl)methacrylamide (PMMA-MA).

The synthesis of the monomer PMMA-MA was performed according to our previous report.[1]

^{1}H NMR (700 MHz, DMSO-d$_6$): δ (ppm) = 7.91 (s, 1H, **a**), 7.87 (s, 1H, **b**), 5.62 (s, 1H, **c**), 5.31 (s, 1H, **d**), 3.08 (q, *J* = 6.8 Hz, 2H, **e**), 3.02 (q, *J* = 6.8 Hz, 2H, **f**), 2.62 (t, *J* = 7.4 Hz, 2H, **g**), 2.35 (t, *J* = 7.4 Hz, 2H, **h**), 1.98 (s, 3H, **i**), 1.84 (s, 3H, **j**), 1.53 (quin, *J* = 8.4 Hz, 2H, **k**).

^{13}C NMR (176 MHz, DMSO-d$_6$): δ (ppm) = 170.61 (**a**), 167.64 (**b**), 166.61 (**c**), 166.15 (**d**), 143.12 (**e**), 141.22 (**f**), 140.27 (**g**), 119.04 (**h**). 36.90 (**i+j**), 32.87 (**k**), 29.58 (**l**), 20.51 (**m**), 19.08 (**n**), 9.68 (**o**).

ESI-MS [m/z] = 309.10 $[M+H]^+$ (calc. 309.15), 331.15 $[M+Na]^+$ (calc. 331.13), 347.10 $[M+K]^+$ (calc. 347.10).

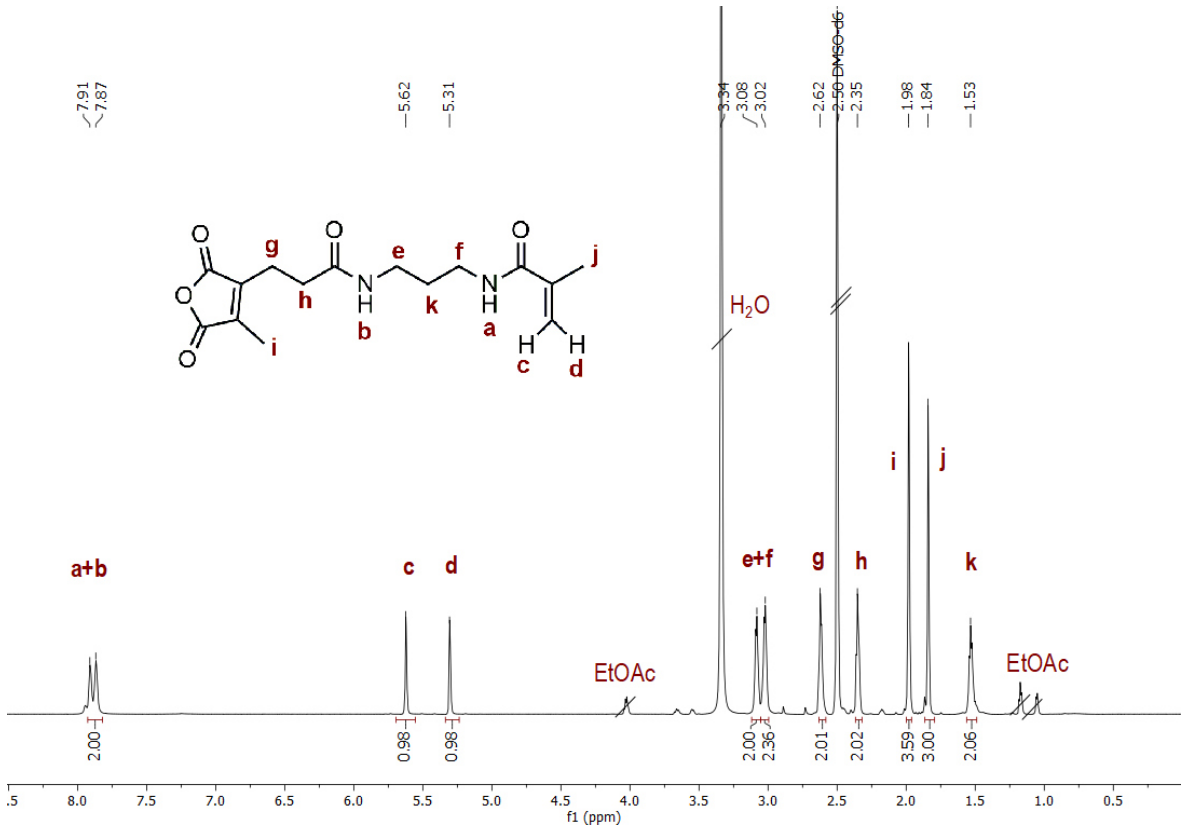

Figure S2: ^{1}H NMR spectrum (700 MHz) of the monomer N-(3-(3-(4-methyl-2,5-dioxo-2,5-dihydrofuran-3-yl)propanamido)-propyl)methacrylamide (PMMA-MA) in DMSO-d_6.

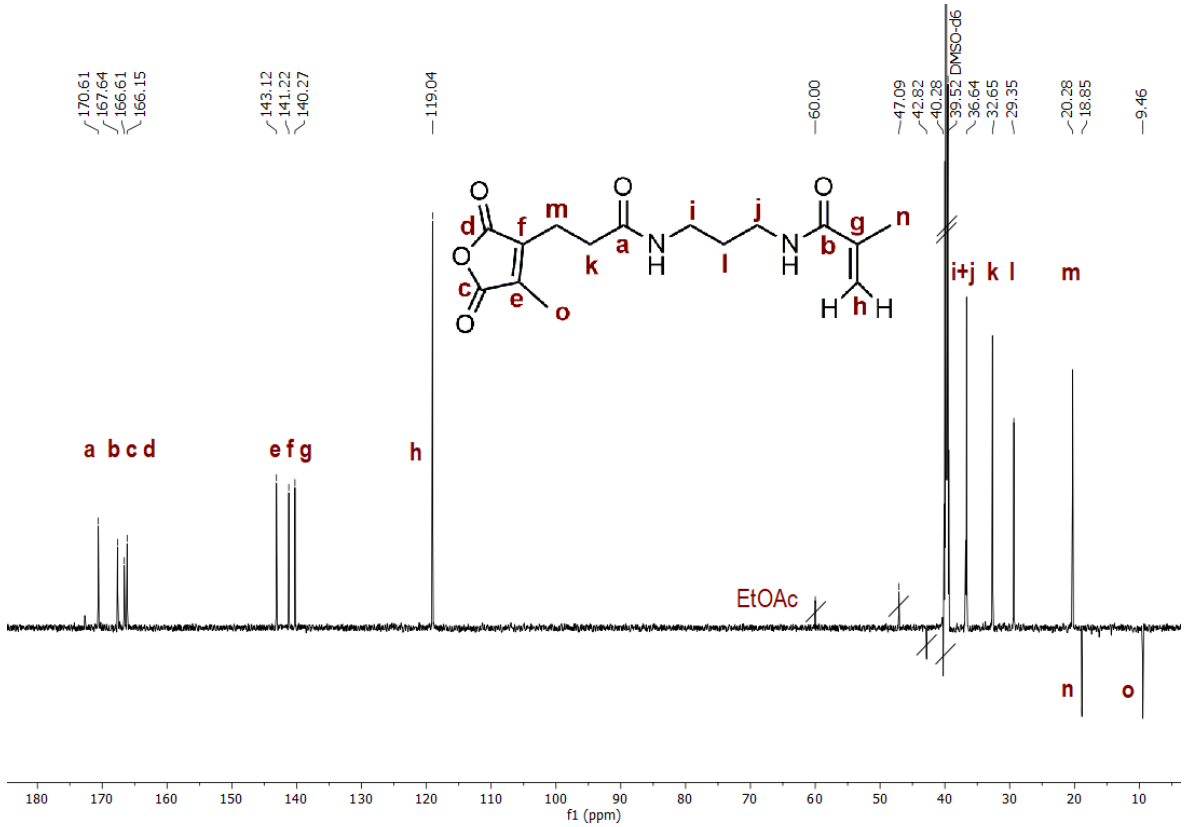

Figure S3: ^{13}C NMR spectrum (176 MHz) of the monomer N-(3-(3-(4-methyl-2,5-dioxo-2,5-dihydrofuran-3-yl)propanamido)-propyl)methacrylamide (PMMA-MA) in DMSO-d_6.

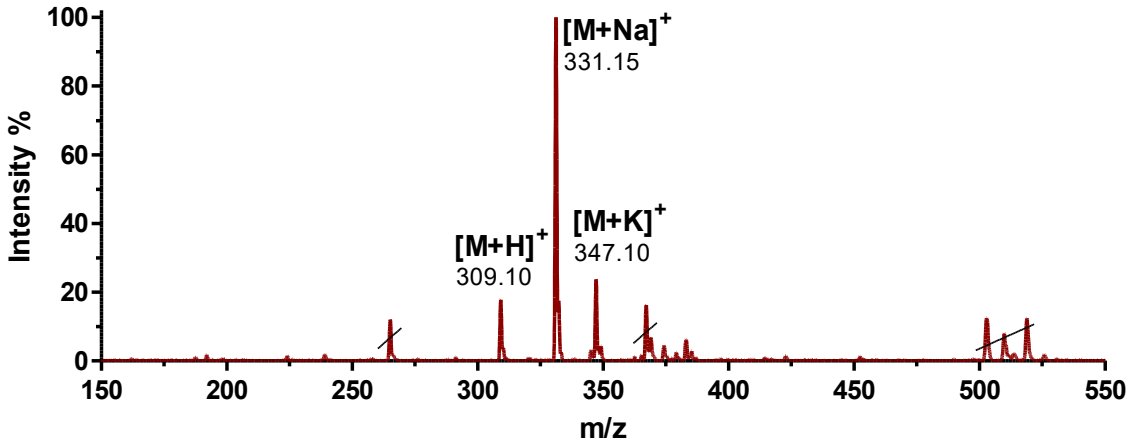

Figure S4: ESI-MS spectrum of the monomer N-(3-(3-(4-methyl-2,5-dioxo-2,5-dihydrofuran-3-yl)propanamido)-propyl)methacrylamide (PMMA-MA) in MeOH (positive ion mode).

Macro-Trithiocarbonate Chain Transfer Agent (macro-TTC-CTA)

Synthesis of Pentafluorophenyl-Trithiocarbonate Chain Transfer Agent (PFP-TTC-CTA)

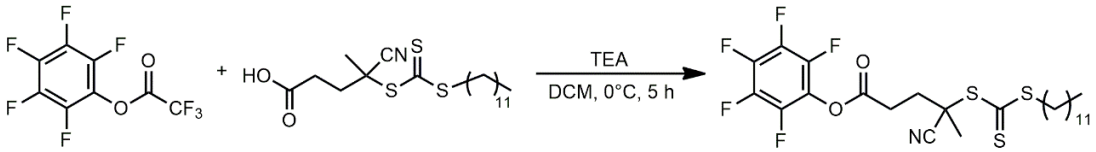

Figure S5: Synthesis of the pentafluorophenyl-trithiocarbonate chain transfer agent (PFP-TTC-CTA).

According to earlier reports[2,3], 4-cyano-4-[(dodecylsulfanylthiocarbonyl)sulfanyl]-pentanoic acid (TTC-CTA) (1.0 g, 2.5 mmol, 1 eq) was dissolved in anhydrous DCM (25 mL) under nitrogen atmosphere. After addition of triethylamine (TEA) (1.0 mL, 7.5 mmol, 3 eq) the reaction mixture was cooled to 0 °C using an ice bath and protected from light pentafluorophenyl trifluoroacetate (1.1 mL, 6.3 mmol, 2.5 eq) was slowly dropped to the solution. The reaction mixture was then stirred for 5 h at 0 °C, followed by dilution with DCM (15 mL) and extraction with water (3x25 mL). The resulting organic layer was dried over Na_2SO_4, filtrated, and dried *in vacuo*. The crude product was purified by silica column chromatography (PE/EA 15:1) yielding pentafluorophenyl-trithiocarbonate chain transfer agent (PFP-TTC-CTA) as yellow oil (1.02 g, 72 %).

^{1}H NMR (700 MHz, $CDCl_3$): δ (ppm) = 3.34 (t, J = 7.4 Hz, 2H, **a**), 3.05-2.98 (m, 2H, **b**), 2.68 (dt, J = 15.5 Hz, J = 8.0 Hz 1H, **c**), 2.53 (dt, J = 14.2 Hz, J = 7.6 Hz 1H, **c'**), 1.93 (s, 3H, **d**), 1.70 (quin, J = 7.1 Hz, 2H, **e**), 1.44-1.36 (m, 2H, **f**), 1.26 (s, 16H, **g**), 0.88 (t, J = 7.0 Hz, 3H, **h**).

^{19}F NMR (659 MHz, $CDCl_3$): δ (ppm) = -152.51 (d, J = 18 Hz, 2F, **a**), -157.29 (t, J = 21.6 Hz, 1F, **b**), -161.89 (d, J = 19.9 Hz, 2F, **c**).

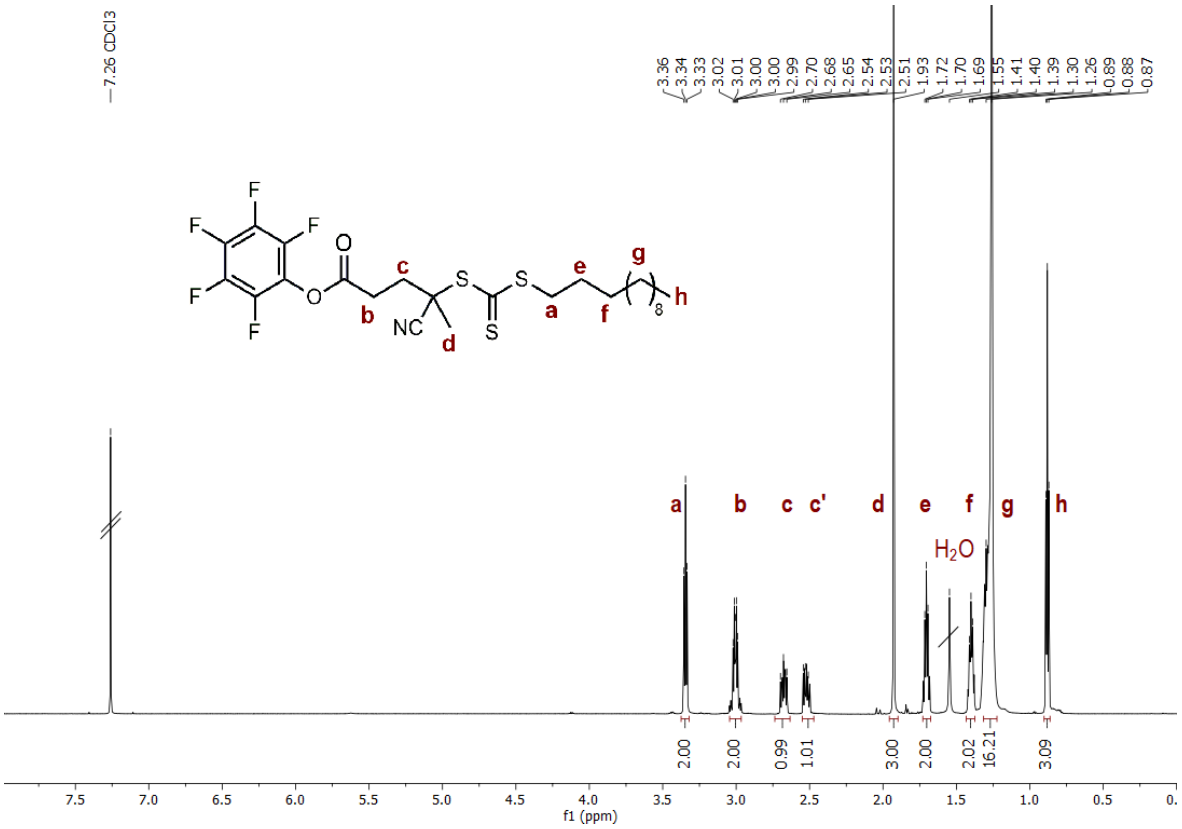

Figure S6: ^{1}H NMR spectrum (700 MHz) of the pentafluorophenyl-trithiocarbonate chain transfer agent (PFP-TTC-CTA) in $CDCl_3$.

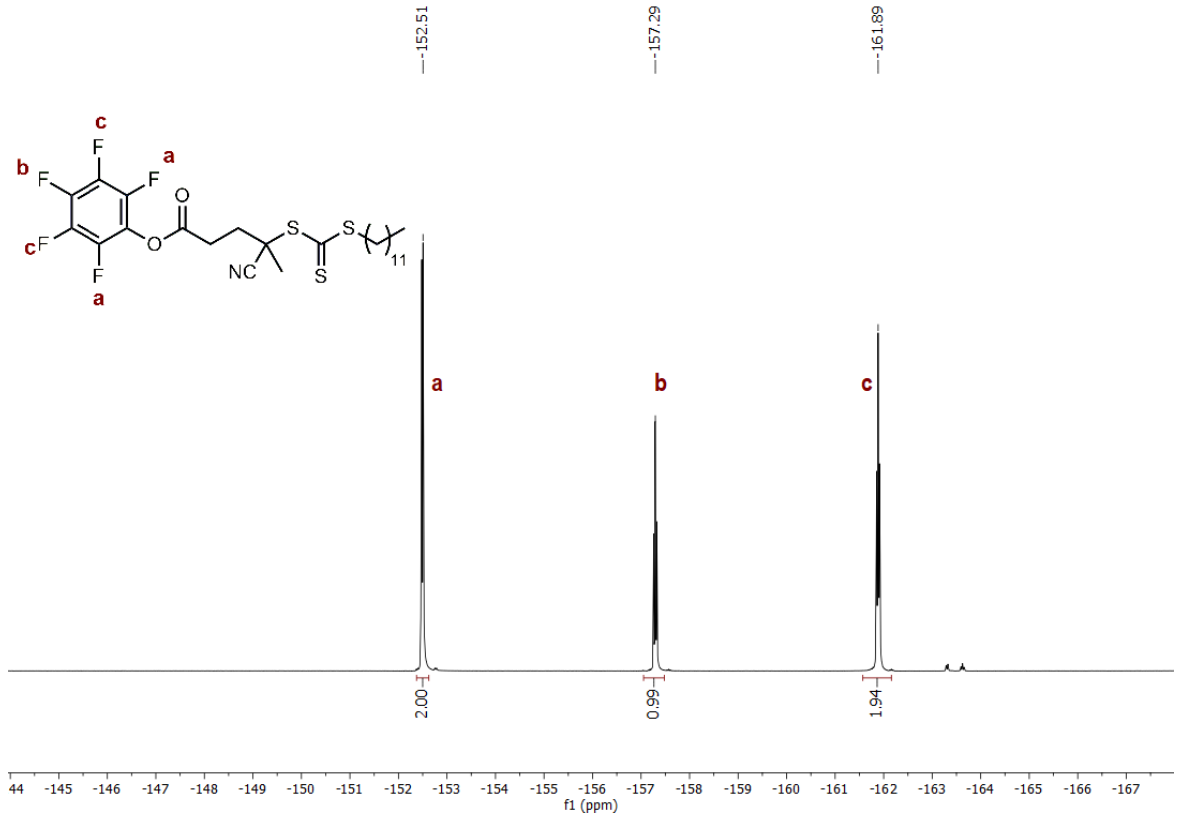

Figure S7: ^{19}F NMR spectrum (659 MHz) of the pentafluorophenyl-trithiocarbonate chain transfer agent (PFP-TTC-CTA) in $CDCl_3$.

Synthesis of Poly(ethylene Glycol)-Trithiocarbonate Chain Transfer Agent (PEG-TTC-CTA)

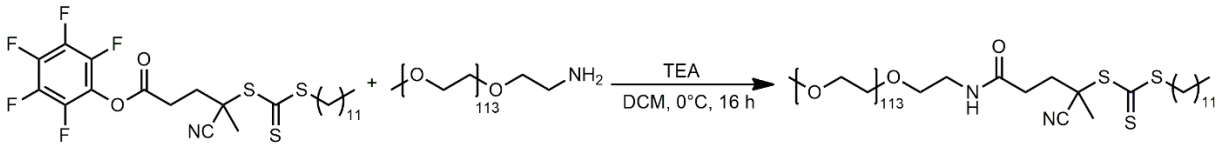

Figure S8: Synthesis of the poly(ethylene glycol)-trithiocarbonate chain transfer agent (PEG-TTC-CTA).

In analogy to previous reports[2,3], pentafluorophenyl-trithiocarbonate chain transfer agent (PFP-TTC-CTA) (0.57 g, 1.0 mmol, 5 eq) was dissolved in anhydrous DCM (5 mL) under nitrogen atmosphere in a pre-dried round bottom flask. Protected from light methoxypoly(ethylene glycol)amine (mPEG-NH_2, M_n: 5 kDa) (1.00 g, 0.20 mmol, 1 eq) dissolved in 10 mL dry DCM and TEA (0.10 g, 1.00 mmol, 5 eq) was added dropwise under ice cooling *via* dropping funnel. After stirring at room temperature overnight the mixture was concentrated under reduced pressure and precipitated three times in cold diethyl ether (-20 °C). The crude product was dissolved in millipore water (45 mL), transferred into a dialysis membrane (MWCO 1.0 kDa) and dialyzed against millipore water for two days. Lyophilization afforded the PEG-TTC-CTA as yellow powder (0.95 g, 74 %).

^{1}H NMR (500 MHz, $CDCl_3$): δ (ppm) = 6.43 (s, 1H, **a**), 3.38-3.73 (m, 2H, **b**), 2.68 (s, 419H, **c**), 3.46-3.41 (m, 2H, **d**), 3.37 (s, 3H, **e**), 3.34-3.27 (m, 2H, **f**), 2.66-2.20 (m, 4H, **g**), 1.89 (s, 3H, **h**), 1.73-1.64 (m, 2H, **i**), 1.44-1.34 (m, 2H, **j**), 1.25 (s, 16H, **k**), 0.87 (t, *J* = *6.8*, 3H, **l**).

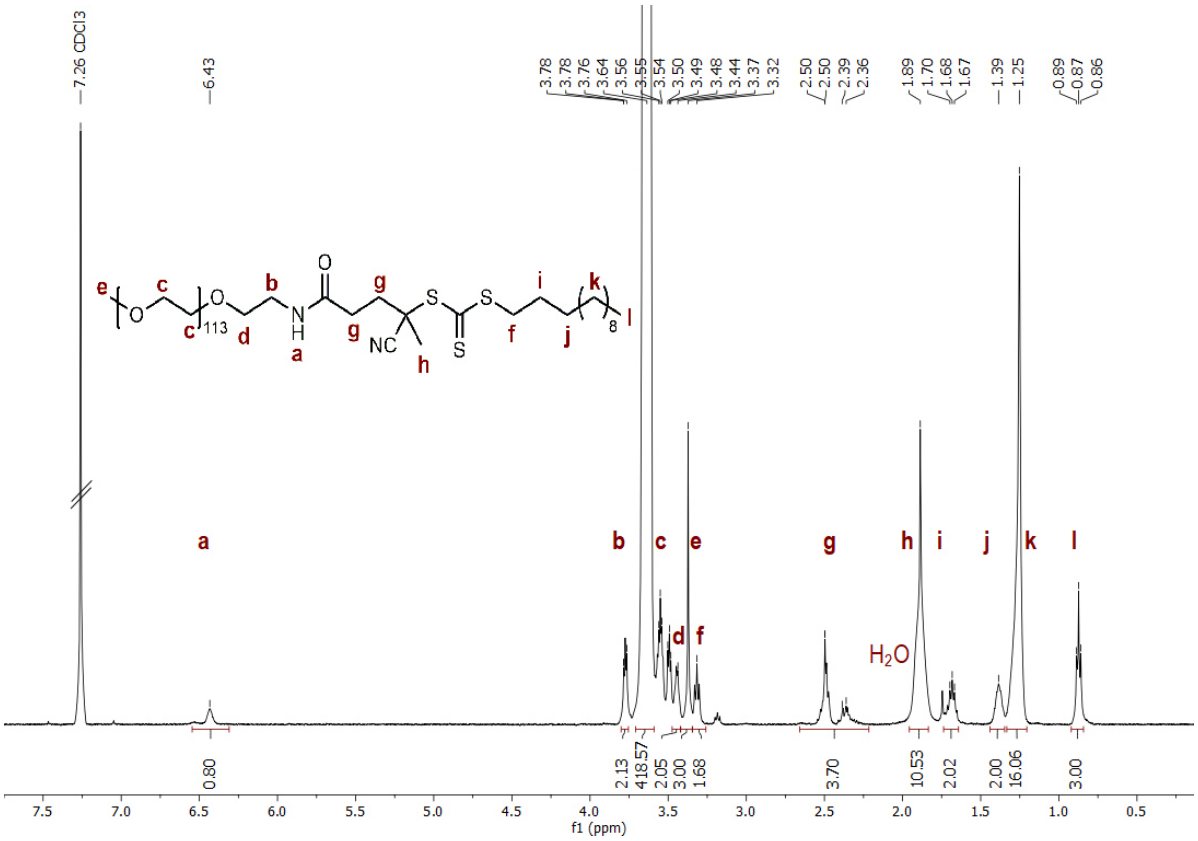

Figure S9: ^{1}H NMR spectrum (700 MHz) of the poly(ethylene glycol)-trithiocarbonate chain transfer agent (PEG-TTC-CTA) in $CDCl_3$.

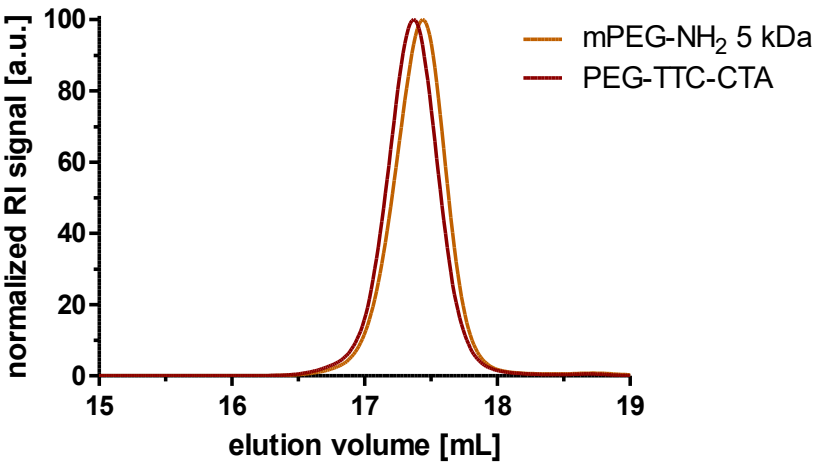

Figure S10: HFIP SEC traces of methoxy(polyethylene glycol)amine (mPEG-NH_2, M_n 5 kDa, orange) and poly(ethylene glycol)-trithiocarbonate chain transfer agent (PEG-TTC-CTA, red).

Block Copolymerization Procedure

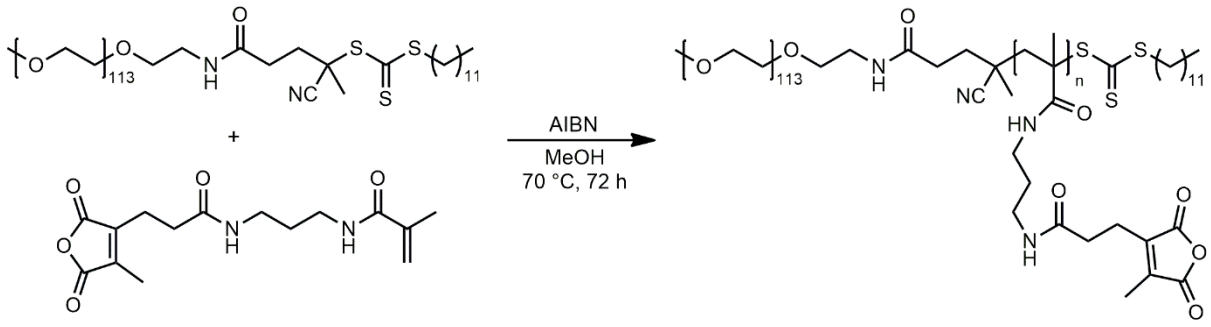

Figure S11: Synthesis of the block copolymer $mPEG_{113}$-*b*-p(PMMA-MA)$_n$ with PEG-TTC-CTA and AIBN in MeOH for 72 h.

The synthesis of the block copolymer $mPEG_{113}$-*b*-p(PMMA-MA)$_n$ was adapted from the literature and modified.[2–4,] PEG-TTC-CTA as macro-CTA (35.03 mg, 0.0065 mmol, 1 eq) and AIBN as initiator (0.33 mg, 0.002 mmol, 0.3 eq) were weighed into a pre-dried Schlenk tube with a stir bar and dissolved in 0.3 mL dry methanol (MeOH). Then, the synthesized monomer PMMA-MA (100 mg, 0.32 mmol, 50 eq) was dissolved in the same amount anhydrous MeOH and added to the reaction mixture. After four freeze-pump-thaw cycles the degassed solution was transferred into an oil bath and stirred for 72 hours at 70 °C. ^{1}H NMR analysis of a reaction aliquot in DMSO-d_6 showed a monomer conversion of 62%. The resulting block copolymer was purified by repeated (3x) precipitation in cold diethyl ether (-20 °C) and centrifugation. After drying under reduced pressure overnight $mPEG_{113}$-*b*-p(PMMA-MA)$_{22}$ was isolated as colorless solid (73 mg, 91%).

^{1}H NMR (500 MHz, $CDCl_3$): δ (ppm) = 6.43 (s, 1H, **a**), 3.38-3.73 (m, 2H, **b**), 2.68 (s, 419H, **c**), 3.46-3.41 (m, 2H, **d**), 3.37 (s, 3H, **e**), 3.34-3.27 (m, 2H, **f**), 2.66-2.20 (m, 4H, **g**), 1.89 (s, 3H, **h**), 1.73-1.64 (m, 2H, **i**), 1.44-1.34 (m, 2H, **j**), 1.25 (s, 16H, **k**), 0.87 (t, *J* = *6.8*, 3H, **l**).

SEC (HFIP) PEG-TTC-CTA: M_n = 32755 g/mol, M_w = 33924 g/mol, Đ = 1.04

SEC (HFIP) $mPEG_{113}$-*b*-p(PMMA-MA)$_{22}$: M_n = 35909 g/mol, M_w = 37438 g/mol, Đ = 1.04

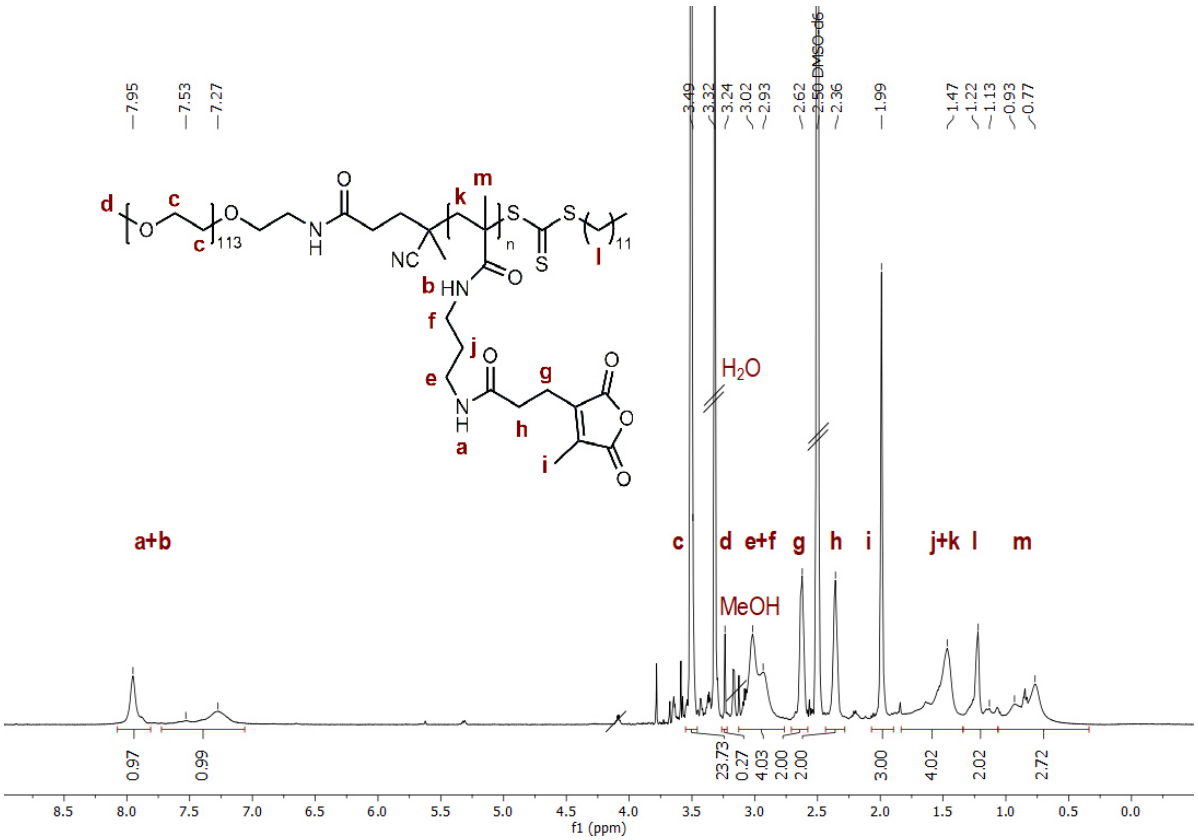

Figure S12: ^{1}H NMR spectrum (700 MHz) of the block copolymer mPEG$_{113}$-*b*-p(PMMA-MA)$_{22}$ synthesized with the PEG-TTC-CTA under RAFT conditions in DMSO-d$_6$.

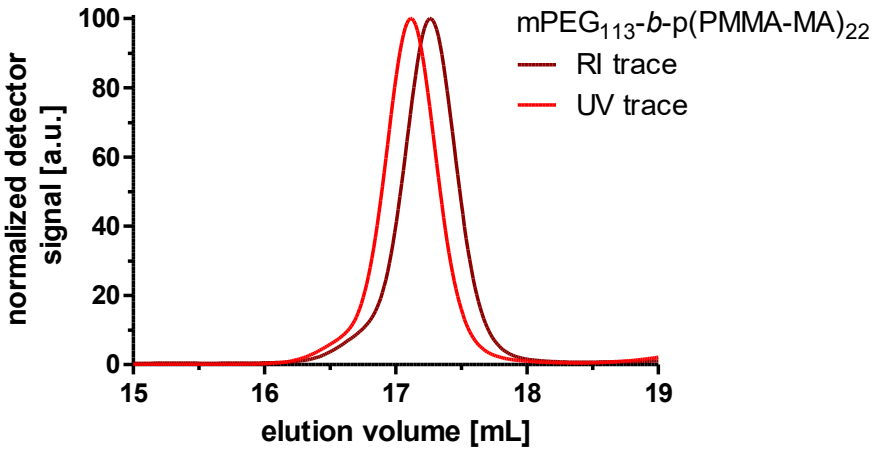

Figure S13: HFIP SEC RI detected (dark red) or UV detected (light red) elugram of the block copolymer mPEG$_{113}$-*b*-p(PMMA-MA)$_{22}$.

pH-Dependent Micelle Formulation

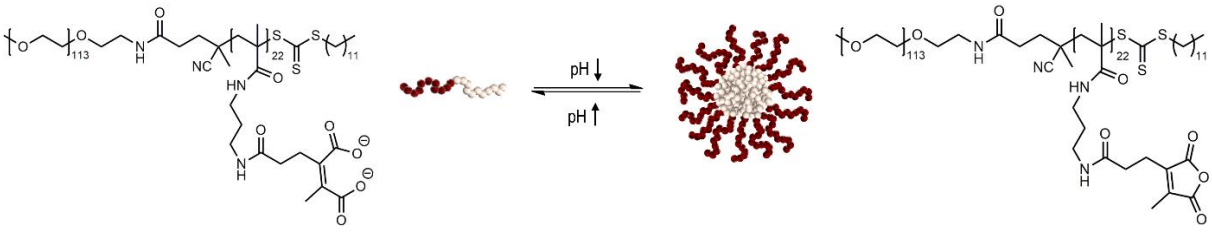

Figure S14: Micelle formulation scheme of the block copolymer mPEG$_{113}$-*b*-p(PMMA-MA)$_{22}$.

The block copolymer mPEG$_{113}$-*b*-p(PMMA-MA)$_{22}$ was dispersed in millipore water with a concentration of 1 mg/mL. Ultrasonication of the dispersion for 1.5 h enabled the formulation of self-assembled polymeric micelles characterized by DLS measurements. For the pH-dependent self-assembly of the block copolymer the dispersion was treated with 1% of a 1M hydrochloric acid (HCl) or 1M sodium hydroxide (NaOH) solution and further characterized by DLS and TEM measurement. In case of a detailed pH-sensitive micelle formulation mPEG$_{113}$-*b*-p(PMMA-MA)$_{22}$ was dispersed in aqueous solutions in a pH-range of 3.5-7.4 and ultrasonicated for 1.5 h. Each dispersion was analyzed by DLS measurements.

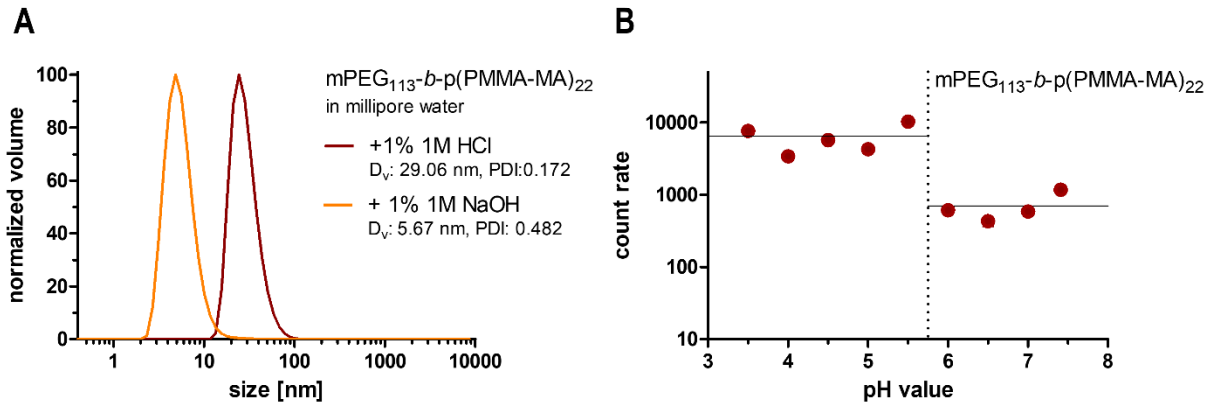

Figure S15: DLS analysis of the block copolymer mPEG$_{113}$-*b*-p(PMMA-MA)$_{22}$ stability under basic or acidic conditions in millipore water (A) and the corresponding count rate at different pH values (B).

Polymer Modification by Amidation with Primary or Secondary Amines

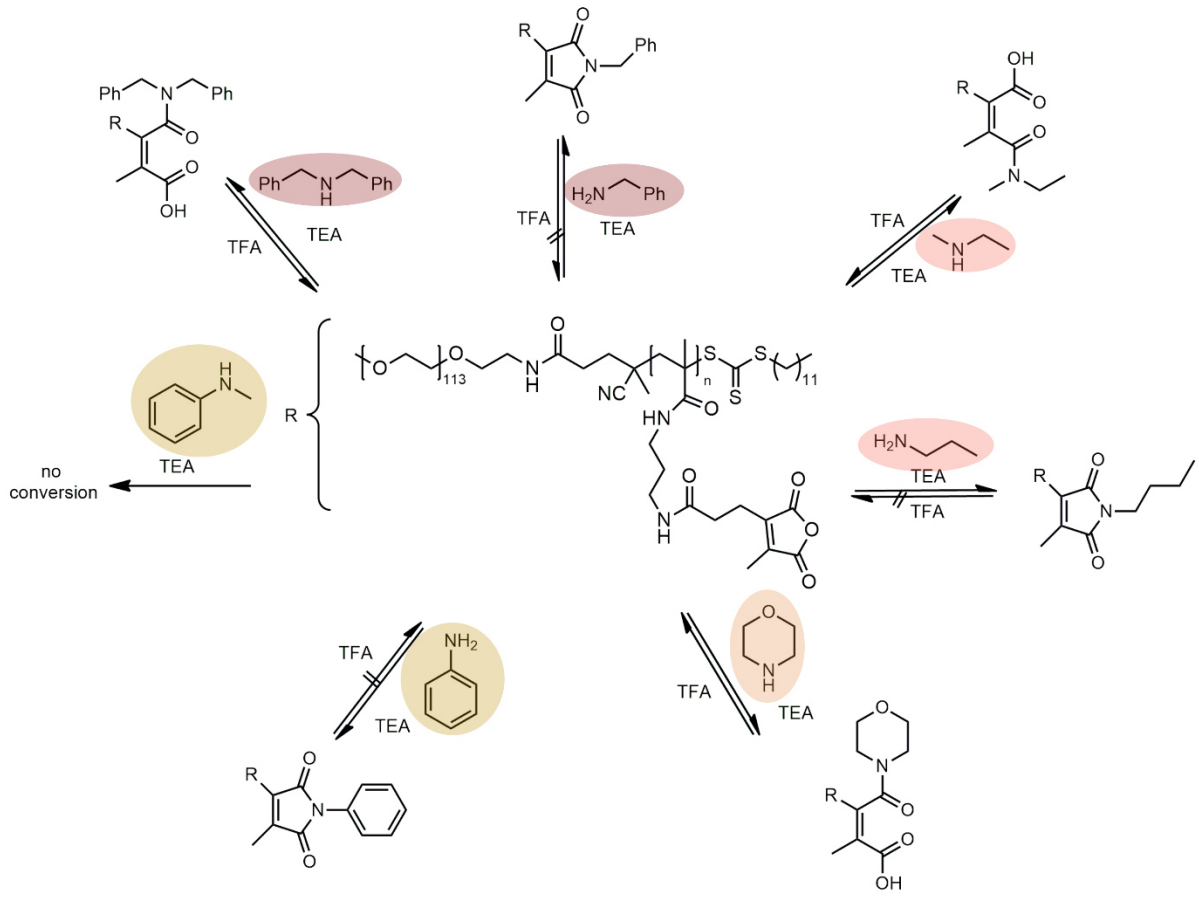

Figure S16: Reaction scheme of 2-propionic-3-methylmaleic anhydride containing block copolymer $mPEG_{113}$-*b*-$p(PMMA\text{-}MA)_{22}$ with different primary or secondary amines.

The potential for pH-sensitive amine modification of the 2-propionic-3-methylmaleic anhydride groups of the previously synthesized block copolymer $mPEG_{113}$-*b*-$p(PMMA\text{-}MA)_{22}$ was analyzed in analogy to earlier reports[1,3] by the reaction with different primary or secondary amines. Therefore, $mPEG_{113}$-*b*-$p(PMMA\text{-}MA)_{22}$ (15 mg, 1.23 µmol/27.09 µmol reactive anhydride groups, 1 eq) was weighted in a Schlenk flask equipped with a stir bar and dissolved in 0.6 mL DMSO under nitrogen atmosphere. After addition of triethylamine (TEA, 18.78 µL, 135.45 µmol, 5 eq) and corresponding primary amines, such as aniline (7.42 µL, 81.27 µmol, 3 eq) or secondary amines like morpholine (7.08 µL, 81.27 µmol, 3 eq) the reaction mixture was stirred at 50 °C overnight. The modified polymers were purified by threefold precipitation into diethyl ether and dried *in vacuo* for 16 h affording pale-yellow powders (18 mg, quantitative).

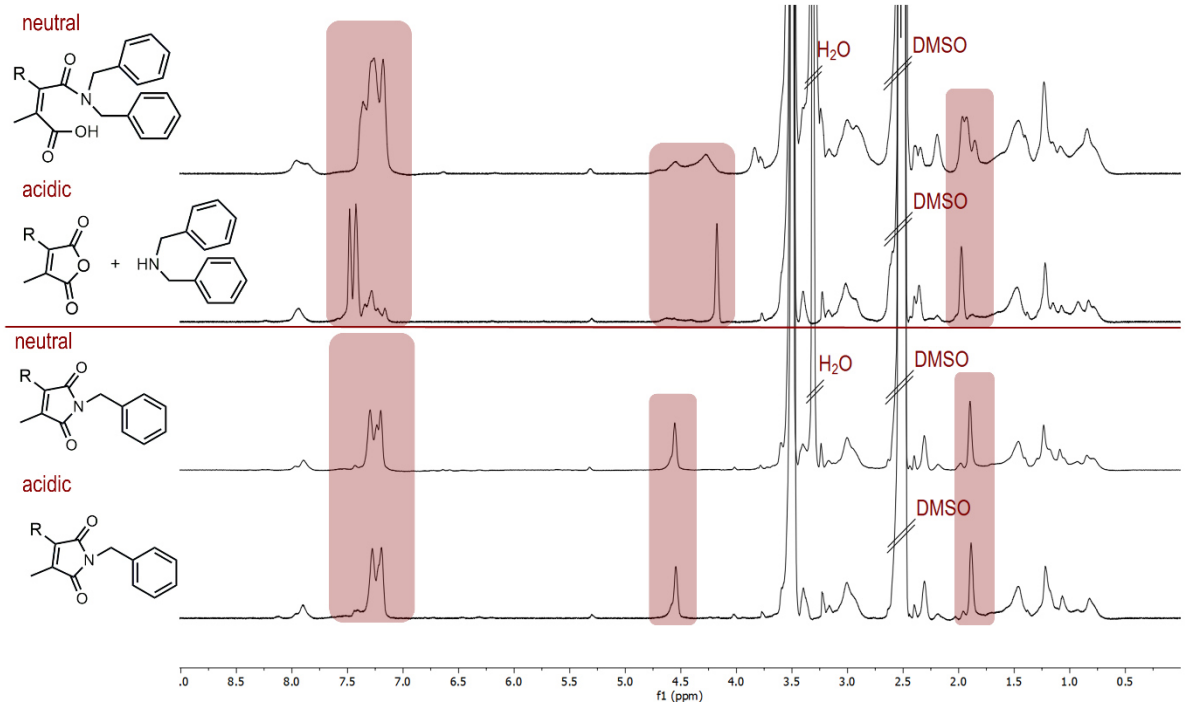

Figure S17: ^{1}H NMR spectra (700 MHz) of the block copolymer mPEG$_{113}$-*b*-p(PMMA-MA)$_{22}$ after the reaction with dibenzylamine or benzylamine under neutral and acidic conditions in DMSO-d$_6$.

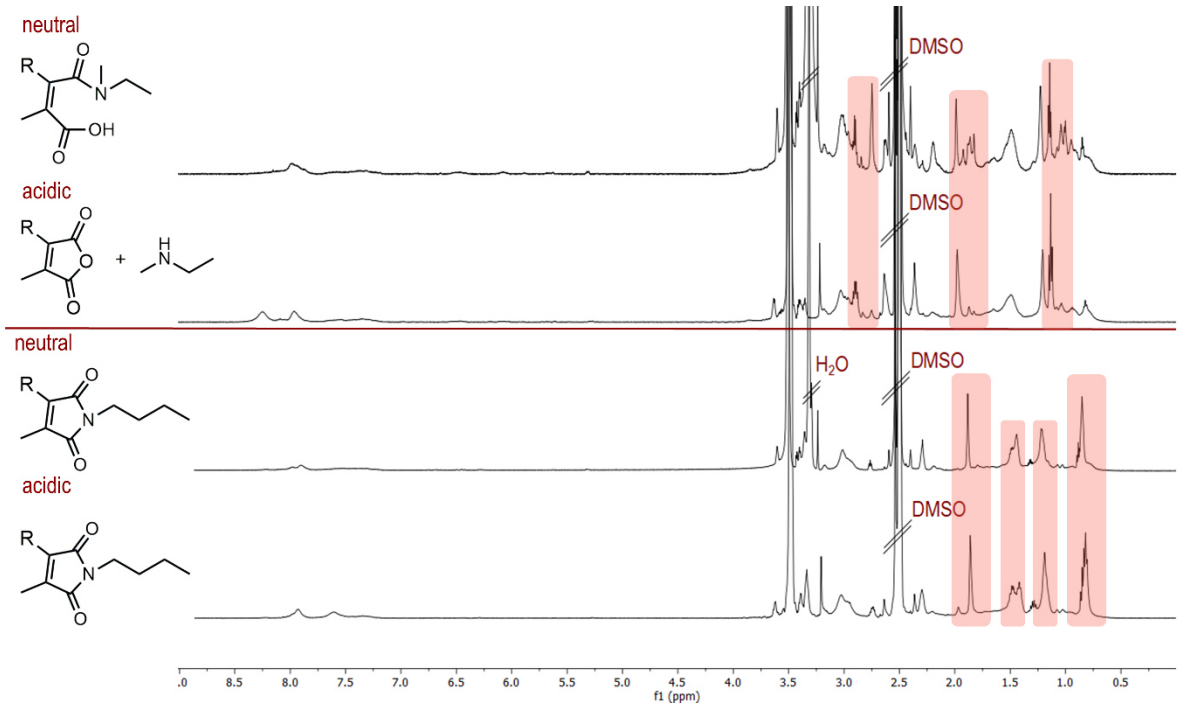

Figure S18: ^{1}H NMR spectra (700 MHz) of the block copolymer mPEG$_{113}$-*b*-p(PMMA-MA)$_{22}$ after the reaction with ethylmethylamine or butylamine under neutral and acidic conditions in DMSO-d$_6$.

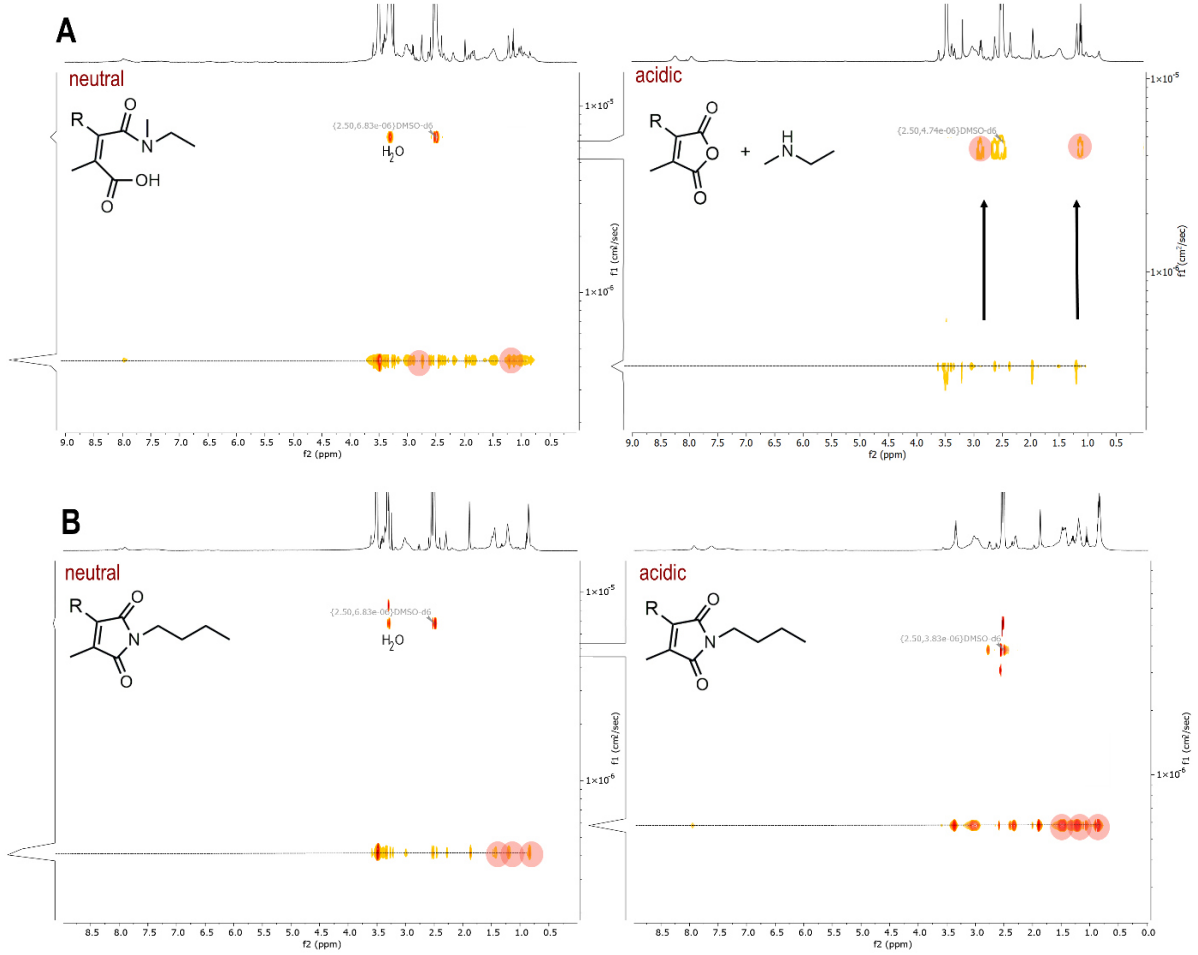

Figure S19: DOSY NMR spectra (700 MHz) of the block copolymer mPEG$_{113}$-*b*-p(PMMA-MA)$_{22}$ after the reaction with ethylmethylamine (A) or butylamine (B) under neutral and acidic conditions in DMSO-d$_6$.

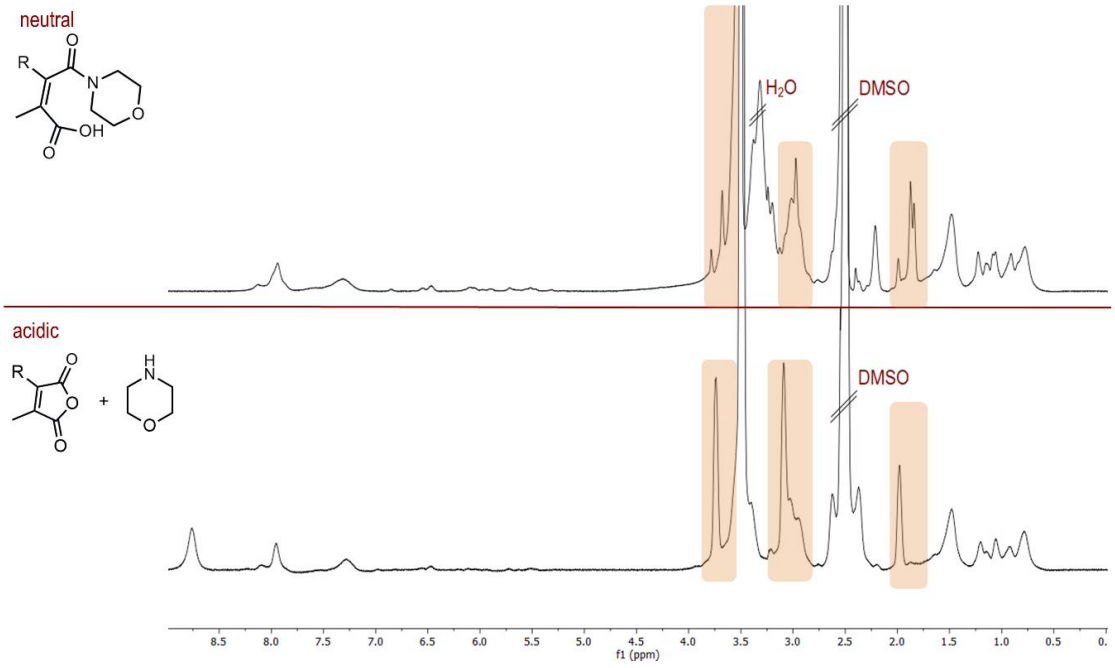

Figure S20: ^{1}H NMR spectra (700 MHz) of the block copolymer mPEG$_{113}$-*b*-p(PMMA-MA)$_{22}$ after the reaction with morpholine under neutral and acidic conditions in DMSO-d$_6$.

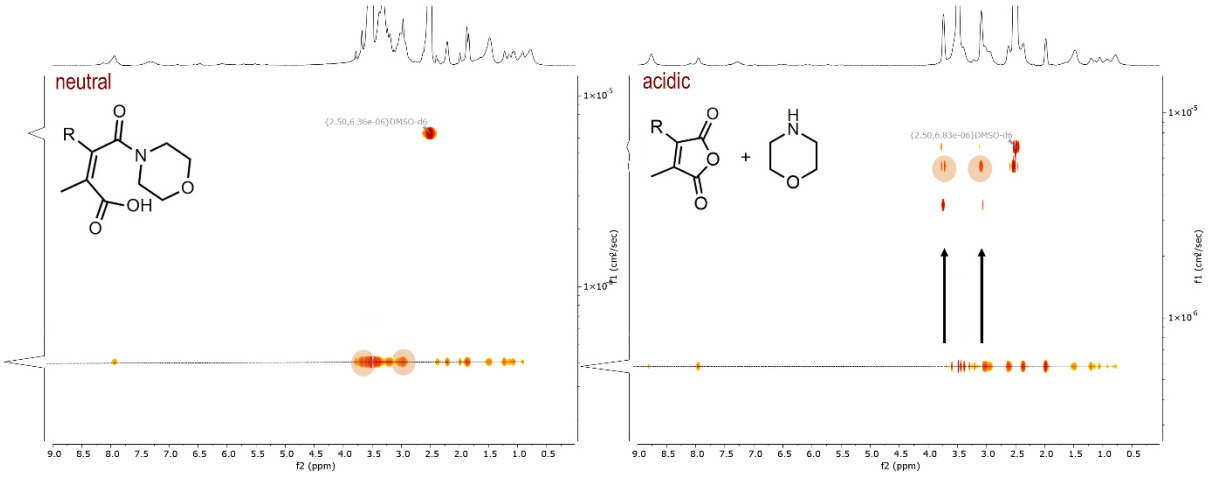

Figure S21: DOSY NMR spectra (700 MHz) of the block copolymer mPEG$_{113}$-*b*-p(PMMA-MA)$_{22}$ after the reaction with morpholine under neutral and acidic conditions in DMSO-d$_6$.

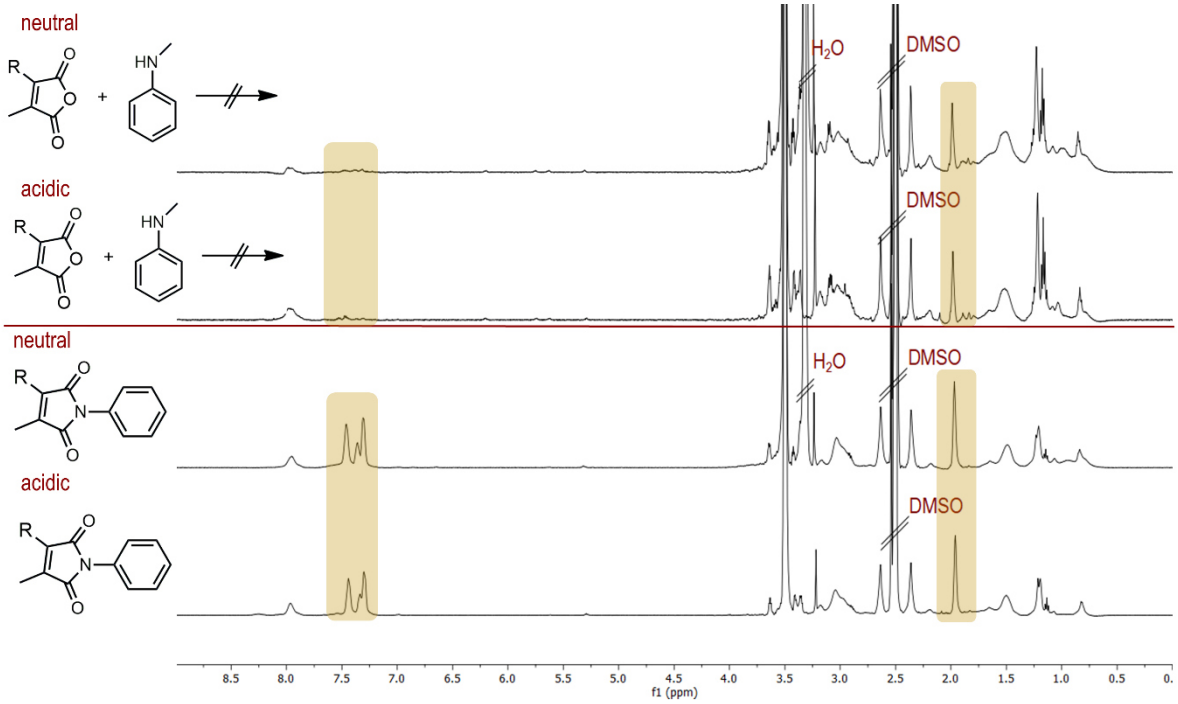

Figure S22: ^{1}H NMR spectra (500 MHz) of the block copolymer mPEG$_{113}$-*b*-p(PMMA-MA)$_{22}$ after the reaction with N-methylaniline or aniline under neutral and acidic conditions in DMSO-d$_6$.

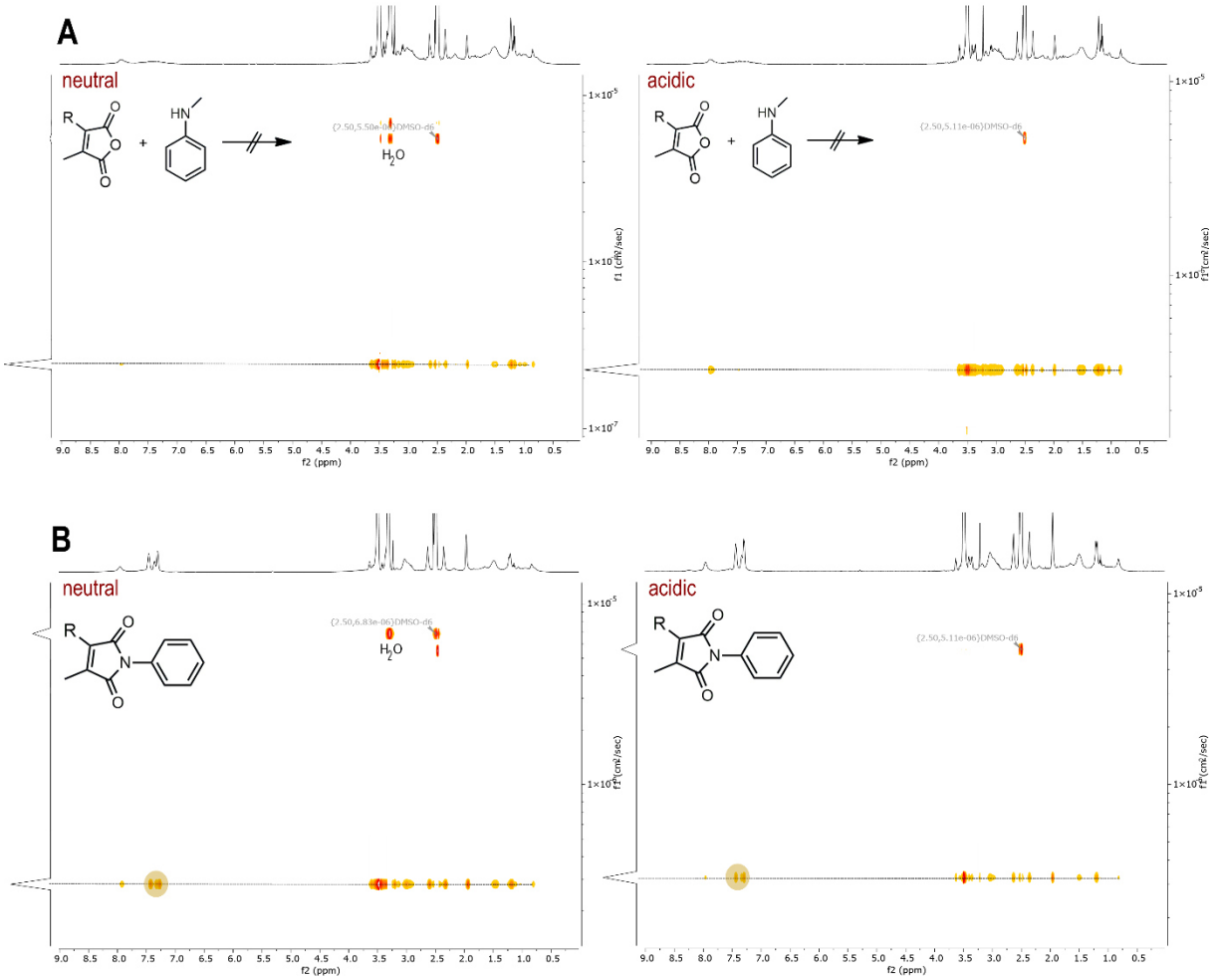

Figure S23: DOSY NMR spectra (500 MHz) of the block copolymer mPEG$_{113}$-*b*-p(PMMA-MA)$_{22}$ after the reaction with N-methylaniline (A) or aniline (B) under neutral and acidic conditions in DMSO-d$_6$.

Self-Assembled Micelles after 2-Propionic-3-Methylmaleic-Anhydride Modification of the Block Copolymer

Synthesis and Micelle Formulation of Dibenzyl- or Benzylamine-Modified Block Copolymer

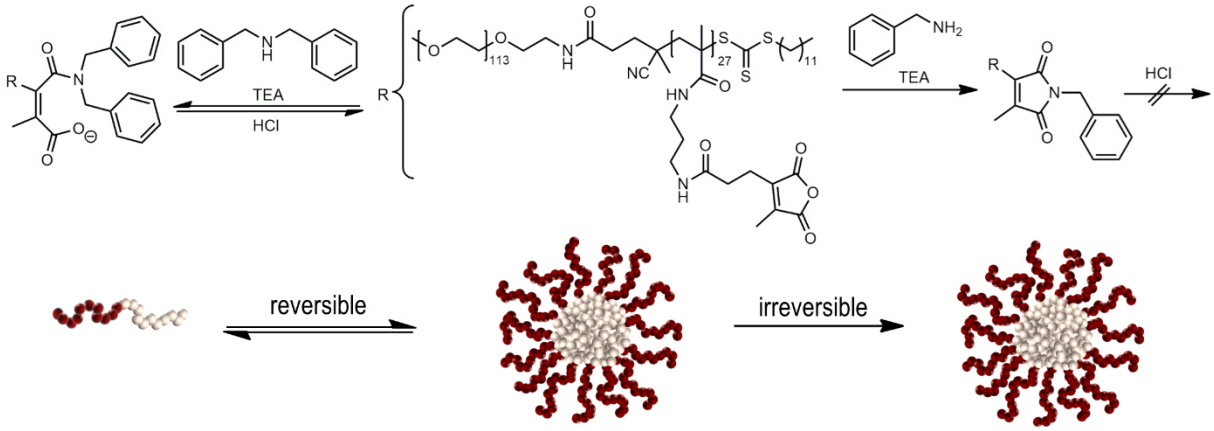

Figure S24: Synthesis and micelle formulation of anhydride containing block copolymer $mPEG_{113}$-*b*-$p(PMMA\text{-}MA)_{27}$ reacted with dibenzylamine or benzylamine.

The block copolymer $mPEG_{113}$-*b*-$p(PMMA\text{-}MA)_{27}$ was modified analogously to the previously described modifications. Consequently, 10 mg of the bock copolymer (0.73 µmol/19.67 µmol reactive anhydride groups, 1 eq) was dissolved in DMSO and treated with TEA (13.63 µL, 98.36 µmol, 5 eq) and dibenzylamine (11.35 µL, 59.01 µmol, 3 eq) or benzylamine (6.45 µL, 59.01 µmol, 3 eq). After reaction overnight at 50 °C the three times precipitated bock copolymers were dried under reduced pressure. Finally, bock copolymer dispersions of the secondary or primary amine-modified systems were prepared in millipore water at a concentration of 1 mg/mL, followed by ultrasonication for 1.5 h. Formation of polymeric micelles and related pH sensitivity was verified by DLS measurements.

SEC (HFIP) $mPEG_{113}$-*b*-$p(PMMA\text{-}MA)_{27}$: M_n = 32041 g/mol, M_w = 34333 g/mol, Đ = 1.07

SEC (HFIP) $mPEG_{113}$-*b*-$p(PMMA\text{-}MA)_{27}$ (+dibenzylamine): M_n = 31647 g/mol, M_w = 34318 g/mol, Đ = 1.08

SEC (HFIP) $mPEG_{113}$-*b*-$p(PMMA\text{-}MA)_{27}$ (+benzylamine): M_n = 33151 g/mol, M_w = 36125 g/mol, Đ = 1.09

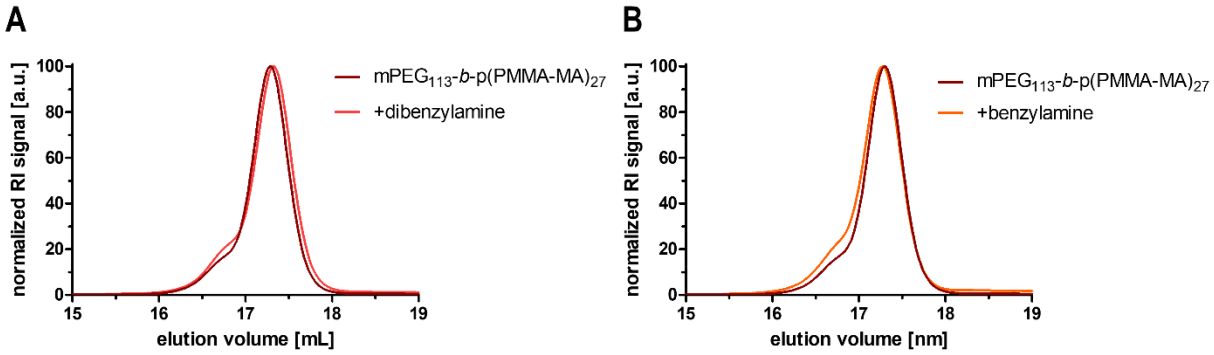

Figure S25: SEC traces of the block copolymer $mPEG_{113}$-*b*-$p(PMMA\text{-}MA)_{27}$ before and after reaction with benzylamine (A) or dibenzylamine (B).

Synthesis and Micelle Formulation of Dual 2-Propionic-3-Methylmaleic-Anhydride Modification of the Block Copolymer

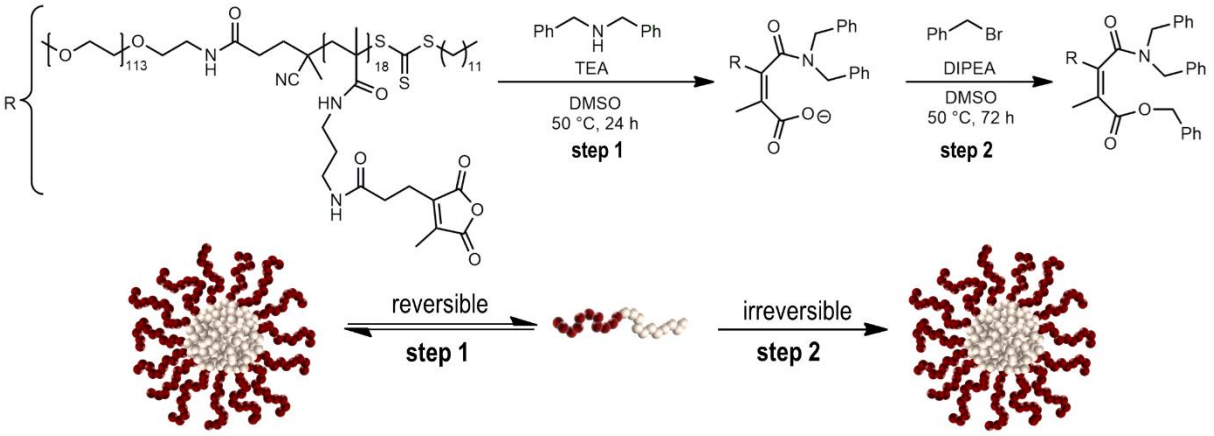

Figure S26: Reaction scheme and micelle formulation of anhydride-containing block copolymer $mPEG_{113}$-*b*-$p(PMMA\text{-}MA)_{18}$ with dibenzylamine and further conjugation of benzyl bromide.

The dual modification of the block copolymers' 2-propionic-3-methylmaleic anhydride groups was adapted from an earlier report with minor modification.[1,3] $mPEG_{113}$-*b*-$p(PMMA\text{-}MA)_{18}$ (15mg, 1.37 µmol/24.66 µmol reactive anhydride groups, 1 eq) was weighted into a pre-dried Schlenk flask and 0.6 mL DMSO was added under nitrogen atmosphere. Next, TEA (10.25 µL, 73.98 µmol, 3 eq) and dibenzylamine (7.11 µL, 36.99 µmol, 1.5 eq) were dropped to the reaction mixture. After a reaction time of 16 h at 50 °C the conjugated polymer was precipitated three times in diethyl ether and then dried under high vacuum. The isolated block copolymer (15 mg, 1.03 µmol/18.62 µmol reactive anhydride groups, 1 eq) was redissolved in 0.6 mL DMSO under nitrogen atmosphere, followed by the addition of *N*,*N*-diisopropylethylamine (DIPEA) (31.67 µL, 186.2 µmol, 10 eq) and benzyl bromide (8.85 µL, 74.48 µmol, 4 eq). The reaction mixture was allowed to stir for 72 h at 50 °C. After threefold

precipitation into diethyl ether and subsequent centrifugation the modified polymer was dried *in vacuo* overnight. mPEG$_{113}$-*b*-p(PMMA-MA)$_{18}$ (+dibenzylamine, benzylbromide) was obtained as colorless solid (23 mg, 96%). Finally, polymer micelles of the first and second synthesis step were formed by ultrasonication of the corresponding modified block copolymers in millipore water (1 mg/mL). Resulting micelles and their pH-dependency were characterized by DLS measurements.

SEC (HFIP) mPEG$_{113}$-*b*-p(PMMA-MA)$_{18}$: M_n = 29830 g/mol, M_w = 32030 g/mol, Đ = 1.07

SEC (HFIP) mPEG$_{113}$-*b*-p(PMMA-MA)$_{18}$ (+dibenzylamine step 1): M_n = 30986 g/mol, M_w = 32507 g/mol, Đ = 1.05

SEC (HFIP) mPEG$_{113}$-*b*-p(PMMA-MA)$_{18}$ (+dibenzylamine, benzyl bromide, step 2): M_n = 34414 g/mol, M_w = 36880 g/mol, Đ = 1.07

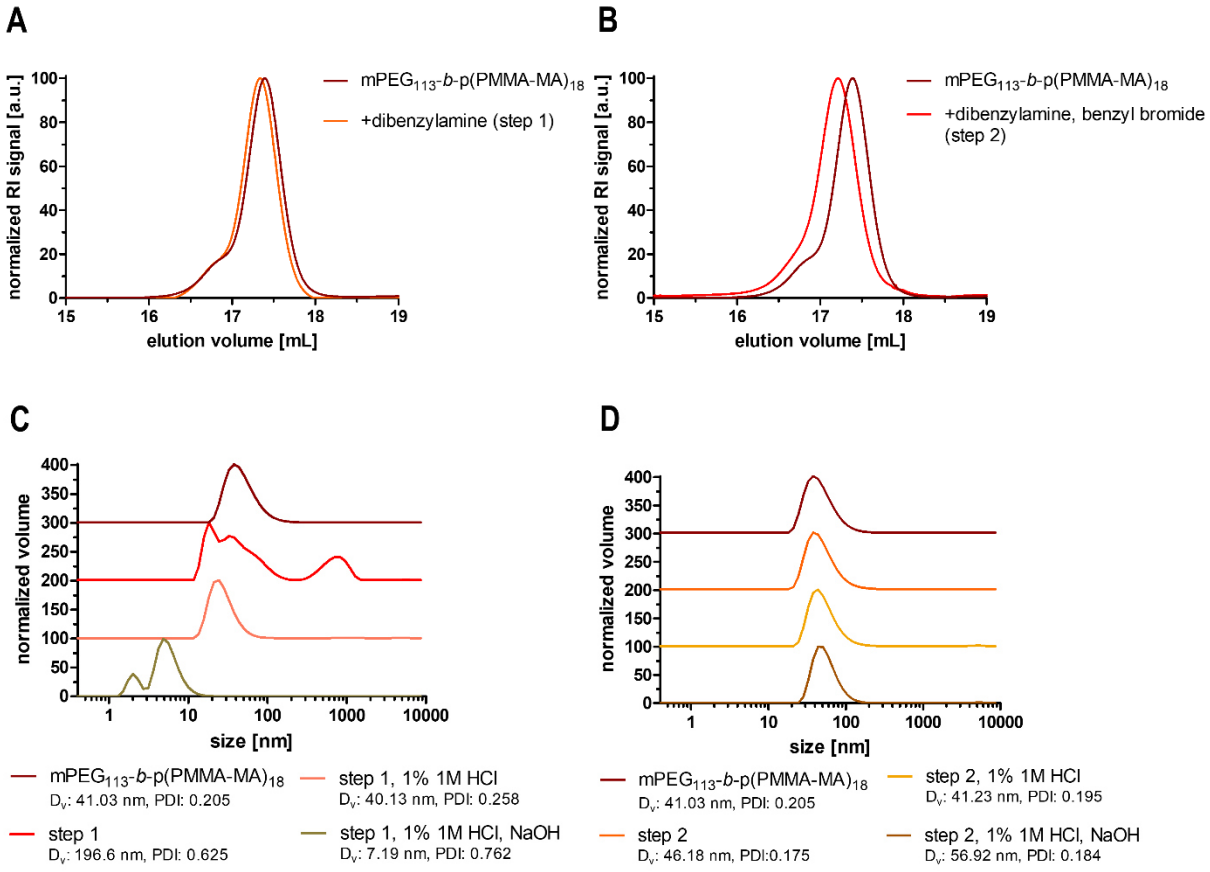

Figure S27: SEC elugrams of the block copolymer mPEG$_{113}$-*b*-p(PMMA-MA)$_{18}$ before and after modification with dibenzylamine (step 1, A) and benzyl bromide (step 2, B). DLS analysis of the block copolymer reacted with dibenzylamine (step 1, C) and benzyl bromide (step 2, D) in millipore water under basic and acidic conditions.

Block Copolymer Dye Labeling Reaction and Resulting Fluorescence Resonance Energy Transfer (FRET) Characteristics

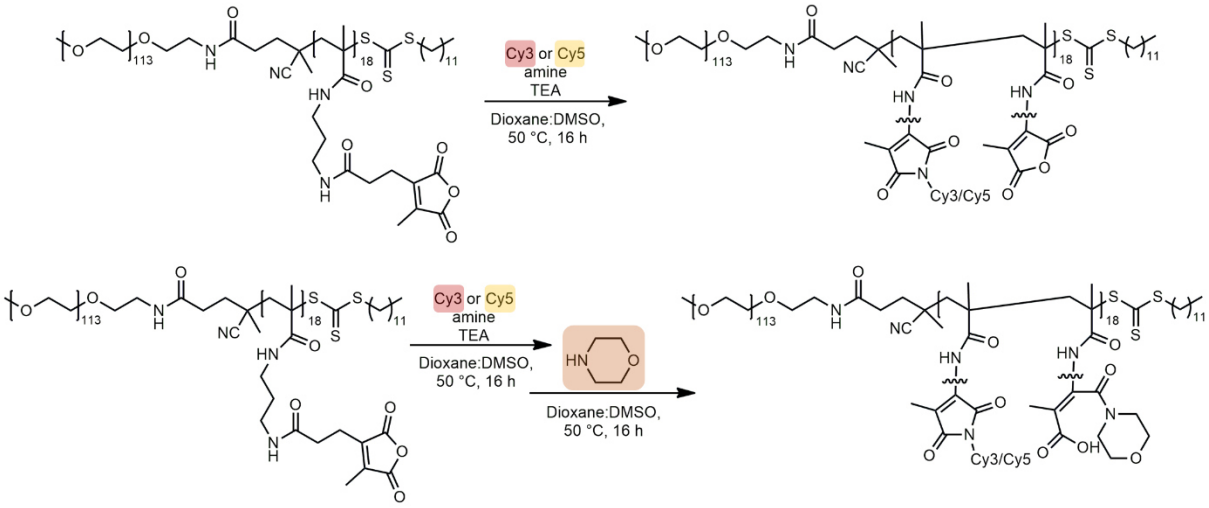

Figure S28: Schematic reaction of the block copolymer $mPEG_{113}$-*b*-p(PMMA-MA)$_{18}$ with Cy3 or Cy5 cadaverine and $mPEG_{11}$-amine.

Two different types of dye-labeled block copolymers were synthesized according to the literature and modified.[5] Therefore, the block copolymer $mPEG_{113}$-*b*-p(PMMA-MA)$_{18}$ (2x30 mg, 2.74 µmol, 1 eq) was dissolved in 1.5 mL dry dioxane under nitrogen atmosphere. Then, TEA (2x1.14 µL, 8.22 µmol, 3 eq) and Cy3 cadaverine (68.8 µL of 25 mg/mL stock solution, 2.74 µmol, 1 eq) or Cy5 cadaverine (71.65 µL of 25 mg/mL stock solution, 2.74 µmol, 1 eq) were dropped to the solution, followed by the addition of 0.5 mL DMSO to each solution to ensure efficient solubility of the added dyes. The reaction mixtures were stirred overnight at room temperature. Afterwards, 15 mg of the dye-labeled block copolymers (1.30 µmol/22.1 µmol reactive anhydride groups, 1 eq) were separated into new Schlenk flasks and treated with and excess of morpholine (5.72 µL, 66.3 µmol, 3 eq) and TEA (9.19 µL, 66.3 µmol, 3 eq). The reaction mixtures were allowed to stir for further 16 h at room temperature. At last, the dye-labeled block copolymers with and without morpholine were purified by repeated (3x) precipitation in an excess of diethyl ether. After drying *in vacuo* overnight $mPEG_{113}$-*b*-p(PMMA-MA)$_{18}$ with and without morpholine +Cy3 or +Cy5 were isolated as intensive blue and pink powder.

SEC (HFIP) $mPEG_{113}$-*b*-p(PMMA-MA)$_{18}$: M_n = 29830 g/mol, M_w = 32030 g/mol, Đ = 1.07

SEC (HFIP) $mPEG_{113}$-*b*-p(PMMA-MA)$_{18}$ (+Cy3): M_n = 32794 g/mol, M_w = 34975 g/mol, Đ = 1.07

SEC (HFIP) $mPEG_{113}$-*b*-p(PMMA-MA)$_{18}$ (+Cy5): M_n = 33392 g/mol, M_w = 35966 g/mol, Đ = 1.08

SEC (HFIP) $mPEG_{113}$-*b*-p(PMMA-MA)$_{18}$ (+morpholine, Cy3): M_n = 32831 g/mol, M_w = 35080 g/mol, Đ = 1.07

SEC (HFIP) $mPEG_{113}$-*b*-p(PMMA-MA)$_{18}$ (+morpholine, Cy5): M_n = 33181 g/mol, M_w = 35765 g/mol, Đ = 1.08

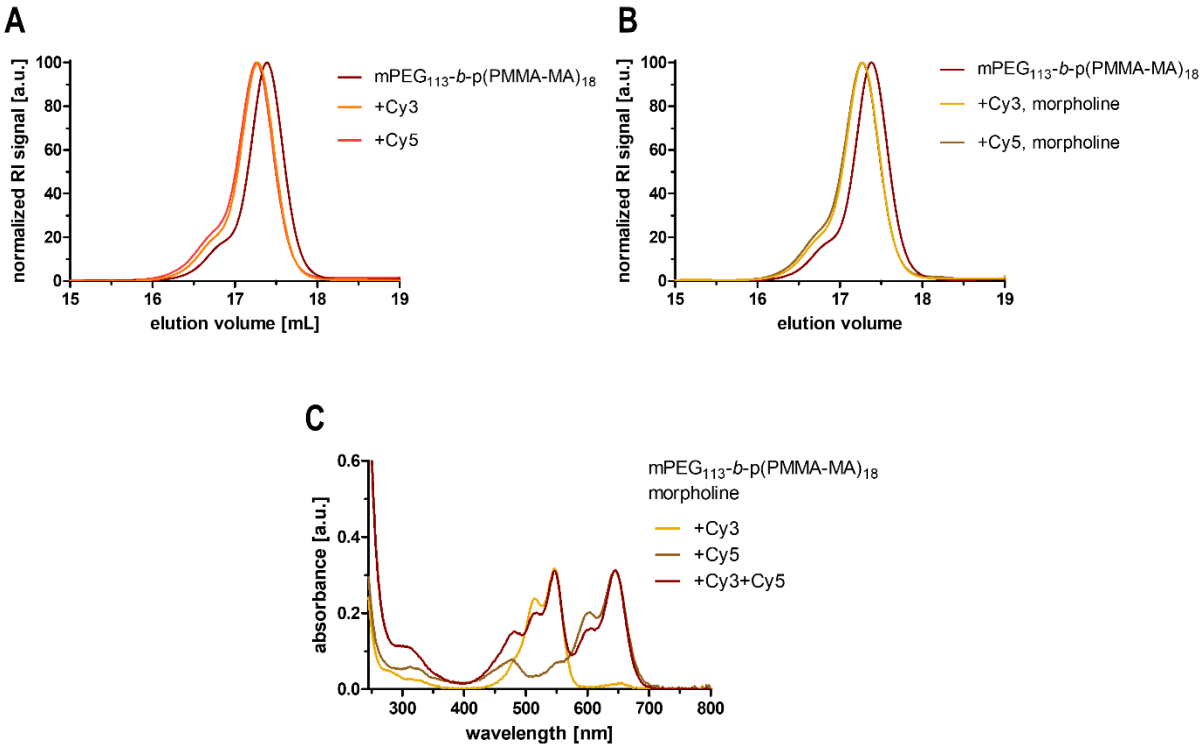

Figure S29: HFIP SEC traces of the block copolymer $mPEG_{113}$-*b*-p(PMMA-MA)$_{18}$ with and without attached fluorescent Cy3 cadaverine or Cy5 cadaverine (A) and further hydrophilized with morpholine (B). UV-Vis characterization of the dye-labeled block copolymers hydrophilized with morpholine separated or as mixture (+Cy3+Cy5) in PBS (C).

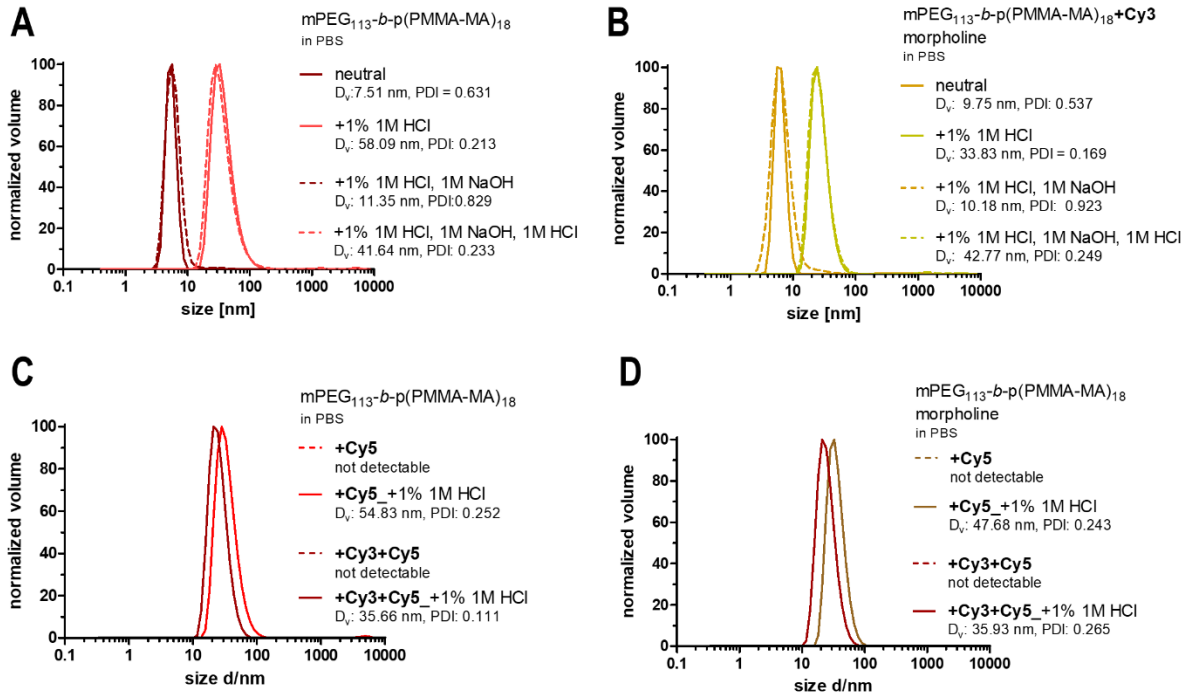

Figure S30: pH-reversible DLS characterization of the block copolymer $mPEG_{113}$-*b*-p(PMMA-MA)$_{18}$ in PBS (A). Additional pH-sensitive DLS analysis of the dye-labeled block copolymers (B-D). Cy5-conjugated block copolymer can only be measured under acidic conditions formulating micellar structures (C+D).

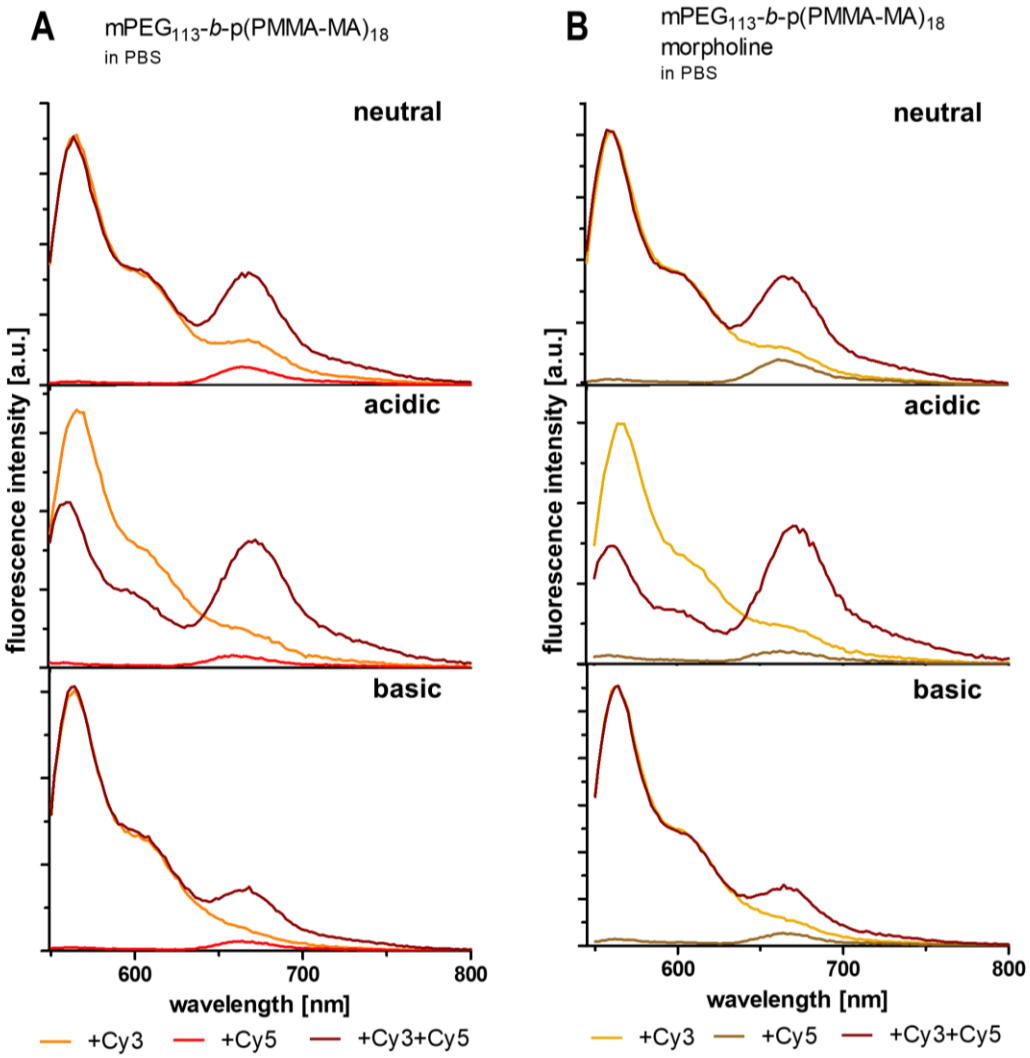

Figure S31: Fluorescence intensity spectra (excitation at 550 nm) of the dye-labeled block copolymers with (B) and without (A) additional hydrophilization with morpholine in PBS and treated with 1% 1M HCl or 1% 1M NAOH.

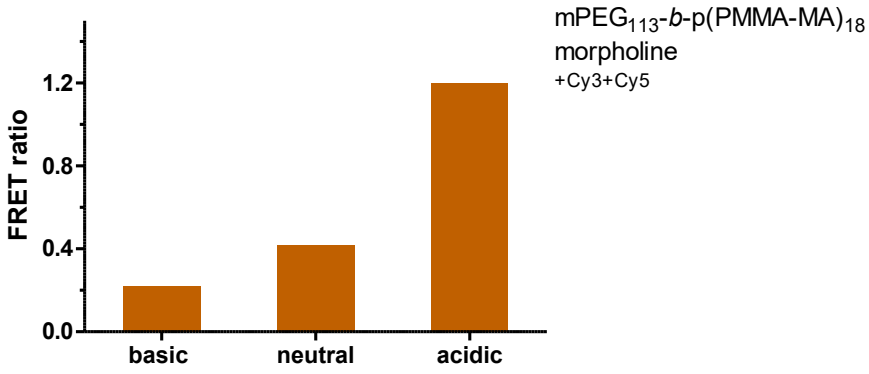

Figure S32: Calculated FRET ratios of mixed Cy3 or Cy5 dye-labeled block copolymers $mPEG_{113}$-*b*-$p(PMMA\text{-}MA)_{18}$ hydrophilized with morpholine in PBS and treated with 1% 1M HCl or 1% 1M NAOH

In vitro Experiments

Determination of RAW-Dual Macrophages Cell Viability by MTT Assay

Cellular metabolic activity of RAW-Dual macrophages was analyzed by a colorimetric MTT assay. Consequently, RAW-Dual macrophages were seeded into a 96-well plate (90000 cells/well in 180 µL) and incubated for 16 h at 37 °C. Afterwards, 20 µL of the block copolymer $mPEG_{113}$-*b*-$p(PMMA\text{-}MA)_{18}$, PBS (positive control) or DMSO (negative control) were added to the cells at given concentration (n=4) and incubated for 24 h at 37 °C. Next, cells were treated with 30 µL of a 2 mg/mL 3-(4,5-dimethylthiazol-2-yl)-2,5-diphenyltetrazolium bromide solution in PBS for 1.5 h at 37 °C and then, formed formazan crystals were dissolved by incubation with 100 µL of a 10% m/v SDS/0.01 M HCl solution overnight. Resulting cell viability was quantified by absorbance measurement at 570 nm using a plate reader.

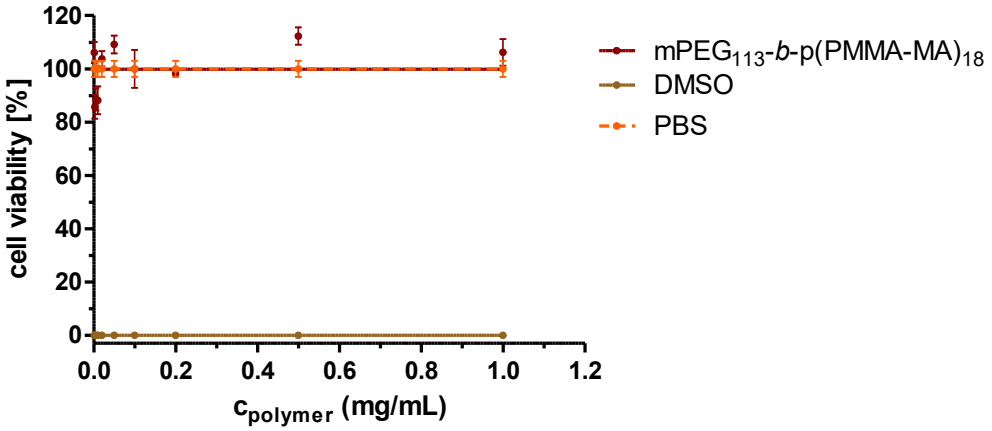

Figure S33: Cell viability of RAW-Dual macrophages incubated with the block copolymer $mPEG_{113}$-*b*-$p(PMMA\text{-}MA)_{18}$, PBS (positive control) or DMSO (negative control) characterized by MTT assay (n=4).

Cell Uptake and Resulting FRET Determination in RAW-Dual Macrophages by Flow Cytometry

For cell uptake studies and time dependent intracellular micelle formulation causing a FRET signal RAW-Dual macrophages were seeded into 24-well plates in a density of 250000 cells/well in 900 µL cell culture medium and incubated overnight at 37 °C for cell adhesion before starting the experiment. Then, 100 µL of a +Cy3 dye-labeled block copolymer, +Cy5 dye-labeled block copolymer or a mixture of both dye-labeled block copolymers (+Cy3+Cy5) with and without morpholine in PBS was added to the cell solution (yielding a final concentration of 30 µg/mL). Cells were incubated for different time frames going from 4, 8, 12, 24 to 48 h at 37 °C. For cells incubated longer than 24 h cell medium was changed after one day. After incubation for the corresponding time, the cell culture medium was aspired and cells were washed with 1 mL PBS followed by incubation in 500 µL dissociation buffer for 15 minutes at 37 °C. Resulting cell suspensions were transferred into Eppendorf tubes on ice and centrifuged immediately at 300 g for 10 minutes at 5 °C. Cell supernatants were removed, and the cell pellets were resuspended in 200-500 µL PBS. To ensure the cell integrity all cell suspensions were stored on ice before flow cytometric analysis on a BD Accuri C6 (BD Biosciences). All data were processed by FlowJo Software. All samples were run in triplicates (n=3).

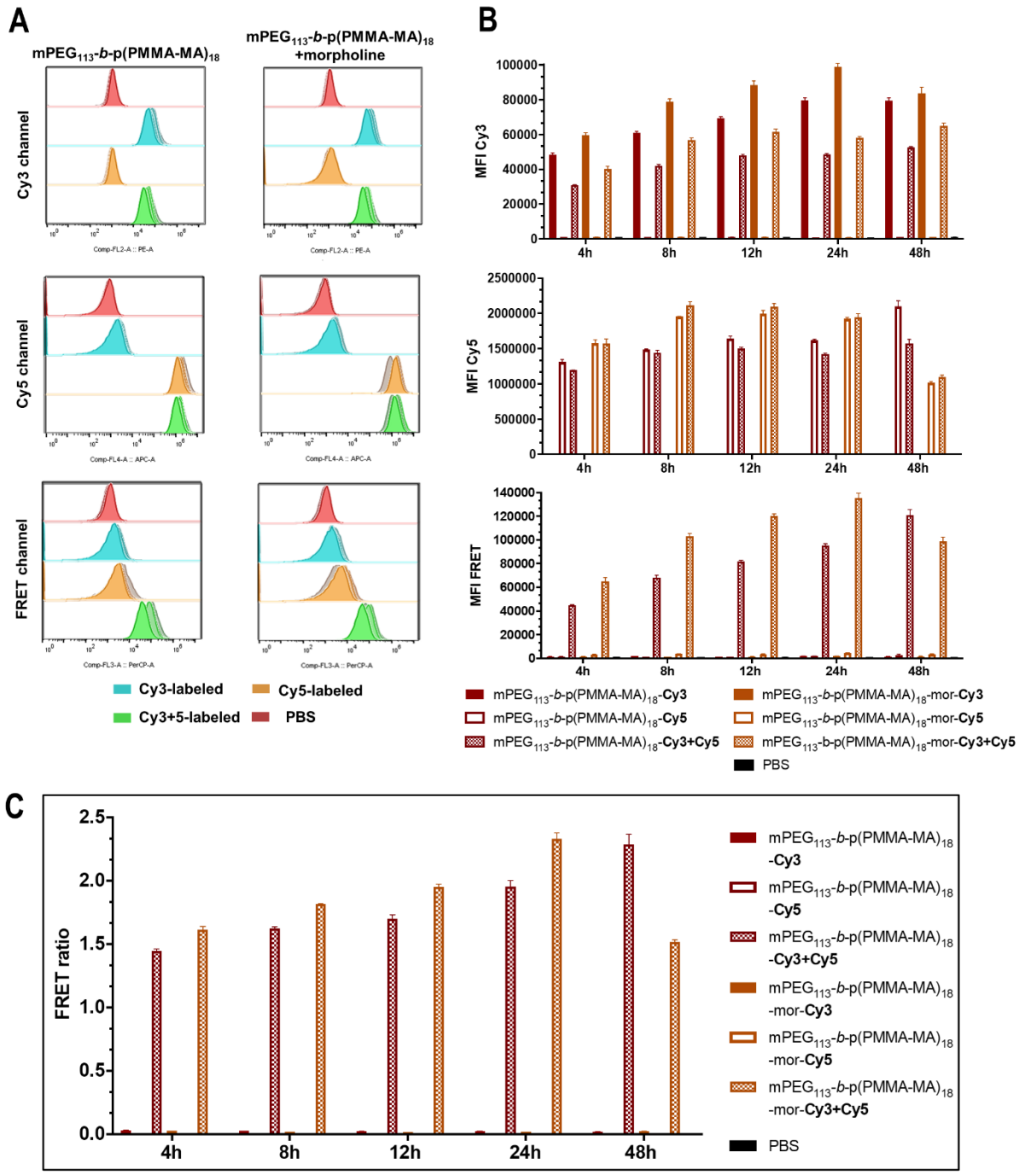

Figure S34: Flow cytometry time dependent cellular uptake analysis in RAW-Dual macrophages incubated with PBS (control), Cy3- or Cy5-labeled block copolymer, as well as a mixture of the dye-labeled block copolymers with and without morpholine quenching at 30 µg/mL for 4, 8, 12, 24 and 48h. Flow cytometry histograms (A) and mean fluorescence intensity (MFI) (B) of Cy3, Cy5 as well as FRET signal for RAW-Dual macrophages. Interestingly, only in case of the dye-labeled block copolymer mixtures a FRET signal is found, that gradually increases (expect for morpholine quenched polymers after 48 h). Based on the flow cytometry data time, the time-dependent FRET ratio was calculated as ratio of FRET MFI to Cy3 MFI.

Fluorescence Confocal Laser Scanning Microscopy Imaging and Lifetime Imaging

For analysis of intracellular micellar formulation by fluorescence confocal laser scanning microscopy RAW-Dual macrophages were seeded in an Ibidi µ-slide 8-well confocal microscopy chamber (50000 cells/well in 180 µL culture medium) and left to adhere overnight at 37 °C. Then, 20 µL of the Cy3- or Cy5-labeled block copolymer, as well as a mixture of both dye-labeled block copolymers with and without morpholine in PBS (total concentration of 10 µg/mL) were added to the cells. After incubation for 4 h at 37 °C cells were analyzed in their cell medium solution without fixation or cell nuclei staining on an incubator-equipped Leica Stellaris® 8 microscope (40x glycerol immersion objective) with fast lifetime contrast (FALCON) module (Leica Microscopy GmbH, Wetzlar, Germany). All samples were pulsed with a 40 MHz white laser at 469 nm measuring the intensity and fluorescence lifetime. The emitted photons were recorded on a HyD® X (GaAsP hybrid photocathode) detector with a filter window at 480 nm to 650 nm.

For fluorescence lifetime imaging (FLIM) over time cells were treated with a mixture of Cy3- or Cy5-labeled block copolymer and immediately analyzed on the incubator-equipped Leica Stellaris® 8 microscope. In this case, cells were hold at 37 °C, 5 % CO_2 with 90% relative humidity. Images were detected at intervals of 1.5 min for 4 h, with a scanning resolution of 1024x1024 pixels at 200 Hz. Consequently, 158 images were detected and generated photons were counted according to FALCON-modified time correlated single photon counting (TCSPC) method. Based on following equation each pixel was transformed into a phasor plot.

$$g_{ij}(\omega) = \int_0^T I(t) \cdot \cos(n\omega t)\,\mathrm{d}t \;/\; \int_0^T I(t)\mathrm{d}t$$

$$s_{ij}(\omega) = \int_0^T I(t) \cdot \sin(n\omega t)\,\mathrm{d}t \;/\; \int_0^T I(t)\mathrm{d}t$$

$G_{ij}(\omega)$ and $s_{ij}(\omega)$ correspond to the x and y coordinates of the phasor plot, while n and ω are the harmonic and angular frequency of excitation. T is the repeated frequency of the acquisition. The frequency domain data acquisition from each pixel is transformed to phasor points based on the following transformation:

$$g_{ij}(\omega) = m_{ij} \cdot \cos(\phi_{ij})$$

$$s_{ij}(\omega) = m_{ij} \cdot \sin(\phi_{ij})$$

In this case $m_{ij}(\omega)$ and $\phi_{ij}(\omega)$ correspond to the modulation and phase shift respectively to the frequency domain measurement at pixel ij. Consequently, the decay of each pixel can be

transformed to a point in the phasor plot. All images and phasor components were processes by Leica Application Suite X 3.7.4.23463 of the Leica Microsystem.

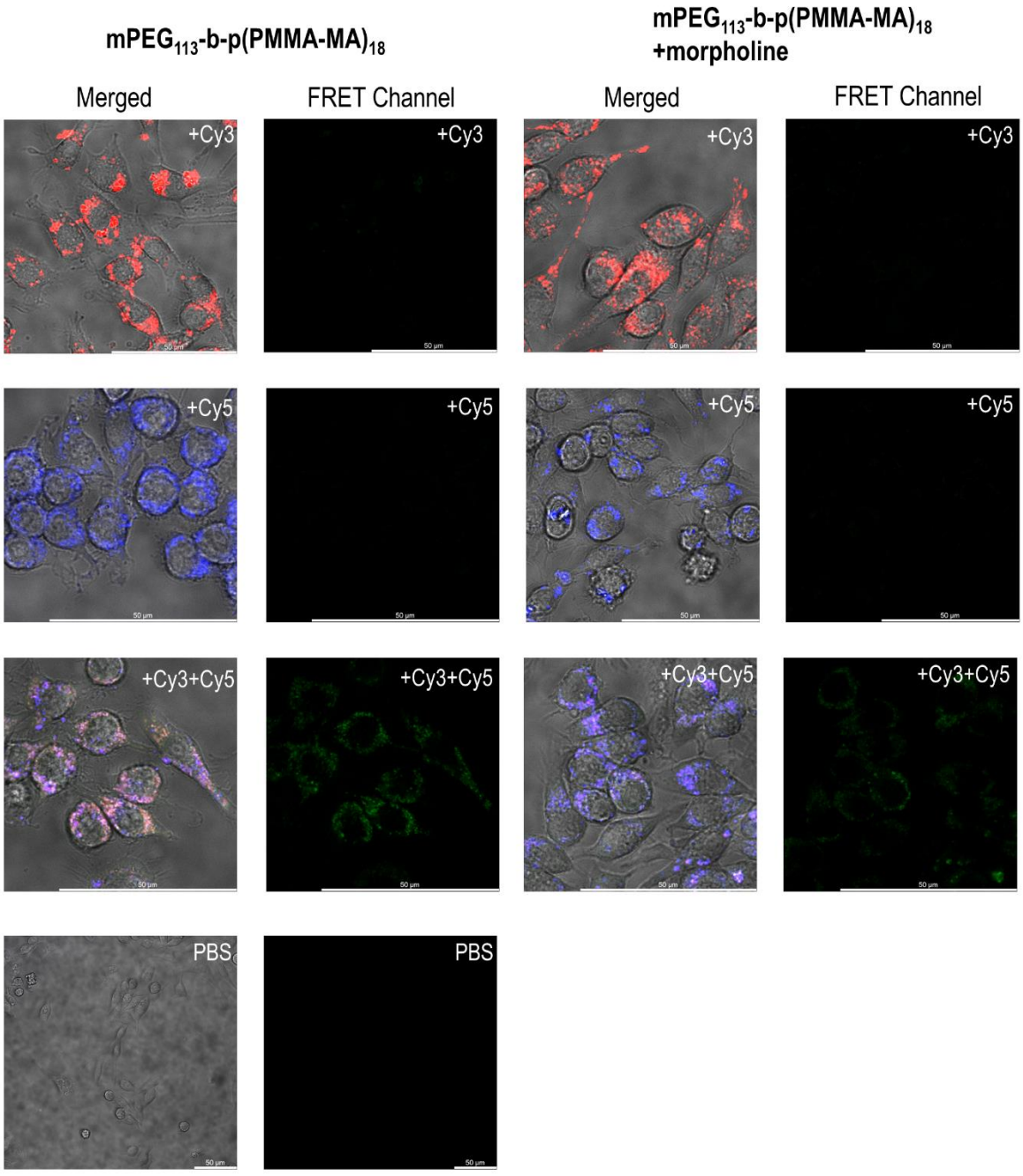

Figure S35: Fluorescence confocal microscopy images of RAW-Dual macrophages treated with Cy3- or Cy5-conjugated block copolymer as well as a mixture of both dye-labeled block copolymers with and without morpholine at 10 µg/mL or PBS as control for 4 h (red: Cy3-labeled polymer, blue: Cy5-conjugated polymer, pink: mixture of Cy3- or Cy5-labeled polymer, green: FRET signal).

Correlative Light and Electron Microscopy (CLEM) Cell Imaging

For cellular uptake and intracellular self-assembly of Cy5-labeled block copolymer RAW-Dual macrophages were seeded onto 3 mm sapphire disks (M. Wohlwend GmbH, Switzerland) in a Ibidi µ-slide 8-well confocal microscopy chamber (30000 cells/well in 180 µL culture medium) and left to adhere overnight at 37 °C. Prior to use, the sapphire disks were coated with a 10 nm-thick carbon layer by an EM MED020 instrument (Leica, Germany), dried and sterilized at 120 °C for 16 h. Afterwards, 20 µL of the Cy5-labled block copolymer $mPEG_{113}$-*b*-$p(PMMA\text{-}MA)_{18}$ (total concentration of 30 µg/mL) was added to the cells and incubated for 4 h at 37 °C. Subsequently, the sapphire disks were collected, immersed into 1-hexadecene, and fixed between two aluminum plates (3 mm, Plano). Afterwards, used aluminum 'sandwich' structure was rapidly frozen for a duration of 2-3 seconds using a Wohlwend HPF Compact 01 high-pressure freezer at a pressure of 2100 bar. The specimen holder was submerged into liquid nitrogen, followed by the relocation to a container filled with liquid nitrogen. After removal from the aluminum sandwich, the frozen sapphire discs were transferred into 1 mL pre-cooled freeze substitution medium (0.2% (w/v) osmium tetroxide, 0.1% (w/v) uranyl acetate, 5% (v/v) distilled water in acetone) and further processed in a freeze substitution unit (AFS2, Leica, Germany). Samples were allowed to warm up to 0 °C over 20 h, before being warmed to room temperature. The substitution medium was removed by washing with acetone (3x) every 30 minutes. Subsequently the discs were infiltrated in gradient acetone-epoxy resin mixtures (2:1, 1:1 and 1:2) for each 1 h. In a last step, the samples were infiltrated in 100% epoxy resin overnight. To initiate the polymerization process of the resin, each disk was transferred into a new Eppendorf tube containing fresh epoxy resin and maintained at 60 °C for 24 h.

Sectioning

After polymerization, sapphire disks were detached from the EPON block by immersion into liquid nitrogen. Next, the resin blocks were trimmed and sectioned on a Leica Ultramicrotom EM UC7. Sectioning was carried out utilizing an ultra 45° Jumbo diamond knife (Diatome, Switzerland) and the resulting cuts were collected in a basin filled with water. Afterwards, the cuts were transferred either on ITO coated coverslips (Plano, Germany, Wetzlar) for later SEM imaging or on Type H6 100mesh finder grids (Plano, Germany, Wetzlar) for TEM imaging.

Confocal imaging

Images were recorded on an SP5 Leica Laser Scanning Confocal Microscope (Leica Wetzlar, Germany). To enable the detection of later SEM images, cuts on ITO were analyzed by a 63x1.2 NA water immersion objective. Cuts on TEM Finder Grids were deposited on coverslips and

imaged with an 20x0.75 NA dry objective. In both cases, 458 nm laser line was used for acquisition of reflected light images and simultaneously 488 laser line was used for the excitation of the Cy5-labeled block copolymer. Reflected light was recorded on a photomultiplier whereas fluorescent light in a range of 600-670 nm was measured on a APD avalanche photodiode.

TEM

TEM images were recorded on a Jeol JEM 1400 with an acceleration voltage of 100kV. SEM cuts on ITO were imaged on a HITACHI SU8000 using SE+BSE mode with 1.5kV landing voltage at 18000nA EmissionCurrent.

CLEM

Precise detection of confocal and electron microscopy images enables the identification of specific molecules by confocal fluorescence microscopy, while also offering a detailed visualization of the cellular environment on high resolution electron microscopy images. To this end reflected light and fluorescent light confocal images were recorded simultaneously. The outline and certain internal structural characteristics of the cells can clearly be seen in the reflected light images and can further be identified in the high-resolution EM image. By manually setting landmarks on these structural characteristics a transformation of the EM Image to the confocal image is calculated using the "landmark correspondence" plugin of ImageJ (in combination with an inhouse Macro).

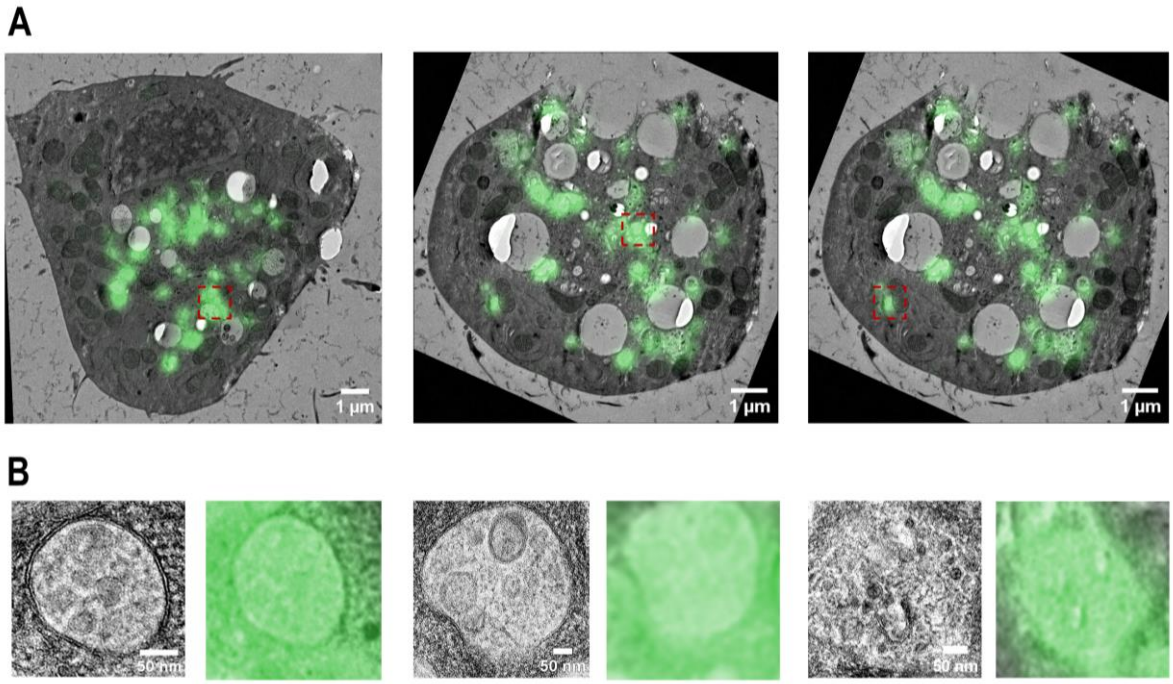

Figure S36: CLEM images of RAW-Dual macrophages incubated with Cy5-labeled block copolymer at 30 µg/mL for 4 h, showing micellar structures after endosomal uptake (green: cell organelles with Cy5-labeled-polymer/micelles).

Additional References

(1) Heck, A. G.; Stickdorn, J.; Rosenberger, L. J.; Scherger, M.; Woller, J.; Eigen, K.; Bros, M.; Grabbe, S.; Nuhn, L. Polymerizable 2-Propionic-3-Methylmaleic Anhydrides as a Macromolecular Carrier Platform for PH-Responsive Immunodrug Delivery. *J. Am. Chem. Soc.* **2023**, *145* (50), 27424–27436.

(2) Huppertsberg, A.; Kaps, L.; Zhong, Z.; Schmitt, S.; Stickdorn, J.; Deswarte, K.; Combes, F.; Czysch, C.; De Vrieze, J.; Kasmi, S.; Choteschovsky, N.; Klefenz, A.; Medina-Montano, C.; Winterwerber, P.; Chen, C.; Bros, M.; Lienenklaus, S.; Sanders, N. N.; Koynov, K.; Schuppan, D.; Lambrecht, B. N.; David, S. A.; De Geest, B. G.; Nuhn, L. Squaric Ester-Based, PH-Degradable Nanogels: Modular Nanocarriers for Safe, Systemic Administration of Toll-like Receptor 7/8 Agonistic Immune Modulators. *J. Am. Chem. Soc.* **2021**, *143* (26), 9872–9883.

(3) Heck, A. G.; Medina-Montano, C.; Zhong, Z.; Deswarte, K.; Eigen, K.; Stickdorn, J.; Kockelmann, J.; Scherger, M.; Sanders, N. N.; Lienenklaus, S.; Lambrecht, B. N.; Grabbe, S.; De Geest, B. G.; Nuhn, L. PH-Triggered, Lymph Node Focused Immunodrug Delivery by Polymeric 2-Propionic-3-Methylmaleic Anhydrides with Cholesterol End Group. **2024-submitted**.

(4) Stickdorn, J.; Stein, L.; Arnold-Schild, D.; Hahlbrock, J.; Medina-Montano, C.; Bartneck, J.; Ziß, T.; Montermann, E.; Kappel, C.; Hobernik, D.; Haist, M.; Yurugi, H.; Raabe, M.; Best, A.; Rajalingam, K.; Radsak, M. P.; David, S. A.; Koynov, K.; Bros, M.; Grabbe, S.; Schild, H.; Nuhn, L. Systemically Administered TLR7/8 Agonist and Antigen-Conjugated Nanogels Govern Immune Responses against Tumors. *ACS Nano* **2022**, *16* (3), 4426–4443.

(5) Nuhn, L.; Van Herck, S.; Best, A.; Deswarte, K.; Kokkinopoulou, M.; Lieberwirth, I.; Koynov, K.; Lambrecht, B. N.; De Geest, B. G. FRET Monitoring of Intracellular Ketal Hydrolysis in Synthetic Nanoparticles. *Angew. Chemie - Int. Ed.* **2018**, *57* (33), 10760–10764.

CHAPTER IV: INTRODUCING TARGETING UNITS OR pH-RELEASABLE IMMUNODRUGS INTO CORE-CLICKABLE NANOGELS

The following chapter was submitted to the European Polymer Journal and is in revision. As first author, I designed the core-clickable nanogels and performed all synthesis steps of the DBCO-modified block copolymer. In this regard, I characterized the block copolymer by different methods and fabricated hydrophilic nanogels. Transmission Electron Microscopy (TEM) images were recorded by David Schwiertz. I investigated the accessibility of the DBCO function and synthesized the azide-containing, pH-sensitive linker for the fabrication of pH-responsive drug-loaded nanogels. Further biological evaluations on RAW-Dual macrophages were conducted by me. The small molecular drug IMDQ was synthesized by Maximilan Scherger, while further modifications were conducted by me. Additionally, I formulated trimannose-loaded nanogels and studied their *in vitro* targeting behavior on CHO^{MMR+} and CHO^{MMR-} cells by support of Bellinda Lantzberg. The azide-modified trimannose was provided by Robert Forster and confocal microscopy images were recorded by Ha-Chi Nguyen. The manuscript was prepared by me and feedback from all co-authors was included.

INTRODUCING TARGETING UNITS OR PH-RELEASABLE IMMUNODRUGS INTO CORE-CLICKABLE NANOGELS

Alina G. Heck[1], David Schwiertz[2], Bellinda Lantzberg[1], Ha-Chi Nguyen[1], Robert Forster[3], Maximilian Scherger[1], Till Opatz[3], Jo A. Van Ginderachter[4], and Lutz Nuhn[1,5]*

1: Max Planck Institute for Polymer Research, 55128 Mainz, Germany

2: Biotherapeutics Division, Leiden Academic Centre for Drug Research (LACDR), Leiden University, 2333CC Leiden, The Netherlands

3: Johannes Gutenberg-University Mainz, Department of Chemistry, 55128 Mainz, Germany

4: Brussels Center for Immunology, Vrije Universiteit Brussel, 1050 Brussels, Belgium
Myeloid Cell Immunology Lab, VIB Center for Inflammation Research, 1050 Brussels, Belgium

5: Chair of Macromolecular Chemistry, Julius-Maximilians-Universität Würzburg, 97070 Würzburg, Germany

*: corresponding author: Prof. Dr. Lutz Nuhn (E-mail: lutz.nuhn@uni-wuerzburg.de)

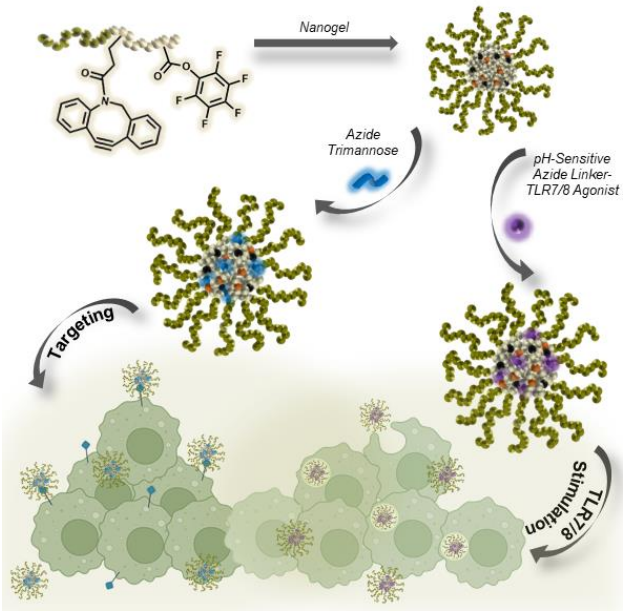

Keywords: DBCO click chemistry, RAFT-polymerization, mannose targeting, 2-propionic-3-methylmaleic anhydride linker, DBCO nanogels, pH-reversible drug-loaded nanogels, immunodrug delivery.

Abstract

The development of nano-sized carrier systems plays a fundamental role in immunodrug delivery and the treatment of cancer. Especially functional materials, coupled with a stimuli-responsive drug release, control the selective delivery of small molecular drugs to the target site and avoid systemic side effects. Based on this, we introduce a DBCO core-functionalized nanogel platform for pH-reversible conjugation of highly potent TLR7/8-activating imidazoquinolines and the selective targeting of macrophage mannose receptor (MMR/ CD206) expressed by immunosuppressive macrophages. DBCO-PEG_4-amine functionalized polymethacrylates are synthesized by controlled RAFT polymerization and self-assembled into precursor micelles in polar aprotic solvents. Corresponding nanogels are generated *via* reactive ester chemistry, while conjugated DBCO-units are incorporated into the core, still accessible for click reaction with azide-functionalized structures. Regarding the preparation of targeted nanogels, trimannose equipped with azide moieties can be conjugated to the DBCO nanogels, revealing the efficient targeting of macrophages' mannose receptor *in vitro*. Moreover, the broad applicability of the DBCO nanogel is demonstrated by the synthesis of an azide-containing 2-propionic-3-methylmaleic anhydride-based linker sensitive for the pH-reversible conjugation of secondary amine-modified immune modulators, such as IMDQ-Me. *Via* bioorthogonal DBCO click reaction, the immune modulator can reversibly be conjugated, affording pH-responsive drug-loaded nanogels that conserve the desired immune stimulatory effect *in vitro*. Overall, these findings highlight the potential of core-functionalized DBCO nanogels, a promising carrier system for pH-sensitive conjugated immunodrugs as well as an attractive platform for controlled targeting of MMR. Altogether, the versatile application of core-functionalized DBCO nanogels may pave the way for enhancing bioorthogonal multifunctionality inside nanocarrier systems that assist in addressing multiple targets in cancer immunotherapy.

Introduction

Nano-scaled polymeric micelles have demonstrated a high potential as drug delivery system in diagnostics and therapeutics. The variation of the pharmacokinetic profile, as well as the improved bioavailability and reduced toxicity of small-molecular drugs increased the application of nanoparticles in anticancer therapy. Thus far, efficient targeted drug delivery has primarily been accomplished by the accumulation of long circulating drug nano-formulations using the enhanced permeability and retention (EPR) effect of solid tumors.[1–4] Based on the high demand for nutrients and oxygen, fast growing tumors present various leaky vessels which increases the permeability to nanomaterials, while contributing to the retention time through the lack of normal lymphatic drainage.[5,6] Compared to passive targeting, active targeting relies on the application of targeting structures conjugated to nanoparticles. Accumulated in the tumor microenvironment, biological ligands can interact with specific receptors or markers overexpressed on tumor or immune cells affording a cell-specific drug delivery.[6,7] Already illustrated by the Ringsdorf model for pharmacologically active polymers[8,9] targeted carrier structures improve the efficacy at the site of the disease. Small structures like nanobodies[10,11] or saccharides[12] are promising mediators for a cell-selective drug targeting. Mannose receptors are expressed on important immune cells, including dendritic cells and macrophages.[12,13] Among these cells, macrophages are represented in all tissues, while playing a dominant role in tumor progression and metastasis. Tumor-associated macrophages (TAMs) are located in the tumor microenvironment, often displaying a high immunosuppressive activity and strong expression of the Macrophage Mannose Receptor (MMR, CD206). Hence, TAMs can be considered as an attractive target for cancer immunotherapy.[11,14–17]

Access to nano-sized drug delivery systems can be generated by the synthesis of self-assembling block copolymers.[1,18] Subsequent core-crosslinking will then assist in providing advanced properties for applications in complex biological environments.[4,19,20] As already reported from our laboratories, well-defined core-shell systems can be formulated by the Reversible Addition-Fragmentation Chain Transfer (RAFT) polymerization of methoxy tri(ethylene glycol) methacrylate (mTEGMA) and the reactive ester pentafluorophenyl methacrylate (PFPMA).[21] The resulting amphiphilic block copolymers provide efficient shielding properties and stability based on the hydrophilic PEG-like structure, whereas the hydrophobic PFPMA enables controlled self-assembly and amine modification.[22–24] Consequently, self-assembled micelles can be further functionalized by dye-labeling or core-crosslinking, promoting the nanoparticle stability and integrity.[22,25] So far, additional surface decoration with azides enabled the conjugation of DBCO-functional proteins or

peptides and the generation of antigen-decorated nanogels.[25,26] Additionally, MMR-targeting nanobodies were also immobilized onto such nanogels for targeting $CD206^+$ cells.[10,14] However, the core-functionalization with amine-containing dibenzocyclooctynes (DBCO) has not been reported yet and could further extend the application of our nanoparticle system.

In recent years, click chemistry has become an important tool in nanomedicine and pharmaceutical sciences. Since the first reports by Sharpless and coworkers in 2001, click chemistry has been defined as high-yielding reactions, providing non-reacting by-products under mild reaction conditions.[27,28] Various bioorthogonal reactions such as the copper-catalyzed azide-alkyne cycloaddition (CuAAC) or the tetrazine ligation by an inverse electron-demand Diels-Alder reaction (IEDDA) have paved the way for a fast and selective chemical reaction between biomolecules and synthesized functional groups. Due to the general concern of copper in materials for biomedical applications, the Cu-free azide-alkyne cycloaddition (SPAAC) demonstrates efficient reaction properties with milder and more versatile application features. Strained cyclooctynes such as DBCO form chemically and metabolically robust bonds to orthogonal azides in a [3+2] cycloaddition, making the reaction an attractive candidate for numerous *in situ* applications.[29–31]

Hence, SPAAC reactions can be used to modify nanocarriers with additional functional groups or stimuli responsive systems. Supplementation of nano-sized drug carriers with stimuli responsive motives promotes a controlled drug efficacy at the target-site with minimized side effects. Among the variety of stimuli such as light or redox potential, pH-sensitive formulations gained an important role in next generation nanomaterials.[32–34] Between frequently used ketal[24] or hydrazone structures,[35] disubstituted maleic anhydride systems have been employed as excellent structures able to release conjugated amines in their native form without the generation of by-products.[36,37] Already a mildly acidic pH (5.5-6.8) initiates the fast attack by the β-positioned free carboxylic acid to the amide, resulting in the re-formation of the anhydride system and precursor amines.[34,38,39] In addition, modification of the *cis*-double bond by variation of adjacent substituents impacts the angle between maleic acid amide derivates and the β-carboxylate and, thus, the pH sensitivity of the system.[40–42] When primary amines are conjugated, we recently reported the formation of cyclic imides on polymeric maleic anhydrides resulting in the lack of pH sensitivity.[43] Only for secondary amines, reversibility of the conjugate is found. Consequently, we could support the pH-reversible conjugation of secondary amine-containing drugs, such as the small-molecular Toll-like receptor 7/8 (TLR7/8) agonist 1-(4-((methylamino)methyl)-benzyl)-2-butyl-1*H*-imidazo[4,5-c]quinolin-4-amine (IMDQ-Me).[43]

Upon administration most TLR agonists activate various antigen-presenting cells (APCs) leading to the secretion of cytokines like type-I IFN and IL-12 and the stimulation of cytotoxic T-cells. Nevertheless, most injected compounds rapidly distribute through the body, resulting in an undesired inflammatory reaction.[23,24,44,45] Previous reports demonstrated a controlled immune activation by covalent conjugation of small molecular TLR agonists to different types of nanocarriers.[25,46–48] In this context, the additional application of stimuli-responsive linkers could contribute to the efficacy and targeted immune stimulation.

Herein, we describe the conjugation of an amine-functionalized DBCO to an amphiphilic block copolymer consisting of methoxy tri(ethylene glycol) methacrylate (mTEGMA) and reactive ester pentafluorophenyl methacrylate (PFPMA), followed by the conversion of the block copolymer micelles into completely hydrophilic dye-labeled and core-crosslinked nanogels (Figure 1). Investigating the accessibility of the nanogels' core-localized DBCO groups with azide-containing dyes, the favourable click reaction is shown and paving the way for biological applications. While the nanogel itself shows no MMR affinity, covalent conjugation of an azide-functionalized trimannose triggers the selective targeting and internalization into MMR-expressing cells. Further generation of an azide-modified disubstituted maleic anhydride linker offers a smart platform for the pH-sensitive conjugation of different amines as well as secondary amine-modified immune-stimulating TLR 7/8 agonist IMDQ-Me with high *in vitro* activity. Overall, extending the nanogel platform for DBCO click reactions therefore provides beneficial features for a targeted and pH-sensitive (immuno)-drug delivery.

Results and Discussion

Design, Synthesis and Characterization of a DBCO-functionalized Nanogel Platform

To establish a synthetic pathway for DBCO-conjugated amphiphilic block copolymers, pentafluorophenyl (PFP) reactive ester monomers were employed.[49,50] With their high solubility in different organic solvents, their high reactivity for a broad range of amines and their easy direction of reaction kinetics,[51,52] pentafluorophenyl methacrylate (PFPMA) monomers were accessed by treatment of methacryloyl chloride with pentafluorophenol (Figure S1-S4). Next, Reversible Addition-Fragmentation Chain Transfer (RAFT) polymerisation should enable the controlled synthesis of the block copolymer p(mTEGMA)$_n$-*b*-p(PFPMA)$_m$ to form block copolymer micelles, followed by the conversion into hydrophilic nanogels. Therefore, commercially available tri(ethylene glycol)methyl ether methacrylate (mTEGMA) was polymerized by the chain transfer agent 4-cyano-4-((phenylcarbonothioyl)thio)pentanoic

acid and the initiator azobisisobutyronitrile (AIBN, Figure S5). Precipitation in hexane yielded the homopolymer p(mTEGMA)$_{20}$ with a number-average molecular weight (M_n) of 2660 app (apparent molar mass) and a narrow *Đ* of 1.22 (Figure S6+S7). Afterwards, similar reaction conditions were applied during block copolymerization with PFPMA (Figure S8) yielding a narrowly dispersed block copolymer with a *Đ* of 1.28 and number-average molecular weight (M_n) of 10941 app. Thereby, a significant shift of the block copolymer by size exclusion chromatography (SEC) compared to the homopolymer clearly attested the attachment of PFPMA to the homopolymer (Figure S11). Further ^{1}H NMR and ^{19}F NMR spectroscopy characterization (Figure S9 and S10) confirmed the successful synthesis of the block copolymer p(mTEGMA)$_{20}$-*b*-p(PFPMA)$_{36}$. To ensure no interaction of the dithiobenzoate end groups with amines present during the nanogel formulation, the block copolymer was further reacted with an excess of AIBN (Figure S13). Here, the removal of the end groups was confirmed by UV-Vis spectroscopy but had no effect on the structural properties of the block copolymer (Figure S13-S15).

In a final step, the block copolymer was partially functionalized with DBCO through aminolysis by DBCO-PEG$_4$-amine (Figure 1A and Figure S16). The modified block copolymer chains were targeted to be equipped with three DBCO-PEG$_4$-units per chain and could then be isolated by precipitation in diethyl ether. Detailed characterization was conducted by ^{1}H, ^{19}F NMR and UV-Vis spectroscopy, as well as size exclusion chromatography (SEC, Figure S17-S19) which all confirmed the covalent conjugation of the DBCO group onto the p(PFPMA) block.

For the preparation of fully hydrophilic nanogels, precursor micelles were prepared from p(mTEGMA)$_{20}$-*b*-p(PFPMA)$_{36}$ with or without additional DBCO modification. Both block copolymers could be self-assembled in DMSO by ultrasonication and analyzed by dynamic light scattering (DLS). The two systems provided narrowly distributed micelles with a z-average hydrodynamic diameter (D_z) between 20 to 30 nm and a PDI of 0.20. Interestingly, the DBCO micelles tended to be slightly smaller, considering their lower degree of fluorination which governs the polymers' self-assembly in DMSO (Figure 1C and Figure S19). Following the synthesis concept of Figure 1B (and Figure S20), the remaining PFP units were subsequently aminolyzed by traces of tetramethylrhodamine cadaverine (TMR) for dye labeling and 0.5 equivalents of 2,2-(ethylenedioxy)bis(ethylamine) for cross-linking. Final hydrophilization by an excess of 2-aminoethanol, followed by purification *via* dialysis against millipore water supplemented with 0.1% ammonia resulted in two types of nanogels (NG and NG with DBCO).

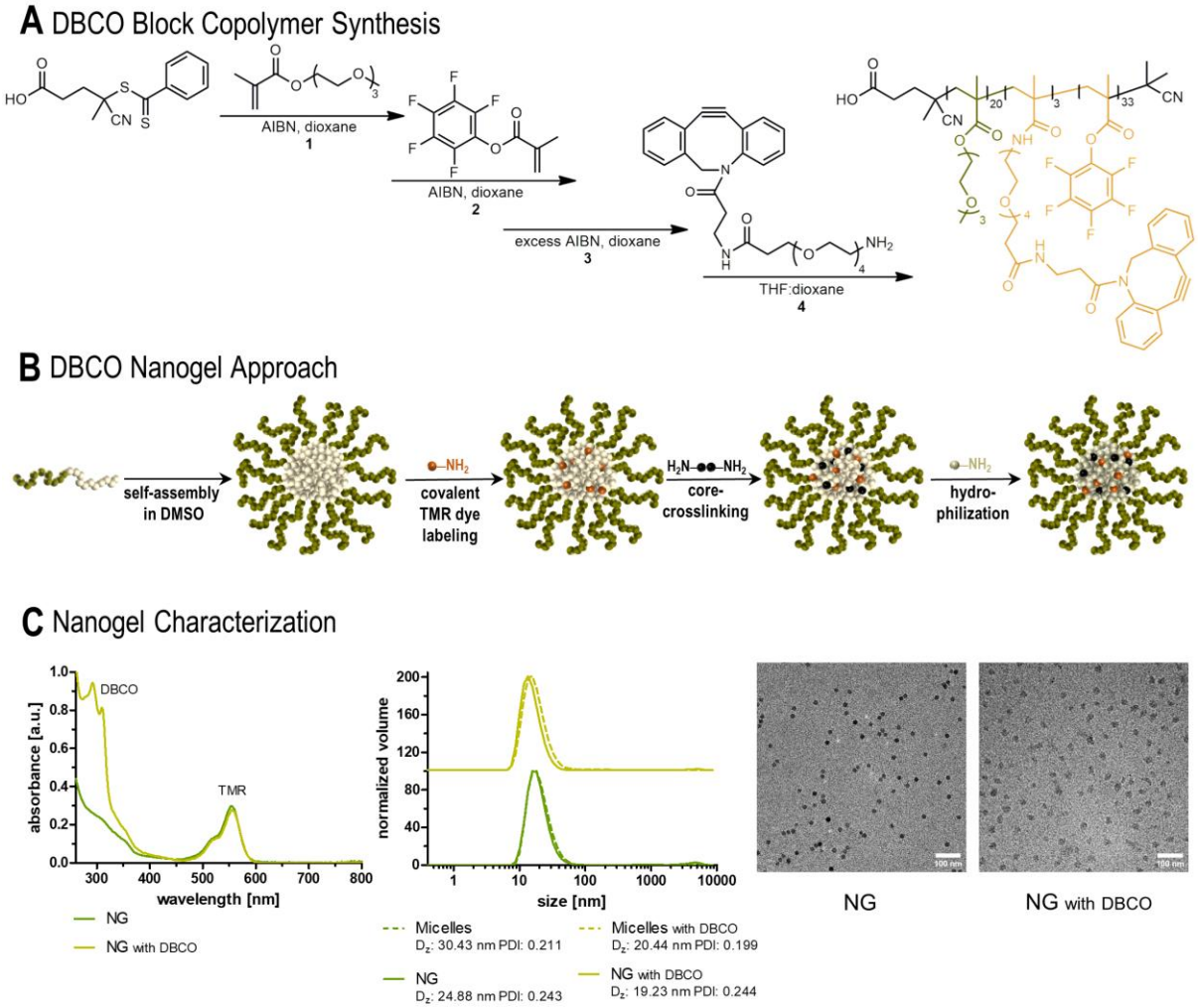

Figure 1. Preparation of core-functionalized DBCO nanogels from DBCO-containing reactive ester block copolymer. (**A**) Synthesis scheme for the controlled RAFT block copolymerization of p(mTEGMA) with PFPMA initiated by AIBN affording the block copolymer p(mTEGMA)$_{20}$-*b*-p(PFPMA)$_{36}$, followed by partial modification through aminolysis with DBCO-PEG$_4$-amine. (**B**) Sequential fabrication process for the core-localized DBCO nanogels derived from the self-assembled precursor micelles in DMSO. The remaining reactive ester chemistry units enable the generation of tetramethylrhodamine dye (TMR)-labeled and core-crosslinked, hydrophilic nanogels. (**C**) Characterization data for the DBCO nanogels compared to nanogels without DBCO. In the UV-spectra of both TMR-labeled nanogels, the absorbance maxima around 300 nm can be related to the nanogel core-conjugated DBCO units. Dynamic light scattering (DLS) measurements of the precursor micelles and fabricated nanogels both with and without DBCO-conjugated. Subsequent transmission electron microscopy (TEM) images confirm the homogeneity of both nanogels with and without DBCO.

To ensure the integrity of the nanogels and their core-localized DBCO units, UV-Vis absorbance spectra and DLS measurement were recorded in millipore water containing 0.1% ammonia (Figure 1C and Figure S21). Thereby, both systems revealed the successful generation of TMR-labeled nanogels with narrow monomodal distribution in a similar size range (D_z of 19.23 nm and 24.88 nm – the DBCO functionality does obviously not interfere with the nanogel later on, as the particle sizes were pre-determined by self-assembled smaller precursor micelles). In addition, the core-crosslinked nanogels could be imaged in dry state by transmission electron microscopy (TEM) and confirmed the presence of homogenously

distributed spherically shaped nanoparticles. Interestingly, DBCO-functionalized nanoparticles illustrated a spherical morphology with slightly reduced contrast (Figure 1C - perhaps the loss of fluorine content may slightly disturb the intramicellar nanophase separation of the precursor micelles).

With respect to the further preparation of drug-loaded or targeted nanogels, the accessibility of the nanogels' DBCO-units during bioorthogonal conjugation had to be confirmed. Consequently, a commercially available azide-modified fluorescent dye (Oregon Green 488 azide, OG488 azide) was used for tracing its click attachment to the nanogel, while potentially unreacted dyes could be removed *via* spin-filtrations, particularly important for control nanogels that do not contain any DBCO-groups. The isolated nanogels were analyzed by UV-Vis and DLS measurement, showing an additional absorbance maximum at 496 nm only for the DBCO nanogels (Figure 2B and 2C). In contrast, OG488 azide-treated control nanogels (NG) revealed only one absorbance maximum at 550 nm, derived from the conjugated TMR. In conclusion, the nanogels' DBCO-groups can be addressed for click chemistry and represent an ideal candidate for selective drug delivery by post-modification inside the nanogels' cores. This observation matches well with our recent observations on similar micelle-derived core-crosslinked and hydrophilized nanogels. They seem to provide a more porous structure and allow not only water to enter the nanoparticle but also other guest molecules to diffuse into the nanogel core.[53]

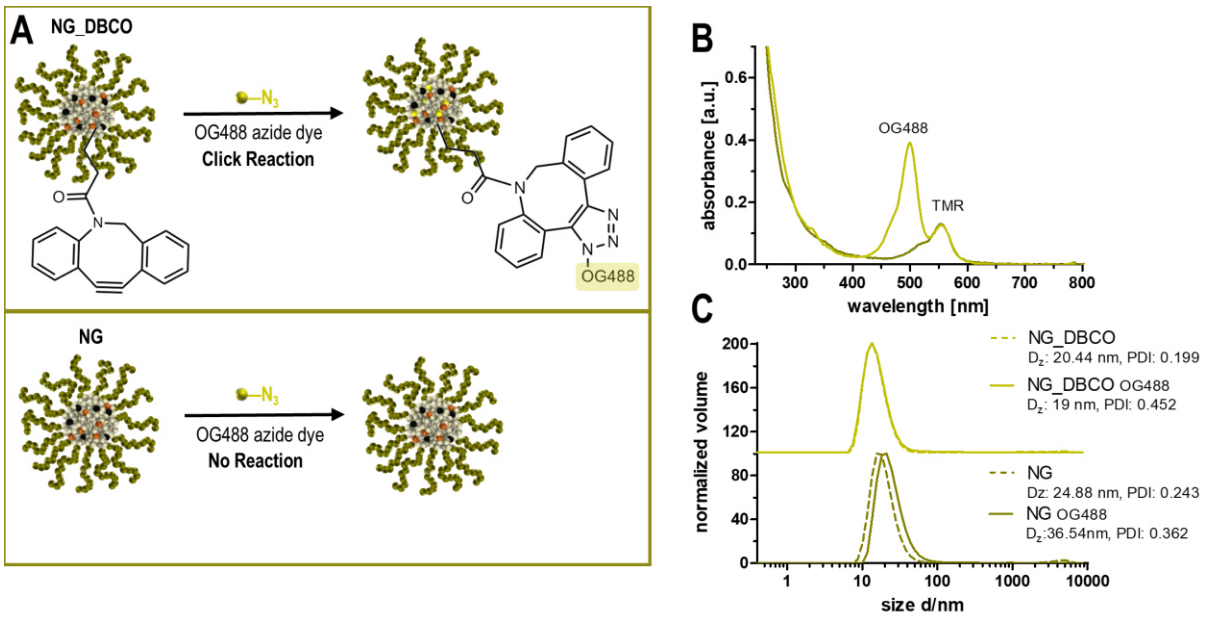

Figure 2. Analyzing the accessibility of the nanogels' core-localized DBCO-units. (**A**) Schematic reaction of the DBCO nanogel with the azide-containing fluorescent dye Oregon Green 488 azide (OG488 azide) compared to nanogels without core-localized DBCO. (**B**) UV-Vis spectra of the dye-functionalized DBCO nanogels, revealing an

additional absorbance maximum at 496 nm only for the DBCO nanogels while the control nanogels show no reaction with OG488 azide. (**C**) DLS measurements of the DBCO nanogels and control nanogels before and after treatment with OG488 azide.

Modification of DBCO Nanogels with Azide-Trimannose for Controlled MMR Targeting

Glycosylation can confer excellent targeting properties and consequently aid in understanding of a variety of cellular recognition processes. Due to its high specificity and effectiveness, mannosylation can be used for selective targeting of immune cells that highly express the mannose receptor, such as macrophages or dendritic cells, paving the way towards improved drug delivery and controlled immunotherapy.[13,14,16,54–57] Therefore, we aimed at conjugating azide-containing trimannose motifs[58,59] to the DBCO-functionalized nanogels (Figure 3A and Figure S38).

For comprehensive confirmation of successful trimannose conjugation, the nanogels were further treated with an azide-functionalized fluorescent dye (AF488 azide) after azide trimannose modification (Figure 3A). If successful trimannose conjugation occurred first, the dye can afterwards not conjugate compared to previous experiments. Additional control reactions on nanogels without DBCO should serve as further proof for a selective trimannose nanogel formation (Figure S38). Following the reaction scheme of Figure 3A (and Figure S38), all nanogels were subsequently purified by excessive spin-filtration for removal of unconjugated compounds, and then characterized by DLS and UV-measurement. Trimannose conjugation or dye-labeling did not affect the size of the nanogels (Figure 3B).

Furthermore, DBCO nanogels solely treated with AF488 azide demonstrated a significant absorbance maximum at 496 nm (Figure 3C). In stark contrast, DBCO nanogels which first reacted with azide trimannose led to the conversion of all potential DBCO-groups, and consequently no AF488 dye could be bound but was removed during the purification step. In case of control nanogel reactions without DBCO, a conjugation with neither azide trimannose nor AF488 azide was observed. Thus, these UV-Vis spectrophotometry data confirm the successful azide trimannose conjugation to the DBCO nanogels (Figure 3C).

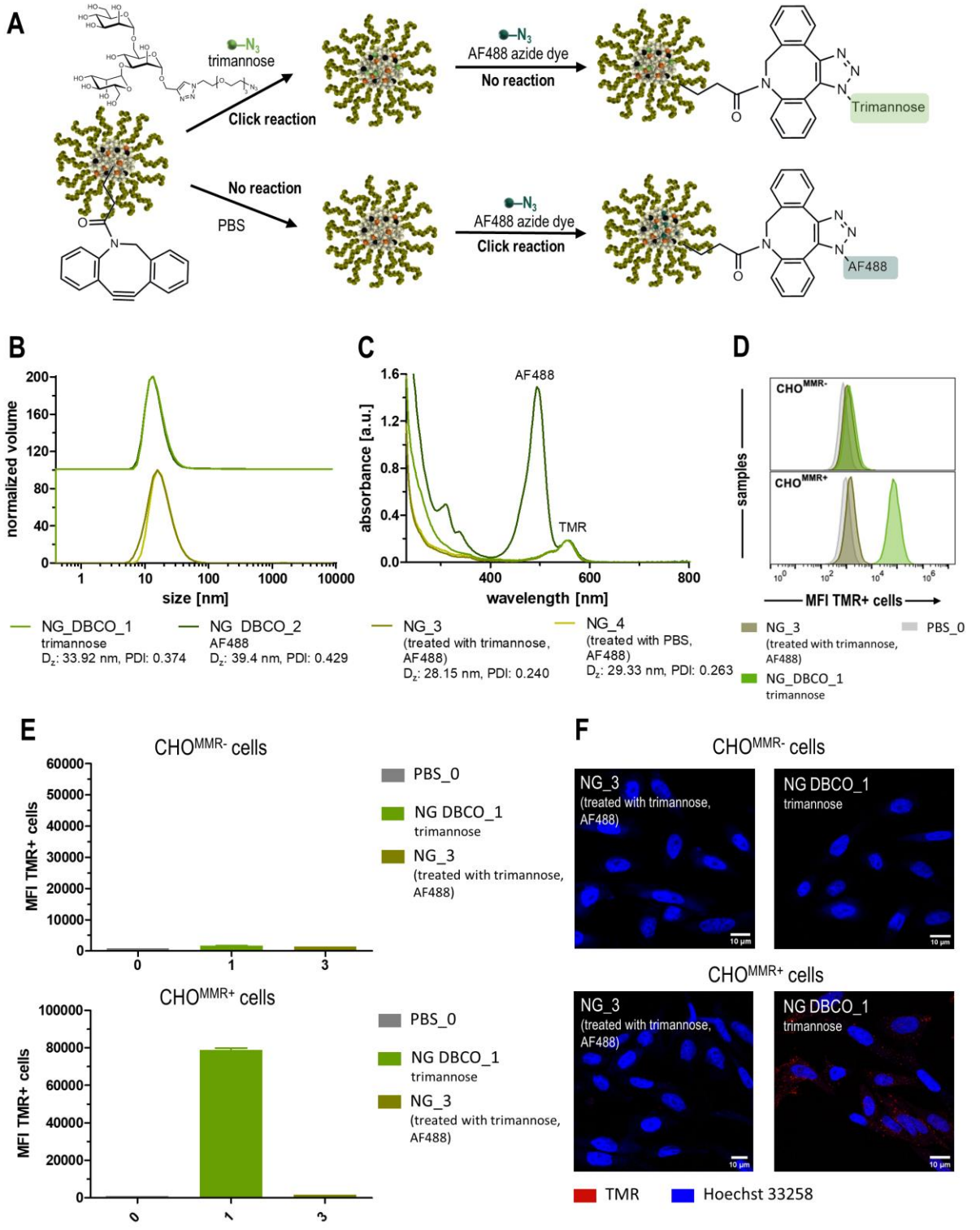

Figure 3. Formulation of trimannose conjugated DBCO nanogels for specific targeting of the macrophage mannose receptor (MMR) *in vitro*. (**A**) Reaction scheme for the sequential attachment of trimannose and Alexa Fluor 488 azide (AF488 azide) to the DBCO nanogel core by click reaction. (**B**) DLS measurement of the trimannose (NG_DBCO_1) and AF488-labeled (NG_DBCO_2) nanogels as well as corresponding control nanogels without DBCO (NG_3 and NG_4), which were treated accordingly to the DBCO nanogels but cannot undergo any conjugation. (**C**) UV-Vis spectrophotometry data of the nanoparticles shows an additional absorbance maximum at 488 nm only for NG_DBCO_2 solely treated with AF488 azide, while NG_DBCO_1 has previously been reacted with trimannose and, thus, shows no additional absorbance maximum. It can consequently be assumed to be successfully conjugated

to trimannose. (**D**) Cellular histogram of $CHO^{MMR+/MMR-}$ cells incubated with trimannose-labeled DBCO nanogels and PBS as a reference at 10 µg/mL for 24 h (n=3). (**E**) Mean fluorescence intensities (MFI) of $CHO^{MMR+/MMR-}$ cells incubated with TMR-labeled nanogels which were treated with trimannose and then AF448 azide (DBCO_NG_1 or NG_3) at 10 µg/mL for 24 h (n=3). Only the DBCO_NG_1, accessible for trimannose click reaction, demonstrated a specific uptake in CHO^{MMR+} cells. (**F**) Confocal microscopy images of $CHO^{MMR+/MMR-}$ cells incubated with DBCO_NG_1 or NG_3 at 10 µg/mL for 24 h (red: TMR-labeled nanogels, blue: nuclei stained with Hoechst 33258).

To assess the conserved bioactivity of trimannose towards interacting with the MMR/CD206 receptor and trigger a receptor-mediated cellular uptake for nanogels, we next performed *in vitro* experiments on Chinese Hamster Ovary cells that were genetically modified to express the MMR/CD206 receptor (CHO^{MMR+}), while wild type CHO cells without the MMR/CD206 receptor (CHO^{MMR-}) served as controls. For this purpose, both cell lines were incubated with the trimannose- or AF488-modified DBCO nanogel samples or the control nanogels for 24 h at 37 °C and characterized by flow cytometry and fluorescence confocal microscopy analyses. Thereby, our *in vitro* tests confirmed an exclusively boosted cellular uptake of trimannose-conjugated DBCO nanogels by CHO^{MMR+} cells compared to CHO^{MMR-}, visualized by the histogram plot (Figure 3D) and mean fluorescence intensities (Figure 3E), both recorded by flow cytometry. Control nanogels without DBCO showed no cellular uptake in both cell lines (Figure S49-S51). Presumably based on the increased hydrophobicity of the fluorescent dye AF488 into the nanogel core, the corresponding dye-labeled DBCO nanogels revealed an unspecific increased cellular uptake in both CHO^{MMR+} and CHO^{MMR-} cells compared to highly selective trimannose-conjugated DBCO nanogels (Figure S49-S51). Consequently, the carbohydrate click modification not only mediates specific binding but can also serve as a sufficient shielding domain, as we observed earlier, too.[54,55] Our findings were further supported by confocal microscopy images of CHO^{MMR+} and CHO^{MMR-} cells. All cells provided an internalization of AF488-labled DBCO nanogels, whereas trimannose-conjugation caused an exclusive cellular uptake in CHO^{MMR+} cells, confirming the successful targeting of the MMR/CD206 receptor by trimannose, followed by nanoparticle cell internalization (Figure 3F and Figure S52-S53).

Altogether, the obtained results demonstrate the successful conjugation of trimannose-species in the core of the DBCO nanogels by click reaction without affecting their ability to selectively target the MMR receptor on CHO cells, leading to an enhanced specific cellular uptake.

Synthesis and Characterization of an Azide Containing 2-Propionic-3-Methylmaleic Anhydride Linker for pH-Reversible Amidation Reaction

Based on these promising results, we wanted to verify whether the DBCO group inside the nanogel can also be explored for pH-sensitive covalent drug loading. Disubstituted maleic anhydride systems show a high sensitivity to slightly acidic environments, such as the tumor microenvironment (pH ≈ 6.5), able to release conjugated amines in their native form. Due to these features, maleic anhydrides are often referred to as traceless linkers.[36,60] We have recently reported on a polymer maleic anhydride system with remarkable drug delivery performances for immunostimulatory drugs, however, only when equipped with secondary amines.[43] To conjugate such a pH-sensitive linker into the core of our DBCO-functionalized nanogels, a disubstituted maleic anhydride needs to be equipped with an additional azide functionality for biorthogonal DBCO click reaction.

To this end, 2-propionic-3-methylmaleic anhydride was converted in a two-step reaction, starting with the transformation into a highly amine reactive acid chloride. Next, this reactive group was treated with the commercially available 11-azido-3,6-9-trioxaundecan-1-amine (Figure 4A, Figure S22) affording a bifunctional linker that is both accessible for pH-reversible conjugation of secondary amines as well as azide click reaction to DBCO groups. With regard to this amidation reaction, we opted for the design of a stable amide bond as linker between the azide and the maleic anhydride than an ester bond. Thus, we circumvent premature ester hydrolysis that would compete with the acid-triggered drug release from the anhydride system. Finally, the resulted linker was characterized by ^{1}H and 2D NMR spectroscopy as well as IR spectroscopy measurement (Figure 4B and Figure S23-S28).

After successful synthesis of the bifunctional linker, we evaluated its pH-reversible amine conjugation for fluorescent dyes in organic solvents. In this context, the azide-containing 2-propionic-3-methylmaleic anhydride linker was dissolved in DMSO supplemented with triethylamine (TEA) and treaded with the synthesized secondary amine dye 4-nitro-7-piperazino-2,1,3-benzoxadiazole (NBD-PZ/NBD, Figure S29-S31) or the commercially available primary amine dye dansyl cadaverine (Figure S32). Both fluorescent dyes demonstrated successful amidation of the anhydride system, although only the secondary amine containing NBD-PZ revealed an acidic release of the conjugated dye characterized by ^{1}H NMR spectroscopy measurements (Figure 4C).

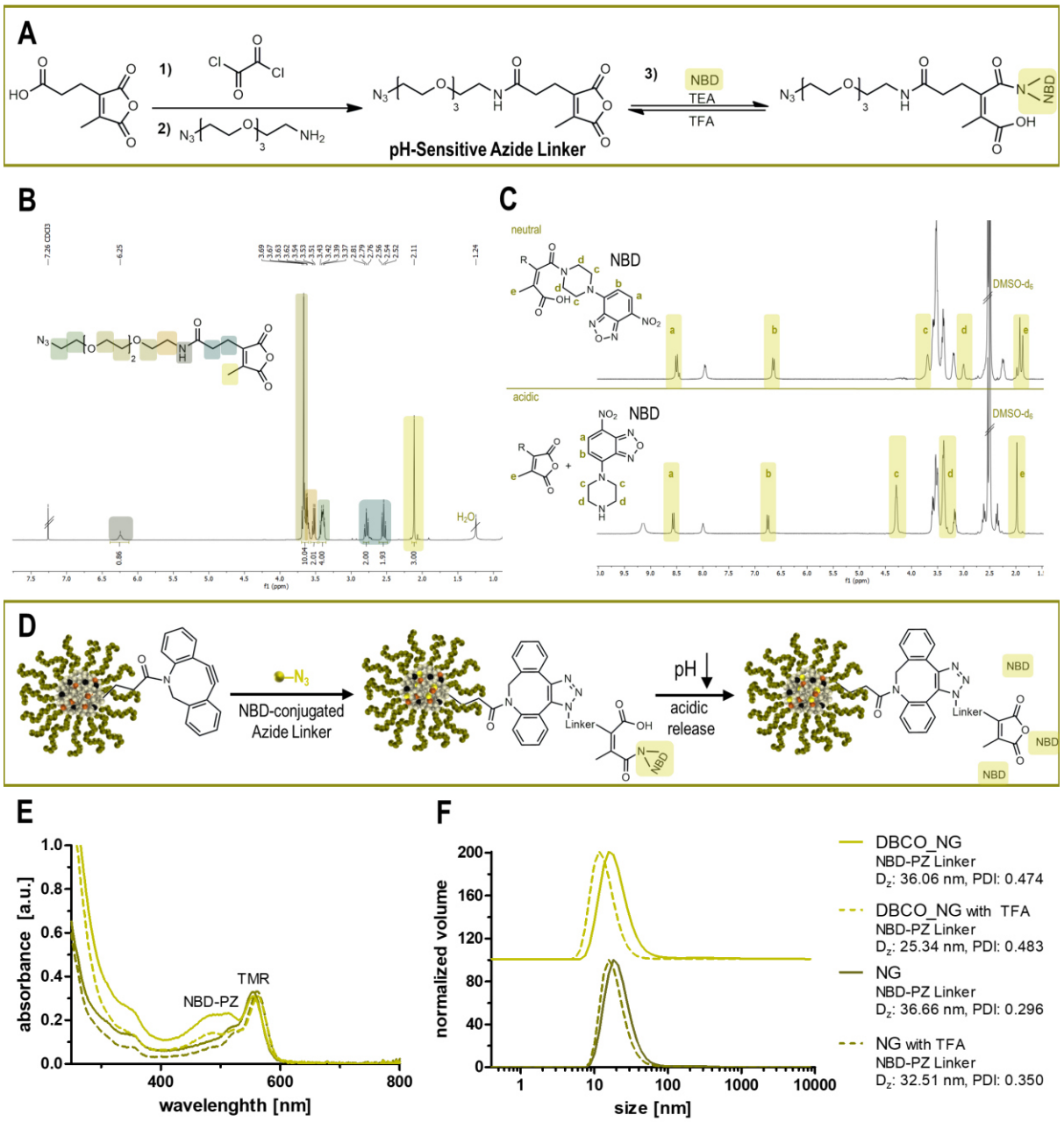

Figure 4. Synthesis of a bifunctional linker, accessible for pH-reversible conjugation of secondary amines and azide click reaction to DBCO core-functionalized nanogels. (**A**) Synthesis route for the fabrication of a pH-sensitive linker based on 2-propionic-3-methylmaleic anhydride with additional azide functionality, followed by pH-reversible dye-labeling with the fluorescent dye NBD-PZ/NBD. (**B**) ^{1}H NMR spectrum of the pH-sensitive azide linker recorded in $CDCl_3$. (**C**) ^{1}H NMR spectra of the NBD-conjugated azide linker under neutral conditions and upon acidification showing the reversible conjugation and release of the fluorescent dye 4-nitro-7-piperazino-2,1,3-benzoxadiazole (NBD), in particular by the two asymmetric regioisomer signals of the α-methyl signal e that re-form again into one single sharp peak e upon acid-triggered anhydride formation. (**D**) Synthetic concept for the formation of pH-reversible NBD-labeled DBCO nanogels by reaction with the dye-conjugated azide linker. (**E**) UV-Vis spectroscopy measurements of the DBCO nanogel reacted with the NBD-labeled azide linker under neutral and acidic conditions (light green) compared to control nanogels treated with the dye-labeled linker (dark green). DBCO nanogels undergo a successful conjugation with the NBD-labeled linker (absorbance maximum at 480 nm) and release NBD after treatment with trifluoroacetic acid (TFA), while control nanogels remain unlabeled. (**F**) DLS measurement of the DBCO nanogels (light green) and control nanogels (dark green) that reacted with the dye-labeled linker as well as after treatment with TFA.

Interestingly, secondary amines led to the formation of two asymmetric regioisomers and, consequently, the α-methyl signal of the *cis*-oriented double bond splits into two sharp signals (Figure 4C, Signal e, neutral – and MALDI ToF MS measurements, Figure S33). Followed acidification with trifluoroacetic acid (TFA) forced the reformation of the disubstituted maleic anhydride structure by generation of one sharp α-methyl signal and the release of NBD-PZ (Figure 4C, Signal e, acidic). Contrarily, the reaction with the primary amine dye dansyl cadaverine showed the formation of a pH-resistant imide structure, as confirmed both by ^{1}H NMR (affording one sharp α-methyl signal after amidation, Figure S34) as well as ESI-MS measurement (for the cyclized imide the molecular mass is reduced by 18 g/mol due to water elimination, Figure S35). These findings were again in agreement with our previous studies on polymeric maleic anhydrides also exhibiting an exclusive pH reversibility only upon reaction with secondary amines in DMSO.[43] Consequently, we focused our attention on the reversible conjugation of secondary amine-functionalized dyes and drugs during the following nanogel experiments.

For the preparation of pH-reversibly dye-labeled DBCO nanogels, NBD-PZ-modified azide-functionalized maleic anhydride linkers were introduced to the core-localized DBCO units or added to the control nanogels (Figure 4D). To ensure the absence of unconjugated linkers, all samples were analogously purified by extensive spin-filtration (MWCO 10000 g/mol) with water supplemented with 0.1% ammonia. Based on the previous fluorescent labeling of the azide-functionalized maleic anhydride linker, the nanogel dye modification could again be confirmed by UV-Vis spectroscopy, showing a further absorbance maximum at 480 nm only for the DCBO nanogels compared to the control nanogels (Figure 4E). Additional treatment with TFA caused a successful release of conjugated NBD-PZ and removal during the following spin-filtration processes (Figure 4E). All nanogels exhibited almost identical particle sizes after the treatment with the dye-labeled linker and slightly decreased by treatment with TFA (Figure 4F). Thus, azide-containing 2-propionic-3-methylmaleic anhydride-based linkers represent ideal properties for pH-reversible conjugation of secondary amines and further modification of core-functionalized DBCO nanogels. Such pH-driven release scenarios may for instance become relevant with regards to intracellular endosomal drug delivery.

Formation of pH-Releasable Immunostimulatory DBCO Nanogels

After having demonstrated efficient functionalization of DBCO nanogels with azide-clickable linkers which further provide additional pH-sensitive release properties for conjugated secondary amines, we used our bifunctional linker system for reversible covalent drug loading

into our core-crosslinked nanoparticles. Potent small molecular activators of the Toll-like receptor 7 and 8 (TLR 7/8) demonstrate an attractive drug category for cancer immunotherapy. Already presented by us in several studies, conjugation of TLR 7/8 agonists promote their selective immune stimulation spatiotemporally while reducing unspecific side effects. Unfortunately, after conjugation to nano-sized carrier systems the immunodrug IMDQ often lacks its high nanomolar drug activity.[22,44,47,48,61,62] Therefore, we investigated the immune stimulatory profile of a pH-reversible IMDQ-loaded DBCO nanogel which would be able to release the conjugated drug under endolysosomal pH conditions by following the introduced bifunctional linker strategy (Figure 5A).

First, the imidazoquinoline-based TLR 7/8 agonist IMDQ was modified in a two-step reaction, generating a secondary amine (IMDQ-Me, Figure S40-S43) for pH-reversible conjugation to the azide-clickable linker system (Figure S44 and S45). Next, the linker-drug conjugate could be attached to the DBCO nanogels and compared to control nanogels with no DBCO-groups and, thus, unable for click reactions (Figure 5A). Prior to the first *in vitro* test, unbound linker-IMDQ-Me-conjugate was removed for all samples - in analogy to the previous experiments - by spin-filtration and the resulting drug load verified by UV-Vis spectroscopy. Thereby, only DBCO-functionalized nanogels revealed a successful conjugation with typical IMDQ-Me drug absorbances around 324 nm, corresponding to a drug loading of 3.1 wt% (Figure 5B and Figure S48).

To finally investigate the IMDQ-Me-mediated TLR7/8 activity, RAW-Dual macrophages' reporter function was employed. Engineered RAW-Dual macrophages enable the screening of different TLR activities, for example, by evaluating the expression of embryonic alkaline phosphatase in response to NF-κB activation. Thereby, secreted embryonic alkaline phosphatase (SEAP) can easily be detected by UV-Vis spectroscopy of the cell culture supernatant after applying the Quanti Blue Assay. Consequently, RAW-Dual macrophages were incubated with increasing concentrations of the IMDQ-Me-linker-conjugated DBCO nanogel or soluble IMDQ-Me. Additionally, different control nanogels such as the empty nanogels (DBCO NG and NG) as well as nanogel (NG) treated with the linker-drug conjugate were analyzed. Remarkably, both the IMDQ-Me-loaded DBCO nanogel and soluble IMDQ-Me provided a strong TLR activation at the same sub-micromolar concentration range, while all empty controls induced no TLR stimulation and remained immunologically silent (Figure 5D).

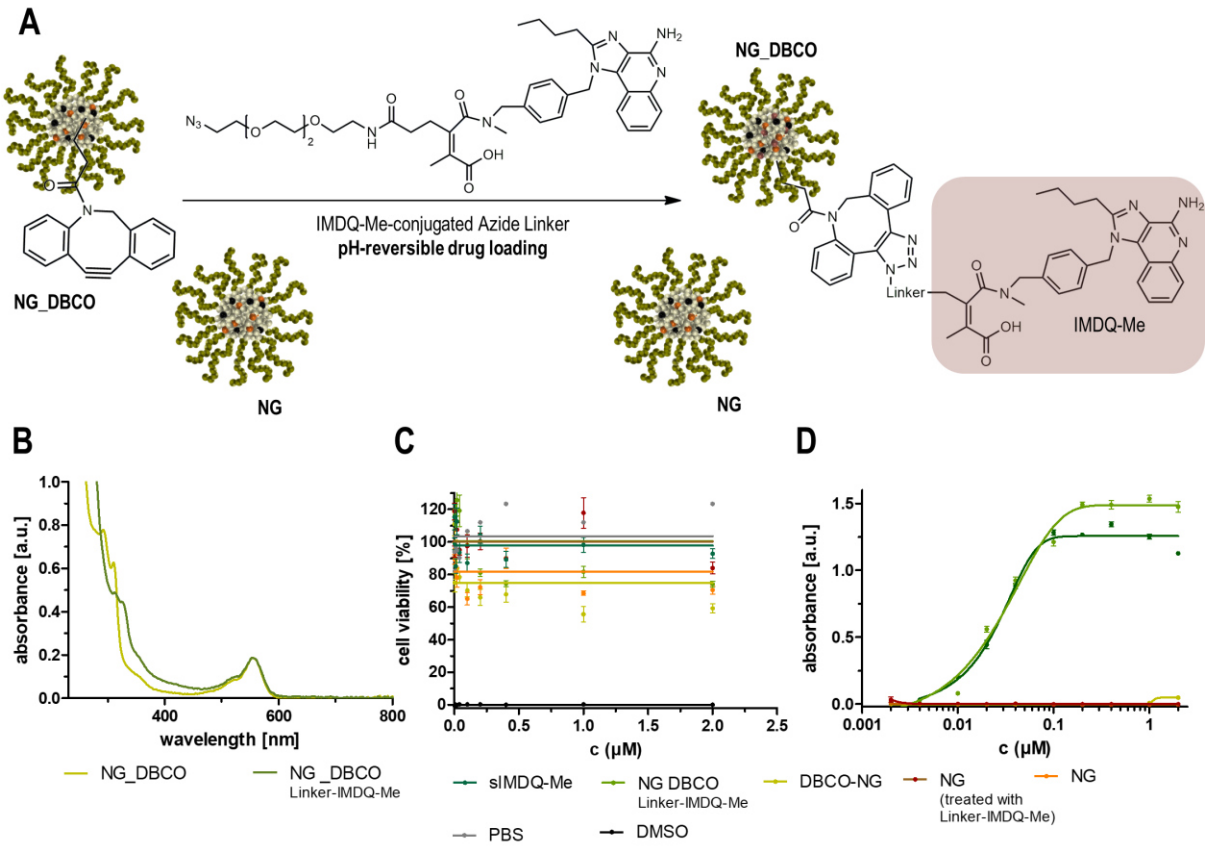

Figure 5. *In vitro* evaluation of TMR-labeled DBCO nanogels with pH-reversibly attached immune stimulatory TLR 7/8 agonist IMDQ-Me. (**A**) Reaction strategy for the synthesis of immunodrug-loaded DBCO nanogels by treatment with IMDQ-Me-conjugated azide linker compared to nanogels without DBCO. (**B**) UV-Vis spectroscopy analysis of the fluorescently labeled DBCO nanogel before (dark green) and after pH-sensitive drug loading (light green). (**C**) Cell viability of RAW-Dual macrophages incubated with the drug-loaded DBCO nanogel, soluble IMDQ-Me, different control nanogels, as well as PBS and DMSO, quantified by MTT assay (n=4). (**D**) TLR 7/8 receptor activation of soluble IMDQ-Me and the pH-reversibly IMDQ-Me-loaded DBCO nanogel compared to the empty DBCO nanogel and control nanogels determined by Quanti Blue assay (n=4).

The obtained results indicate for the first time similar TLR activation for a covalently bound agonist versus its soluble counterpart. This confirms successful acidic-triggered release of IMDQ-Me from the DBCO nanogel (presumably inside the endolysosomes) and, thus, explains its equal stimulatory effect to soluble IMDQ-Me. Additionally, RAW-Dual cell viability was quantified by a MTT Assay. Thereby, all tested samples demonstrated no significant toxicity in the studied concentration regime (Figure 5C).

Conclusions

Overall, we have successfully demonstrated the RAFT-based synthesis and formulation of a core-functionalized DBCO nanogel platform serving as a chemically diverse toolbox for (reversible) bioorthogonal attachment of targeting units or small immunostimulatory molecules. In a subsequent controlled RAFT polymerization, reactive ester block copolymers were synthesized and partially DBCO modified. Based on the self-assembly properties in DMSO, precursor micelles could be generated, followed by amidation of the reactive ester side chains into core-crosslinked, hydrophilic nanogels. Besides the bioorthogonally well-addressable DBCO groups localized in the core, their sterical accessibility for click reactants corresponds well to the view of a more porous structure we could recently gain for similar micelle-derived core-crosslinked and hydrophilized nanogels.[53] In the current study, we could practice this with azide-functionalized dyes that could successfully be covalently incorporated into the nanogel cores. Moreover, the nanocarriers' potential for specific attachment of azide-containing bioactive groups was further demonstrated by the conjugation of a clickable trimannose as targeting unit for mannose-decorated immune cells, such as TAMs. First *in vitro* experiments demonstrated the selective delivery into MMR^+ CHO cells and, thus, encouraged the development of further pH-releasable drug delivery systems. By the synthesis of an azide-containing 2-propionic-3-methylmaleic anhydride-based linker we afforded a bifunctional linker with the ability for pH-reversible conjugation of secondary amines in polar aprotic solvents, such as DMSO, and further DBCO click reaction to the nanogels. Subsequently, secondary amine-modified IMDQ-Me, a highly potent TLR 7/8 agonist, was conjugated to the linker and then attached to the DBCO nanogels. Remarkably, the pH-sensitive drug-loading resulted in strong TLR 7/8 receptor stimulations *in vitro* that were of equal activity as the soluble drug itself. These finding underline the efficacy of the core-functionalized DBCO nanogels as a carrier platform for specific targeting of immune cells and the pH-reversible endosomal delivery potential for small immune modulators. Consequently, the development of these nanogels may pave the way for novel multifunctional carrier systems for therapeutic applications in cancer immunotherapy.

Author Contributions

The manuscript was written through contributions of all authors. All authors have given approval to the final version of the manuscript.

Notes

The authors declare no conflict of interest.

Acknowledgements

The authors' work was gratefully supported by the DFG through the Emmy Noether program and the CRC/SFB 1066 projects B03 and B04 (both to L.N.). Moreover, support by the BMBF Clusters4Futer curATime (projects curAIntervent and megATarget, both to L.N.) is kindly acknowledged. Manfred Wagner, Stefan Spang, Stephan Türk, Jutta Schnee and Detlev-Walter Scholdei are gratefully acknowledged for technical assistance during the analytical measurements. Moreover, we would like to thank Tanja Weil for providing access to excellent laboratory facilities.

References

(1) Cabral, H.; Miyata, K.; Osada, K.; Kataoka, K. Block Copolymer Micelles in Nanomedicine Applications. *Chem. Rev.* **2018**, *118* (14), 6844–6892.

(2) Sur, S.; Rathore, A.; Dave, V.; Reddy, K. R.; Chouhan, R. S.; Sadhu, V. Recent Developments in Functionalized Polymer Nanoparticles for Efficient Drug Delivery System. *Nano-Structures and Nano-Objects* **2019**, *20*, 100397.

(3) Kumari, A.; Yadav, S. K.; Yadav, S. C. Biodegradable Polymeric Nanoparticles Based Drug Delivery Systems. *Colloids Surfaces B Biointerfaces* **2010**, *75* (1), 1–18.

(4) Talelli, M.; Barz, M.; Rijcken, C. J. F.; Kiessling, F.; Hennink, W. E.; Lammers, T. Core-Crosslinked Polymeric Micelles: Principles, Preparation, Biomedical Applications and Clinical Translation. *Nano Today* **2015**, *10* (1), 93–117.

(5) Shi, Y.; van der Meel, R.; Chen, X.; Lammers, T. The EPR Effect and beyond: Strategies to Improve Tumor Targeting and Cancer Nanomedicine Treatment Efficacy. *Theranostics* **2020**, *10* (17), 7921–7924.

(6) Attia, M. F.; Anton, N.; Wallyn, J.; Omran, Z.; Vandamme, T. F. An Overview of Active and Passive Targeting Strategies to Improve the Nanocarriers Efficiency to Tumour Sites. *J. Pharm. Pharmacol.* **2019**, *71* (8), 1185–1198.

(7) Pearce, A. K.; O'Reilly, R. K. Insights into Active Targeting of Nanoparticles in Drug Delivery: Advances in Clinical Studies and Design Considerations for Cancer Nanomedicine. *Bioconjug. Chem.* **2019**, *30* (9), 2300–2311.

(8) Gros, L.; Ringsdorf, H. Polymeric Antitumour Agents on a Molecular and on a Cellular Level? *Polym. Sci. Technol.* **1983**, *23*, 23–32.

(9) Ringsdorf, H. Structure and Properties of Pharmacologically Active Polymers. *J Polym Sci Polym Symp* **1975**, *153* (51), 135–153.

(10) Scherger, M.; Bolli, E.; Antunes, A. R. P.; Arnouk, S.; Stickdorn, J.; Van Driessche, A.; Schild, H.; Grabbe, S.; De Geest, B. G.; Van Ginderachter, J. A.; Nuhn, L. Transient Multivalent Nanobody Targeting to CD206-Expressing Cells via PH-Degradable Nanogels. *Cells* **2020**, *9* (10).

(11) Bolli, E.; Scherger, M.; Arnouk, S. M.; Pombo Antunes, A. R.; Straßburger, D.; Urschbach, M.; Stickdorn, J.; De Vlaminck, K.; Movahedi, K.; Räder, H. J.; Hernot, S.; Besenius, P.; Van Ginderachter, J. A.; Nuhn, L. Targeted Repolarization of Tumor-Associated Macrophages via Imidazoquinoline-Linked Nanobodies. *Adv. Sci.* **2021**, *8* (10), 1–12.

(12) Kawakami, S.; Hashida, M. Glycosylation-Mediated Targeting of Carriers. *J. Control. Release* **2014**, *190*, 542–555.

(13) Irache, J. M.; Salman, H. H.; Gamazo, C.; Espuelas, S. Mannose-Targeted Systems for the Delivery of Therapeutics. *Expert Opin. Drug Deliv.* **2008**, *5* (6), 703–724.

(14) Nuhn, L.; Bolli, E.; Massa, S.; Vandenberghe, I.; Movahedi, K.; Devreese, B.; Van Ginderachter, J. A.; De Geest, B. G. Targeting Protumoral Tumor-Associated Macrophages with Nanobody-Functionalized Nanogels through Strain Promoted Azide Alkyne Cycloaddition Ligation. *Bioconjug. Chem.* **2018**, *29* (7), 2394–2405.

(15) Ruffell, B.; Coussens, L. M. Macrophages and Therapeutic Resistance in Cancer. *Cancer Cell* **2015**, *27* (4), 462–472.

(16) Duan, Z.; Luo, Y. Targeting Macrophages in Cancer Immunotherapy. *Signal Transduct. Target. Ther.* **2021**, *6* (1), 1–21.

(17) Mantovani, A.; Marchesi, F.; Malesci, A.; Laghi, L.; Allavena, P. Tumor-Associated Macrophages as Treatment Targets in Oncology. *Nat Rev Clin Oncol* **2017**, *14* (7), 399–416.

(18) Blanazs, A.; Armes, S. P.; Ryan, A. J. Self-Assembled Block Copolymer Aggregates: From Micelles to Vesicles and Their Biological Applications. *Macromol. Rapid Commun.* **2009**, *30* (4–5), 267–277.

(19) Kockelmann, J.; Zentel, R.; Nuhn, L. Post-Polymerization Modifications to Prepare Biomedical Nanocarriers with Varying Internal Structures, Their Properties and Impact on Protein Corona Formation. *Macromol. Chem. Phys.* **2023**, *2300199*, 1–15.

(20) Leber, N.; Nuhn, L.; Zentel, R. Cationic Nanohydrogel Particles for Therapeutic Oligonucleotide Delivery. *Macromol. Biosci.* **2017**, *17* (10), 1–15.

(21) Nuhn, L.; Hirsch, M.; Krieg, B.; Koynov, K.; Fischer, K.; Schmidt, M.; Helm, M.; Zentel, R. Cationic Nanohydrogel Particles as Potential SiRNA Carriers for Cellular Delivery. *ACS Nano* **2012**, *6* (3), 2198–2214.

(22) Stickdorn, J.; Nuhn, L. Reactive-Ester Derived Polymer Nanogels for Cancer Immunotherapy. *Eur. Polym. J.* **2020**, *124* (September 2019), 109481.

(23) Nuhn, L.; De Koker, S.; Van Lint, S.; Zhong, Z.; Catani, J. P.; Combes, F.; Deswarte, K.; Li, Y.; Lambrecht, B. N.; Lienenklaus, S.; Sanders, N. N.; David, S. A.; Tavernier, J.; De Geest, B. G. Nanoparticle-Conjugate TLR7/8 Agonist Localized Immunotherapy Provokes Safe Antitumoral Responses. *Adv. Mater.* **2018**, *30* (45), 1–9.

(24) Nuhn, L.; Vanparijs, N.; De Beuckelaer, A.; Lybaert, L.; Verstraete, G.; Deswarte, K.; Lienenklaus, S.; Shukla, N. M.; Salyer, A. C. D.; Lambrecht, B. N.; Grooten, J.; David, S. A.; De Koker, S.; De Geest, B. G. PH-Degradable Imidazoquinoline-Ligated Nanogels for Lymph Node-Focused Immune Activation. *Proc. Natl. Acad. Sci. U. S. A.* **2016**, *113* (29), 8098–8103.

(25) Stickdorn, J.; Stein, L.; Arnold-Schild, D.; Hahlbrock, J.; Medina-Montano, C.; Bartneck, J.; Ziß, T.; Montermann, E.; Kappel, C.; Hobernik, D.; Haist, M.; Yurugi, H.; Raabe, M.; Best, A.; Rajalingam, K.; Radsak, M. P.; David, S. A.; Koynov, K.; Bros, M.; Grabbe, S.; Schild, H.; Nuhn, L. Systemically Administered TLR7/8 Agonist and Antigen-Conjugated Nanogels Govern Immune Responses against Tumors. *ACS Nano* **2022**, *16* (3), 4426–4443.

(26) Stickdorn, J.; Czysch, C.; Medina-Montano, C.; Stein, L.; Xu, L.; Scherger, M.; Schild, H.; Grabbe, S.; Nuhn, L. Peptide-Decorated Degradable Polycarbonate Nanogels for Eliciting Antigen-Specific Immune Responses. *Int. J. Mol. Sci.* **2023**, *24* (20).

(27) D. Hein, Christopher. Liu, Xin-Ming. Wang, D. Click Chemistry, a Powerful Tool for Pharmaceutical Sciences. *Natl. Inst. Heal. J.* **2008**, *25* (10), 1–7.

(28) Kolb, H. C.; Finn, M. G.; Sharpless, K. B. Click Chemistry: Diverse Chemical Function from a Few Good Reactions. *Angew. Chemie - Int. Ed.* **2001**, *40* (11), 2004–2021.

(29) Scinto, S. L.; Bilodeau, D. A.; Hincapie, R.; Lee, W.; Nguyen, S. S.; Xu, M.; am Ende, C. W.; Finn, M. G.; Lang, K.; Lin, Q.; Pezacki, J. P.; Prescher, J. A.; Robillard, M. S.; Fox, J. M. Bioorthogonal Chemistry. *Nat. Rev. Methods Prim.* **2021**, *1* (1).

(30) Bird, R. E.; Lemmel, S. A.; Yu, X.; Zhou, Q. A. Bioorthogonal Chemistry and Its Applications. *Bioconjug. Chem.* **2021**, *32* (12), 2457–2479.

(31) Agard, N. J.; Prescher, J. A.; Bertozzi, C. R. A Strain-Promoted [3 + 2] Azide-Alkyne Cycloaddition for Covalent Modification of Biomolecules in Living Systems. *J. Am. Chem. Soc.* **2004**, *126* (46), 15046–15047.

(32) Schattling, P.; Jochum, F. D.; Theato, P. Multi-Stimuli Responsive Polymers-the All-in-One Talents. *Polym. Chem.* **2014**, *5* (1), 25–36.

(33) Tong, R.; Tang, L.; Ma, L.; Tu, C.; Baumgartner, R.; Cheng, J. Smart Chemistry in Polymeric Nanomedicine. *Chem. Soc. Rev.* **2014**, *43* (20), 6982–7012.

(34) Fleige, E.; Quadir, M. A.; Haag, R. Stimuli-Responsive Polymeric Nanocarriers for the Controlled Transport of Active Compounds: Concepts and Applications. *Adv. Drug Deliv. Rev.* **2012**, *64* (9), 866–884.

(35) Van Driessche, A.; Kocere, A.; Everaert, H.; Nuhn, L.; Van Herck, S.; Griffiths, G.; Fenaroli, F.; De Geest, B. G. PH-Sensitive Hydrazone-Linked Doxorubicin Nanogels via Polymeric-Activated Ester Scaffolds: Synthesis, Assembly, and in Vitro and in Vivo Evaluation in Tumor-Bearing Zebrafish. *Chem. Mater.* **2018**, *30* (23), 8587–8596.

(36) Du, J. Z.; Li, H. J.; Wang, J. Tumor-Acidity-Cleavable Maleic Acid Amide (TACMAA): A Powerful Tool for Designing Smart Nanoparticles to Overcome Delivery Barriers in Cancer Nanomedicine. *Acc. Chem. Res.* **2018**, *51* (11), 2848–2856.

(37) Kanamala, M.; Wilson, W. R.; Yang, M.; Palmer, B. D.; Wu, Z. Mechanisms and Biomaterials in PH-Responsive Tumour Targeted Drug Delivery: A Review. *Biomaterials* **2016**, *85*, 152–167.

(38) Spanedda, M. V.; Bourel-Bonnet, L. Cyclic Anhydrides as Powerful Tools for Bioconjugation and Smart Delivery. *Bioconjug. Chem.* **2021**, *32* (3), 482–496.

(39) Zhang, X.; Zhang, K.; Haag, R. Multi-Stage, Charge Conversional, Stimuli-Responsive Nanogels for Therapeutic Protein Delivery. *Biomater. Sci.* **2015**, *3* (11), 1487–1496.

(40) Zhang, A.; Yao, L.; An, M. Reversing the Undesirable PH-Profile of Doxorubicin: Via Activation of a Di-Substituted Maleamic Acid Prodrug at Tumor Acidity. *Chem. Commun.* **2017**, *53* (95), 12826–12829.

(41) Su, S.; Du, F. S.; Li, Z. C. Synthesis and PH-Dependent Hydrolysis Profiles of Mono- and Dialkyl Substituted Maleamic Acids. *Org. Biomol. Chem.* **2017**, *15* (39), 8384–8392.

(42) Song, Y.; Jung, D.; Kang, S.; Lee, Y. Amine-Selective Affinity Resins Based on PH-Sensitive Reversible Formation of Covalent Bonds. *Soft Matter* **2017**, *13* (12), 2295–2298.

(43) Heck, A. G.; Stickdorn, J.; Rosenberger, L. J.; Scherger, M.; Woller, J.; Eigen, K.; Bros, M.; Grabbe, S.; Nuhn, L. Polymerizable 2-Propionic-3-Methylmaleic Anhydrides as a Macromolecular Carrier Platform for PH-Responsive Immunodrug Delivery. *J. Am. Chem. Soc.* **2023**, *145* (50), 27424–27436.

(44) Van Herck, S.; De Geest, B. G. Nanomedicine-Mediated Alteration of the Pharmacokinetic Profile of Small Molecule Cancer Immunotherapeutics. *Acta Pharmacol. Sin.* **2020**, *41* (7), 881–894.

(45) Lybaert, L.; Vermaelen, K.; De Geest, B. G.; Nuhn, L. Immunoengineering through Cancer Vaccines – A Personalized and Multi-Step Vaccine Approach towards Precise Cancer Immunity. *J. Control. Release* **2018**, *289*, 125–145.

(46) Kockelmann, J.; Stickdorn, J.; Kasmi, S.; De Vrieze, J.; Pieszka, M.; Ng, D. Y. W.; David, S. A.; De Geest, B. G.; Nuhn, L. Control over Imidazoquinoline Immune Stimulation by PH-Degradable Poly(Norbornene) Nanogels. *Biomacromolecules* **2020**, *21* (6), 2246–2257.

(47) Czysch, C.; Medina-Montano, C.; Zhong, Z.; Fuchs, A.; Stickdorn, J.; Winterwerber, P.; Schmitt, S.; Deswarte, K.; Raabe, M.; Scherger, M.; Combes, F.; De Vrieze, J.; Kasmi, S.; Sandners, N. N.; Lienenklaus, S.; Koynov, K.; Räder, H. J.; Lambrecht, B. N.; David, S. A.; Bros, M.; Schild, H.; Grabbe, S.; De Geest, B. G.; Nuhn, L. Transient Lymph Node Immune Activation by Hydrolysable Polycarbonate Nanogels. *Adv. Funct. Mater.* **2022**, *32* (35), 2203490.

(48) Huppertsberg, A.; Kaps, L.; Zhong, Z.; Schmitt, S.; Stickdorn, J.; Deswarte, K.; Combes, F.; Czysch, C.; De Vrieze, J.; Kasmi, S.; Choteschovsky, N.; Klefenz, A.; Medina-Montano, C.; Winterwerber, P.; Chen, C.; Bros, M.; Lienenklaus, S.; Sanders, N. N.; Koynov, K.; Schuppan, D.; Lambrecht, B. N.; David, S. A.; De Geest, B. G.; Nuhn, L. Squaric Ester-Based, PH-Degradable Nanogels: Modular Nanocarriers for Safe, Systemic Administration of Toll-like Receptor 7/8 Agonistic Immune Modulators. *J. Am. Chem. Soc.* **2021**, *143* (26), 9872–9883.

(49) Eberhardt, M.; Mruk, R.; Zentel, R.; Théato, P. Synthesis of Pentafluorophenyl(Meth)Acrylate Polymers: New Precursor Polymers for the Synthesis of Multifunctional Materials. *Eur. Polym. J.* **2005**, *41* (7), 1569–1575.

(50) Gibson, M. I.; Froehlich, E.; Klok, H.-A. Postpolymerization Modification of Poly(Pentafluorophenylmethacrylate): Synthesis of a Divers Water-Soluble Polymer Library. *J. Polym. Sci. Part A Polym. Chem.* **2009**, *47*, 4332–4345.

(51) Mohr, N.; Barz, M.; Forst, R.; Zentel, R. A Deeper Insight into the Postpolymerization Modification of Polypenta Fluorophenyl Methacrylates to Poly(N-(2-Hydroxypropyl) Methacrylamide). *Macromol. Rapid Commun.* **2014**, *35* (17), 1522–1527.

(52) Das, A.; Theato, P. Activated Ester Containing Polymers: Opportunities and Challenges for the Design of Functional Macromolecules. *Chem. Rev.* **2016**, *116* (3), 1434–1495.

(53) Huppertsberg, A.; Leps, C.; Alberg, I.; Rosenauer, C.; Morsbach, S.; Landfester, K.; Tenzer, S.; Zentel, R.; Nuhn, L. Squaric Ester-Based Nanogels Induce No Distinct Protein Corona but Entrap Plasma Proteins into Their Porous Hydrogel Network. *Macromol. Rapid Commun.* **2022**, *43* (19), 1–9.

(54) Leber, N.; Kaps, L.; Yang, A.; Aslam, M.; Giardino, M.; Klefenz, A.; Choteschovsky, N.; Rosigkeit, S.; Mostafa, A.; Nuhn, L.; Schuppan, D.; Zentel, R. α-Mannosyl-Functionalized Cationic Nanohydrogel Particles for Targeted Gene Knockdown in Immunosuppressive Macrophages. *Macromol. Biosci.* **2019**, *19* (7), 1–12.

(55) Kaps, L.; Leber, N.; Klefenz, A.; Choteschovsky, N.; Zentel, R.; Nuhn, L.; Schuppan, D. In Vivo SiRNA Delivery to Immunosuppressive Liver Macrophages by α-Mannosyl-Functionalized Cationic Nanohydrogel Particles. *Cells* **2020**, *9* (8).

(56) De Coen, R.; Vanparijs, N.; Risseeuw, M. D. P.; Lybaert, L.; Louage, B.; De Koker, S.; Kumar, V.; Grooten, J.; Taylor, L.; Ayres, N.; Van Calenbergh, S.; Nuhn, L.; De Geest, B. G. PH-Degradable Mannosylated Nanogels for Dendritic Cell Targeting. *Biomacromolecules* **2016**, *17* (7), 2479–2488.

(57) De Coen, R.; Nuhn, L.; De Geest, B. G. Engineering Mannosylated Nanogels with Membrane-Disrupting Properties. *Polym. Chem.* **2019**, *10* (31), 4297–4304.

(58) Wagener, K.; Bros, M.; Krumb, M.; Langhanki, J.; Pektor, S.; Worm, M.; Schinnerer, M.; Montermann, E.; Miederer, M.; Frey, H.; Opatz, T.; Rösch, F. Targeting of Immune Cells with Trimannosylated Liposomes. *Adv. Ther.* **2020**, *3* (6), 1–10.

(59) Krumb, M.; Frey, M. L.; Langhanki, J.; Forster, R.; Kowalczyk, D.; Mailänder, V.; Landfester, K.; Opatz, T. Multivalency Beats Complexity: A Study on the Cell Uptake of Carbohydrate Functionalized Nanocarriers to Dendritic Cells. *Cells* **2020**, *9* (9).

(60) Maier, K.; Wagner, E. Acid-Labile Traceless Click Linker for Protein Transduction. *J. Am. Chem. Soc.* **2012**, *134* (24), 10169–10173.

(61) Lynn, G. M.; Laga, R.; Jewell, C. M. Induction of Anti-Cancer T Cell Immunity by in Situ Vaccination Using Systemically Administered Nanomedicines. *Cancer Lett.* **2019**, *459* (January), 192–203.

(62) Shields, C. W.; Wang, L. L. W.; Evans, M. A.; Mitragotri, S. Materials for Immunotherapy. *Adv. Mater.* **2020**, *32* (13), 1–56.

INTRODUCING TARGETING UNITS OR PH-RELEASABLE IMMUNODRUGS INTO CORE-CLICKABLE NANOGELS

-Supporting Information-

Alina G. Heck[1], David Schwiertz[2], Bellinda Lantzberg[1], Ha-Chi Nguyen[1], Robert Forster[3], Maximilian Scherger[1], Till Opatz[3], Jo A. Van Ginderachter[4], and Lutz Nuhn[1,5]*

1: Max Planck Institute for Polymer Research, 55128 Mainz, Germany

2: Biotherapeutics Division, Leiden Academic Centre for Drug Research (LACDR), Leiden University, 2333CC Leiden, The Netherlands

3: Johannes Gutenberg-University Mainz, Department of Chemistry, 55128 Mainz, Germany

4: Brussels Center for Immunology, Vrije Universiteit Brussel, 1050 Brussels, Belgium
Myeloid Cell Immunology Lab, VIB Center for Inflammation Research, 1050 Brussels, Belgium

5: Chair of Macromolecular Chemistry, Julius-Maximilians-Universität Würzburg, 97070 Würzburg, Germany

*: corresponding author: Prof. Dr. Lutz Nuhn (E-mail: lutz.nuhn@uni-wuerzburg.de)

Materials and Methods

All reagents and solvents were purchased from Sigma Aldrich (Taufkirchen, Germany), TCI Chemicals (Tokyo, Japan) or Rapp Polymers (Tübingen, Germany) and used without further purification. Chloroform ($CHCl_3$), dichloromethane (DCM), dioxane, dimethyl sulfoxide (DMSO), *N,N*-dimethylformamide (DMF), ethyl acetate (EA), ethanol, tetrahydrofurane (THF) all deuterated solvents as well as benzylamine, dibenzylamine, triethylamine (TEA), pentafluorophenol and methacryloyl chloride were purchased from Sigma Aldrich. Prior to use dioxane and THF were dried over sodium. Oxalyl chloride, trifluoroacetic acid (TFA), Oregon Green 488 azide (OG488-azide) and Alexa Fluor 488 azide (AF488-azide) were purchased from Thermo Fisher Scientific (Waltham, MA, USA). Tetramethylrhodamine cadaverine (TMR) was bought from Biotium (Fermont, CA, USA). Dibenzylcyclooctyne-PEG_4-Amine (DBCO-PEG_4-Amine) was obtained from Jena Bioscience GmbH (Jena, Germany) and 11-Amino-1-azido-3,6,9-trioxaundecane was purchased from TCI Chemicals (Tokyo, Japan). Azobisisobutyronitrile (AIBN) was recrystallized from ethanol twice.

TLR7/8 agonist 1-(4-(aminomethyl)benzyl)-2-butyl-1*H*-imidazo[4,5-c]quinoline-4-amine (IMDQ) was kindly provided by Maximilian Scherger (Max Planck Institute for Polymer Research, Germany)[1–3] and the clickable trimannose azide (1-(11-azido-3,6,9-trioxaundec-1-yl)-1*H*-1,2,3-triazol-4-yl)-methyl 3,6-Di-*O*-(α-d-mannopyranosyl)-α-d-mannopyranosid was synthesized by Robert Forster (Johannes Gutenberg-University, Germany).[4,5]

Hexafluoroisopropanol (HFIP) was obtained from Fluorochem Ltd. (Hadfield, UK). Millipore (mp) water was prepared using a MILLI-Q® Reference A+ System. Water was used at a resistivity of 18.2 MΩ·cm and total organic caron of <5 ppm. For silica gel chromatography silica with particle size of 0.063-0.2 mm from Macherey-Nagel GmbH & Co. KG (Dueren, Germany) was used. Dialysis was performed with Spectra/Por7™ dialysis membranes with a molecular weight cut-off of 1000 g/mol obtained from Spectrum Labs (Schwerte, Germany).

Dulbecco's phosphate-buffered saline (PBS), cell culture medium and supplements were obtained from Thermo Fisher Scientific. RAW-Dual™ (IRF-Lucia/KI-[MIP-2]SEAP) murine macrophage reporter cell line and the QUANTI-Blue™ solution were obtained from InvivoGen (San Diego, CA, USA). RAW-Dual™ cells were cultured in Dulbecco's modified Eagle's medium DMEM, containing 10% fetal bovine serum, 1% penicillin/streptomycine, 0.02% normocine, and 0.01% zeocin at 37 °C with 5% CO_2 saturation.

Immortalized Chinese Hamster Ovary cells without the MMR/CD206 receptor (CHO^{MMR-}) were cultured in Dulbecco's modified Eagle's medium/Ham's F-12 nutrients (DMEM/F12 (1:1)) containing 10% fetal bovine serum, 1% penicillin/streptomycin, 2 mM L-glutamine and 1 mM sodium pyruvate at 37 °C with 5% CO_2 saturation. Genetically modified CHO^{MMR+} expressing the MMR/CD206 receptor were cultured in the same medium additionally supplemented with 0.06% geneticin (G418).

Instrumentation

Nuclear Magnetic Resonance (NMR) Spectroscopy

^{1}H, ^{13}C, ^{19}F and 2D NMR spectra were recorded on a Bruker Avance III 300 MHz, Bruker Avance III 400 MHz, Bruker Avance III 500 MHz or Bruker Avance III 700 MHz spectrometer at room temperature. The chemical shifts are reported in parts per million (ppm) relative to tetramethylsilane (TMS) All samples were dissolved in deuterated solvents and calibration of the spectra was achieved using the solvent signal. NMR spectra were analyzed using MestReNova 14.2.0 by Mestrelab Research.

Size Exclusion Chromatography (SEC)

Analytical SEC characterization was performed using HFIP as an eluant, supplemented with 3 g/L potassium trifluoroacetate, while the flow rate was set at 0.8 mL/min and 40 °C. The columns material was composed of modified silica gel (PFG columns, particle size 7 µM, porosity: 100 Å and 1000 Å), obtained from PSS Polymer Standards Service GmbH, Mainz, Germany. Poly(methyl methacrylate) (PMMA) standards were utilized for calibration, obtained from PSS, Mainz. The SECcurity^{2}instrument from PPS, Mainz was equipped with a SECcurtity^{2}isocratic pump, a degasser, an autosampler, a column thermostat, an UV and RI detector. Polymer samples were dissolved at 1mg/mL and filtered through GHP syringe filters (0.2 µm pore size, Acrodisc).

Additional SEC measurements with THF as eluent were carried out on an instrument consisting of a pump PU1580, an autosampler AS1555, UV and RI detector from JASCO and a column thermostat. The columns were packed with MZ-Gel SDpuls 10^{2} Å and MZ-Gel SDpuls 10^{6} Å purchased from MZ-Analysentechnik. Poly(methyl methacrylate) (PMMA) standard was used for calibration, purchased from PSS, Mainz and toluene was applied as internal standard. Polymer samples were dissolved at 1mg/mL, filtered through GHP syringe filters (0.2 µm pore size, Acrodisc) and recorded at a flow rate of 0.8 mL/min at 40 °C.

Dynamic Light Scattering (DLS)

Single-angle DLS measurements were performed on a Malvern Z Nano instrument endued with a He-Ne-Laser (λ = 632.8 nm) and by utilization of the ZetaSizer Software 7.12. Samples were recorded in triplicates at 25 °C and a detection angle of 173°. DLS data were processed analyzed by cumulant fitting for z-average mean diameter and PDI, or by CONTIN fitting method for intensity-, volume-, and number-weighted particle size distribution. Samples were dissolved at 0.1 mg/mL and filtrated through GHP syringe filters (0.2 µm pore size, Acrodisc).

Ultraviolet-Visible Spectroscopy (UV-Vis) and Fluorescence Spectroscopy

UV-Vis spectra were measured on a Thermo Scientific™ NanoDrop™ 2000c spectrophotometer with a Hellma Quartz Cuvette or with a Jasco V-630 spectrophotometer equipped with a JASCO ETC-717 peltier thermostatted cell holder. Measurements were carried out at 20 °C using a water thermostat (A. Knüss Optronic V50).

Fluorescence spectroscopy and absorbance read-out of RAW-blue and MTT assay were recorded on a Spark 20M Multimode Microplate Reader from Tecan Trading AG (Mannedorf, Switzerland).

Mass Spectrometry (ESI-MS and MALDI-ToF)

ESI mass spectra were carried out on an Agilent 6545 QTOF-MS (Santa Clara, CA, USA). All samples were dissolved in methanol at 0.1 mg/mL. Mass spectrometry data were processed and analyzed using the Advion Data Express software and mMass.

Matrix Assisted Laser Desorption Ionization-Time of Flight (MALDI-ToF) measurements were conducted on a rapifleX^{TM} MALDI-ToF/ToF mass spectrometer from Bruker Daltonik GmbH (Bremen, Germany). The instrument was fitted with a 10 kHz scanning smartbeam Nd:YAG laser at 355 nm wavelength and a 10 bit 5 GHz digitizer. Mass spectra were measured in a positive ion mode using DCTB (trans-2-[3-(4-tbutylphenyl)-2-methyl-2-propenylidene]-malononitrile) acid as a matrix. All Samples were prepared at 0.1 mg/mL and the resulting data were processed by mMass software.

Transmission Electron Microscopy (TEM)

TEM measurements were conducted on a FEI Tecnai G2 Spirit microscope equipped with a Gatan US1000 2k x 2k CCD camera an LaB_6 cathode operated at 120 kV. Images were measured on freshly glow discharged carbon copper grids (CF300-Cu, 300 mesh). 5 µL of a nanogel solution (c = 25 mg·L^{-1}, dissolved in Millipore water containing 0.1 % NH_3 was

transferred onto the TEM grid and removed with a filter paper after 1 minute. Afterwards, 5 µL uranyl acetate solution (2 wt% in ethanol) was added and removed after 15 s incubation time. All sample-deposited grids were air-dried overnight. Transmission electron microscopy data were processed using ImageJ 1.52 software (National Institutes of Health, USA).

Fluorescent Confocal Microscopy

Fluorescent confocal laser scanning microscopy images were performed on a STELLARIS 8 Leica DMi8 confocal microscope with a HC PL APO CS2 40x/1.25 GLYC oil immersion objective. Images were analyzed using Leica Application Suite X 3.7.4.23463 by Leica Microsystems and ImageJ 1.52 software (National Institutes of Health, USA).

Fluorescence-Activated Cell Scanning (FACS)

Flow cytometric analyses were measured on a BD Accuri C6 from BD Biosciences. Resulting data were processed using FloJo™_v10.8.1_CL by BD Biosciences.

Syntheses

Synthesis of the Monomer Pentafluorophenyl Methacrylate (PFPMA)

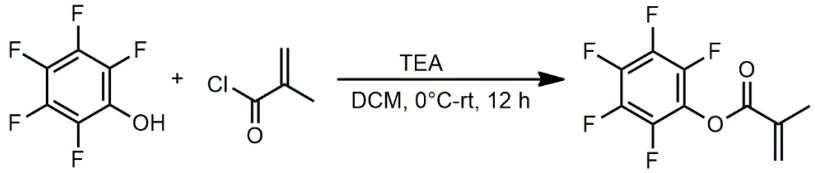

Figure S1: Synthesis of the monomer pentafluorophenyl methacrylate (PFPMA).

Pentafluorophenyl methacrylate (PFPMA) was synthesized according to the literature with minor modification.[6] In a three neck round bottom flask equipped with a dropping funnel and magnetic stir bar pentafluorophenol (20.0 g, 0.108 mol, 1 eq) was dissolved in anhydrous DCM (200 mL) under nitrogen atmosphere. The solution was cooled on an ice bath while triethylamine (TEA, 16.6 mL, 0.119 mol, 1.1 eq) was dropped to the solution, followed by the addition of methacryloyl chloride (10.1 mL, 0.119 mol, 1.1 eq) *via* dropping funnel. The reaction mixture was stirred for another 20 minutes at 0 °C and then allowed to react at room temperature for 12 h. Afterwards, the reaction mixture was washed with water (3x100 mL), dried over $MgSO_4$, filtrated, and concentrated *in vacuo*. The crude product was purified by subsequent vacuum distillation yielding pentafluorophenyl methacrylate as a colorless oil at 35 °C ($1x10^{-3}$ mbar) (14.20 g, 56%).

^{1}H NMR (400 MHz, $CDCl_3$): δ (ppm) = 6.45 (m, 1H, **a**), 5.91 (m, 1H, **b**), 2.08 (s, 1H, **c**).

^{19}F NMR (376 MHz, $CDCl_3$): δ (ppm) = -153.94 (d, J = 17.1 Hz, 2F, **a**), -159.33 (t, J = 21.7 Hz, 1F, **b**), -163.62 (m, 2F, **c**).

IR (ATR) ũ [cm^{-1}] = 2991 (w), 2936 (w), 1758 (s, υ, -C=O), 1638 (w), 1515 (s, δ, -C=C arom.), 1457 (m), 1438 (w), 1404 (w), 1381 (w), 1364 (s); 1326 (w), 1301 (m, υ, -C-O-C-), 1146 (m), 1086 (s, υ, -C-O-C-), 1046 (m), 992 (s, δ, =C-H), 951 (m), 933 (m), 858 (m, υ, -C-Hal), 801 (m, υ, -C-Hal).

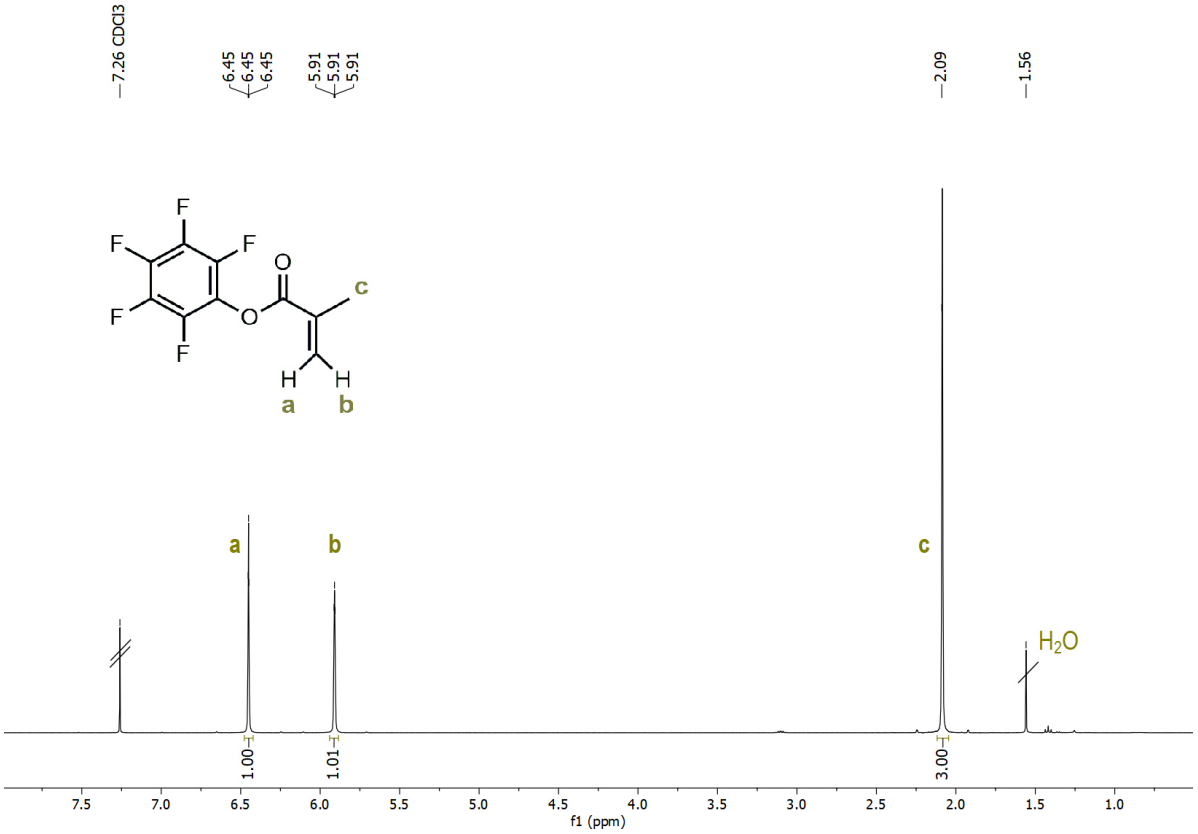

Figure S2: ^{1}H NMR spectrum (400 MHz) of the monomer pentafluorophenyl methacrylate (PFPMA) in $CDCl_3$.

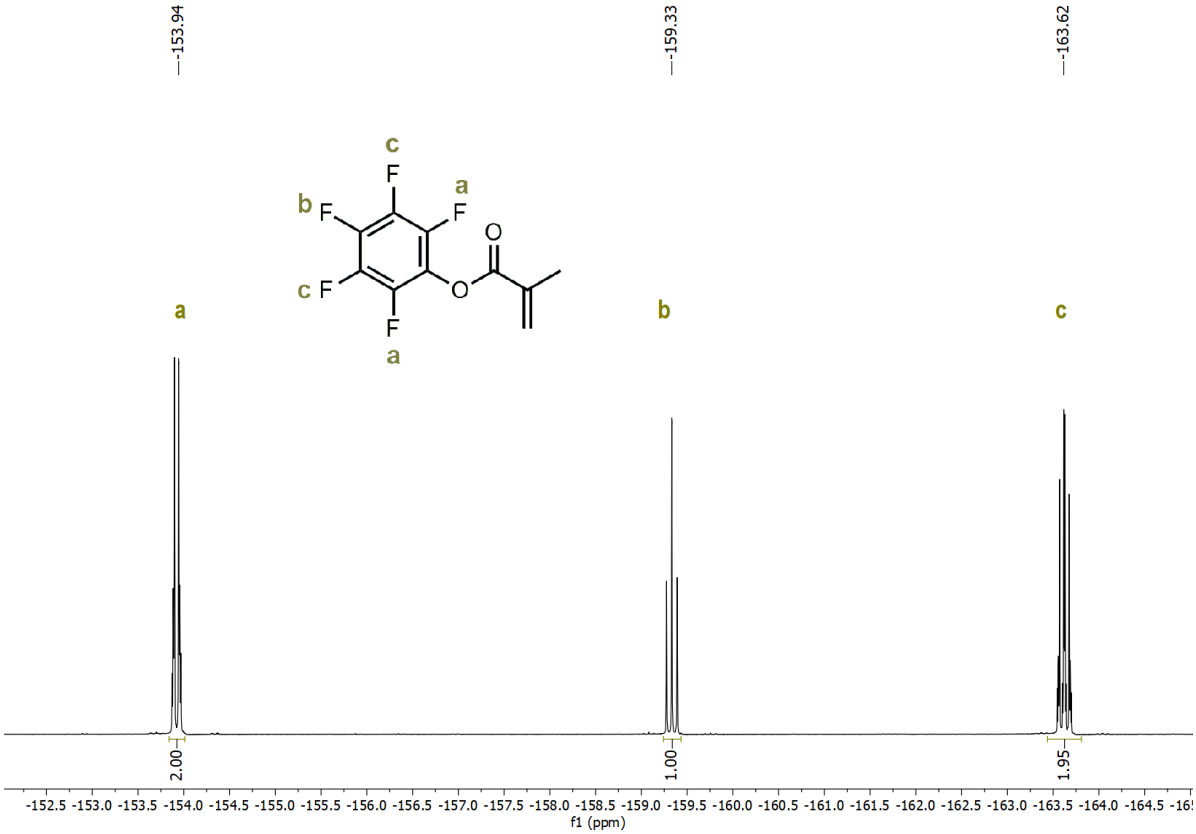

Figure S3: ^{19}F NMR spectrum (376 MHz) of the monomer pentafluorophenyl methacrylate (PFPMA) in $CDCl_3$.

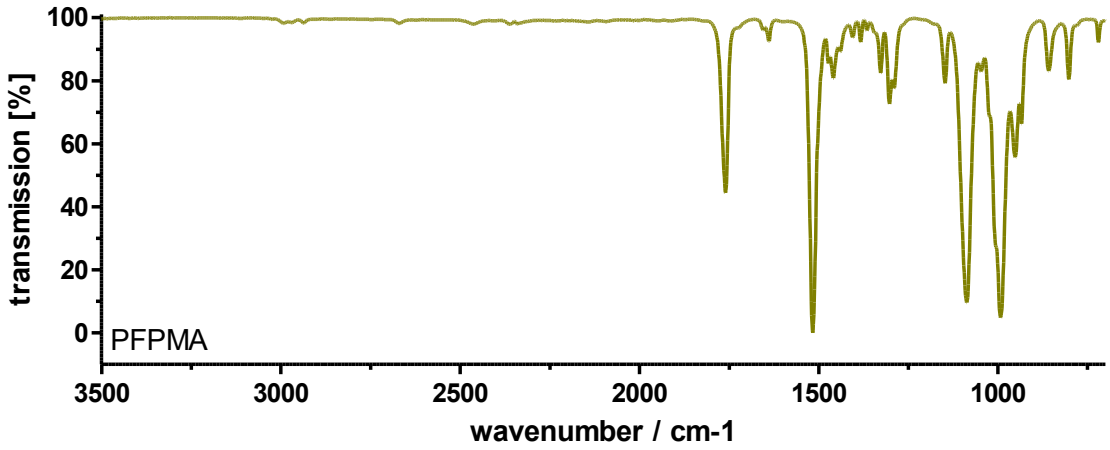

Figure S4: IR spectrum of the monomer PFPMA.

Polymerization Procedure

Synthesis of the Homopolymer p(mTEGMA)$_n$

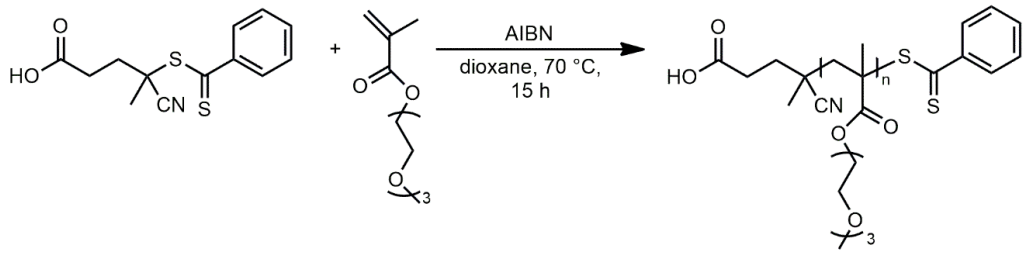

Figure S5: Synthesis of the homopolymer p(mTEGMA)$_n$ with AIBN in dioxane at 70 °C for 15 hours.

The homopolymer p(mTEGMA)$_n$ was synthesized *via* RAFT-polymerization according to the literature and modified.[7,8] 4-cyano-4-((phenylcarbonothioyl)thio)pentanoic acid (40.0 mg, 0.143 mmol, 1 eq) and AIBN (2.40 mg, 0.014 mmol, 0.1 eq) were weighed into a pre-dried Schlenk flask and dissolved in 2 mL anhydrous dioxane under argon atmosphere. Tri(ethylene glycol)methyl ether methacrylate (833 mg, 3.586 mmol, 20 eq) was added to the solution and the reaction mixture was degassed by three freeze-pump-thaw cycles. The solution was heated in an oil bath at 70 °C in its evacuated state. After a reaction time of 15 h, a reaction aliquot was characterized by ^{1}H NMR analysis indicating a conversion of 53%. The solution was cooled to room temperature and the homopolymer was purified by precipitation in an excess of cold hexane (-20 °C), centrifuged (4500 rpm, 10 min) and decanted. After redissolving the residue in ~ 2 mL dioxane the precipitation process was repeated three times. The product was dried under reduced pressure for 16 h. The homopolymer p(mTEGMA)$_{20}$ was isolated as a red oil (512 mg, 67%).

^{1}H NMR (400 MHz, $CDCl_3$): δ (ppm) = 7.98-7.30 08 (m, 5H, **a**), 4.08 (m, 2H, **b**), 3.70-3.60 (m, 8H, **c**), 3.56 (m, 2H, **d**), 3.38 (m, 3H, **e**), 2.05-1.65 (m, 2H, **f**), 1.53-0.74 (m, 3H, **g**).

SEC (THF) p(mTEGMA)$_{20}$: M_n = 2660 app (apparent molar mass), M_w = 3251 g/mol, Đ = 1.22

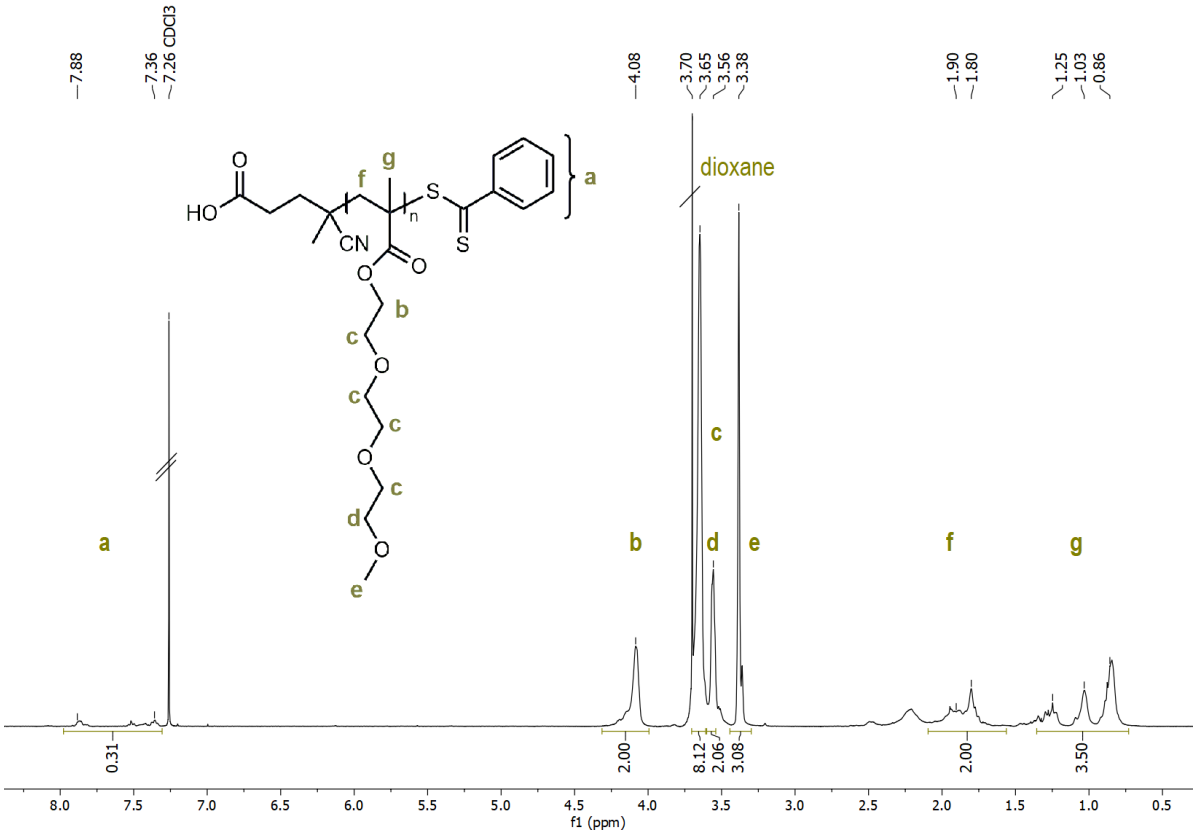

Figure S6: ^{1}H NMR spectrum (700 MHz) of the homopolymer p(mTEGMA)$_{20}$ in $CDCl_3$.

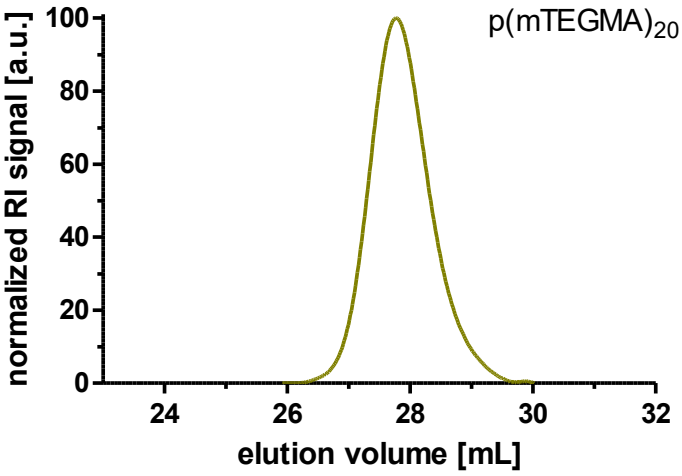

Figure S7: THF SEC trace of the homopolymer p(mTEGMA)$_{20}$.

Synthesis of the Block Copolymer p(mTEGMA)$_n$-*b*-p(PFPMA)$_m$

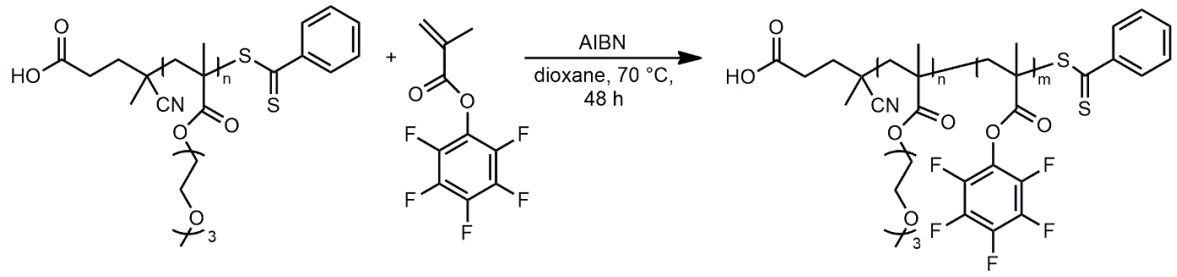

Figure S8: Synthesis of the block copolymer p(mTEGMA)$_n$-*b*-p(PFPMA)$_m$ with AIBN in dioxane at 70 °C for 48 hours.

The block copolymer p(mTEGMA)$_n$-*b*-p(PFPMA)$_m$ was synthesized *via* RAFT polymerization by an adapted literature protocol.[7,8] P(mTEGMA)$_{20}$ (500 mg, 0.125 mmol, 1 eq) and AIBN (2.05 mg, 0.013 mmol, 0.1 eq) were weighted into an oven dried Schlenk flask and dissolved in anhydrous dioxane (2 mL) under argon atmosphere. Then, pentafluorophenyl methacrylate (1.01 g, 4.0 mmol, 32 eq) was dropped to the solution, followed by three freeze-pump-thaw cycles. The reaction mixture was stirred for 48 h at 70 °C in the absence of oxygen and light. The solution was cooled to room temperature and the block copolymer was three times precipitated into cold hexane (-20 °C) and dried under reduced pressure for 16 h. The block copolymer p(mTEGMA)$_{20}$-*b*-p(PFPMA)$_{36}$ was isolated as red powder (1.41 g, quant.).

^{1}H NMR (400 MHz, $CDCl_3$): δ (ppm) = 8.02-7.28 (m, 5H, **a**), 4.09 (m, 2H, **b**), 3.72-3.59 (m, 8H, **c**), 3.56 (m, 2H, **d**), 3.38 (m, 3H, **e**), 2.61-2.31 (m, 2H, **f**), 2.01-1.46 (m, 2H, **g**), 1.53-1.31 (m, 3H, **h**), 1.10-0.72 (m, 3H, **i**).

^{19}F NMR (376 MHz, $CDCl_3$): δ (ppm) = -151.50-152.63 (m, 2F, **a**), -158.04 (m, 1F, **b**), -163.22 (m, 2F, **c**).

SEC (THF) p(mTEGMA)$_{20}$: M_n = 2660 app, M_w = 3251 g/mol, Đ = 1.22

SEC (THF) p(mTEGMA)$_{20}$-*b*-p(PFPMA)$_{36}$: M_n = 10941 app, M_w = 14028 g/mol, Đ = 1.28

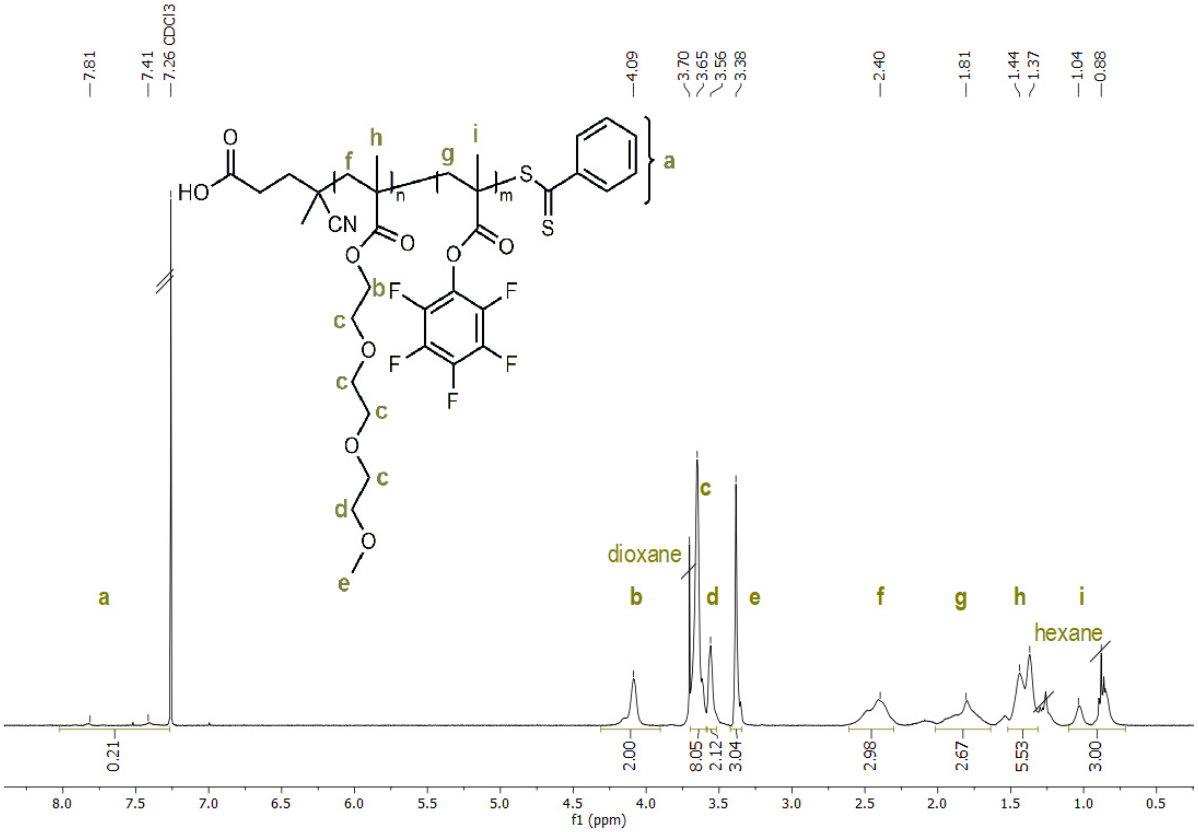

Figure S9: ^{1}H NMR spectrum (400 MHz) of the block copolymer p(mTEGMA)$_{20}$-*b*-p(PFPMA)$_{36}$ in $CDCl_3$.

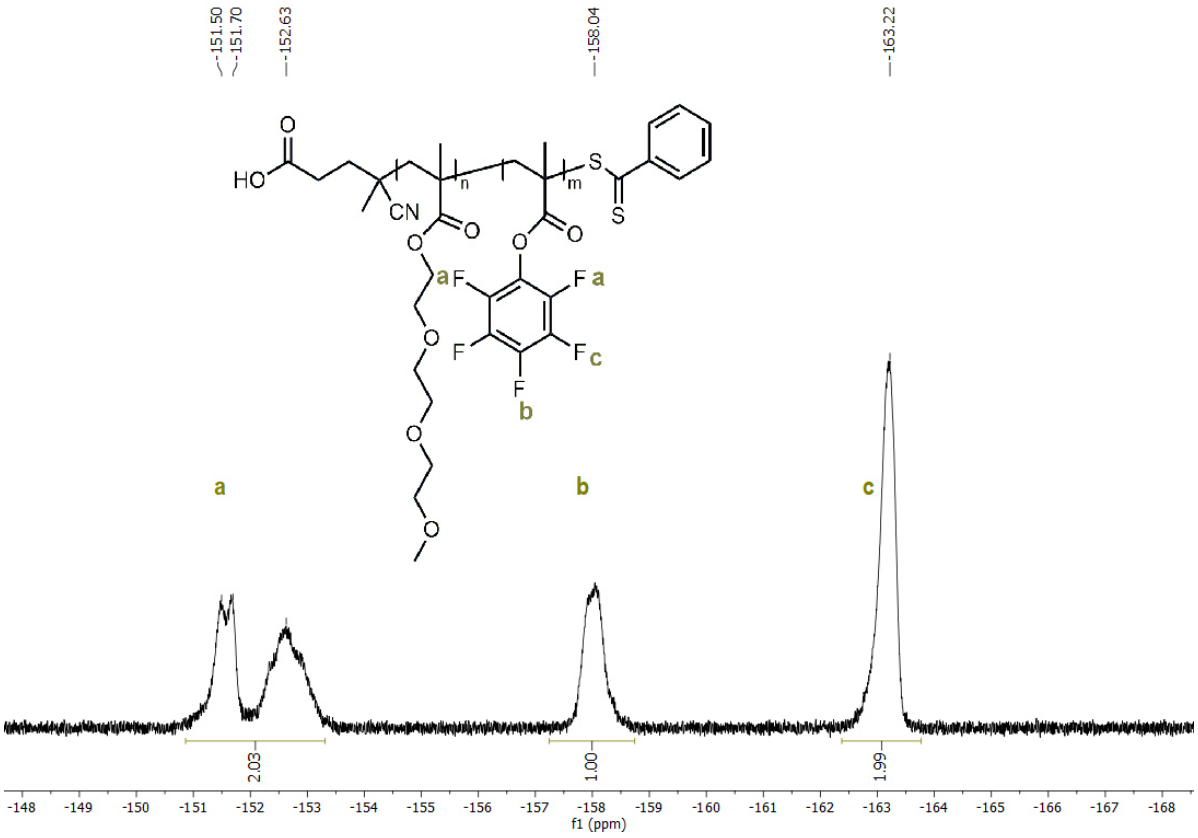

Figure S10: ^{19}F NMR spectrum (376 MHz) of the block copolymer p(mTEGMA)$_{20}$-*b*-p(PFPMA)$_{36}$ in $CDCl_3$.

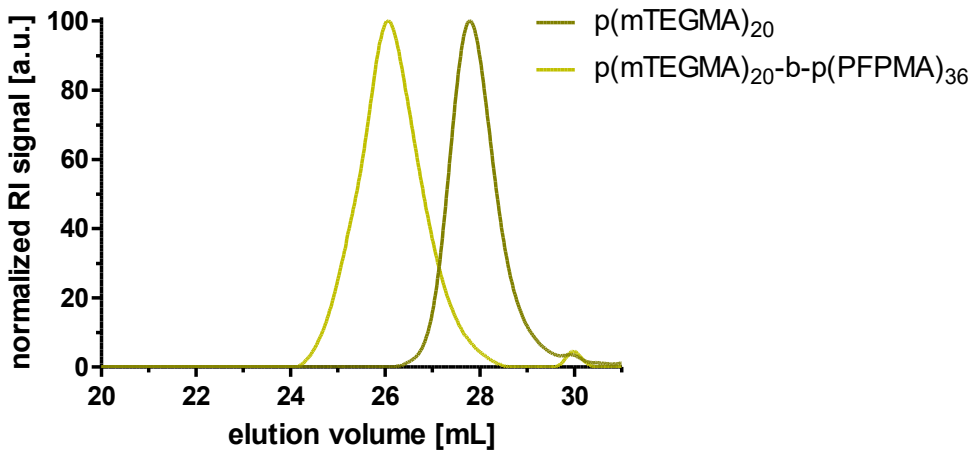

Figure S11: THF SEC traces of the homopolymer p(mTEGMA)$_{20}$ (light green) and the block copolymer p(mTEGMA)$_{20}$-*b*-p(PFPMA)$_{36}$ (dark green).

Removal of Dithiobenzoate End Groups of the Block Copolymer p(mTEGMA)$_{20}$-*b*-p(PFPMA)$_{36}$

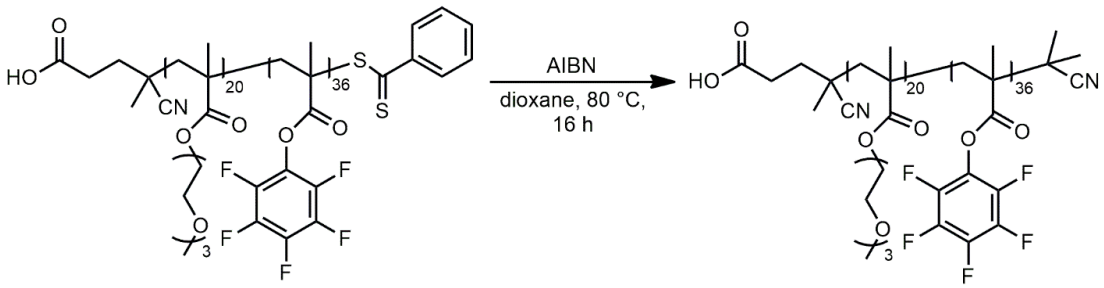

Figure S12: Reaction scheme for the removal of dithiobenzoate end groups of the block copolymer p(mTEGMA)$_{20}$-*b*-p(PFPMA)$_{36}$ with an excess of AIBN in dioxane at 80 °C for 16 hours.

The removal of dithiobenzoate end groups was conducted according to the literature.[7,8] The block copolymer p(mTEGMA)$_{20}$-*b*-p(PFPMA)$_{36}$ (1.20 g, 0.094 mmol, 1 eq) and an excess of AIBN (463 mg, 2.82 mmol, 30 eq) were transferred into a Schlenk tube and dissolved in 3 mL anhydrous dioxane under argon atmosphere. The clear, red solution was stirred at 80 °C for 24 h. Afterwards, the colorless block copolymer was precipitated into cold hexane (-20 °C) three times, centrifuged (3x10 min at 4500 rpm) and dried *in vacuo* for 16 h. The product was isolated as colorless powder (1.17 g, 83%).

^{1}H NMR (400 MHz, $CDCl_3$): δ (ppm) = 4.09 (m, 2H, **b**), 3.70-3.59 (m, 8H, **c**), 3.56 (m, 2H, **d**), 3.38 (m, 3H, **e**), 2.61-2.25 (m, 2H, **f**), 1.99-1.72 (m, 2H, **g**), 1.49-1.33 (m, 3H, **h**), 1.15-0.70 (m, 3H, **i**).

^{19}F NMR (376 MHz, $CDCl_3$): δ (ppm) = -151.47-152.92 (m, 2F, **a**), -158.07 (m, 1F, **b**), -163.24 (m, 2F, **c**).

SEC (THF) p(mTEGMA)$_{20}$-*b*-p(PFPMA)$_{36}$ with end group: M_n = 10633 app, M_w = 14228 g/mol, Đ = 1.28

SEC (THF) p(mTEGMA)$_{20}$-*b*-p(PFPMA)$_{36}$ without end group: M_n = 10379 app, M_w = 13117 g/mol, Đ = 1.26

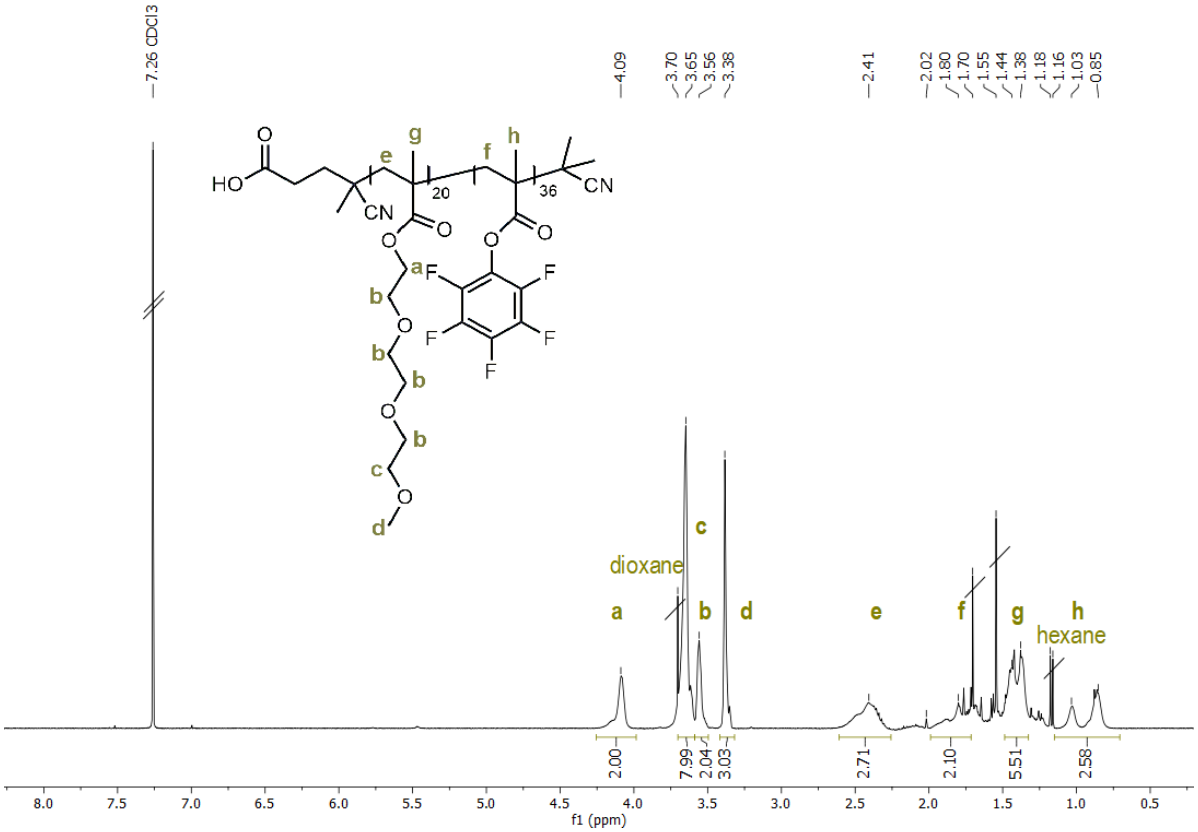

Figure S13: ^{1}H NMR spectrum (400 MHz) of the block copolymer p(mTEGMA)$_{20}$-*b*-p(PFPMA)$_{36}$ after end group removal in $CDCl_3$.

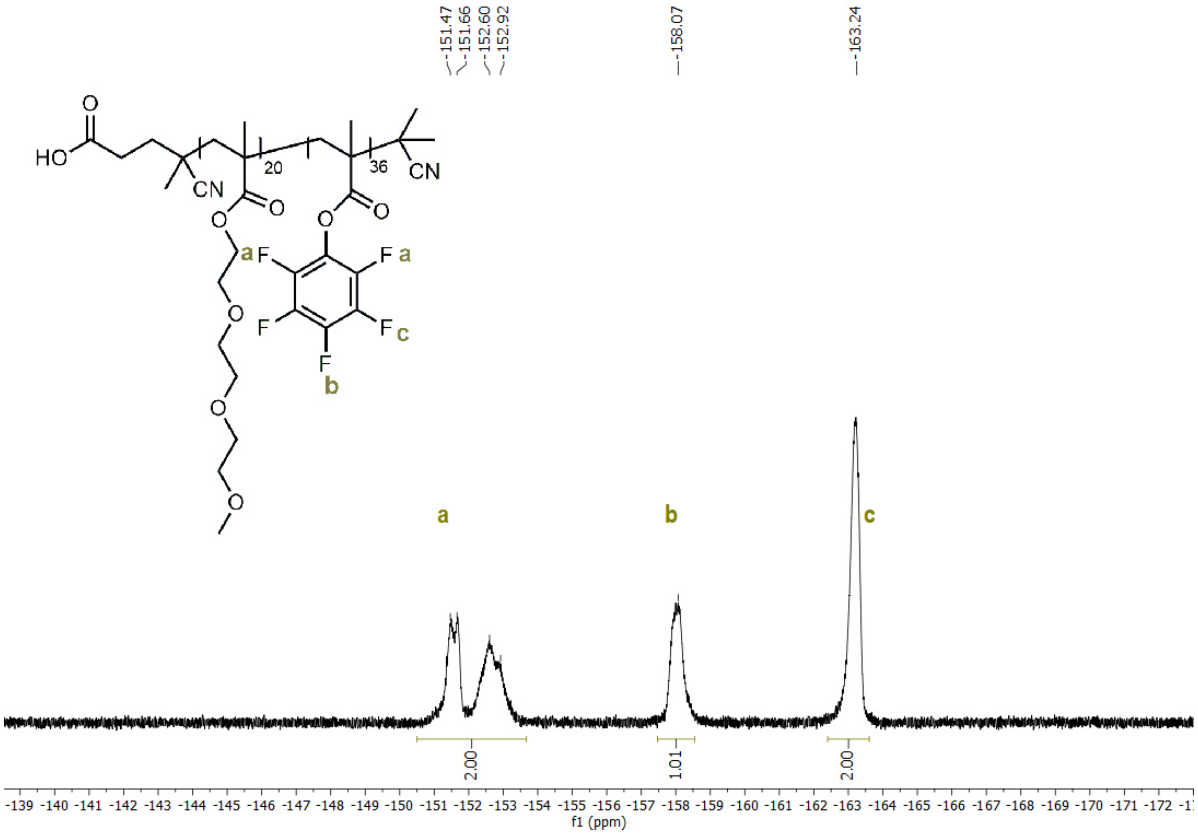

Figure S14: ^{19}F NMR spectrum (400 MHz) of the block copolymer p(mTEGMA)$_{20}$-*b*-p(PFPMA)$_{36}$ after end group removal in $CDCl_3$.

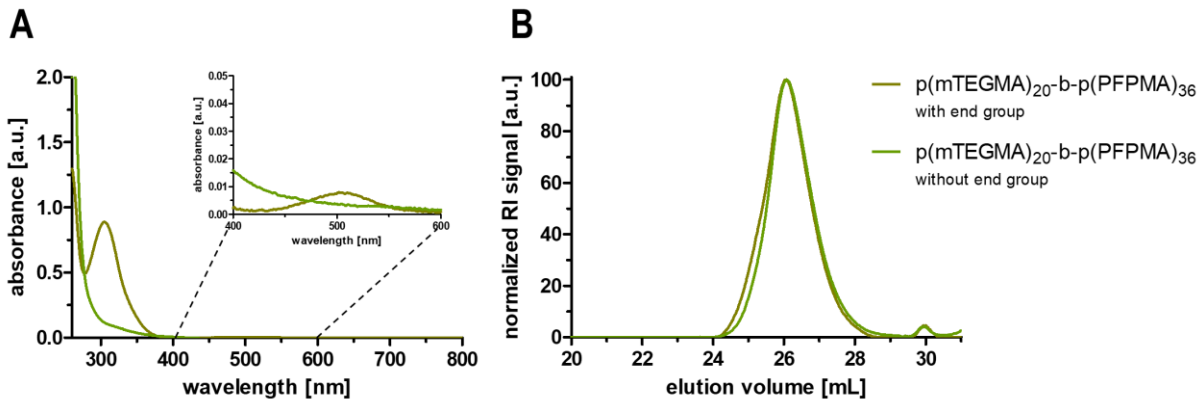

Figure S15: UV-Vis spectra of the block copolymer p(mTEGMA)$_{20}$-*b*-p(PFPMA)$_{36}$ before and after end group removal in dioxane (A) and the corresponding THF SEC traces (B).

DBCO Conjugation to the Block Copolymer

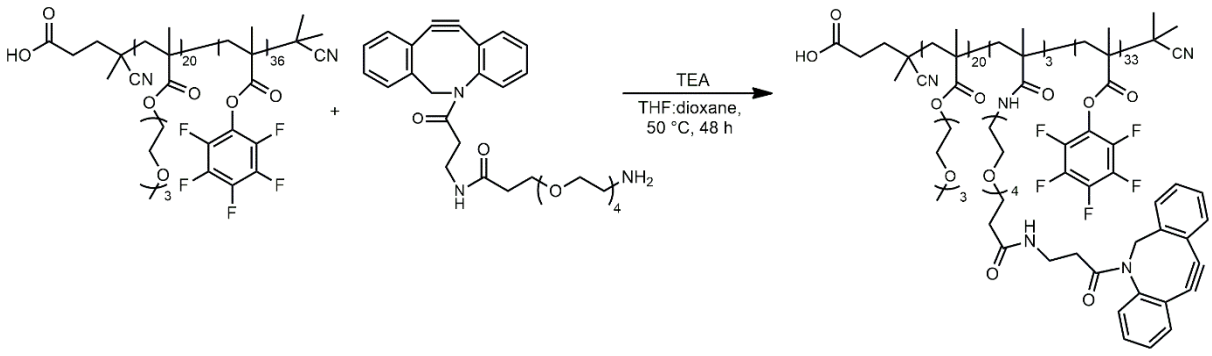

Figure S16: Reaction scheme for the conjugation of DBCO-PEG$_4$-Amine to the block copolymer p(mTEGMA)$_{20}$-*b*-p(PFPMA)$_{36}$ in a mixture of THF and dioxane at 50 °C for 48 hours.

In two pre-dried Schlenk flasks equipped with a stir bar the block copolymer p(mTEGMA)$_{20}$-*b*-p(PFPMA)$_{36}$ (2x30 mg, 2.14 µmol/77.04 µmol reactive ester groups, 1 eq) was dissolved in a mixture of anhydrous THF and dioxane (1:1) under nitrogen atmosphere. TEA (2.67 µL, 19.25 µmol, 0.25 eq) was added to both solutions, followed by the addition of DBCO-PEG$_4$-Amine (223 µL of a 15 mg/mL stock solution in DMSO, 6.39 µmol, 0.083 eq) or 223 µL DMSO as a control. Both reaction mixtures were stirred for 48 h at 50 °C. Analysis by ^{1}H NMR and ^{19}F NMR of reaction aliquots in DMSO showed successful conversion of three PFP units by DBCO-PEG$_4$-Amine. Both block copolymers were purified by threefold precipitation in a mixture of hexane and diethyl ether (2:1). After drying at high vacuum for 16 h the DBCO modified block copolymer was obtained as yellow powder (34 mg, quant), while the unmodified block copolymer yielded a colorless solid (31 mg, quant).

^{1}H NMR (400 MHz, $CDCl_3$): δ (ppm) = 7.69-7.30 (m, 7H, **a**), 7.22-6.88 (m, 1H, **b**), 5.35-5.11 (m, 1H, **c**), 4.09 (m, 2H, **d**), 3.76-3.61 (m, 8H, **e**), 3.57 (m, 2H, **f**), 3.38 (m, 3H, **g**), 2.36-2.23 (m, 3H, **h**), 2.24-1.75 (m, 2H, **i**), 1.51-1.34 (m, 2H, **j**), 1.21-079 (m, 2H, **k**).

^{19}F NMR (376 MHz, $CDCl_3$): δ (ppm) = -150.34-151.44 (m, 2F, **a**), -156.98 (m, 1F, **b**), -162.07 (m, 2F, **c**).

SEC (HFIP) p(mTEGMA)$_{20}$-*b*-p(PFPMA)$_{36}$: M_n = 15311 app, M_w = 17709 g/mol, Đ = 1.16

SEC (HFIP) p(mTEGMA)$_{20}$-*b*-p(PFPMA)$_{36}$ with DBCO: M_n = 16518 app, M_w = 21749 g/mol, Đ = 1.31

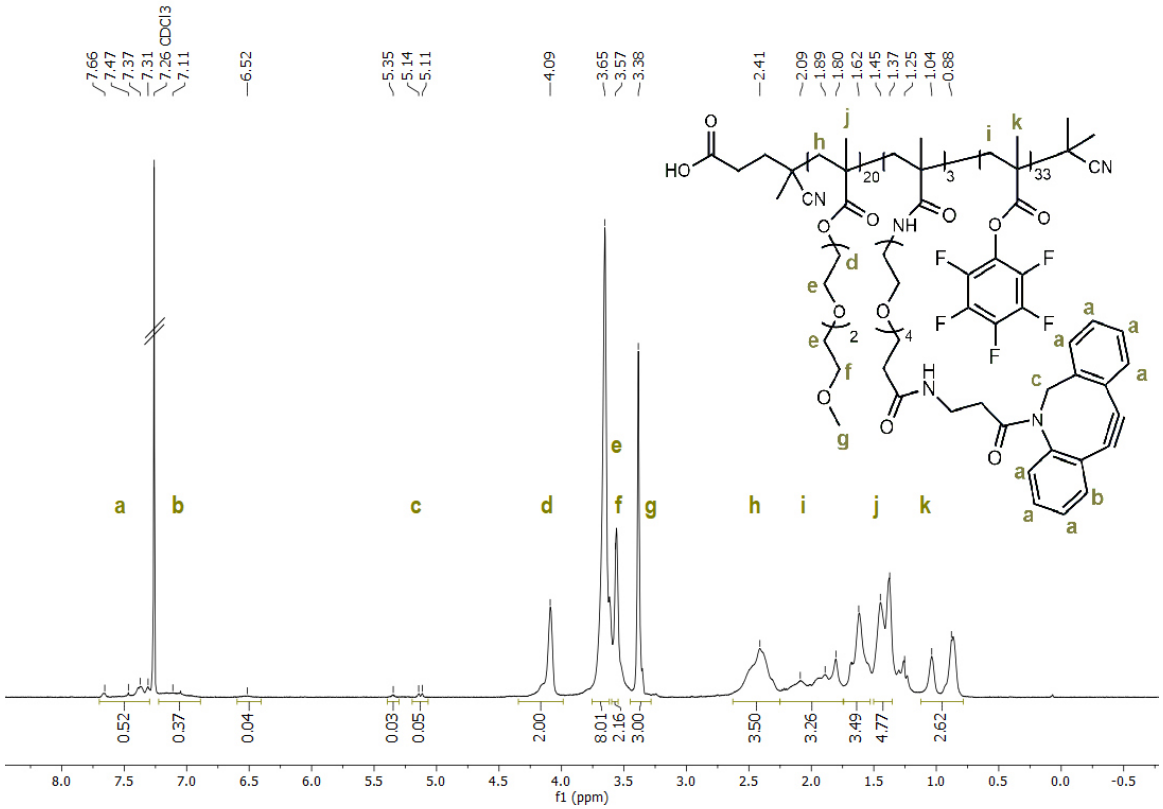

Figure S17: ^{1}H NMR spectrum (500 MHz) of the block copolymer p(mTEGMA)$_{20}$-*b*-p(PFPMA)$_{36}$ after DBCO-PEG$_4$-Amine conjugation in $CDCl_3$.

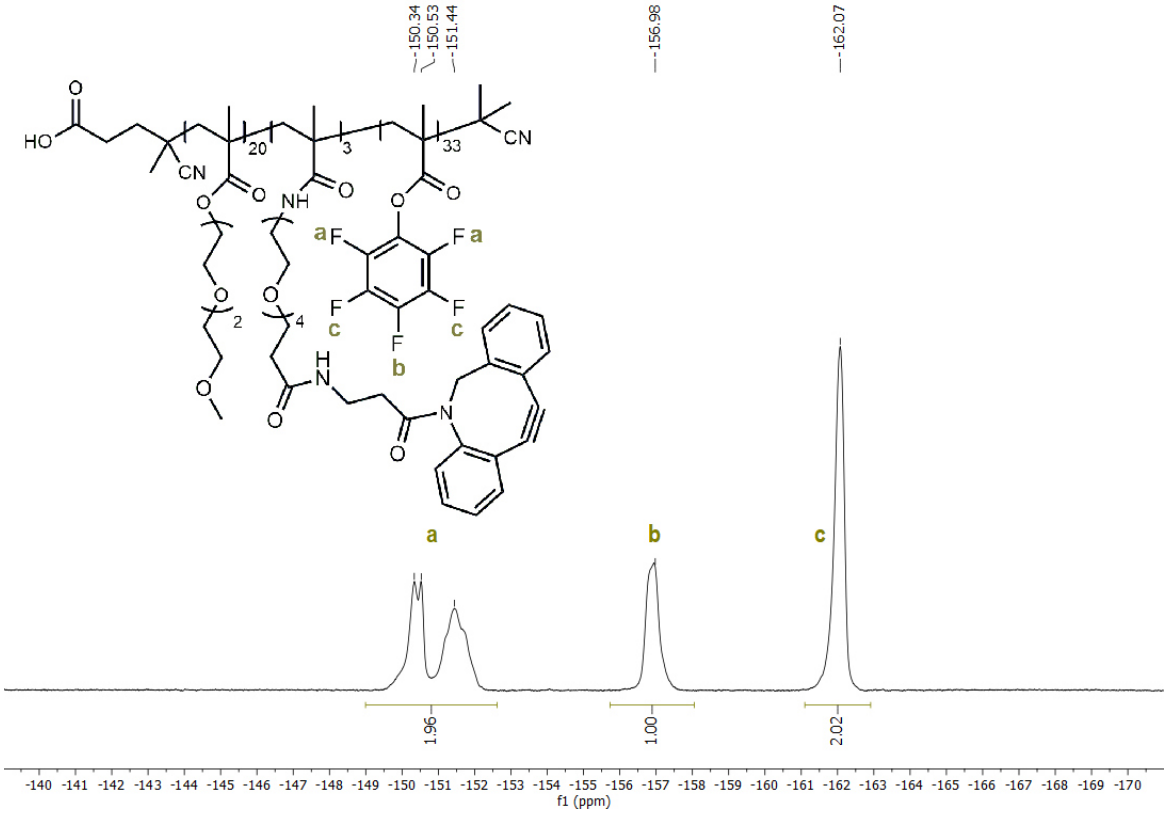

Figure S18: ^{19}F NMR spectrum (471 MHz) of the block copolymer p(mTEGMA)$_{20}$-*b*-p(PFPMA)$_{36}$ after DBCO-PEG$_4$-Amine conjugation in $CDCl_3$.

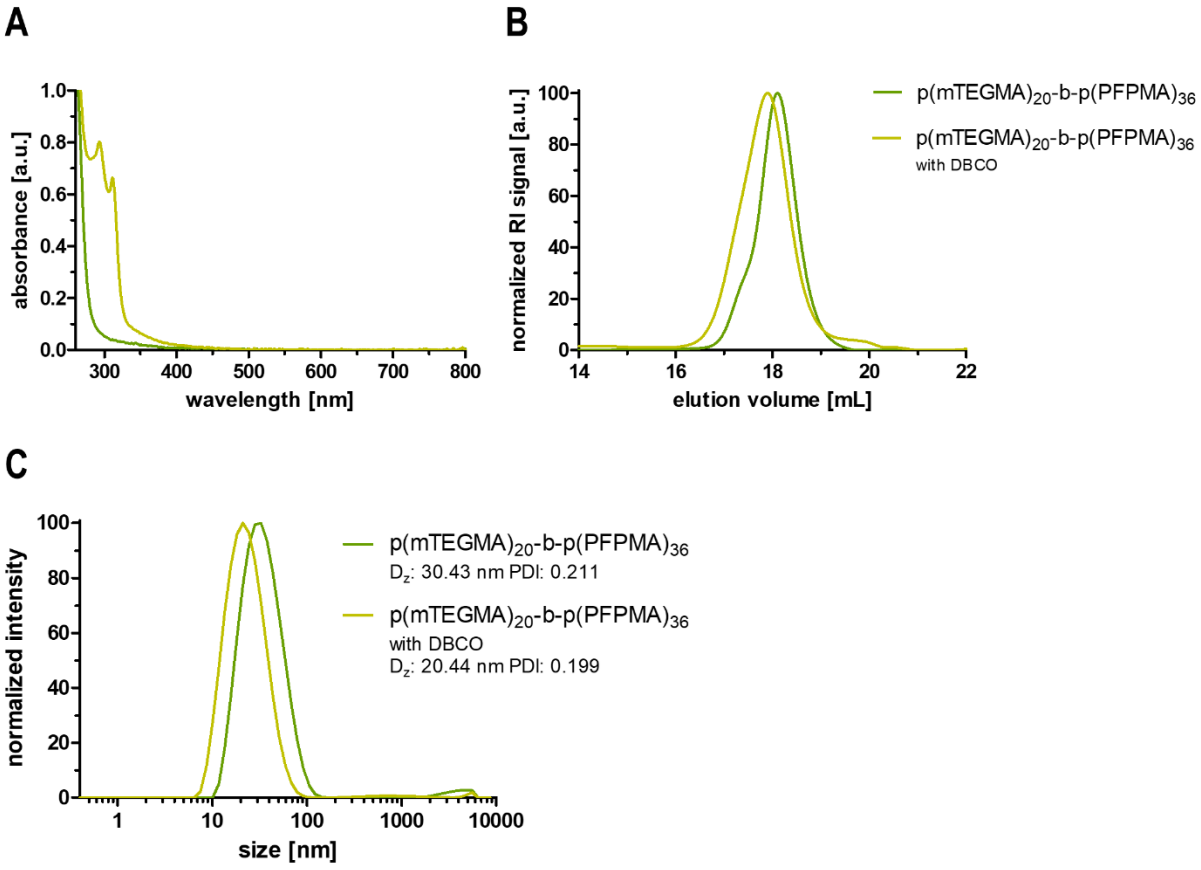

Figure S19: UV-Vis spectra of the block copolymer p(mTEGMA)$_{20}$-*b*-p(PFPMA)$_{36}$ before (dark green) and after (light green) conjugation of DBCO-PEG$_4$-Amine in dioxane (A), the corresponding HFIP SEC elugrams (B) and DLS analysis of the self-assembled block copolymer p(mTEGMA)$_{20}$-*b*-p(PFPMA)$_{36}$ (dark green) and DBCO-PEG$_4$-Amine conjugated block copolymer (light green) in DMSO (10mg/mL), showing the normalized intensity sizes.

Nanogel Formulation

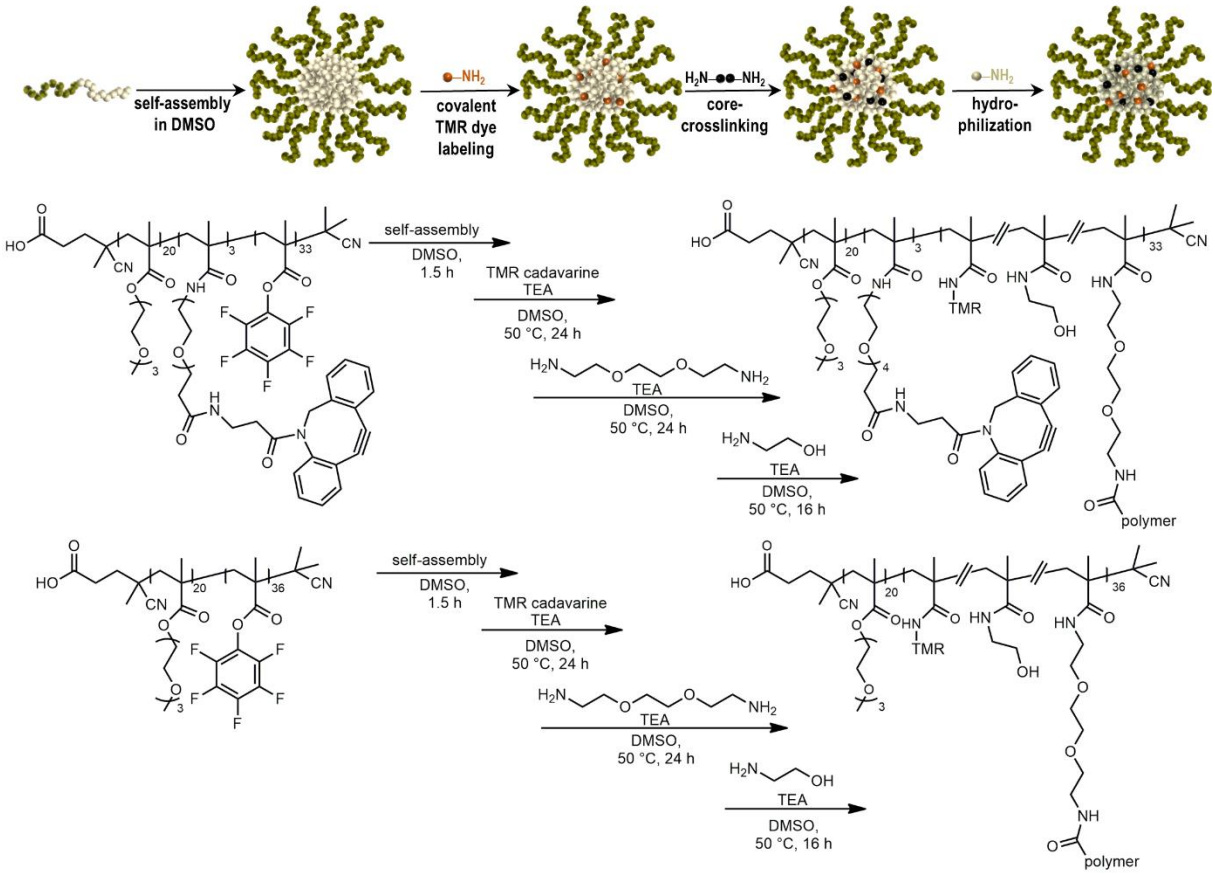

Figure S20: Reaction scheme for the sequential formulation of hydrophilic nanogels.

The formulation of hydrophilic nanogels was adapted from the literature and modified.[7,8] Two types of core-crosslinked and dye-labeled nanogels with DBCO and without DBCO were generated in DMSO. Therefore, DBCO-conjugated block copolymer p(mTEGMA)$_{20}$-*b*-p(PFPMA)$_{36}$ (25 mg, 1.66 µmol/54.78 µmol reactive ester groups, 1 eq) or block copolymer without DBCO (25 mg, 1.78 µmol/64.08 µmol reactive ester groups, 1 eq) were dispersed in 2.5 mL anhydrous DMSO under nitrogen atmosphere and ultrasonicated for two hours. Self-assembly of the polymeric micelles was analyzed by DLS measurements and resulted micellar dispersions were used for nanogel formulation. For dye-labeling both micellar solutions were treated with tetramethylrhodamine cadaverine (TMR, 28.20 µL from a 5 mg/mL stock solution in DMSO, 0.274 µmol, 0.005 eq (with DBCO)), (32.94 µL, 0.32 µmol (without DBCO)) and TEA (1.71 µL, 12.33 µmol, 0.225 eq (with DBCO)), (1.99 µL, 14.418 µmol (without DBCO)). The reaction mixtures were stirred at 50 °C for 48 h. Then, the core-crosslinking reagent 2,2-(ethylenedioxy)bis(ethylamine) (2.40 µL, 16.43 µmol, 0.3 eq (with DBCO)), (2.81 µL, 19.22 µmol (without DBCO)) and TEA (22.78 µL, 164.34 µmol, 3 eq (with DBCO)), (26.65

µL, 192.24 µmol (without DBCO)) were added to the solutions and further stirred for 24 h at 50 °C. To obtain completely hydrophilic nanogels an excess of 2-aminoethanol (9.92 µL, 164.34 µmol, 3 eq (with DBCO)), (11.60 µL, 192.24 µmol (without DBCO)) and TEA (22.78 µL, 164.34 µmol, 3 eq (with DBCO)), (26.65 µL, 192.24 µmol (without DBCO)) were dropped to the reaction mixtures and allowed to stir overnight at 50 °C. Subsequently, the formulated nanogels were transferred into dialysis membranes (MWCO 1.0 kDa) and dialyzed against water supplemented with 0.1% ammonia for five days and water exchange twice a day. After lyophilization the resulting nanogels were obtained as pale-pink powder.

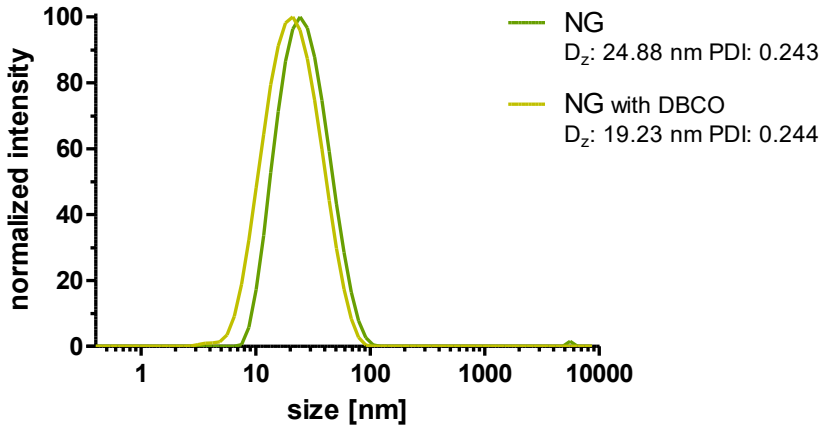

Figure S21: DLS study of the formulated nanogels with (light green) and without DBCO (dark green) in millipore water + 0.1% NH_3. (1mg/mL).

Synthesis of Azide Containing 2-Propionic-3-Methylmaleic Anhydride Linker

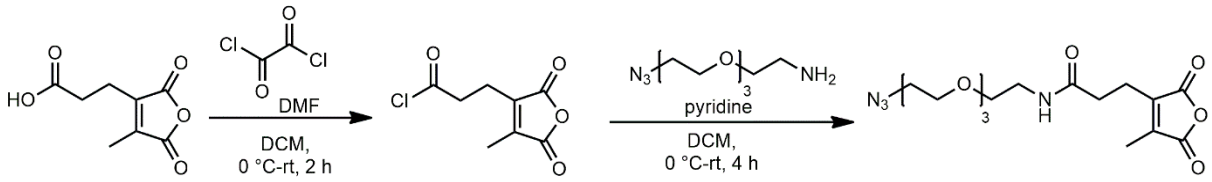

Figure S22: Synthesis of N-(2-(2-(2-azidoethoxy)ethoxy)ethyl)-3-(4-methyl-2,5-dioxo-2,5-dihydro-furan-3-yl)propanamid in two steps.

The azide-containing 2-propionic-3-methylmaleic anhydride linker N-(2-(2-(2-azidoethoxy)ethoxy)ethyl)-3-(4-methyl-2,5-dioxo-dihydrofuran-3-yl)propanamid was synthesized in analogy to the literature and modified.[9–11] 2-propionic-3-methylmaleic anhydride (1.2 g, 6.52 mmol, 1 eq) was weighted into a round bottom flask and dissolved in anhydrous DCM (35 mL) under nitrogen atmosphere. The solution was cooled to 0 °C using an ice bath, then 5 drops DMF and oxalyl chloride (1.85 mL, 21.52 mmol, 3.3 eq) were slowly dropped to the reaction mixture. After additional stirring for 30 min at 0 °C the solution was

allowed to stir at room temperature for 2 h. The solvent was evaporated and resulting acetyl chloride activated 2-propionic-3-methylmaleic anhydride linker was redissolved in 35 mL anhydrous DCM under nitrogen atmosphere. Pyridine (0.527 mL, 6.62 mmol, 1 eq) and 11-azido-3,6-9-trioxaundecan-1-amine (1.5 mL, 7.56 mmol, 1.16 eq) were slowly dropped to the solution *via* syringe and ice cooling. Afterwards, the reaction mixture was stirred for further 30 min at 0 °C, before stirred at room temperature for 4 h. Then, the solution was extracted with a saturated ammonium chloride aqueous solution (4x50 mL). The organic layer was dried over Na_2SO_4, filtrated, and evaporated under reduced pressure. The crude product was purified by silica gel chromatography using ethyl acetate as eluent. The pure product was isolated as slightly yellow oil (1.39 g, 56%).

^{1}H NMR (300 MHz, $CDCl_3$): δ (ppm) = 6.25 (s, 1H, **a**), 3.71-3.59 (m, 10H, **b**), 3.57-3.47 (m, 2H, **c**), 3.46-3.35 (m, 4H, **d+e**), 2.79 (t, *J* = 7.0 Hz, 2H, **f**), 2.54 (t, *J* = 7.0 Hz, 2H, **g**), 2.11 (s, 3H, **h**).

^{13}C NMR (75 MHz, $CDCl_3$): δ (ppm) = 170.59 (**a**), 166.13 (**b**), 166.04 (**c**), 142.91 (**d**), 142.32 (**e**), 70.79 (**f**), 70.72 (**g**), 70.62 (**h**), 70.36 (**i**), 70.12 (**j**), 69.68 (**k**), 50.79 (**l**), 39.49 (**m**), 32.90 (**n**), 20.49 (**o**), 9.80 (**p**.

IR (ATR) ũ [cm^{-1}] = 3318 (w), 3081 (w), 2920 (m, υ, -N-D-), 2867 (m, υ, -N-D-), 2361 (w), 2340 (w), 2100 (s, υ, $-N_3$), 1824 (s, υ, -C=O- anhy.), 1760 (s, υ, -C=O- anhy.), 1670 (s, υ, -C=O- amide), 1537 (m), 1442 (m), 1386 (w), 1348 (m-s, υ, -C-N-) , 1278 (w), 1180 (w), 1116 (s, υ, -C-O-C- ether), 908 (s), 851 (w), 732 (w).

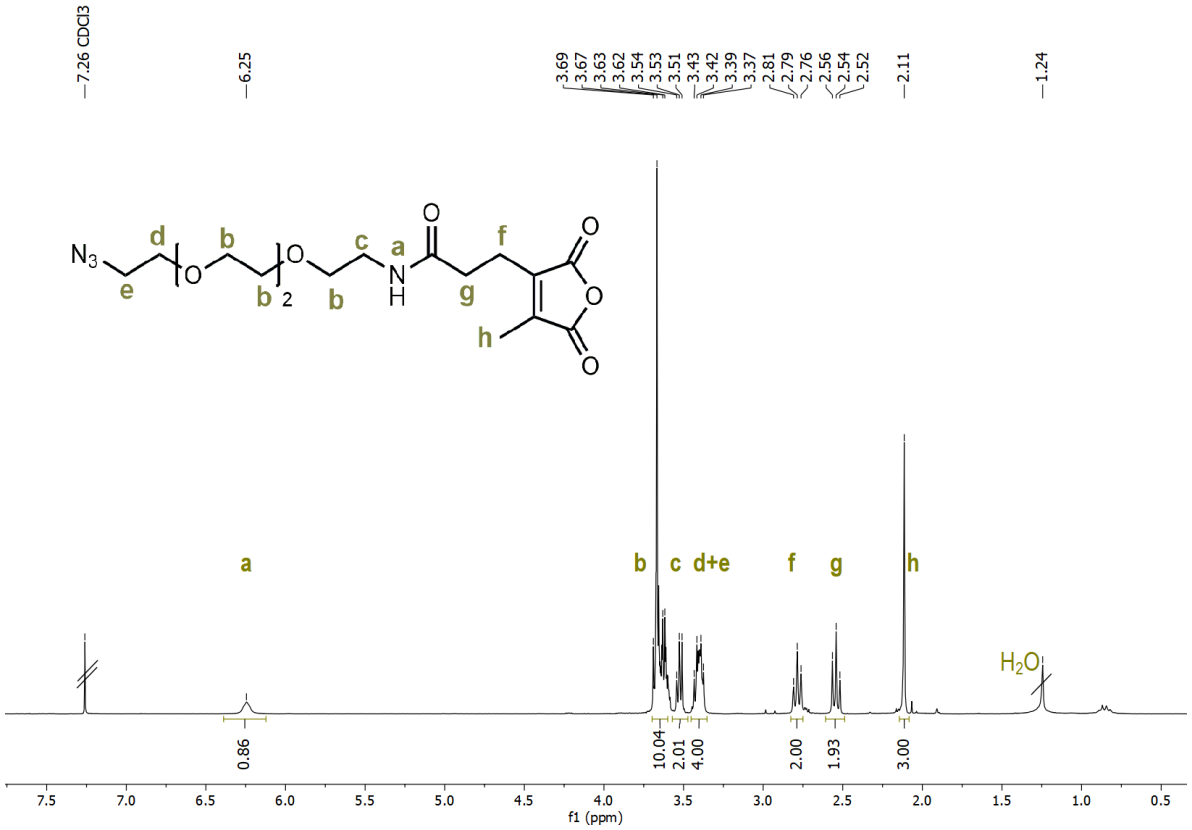

Figure S23: ^{1}H NMR spectrum (300 MHz) of N-(2-(2-(2-azidoethoxy)ethoxy)ethyl)-3-(4-methyl-2,5-dioxo-2,5-dihydro-furan-3-yl)propanamid in $CDCl_3$

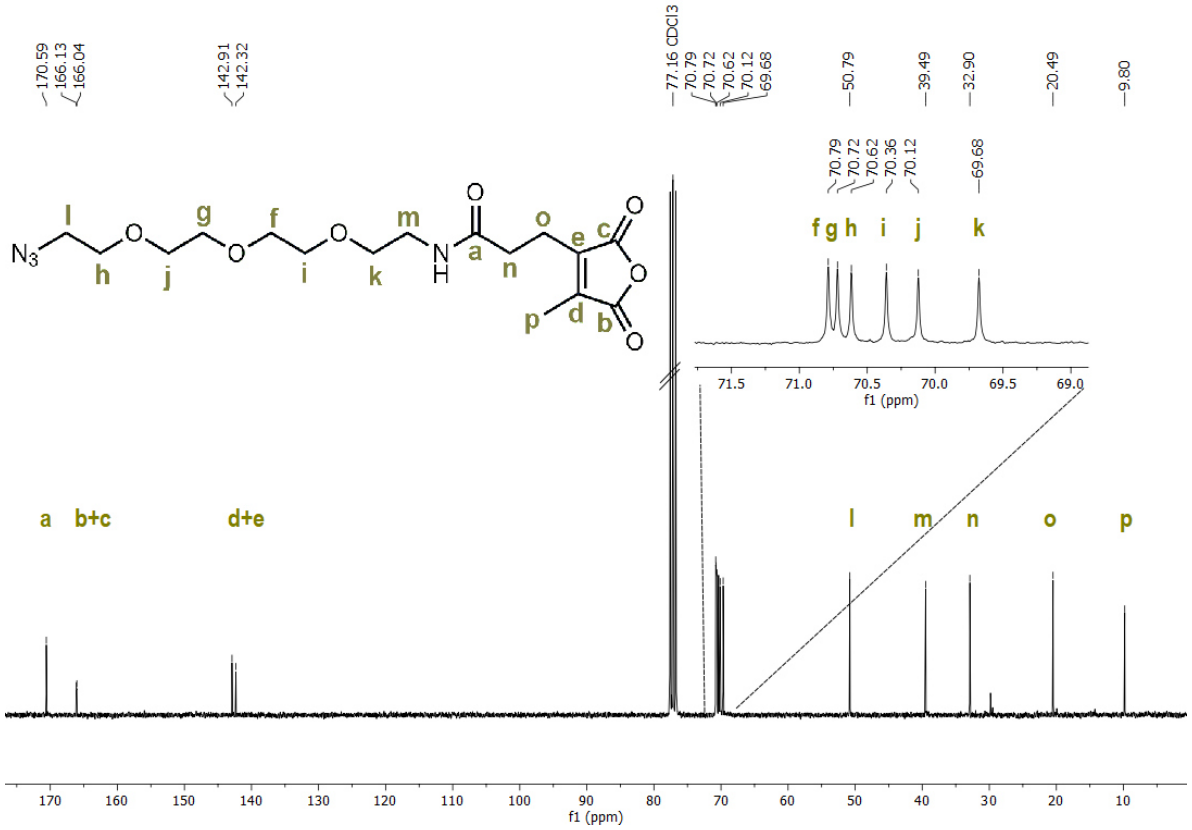

Figure S24: ^{13}C NMR spectrum (75 MHz) of N-(2-(2-(2-azidoethoxy)ethoxy)ethyl)-3-(4-methyl-2,5-dioxo-2,5-dihydro-furan-3-yl)propanamid in $CDCl_3$

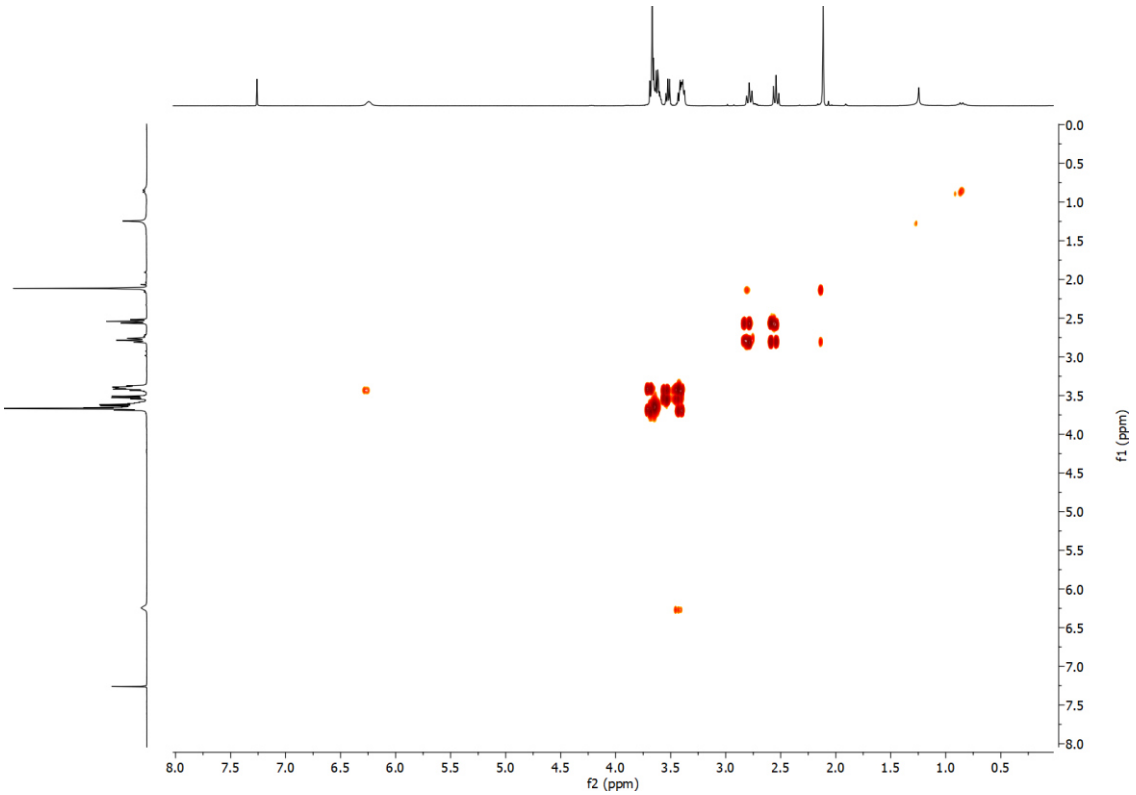

Figure S25: 2D COSY NMR spectrum of N-(2-(2-(2-azidoethoxy)ethoxy)ethyl)-3-(4-methyl-2,5-dioxo-2,5-dihydrofuran-3-yl)propanamid in $CDCl_3$.

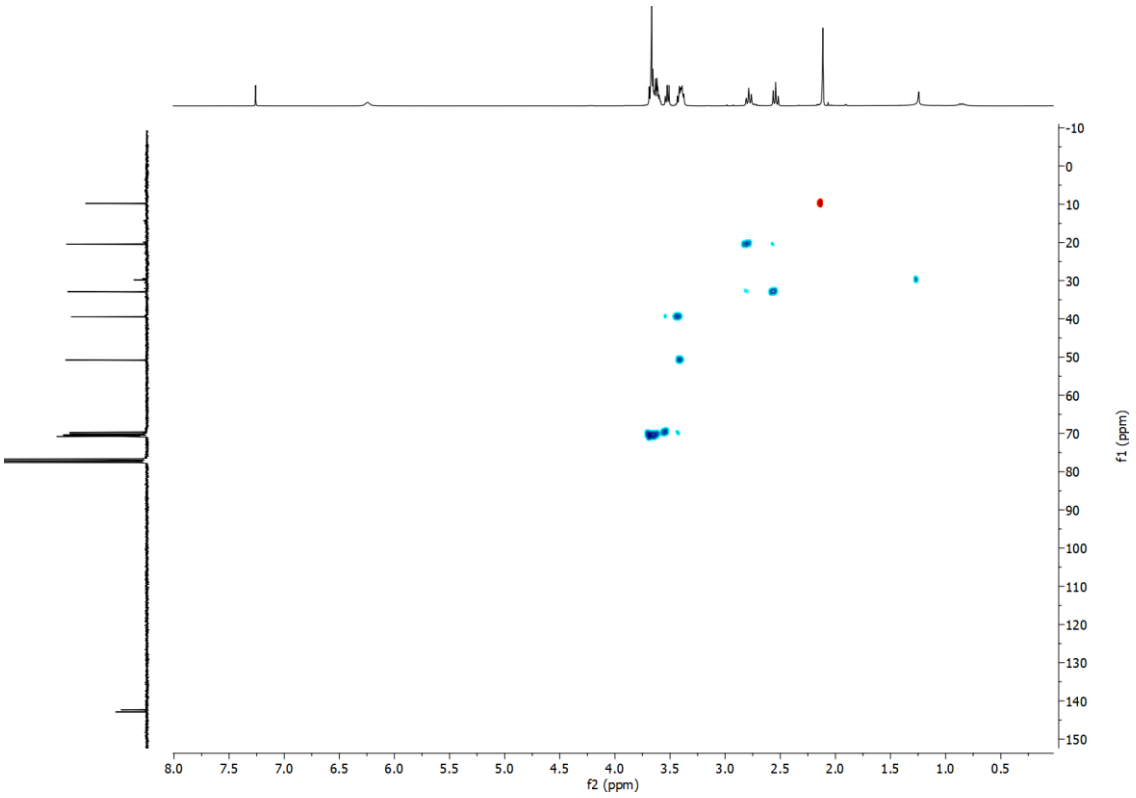

Figure S26: 2D HSQC NMR spectrum of N-(2-(2-(2-azidoethoxy)ethoxy)ethyl)-3-(4-methyl-2,5-dioxo-2,5-dihydrofuran-3-yl)propanamid in $CDCl_3$.

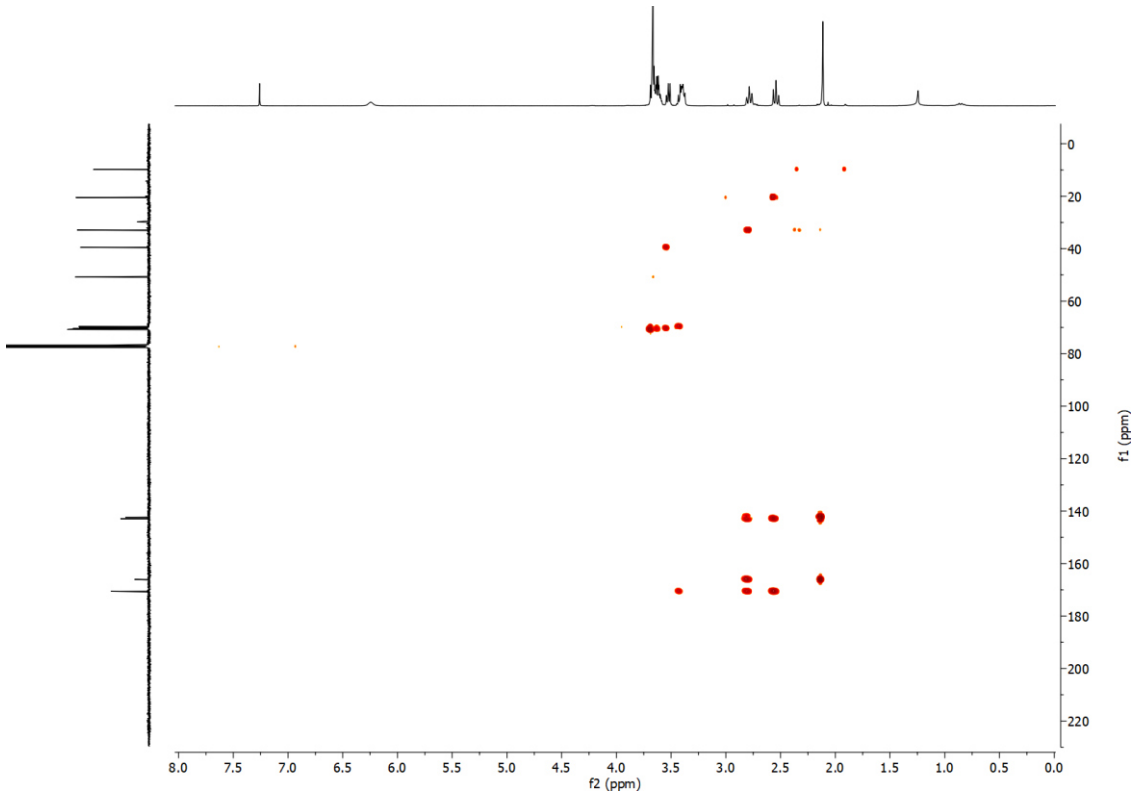

Figure S27: 2D HMBC NMR spectrum of N-(2-(2-(2-azidoethoxy)ethoxy)ethyl)-3-(4-methyl-2,5-dioxo-2,5-dihydro-furan-3-yl)propanamid in $CDCl_3$.

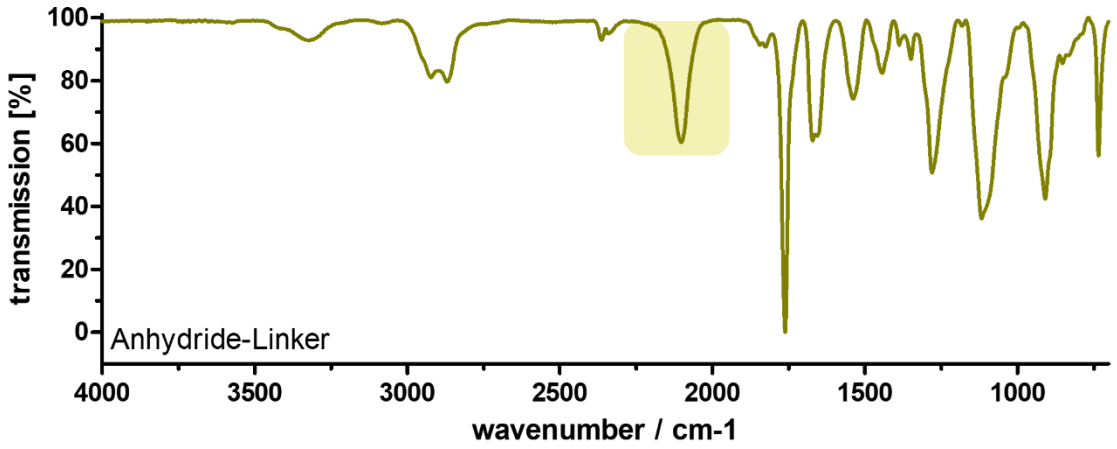

Figure S28: IR spectrum of N-(2-(2-(2-azidoethoxy)ethoxy)ethyl)-3-(4-methyl-2,5-dioxo-2,5-dihydro-furan-3-yl)propanamid.

Preparation of pH-Reversible and Irreversible Dye-Labeled Azide Containing 2-Propionic-3-Methylmaleic Anhydride Linker by Amidation

Synthesis of 4-Nitro-7-Piperazino-2,1,3-Benzoxadiazole (NBD-PZ)

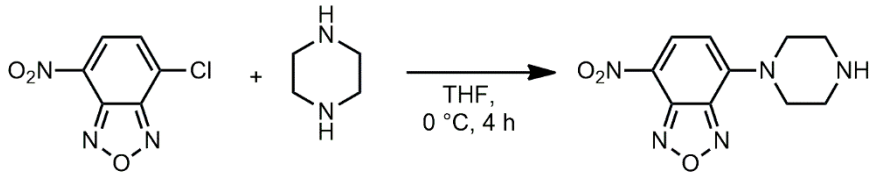

Figure S29: Synthesis of 4-Nitro-7-piperazino-2,1,3-benzoxadiazole (NBD-PZ).

The synthesis of the fluorescent dye 4-Nitro-7-piperazino-2,1,3-benzoxadiazole (NBD-PZ) was performed similar as previously reported.[11]

^{1}H NMR (500 MHz, DMSO-d$_6$): δ (ppm) = 8.44 (d, J = 9.2 Hz, 1H, **a**), 6.63 (d, J = 9.3 Hz, 1H, **b**), 4.07 (m, 4H, **c**), 2.92 (m, 4H, **d**).

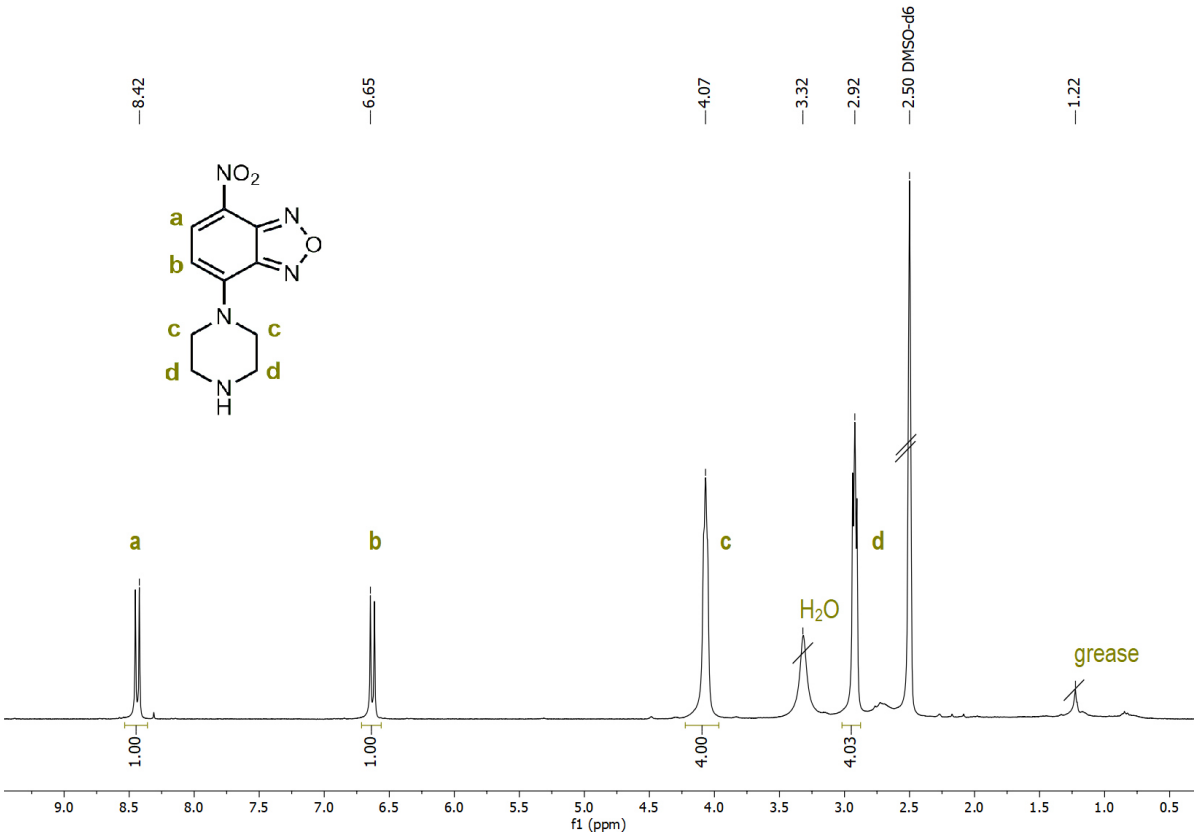

Figure S30: ^{1}H NMR spectrum (500 MHz) of 4-Nitro-7-piperazino-2,1,3-benzoxadiazole (NBD-PZ) in DMSO-d$_6$.

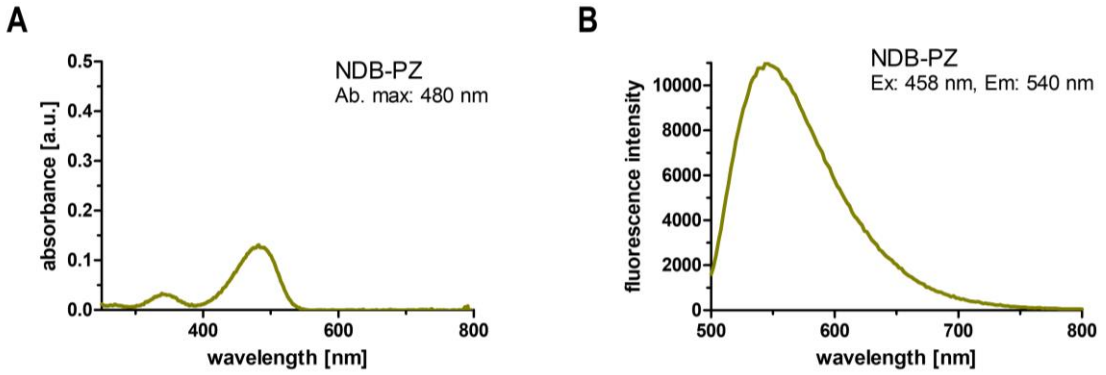

Figure S31: UV-Vis spectrum of 4-Nitro-7-piperazino-2,1,3-benzoxadiazole (A) and the corresponding fluorescence intensity spectrum in PBS (B).

Linker Dye Labeling Reaction by Covalent Attachment of Primary and Secondary Amines

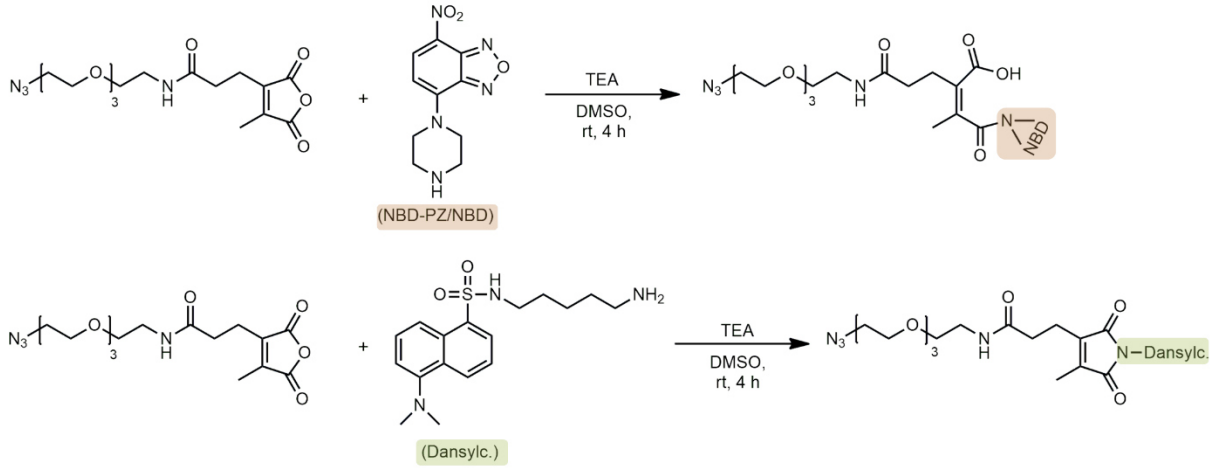

Figure S32: Synthesis of pH-reversible and irreversible dye-labeled azide 2-propionic-3-methylmaleic anhydride linker in DMSO at room temperature for four hours.

In a Schlenk tube equipped with a magnetic stir bar the azide-containing 2-propionic-3-methylmaleic anhydride linker (120 mg, 0.313 mmol, 1 eq) was dissolved in 6 mL anhydrous DMSO under nitrogen atmosphere. TEA (122 µL, 0.88 mmol, 3 eq) was dropped to the solution and then 60 mg of the linker was transferred into a new Schlenk tube. Protected from light dansyl cadaverine (Dansylc, 53.60 mg, 1 eq) or 4-nitro-7-piperazino-2,1,3-benzoxadiazole (NBD-PZ, 39.88 mg, 1 eq) were added to the reaction mixtures and stirred for 4 h at room temperature. The formulated dye-labeled linkers were purified by threefold precipitation into diethyl ether, centrifuged (3x15 min, 4000 rpm) and decanted. Drying for 16 h at reduced pressure afforded the dye-conjugated linkers as intensive red or yellow oil (89 mg, 93%).

MALDI-ToF MS [m/z] (with NBD-PZ) = 634.25 $[M+H]^+$ (calc. 634.62), 656.24 $[M+Na]^+$ (calc. 656.61), 672.21 $[M+K]^+$ (calc. 672.72).

ESI-MS [m/z] (with dansylc.) = 724.78 $[M+Na]^+$ (calc. 724.82), 740.80 $[M+K]^+$ (calc. 740.93).

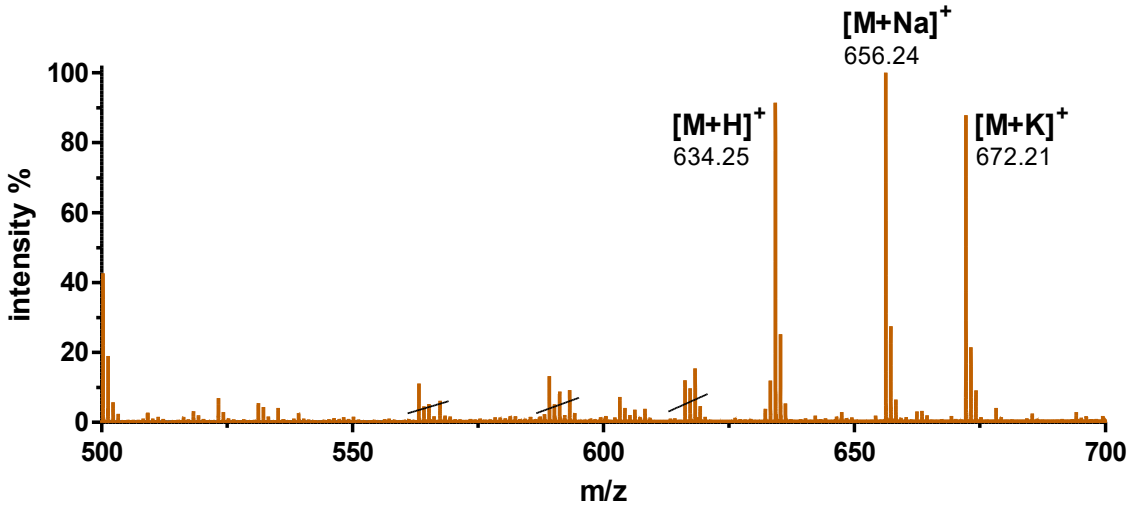

Figure S33: MALDI-ToF MS spectrum of the azide 2-propionic-3-methylmaleic anhydride linker after NBD-PZ conjugation in DCM.

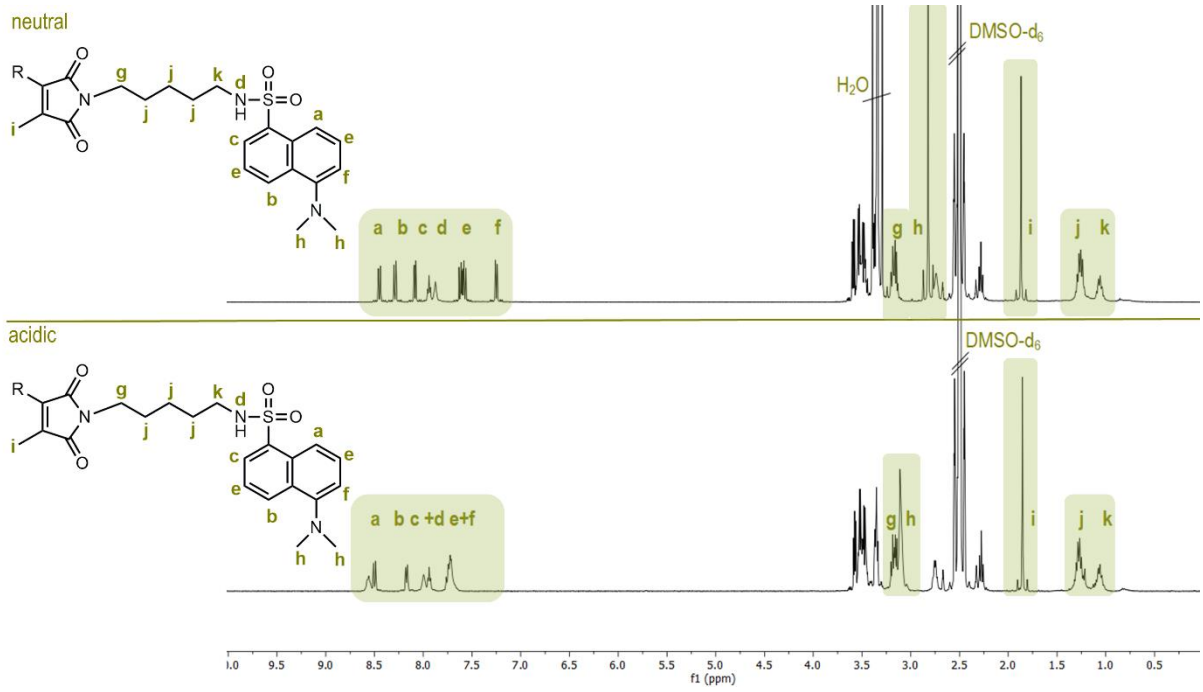

Figure S34: ^1H NMR spectra (400 MHz) of the dansyl cadaverine (dansylc.) conjugated azide 2-propionic-3-methylmaleic anhydride linker under neutral and acidic conditions in DMSO-d_6.

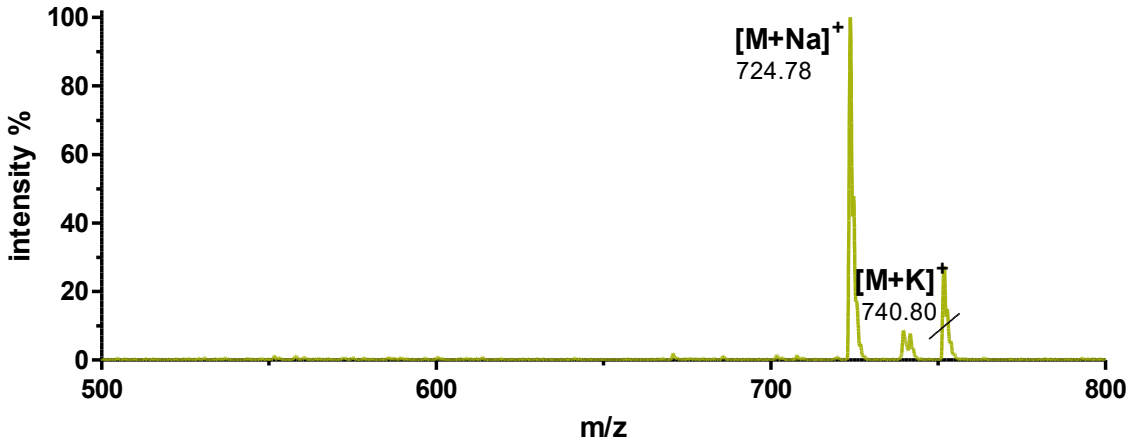

Figure S35: ESI-MS spectrum of the azide 2-propionic-3-methylmaleic anhydride linker after dansyl cadaverine (dansylc.) conjugation in MeOH.

Nanogel DBCO Click Reaction

Nanogel DBCO Click Reaction with Fluorescent Azide-Dye

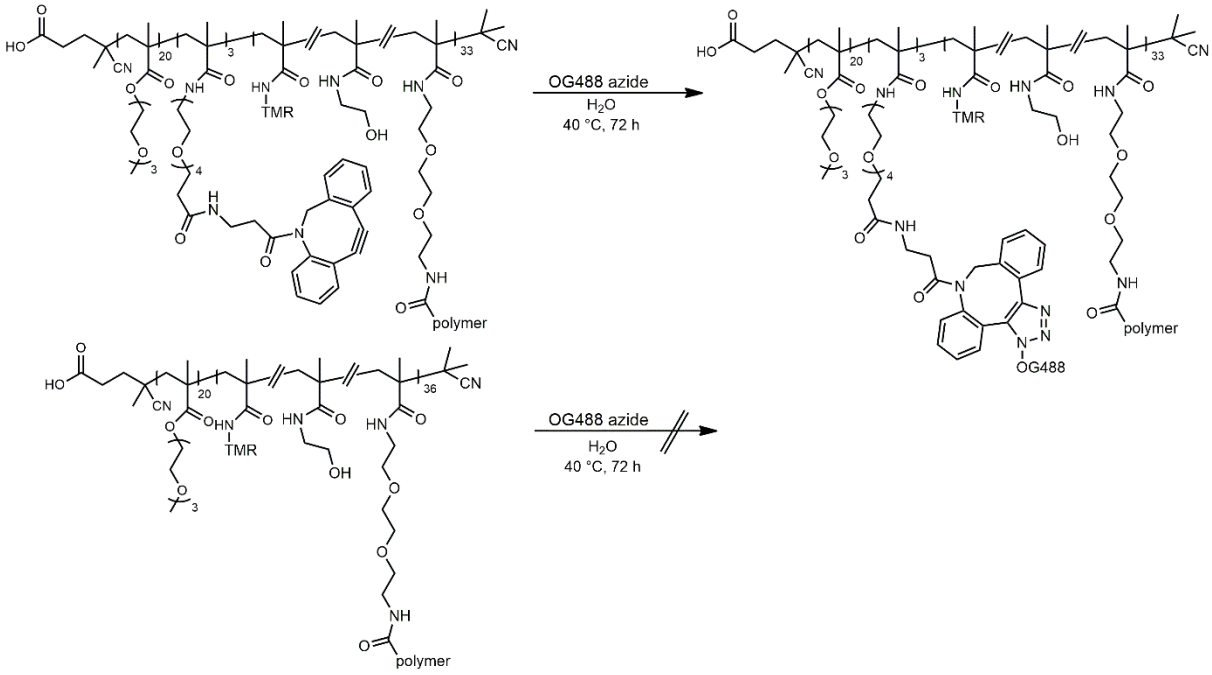

Figure S36: Scheme for the Oregon green 488 azide (OG488 azide) click reaction to the DBCO nanogel (NG DBCO) and control reaction with non-containing DBCO nanogel (NG) in millipore water with 0.1% NH_3 at 40 °C for 72 hours.

To ensure the DBCO-accessibility the corresponding nanogel was used in a DBCO click reaction with an azide-containing fluorescent dye. Therefore, 0.5 mg DBCO nanogel (NG DBCO, 0.046 µmol/0.137 µmol reactive DBCO groups, 1 eq) or control nanogel without

DBCO (NG, 0.5 mg, 0.052 µmol, 1 eq) were redispersed in water supplemented with 0.1% NH_3. After sonication for 1.5 h Oregon Green 488 azide (OG488 azide, 44.32 µL from a 2.5 mg/mL stock solution, 0.17 µmol, 1.25 eq) was added to the two different nanogel solutions and shaken for 3 days at 40 °C in the absence of light. Finally, the solutions were purified by repetitive spin-filtration (MWCO 10000 g/mol) with a mixture of ethanol and 0.1 % ammonia containing water (3x) as well as millipore water. Successful reaction could be monitored by UV-Vis spectroscopy.

Nanogel DBCO Click Reaction with pH-Reversible and Irreversible Dye-Labeled Azide Containing 2-Propionic-3-Methylmaleic Anhydride Linker

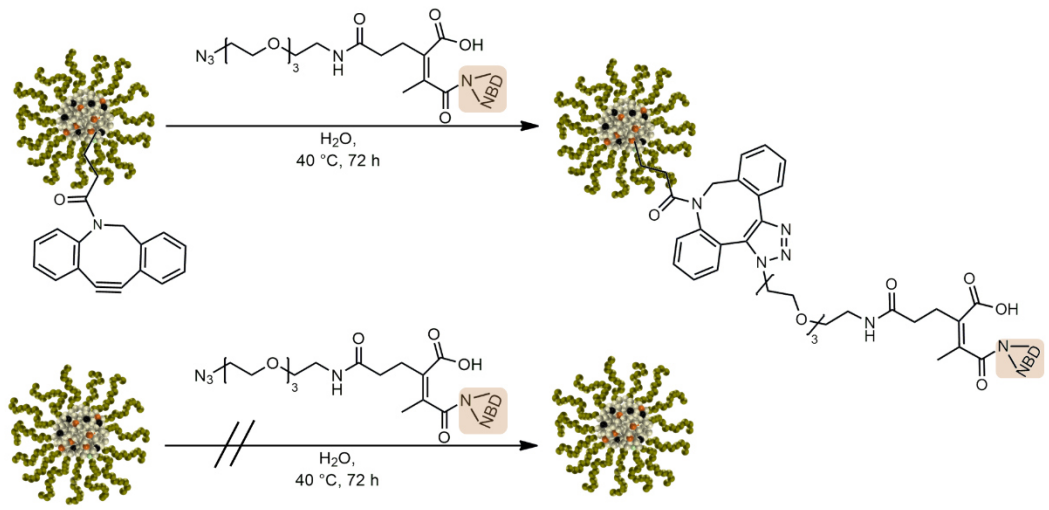

Figure S37: Reaction scheme for the click reaction of reversible dye-labeled azide 2-propionic-3-methylmaleic anhydride linker to the DBCO nanogel (NG DBCO) or control nanogel without DBCO (NG) in millipore water with 0.1% NH_3 at 40 °C for 72 hours.

The nanogel modification with dye-labeled azide-containing 2-propionic-3-methylmaleic anhydride linker was formulated analogously to the OG488 azide click reaction. 1 mg DBCO nanogel (NG DBCO, 0.091 µmol/0.273 µmol reactive DBCO groups, 1 eq) or control nanogel (NG, 0.105 µmol, 1 eq) were dissolved in 1 mL water supplemented with 0.1% NH_3 and sonicated for 1.5 h. Then, each nanogel solution was treated with the synthesized NBD-PZ-conjugated azide linker (259 µL from a 10 mg/mL stock solution, 4.09 µmol, 15 eq). The reaction mixtures were shaken for 3 days at 40 °C protected from light. After repeated spin-filtration (MWCO 10000 g/mol) with 0.1% NH_3 water the nanogels were analyzed by UV-Vis and DLS measurement. To determine the pH-sensitive release of NBD-PZ under acidic

conditions both nanogels were treated with 1% trifluoroacetic acid (TFA) solution and further spin-filtrated, followed by UV-Vis and DLS characterization.

DBCO Nanogel Targeting by Click Reaction with Azide-Trimannose

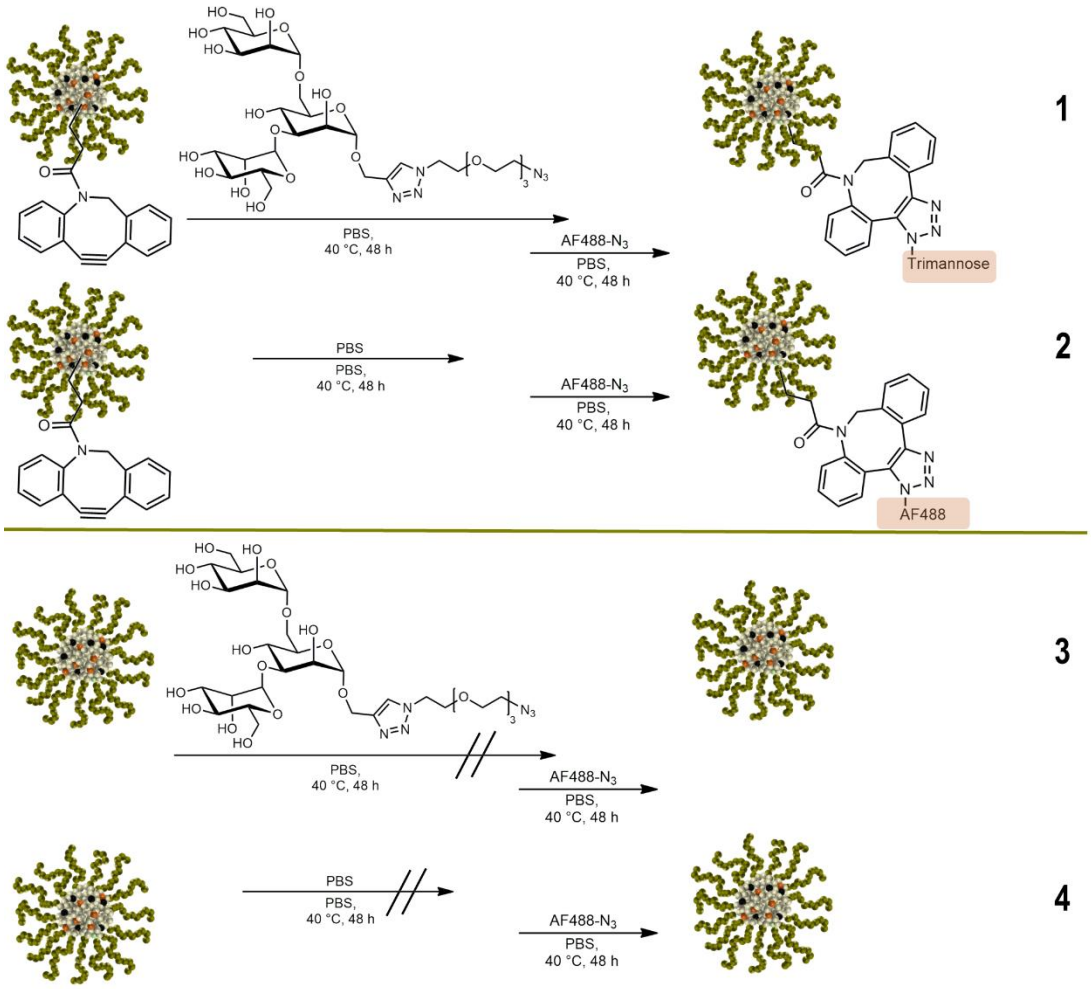

Figure S38: Scheme for stepwise preparation of azide-trimannose- or AF488-azide-conjugated DBCO nanogels (NG DBCO) or corresponding control nanogels (NG) in PBS at 40 °C for four days.

For targeting of the macrophage mannose receptor (MMR) azide-containing trimannose was conjugated to the DBCO nanogel (NG DBCO). Therefore, a 2 mg DBCO nanogel or control nanogel (NG) solution was generated in 2 mL PBS. After sonication for 1.5 h 1 mg of the DBCO nanogel (0.091 µmol/0.273 µmol reactive DBCO groups, 1 eq) or control nanogel (0.104 µmol, 1 eq) were transferred into a new Eppendorf tube. The DBCO and control nanogel were treated with either azide-trimannose (304 µL of a 2 mg/mL stock solution in PBS, 0.819 µmol, 3 eq) or blank PBS (304 µL) and shaken for 48 h at 40 °C. Then, Alexa Fluor 488 azide (AF488 azide, 67.57 µL from a 5 mg/mL stock solution, 0.409 µmol, 1.5 eq) was added to all solutions and shaken for further 48 h at 40 °C protected from light. The resulted nanogels were purified

by repeated spin-filtration with a mixture of ethanol and 0.1 % ammonia containing water (3x) as well as millipore water. Successful conjugation was characterized by UV-Vis spectroscopy and fluorescence intensity measurement.

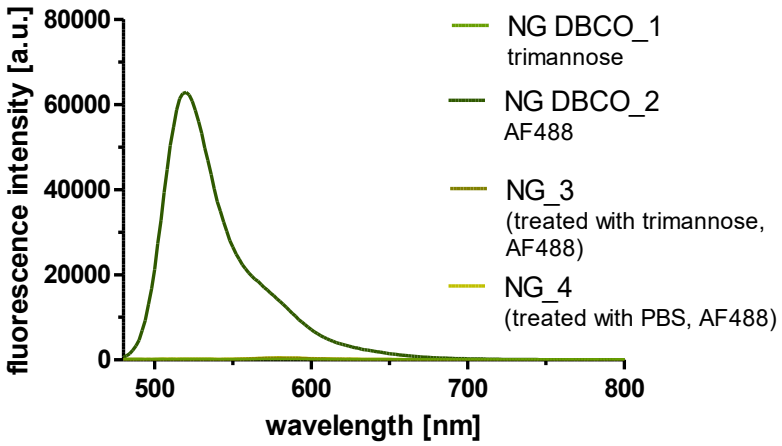

Figure S39: Fluorescence intensity spectra (excitation at 450 nm) of azide-trimannose or AF488-azide-labeled DBCO nanogels and corresponding control nanogels.

DBCO Nanogel Drug Conjugation by Covalent Attachment of IMDQ or IMDQ-Me to the Azide 2-Propoinic-3-Methylmaleic Anhydride Linker

Immune Stimulatory Drug Imidazoquinoline IMDQ Modification by Methylation

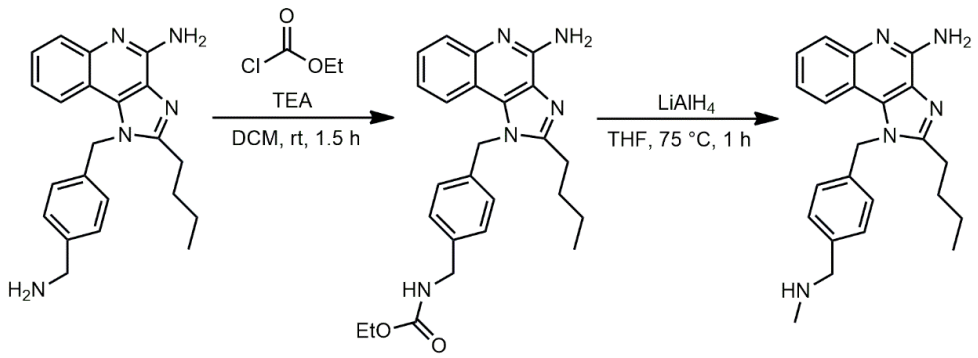

Figure S40: Synthesis of 2-butyl-1-(4-((methylamino)methyl)benzyl)-1H-imidazo[4,5-c]quinolin-4-amine (IMDQ-Me).

IMDQ-Me was synthesized as previously reported.[11]

^{1}H NMR (700 MHz, DMSO-d$_6$): δ (ppm) = 7.78 (d, J = 8.8 Hz,1H, **a**), 7.57 (d, J = 8.8 Hz, 1H, **b**), 7.37 (m, 3H, **c+d**), 7.01 (m, 3H, **e+f**), 6.53 (s, 2H, **g**), 5.85 (s, 2H, **h**), 3.73 (s, 2H, **i**), 2.90 (m, 2H, **j**), 2.30 (s, 3H, **k**), 1.70 (m, 2H, **l**), 1.38 (m, 2H, **m**), 1.23 (s, 1H, **n**), 0.86 (t, 3H, **o**).

^{13}C NMR (176 MHz, DMSO-d$_6$): δ (ppm) = 153.68 (**a**), 151.82 (**b**), 144.91 (**c**), 135.89 (**d**), 132.95 (**e**), 129.24 (**f**), 126.57-125.60 (**g-k**), 120.95 (**l**). 120.19 (**m**), 114.68 (**n**), 53.47 (**o**), 47.96 (**p**), 34.50 (**q**), 29.71 (**r**), 26.34 (**s**), 21.95 (**t**), 13.83 (**u**).

ESI-MS [m/z] = 374.24 $[M+H]^+$ (calc. 374.49).

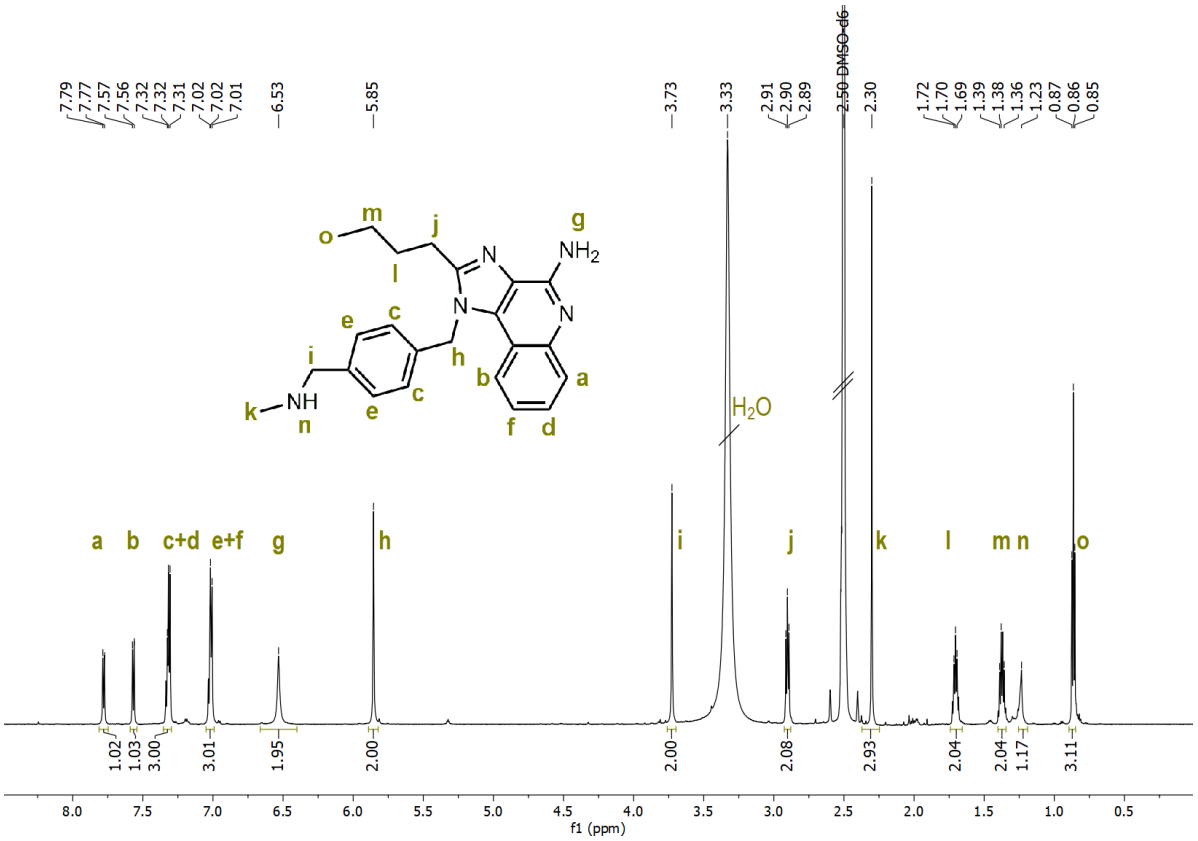

Figure S41: ^{1}H NMR spectrum (700 MHz) of 2-butyl-1-(4-((methylamino)methyl)benzyl)-1H-imidazo[4,5-c]quinolin-4-amine (IMDQ-Me) in DMSO-d$_6$.

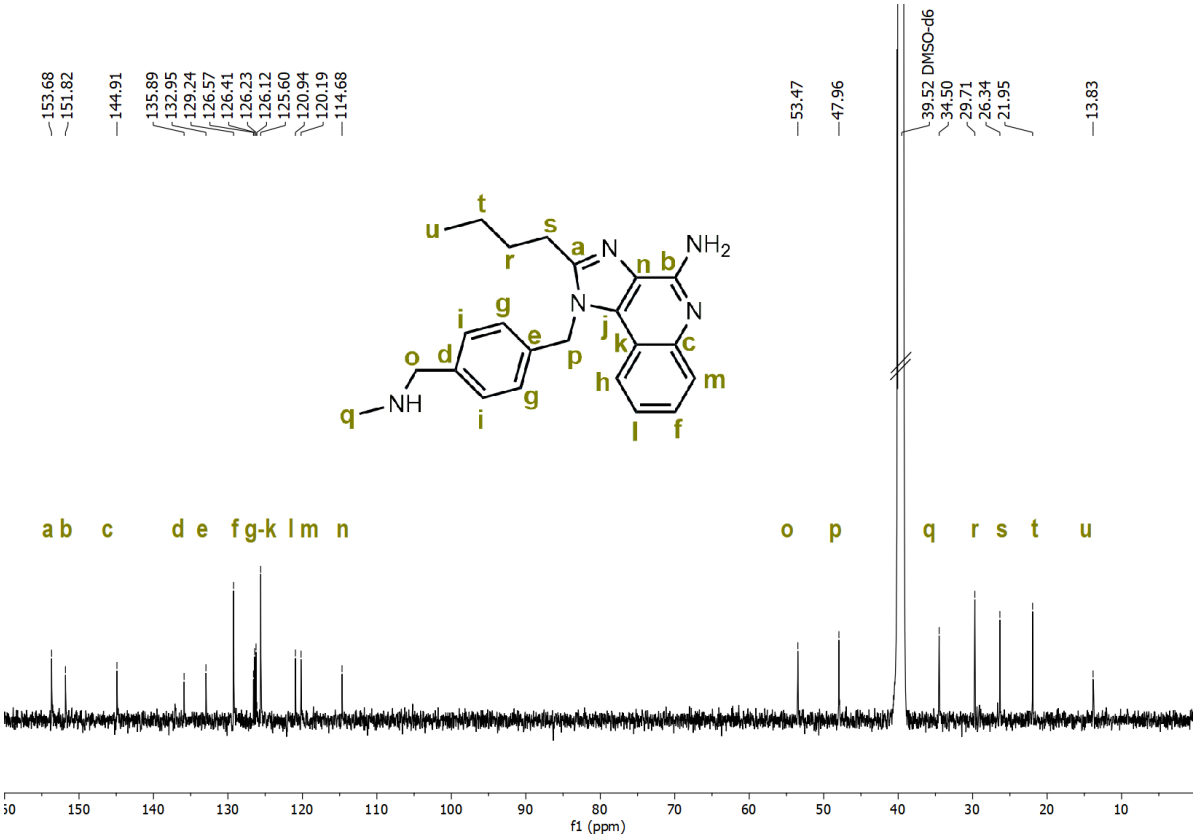

Figure S42: ^{13}C NMR spectrum (700 MHz) of 2-butyl-1-(4-((methylamino)methyl)benzyl)-1H-imidazo[4,5-c]quinolin-4-amine (IMDQ-Me) in DMSO-d_6.

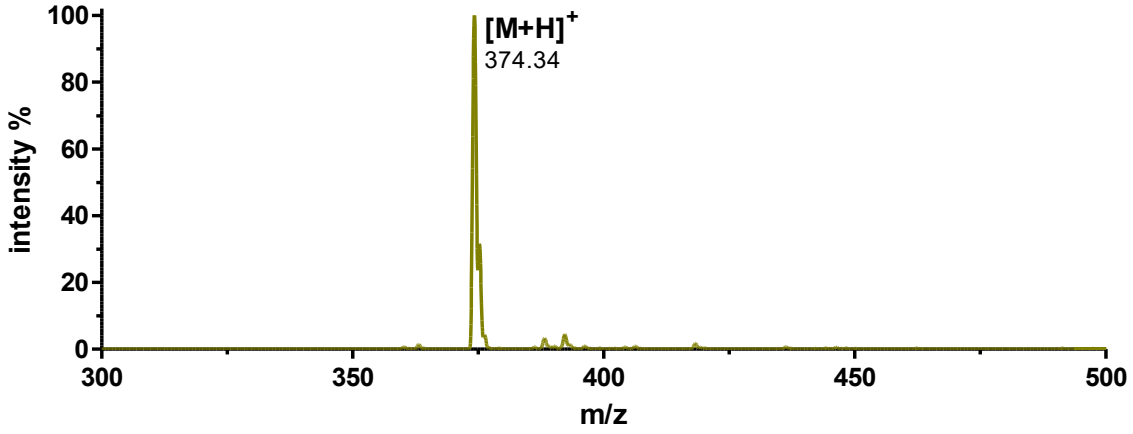

Figure S43: ESI-MS spectrum of 2-butyl-1-(4-((methylamino)methyl)benzyl)-1H-imidazo[4,5 c]quinoline-4-amine (IMDQ-Me) in MeOH (positive ion mode).

pH-Reversible IMDQ-Me Conjugation to the Azide 2-Propionic-3-Methylmaleic Anhydride Linker

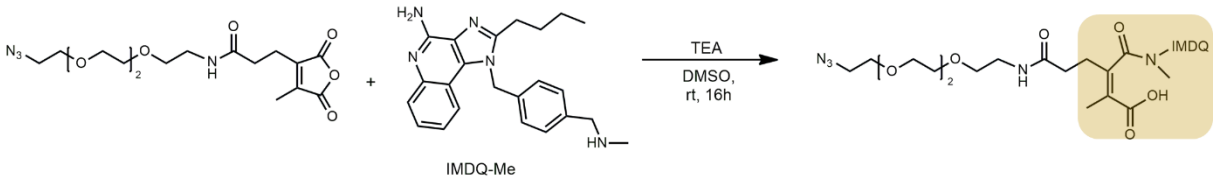

Figure S44: Schematic reaction of the azide 2-propionic-3-methylmaleic anhydride linker with IMDQ-Me in DMSO for 16 h.

7.5 mg of the azide-containing 2-propionic-3-methylmaleic anhydride linker (0.02 mmol, 1 eq) was weighted into two oven-dried Schlenk tubes and dissolved in 0.3 mL DMSO-d_6 under nitrogen atmosphere. TEA (2x8.11 µL, 0.058 mmol, 3 eq) was dropped to the solution, followed by the addition of IMDQ-Me (14.57 mg, 0.039 mmol, 2 eq). The reaction mixture was allowed to stir at room temperature overnight. The drug-conjugated linker was characterized by ^{1}H NMR measurement.

^{1}H NMR (400 MHz, DMSO-d_6): δ (ppm) Linker-IMDQ-Me = 7.86-7-76 (m, 1H, **a**), 7.63-7-54 (m, 1H, **b**), 7.37-7.22 (m, 3H, **c+d**), 7.10-6.91 (m, 3H, **e+f**), 6.66 (s, 2H, **g**), 5.84 (d, 2H **h**), 3.61-3.44 (m, 12H, **i+j**), 3.43-3.33 (m, 4H, **k**), 3.21-3.11 (m, 2H, **l**), 2.89 (t, *J* = 7.7 Hz, 2H, **m**), 2.64 (s, 3H, **n**), 2.43-2.36 (m, 2H, **o**), 2.22-2.12 (m, 2H, **p**) 1.78 (m, 3H, **q**), 1.73-1.64 (m, 2H, **r**), 1.43-1-30 (m, 3H, **s**), 0.84 (m, 3H, **t**).

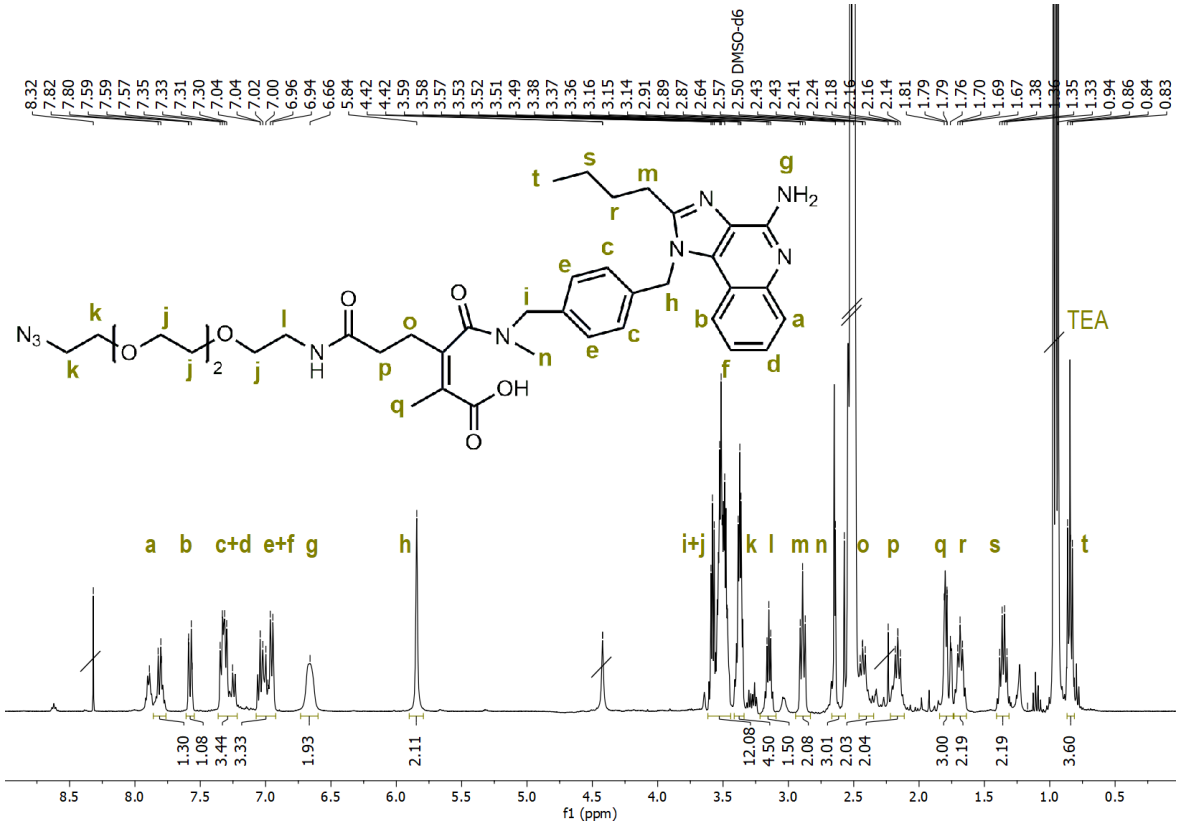

Figure S45: ^{1}H NMR spectrum (400 MHz) of IMDQ-Me-conjugated azide 2-propionic-3-methylmaleic anhydride linker in DMSO-d_6.

DBCO Nanogel Drug Loading by Click Reaction with IMDQ-Me Conjugated Azide Linker

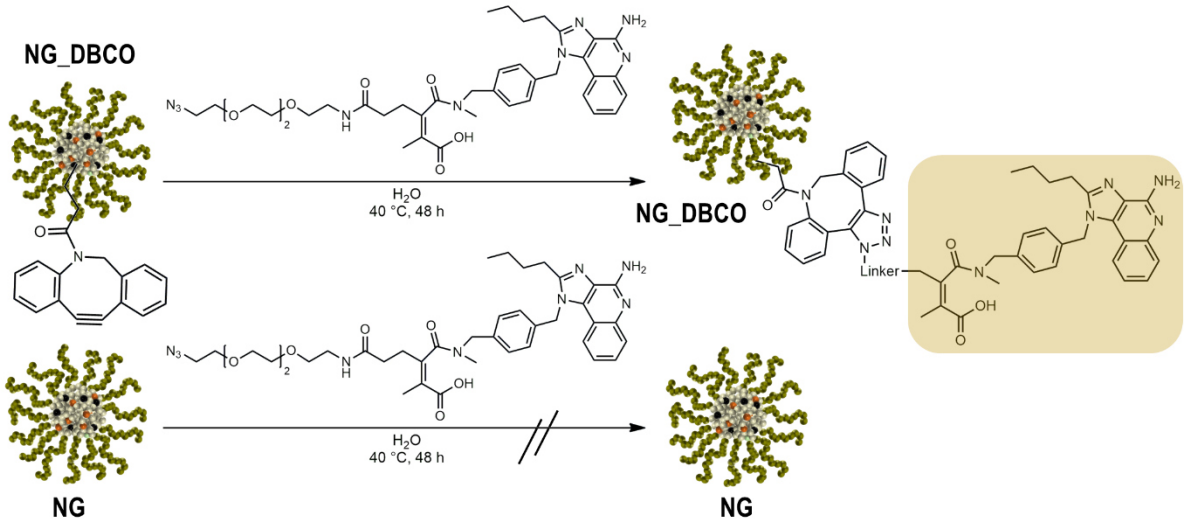

Figure S46: Schematic reaction of DBCO nanogel (NG DBCO) with IMDQ-Me-conjugated azide 2-propionic-3-methylmaleic anhydride linker in water supplemented with 0.1% NH_3 for 48 h.

For the pH-reversible drug-loading of DBCO nanogels IMDQ-Me-conjugated azide 2-propionic-3-methylmaleic anhydride linker was conjugated to the DBCO nanogel

(NG_DBCO). Therefore, 1.0 mg DBCO nanogel (0.091 µmol/0.273 µmol reactive DBCO units, 1 eq) or control nanogel (NG, 1mg, 0.104 µmol, 1 eq) were dissolved in 1 mL water supplemented with 0.1% ammonia and sonication for 1.5 h. IMDQ-Me-conjugated azide 2-propionic-3-methylmaleic anhydride linker (74.78 µL from a 8 mg/mL stock solution in DMSO, 0.819 µmol, 3 eq) was added to both solutions and shaken for 48 h at 40 °C protected from light. Finally, the nanogel solutions were purified by repeated spin-filtration (MWCO 10000 g/mol) with millipore water containing 0.1 % ammonia. The resulting nanogels were characterized by UV-Vis and DLS measurement.

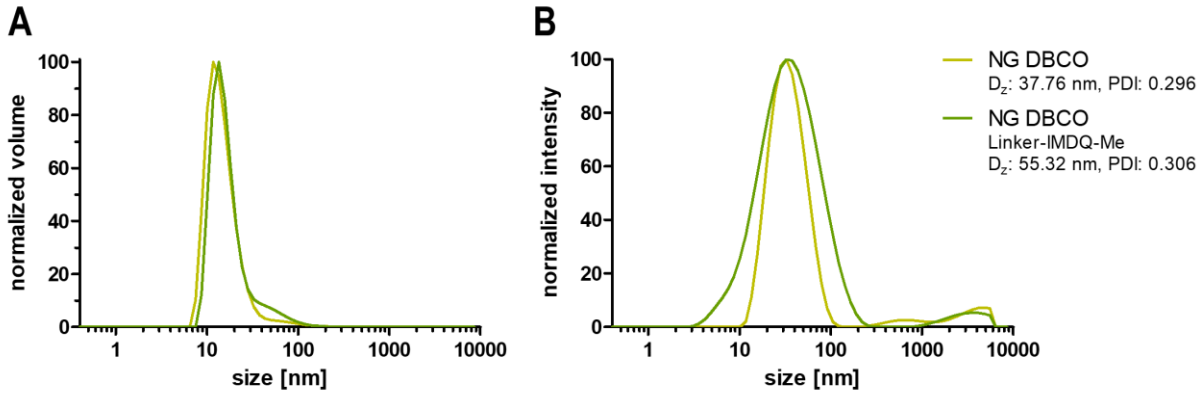

Figure S47: DLS measurement of the corresponding DBCO nanogels in water supplemented with 0.1% NH_3 showing the volume size (A) and intensity size distribution (B).

Determination of IMDQ-Me Drug Loading by UV-Vis Characterization

In order to investigate the IMDQ-Me drug load to the DBCO nanogel standard curves ranging from 0.1 to 0.0031 mg/mL were measured by UV-Vis. For estimation free drug stock solutions (10 mg/mL) were diluted in PBS and characterized by UV-Vis measurement. According to previous reports and adjusted equations the drug load to the nanogel could be evaluated.[8] The free drug showed a high absorbance maximum at 322 nm, while it shifted to 324 nm in case of the drug loaded nanogels.

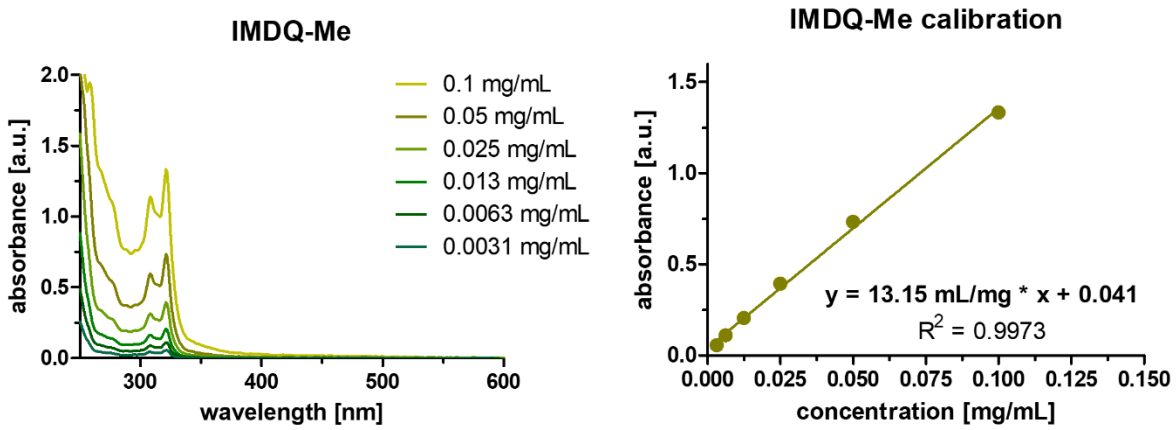

Figure S48: UV-Vis spectra of IMDQ-Me at different concentrations in PBS (left) and the corresponding calibration curve (right).

Calculation of the IMDQ-Me drug load to the NG DBCO:

$$X = \frac{(\Delta A - b)}{m - (A_{empty} / c)}$$

$X = 0.016 / 0.5$ mg/mL

$X =$ **3.1 wt%**

$\mathbf{\Delta A} = A_{max}$ (IMDQ-Me DBCO NG) $- A_{max}$ (DBCO NG)
$= 0.447 - 0.207 = 0.240$

$\mathbf{b} = 0.041$

$\mathbf{m} = 13.15$ mL/mg

$\mathbf{A_{empty}} = 0.207$

$\mathbf{c} = 0.5$ mg/mL

In vitro Experiments

Determination of Trimannose DBCO Nanogel Cell Uptake in CHO$^{MMR+/-}$ Cells by Flow Cytometry (FACS)

To investigate the trimannose-conjugated nanoparticle uptake by flow cytometry CHO$^{MMR+/-}$ cells were seeded into 24-well plates in a density of 250000 cells/well in 900 µL cell culture medium and incubated overnight at 37 °C for cell sedimentation and adhesion to the bottom of the well. Afterwards, 100 µL DBCO nanogel or control nanogel samples in PBS were added to each well (yielding a final concentration of 10 µg/mL). All samples were run in triplicates and incubated for 24 h at 37 °C. Next, the cell culture medium was aspired, cells were washed with 1 mL PBS and incubated with 500 µL dissociation buffer for 15 minutes at 37 °C. The cells were detached and resulting suspensions were then transferred into Eppendorf tubes on ice and centrifuged at 300 g for 10 minutes at 5 °C. The supernatants were aspired, and the cell pellets were resuspended in 200 µL PBS. Prior to flow cytometry analysis on a BD Accuri C6

(BD Biosciences) the cell suspensions were stored on ice. All data were processed by FlowJo Software.

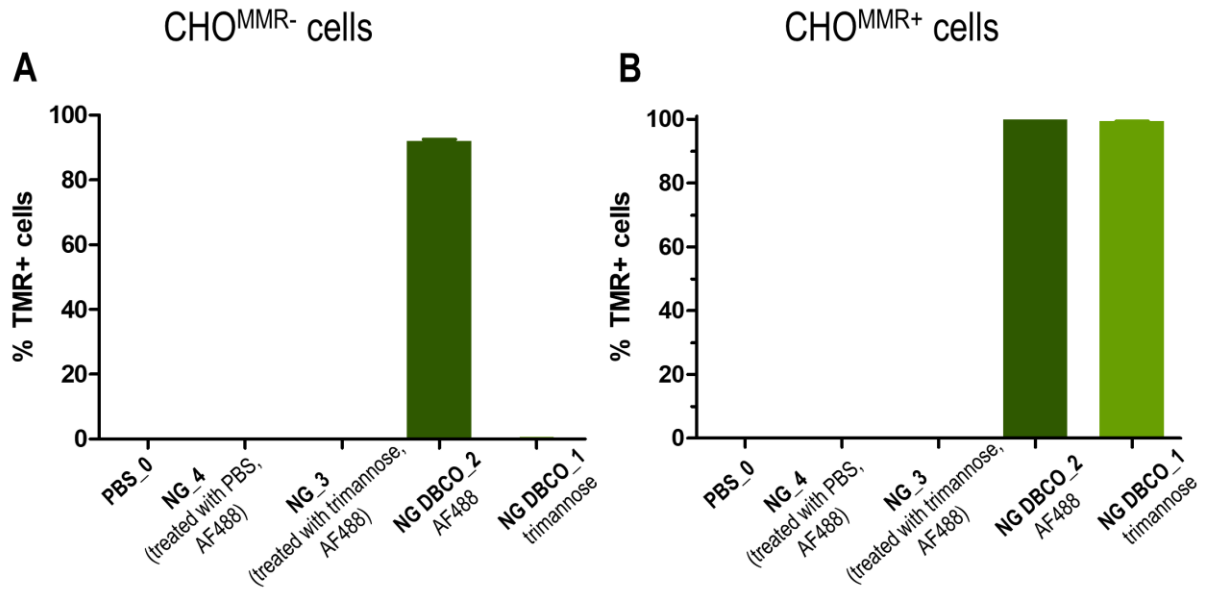

Figure S49: Result of the flow cytometry analysis of CHO$^{MMR+/-}$cells incubated with trimannose- or AF488-labeled DBCO nanogels (NG DBCO_1,2) or the corresponding nanogels without DBCO (NG_3,4) at 10 µg/mL or PBS as control for 24 h. Demonstrating the percentage of TMR positive cells (% TMR+ cells) (n=3).

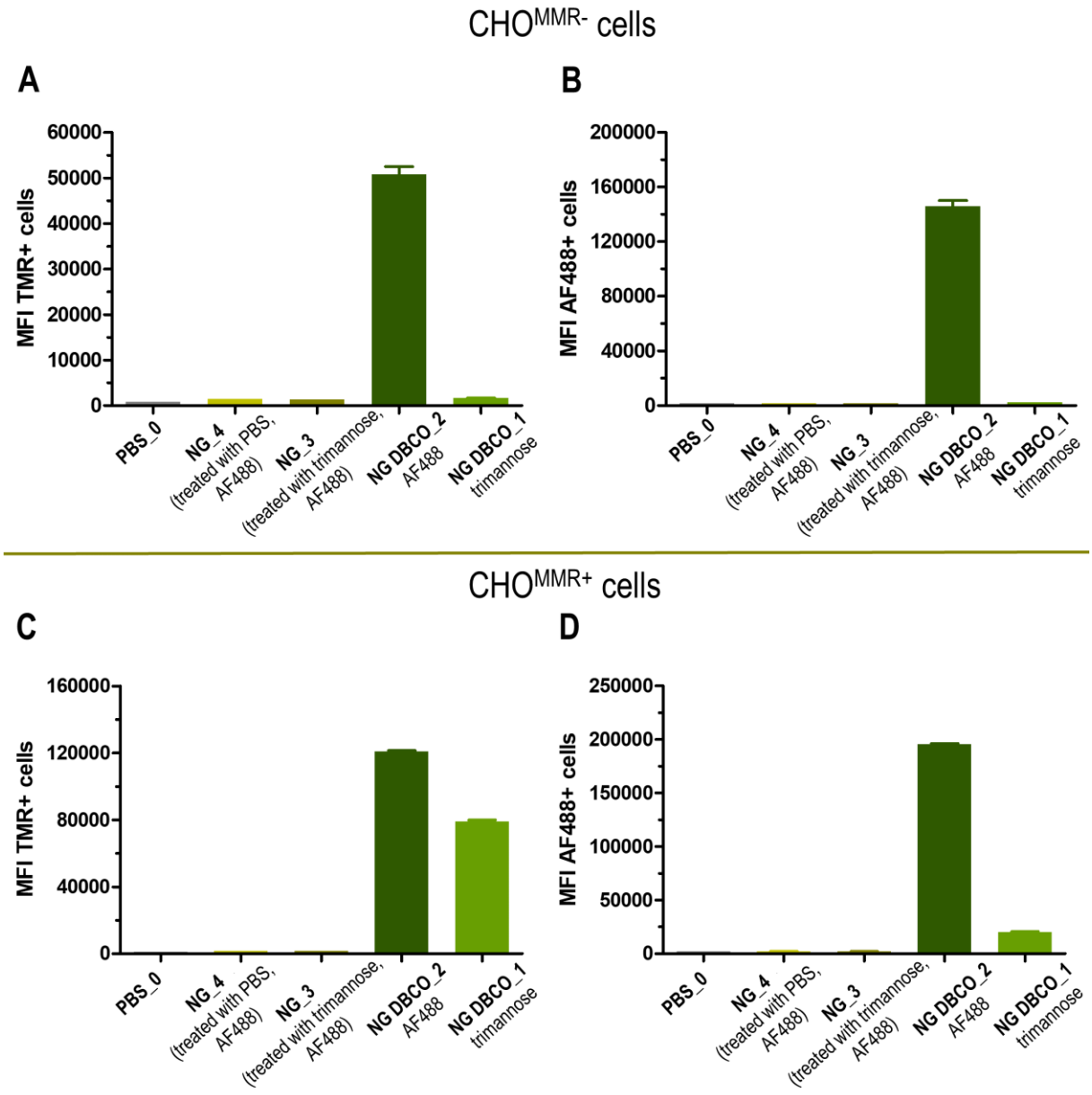

Figure S50: Flow cytometry characterization of CHO$^{MMR+/-}$cells incubated with PBS (control), trimannose- or AF488-conjugated DBCO nanogels (NG DBCO_1,2) or the corresponding nanogels without DBCO (NG_3,4) at 10 µg/mL for 24 h showing the mean fluorescence intensity (MFI) of TMR or AF488 positive cells (MFI TMR+ or AF488+ cells) (n=3).

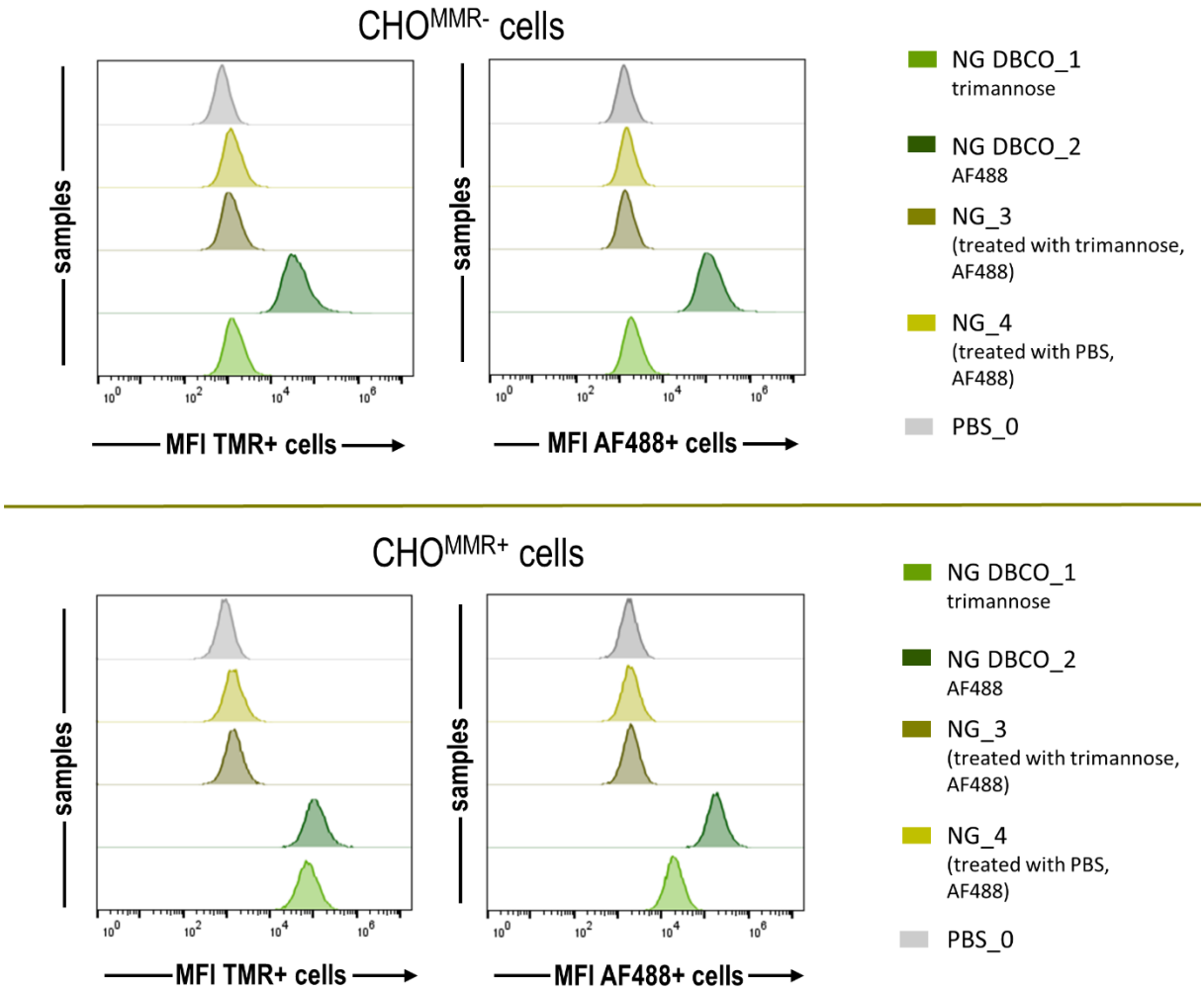

Figure S51: Flow cytometry analysis of CHO$^{MMR+/-}$cells incubated with PBS (control), trimannose- or AF488-conjugated DBCO nanogels (NG DBCO_1,2) or the corresponding nanogels without DBCO (NG_3,4) at 10 µg/mL for 24 h showing the histograms of TMR or AF488 positive cells (MFI TMR+ or AF488+ cells) (n=3).

Fluorescence Confocal Laser Scanning Microscopy Imaging

CHO$^{MMR+/-}$ cells were seeded in an Ibidi µ-slide 8-well chamber (50000 cells/well in 180 µL culture medium) and incubated overnight for adhesion. Then, 20 µL DBCO nanogel or control nanogel in PBS (total concentration of 10 µg/mL) was added to the cells. After incubation for 24 h at 37 °C the cell medium was aspired, and cells were washed with PBS (3x). 200 µL 4% paraformaldehyde solution was added and allowed to fixate for 15 min at 37 °C. Next, cells were washed three times with PBS and cell nuclei were stained with 125 µL 4′,6-diamidino-2-phenylindole (DAPI) (80 µg/mL in PBS) for 20 min at room temperature protected from light. Finally, cells were washed with PBS three times and stored under aqueous mounting medium. All cells were analyzed on a STELLARIS 8 Leica DMi8 confocal microscope (Wetzlar, Germany) with a HC PL APO CS2 40x/1.25 GLYC oil immersion objective. The images were processes by Leica Application Suite X 3.7.4.23463 of the Leica Microsystem.

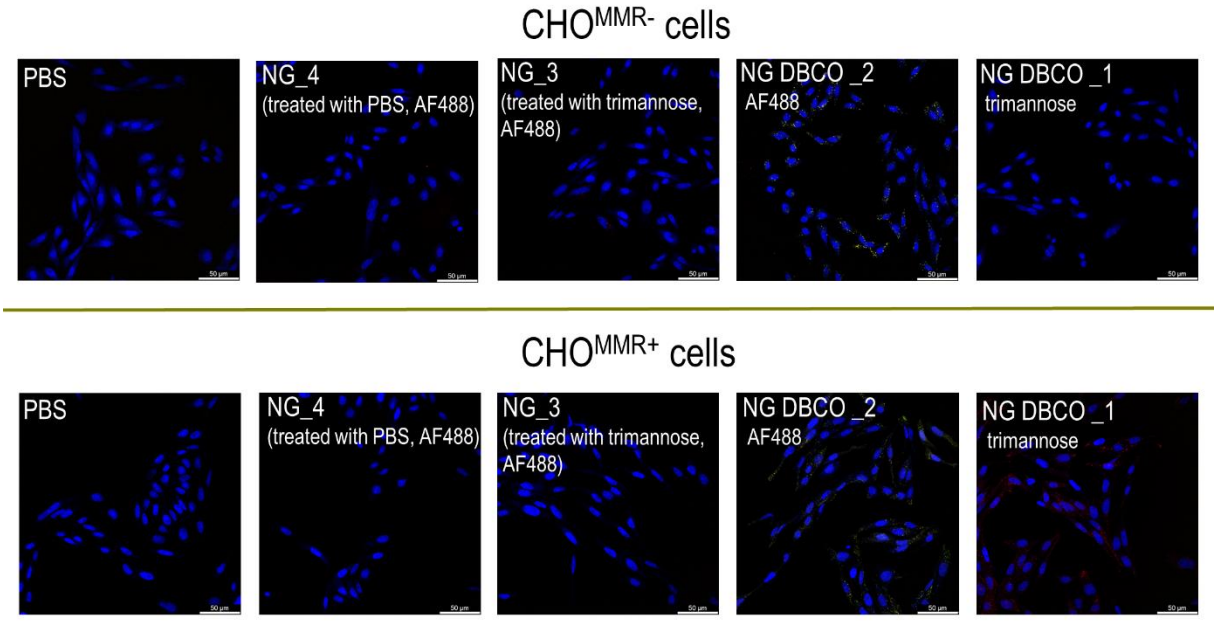

Figure S52: Fluorescence confocal microscopy images of CHO$^{MMR+/-}$cells incubated with trimannose- or AF488-DBCO nanogels (NG DBCO_1,2) or the corresponding nanogels without DBCO (NG_3,4) at 10 µg/mL or PBS as control for 24 h (blue: nuclei stained with Hoechst 33258, red: TMR-labeled nanogel, yellow:AF488-conjugated nanogel).

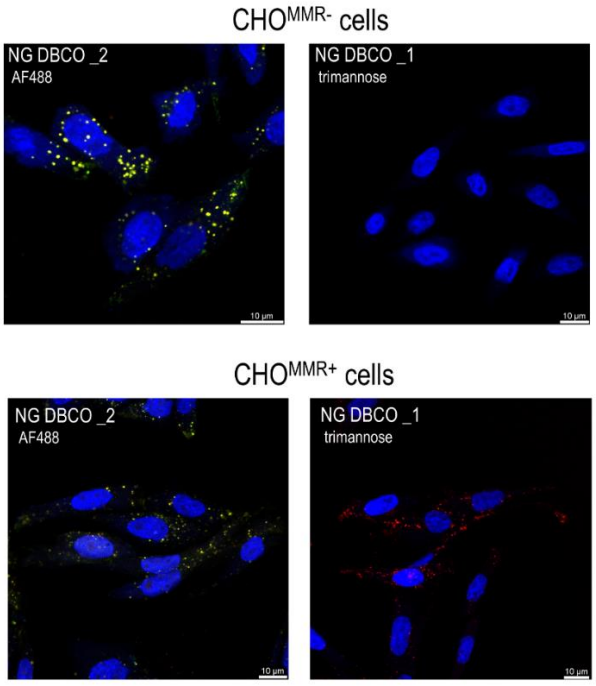

Figure S53: Fluorescence confocal microscopy zoom in images of CHO$^{MMR+/-}$cells incubated with trimannose- or AF488-conjugated DBCO nanogels (NG DBCO_1,2) or the corresponding nanogels without DBCO (NG_3,4) at 10 µg/mL for 24 h (blue: nuclei stained with Hoechst 33258, red: TMR-labeled nanogel, yellow:AF488-conjugated nanogel).

Determination of RAW-Dual Macrophages Cell Viability by MTT Assay

RAW-Dual macrophages were seeded into a 96-well plate (90000 cells/well in 180 µL) and incubated for 16 h at 37 °C for adhesion. Then, 20 µL of the linker-IMDQ- or linker-IMDQ-Me-loaded DBCO nanogels, corresponding nanogels without DBCO, the soluble drugs and PBS (positive control) or DMSO (negative control) were added to the cells at given concentrations (n=4). After incubation for 24 h at 37 °C, 30 µL of a 2 mg/mL 3-(4,5-dimethylthiazol-2-yl)-2,5-diphenyltetrazolium bromide solution in PBS was added to each well, followed by incubation for 1.5 h at 37 °C. Next, 100 µL of a 10% m/v SDS/0.01 M HCl solution was added to the cells to dissolve formed formazan crystals by incubation overnight at 37 °C. Resulting cell viability was determined by UV-Vis measurement at 570 nm using a plate reader.

RAW-Dual Macrophage TLR Reporter Assay (QUANTI-Blue Assay)

To analyze the TLR receptor stimulation by IMDQ-Me-loaded DBCO nanogels, TLR reporter assay was performed on RAW-Dual macrophages as recommended by the manufacturer (InvivoGen). The IMDQ-induced activation of NF-κB/AP-1 was detected by the secretion of embryonic alkaline phosphatase (SEAP). RAW-Dual cells were seeded as previously described for MTT assay. Next, 20 µL of the respective nanogel solution at the given IMDQ-Me concentrations was added to each well and incubation for 24 h at 37 °C. Afterwards, 50 µL of the supernatant of each well was transferred into a new 96-well plate and the SEAP levels was determined by QUANTI-Blue Assay (Invivogen). Therefore, 150 µL QUANTI-Blue solution was added and cells were incubated for 2 h at 37 °C, followed by absorbance measurement at 620 nm using a plate reader. All experiments were performed at n=4.

Additional References

(1) Bolli, E.; Scherger, M.; Arnouk, S. M.; Pombo Antunes, A. R.; Straßburger, D.; Urschbach, M.; Stickdorn, J.; De Vlaminck, K.; Movahedi, K.; Räder, H. J.; Hernot, S.; Besenius, P.; Van Ginderachter, J. A.; Nuhn, L. Targeted Repolarization of Tumor-Associated Macrophages via Imidazoquinoline-Linked Nanobodies. *Adv. Sci.* **2021**, *8* (10), 1–12. https://doi.org/10.1002/advs.202004574.

(2) Scherger, M.; Pilger, Y. A.; Stickdorn, J.; Komforth, P.; Schmitt, S.; Arnouk, S. M.; Lebegge, E.; Koynov, K.; Räder, H. J.; Van Ginderachter, J. A.; Nuhn, L. Self-Immolative Nanobody-Cysteine Residue Modification for Controlled Immunodrug Delivery. *Adv. Ther.* **2023**, *6* (2300076), 1–8. https://doi.org/10.1002/adtp.202300076.

(3) Scherger, M.; Pilger, Y. A.; Stickdorn, J.; Komforth, P.; Schmitt, S.; Koynov, K.; Räder, H. J.; Nuhn, L. Efficient Self-Immolative RAFT End Group Modification for Macromolecular Immunodrug

Delivery. *Biomacromolecules* **2023**, *24* (5), 2380–2391. https://doi.org/10.1021/acs.biomac.3c00239.

(4) Krumb, M.; Frey, M. L.; Langhanki, J.; Forster, R.; Kowalczyk, D.; Mailänder, V.; Landfester, K.; Opatz, T. Multivalency Beats Complexity: A Study on the Cell Uptake of Carbohydrate Functionalized Nanocarriers to Dendritic Cells. *Cells* **2020**, *9* (9). https://doi.org/10.3390/cells9092087.

(5) Wagener, K.; Bros, M.; Krumb, M.; Langhanki, J.; Pektor, S.; Worm, M.; Schinnerer, M.; Montermann, E.; Miederer, M.; Frey, H.; Opatz, T.; Rösch, F. Targeting of Immune Cells with Trimannosylated Liposomes. *Adv. Ther.* **2020**, *3* (6), 1–10. https://doi.org/10.1002/adtp.201900185.

(6) Nuhn, L.; Hirsch, M.; Krieg, B.; Koynov, K.; Fischer, K.; Schmidt, M.; Helm, M.; Zentel, R. Cationic Nanohydrogel Particles as Potential SiRNA Carriers for Cellular Delivery. *ACS Nano* **2012**, *6* (3), 2198–2214. https://doi.org/10.1021/nn204116u.

(7) Stickdorn, J.; Stein, L.; Arnold-Schild, D.; Hahlbrock, J.; Medina-Montano, C.; Bartneck, J.; Ziß, T.; Montermann, E.; Kappel, C.; Hobernik, D.; Haist, M.; Yurugi, H.; Raabe, M.; Best, A.; Rajalingam, K.; Radsak, M. P.; David, S. A.; Koynov, K.; Bros, M.; Grabbe, S.; Schild, H.; Nuhn, L. Systemically Administered TLR7/8 Agonist and Antigen-Conjugated Nanogels Govern Immune Responses against Tumors. *ACS Nano* **2022**, *16* (3), 4426–4443. https://doi.org/10.1021/acsnano.1c10709.

(8) Nuhn, L.; Vanparijs, N.; De Beuckelaer, A.; Lybaert, L.; Verstraete, G.; Deswarte, K.; Lienenklaus, S.; Shukla, N. M.; Salyer, A. C. D.; Lambrecht, B. N.; Grooten, J.; David, S. A.; De Koker, S.; De Geest, B. G. PH-Degradable Imidazoquinoline-Ligated Nanogels for Lymph Node-Focused Immune Activation. *Proc. Natl. Acad. Sci. U. S. A.* **2016**, *113* (29), 8098–8103. https://doi.org/10.1073/pnas.1600816113.

(9) Takemoto, H.; Miyata, K.; Hattori, S.; Ishii, T.; Suma, T.; Uchida, S.; Nishiyama, N.; Kataoka, K. Acidic PH-Responsive SiRNA Conjugate for Reversible Carrier Stability and Accelerated Endosomal Escape with Reduced IFNα-Associated Immune Response. *Angew. Chemie - Int. Ed.* **2013**, *52* (24), 6218–6221. https://doi.org/10.1002/anie.201300178.

(10) Ding, Y.; Du, C.; Qian, J.; Zhou, L.; Su, Y.; Zhang, R.; Dong, C. M. Tumor PH and Intracellular Reduction Responsive Polypeptide Nanomedicine with a Sheddable PEG Corona and a Disulfide-Cross-Linked Core. *Polym. Chem.* **2018**, *9* (25), 3488–3498. https://doi.org/10.1039/c8py00579f.

(11) Heck, A. G.; Stickdorn, J.; Rosenberger, L. J.; Scherger, M.; Woller, J.; Eigen, K.; Bros, M.; Grabbe, S.; Nuhn, L. Polymerizable 2-Propionic-3-Methylmaleic Anhydrides as a Macromolecular Carrier Platform for PH-Responsive Immunodrug Delivery. *J. Am. Chem. Soc.* **2023**, *145* (50), 27424–27436. https://doi.org/10.1021/jacs.3c08511.

Chapter V: Restoring the pH-Responsiveness for Amine-Conjugated 2-Propionic-3-Methylmaleic Anhydride Linkers

The following chapter was submitted to a peer-reviewed journal and describes the further analysis of the bifunctional linker based on 2-propionic-3-methylmaleic anhydride for the pH-reversible conjugation of amine-bearing systems and the solvent-dependent sensitivity for side-reactions. I synthesized the pH-responsive bifunctional linker and used it for several primary and secondary amine conjugations in different solvents. Then, I investigated their pH reversibility and the competing formation of irreversible imide structures. The manuscript was prepared by me with feedback from all co-authors.

RESTORING THE PH-RESPONSIVENESS FOR AMINE-CONJUGATED 2-PROPIONIC-3-METHYLMALEIC ANHYDRIDE LINKERS

Alina G. Heck[1,2] and Lutz Nuhn[1,2]*

Dedicated to Professor Frank Würthner on the occasion of his 60th birthday.

1: Chair of Macromolecular Chemistry, Julius-Maximilians-Universität Würzburg, 97070 Würzburg, Germany

2: Max Planck Institute for Polymer Research, 55128 Mainz, Germany

*: corresponding author: Prof. Dr. Lutz Nuhn (E-mail: lutz.nuhn@uni-wuerzburg.de)

Keywords: 2-propionic-3-methylmaleic anhydride linker, pH reversibility, amidation, dynamic covalent bond.

Abstract

The controlled pH-reversible conjugation of amine-functionalized molecules to nano-sized carrier systems is a promising achievement to enhance the efficacy of small molecular drugs at the target site. Various pH-responsive structures, such as ketals or hydrazones are accessible for drug delivery but suffer from high pH-gradients and elaborative modifications. The latter often further affects the specific activity of the released drugs. In this study, we establish the synthesis of a highly pH-sensitive bifunctional linker based on 2-propionic-3-methylmaleic anhydride. The underlying chemical structure enables the pH-reversible conjugation of different amines, although the attachment of primary amines competes with the formation of a pH-resistant imide structure. Remarkably, by analysis of the pH-reversible amidation profile in different solvents, the ring-opened amide structures are generated with primary amines in diethyl ether. The formed conjugates rapidly phase separate and preserve the pH sensitivity of the linker system. Based on these findings, this manufacturing process is highly relevant in providing amine-conjugated 2-propionic-3-methylmaleic anhydride linkers and restoring their pH-responsiveness, particularly for primary amine-bearing drugs. This can pave their way for future applications, for instance, in nanomedicine.

Introduction

In recent years, a variety of inflammatory tissues have been addressed by passively or actively targeted drug delivery systems. They can improve the therapeutic efficacy while reducing undesired side-effects. Thereby, the addition of stimuli-responsive delivery elements significantly improved the application of targeted nanocarriers, particularly in addressing infectious diseases and cancer. For instance, the incorporation of stimuli-responsive linkers afforded active carrier systems that became sensitive to specific physiological triggers and released drugs selectively at the target sites.[1–4] Among a variety of stimuli-responsive systems, pH-triggered linkers represent one of the chemically most relevant applied stimuli, as several tissues and cellular regions display (patho-)physiologically relevant pH-gradients, such as the tumor microenvironment (pH 6.5-6.9) or endosomes and lysosomes (pH 4.5-5.5). After reaching the acidified areas, the conjugated therapeutics are released by distinct chemical cues following charge conversion, pH-sensitive crosslinkers or cleavable linker systems.[5–9]

One potent category of pH-dependent structures are disubstituted maleic anhydride based-linkers. These structures exhibit a remarkable pH sensitivity (5.5-6.8) similar to the tumor microenvironment, primarily attributed to the presence of a *cis*-oriented double bond.[1,10] After direct covalent attachment of amine-containing small molecules, ring-opened anhydrides provide a negatively charged carboxylate group. This can become beneficial for the charge conversion of corresponding molecules and further traceless hydrolysis of the amide bond under mild acidic conditions. Therefore, disubstituted maleic anhydrides can be applied as multifunctional pH-labile linkers to overcome shortcomings of small molecular drugs or provide advantageous charge conversion properties to biomolecules and nanocarriers.[6,11–13] However, primary amine-mediated conjugation reactions with disubstituted maleic anhydride structures are not sufficiently pH-reversible, affording most likely the pH-irreversible imide structure.[14] Although many publications report on the successful pH-reversible conjugation of primary amines to disubstituted maleic anhydride structures, only limited studies demonstrate the pH-sensitive profile of the generated conjugates or reveal the formation of the corresponding imide.[9,15,16]

By carefully choosing the bifunctional 2-propionic-3-methylmaleic anhydride linker with an additional azide group for bioorthogonal click chemistry, we recently verified that a pH-sensitive release can only be guaranteed for secondary amines, but not for primary amines, and we subsequently applied it for nanogel-mediated endosomal immunodrug delivery.[17] In this study, we now aimed at further investigating the pH reversibility of the anhydride system

for primary amines and were successfully able to restore it, depending on the reaction solvent during the fabrication process. When treated with fluorescent dyes bearing primary amines in DMSO, the bifunctional linker forms the corresponding imide systems, whereas functionalization in diethyl ether avouches the formation of regioisomer amides that can get released upon acidification (Figure 1). Our observations ensure how to control 2-propionic-3-methylmaleic anhydride amidation and restore their pH sensitivity for both primary and secondary amine functionalized cargos.

Results and Discussion

For the formulation of an azide-clickable and pH-reversible linker, 2-propionic-3-methylmaleic anhydride was converted in a two-step reaction by treatment with oxalyl chloride and 11-azido-3,6-9-trioxaundecan-1-amine (Figure S1). The resulting bifunctional linker was analyzed by ^{1}H and 2D NMR spectroscopy studies (Figure S2-S6) as well as IR-spectroscopy measurements (Figure S7). Next, the pH-reversible conjugation of primary and secondary amines was first verified in DMSO (Figure 1A-C and Figure S11).

In analogy to our previous studies[17], the reaction with the secondary amine-bearing fluorescent dye 4-nitro-7-piperazino-2,1,3-benzoxadiazole (NBD-PZ, Figure S8-S10) resulted in a pH-reversible conjugation to the linker system (Figure 1B), as indicated by the formation of two ring-opened regioisomers. While mass spectrometry revealed one adduct (Figure S12), the ^{1}H NMR spectrum provided two signals for the corresponding α-positioned methyl signals of the two regioisomers under neutral conditions. Upon treatment with TFA, they afforded again one signal corresponding to the anhydride structure (Figure 1B). In contrast, the reaction of 2-propionic-3-methylmaleic anhydride with the primary amine-containing fluorescent dye dansyl cadaverine afforded the formation of a pH-resistant imide system in DMSO. *Via* mass spectrometry, the adduct afforded a molecular weight that was reduced by 18 g/mol (Figure S12), and instead of two α-positioned methyl regioisomers only one signal was recorded by the ^{1}H NMR spectroscopy (Figure 1C). Furthermore, this compound did not provide any pH sensitivity, as no changes in the ^{1}H NMR spectrum could be detected even upon acidification (Figure 1C). Therefore, we investigated the feasibility for pH-sensitive amidation in alternative solvents and selected diethyl ether, in which the formed adducts immediately caused a phase separation by salt formation. Using analogous reaction conditions, benzylamine, dibenzylamine or *N*-methyl-piperazine were conjugated to the linker system and analyzed under neutral and acidic conditions (Figure 1A, D-E and Figure S14).

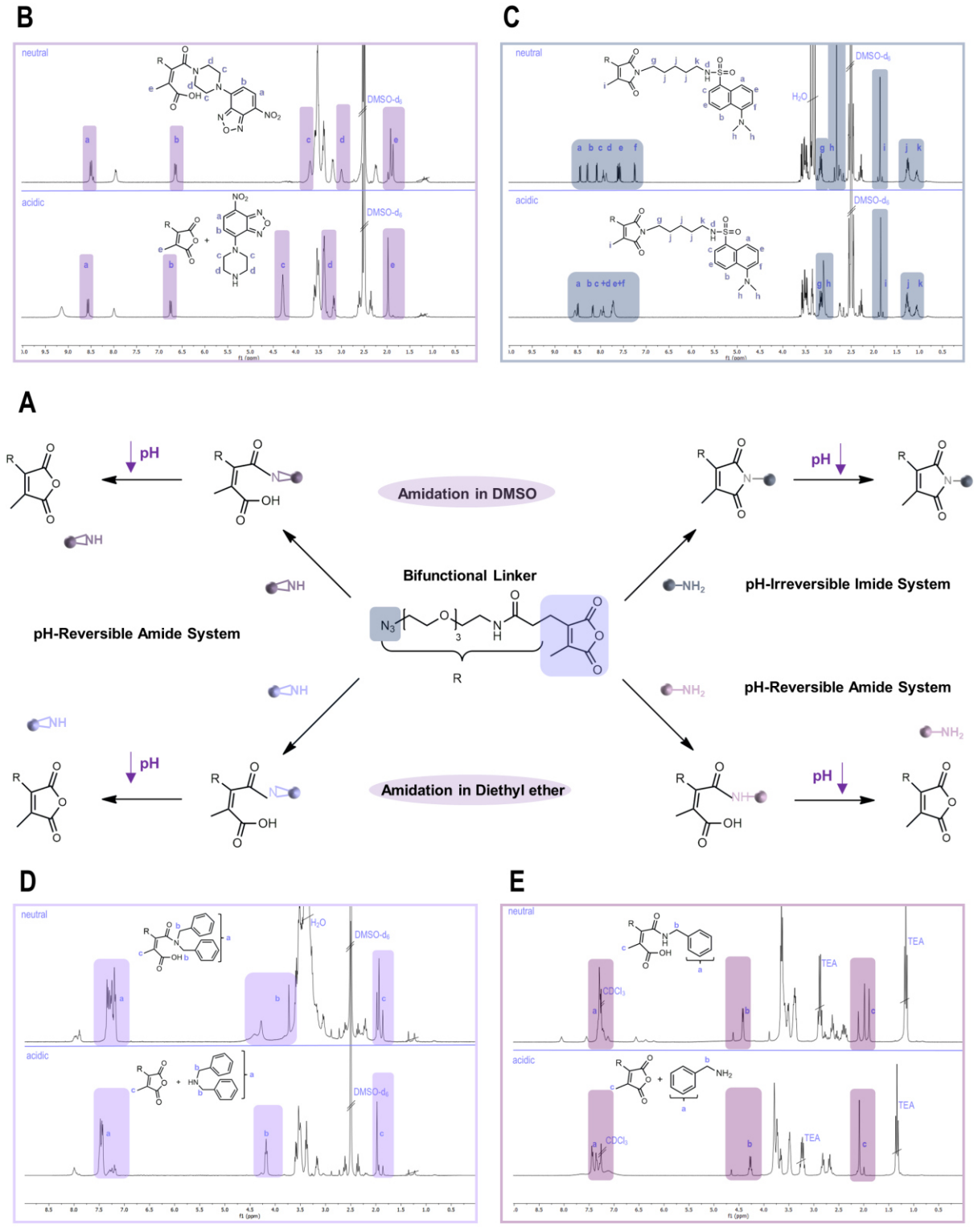

Figure 1. pH-reversible amidation profile of a synthesized bifunctional linker based on 2-propionic-3-methylmaleic anhydride. (**A**) Reaction scheme for the conversion of 2-propionic-3-methylmaleic anhydride with several primary or secondary amines in different solvents under neutral and acidic conditions. (**B**) ^{1}H NMR spectra of NDB-PZ-conjugated linker underlining the pH-reversible conjugation only for secondary amines in DMSO. (**C**) ^{1}H NMR spectra of dansyl cadaverine-modified linker under neutral and acidic conditions in DMSO, showing the loss of pH sensitivity by imide formation. (**D+E**) ^{1}H NMR analyses demonstrating the pH-reversible amidation with dibenzyl- and benzylamine in diethyl ether by providing two α-positioned methyl signals (c) of the two regioisomers that upon acidification become again one signal for the corresponding anhydride.

Remarkably, ^{1}H NMR spectroscopy and mass spectrometry revealed the successful pH-reversible amidation of benzylamine, dibenzylamine and *N*-methyl-piperazine. Respective ring-opened signals of the primary amine-modified structure could be identified by mass spectrometry and ^{1}H NMR spectroscopy measurements (Figure S15 - S18). Upon acidification, a significant shift was now evident upon acidification (Figure 1E) similar to the modification with secondary amine bearing dibenzylamine (Figure 1D).

Compared to the amidation reaction conditions of the primary amines in DMSO, the changed solubility properties in diethyl ether afforded the benzylamine-conjugated linker after anhydride ring opening to quickly phase separate as the corresponding triethylamine salt. This subsequently prevents the further conversion into the irreversible imide. In comparison, first amidation reactions in DMSO ensured high solubility of all conjugated products and, thus, resulted in ring closure and release of water. These contradictory reaction conditions show how the potential dynamic covalent bond properties of disubstituted maleic anhydride systems are also influenced by respective solvents.[15,18] Our findings emphasize the high sensitivity of our azide-clickable and pH-reversible linker based on 2-propionic-3-methylmaleic anhydride for the conjugation with primary and secondary amines. This conjugation can be finetuned by respective selective solvents in order to restore the linkers' pH sensitivity.

Conclusions

In summary, we reported on an azide-clickable and pH-reversible 2-propionic-3-methylmaleic anhydride-based linker platform that allows for the covalent conjugation of different amine functionalities. By careful analysis of the disubstituted maleic anhydride systems, the previously reported reaction conditions for primary amines yielded pH-resistant imides in DMSO. Towards their reversible conjugation with remaining pH sensitivity, amidations could also be conducted in diethyl ether. Interestingly, this approach did not only reveal fast conjugation with various amines, but it also conserved the pH reversibility for primary amines. Under these conditions the corresponding triethylamine salts phase separate from diethyl ether and prevent any further ring-closure reaction. Overall, 2-propionic-3-methylmaleic anhydride-based linkers demonstrate altering solubilities after amidation reaction in different solvents affecting the subsequent imide formation. In this regard, diethyl ether appears to be highly suitable for the reaction with primary amines in order to restore the linkers pH sensitivity and, thus, pave the way for these linker systems towards pH-reversible delivery of primary amine-containing drugs.

Author Contributions

The manuscript was written through contributions of all authors. All authors have given approval to the final version of the manuscript.

Notes

The authors declare no competing financial interest.

Acknowledgements

The authors' work was gratefully supported by the DFG through the Emmy Noether program, the CRC/SFB 1066 projects B03 and B04 and the CRC/TRR 225 project B08. Moreover, support by the BMBF Clusters4Futer curATime (projects curAIntervent and megATarget) is kindly acknowledged. AGH and LN would like to thank Manfred Wagner, Stefan Spang, Stephan Türk and Jutta Schnee for technical assistance during the analytical measurements. Additionally, Tanja Weil is gratefully acknowledged for providing access to excellent laboratory facilities.

References

(1) Fleige, E.; Quadir, M. A.; Haag, R. Stimuli-Responsive Polymeric Nanocarriers for the Controlled Transport of Active Compounds: Concepts and Applications. *Adv. Drug Deliv. Rev.* **2012**, *64* (9), 866–884.

(2) Schattling, P.; Jochum, F. D.; Theato, P. Multi-Stimuli Responsive Polymers-the All-in-One Talents. *Polym. Chem.* **2014**, *5* (1), 25–36.

(3) Ganta, S.; Devalapally, H.; Shahiwala, A.; Amiji, M. A Review of Stimuli-Responsive Nanocarriers for Drug and Gene Delivery. *J. Control. Release* **2008**, *126* (3), 187–204.

(4) Kalaydina, R. V.; Bajwa, K.; Qorri, B.; Decarlo, A.; Szewczuk, M. R. Recent Advances in "Smart" Delivery Systems for Extended Drug Release in Cancer Therapy. *Int. J. Nanomedicine* **2018**, *13*, 4727–4745.

(5) Hajebi, S.; Rabiee, N.; Bagherzadeh, M.; Ahmadi, S.; Rabiee, M.; Roghani-Mamaqani, H.; Tahriri, M.; Tayebi, L.; Hamblin, M. R. Stimulus-Responsive Polymeric Nanogels as Smart Drug Delivery Systems. *Acta Biomater.* **2019**, *92*, 1–18.

(6) Jazani, A. M.; Oh, J. K. Development and Disassembly of Single and Multiple Acid-Cleavable Block Copolymer Nanoassemblies for Drug Delivery. *Polym. Chem.* **2020**, *11* (17), 2934–2954.

(7) Gao, W.; Chan, J. M.; Farokhzad, O. C. Reviews PH-Responsive Nanoparticles for Drug Delivery. *Mol. Pharm.* **2010**, *7* (6), 1913–1920.

(8) Deirram, N.; Zhang, C.; Kermaniyan, S. S.; Johnston, A. P. R.; Such, G. K. PH-Responsive Polymer Nanoparticles for Drug Delivery. *Macromol. Rapid Commun.* **2019**, *40* (10), 1–23.

(9) Dal Corso, A.; Pignataro, L.; Belvisi, L.; Gennari, C. Innovative Linker Strategies for Tumor-Targeted Drug Conjugates. *Chem. - A Eur. J.* **2019**, *25* (65), 14740–14757.

(10) Du, J. Z.; Li, H. J.; Wang, J. Tumor-Acidity-Cleavable Maleic Acid Amide (TACMAA): A Powerful Tool for Designing Smart Nanoparticles to Overcome Delivery Barriers in Cancer Nanomedicine. *Acc. Chem. Res.* **2018**, *51* (11), 2848–2856.

(11) Spanedda, M. V.; Bourel-Bonnet, L. Cyclic Anhydrides as Powerful Tools for Bioconjugation and Smart Delivery. *Bioconjug. Chem.* **2021**, *32* (3), 482–496.

(12) Lyu, M.; Yazdi, M.; Lin, Y.; Höhn, M.; Lächelt, U.; Wagner, E. Receptor-Targeted Dual PH-Triggered Intracellular Protein Transfer. *ACS Biomater. Sci. Eng.* **2022**.

(13) Zhang, X.; Zhang, K.; Haag, R. Multi-Stage, Charge Conversional, Stimuli-Responsive Nanogels f or Therapeutic Protein Delivery. *Biomater. Sci.* **2015**, *3* (11), 1487–1496.

(14) Heck, A. G.; Stickdorn, J.; Rosenberger, L. J.; Scherger, M.; Woller, J.; Eigen, K.; Bros, M.; Grabbe, S.; Nuhn, L. Polymerizable 2-Propionic-3-Methylmaleic Anhydrides as a Macromolecular Carrier Platform for PH-Responsive Immunodrug Delivery. *J. Am. Chem. Soc.* **2023**, *145* (50), 27424–27436.

(15) Zhang, A.; Yao, L.; An, M. Reversing the Undesirable PH-Profile of Doxorubicin: Via Activation of a Di-Substituted Maleamic Acid Prodrug at Tumor Acidity. *Chem. Commun.* **2017**, *53* (95), 12826–12829.

(16) Su, S.; Du, F. S.; Li, Z. C. Synthesis and PH-Dependent Hydrolysis Profiles of Mono- and Dialkyl Substituted Maleamic Acids. *Org. Biomol. Chem.* **2017**, *15* (39), 8384–8392.

(17) Heck, A. G.; Schwiertz, D.; Lantzberg, B.; Nguyen, H.-C.; Forster, R.; Scherger, M.; Opatz, T.; Van Ginderacher, J. A.; Nuhn, L. Introducing Targeting Units or PH-Releasable Immunodrugs into Core-Clickable Nanogels. *Eur. Polym. J.* **2024**, **in revision**.

(18) Matysiak, B. M.; Monreal Santiago, G.; Otto, S. Teaching an Old Compound New Tricks: Reversible Transamidation in Maleamic Acids. *Chem. - A Eur. J.* **2022**, *28* (40).

RESTORING THE PH-RESPONSIVENESS FOR AMINE-CONJUGATED 2-PROPIONIC-3-METHYLMALEIC ANHYDRIDE LINKERS

-Supporting Information-

Alina G. Heck[1] and Lutz Nuhn[1,2]*

Dedicated to Professor Frank Würthner on the occasion of his 60th birthday.

1: Chair of Macromolecular Chemistry, Julius-Maximilians-Universität Würzburg, 97070 Würzburg, Germany

2: Max Planck Institute for Polymer Research, 55128 Mainz, Germany

*: corresponding author: Prof. Dr. Lutz Nuhn (E-mail: lutz.nuhn@uni-wuerzburg.de)

Materials and Methods

Unless otherwise stated, all reagents and solvents were obtained from Sigma Aldrich (Taufkirchen, Germany) or TCI Chemicals (Tokyo, Japan) and used without further purification. Dichloromethane (DCM), dimethyl sulfoxide (DMSO), *N*,*N*-dimethylformamide (DMF), ethyl acetate (EA), all deuterated solvents as well as benzylamine, dibenzylamine, triethylamine (TEA), N-methylpiperazine or dansyl cadaverine were purchased from Sigma Aldrich. Oxalyl chloride, trifluoroacetic acid (TFA) were bought from Thermo Fisher Scientific (Waltham, MA, USA) and 11-amino-1-azido-3,6,9-trioxaundecane was obtained from TCI Chemicals (Tokyo, Japan). For silica gel chromatography silica with particle size of 0.063-0.2 mm from Macherey-Nagel GmbH & Co. KG (Dueren, Germany) was used.

Instrumentation

Nuclear Magnetic Resonance (NMR) Spectroscopy

^{1}H, ^{13}C and 2D NMR spectra were recorded on a Bruker Avance III 300 MHz, Bruker Avance III 400 MHz or Bruker Avance III 500 MHz spectrometer at room temperature. All samples were prepared using deuterated solvents and residual non-deuterated solvent signals were used as reference. Resulting spectra were processed using MestReNova 14.2.0 by Mestrelab Research.

Ultraviolet-Visible Spectroscopy (UV-Vis) and Fluorescence Spectroscopy

UV-Vis spectra were recorded on a Thermo Scientific™ NanoDrop™ 2000c spectrophotometer with a Hellma Quartz Cuvette.

Fluorescence spectroscopy was measured on a Spark 20M Multimode Microplate Reader from Tecan Trading AG (Mannedorf, Switzerland).

Mass Spectrometry (ESI-MS and MALDI-ToF)

ESI mass spectra were carried out on an Agilent 6545 QTOF-MS (Santa Clara, CA, USA). All samples were dissolved in methanol at 0.1 mg/mL. Mass spectrometry data were processed and analyzed using the Advion Data Express software and mMass.

Matrix Assisted Laser Desorption Ionization-Time of Flight (MALDI-ToF) measurement were carried out on a rapifleX™ MALDI-ToF/ToF mass spectrometer from Bruker Daltonik GmbH (Bremen, Germany) fitted with a 10 kHz scanning smartbeam Nd:YAG laser at 355 nm

wavelength and a 10 bit 5 GHz digitizer. Mass spectra were recorded in positive ion mode using DCTB (trans-2-[3-(4-tbutylphenyl)-2-methyl-2-propenylidene]-malononitrile) acid as a matrix. All samples were prepared at 0.1 mg/mL and the obtained data were analyzed by mMass software.

Syntheses

Synthesis of an Azide-Functional and pH-Sensitive 2-Propionic-3-Methylmaleic Anhydride-Based Linker

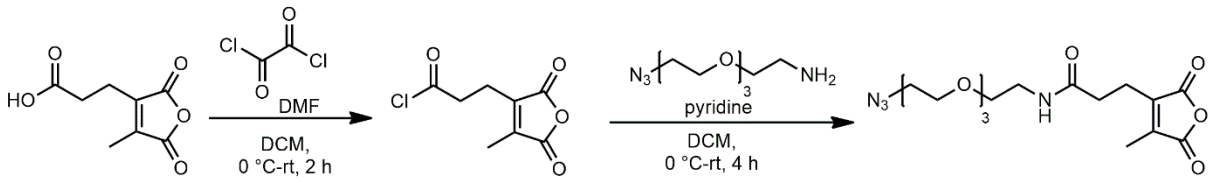

Figure S1: Synthesis of N-(2-(2-(2-azidoethoxy)ethoxy)ethyl)-3-(4-methyl-2,5-dioxo-2,5-dihydro-furan-3-yl)propanamid in two steps.

The azide-functional and pH-reversible 2-propionic-3-methylmaleic anhydride based linker N-(2-(2-(2-azidoethoxy)ethoxy)ethyl)-3-(4-methyl-2,5-dioxo-dihydrofuran-3-yl)propanamid was synthesized in analogy to previous reports.[1–3] The pure product was obtained as yellow oil (1.21 g, 49%).

^{1}H NMR (300 MHz, $CDCl_3$): δ (ppm) = 6.25 (s, 1H, **a**), 3.71-3.59 (m, 10H, **b**), 3.57-3.47 (m, 2H, **c**), 3.46-3.35 (m, 4H, **d+e**), 2.79 (t, *J* = 7.0 Hz, 2H, **f**), 2.54 (t, *J* = 7.0 Hz, 2H, **g**), 2.11 (s, 3H, **h**).

^{13}C NMR (75 MHz, $CDCl_3$): δ (ppm) = 170.59 (**a**), 166.13 (**b**), 166.04 (**c**), 142.91 (**d**), 142.32 (**e**), 70.79 (**f**), 70.72 (**g**), 70.62 (**h**), 70.36 (**i**), 70.12 (**j**), 69.68 (**k**), 50.79 (**l**), 39.49 (**m**), 32.90 (**n**), 20.49 (**o**), 9.80 (**p**.

IR (ATR) ũ [cm^{-1}] = 3318, 3081, 2920, 2867, 2361, 2340, 2100, 1824, 1760, 1670, 1537, 1442, 1386, 1348, 1278, 1180, 1116, 908, 851, 732.

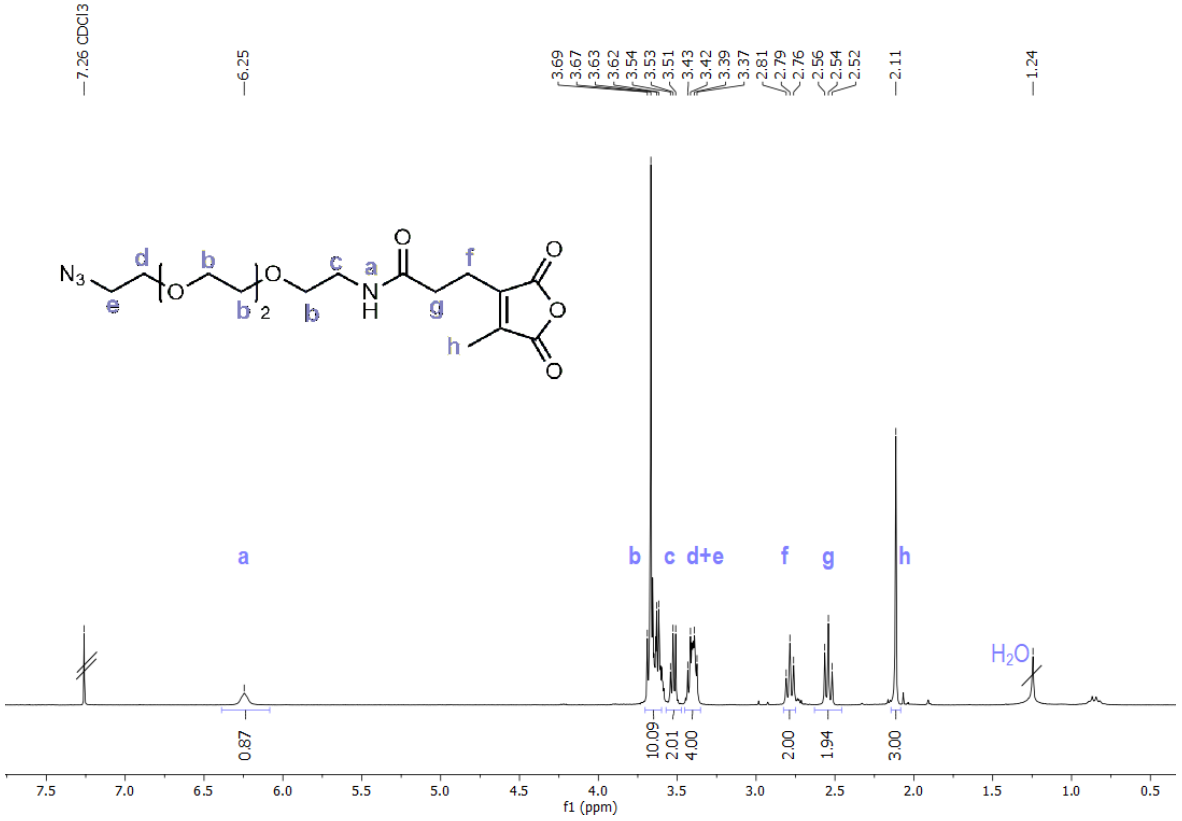

Figure S2: ^{1}H NMR spectrum (300 MHz) of N-(2-(2-(2-azidoethoxy)ethoxy)ethyl)-3-(4-methyl-2,5-dioxo-2,5-dihydro-furan-3-yl)propanamid in $CDCl_3$.

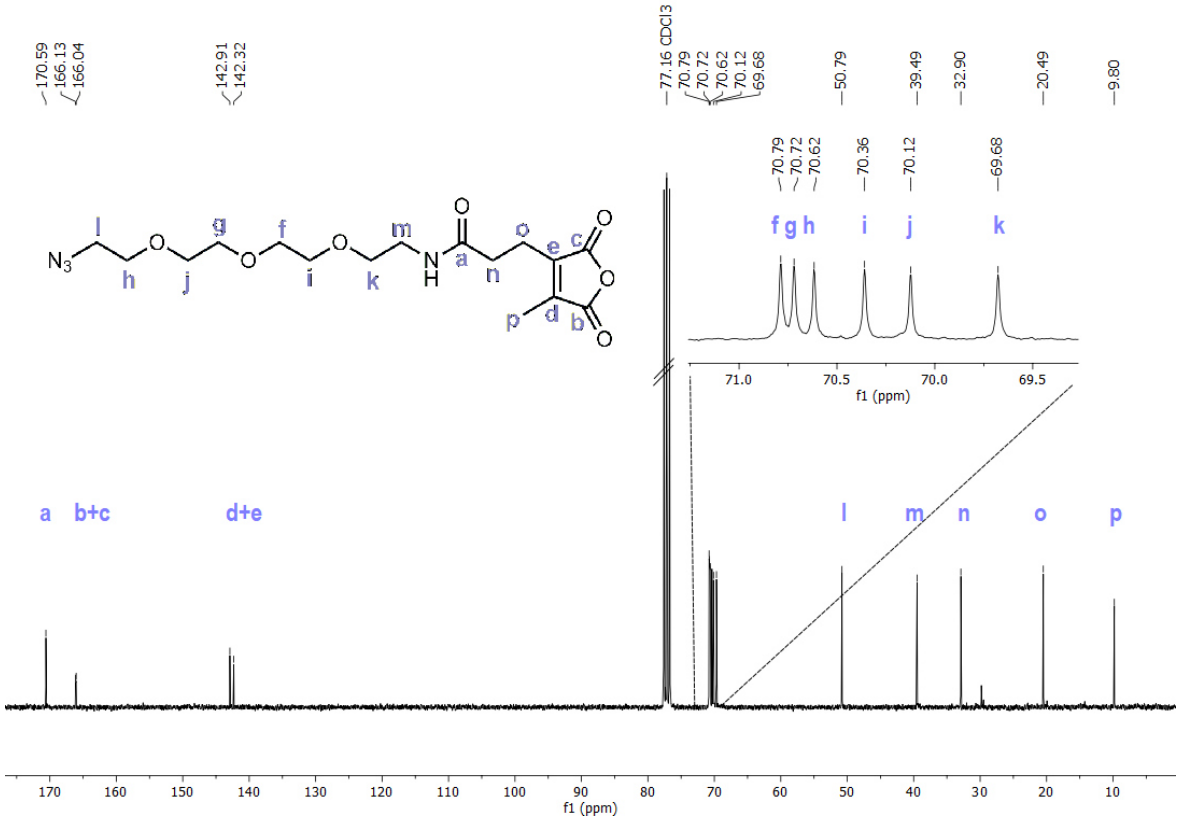

Figure S3: ^{13}C NMR spectrum (75 MHz) of N-(2-(2-(2-azidoethoxy)ethoxy)ethyl)-3-(4-methyl-2,5-dioxo-2,5-dihydro-furan-3-yl)propanamid in $CDCl_3$.

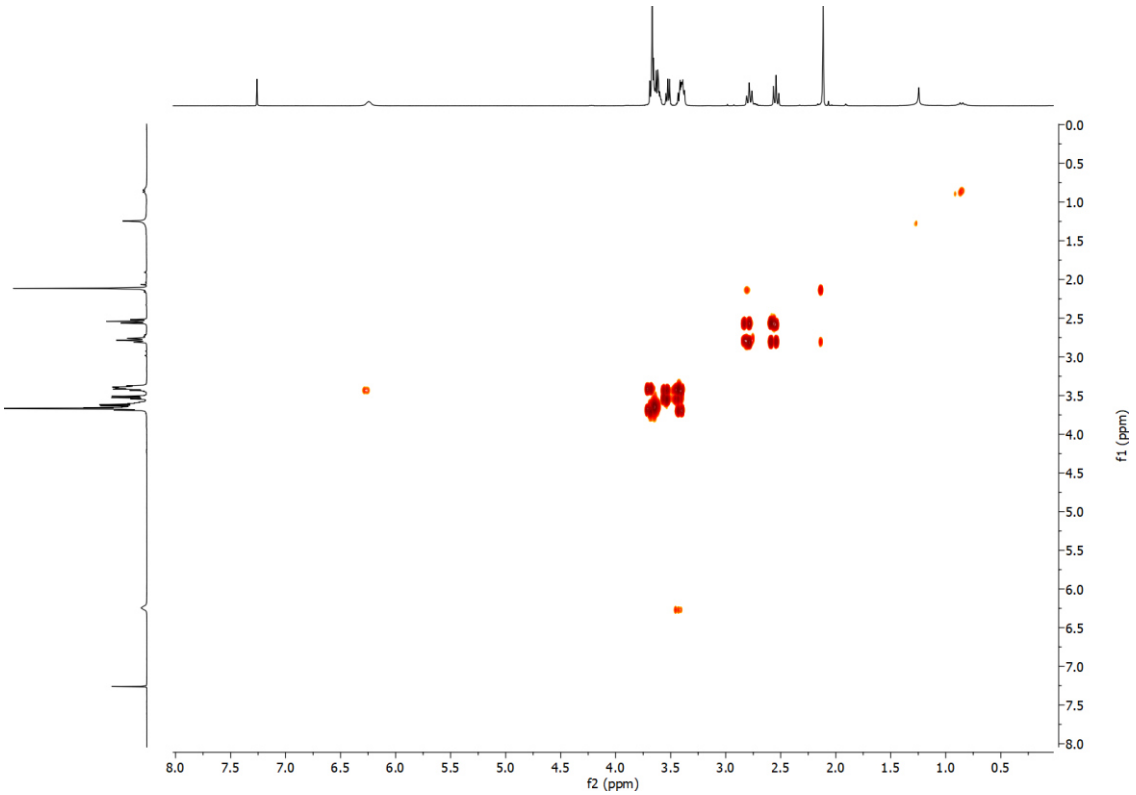

Figure S4: 2D COSY NMR spectrum of N-(2-(2-(2-azidoethoxy)ethoxy)ethyl)-3-(4-methyl-2,5-dioxo-2,5-dihydrofuran-3-yl)propanamid in $CDCl_3$.

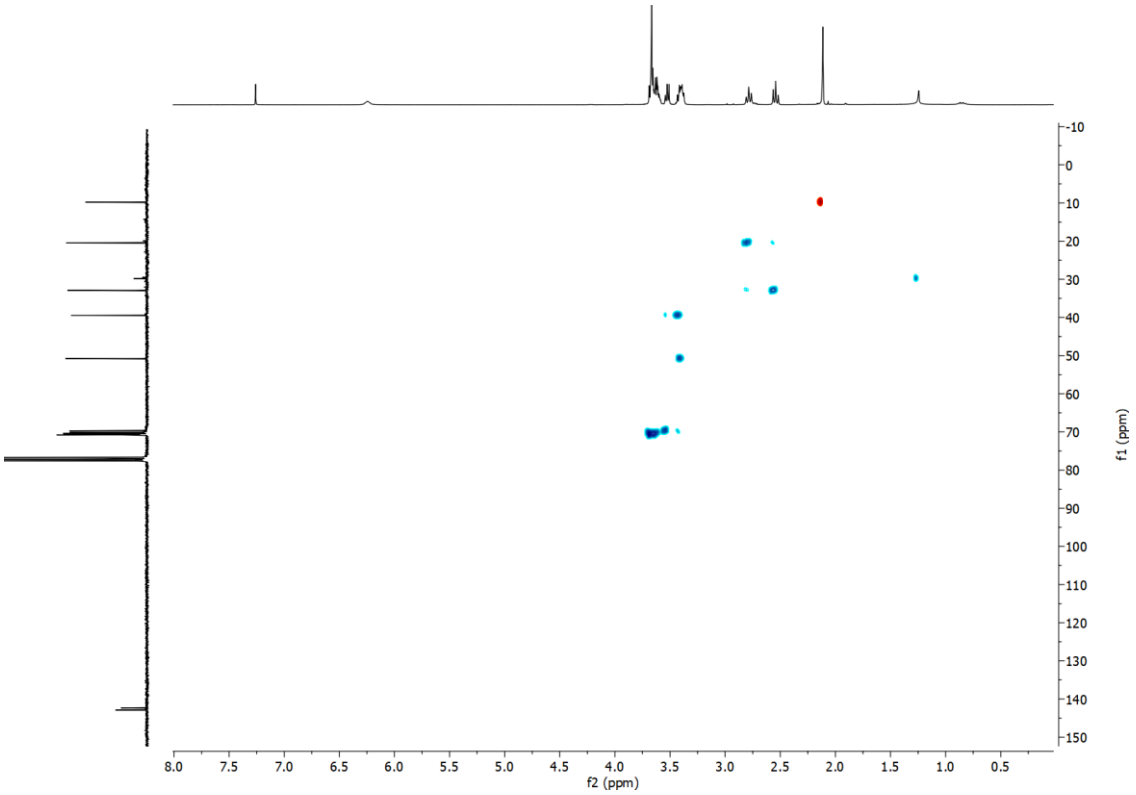

Figure S5: 2D HSQC NMR spectrum of N-(2-(2-(2-azidoethoxy)ethoxy)ethyl)-3-(4-methyl-2,5-dioxo-2,5-dihydrofuran-3-yl)propanamid in $CDCl_3$.

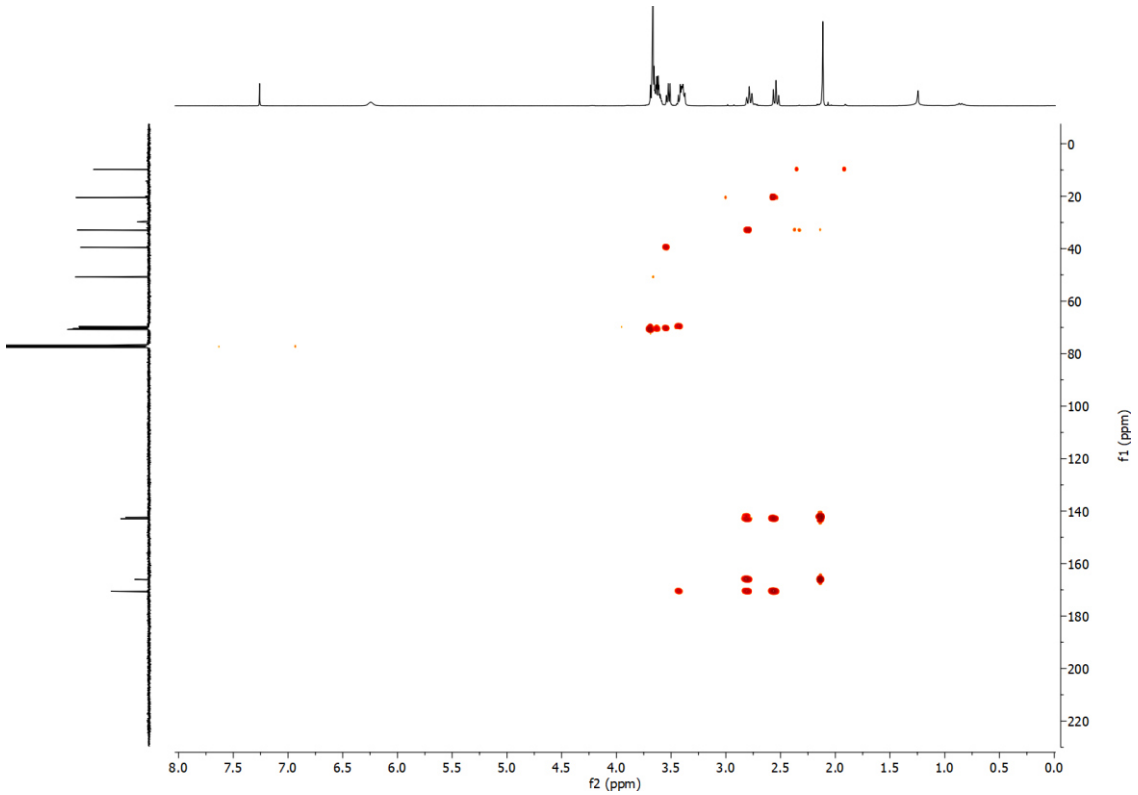

Figure S6: 2D HMBC NMR spectrum of N-(2-(2-(2-azidoethoxy)ethoxy)ethyl)-3-(4-methyl-2,5-dioxo-2,5-dihydro-furan-3-yl)propanamid in $CDCl_3$.

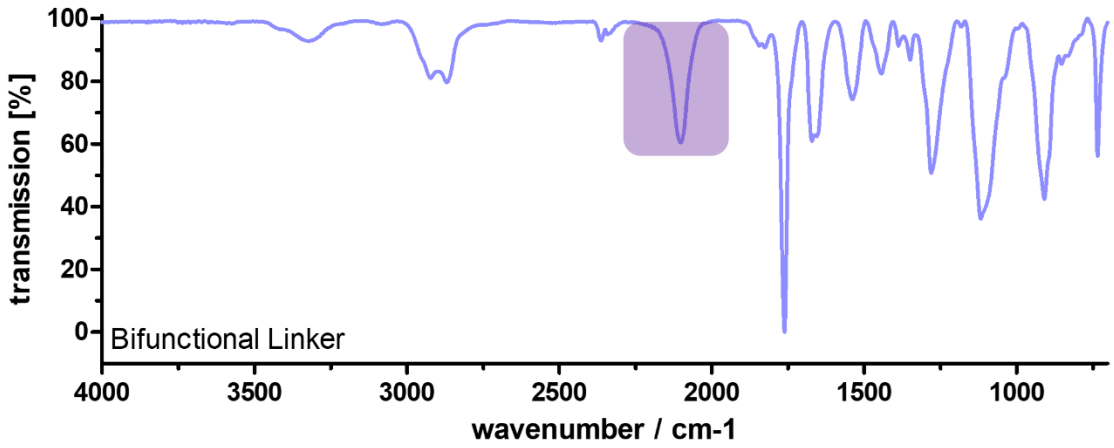

Figure S7: IR spectrum of N-(2-(2-(2-azidoethoxy)ethoxy)ethyl)-3-(4-methyl-2,5-dioxo-2,5-dihydro-furan-3-yl)propanamid.

pH-Reversible and Irreversible Amidation of Azide-Functional 2-Propionic-3-Methylmaleic Anhydride Linker by Amidation with Primary or Secondary Amine Dyes in DMSO

Synthesis of 4-Nitro-7-Priperazino-2,1,3-Benzoxadiazole (NBD-PZ/NBD)

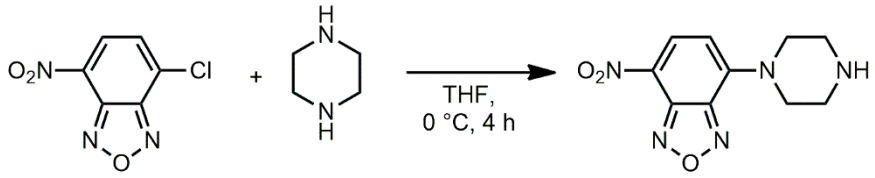

Figure S8: Synthesis of 4-Nitro-7-piperazino-2,1,3-benzoxadiazole (NBD-PZ).

The fluorescent dye 4-Nitro-7-piperazino-2,1,3-benzoxadiazole (NBD-PZ) was synthesized similar as previously reported.[4]

^{1}H NMR (500 MHz, DMSO-d$_6$): δ (ppm) = 8.44 (d, J = 9.2 Hz, 1H, **a**), 6.63 (d, J = 9.3 Hz, 1H, **b**), 4.07 (m, 4H, **c**), 2.92 (m, 4H, **d**).

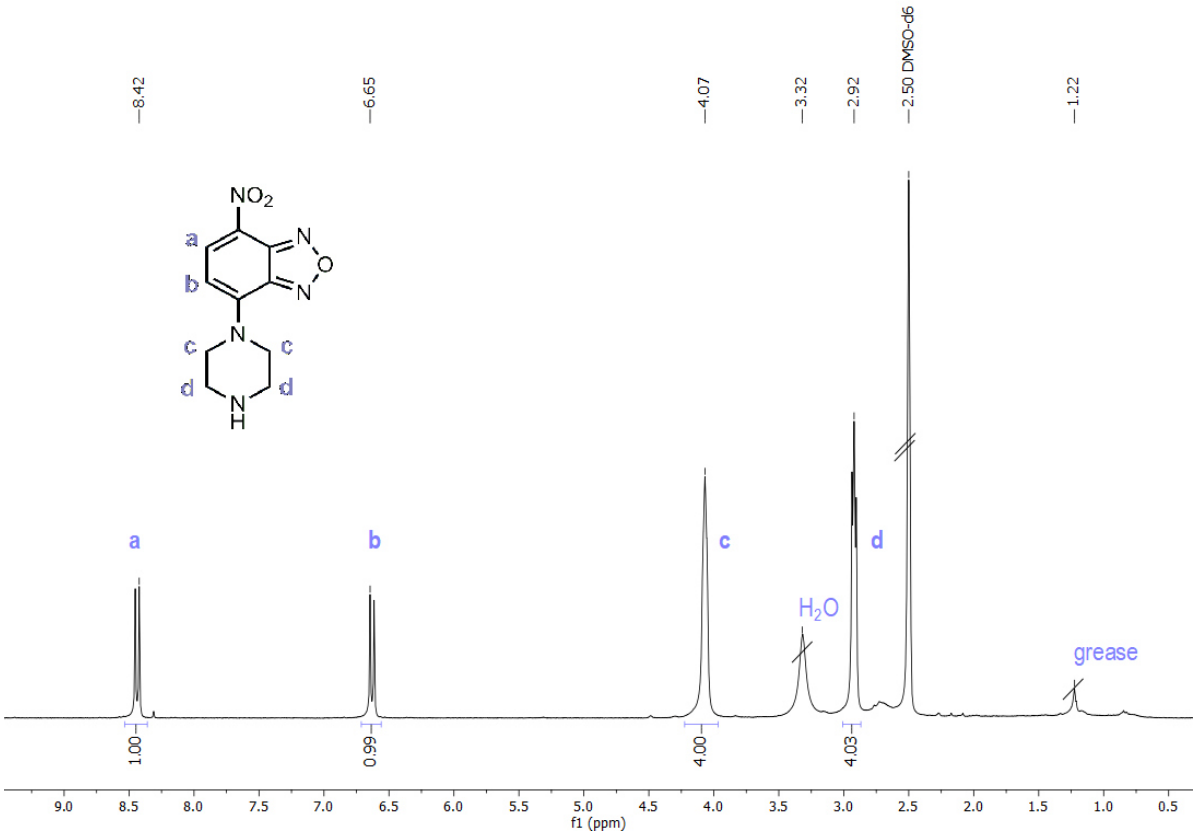

Figure S9: ^{1}H NMR spectrum (500 MHz) of 4-Nitro-7-piperazino-2,1,3-benzoxadiazole (NBD-PZ) in DMSO-d$_6$.

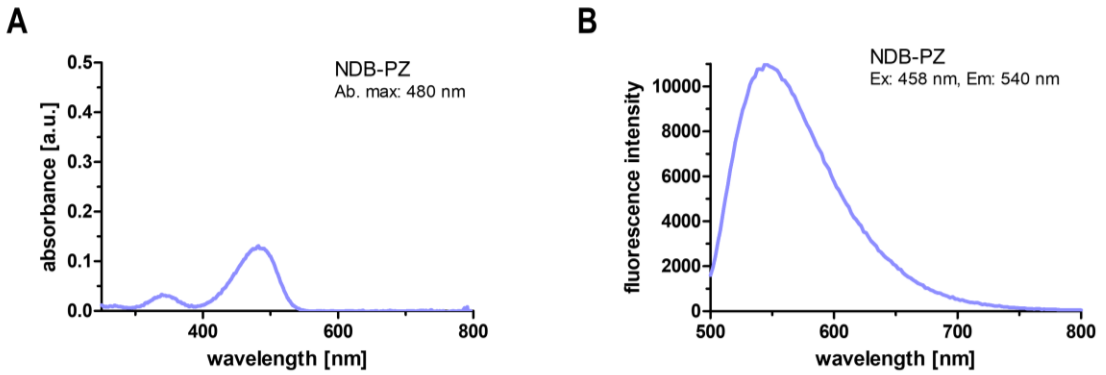

Figure S10: UV-Vis spectrum of NBD-PZ (A) and the corresponding fluorescence intensity spectrum in PBS (B).

pH-Reversible or Irreversible Attachment of Fluorescent Dyes to the Azide-Functional 2-Propionic-3-Methylmaleic Anhydride Linker

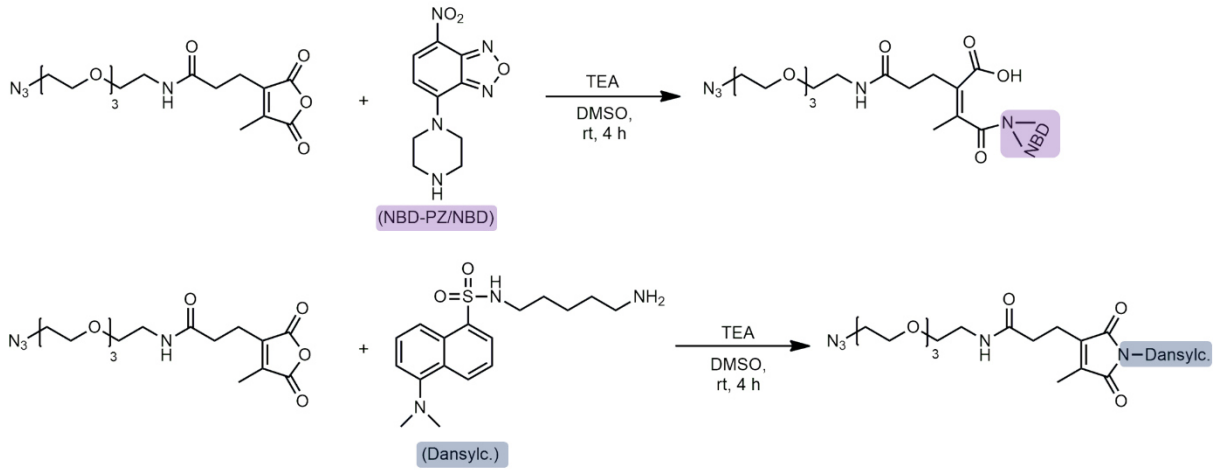

Figure S11: Synthesis of pH-reversible and irreversible dye-labeled azide-functional 2-propionic-3-methylmaleic anhydride linker in DMSO at room temperature for four hours.

The pH-reversible or irreversible dye-labeling reaction of azide-containing 2-propionic-3-methylmaleic anhydride linker in DMSO was conducted according to previously reported modification reactions.[3] 80 mg of the bifunctional linker (0.208 mmol, 1 eq) was weighted in a Schlenk tube and dissolved in 4 mL dry DMSO and TEA (86.5 µL, 0.624 mmol, 3 eq) under nitrogen atmosphere. Afterwards, 40 mg of the bifunctional linker was transferred into a new Schlenk tube followed by the addition of dansyl cadaverine (dansylc., 34.89 mg, 0.104 mmol, 1 eq) or 4-nitro-7-piperazino-2,1,3-benzoxadiazole (NBD-PZ/NBD, 25.92 mg, 0.104 mmol, 1 eq). The reaction mixtures were stirred for 4 h at room temperature protected from light. Then, the dye-labeled linkers were precipitated into diethyl ether (3x), centrifuged (3x15 min, 4000 rpm) and decanted. After drying *in vacuo* overnight the dye-labeled linkers were obtained as intensive red or yellow oil (63 mg, 96%).

MALDI-ToF [m/z] (with NBD-PZ) = 634.25 $[M+H]^+$ (calc. 634.62), 656.24 $[M+Na]^+$ (calc. 656.61), 672.21 $[M+K]^+$ (calc. 672.72).

ESI-MS [m/z] (with dansylc.) = 724.78 $[M+Na]^+$ (calc. 724.82), 740.80 $[M+K]^+$ (calc. 740.93).

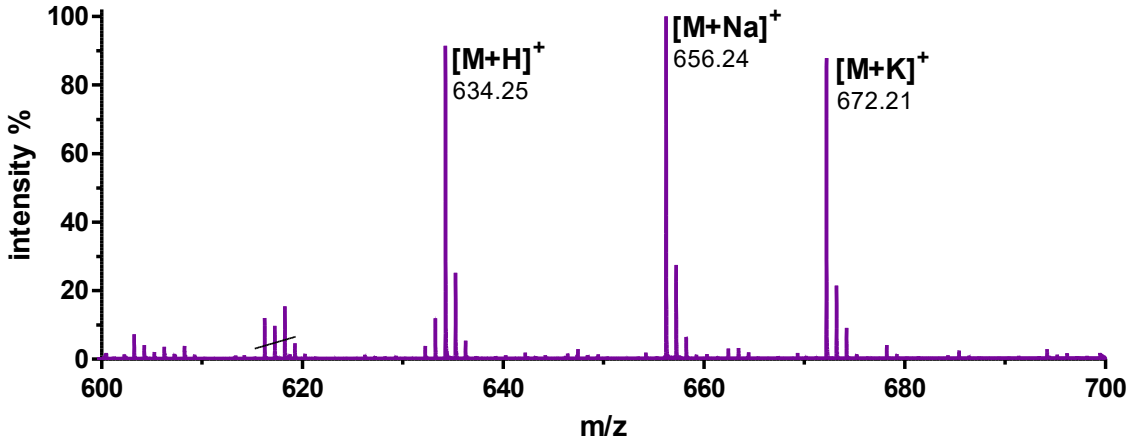

Figure S12: MALDI-ToF spectrum of the azide 2-propionic-3-methylmaleic anhydride linker after NBD-PZ conjugation in DCM.

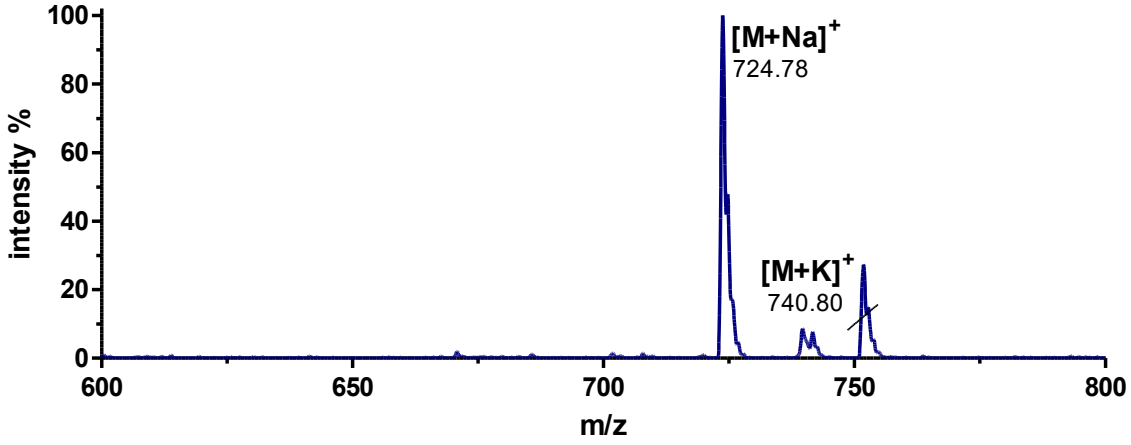

Figure S13: ESI-MS spectrum of the azide 2-propionic-3-methylmaleic anhydride linker after dansyl cadaverine (dansylc.) conjugation in MeOH.

pH-Reversible Azide-Functional 2-Propionic-3-Methylmaleic Anhydride Linker Modification by Amidation with Primary and Secondary Amines in Diethyl ether

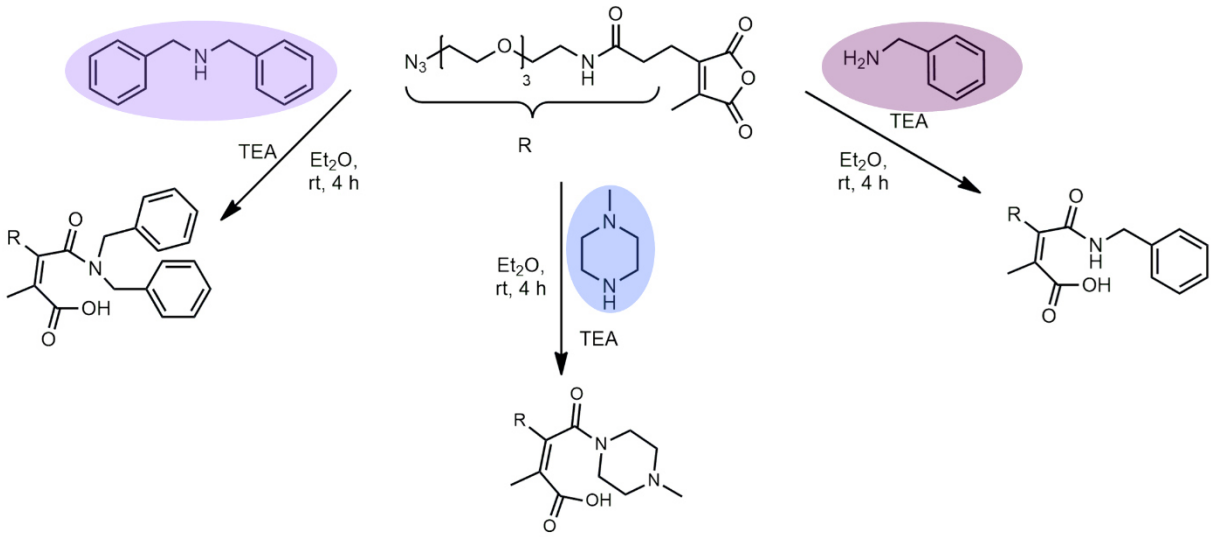

Figure S14: Schematic pH-reversible amidation reaction of the azide-containing 2-propionic-3-methylmaleic anhydride linker with different secondary or primary amines in diethyl ether for 4 hours.

To characterize the accessibility for amine modification in diethyl ether the synthesized azide-containing 2-propionic-3-methylmaleic anhydride linker was reacted with different primary or secondary amines in analogy to previous reports.[4] Consequently, 60 mg of the linker (0.16 mmol, 1.1 eq) was transferred into a round bottom flask and dissolved in diethyl ether (3 mL) under nitrogen atmosphere. TEA (61 µL, 0.44 mmol, 3 eq) was dropped to the solution, followed by the addition of the corresponding amines, like *N*-methyl-piperazine (16.08 µL, 0.145 mmol, 1 eq). The reaction mixture was stirred for 2 h at room temperature. Then, TEA (61 µL, 0.44 mmol, 3 eq) was added a second time and the reaction mixture was stirred for further 2 h. Subsequently, the solvent was evaporated, and the product was dried *in vacuo* for 16 h. The modified linkers were obtained as yellow solid (67 mg, 87%).

MALDI-ToF [m/z] (with dibenzylamine) = 582.23 $[M+H]^+$ (calc. 582.66), 604.23 $[M+Na]^+$ (calc. 604.65), 620.20 $[M+K]^+$ (calc. 620.76).

MALDI-ToF [m/z] (with benzylamine) = 474 $[M\text{-imide}+H]^+$ (calc. 474.52), 492.32 $[M+H]^+$ (calc. 492.54), 496 $[M\text{-imide}+Na]^+$ (calc. 496.51), 514.30 $[M+Na]^+$ (calc. 514.53), 530.27 $[M+K]^+$ (calc. 530.64).

MALDI-ToF [m/z] (with N-methylpiperazine) = 485.54 $[M+H]^+$ (calc. 485.55), 507.46 $[M+Na]^+$ (calc. 507.54), 523.38 $[M+K]^+$ (calc. 523.65).

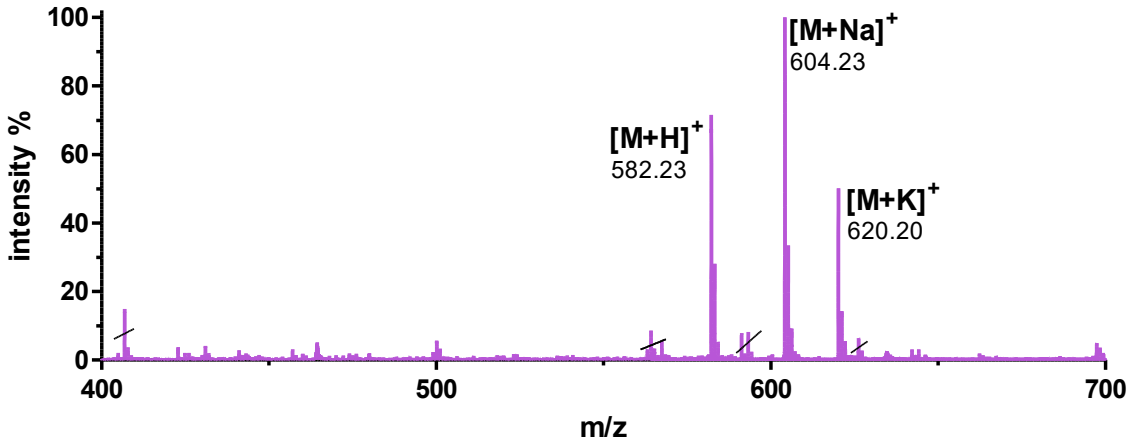

Figure S15: MALDI-ToF spectrum of the dibenzylamine-conjugated azide-containing 2-propionic-3-methylmaleic anhydride linker in DCM.

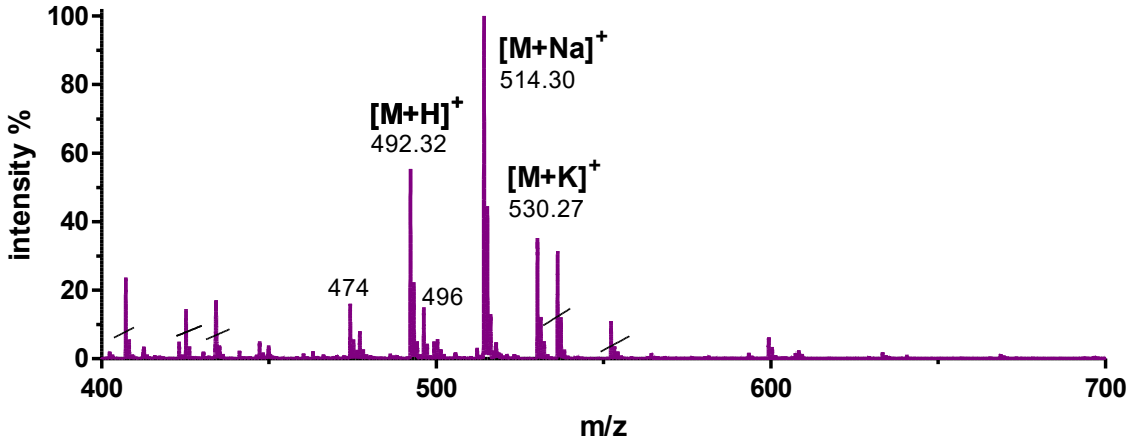

Figure S16: MALDI-ToF spectrum of the benzylamine-conjugated azide 2-propionic-3-methylmaleic anhydride linker in DCM.

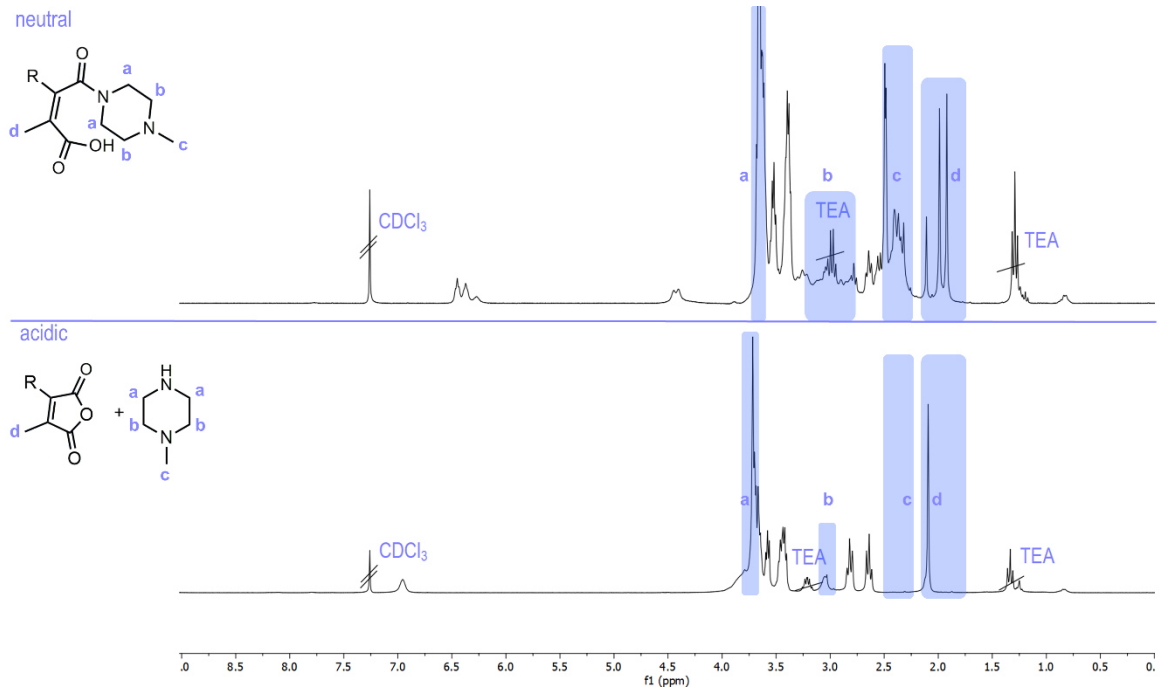

Figure S17: ^{1}H NMR spectra (300 MHz) of the azide-containing 2-propionic-3-methylmaleic anhydride linker after modification with N-methylpiperazine under neutral and acidic conditions in $CDCl_3$.

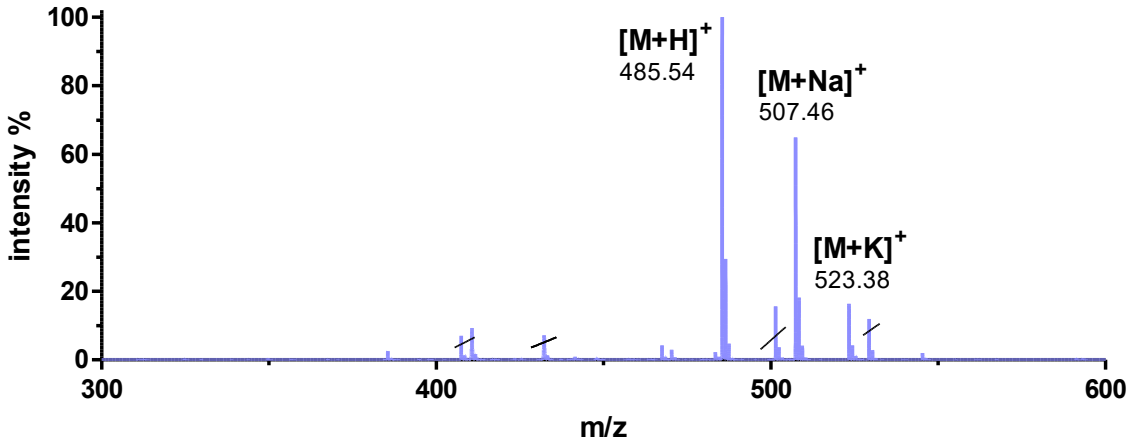

Figure S18: MALDI-ToF spectrum of the N-methylpiperazine-conjugated azide 2-propionic-3-methylmaleic anhydride linker in DCM.

Additional References

(1) Takemoto, H.; Miyata, K.; Hattori, S.; Ishii, T.; Suma, T.; Uchida, S.; Nishiyama, N.; Kataoka, K. Acidic PH-Responsive SiRNA Conjugate for Reversible Carrier Stability and Accelerated Endosomal Escape with Reduced IFNα-Associated Immune Response. *Angew. Chemie - Int. Ed.* **2013**, *52* (24), 6218–6221.

(2) Ding, Y.; Du, C.; Qian, J.; Zhou, L.; Su, Y.; Zhang, R.; Dong, C. M. Tumor PH and Intracellular Reduction Responsive Polypeptide Nanomedicine with a Sheddable PEG Corona and a Disulfide-Cross-Linked Core. *Polym. Chem.* **2018**, *9* (25), 3488–3498.

(3) Heck, A. G.; Schwiertz, D.; Lantzberg, B.; Nguyen, H.-C.; Forster, R.; Scherger, M.; Opatz, T.; Van Ginderacher, J. A.; Nuhn, L. Introducing Targeting Units or PH-Releasable Immunodrugs into Core-Clickable Nanogels. *Eur. Polym. J.* **2024**, **in revision**.

(4) Heck, A. G.; Stickdorn, J.; Rosenberger, L. J.; Scherger, M.; Woller, J.; Eigen, K.; Bros, M.; Grabbe, S.; Nuhn, L. Polymerizable 2-Propionic-3-Methylmaleic Anhydrides as a Macromolecular Carrier Platform for PH-Responsive Immunodrug Delivery. *J. Am. Chem. Soc.* **2023**, *145* (50), 27424–27436.

SUMMARY

This thesis aimed at investigating functional polymers and expanding their potential as a stimuli-responsive macromolecular carrier platform for the controlled delivery of immune stimulatory drugs. In the development of smart nanocarriers, pH as endogenous stimulus proved to be a promising trigger for the controlled targeting and release of small molecular drugs in nanomedicine. Therefore, pH-sensitive macromolecular structures were synthesized by controlled radical polymerization and further modified to act as an efficient carrier system for various immunodrug delivery purposes. In this regard, applying 2-propionic-3-methylmaleic anhydride-based systems as a pH-sensitive motif presented a high flexibility not only as a polymerizable structure for the generation of stimuli-responsive macromolecular carriers or the controlled formation of intracellularly self-assembling nanocompartments, but also as a potential, bifunctional linker with high potential in cancer immunotherapy.

The first chapter of this thesis focused on the synthesis of polymetharcylamides with pendant 2-propionic-3-methylmaleic anhydride side groups and their ability to conjugate primary and secondary amine-bearing small molecules for a controlled immunostimulation. After optimization of the reaction conditions, a 2-propionic-3-methylmaleic anhydride methacrylamide monomer was deployed and polymerized under RAFT conditions. The amine-reactive anhydrides were converted with different primary or secondary amines and their pH sensitivity was investigated in DMSO. Indeed, only secondary amines revealed a quantitative release of attached amines under acidic conditions, while primary amines induced the formation of pH-resistant imide structures. Thereby, it was found that a dual modification of the anhydride system induced the loss of pH sensitivity and highlighted the characteristic chemical release mechanism of the 2-propionic-3-methylmaleic anhydride structure. By sequential post-polymerization modification with hydrophilic secondary amines and fluorescent dyes, corresponding polymers could be transformed into fully water-soluble, non-toxic structures with efficient cellular uptake and remaining pH sensitivity, as investigated in RAW-Dual macrophages. These beneficial properties were assigned to the formation of pH-responsive drug-loaded macromolecular carriers. Accordingly, a novel secondary amine-bearing imidazoquinoline-based TLR 7/8 agonists (IMDQ-Me) was synthesized and conjugated to the system. Based on the exclusive intracellular pH-sensitive release of secondary amines, IMDQ-Me drug-loaded polymers demonstrated an improved receptor stimulation *in vitro* comparted to irreversibly IMDQ-modified macromolecular carriers.

Next, the pH-responsive macromolecular carrier approach was extended to assure a localized stimulation of antigen presenting cells (APCs) in the draining lymph nodes upon subcutaneous injection in the foot pad of mice (chapter II). In general, cholesteryl-modified systems have been demonstrated an enhanced accumulation in the draining lymph nodes by albumin-hitchhiking mechanisms followed by improved immune cell uptake. Starting from the synthesis of a cholesteryl-modified chain transfer agent (chol-CTA), the methacrylamide-based monomer with pendant 2-propionic-3-methylmaleic anhydride group was grafted onto a chol-CTA *via* RAFT polymerization, providing a polymer with the potential to accumulate in the lymph nodes as well as enabling a pH-sensitive drug attachment. Following the pH-reversible amidation profile of the anhydride groups, the functional polymers were pH-irreversibly or reversibly conjugated with amine-functionalized dyes or drugs. Aminolysis of the remaining functional groups with short mPEG-amines enabled the generation of a hydrophilic macromolecular carrier platform with sufficient water-solubilities and further efficient cellular uptake properties, as confirmed by flow cytometry and confocal microscopy. Interestingly, pH-reversibly IMDQ-Me-loaded polymers focused a strong *in vitro* TLR 7/8 receptor stimulation in macrophages, and moreover elicited a profound activation of primary immune cells relative to the irreversibly drug-loaded polymer system. Additional, detailed *in vivo* evaluations elucidated the beneficial properties of the cholesteryl-modified macromolecular carriers and confirmed the promoted activation of antigen presenting cells (APC) in the draining lymph nodes. The design of cholesteryl-linked polymetharcylamides with appended 2-propionic-3-methylmaleic anhydride groups revealed to be a versatile macromolecular platform for the controlled delivery and release of small molecular immunotherapeutics.

The third chapter encompassed the investigation of pH-responsive, amphiphilic block copolymers for the installed formulation of micellar systems in biological relevant compartments. For this purpose, amphiphilic block copolymers of polyethylene glycol and polymetharcylamides with 2-propionic-3-methylmaleic anhydride side groups were synthesized *via* RAFT polymerization and analyzed at varying pH conditions. When exposed to slightly acidic pH values the block copolymers immediately self-assembled into narrowly distributed spherical micelles with high stability over two weeks, whereas increasing pH values induced a rapid disassembly into soluble polymer chains where the pendant maleic anhydrides were ring-opened as carboxylates. A library of primary amines was conjugated to the block copolymer and characterized in detail, resulting in the formation of pH-resistant, stable polymeric micelles. Moreover, the attachment of secondary amines ensured the pH-responsive release and pH-reversible self-assembly of the system, as demonstrated by ^{1}H NMR

spectroscopy, DOSY experiments and DLS measurements. These findings translated to a biological context would lead to the formation of new micellar compartments inside cells. As a proof of concept, the FRET communicating dyes Cy3-amine and Cy5-amine were separately and irreversibly installed onto the block copolymer and subsequently characterized by DLS measurement as well as UV-Vis and fluorescence spectroscopy. Application of an acidic environment to a mixture of the dye-labeled block copolymers confirmed the formation of micelles and provided a strong FRET signal. First *in vitro* studies revealed an efficient time-dependent cellular uptake, with high tolerability and the generation of FRET inside cells, as quantified by flow cytometry, confocal microscopy, and fluorescent lifetime imaging (FLIM). Remarkably, correlative light and electron microscopy (CLEM) demonstrated the intracellular formation of reversible spherical structures inside acidic endolysosomal compartments. Thus, the chemical design might facilitate altered biomedical processes *in vitro* and can be used as a versatile and adaptable system.

Regarding the advances of smart macromolecular carrier systems, the fourth chapter explored the efficient post-polymerization modification of reactive ester-containing block copolymers for the fabrication of DBCO core-functionalized nanogels that can be used as versatile bioorthogonally addressable platform to install a localized and pH-responsive immune stimulation. Synthetic access was provided by reactive precursor block copolymers consisting of hydrophilic methoxy tri(ethylene glycol) methacrylates (mTEGMA) and hydrophobic reactive ester methacrylates (PFPMA). In this regard, the reactive ester units enabled a covalent attachment of DBCO-PEG_4-amine and the fabrication of dye-labeled and core-crosslinked nanogels. The fabrication process not only provided access to fully hydrophilic nanogels, but also afforded the introduction of DBCO-units into the nanogels' core. These nanogels presented stable, uniform particles with sufficient accessibility for DBCO click reaction with azide-functional structures. Accordingly, azide-bearing trimannose as a targeting unit for mannose receptor expressing immune cells was conjugated to the nanogels and extensively characterized. Afterwards, trimannose-modified nanogels and additional control particles were applied to Chinese Hamster Ovary cells with or without the MMR/CD206 receptor (CHO^{MMR+}/ CHO^{MMR-}). Thorough investigation by flow cytometry and confocal microscopy studies demonstrated a trimannose mediated targeting and internalization of the nanogels and, thus, further emphasizing the DBCO-nanogels' ability for the conjugation of azide-functionalized bioactive molecules. Furthermore, the advantageous properties of the DBCO-nanogels facilitated the attachment of bifunctional linkers with the 2-propionic-3-methylmaleic anhydride motif that enabled the pH-reversible introduction of secondary amine-modified

immunostimulatory drugs (IMDQ-Me). Application of the pH-sensitive drug-loaded nanogel to RAW-Dual macrophages revealed a strong immunoactivation by the TLR 7/8 receptor that was not affected by the conjugation chemistry. The adaptability of the reactive ester polymer chemistry enables the versatile syntheses of DBCO-functional materials and explores their potential in various biological applications.

Based on the formulation of pH-reversible nanogels by bioorthogonal click reaction with an azide-bearing 2-propionic-3-methylmaleic anhydride linker, the fifth chapter investigated the pH-reversible amidation profile of the bifunctional linker in varying solvents. Former synthetic efforts with primary amines and 2-propionic-3-methylmaleic anhydride systems in DMSO revealed the generation of pH-resistant imides. In order to achieve a controlled amidation with primary amines and maintain pH reversibility, additional modifications were performed in diethyl ether. Detailed analyses of resulting amine-modified linkers under varying pH conditions demonstrated a fast reaction and remaining pH reversibility of the azide-functionalized 2-propionic-3-methylmaleic anhydride linker. These conditions might be a suitable strategy for the directed, pH-sensitive modification of dimethylmaleic anhydride-based structures with primary amines while preserving their biological activity.

In conclusion, this thesis explored the high potential of 2-propionic-3-methylmaleic anhydride as an efficient pH-sensitive motif for nano-sized drug delivery applications. The synthesis of functional polymers providing reversible stimuli-responsive post-polymerization modification properties enabled the design of adaptable macromolecular carriers with improved performances in nanomedicine. Particularly, chemical investigations on the material properties by fine-tuning the pH-sensitive functionalization of the carrier platform allowed for a precise modulation of immunotherapeutic activities. Based on the fabrication processes, additional advantageous features of the macromolecular carrier platform ensured the controlled delivery of small molecular drugs to the draining lymph nodes and further promoted the activation of antigen presenting cells (APC). At the same time amphiphilic block copolymers provided a spatiotemporal control for the formulation of micellar systems upon accumulation inside acidic cellular compartments. Furthermore, nanoparticles with the ability for bioorthogonal core functionalization provided a broad opportunity for a pH-reversible and targeted drug delivery of therapeutic agents and, finally, extended the applicability of the 2-propionic-3-methylmaleic anhydride motif to other carrier platforms. The presented design concept of stimuli-responsive macromolecular carriers based on 2-propionic-3-methylmaleic anhydride structures may, thus, paved the way for adaptive and smart drug delivery systems in cancer immunotherapy.

OUTLOOK

This thesis explored the synthetic potential to generate pH-sensitive macromolecular carriers as highly efficient drug delivery systems. Synthetic approaches towards 2-propionic-3-methylmaleic anhydride-based molecular polymers and micellar formulations as well as the implementation to established nano-sized carrier systems were successfully investigated and evaluated for their bio-applicability in nanomedicine.

Concerning the realization of advanced polymer-based carrier systems in nanomedicine, RAFT polymerization emerged as a robust and efficient method. The synthesis of a novel 2-propionic-3-methylmaleic anhydride methacrylamide monomer demonstrated great potential as reactive agent for the generation of pH-responsive macromolecular carriers. Further amplification for controlled radical polymerization by the implementation of a cholesterol-based chain transfer agent (chol-CTA) enabled the controlled and pH-triggered stimulation of antigen presenting cells (APCs) *in vivo*. Nevertheless, further efforts towards the passive accumulation in lymphatic organs by albumin-hitchhiking may be necessary, also following intravenous applications. Based on the fast and high pH sensitivity of the dimethylmaleic anhydride structures, additional time point as well as the detailed investigation of lymphatic organs could provide beneficial insights into the smart carrier system.

Regarding the application of amphiphilic block copolymers with pendant 2-propionic-3-methylmaleic anhydride groups, readily, pH-reversible self-assembly was achieved *ex vitro* as well as *in vitro*. These characteristics make the block copolymers an attractive system for the controlled formulation of transiently appearing intracellular compartments. Additionally, the anhydride functionality enables the permanent or pH-reversible conjugation of amine-bearing molecules. The combination of both properties has been partly realized by fluorescence measurements following the intracellular fate of the structures. The transfer of the strategy to a physical entrapment or the activation of drugs as well as the promotion of biological or chemical reactions could open novel possibilities in controlling cellular functions, also towards advanced cancer therapies. These attempts may, for instance, be attained chemically by bringing two reaction partners close to each other inside endolysosomes and enforcing their reaction (e.g. by *in vivo* “click-to-release” approaches).

Furthermore, this thesis introduced the successful formulation of DBCO-core functionalizable nanogels as a versatile bioorthogonal click platform for the conjugation of mannose-targeting units or the pH-reversible introduction of immunostimulatory drugs through a 2-propionic-3-

methylmaleic anhydride-azide linker. These nanogels will be further tested according to their stability and biological application *in vitro* as well as *in vivo*. Moreover, current experiments cover the separate introduction of mannose-targeting units or the conjugation of a bifunctional 2-propionic-3-methylmaleic anhydride-based linker. Additional studies for a combined introduction of both systems might be of interest for the development of a smart dual carrier system. Altogether, these nanogels provide versatile opportunities for the simultaneous conjugation of multiple azide-functional molecules beyond targeting units, drugs, and dyes.

Referring to the pH resistance of the bifunctional linker towards primary amines in DMSO, the application of diethyl ether as reaction solvent restored the pH sensitivity of the 2-propionic-3-methylmaleic anhydride-based linker for primary amines. These reaction conditions can be further evaluated with respect to their pH reversibility with different types of primary amines, the conjugation of active drugs to relevant carrier systems, as well as the transfer of these findings to the 2-propionic-3-methylmaleic anhydride-based polymer systems. In the future, the dimethylmaleic anhydride motif may be transferred to further biodegradable polymer structures, including polycarbonates which enable the formulation of pH-sensitive biodegradable drug delivery systems.

All these results will enhance the advantageous relevance and robust versatility of carrier systems bearing 2-propionic-3-methylmaleic anhydrides towards individualized treatment of various diseases and simultaneously fine-tuning controlled immune responses with improved therapeutic outcomes.

DANKSAGUNG

[redacted]

[redacted]

LIST OF PUBLICATIONS

The following list presents all publications written or contributed to during this PhD thesis.

Contributions as first author:

A. G. Heck, J. Stickdorn, L. R. Rosenberger, M. Scherger, J. Woller, K. Eigen, M. Bros, S. Grabbe, L. Nuhn, *J. Am. Chem. Soci.* **2023**, *145*, 27424, DOI: 10.1021/jacs.3c08511.

→ **Chapter I**

A. G. Heck, C. Medina-Montano, Z. R. Zhong, K. Deswarte, K. Eigen, J. Stickdorn, J. Kockelmann, M. Scherger, N. N. Sanders, S. Lienenklaus, B. N. Lambrecht, S. Grabbe, B. G. De Geest, L. Nuhn **2024**, **submitted**.

→ **Chapter II**

A. G. Heck, J. Stickdorn, D. Schwiertz, J. Woller, A. Kaltbeitzel, I. Lieberwirth, D. Y. W. Ng, K. Landfester, T. Weil, L. Nuhn, **to be submitted**.

→ **Chapter III**

A. G. Heck, D. Schwiertz, B. Lantzberg, H.-C. Nguyen, R. Forster, M. Scherger, T. Opatz, J. A. Van Ginderachter, L. Nuhn, *Eur. Polym. J.* **2024**, **in revision**.

→ **Chapter IV**

A. G. Heck, L. Nuhn **2024**, **submitted**.

→ **Chapter V**

Contributions as co-author:

A. Prudlik, N. Mohebatti, L. Hildebrandt, A. Heck, L. Nuhn, R. Francke, *Chem. Eur. J.* **2023**, *29*, e202202730, DOI: 10.1002/chem.202202730.

D. Schwiertz, A. Heck, C. Muhl, L. Su, M. Barz, *Eur. Polym. J.* **2024**, *210*, 112989, DOI: 10.1016/j.eurpolymj.2024.112989.